

SCIENCE  
SYMPOSIUM PROCEEDINGS

AD-A253 089

IE 175

# Multifunctional Materials

EDITORS

Alan Buckley

George Gallagher-Daggitt

Frank E. Karasz

Donald R. Ulrich



The document has been approved  
for public release and sale; its  
distribution is unlimited.

H253099

REPORT DOCUMENTATION PAGE			Form Approved OMB No. 0704-0188
Public reporting burden for this collection of information is estimated to average 1 hour per response, including the time for reviewing instructions, searching existing data sources, gathering and maintaining the data needed, and completing and reviewing the collection of information. Send comments regarding this burden estimate or any other aspect of this collection of information, including suggestions for reducing the burden, to Washington Headquarters Services, Directorate for Information Operations and Resources, 1215 Jefferson Davis Highway, Suite 1202, Arlington, VA 22202-4162, and to the Office of Management and Budget, Paperwork Reduction Project (0704-0188), Washington, DC 20503.			
1. AGENCY USE ONLY (Leave Blank)	2. REPORT DATE	3. REPORT TYPE AND DATES COVERED	
	February 1991	Final Report 9/14/89 - 9/13/90	
4. TITLE AND SUBTITLE	5. FUNDING NUMBERS		
Materials Research Society Symposium on Multifunctional Materials	61102F 2303/A3		
6. AUTHOR(S)	8. PERFORMING ORGANIZATION REPORT NUMBER		
Alan Buckley, George Gallagher-Daggitt, Frank E. Karasz, and D. R. Ulrich	AFOSR-TR- 91 0128		
7. PERFORMING ORGANIZATION NAME(S) AND ADDRESS(ES)	9. SPONSORING/MONITORING AGENCY NAME(S) AND ADDRESS(ES)		
Materials Research Society 9800 McKnight Road, Suite 327 Pittsburgh, PA 15237	AFOSR/NC Bldg 410 Bolling AFB, DC 20332-6448		
10. SPONSORING/MONITORING AGENCY REPORT NUMBER			
AFOSR-89-0522			
11. SUPPLEMENTARY NOTES			
12a. DISTRIBUTION/AVAILABILITY STATEMENT		12b. DISTRIBUTION CODE	
Approved for public release; distribution is unlimited			
13. ABSTRACT (Maximum 200 words)			
<p>This contract supported the Symposium on Multifunctional Materials which was held as part of the Materials Research Society Fall Meeting, in Boston, Massachusetts, November 27 - December 2, 1989.</p> <p>The work described covers a broad range of interdisciplinary activities relevant to developing functionalities in ceramics and polymers.</p> <p>The proceedings of this conference were published as the following volume: <i>Multifunctional materials, Materials Research Society Symposium Proceedings</i>, Vol. 175, A. Buckley, G. Gallagher-Daggitt, F. E. Karasz, and D. R. Ulrich (Eds.), Materials Research Society, Pittsburgh (1990).</p>			
14. SUBJECT TERMS		15. NUMBER OF PAGES 381	
		16. PRICE CODE	
17. SECURITY CLASSIFICATION OF REPORT	18. SECURITY CLASSIFICATION OF THIS PAGE	19. SECURITY CLASSIFICATION OF ABSTRACT	20. LIMITATION OF ABSTRACT

## **Multifunctional Materials**

**Symposium held November 29-December 1, 1989, Boston,  
Massachusetts, U.S.A.**

**EDITORS:**

**Alan Buckley**  
Hoechst Celanese Research Company, Summit, New Jersey, U.S.A.

**George Gallagher-Daggitt**  
Ministry of Defence, London, United Kingdom

**Frank E. Karasz**  
University of Massachusetts, Amherst, Massachusetts, U.S.A.

**Donald R. Ulrich**  
Air Force Office of Scientific Research, Washington, D.C., U.S.A.

**92-12516**



**MATERIALS RESEARCH SOCIETY**  
Pittsburgh, Pennsylvania

**92 5 11 1991**

This work was supported by the Air Force Office of Scientific Research, Air Force Systems Command, USAF under Grant Number AFOSR 89-0522.



Accession For	NTIS	CRA&I	1.2	By	Availability Codes	Avail. in Sci. Ctr.
	<input checked="" type="checkbox"/>	<input type="checkbox"/>	<input type="checkbox"/>	Dist		A-1

Single article reprints from this publication are available through University Microfilms Inc., 300 North Zeeb Road, Ann Arbor, Michigan 48106

CODEN: MRSPDH

Copyright 1990 by Materials Research Society.  
All rights reserved.

This book has been registered with Copyright Clearance Center, Inc. For further information, please contact the Copyright Clearance Center, Salem, Massachusetts.

Published by:

Materials Research Society  
9800 McKnight Road  
Pittsburgh, Pennsylvania 15237  
Telephone (412) 367-3003  
Fax (412) 367-4373

Library of Congress Cataloging in Publication Data

Multifunctional materials : symposium held November 29-December 1, 1989, Boston, Massachusetts, U.S.A. / editors, A. Buckley, G. Gallagher-Daggitt, F.E. Karasz, D.R. Ulrich.

p. cm. — (Materials Research Society symposium proceedings : ISSN 0272-9172 ; v. 175)

Includes bibliographical references and index.

ISBN 1-55899-063-1

1. Optical materials—Congresses. 2. Polymers—Congresses. I. Buckley, Alan J. II. Series: Materials Research Society symposium proceedings : v. 175.

QC374.M85 1990  
620.1'9204295—dc20

90-37171  
CIP

Manufactured in the United States of America

## Contents

PREFACE	ix
MATERIALS RESEARCH SOCIETY SYMPOSIUM PROCEEDINGS	xi
PART I: MULTIFUNCTIONALITY IN CERAMICS/POLYMERS	
*NANODESIGNING OF MULTIFUNCTIONAL CERAMIC COMPOSITES J. Liu, M. Sarikaya, W.Y. Shih, and I.A. Aksay	3
*NANOCOMPOSITES - THE MULTIFUNCTIONAL FAMILY OF MATERIALS Rustum Roy	15
*MULTIFUNCTIONAL SILICA OPTICS L.L. Hench and A. Fosmoe	23
PHOTOACTIVE LIQUID CRYSTALLINE POLYMERS AS MULTIFUNCTIONAL MATERIALS David Creed, Anselm C. Griffin, Charles E. Hoyle, and Krishnan Venkataram	35
*MULTI-FUNCTIONAL DEVICE APPLICATIONS OF NONLINEAR OPTICAL POLYMER MATERIALS R. Lytel and G.F. Lipscomb	41
*EXPLORATORY STUDIES OF NEW NLO AND PIEZOELECTRIC POLYMERS H.K. Hall, Jr., Anne B. Padias, Francesco Fuso, Zhende Ni, Michael A. Mitchell, and Thomas M. Leslie	51
NATURE OF THE CHEMICAL BONDS IN POLYMER-SALT COMPLEXES: RAMAN AND IR STUDIES Gholamabbas Nazri, Donald M. MacArthur, and Ricardo Aroca	61
STUDY ON DIOPSIDE WHISKERS PRECIPITATION TYPE HYDROXYAPATITE Toru Nonami	71
PART II: NON-LINEAR OPTICS IN MULTIFUNCTIONAL MATERIALS	
*MULTIFUNCTIONAL MOLECULAR AND POLYMERIC MATERIALS FOR NONLINEAR OPTICS AND PHOTONICS Paras N. Prasad	79
ENHANCEMENT OF THIRD ORDER NONLINEARITY ON PHTHALOCYANINE COMPOUNDS Masahiro Hosoda, Tatsuo Wada, Akira Yamada, Anthony R. Garito, and Hiroyuki Sasabe	89

\*Invited Paper

DESIGN, CHARACTERIZATION, AND OPTICAL PROPERTIES OF PHOSPHAZENE-BASED POLYMERS Gregory J. Exarhos and William D. Samuels	95
ORGANIC, ORGANOMETALLIC AND POLYMERIC MATERIALS WITH NONLINEAR OPTICAL PROPERTIES S.R. Marder, J.W. Perry, W.P. Schaefer, E.J. Ginsburg, C.B. Gorman, and R.H. Grubbs	101
THIRD-ORDER OPTICAL NONLINEARITY IN A POLYMER COMPOSITE K.M. White, R.E. Harelstad, C.V. Francis, D.T. Gerbi, J. Stevens, and P.C. Leung	107
*SYNTHESIS AND PROPERTIES OF MULTIFUNCTIONAL POLYMERS H.A. Goldberg, A.J. East, I.L. Kalnin, R.E. Johnson, H.T. Man, R.A. Keosian, and D. Karim	113
MOLECULAR DESIGN OF SYNTHETIC POLYPEPTIDES FOR NONLINEAR OPTICS T. Ishii, T. Wada, A.F. Garito, H. Sasabe, and A. Yamada	129
*MULTIFUNCTIONAL MACROMOLECULES - SOME DEVICE OPTIONS Michael R. Worboys, Michael S. Griffith, and Nicholas A. Davies	135
 PART III: MULTIFUNCTIONAL INORGANIC MATERIALS	
*MULTIFUNCTIONAL CERAMIC MATERIALS--REVIEW AND PROJECTIONS John D. Mackenzie	149
*MULTIFUNCTIONAL FERROIC NANOCOMPOSITES R.E. Newnham, S.E. McKinstry, and H. Ikawa	161
CONTROL OF $YBa_2Cu_3O_y$ SOL-GEL SOLUTION STRUCTURE BY CHEMICAL MODIFICATION OF ORGANIC ACID AND ITS EFFECTS Haixing Zheng and J.D. Mackenzie	173
SYNTHESIS OF POLYIMIDE-SILICATE HYBRIDS VIA SOL-GEL ULTRASTRUCTURE PROCESSING M. Spinu, A. Brennan, J. Rancourt, G.L. Wilkes, and J.E. McGrath	179
PROTECTIVE COATINGS FOR HIGH TEMPERATURE, LIGHT WEIGHT, STRUCTURAL APPLICATIONS J. Covino, K. Klemm, and J. Dykema	187
*HIGH COMPRESSIVE STRENGTH ORDERED POLYMER FIBERS AND FILMS VIA SOL GEL MICROCOMPOSITE PROCESSING Robert F. Kovar, Richard W. Lusignea, R. Ross Haghighe, Carlo Pantano, and Edwin L. Thomas	193
*THE INFLUENCE OF SOL-GEL GLASS TECHNOLOGY ON COHERENT AND PARTIALLY COHERENT OPTICAL IMAGING SYSTEMS Nicholas J. Phillips	207

\*Invited Paper

DESIGNING PORE-SIZE IN SILICA GELS: [H<sub>2</sub>O] - [TMOS] SYSTEM 219  
H. Kido, P.B. Malla, and S. Komarneni

PART IV: POLYMERS FOR ULTRASTRUCTURES

*DIELECTRIC RELAXATION PROPERTIES AND ALIGNMENT BEHAVIOUR OF LIQUID-CRYSTALLINE SIDE-CHAIN POLYMERS Graham Williams, Ali Nazemi, and Frank F. Karasz	227
*LIQUID CRYSTALLINE MATERIALS FOR POLYMERS WITH ANISOTROPIC ULTRASTRUCTURES George S. Attard	239
MAGNETIC PROPERTIES OF LIQUID CRYSTALS INCORPORATING METAL CENTRES Wolfgang Haase, Stefan Gehring, and Bettina Borchers	249
DIELECTRIC PROPERTIES OF POLYMERIC LIQUID CRYSTALS WITH STRONG LATERAL DIPOLE GROUPS Wolfgang Haase and Matthias Pfeiffer	257
SYNTHESIS AND PROPERTIES OF COMB-LIKE LIQUID CRYSTALLINE POLYMERS WITH ELECTROOPTICALLY ACTIVE MESOGENIC SIDE GROUPS M. Maeda, R.S. Kumar, A. Blumstein, S.K. Tripathy, P. Sixou, and F. Faubert	265
THERMOTROPIC CHIRAL NEMATIC POLYMERS AS OPTICAL MATERIALS S.H. Chen, M.L. Tsai, and S.D. Jacobs	271
*MULTI-LAYERS THIN FILMS OF ACETALIZED POLY(VINYL ALCOHOL) DERIVATIVES OBTAINED BY THE LB METHOD AND THEIR OPTO- ELECTRONIC PROPERTIES Kiyoshi Oguchi, Yasuhiko Yokoh, Kohei Sanui, and Naoya Ogata	277
*DIELECTRIC, TSC AND ELECTROMECHANICAL MEASUREMENTS ON SOME PROSPECTIVE NLO POLYMERS Paul L. Carr, Geoff R. Davies, and Ian M. Ward	289
SILICONE CONTAINING LIQUID CRYSTALLINE POLYURETHANES AND POLYESTERS Robert Kosfeld, F. Braun, L. Willner, and M. Heß	297

PART V: MULTIFUNCTIONAL DESIGN

*MICROSTRUCTURAL CONTROL IN SIDE CHAIN POLYMERS FOR OPTICAL APPLICATIONS Rob Findlay, Tim Lemmon, and Alan Windle	305
*PERIODIC AREA MINIMIZATION SURFACES IN MICROSTRUCTURAL SCIENCE Edwin L. Thomas and Samuel P. Gido	315
BEHAVIOR OF SUPERCONDUCTING CERAMIC-POLYMER COMPOSITE C. Vipulanandan and S. Salib	325

\*Invited Paper

MICROSTRUCTURE AND ELECTRICAL PROPERTIES OF KEVLAR/POLYPYRROLE COMPOSITE FIBERS L.P. Rector, D. DeGroot, T.J. Marks, and S.H. Carr	331
*NEW SYNTHESIS/PROCESSING ROUTES TO MATERIALS EXHIBITING LARGE OPTICAL NONLINEARITY L.R. Dalton and L.P. Yu	337
MICROPHASE SEPARATION IN TRIBLOCK COPOLYMER MELTS Anne M. Mayes and Monica Olvera de la Cruz	345
SYNTHESIS OF SEGMENTED ANISOTROPIC-ISOTROPIC POLY(ARYL ESTER) POLY(ARYLENE ETHER) COPOLYMERS J.E. McGrath, K.L. Cooper, W. Waehamad, H. Huang, and G.L. Wilkes	351
*INORGANIC AND ORGANOMETALLIC PRINCIPLES IN THE DESIGN OF MULTIFUNCTIONAL MATERIALS D. Michael P. Mingos	363
MODELLING MICROSTRUCTURE IN MATERIALS THAT CONTAIN ANISOTROPIC PARTICLES Christopher Viney and Larry A. Chick	371
AUTHOR INDEX	379
SUBJECT INDEX	381
MATERIALS RESEARCH SOCIETY SYMPOSIUM PROCEEDINGS	383

\*Invited Paper

## Preface

This volume represents the proceedings of the Symposium on Multifunctional Materials which was held as part of the Materials Research Society Fall Meeting, in Boston, Massachusetts, November 27 - December 2, 1989.

The work described covers a broad range of interdisciplinary activities relevant to developing functionalities in ceramics and polymers.

The editors are indebted to the authors for their contributions and to the various session chairpersons.

Alan Buckley  
George Gallagher-Daggitt  
Frank E. Karasz  
Donald R. Ulrich

July 1990

---

---

## MATERIALS RESEARCH SOCIETY SYMPOSIUM PROCEEDINGS

---

### *Recent Materials Research Society Symposium Proceedings*

Volume 145—III-V Heterostructures for Electronic/Photonic Devices, C.W. Tu, V.D. Mattera, A.C. Gossard, 1989, ISBN: 1-55899-018-6

Volume 146—Rapid Thermal Annealing/Chemical Vapor Deposition and Integrated Processing, D. Hodul, J. Gelpey, M.L. Green, T.E. Seidel, 1989, ISBN: 1-55899-019-4

Volume 147—Ion Beam Processing of Advanced Electronic Materials, N.W. Cheung, A.D. Marwick, J.B. Roberto, 1989, ISBN: 1-55899-020-8

Volume 148—Chemistry and Defects in Semiconductor Heterostructures, M. Kawabe, T.D. Sands, E.R. Weber, R.S. Williams, 1989, ISBN: 1-55899-021-6

Volume 149—Amorphous Silicon Technology-1989, A. Madan, M.J. Thompson, P.C. Taylor, Y. Hamakawa, P.G. LeComber, 1989, ISBN: 1-55899-022-4

Volume 150—Materials for Magneto-Optic Data Storage, C.J. Robinson, T. Suzuki, C.M. Falco, 1989, ISBN: 1-55899-023-2

Volume 151—Growth, Characterization and Properties of Ultrathin Magnetic Films and Multilayers, B.T. Jonker, J.P. Heremans, E.E. Marinero, 1989, ISBN: 1-55899-024-0

Volume 152—Optical Materials: Processing and Science, D.B. Poker, C. Ortiz, 1989, ISBN: 1-55899-025-9

Volume 153—Interfaces Between Polymers, Metals, and Ceramics, B.M. DeKoven, A.J. Gellman, R. Rosenberg, 1989, ISBN: 1-55899-026-7

Volume 154—Electronic Packaging Materials Science IV, R. Jaccodine, K.A. Jackson, E.D. Lillie, R.C. Sundahl, 1989, ISBN: 1-55899-027-5

Volume 155—Processing Science of Advanced Ceramics, I.A. Aksay, G.L. McVay, D.R. Ulrich, 1989, ISBN: 1-55899-028-3

Volume 156—High Temperature Superconductors: Relationships Between Properties, Structure, and Solid-State Chemistry, J.R. Jorgensen, K. Kitazawa, J.M. Tarascon, M.S. Thompson, J.B. Torrance, 1989, ISBN: 1-55899-029

Volume 157—Beam-Solid Interactions: Physical Phenomena, J.A. Knapp, P. Borgesen, R.A. Zehr, 1989, ISBN 1-55899-045-3

Volume 158—In-Situ Patterning: Selective Area Deposition and Etching, R. Rosenberg, A.F. Bernhardt, J.G. Black, 1989, ISBN 1-55899-046-1

Volume 159—Atomic Scale Structure of Interfaces, R.D. Bringans, R.M. Feenstra, J.M. Gibson, 1989, ISBN 1-55899-047-X

Volume 160—Layered Structures: Heteroepitaxy, Superlattices, Strain, and Metastability, B.W. Dodson, L.J. Schowalter, J.E. Cunningham, F.H. Pollak, 1989, ISBN 1-55899-048-8

Volume 161—Properties of II-VI Semiconductors: Bulk Crystals, Epitaxial Films, Quantum Well Structures and Dilute Magnetic Systems, J.F. Schetzina, F.J. Bartoli, Jr., H.F. Schaake, 1989, ISBN 1-55899-049-6

Volume 162—Diamond, Boron Nitride, Silicon Carbide and Related Wide Bandgap Semiconductors, J.T. Glass, R.F. Messier, N. Fujimori, 1989, ISBN 1-55899-050-X

Volume 163—Irradiation Effects in Semiconductors: Bulk and Layered Structures, J. Bernholc, E.E. Haller, D.J. Wolford, 1989, ISBN 1-55899-051-8

Volume 164—Materials Issues in Microcrystalline Semiconductors, P.M. Fauchet, C.C. Tsai, K. Tanaka, 1989, ISBN 1-55899-052-6

Volume 165—Characterization of Plasma-Enhanced CVD Processes, G. Lucovsky, D.E. Ibbotson, D.W. Hess, 1989, ISBN 1-55899-053-4

Volume 166—Neutron Scattering for Materials Science, S.M. Shapiro, S.C. Moss, J.D. Jorgensen, 1989, ISBN 1-55899-054-2

---

---

## MATERIALS RESEARCH SOCIETY SYMPOSIUM PROCEEDINGS

---

Volume 167—Advanced Electronic Packaging Materials, A. Barfknecht, J. Partridge, C.-Y. Li, C.J. Chen, 1989, ISBN 1-55899-055-0

Volume 168—Chemical Vapor Deposition of Refractory Metals and Ceramics, T.M. Besmann, B.M. Gallois, 1989, ISBN 1-55899-056-9

Volume 169—High Temperature Superconductors: Fundamental Properties and Novel Materials Processing, J. Narayan, C.W. Chu, L.F. Schneemeyer, D.K. Christen, 1989, ISBN 1-55899-057-7

Volume 170—Tailored Interfaces in Composite Materials, C.G. Pantano, E.J.H. Chen, 1989, ISBN 1-55899-058-5

Volume 171—Polymer Based Molecular Composites, D.W. Schaefer, J.E. Mark, 1989, ISBN 1-55899-059-3

Volume 172—Optical Fiber Materials and Processing, J.W. Fleming, G.H. Sigel, S. Takahashi, P.W. France, 1989, ISBN 1-55899-060-7

Volume 173—Electrical, Optical and Magnetic Properties of Organic Solid-State Materials, L.Y. Chiang, D.O. Cowan, P. Chaikin, 1989, ISBN 1-55899-061-5

Volume 174—Materials Synthesis Utilizing Biological Processes, M. Alper, P.D. Calvert, P.C. Rieke, 1989, ISBN 1-55899-062-3

Volume 175—Multi-Functional Materials, D.R. Ulrich, F.E. Karasz, A.J. Buckley, G. Gallagher-Daggitt, 1989, ISBN 1-55899-063-1

Volume 176—Scientific Basis for Nuclear Waste Management XIII, V.M. Oversby, P.W. Brown, 1989, ISBN 1-55899-064-X

Volume 177—Macromolecular Liquids, C.R. Safinya, S.A. Safran, P.A. Pincus, 1989, ISBN 1-55899-065-8

Volume 178—Fly Ash and Coal Conversion By-Products: Characterization, Utilization and Disposal VI, F.P. Glasser, R.L. Day, 1989, ISBN 1-55899-066-6

Volume 179—Specialty Cements with Advanced Properties, H. Jennings, A.G. Landers, B.E. Scheetz, I. Odler, 1989, ISBN 1-55899-067-4

---

---

## MATERIALS RESEARCH SOCIETY MONOGRAPH

---

Atom Probe Microanalysis: Principles and Applications to Materials Problems, M.K. Miller, G.D.W. Smith, 1989; ISBN 0-931837-99-5

*Earlier Materials Research Society Symposium Proceedings listed in the back.*

---

---

**PART I**

**Multifunctionality in  
Ceramics/Polymers**

92-18232



AD-P007 452



3

## NANODESIGNING OF MULTIFUNCTIONAL CERAMIC COMPOSITES

J. LIU, M. SARIKAYA, W. Y. SHIH, W.-H. SHIH, and I. A. AKSAY

Department of Materials Science and Engineering; and  
Advanced Materials Technology Center, Washington Technology Centers,  
University of Washington, Seattle, WA, USA 98195

*Nanodesigning of multifunctional ceramic composites with colloids is discussed from a fundamental point of view. We start with one-component systems, where packing density is the primary concern. Then we extend the discussion to binary systems and deal with the problem of homogeneity. We show that the structure is controlled by the nature of bonding between the particles and by the particle-particle interaction. Surfactants are used to modify these properties, by, first, protecting the active particle surfaces to prevent solid bond formation, and, second, altering the interparticle interaction to provide a "lubricating" effect. In weakly attractive multicomponent systems, not only are we able to achieve high-density packing through restructuring, but we can also control the scale of homogeneity.*

### 1.0 INTRODUCTION

There has been a growing interest in the colloidal processing of nanocomposites because of the advantages of using nanometer-sized particles.<sup>1-3</sup> For example, it is possible to mix different components on a nanometer scale and achieve improved electronic and structural properties for multifunctional applications.<sup>3-5</sup> Another advantage is that the materials can be processed to full density at much lower temperatures than by conventional methods.

Previous literature has discussed some of the advantages and difficulties in colloidal processing with nanometer-sized particles compared to the processing of micrometer and submicrometer-sized particles.<sup>1,2</sup> The most significant difficulty is that nanometer-sized particles in general result in the formation of low-density gels which display large shrinkages during solvent extraction and, therefore, cracking during drying or sintering.<sup>6,7</sup> In this paper, we discuss this problem from a more fundamental point of view and summarize our recent work in this area. We then extend our discussion to binary systems, which have not been understood as well. The study and understanding of multicomponent systems is essential for processing composite materials with two or more components. Through such an understanding, high-packing density can be realized, and also the distribution of species can be controlled so that regularity in the structure and the scale of homogeneity in composition can be predicted.

### 2.0 RESULTS AND DISCUSSION

#### 2.1 One-Component System: Effect of Restructuring

In processing with micrometer or submicron-sized particles, the microstructure and density of green compacts can be controlled via colloidal processing routes.<sup>8,9</sup> When particle interactions are repulsive, suspensions can be consolidated to high packing density compacts.<sup>2,8,9</sup> In contrast, highly attractive particle systems result in low packing density compacts.<sup>2,8,9</sup> In the attractive

region, low-density fractal clusters or powder compacts could restructure to a higher density at later times under weak attraction conditions.<sup>10,11</sup> This restructuring is controlled by the interaction energy  $E$  and the relaxation time  $\tau_R$ . However, experience has shown that with nanometer-sized particles this restructuring is not easily accomplished without the application of high pressures.<sup>1</sup> Therefore, we conducted systematic studies to determine the unique characteristics of nanometer-sized particles. We used conventional and high-resolution transmission electron microscopy (HRTEM) to study the general structure of the aggregates and the particle-particle interfaces in order to investigate the aggregation behavior of nanometer particles in colloid systems. We also calculated the particle-particle interaction by a modified DLVO theory.<sup>12</sup> First, we found that there is effectively no secondary minimum away from the particle surface in particle-particle interactions for nanometer-sized particles.<sup>13</sup> When nanometer-sized particles begin to aggregate, they fall into the primary minimum and direct contact takes place. Second, solid bonding forms between the particles. For example, Figure 1 shows the interfaces between gold particles in a low-density aggregate; when particles touch one another, solid bonding is formed at the particle contacts. This high binding energy makes it very difficult for the particles to break away and relax to a high density once the aggregates are formed. The low-density (< 30 vol. %) aggregate corresponding to Figure 1 is very strong and cannot be easily consolidated to a higher density. For these two reasons, nanometer-sized particles are different from larger (> 0.1  $\mu\text{m}$ ) particles.



Figure 1. High resolution transmission electron microscope (HRTEM) image revealing structures of interfaces between particles in a colloidal gold aggregate. The solid bonding between the particles makes it difficult for the clusters to relax to a high density.

An obvious solution to the problem stated above is that the active particle surfaces must be protected so that solid bonding cannot occur between the particles. Coating the particles with a layer of surfactant prevents the particle-particle contact. Figure 2 illustrates the high-density packing achieved when a layer of surfactant is adsorbed onto the particle surface. The

particles now are separated by a distance of about 1 to 3 nm, which roughly corresponds to the size of the surfactant. This separation is caused by the adsorption of the surfactant, which spatially protects the particle surface. Yet, in order to have dense packing, the particles must be able to move around freely. Thus, the surfactant must also act as a lubricant.<sup>11</sup>

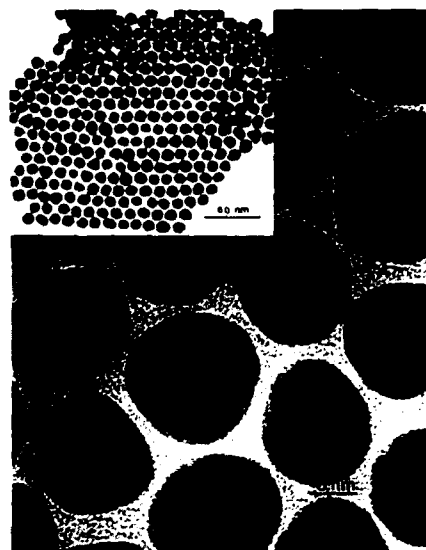


Figure 2. Transmission electron microscope (TEM) images revealing the close packing of gold particles when the particle surfaces are protected by a layer of surfactant. The particles are separated by a distance of 1 to 3 nm, about twice the length of the surfactant.

In order to understand the role of surfactants, the aggregation behavior of the particles was studied at different surfactant concentrations.<sup>14</sup> In this study, a cationic surfactant was added to the colloidal solution containing the negatively-charged gold particles. The surfactant induces aggregation by neutralizing the charges on the particle surface, and since the surfactant layer has a certain thickness, the particles cannot come in contact with one another. The interaction between the particles is thus controlled by the amount of surfactant added to the solution. We then measured the fractal dimension,  $D$ , of the aggregates, which is a measure of the packing density, by light scattering and transmission electron microscopy (TEM). The particle interaction was calculated by the modified DLVO theory<sup>12,15</sup> and the attraction energy  $E$  was taken as the energy of closest approach (taken as 1.5 nm in our case). The relation between  $D$  and  $E$  is plotted in Figure 3, with the computer simulation result<sup>10</sup> plotted as triangles. The experimental results agree very well with the simulation. That is,  $D$  is directly related to  $E$ . Under a weak attraction condition, a high fractal dimension and, thus, high density is obtained. If the attraction energy  $E$  is large (such as in the presence of solid bonding), restructuring is impossible and low  $D$  is observed. Therefore, it is important to provide a small attraction energy to make restructuring possible. This study shows that a surfactant provides a means to help achieve high-density packing for nanometer-sized particles.

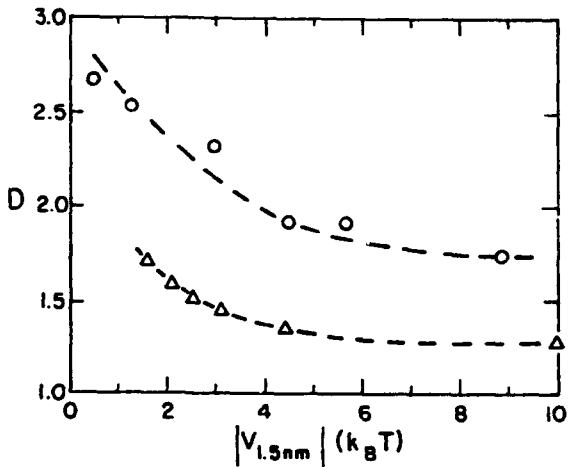


Figure 3. Relationship between the fractal dimension of gold aggregates with surfactants and the binding energy between the particles. The circles are the experimental results and the triangles are the results of the computer simulation in two-dimensions. The fractal structures vary from ramified to compact objects, depending upon the binding energy.

In the case of large particles, macromolecular coatings are used to stabilize suspensions and achieve high solids loading.<sup>16</sup> However, for nanometer-sized particles, macromolecules are not desirable since the amount of the surfactant needed to cover the particle surface increases significantly as the particle size is decreased to the nanometer range, and the effective solid density decreases. There are two methods for solving the problem of excess surfactant. One is to find a surfactant that is short, but very effective, so that the total amount of surfactant incorporated into the system is much less. However, short surfactants may not be large enough to stabilize the particles, but if they have good lubricating properties, the weak aggregates can easily restructure to high density. Studies are underway to identify such surfactants.<sup>17</sup> The second method is to fabricate surfactants (inorganic precursors) which would be transformed into ceramics at a later stage of processing so that they do not need to be eliminated completely. With this method, a nanocomposite could be fabricated in which a surfactant precursor would form the matrix and particles would form the dispersoids.

## 2.2 Binary Systems

In this section, we present theoretical work on binary systems in which the relationship between particle-particle interactions, stability, and phase separation is considered. We then compare the theoretical work with the experiments. The principles discussed here will apply to both large particles and nanosized particles.

### 2.2.1 Model

**2.2.1.1 Repulsive Regime<sup>18,19</sup>** Phase diagrams of highly repulsive colloidal suspensions have been calculated by comparing the free energies of the different phases (specifically, liquids,

and solids with small or large particle-rich phases) in which the particle-particle interactions have been considered. If the particle concentration is not too high or the temperature is not too low, the effective interactions between the colloidal particles are treated with the Debye-Hückel approximation and the stable phase is considered to be the one with the lowest free energy. The free energies of various phases are calculated by means of a variational principle based upon the Gibbs-Bogolyubov inequality.<sup>18</sup> Einstein oscillators are used as the reference system for the solids and a binary hard sphere mixture is used as the reference for the liquids. The solid phase is considered as fcc or bcc substitutional alloys.

**2.2.1.2 Attractive Regime<sup>20</sup>** For attractive interactions, we studied the kinetic effect in systems where the equilibrium state should yield phase separation. A computer simulation was done on a two-dimensional square lattice by using the Monte Carlo method.  $N_1$  represents the number of particles of type 1 with interaction  $E_{11}$ , and  $N_2$  is the number of particles of type 2 with interaction  $E_{22}$ . The particles are placed randomly in a  $M \times M$  lattice with periodic conditions.  $E$  is the interaction between particles. The particles then perform Brownian motion according to the Boltzmann probability  $e^{-\Delta E/RT}$ , where  $\Delta E$  is the energy change due to the motion. Once two particles come together, they form one cluster and move as a whole. In the same way, larger clusters are formed. The mobility of a cluster is assumed to be inversely proportional to the mass of the cluster. In addition, particles can unbind from a cluster according to the Boltzmann probability,  $e^{-\Delta E/RT}$ , where  $\Delta E$  is again the energy change associated with the unbinding.

The free energy of such systems is also calculated according to the cluster variation method (CVM)<sup>21</sup> in which the free energy  $F$  is written as a function of  $x_1$ ,  $x_2$ , as well as the pair parameter  $y_{ij}$ . Here  $x_1$  is the concentration of particle 1;  $x_2$  is the concentration of particle 2; and  $y_{ij}$  is the probability of forming pairs of particle  $i$  and particle  $j$  (including vacancy).  $y_{ij}$  can be obtained by minimizing  $F$  for the equilibrium condition. After  $y_{ij}$  is found, the structure of the suspension is then simulated on a two-dimensional lattice again according to  $x_1$ ,  $x_2$ , and  $y_{ij}$ .<sup>22</sup> The results of the CVM calculation and simulation are compared to the Monte Carlo simulation.

### 2.2.1.3 Results and Discussions

#### 1. Packing Density

Phase diagrams of repulsive binary systems are presented in Figure 4. Large particles have a radius of 545 Å and a surface charge  $Z_t = 300$ . Small particles have a radius  $R = 491$  Å, 445 Å, 409 Å, 382 Å in Figures 4(a), 4(b), 4(c), and 4(d), respectively.  $X$  is the number fraction of the large particles and  $D$  is the total number density. The particle diameter ratio is defined as  $R_{small}/R_{large}$ . The line is the boundary between the solid and liquid phase. It can be seen from the  $D$ - $X$  phase diagram that the boundary line begins to show a maximum as the diameter ratio deviates from unity. The maximum becomes more pronounced as the diameter ratio deviates more from unity, a phenomenon confirmed by experiments.<sup>23</sup> For a diameter (or charge) ratio of 0.7, the solid-liquid boundary almost opens up vertically toward high number densities. The shrinking of the crystalline phase region also signifies the phase separation of the crystalline phases at high concentrations.<sup>18-19</sup> The results of these phase diagrams show that the fluid phase is stable up to a much higher density in a binary system than can be achieved with a one-component system.

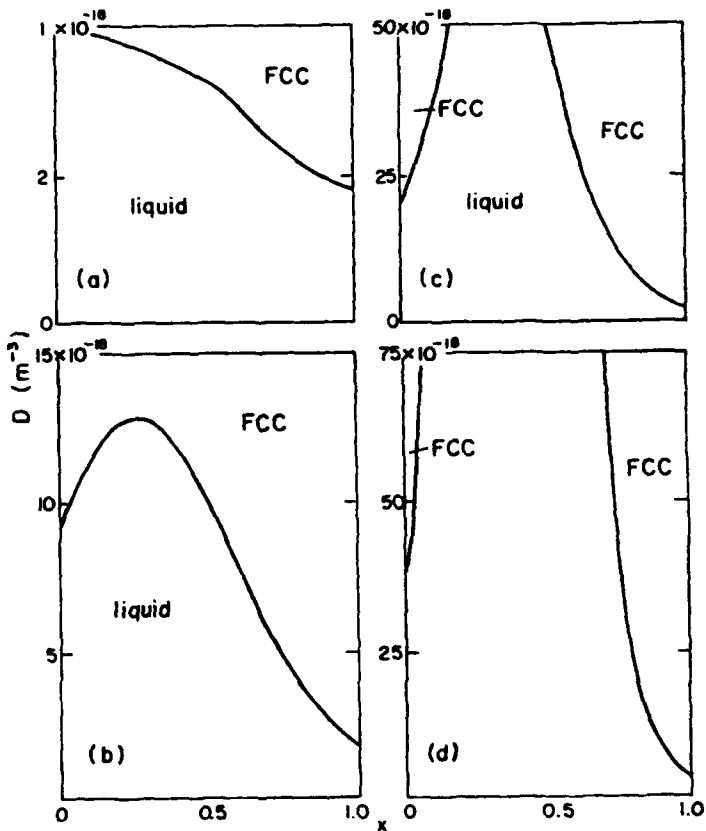


Figure 4. Phase diagrams for repulsive binary systems of large and small particles. Y-axis is density and the x-axis is the number fraction of small particles. From (a) to (d) the diameter ratio of the small to large particles decreases. It can be seen that the fluid region increases to high density as the diameter ratio becomes smaller.

On the other hand, in attractive systems, flocculation is often encountered. In our case, where  $E_{11} < 0$ , the first species flocculates before the second species ( $E_{12} = E_{22} > 0$ ). The addition of the second species has a large effect on the aggregation of the first species. Results from the Monte Carlo simulation are represented in Figure 5. Initially, the addition of the second species always enhances the rate of aggregation. Cluster sizes become larger as the concentration of the second species is increased. However, at a high concentration of the second species, the cluster size begins to decrease again. There is a maximum in the aggregation rate with respect to the second species concentration. This is in agreement with experimental observations.<sup>16</sup> Also to be noted is the effect of aging; as time passes, the clusters become large and the peak position shifts towards a higher concentration of the second species.

From this discussion, it seems that a repulsive system has an advantage over an attractive system since an attractive system flocculates and may show low density. In a repulsive binary system, the fluid phase can still exist at a very high number density, which is helpful in colloidal processing where a high green density compact is desired.<sup>8</sup> However, high density is not always

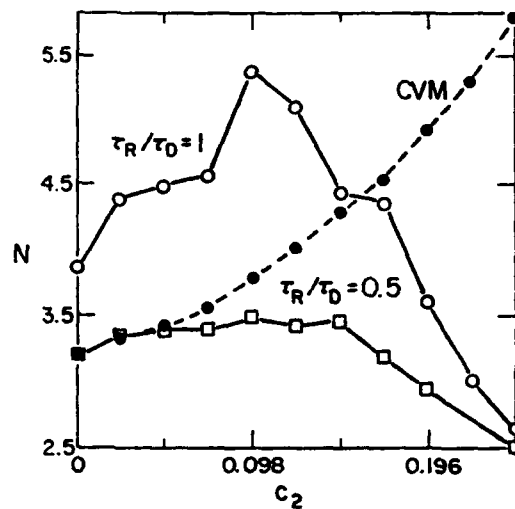


Figure 5. Cluster size vs. second species concentration,  $c_2$ , for comparison between Monte Carlo simulations and CVM calculations where  $E_{11} = -1$ ,  $E_{12} = E_{22} = 8$ , and  $c_1 = 0.245$ . (●) represents CVM, (○) for  $\tau_R/\tau_D = 1$ , and (□) for  $\tau_R/\tau_D = 0.5$ , representing simulations at  $t = 300\tau_D$ . Note that while the simulations show the slowing in the cluster rate at high  $c_2$ , the CVM calculations do not, indicating that the restabilization at higher  $c_2$  is a kinetic effect. In the simulations, a smaller value of  $\tau_R/\tau_D$  represents more sufficient relaxations.

the only requirement for a nanocomposite; one has to also consider the scale of mixing of several components. This aspect of colloidal processing will be discussed in the following section.

### 2.2.2 Scale of Homogeneity

For a nanocomposite, ideally the two components should be distributed with a predictable scale of homogeneity. However, repulsive systems often undergo phase separation, as illustrated in Figure 6. This phase diagram was calculated in a manner similar to Figure 4. It clearly shows that in a binary system, there is a wide two-phase region, one phase rich in small particles, and the other rich in large particles. As the particle concentration increases, phase separation behavior is more pronounced. This indicates that the composite material produced under repulsion conditions will have large domains of different phases of different composition. This then results in an increase in the scale of homogeneity. The phase separation behavior of highly charged particles at high densities has been observed in our experiments. Figure 7 shows colloidal gold and colloidal silica particles mixed under repulsive conditions. The pH of the solution is about 7. Under this condition, the zeta potentials of silica and gold particles are about 60 and 100 mV, respectively, as measured by Doppler shift laser light scattering.<sup>1,14</sup> Given the diameters of both gold and silica particles as 150 Å, the estimated effective charge of a gold particle is about 42 electron charges and that of a silica particle is about 25. The charge ratio is smaller than 0.7. As discussed above, the system should phase separate at high densities. Indeed, this is the case. It can be seen that the gold particles and the silica particles tend to phase-separate into regions consisting of either silica or gold particles. In order to obtain the properties desired for a composite material, the distribution of different components

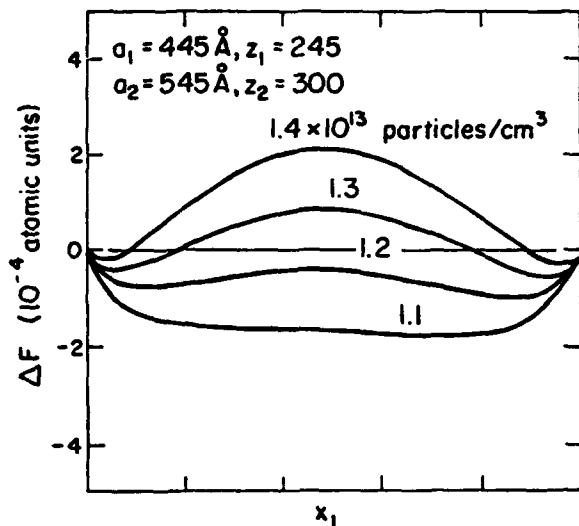


Figure 6. Excess free energy of repulsive binary systems as a function of concentrations of smaller particles,  $x_1$ . A wide two-phase region is usually observed. One atomic unit equals 27.2 eV.

as well as the degree of phase separation, i.e., the scale on which the phase separation takes place--must be controlled. Further understanding of the kinetic process is needed to achieve this control.

From the above discussion, it can be seen that there is a disadvantage in highly repulsive systems due to phase separation. In that sense, weakly interactive systems may have an advantage. A high degree of homogeneity can be achieved in weakly flocculated systems at higher densities.<sup>24</sup> The high degree of homogeneity at high densities is due to slow kinetics, not to equilibrium conditions as shown by aging and also by the comparison of the cluster size calculated by the Monte Carlo method at finite time with that calculated by the CVM method shown in Figure 5. Therefore, in a weakly interactive system, a high degree of homogeneity can still be achieved by slow kinetics at high densities although the equilibrium state should phase separate. The CVM calculation shows that the cluster size increases monotonically with the concentration of the second species. The free energy curve also shows that phase separation should occur over all the concentration ranges. However, the Monte Carlo simulation shows that the aggregation is slowed at high concentration, and there is a maximum. The slowing of the aggregation rate is attributed to the kinetic effect, i.e., the particles (or clusters) are trapped in a kinetic cage and cannot relax to a lower energy state (phase separation state). As the system ages, it moves towards a state of equilibrium.

However, for nanometer-sized particles, aggregate structures formed by adding salt are difficult to consolidate because of the formation of solid bonding between particles. It is necessary to use surfactants to protect the particle surfaces in attractive systems. Under this condition, not only can we achieve a finer scale of homogeneity, but we can also achieve high-density packing through restructuring, as discussed earlier.

To demonstrate the advantage of weakly attractive particles coated with a surfactant, a binary suspension was prepared (Figure 8). A cationic surfactant was introduced into a colloidal suspension consisting of gold and silica particles in order to protect the particle surface and to neutralize the negative charge. This created weakly attractive forces between particles, as evidenced by flocculation. Not only do we achieve a high-packing density (as discussed in Figure 2), but we also find the gold particles to be distributed more homogeneously among the silica particles in what is principally a nanocomposite.



Figure 7. Phase separation of colloidal gold and silica particles under repulsive conditions. The dark particles are gold and the light particles are silica.



Figure 8. A finer scale homogeneous mixture of gold and silica particles under a slightly attractive condition.

### 3.0 SUMMARY

The density and homogeneity of nanocomposite materials can be controlled by regulating the particle-particle interaction. Specifically, we have concluded that a weakly attractive system may be advantageous over a repulsive system: first, it is possible to achieve high density by the restructuring of the clusters in weakly attractive aggregates; second, a weakly attractive binary system can have a finer scale homogeneous distribution of the components regardless of whether the equilibrium state is a phase separation or a mixture. In the case where the equilibrium state is a phase separation, homogeneity is provided by slow kinetics at high densities. The control of particle-particle interaction is realized by using surfactants. The surfactants have two functions. One is to protect the active particle surface to prevent direct particle bonding, which is especially important for small particles. The other is to modify the interparticle interaction, making it possible for the particles to relax to a high-density configuration within the clusters.

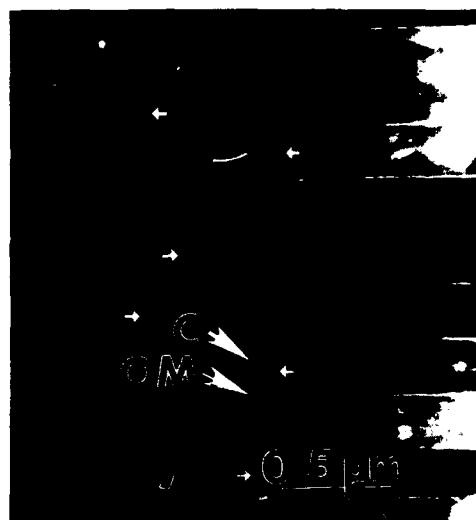


Figure 9. TEM micrograph revealing the typical microstructure of the nacre section of an abalone shell. The microstructure consists of organic material (OM) and ceramic layers (C) arranged in a regular laminated structure.

We should point out that although we have made considerable progress in understanding the properties of nanoparticle systems, as yet we have not been able to achieve precise control of the microstructure. In the above cases of colloidal processing, the final product is a result of a microstructure of small particles randomly configured under certain kinetic conditions. Therefore, the structure is basically determined by entropy. Full control of the final product is extremely difficult, if not impossible, to achieve. However, it is possible to control the processing precisely enough to achieve a final product with a predetermined, highly regular microstructure. In natural processes, there are abundant examples of highly regular microstructures. An example is given in a TEM image in Figure 9 where a cross-sectional view of an abalone shell, consisting of organic (thin-phase, 200 Å) and inorganic (thick-phase, 250 nm) layers, is seen. The phases are arranged in the form of a brick (CaCO<sub>3</sub>) and mortar (organic) microarchitecture. In this case, a highly-ordered microstructure is processed at the molecular level by certain biological process(es) where energy plays the most important role in the *specific* arrangement of the phases.<sup>25</sup> Other than Nature's method, such processes, so far, can only be achieved synthetically in molecular processes such as molecular-beam epitaxy and liquid-phase epitaxy to fabricate materials with a full degree of control at the nanometer level.

## ACKNOWLEDGMENTS

This research was supported by the Air Force Office of Scientific Research (AFOSR) and the Department of Advanced Research Projects Agency (DARPA) and monitored by AFOSR under Grant No. AFOSR-87-0114.

## REFERENCES

1. B. J. Tarasevich, J. Liu, M. Sarikaya, and I. A. Aksay, "Inorganic Gels with Nanometer-Sized Particles," in *Better Ceramics Through Chemistry III, MRS Symp. Proc.*, Vol. 121, edited by C. J. Brinker, D. E. Clark, and D. R. Ulrich (Materials Research Society, Pittsburgh, Pennsylvania, 1988), p. 225.
2. I. A. Aksay, W. Y. Shih, and M. Sarikaya, "Colloidal Processing of Ceramics with Ultrafine Particles," in *Ultrastructure Processing of Advanced Ceramics*, edited by J. D. Mackenzie and D. R. Ulrich (Wiley, New York, 1988), p. 393.
3. See, for instance, papers in *Multicomponent Ultrafine Microstructures, MRS Symp. Proc.*, Vol. 132, edited by L. E. McCandlish, D. E. Polk, R. W. Siegel, and B. H. Kear (Materials Research Society, Pittsburgh, Pennsylvania, 1989).
4. R. E. Newnham, "Composite Electroceramics," *Ferroelectrics*, **68**, 1 (1986).
5. K. Uchino, E. Sadanaga, and T. Hirose, "Dependence of the Crystal Structure on Particle Size in Barium Titanate," *J. Am. Ceram. Soc.*, **72** [8] 1555 (1989).
6. E. M. Rabinovitch, D. W. Johnson, J. B. McChesney, and E. M. Vogel, "Preparation of High-Silica Glasses from Colloidal Gels: I. Preparation for Sintering and Properties of Sintered Glasses," *J. Am. Ceram. Soc.*, **66** [10] 683 (1983).
7. C. J. Brinker and G. W. Scherer, "Relation Between the Sol-to-Gel and Gel-to-Glass Conversions," in *Ultrastructure Processing of Ceramics, Glasses, and Composites*, edited by L. L. Hench and D. R. Ulrich (Wiley, New York, 1984), p. 43.
8. I. A. Aksay, "Principles of Ceramic Shape-Forming with Powder Systems," in *Ceramic Powder Science II, Ceramic Transactions*, Vol. 1, edited by L. E. Messing, E. R. Fuller, Jr., and H. Hausner (American Ceramic Society, Westerville, Ohio, 1988), p. 663.
9. I. A. Aksay and R. Kikuchi, "Structures of Colloidal Solids," in *Science of Ceramic Chemical Processing*, edited by L. L. Hench and D. R. Ulrich (Wiley, New York, 1986), p. 513.
10. W. Y. Shih, I. A. Aksay, and R. Kikuchi, "Reversible-Growth Model: Cluster-Cluster Aggregation with Finite Binding Energies," *Phys. Rev. A*, **36** [10] 5015 (1987).
11. D. Gallagher, Ph.D. Thesis, University of Washington, Seattle, Washington (1988).
12. For example, see J. Th. G. Overbeck, "Recent Developments in the Understanding of Colloid Stability," *J. Colloid Interface Sci.*, **58**, 408 (1977).
13. J. Liu, Ph.D. Thesis, University of Washington, Seattle, Washington (1990).
14. J. Liu, M. Sarikaya, W. Y. Shih, and I. A. Aksay, "Fractal Colloidal Aggregates with Finite Interparticle Interaction: Energy Dependence of the Fractal Dimension," *Phys. Rev. A*, **41** [4] 3206 (1990).

15. W.-H. Shih and D. Stroud, "Theoretical Study of Miscibility and Glass Forming Trends in Mixtures of Polystyrene Spheres," *J. Chem. Phys.*, **80** [9] 4429 (1984).
16. J. Cesarano III, Ph.D. Thesis, University of Washington, Seattle, Washington (1989); M. Yasrebi, Ph.D. Thesis, University of Washington, Seattle, Washington (1988).
17. G. L. Graff, M.S. Thesis (in progress), University of Washington, Seattle, Washington (1990).
18. W. Y. Shih, W.-H. Shih, and I. A. Aksay, "The Stability of Binary Charged Colloidal Crystals," *J. Chem. Phys.*, **90** [8] 4506 (1989).
19. W. Y. Shih, I. A. Aksay, and R. Kikuchi, "Phase Diagrams of Charged Colloidal Particles," *J. Chem. Phys.*, **86**, 5127 (1987).
20. J. Liu, W. Y. Shih, R. Kikuchi, and I. A. Aksay, "On the Clustering of Binary Colloidal Suspensions," in press, *J. Colloid Interface Sci.* (1990).
21. R. Kikuchi, "Ternary Phase Diagram Calculations - I - General Theory," *Acta Metal.*, **25** 195 (1977).
22. R. Kikuchi, "Crystal Growth Model of Lattice-Order Simulation and the Cluster-Variation Method," *Phys. Rev. B*, **22** [8] 3784 (1980).
23. P. M. Chaikin and P. A. Pincus, unpublished.
24. C. Har, I. A. Aksay, and O. J. Whittemore, in *Advances in Materials Characterization II*, edited by R. L. Snyder, R. A. Condrate and P. F. Johnson (Plenum, New York, 1985), p. 339.
25. M. Sarikaya, K. E. Gunnison, M. Yasrebi, and I. A. Aksay, "Mechanical Property-Microstructural Relationships in Abalone Shell," in *Materials Synthesis Utilizing Biological Processes, MRS Symp. Proc.*, Vol. 174, edited by P. C. Rieke, P. D. Calvert, and M. Alper (Materials Research Society, Pittsburgh, Pennsylvania, 1990).





AD-P007 453



15

## NANOCOMPOSITES — THE MULTIFUNCTIONAL FAMILY OF MATERIALS

RUSTUM ROY

Materials Research Laboratory, The Pennsylvania State University, University Park, PA 16802

### ABSTRACT

This paper starts by discussing the concept of multifunctional materials. Multifunctionality can be achieved in a single phase in a composite or a mixture. While a few exceptional single phase materials such as diamond, Al<sub>2</sub>O<sub>3</sub>, CaSrZr<sub>4</sub>P<sub>6</sub>O<sub>24</sub> exhibit peak values of more than one function, it will be argued that the "invention" of the nanocomposite class of materials made by solution sol-gel processing has opened up the potential for designing several multifunctional materials.

Examples will be drawn from our recent results—both successes and failures—in trying to design and synthesize nanocomposites of two or more ceramic phases for various chemical, thermal, and electrical functions.

### INTRODUCTION

#### Multifunctional Materials

The title of the symposium invites some reflection on what the term can mean. Table 1 is an attempt to systematize the very different materials which are multifunctional.

Table 1. Multifunctional Materials

1 Single phase	2 Single Nanocomposite Material	3 Single Composite Material	4 Macroscopic mixture of two phases
Several different properties each showing extreme or interesting values. in the same <b>single phase</b> . e.g. diamond. fields.	Different properties realized by hybridizing <b>different materials on a 1-100 nm scale</b> causing hybrid properties to appear possibly of interest in different <b>Materials</b> 1. Single phase. e.g. optical glasses 2. Metal-ceramic graded composites	Enhancement of certain properties (usually mechanical) by interaction of phases. 3a. <b>Gradient Property</b>	Two functions achieved by addition of separate properties.

The titles of the columns in the table summarizes the first key point. We can achieve multifunctionality by using a single phase or "mixing" at various levels from the unit cell to single composites of 100nm components, to macro-mixtures. Of course, mixtures do not count as a single material. But should the third category—say steel bar-reinforced concrete or a mixture of an oxide support with a catalytic metal—be thought of as "one material." Most composites—glass reinforced plastics—used for their mechanical properties (single function) fall into this category and have been studied for decades. they will not be considered further. We will therefore focus our attention in this paper on the first two categories only of which only the nanocomposites are new.



### Single Phase Materials

Diamond is perhaps the best example of a single phase multifunctional material since several of its properties are very desirable: hardness, thermal conductivity, transparency in the i-r, etc. But Table 2 lists some other single phases which clearly are multifunctional also, with a qualitative numerical ranking (5 high, 0 low) of the relative importance of that property of the material as compared to competitive materials.  $\text{NaZr}_2\text{P}_3\text{O}_{12}$  "NZP" for example, was first discovered as a fast-ion transporter, but later this structure became much more interesting [1] for its controlled (low +, zero, low -) thermal expansion, and also as a ceramic host for radionuclides [2] from standard reactor waste. Garnets are also very versatile: with functions as different as from synthetic gems and magnetic bubbles.  $\text{BaTiO}_3$  conversely, has only one useful function. It would be interesting from the viewpoint of systematic materials synthesis to see if one could discover any guidelines to select materials which would have more than one useful function. It appears to be true that those materials which are outstanding in one property are frequently of some value in others also. The crystal chemistry which is responsible for a highly unusual value for one function is almost certain to result in high values in other functions also, since several of these are strongly correlated.

**Table 2. Single Phase Materials**

Functions	Diamond	Alumina	NZP	Garnet	$\text{BaTiO}_3$	Quartz
Wear	5	4	2	1	0	2
Optical	5	4	0	2	0 (?)	
Thermal						
Exp.	-	-	-	0	-	
Cond.	5	3	5	0	0	
Electrical	5	5	5	0	5	5
Magnetic	0	0	X	5	0	0
Chemical	5	4	5	0	0	5

The disadvantage of such single phase materials as candidates for multifunctionality is that there is absolutely no logical way by which we can predict the existence of such materials. I have discussed elsewhere [3] this impossibility, using the high  $T_c$  superconductors as the classic example, of the inability to attain this goal.

### Nanocomposites: A New Direction for Multifunctional Materials Synthesis

The concept of macro (and micro) composites originated in the idea of blending into one interactive material, two phases, so chosen as to enhance the mechanical properties of the resultant "composite." The science and technology of mechanically improved (stronger, tougher, etc.) composition is a field unto itself. But this concept had not really entered the world of designing materials for any other function: electrical, optical, chemical, etc. Yet scattered empirical evidence suggested that a general principle may be embedded in the concept of hybridizing properties of phases mixed on a nanometer scale. The nature and theory of the interaction was clearly outside the scope of the theory of mechanical composites.

Table 3 lists known families of nanocomposite materials which show extraordinary properties. The apatite-collagen nanocomposite with 1nm fibrils of apatite arranged around collagen hosts is an outstanding natural example even in the area of mechanical properties. And there are hints in the literature [4,5] that nanoscale mixing may provide surprisingly enhanced mechanical properties. However we do not pursue this function further in this paper.

The so-called artificially structured semiconductors based on GaAs and its crystalline solutions are 2.2 manocomposites with each layer 1-10 nanometers thick. Such a nanocomposite has new hybridized electrical properties which are not merely the sum or average of the end number components. This is equally true of the coated cutting tools and the new adsorbents we describe later.

Table 3. Nanocomposite Materials

	Coated cutting tools	Strength	Special magnetic	Adsorbents exchangers	Interleaved sheets
Wear	Multilayer Coating (WC+Co)	Teeth			
Optical					Clays and Rhodamine
Thermal Exp. Cond.			NZP+MgO		
Electrical					GaAs-GaSbAs
Magnetic			NZP+YIG		
Chemical				Zeolites	

It would appear on the face of the concept that **since we can mix very different (or very similar) materials on a nanometer scale, we should be able to build into one material a variety of functions each carried by one phase.** But in addition one may expect new properties to arise because of the interaction between the two (or more) phases. We turn now to the actual realization of both of these hopes.

#### Solution-Sol-Gel (SSG) as the Process of Choice

The first method used to make nanocomposite materials was sputtering alternately from two sources. By this method it was easy to make very thin two dimensional layers (2:2 composites) of different compositions. These vapor phase methods remain, of course, the basis of the routine and research preparation of an array of electronic materials. Multisource sputtering was becoming routinized in the seventies and Messier, Roy and Krishnaswamy [6] applied it explicitly to see if it was possible to make 0:3 nanocomposites of polymers, metals and ceramics, e.g. Teflon and platinum,  $Al_2O_3$  + Au, etc. While this yielded a series of interesting materials, e.g., 2 nm size Au crystals with 5 fold symmetry in noncrystalline  $Al_2O_3$ , it was evident that the method had serious limitations of size and speed. We therefore started to explore new methods to achieve this end.

In 1982 I changed the direction of all sol-gel work away from the single focus towards which it had been aimed by ourselves and all other researchers since our initial work starting in 1948—making ultrahomogeneous ceramics. I saw the possibility of making ceramic materials with maximum heterogeneity instead. If maximum heterogeneity could be defined by the maximum interfacial area between the different phases in a composite, then reduction of size of the phase was certainly the way to achieve this.

When two sols are mixed, provided the mixture remains electrostatically stable, it allows us to achieve "perfect" mixing on the scale of the particle size(s) involved. No chemical interaction or clumping occurs since the charged particles do not differentiate between the chemistries. By tailoring the gelation and desiccation one can therefore produce powders, continuous thin films and small (mm size) bulk objects of an array of 0:3 nanocomposites. Of course some 2:2 composites, albeit with relatively thick layers, can be made by sequential deposition. Many of our key papers in developing di-phasic xerogels (=nanocomposites) are listed in a review of the field. Details on methods for preparation of such nanocomposites have been described in an earlier paper [8]. Table 3 attempts a summary of various kinds of nanocomposites which are known to show the place of SSG-derived nanocomposites in the big picture. We turn now to results which can be achieved via the SSG method.

## RESULTS

Over the last six years we have reported on the preparation and properties of a wide variety of nanocomposites via SSC [9-12]. In this paper I select some examples which illustrate the multifunctionality possible in this family and also choose the rare example where we have been able to build in, by design, multifunctionality into the same material. Table 4 summarizes the different functions which have been synthesized into different nanocomposites in our work. In March 1989 an entire symposium was held in Japan on nanocomposite materials and several interesting examples (e.g. that of Shimada [13]) can be found therein. In most of these cases up to now one can only illustrate the fact that sets of nanocomposites based on some common compositions can be made multifunctional. Each specific combination may have only one function. We only list below the examples which have been described in detail elsewhere.

**Table 4.**

NANOCOMPOSITE CHEMICAL SUBFUNCTIONS	Mullite	Al <sub>2</sub> O <sub>3</sub>	ZrSiO <sub>4</sub>	ThSiO <sub>4</sub>	Cordierite
• Control reaction products		✓		✓	✓
• Control reaction rates and temperatures	✓	✓	✓	✓	✓
• Control microstructure	✓	✓			✓
• Control morphology	✓				
• Control crystallographic orientation				✓	

### Control of Phase Formed

Nanocomposite di-phasic gels of ThSiO<sub>4</sub> (non-crystalline) + ThSiO<sub>4</sub>(huttonite) and ThSiO<sub>4</sub>(NC) + ThSiO<sub>4</sub>(thorite) at 1400°C yield ceramics of 100% huttonite and 100% thorite respectively [12]. With cordierite compositions, likewise, completely different final products can be obtained by compositional and structural nanocomposites [14].

### Control of Reaction Rates and Temperatures

We have demonstrated in several papers in the cases of Al<sub>2</sub>O<sub>3</sub>, ZrSiO<sub>4</sub>, ThSiO<sub>4</sub>, AlPO<sub>4</sub>, etc., by DTA and static thermal reaction studies that reaction temperatures can be lowered by 150°-250°C in appropriately configured nanocomposites [9].

### Control of Microstructure

These same diphasic and triphasic gels can radically alter the microstructure of heated gels from 10-15 $\mu$  grain sizes to submicron sizes [10].

### Control of Morphology

The most successful example of this ability was found in the case of mullite, where compositionally diphasic gels seeded with crystalline mullite gave acicular crystals with a 10:1 aspect ratio contrasted with the usual equant morphology [11].

### Control of Crystallographic Orientation by Solid State Epitaxy

In another paper in this symposium we demonstrate our ability to grow epitaxial layers on large single crystals of quartz, perovskite and rutile structures [15]. In our early studies in

which the surprising results noted above on many functions were found, we claimed that the mechanism for the effects was solid state epitaxial growth. The new data add more evidence to this claim. It is clear that nano-scale second phases can grow, into at least, highly oriented if not single crystals on a substrate totally in the solid state. We believe this is the most direct evidence of solid state epitaxy provided so far.

#### NEW FUNCTIONS CONTROLLED IN NANOCOMPOSITES

One of the most interesting examples of Shimada's work on the enhanced luminescence of 2:2 nanocomposites of say, Rhodamine B, interlayered into a clay mineral. By so modifying radically the crystal field surrounding the molecule, Shimada was able to enhance the luminescence output by an order of magnitude, and to make the material much more thermally stable.

A new target property in our work is the creation of nanocomposites of pillared clays, zeolites and gels to provide a thermodynamically ideal adsorption-desorption cycle for drying of gases. Figure 1 shows the ideally desirable desorption isotherm and both the final nanocomposite performance, and a typical curve of a competitive material.

A third property on which our laboratory has been focusing is on materials which can both selectively adsorb and "fix" at low temperatures selected ions (both radioactive and biologically toxic). In one successful synthesis by a stepwise process we have exchanged out the  $K^+$  in a phlogopite mica using  $NaB(Ph)_4$ , and then used this material to adsorb  $Cs^+$  out of solution. The  $K_d$  or selectivity ratio for this material is a phenomenal 664.000 compared to 1-5000 for the typical good material [16]. The obvious multi-functional goal here is to create a nanocomposite which can selectively adsorb 2, 3 or more targeted ions.

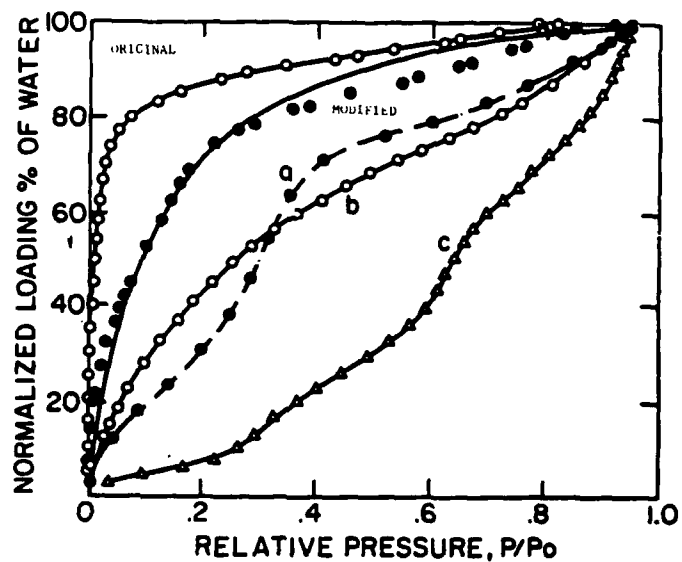


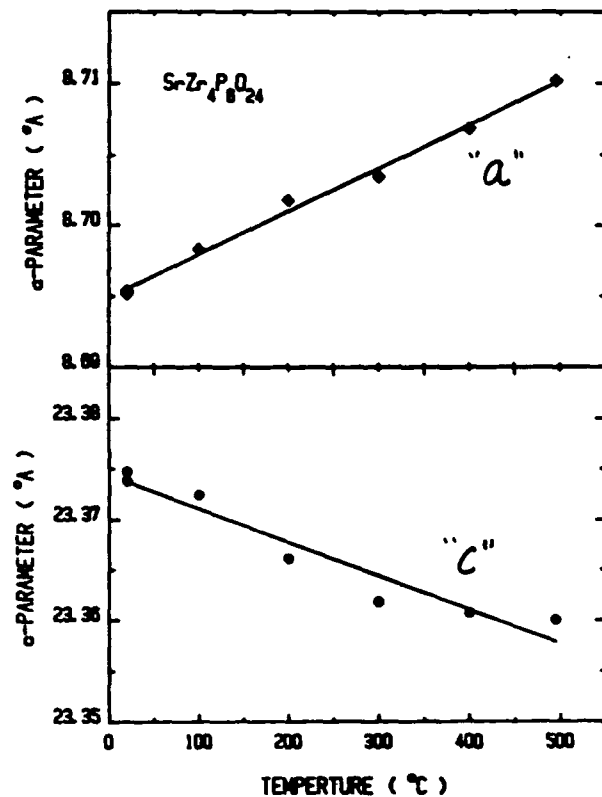
Figure 1. Water adsorption isotherms (upper curves) of: zeolite 13Y original sample (O) with a total capacity of 0.29 g/g; zeolite 13 Y modified sample data (O) shown next to the dark line upper curve. Also below the ideal curve with a total capacity of 0.19 g/g are shown the isotherms for:  $Al_2O_3$  pillared clay (a); hydrophilic  $Al_2O_3$  pillared clay (b); and original montmorillonite clay (c).

#### A Case Study: Making a Zero-expansion Ferrimagnetic Material

I end with a real example of two competing approaches to making a multifunctional phase.

Our successes, based initially on a serendipitous observation, in making a controllable zero expansion ceramic with the NZP or Nasicon or  $\text{Ca}_0.5\text{Ti}_2\text{P}_3\text{O}_{12}$  structurally relied on the anisotropy of  $\alpha$  in the phase (Fig. 2). Emboldened by this success, our sponsors the AFOSR next set a goal of simultaneously having not only a net  $\alpha = 0$  but that the anisotropy of  $\alpha$  in the hexagonal phase also be reduced to zero. Again based on serendipitous observation this goal was also achieved in a phase of composition  $\text{Ca}_3\text{Sr}_4\text{P}_6\text{O}_{24}$ . Finally the AFOSR set a target of a material which would have zero expansion and also be ferrimagnetic in order to provide no radar scattering—a truly multifunctional challenge.

Figure 2. Nearly zero- $\alpha$  achieved in these hexagonal phases by balancing out  $\alpha$ -anisotropy in 'a' and 'c' directions.



For one year my postdocs and I tried the single phase approach to use the NZP structure and substitute in 3d and 4f ions in many combinations. Our original discovery of the ferrimagnetic garnets [17] had provided the first family with three interacting sublattices, respectively, IV, VI and VIII coordinated. Because the "NZP" structure was even more favorable to multiple ion substitution than the garnets and also had at least three sublattices, it appeared very hopeful that this goal could be attained in a single phase.

Yet intensive study of all possible combinations of ions failed to yield a single phase which was both ferrimagnetic and had "zero" thermal expansion.

Finally we were forced to take the alternative route of creating a nanocomposite which would contain these properties. Such a nanocomposite would likely have to withstand moderately high temperatures in processing. Hence in designing it, it was necessary to first find two phases which were thermodynamically compatible, one of which was ferrimagnetic (and had a modest positive net  $\alpha$ ) and another which had a modestly negative net  $\alpha$ . This combination was found by empirical cut and try, and a nanocomposite prepared which was both "zero" expanding and ferrimagnetic, and consisted of YIG and a Na-rich NZP.

## CONCLUSIONS

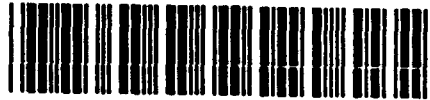
Nanocomposites made by the solution-sol-gel process offer a uniquely large and versatile class of materials which can be tailored to be multi-functional. Yet each example will have to be treated as a unique case, since no common features can be expected. It is only the di-phasic SSG process which is in common.

## REFERENCES

- [1] R. Roy, D.K. Agrawal and H.A. McKinstry, Very Low Thermal Expansion Coefficient Materials, *Ann. Rev. Mater. Sci.* **19**, 39 (1989).
- [2] R. Roy, L.J. Yang, J. Alamo and E.R. Vance, A Single Phase ([NZP]) Ceramic Radioactive Waste Form, *Scientific Basis for Nuclear Waste Management*, Vol. **6**, p. 77, Douglas G. Brookins (Ed.), Elsevier Science Publ. Co., Inc., New York (1983).
- [3] R. Roy, Synthesizing New Materials to Specification, *Solid State Ionics* **32/33**, 3 (1989).
- [4] J.S. Koehler, Attempt to Design a Strong Solid, *Phys. Rev. B* (2), 15 July 1980.
- [5] S.L. Lehoczky, Retardation of Dislocation Generation and Motion in Thin-layered Metal Laminates, *Phys. Rev. Lett.* **41**, 1814 (1978).
- [6] R.A. Roy, R.F. Messier and J.M. Cowley, *Thin Solid Films* **79**, 207 (1971).
- [7] R. Roy, Ceramics by the Solution-Sol-Gel Route, *Science* **238**, 1664 (1987).
- [8] R. Roy, S. Komarneni and W. Yarbrough, Some New Advances with SSG-Derived Nanocomposites, Chapter 42, *Ultrastructure Processing of Advanced Ceramics*, John MacKenzie and Don Ulrich (Eds.), Wiley Interscience, 571 (1988).
- [9] Y. Suwa, R. Roy and S. Komarneni, Lowering Crystallization Temperatures by Seeding in Structurally Diphasic  $\text{Al}_2\text{O}_3$ - $\text{MgO}$  Xerogels, *J. Am. Ceram. Soc.* **68** [9], C-238 (1985).
- [10] W.A. Yarbrough and R. Roy, Extraordinary Effects of Mortar-and-Pestle Grinding on Microstructure of Sintered Alumina Gel, *Nature* **322** (6077), 347 (24 July 1987); Microstructural Evolution in Sintering of ALOOH Gels, *J. Mater. Res.* **2** (4), 494 (July/Aug. 1987).
- [11] S. Komarneni and R. Roy, Diphasic Xerogels, A New Class of Materials Phases in the  $\text{Al}_2\text{O}_3$ - $\text{SiO}_2$ -System—A Reply, *J. Am. Ceram. Soc.* **68**, C-85 (1985).
- [12] G. Vilmin, S. Komarneni and R. Roy, Crystallization of  $\text{ThSiO}_4$  from Structurally and/or Compositionally Diphasic Gels, *J. Mater. Res.* **2** (4), 489 (1987).
- [13] M. Shimada, Preparation and Fluorescence Properties of Clay-Dye Composites, *Proceedings, Seventh Seminar on Frontier Technology*, Oiso, Japan (Feb. 7-10, 1989).
- [14] A. Kazakos-Kijowski, S. Komarneni and R. Roy, Multi-phasic Nanocomposite Sol-Gel Processing of Cordierite, in *Better Ceramics Through Chemistry III*, C.J. Brinker, D.E. Clark and D.R. Ulrich (Eds.), 245 (1988).
- [15] R. Roy, S. Komarneni and U. Selvaraj, Solid State Epitaxy, *Symposium S, Mat. Res. Soc.* (1989).
- [16] S. Komarneni and Rustum Roy, patent applied for.
- [17] M.L. Keith and R. Roy, Structural Relations Among Double Oxides of Trivalent Elements, *Am. Mineralogy* **39**, 1 (1954).
- [18] D.K. Agrawal and R. Roy, Composite Route to 'Zero' Expansion Ceramics, *J. Mats. Sci.* **20**, 4617 (1985).



AD-P007 454



23

MULTIFUNCTIONAL SILICA OPTICS

L. L. HENCH AND A. FOSMOE

Advanced Materials Research Center, University of Florida, One Progress  
Blvd., #14, Alachua, FL 32615

92-18234



ABSTRACT

The sol-gel chemical processing method of producing fully dense silica optics provides an intermediate product termed Type VI silica ideally suited for use in engineering multifunctional silica optics. This paper reviews the sol-gel process, the Type V dense gel-silica produced by this process and the Type VI ultraporous gel-silica intermediate product. Included is a comparison of two different porous ultrastructures with 1.2 nm and 8.0 nm average pore radii. Two uses of the porous gel-silica components as multifunctional optics are described. The first is for use in transpiration cooled windows in high-speed rocket guidance systems. Flow rates of He and N<sub>2</sub> through the 1.2 nm and 8.0 nm ultrastructures are as high as 0.9 m/min at 0.75 MPa. High temperature UV transmission in contact with an impinging oxy-acetylene flame is demonstrated. Use of Type VI gel-silica as a host matrix for fast radiation-hard scintillating detectors is also reviewed.

INTRODUCTION

Precision optics have been made by basically the same process since the time of Galileo; i.e., silica sand has been melted with various fluxes, homogenized at very high temperatures above the liquidus and cast into glass ingots. Sections of the ingots with minimum bubbles, seeds, striae or other defects have been selected by hand for grinding by skilled opticians into the shape of lenses, prisms, windows, or mirrors, followed by successive polishing steps, again performed by highly trained optical technicians. The quality of each optical component is therefore dependent on the summation of the quality of each step of processing, which in turn is a function of the skill, training, and time devoted by technicians. The performance of an optical system is an aggregate of the quality of the individual components and therefore is highly dependent on the availability and skill of technical manpower.

Until recently, optical components have for the most part also served only a single function in an optical system; i.e., lenses refract, mirrors reflect, windows transmit, filters absorb and lasers amplify. As optical systems requirements become ever more demanding there is a great incentive for components to serve more than one function. This need is very difficult to satisfy with traditional methods of making precision optics. The fundamental characteristics of glass as an isotropic, homogeneous solid generally restrict its use to a single optical function.

Sol-gel chemical processing of silica provides a new approach to each of the historical restrictions of silica optical components summarized above; i.e., 1) elimination of hand operations in manufacturing by net shape casting, and 2) development of multifunctional optics by producing ultraporous silica matrices that are optically transparent.

## SOL-GEL PROCESSING

Recent publications have presented in detail the important features of sol-gel technology [1-3]. The use of sol-gel processing for producing monolithic silica optical components has also been previously described [1,2]. In summary, there are three approaches to making sol-gel monoliths:

Method 1 -	Gelation of colloidal powders.
Method 2 -	Hydrolysis and polycondensation of alkoxide precursors, followed by hypercritical drying to form aerogels.
Method 3 -	Hydrolysis and polycondensation of alkoxide precursors followed by aging and drying under ambient atmospheres to form xerogels.

Method 1 has been used by Shoup to make silica for reflective optics. Method 2 has been used by Kistler [4], Fricke [5], Zarzycki [6], and others to make aerogels, which can be used as very low density optical components with an index of refraction close to 1.00 [7], or densified to form silica glass [8].

In order to make net shape multifunctional optics we use Method 3 with an emphasis on controlling at a molecular level each of the seven steps of processing listed in Figure 1.

In our process the alkoxide is tetramethylorthosilicate (TMOS) and the catalyst is either nitric acid or hydrofluoric acid, depending upon the average pore size desired after drying. Full density net shape precision optics termed Type V gel-silica, require all seven steps listed in Figure 1. Partially dense, controlled porosity Type VI gel-silica optics require the first six steps listed in Figure 1.

## TYPE V, DENSE GEL-SILICA

The average pore size of the dried monoliths used in making Type V dense gel-silica is very small, in the range of 1.2 nm, with a very narrow size distribution, see Figure 2. Densification occurs at a low temperature, 1150°C, in a dry atmosphere due to the very small pore radii and very large,  $>700 \text{ m}^2/\text{g}$ , surface area. There is almost no change in pore radii as densification occurs, see Figure 3. As shown by Vasconcelos [9], nearly all the change in texture during the densification is due to a decrease in connectivity of the pore network which decreases the surface area and volume fraction of the pores per unit volume, Figure 3. At 1150°C all the pores are eliminated and the bulk density of the glass is 2.2 g/cc, equivalent to that of vitreous silica, Types I-IV, made by other processes [1].

The shape of the optical component is determined by the shape of the mold used for gelation, Step 2. Nogues et al. [10] report that it is possible to achieve as-cast tolerances for the diameter, thickness, and radius of curvature of silica lenses made by sol-gel processing which are within, or surpass, tolerances achieved by precision grinding and polishing.

The optical properties of Type V gel-silica are also superior than most of the commercial grades of optical silica, as discussed previously [1,11,12]. Figure 4 compares transmission from the vacuum ultraviolet to the visible for

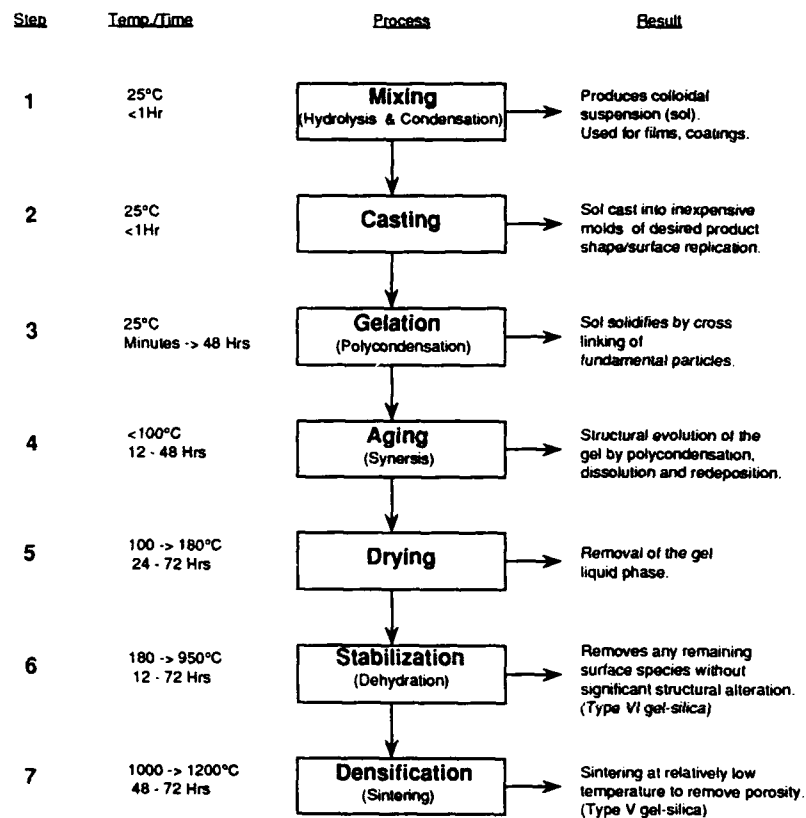


Figure 1. Sol-gel processing sequence for multifunctional optics.

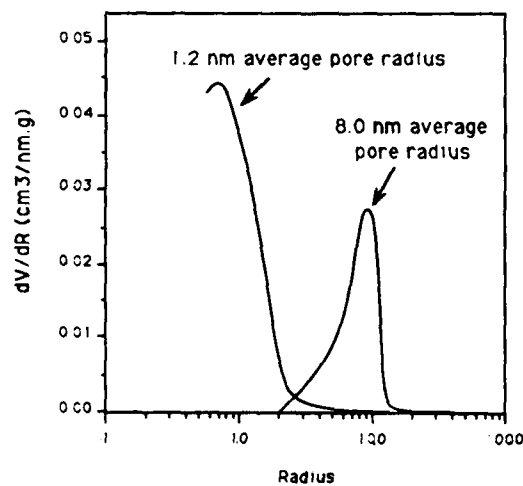


Figure 2. Pore size distribution for dried silica gel monoliths with 1.2 nm and 8.0 nm average pore radii.

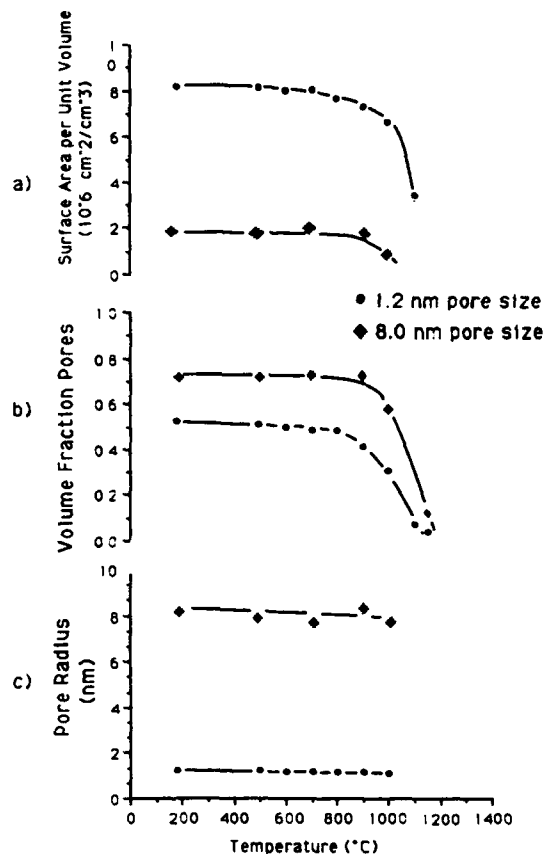


Figure 3. Variation of: a) surface area per unit volume ( $S_v$ ), b) volume fraction of pores ( $V_v$ ), and c) pore radius ( $R$ ), all as a function of temperature.

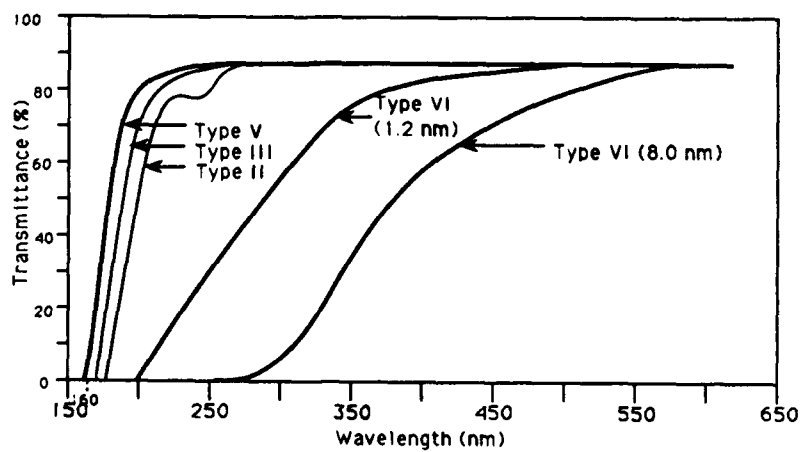


Figure 4. UV cut-offs of Types I, II, III, V, and VI silica.

Type V gel-silica with typical curves for Types II and III optical silicas. Type V gel-silica has a lower wavelength UV cut-off than even Type III silica, made by flame hydrolysis of  $\text{SiCl}_4$ , which is sold for UV applications. Removal of cation and hydroxyl impurities in sol-gel silica processing is responsible for the improvement in optical transmission.

Transmission in the near IR of Type V gel-silica is also excellent, as illustrated in Figure 5. There are no absorption peaks due to hydroxyl impurities, see Table I, unlike Type III optical silicas.

#### TYPE VI, ULTRAPOROUS GEL-SILICA

Figure 3 shows that gel-silica monoliths heated up to 800°C to 900°C still retain a large volume fraction of porosity. Vasconcelos' studies of the topological characteristics of these gels show that this porosity is completely interconnected [9]. Because of the very small size of the pores, Figure 2, the material is optically transparent, Figure 6. By heating to 800-900°C stabilization, Step 7 in Figure 1, the concentration of silanols on the surface of the pore network can be controlled, as illustrated in Figures 5 and 7 thereby making the material chemically stable when exposed to an aqueous environment.

The ultraporous, optically transparent gel-silica, termed Type VI gel-silica [1], is uniquely suited for many multifunctional optical applications, as discussed by Hench et al. [1,12] and Nogues et al. [13].

It is possible to vary the pore size and volume fraction of porosity of the Type VI gel-silica by using HF as a catalyst in Step 1, as discussed by Parsell [14], Vasconcelos [9], and Elias [15]. Figure 2 compares the pore distribution curves for monoliths with 1.2, and 8.0 nm average pore sizes. Details of textural characteristics and the thermal behavior of these, and monoliths with other pore sizes, are presented elsewhere by Vasconcelos [9] and Elias [15]. Increasing the pore size of the network is important for a number of multifunctional optical applications, as shown below. However, the larger pores do degrade the UV cut-off to some extent, from 160nm to 235nm as shown in Figure 4, probably due to Rayleigh scattering, as calculated by West and Elias [15]. The porous Type VI optics also have residual hydroxyls retained on the pore network, Figure 5, with the concentration dependent on the maximum stabilization temperature. Since the larger pore network is more thermally stable,[9,15] the larger pore optics can be heated to higher stabilization temperatures to decrease the OH content and still retain a very large volume fraction of porosity (Figure 3). This increase in volume fraction of porosity and greater thermal stability of the 8.0 nm Type VI gel-silica offers a major advantage for the multifunctional optical applications discussed below.

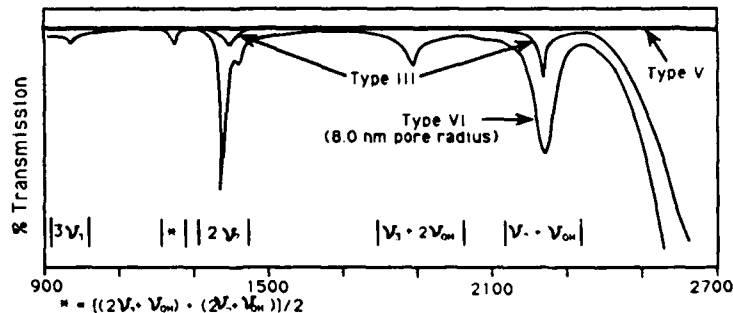


Figure 5. NIR transmission curves for Types III, V and VI silica.

Table I. Si-O-H Fundamental Vibrational Assignments

$\nu_{\text{OH}}$	Si-O-H Out of Plane Bending
$\nu_1$	Si-O-H (Isolated) Stretch
$\nu_2$	Si-O-H (Adjacent) Stretch
$\nu_3$	Si-O-H (Hydrogen Bonded to Water) Stretch

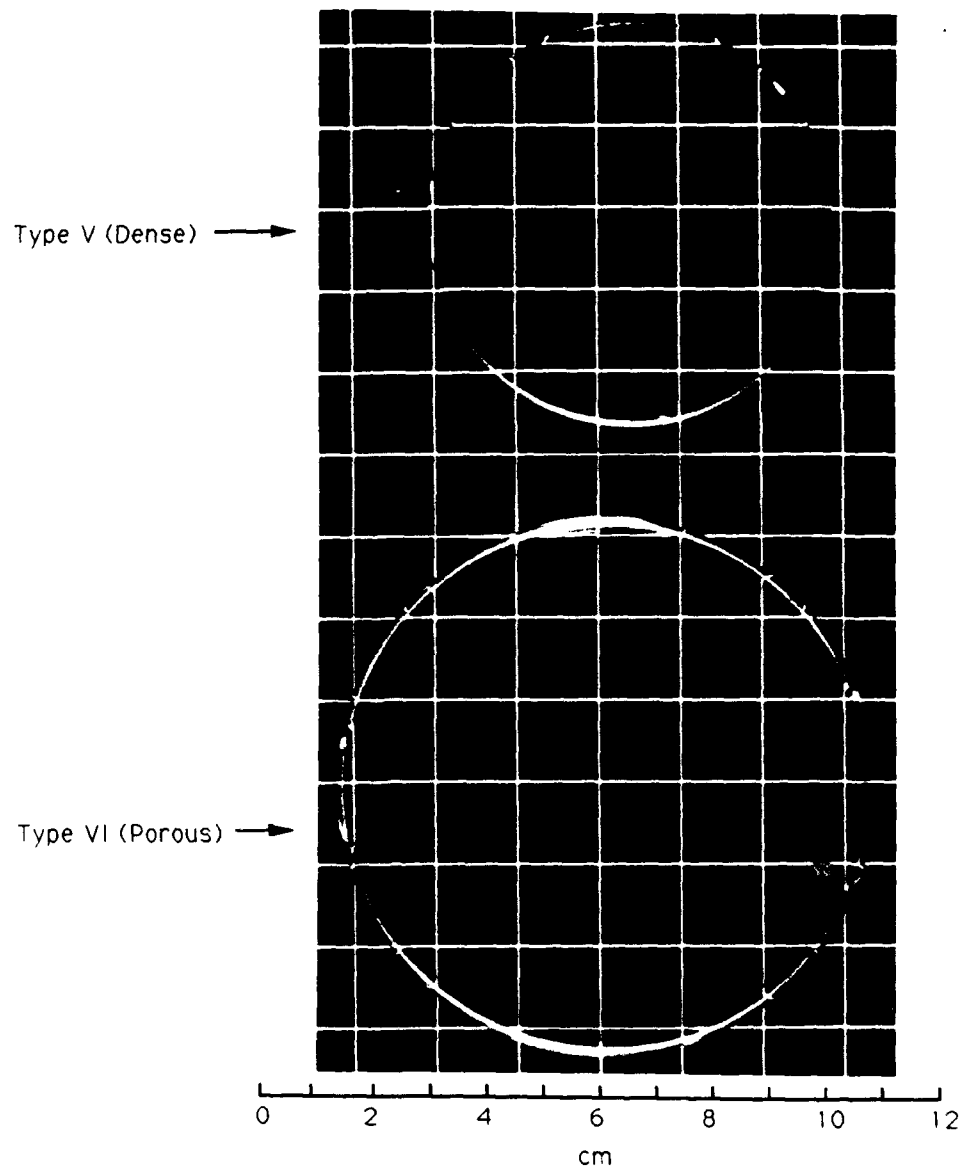


Figure 6. Optical transparency of Type V (dense) and Type VI (porous) gel-silica.

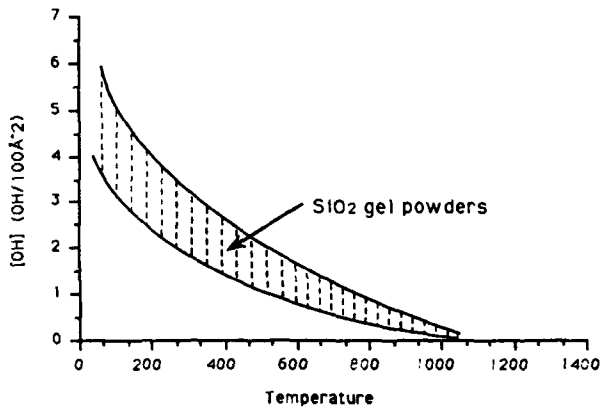


Figure 7. Hydroxyl concentration of silica gel powders as a function of processing temperature (from Davydov, et al. [16]).

#### TRANSPIRATION COOLED UV WINDOWS

Multifunctionality is highly desirable for optically transmitting windows in high speed rocket guidance systems due to severe operating conditions. The windows need to transmit light over a broad range of wavelengths, including the ultraviolet. Most importantly, the optical transmission must not be affected by very high ambient temperatures and impingement of very energetic gases. Reasonably good structural strength, thermal stability, and thermal shock resistance is also required for rocket windows.

A unique approach to achieving thermally resistant properties is to cool the window by passing gases through the window. Such a concept is possible with the ultraporous Type VI gel-silica monoliths.

The objective of the multifunctional optical component is to cool the window via transpiration of gases through the interconnecting pore structure while optical transmission is maintained.

The first step in evaluation of the concept of a transpiration cooled window is to determine whether transpiration of gases is possible through a porous Type VI gel-silica medium. The second step, if transpiration is possible, is to characterize the transpiration rate as a function of pressure, pore radius, sample thickness, and type of gas. The third step is to determine whether UV transmission occurs through the Type VI porous gel-silica window at elevated temperatures and with gases impinging on it. Fourth, thermal shock characterization of the window is also needed.

A preliminary report of these multifunctional performance characteristics follows. A low pressure (<700 psi) test chamber was designed and built to quantify the rate of gas transpiration through the porous optical windows. The results are shown in Figure 8 with the flow rates of helium through samples with pore radii of 1.2nm and 8.0nm (processed to 180°C and 500°C stabilization temperatures) measured as a function of pressure. Figure 9 shows the difference in flow between helium and nitrogen through the sample with 1.2nm pores stabilized to 180°C. The flow rate of the He is considerably

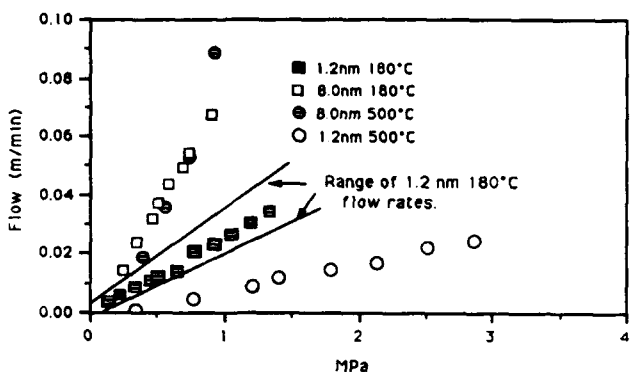


Figure 8. Helium transpiration through 1.2 nm and 8.0 nm porous gel-silica windows.

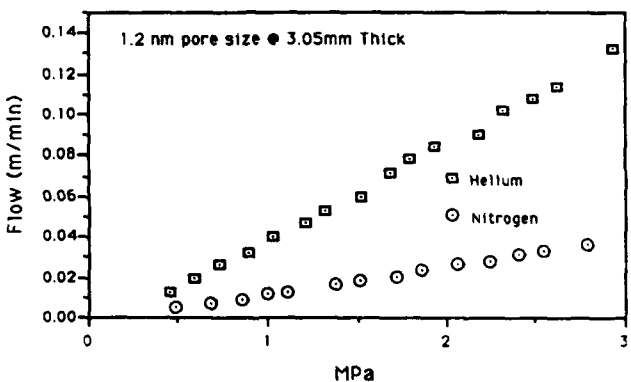


Figure 9. Helium versus nitrogen transpiration flow in a 1.2 nm pore size gel-silica window.

faster than nitrogen due to the difference in size<sup>1</sup> and the diatomic nature of nitrogen; i.e.,  $He = 0.36$  nm,  $N_2 = 0.42$  nm.

To determine the effect of elevated temperature upon the UV transmission of gel-silica, a high temperature test apparatus was constructed, Figure 10. This apparatus includes a UV light source, sample holder with thermocouple, an oxygen-acetylene torch heat source, and a multifunctional gel-silica optical component as a UV detector. This detector component is described in the next section. Fluorescent activity was observed in the detector at  $T > 1000^\circ C$  due to the UV transmission of the window, absorption in the detector and emission at  $\sim 600$  nm by the wavelength shifter. The upper limit of temperature performance of the gel-silica UV window under transpiration cooling is presently unknown but is probably much higher than can be measured in this experimental set-up. Tests are underway and results will be presented at the Spring 1990 MRS meeting.

<sup>1</sup>Sizes (diameters) are approximated using twice the van der Waals radii and adding the  $N = N$  bond length for  $N_2$  (values taken from Huheey [17]).

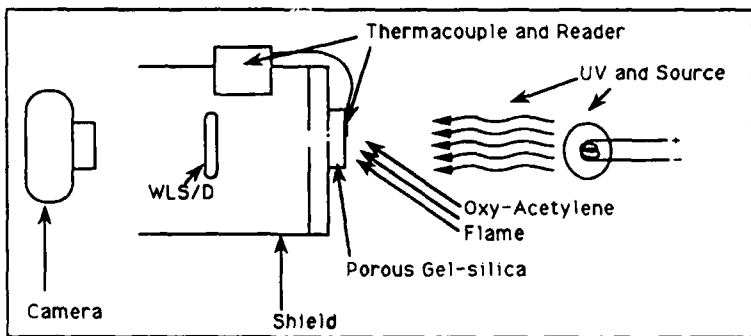


Figure 10. Experimental setup for UV detection at elevated temperature.

#### FAST, RADIATION-HARD SCINTILLATING DETECTOR

The physical features of Type VIA porous gel-silica described above are attractive to use as matrices for doping or impregnation with fluors, non-linear optical polymers or compounds, wavelength shifters, or lasing dyes. The result is a hybrid multifunctional optical component.

Table II lists examples of some organic and inorganic compounds that have been successfully impregnated into several Type VI gel-silica samples [1].

The results described above show that it is possible to select various combinations of second phase loading which are a function of pore size and total pore volume of the porous optical matrix. Previous studies [9] have shown that physical properties such as flexural strength, compressive strength, elastic modulus, coefficient of thermal expansion, density, and microhardness are also a function of pore size and volume fraction of porosity. For example, an 800°C heat treatment of a 1" diameter x 1/4" thick plano-plano Type VI gel-silica blank with 1.2 nm pores produces an optically transparent component that weighs 4.02 g, has a 117 HV microhardness, and has nearly 2500 m<sup>2</sup> surface area with pores ~1.2 nm radius. This component can accept 1.6 cc of a dopant second phase using various impregnation techniques. Thus, 40-50 volume percent of the component can be filled with a second phase.

Table II. Compounds Impregnated into Type VI Porous Gel-Silicas.

<u>Non-Linear Optical Polymers</u>	<u>Transition Metals</u>
-PBT [Phenylenebenzobisthiazole]	- Cu
-MNA [2-Methyl-4-Nitroaniline]	- Ni
<u>Organic Fluors</u>	- Cr
-B-PBD[2-4'-t-Butylphenyl) 5-(4"-Biphenyl)-1,3,4-Oxadiazole]	- Ce
-P-TP [p-Terphenyl]	- Ag
-P-QP [P-Quarterphenyl]	- Fe
<u>Wavelength Shifter</u>	- Co
-3-HF [Hydroxyflavone]	
<u>Laser Dye</u>	<u>Rare-Earths (Lanthanides)</u>
-Rhodamine 6G	- Nd
	- Er

If a harder and stronger component is desired, a 900°C heat treatment can be used although the amount of dopant phase is reduced to 1.31 cc.

The Type VI gel-silicas with larger pore sizes described above make it possible to impregnate the component with higher molecular weight polymers. The same 800°C treatment of a 1" diameter x 1/4" thick sample with 8.0nm pores produces an optical component that weighs 1.98 g, has a 18 HV microhardness, and has nearly 583 m<sup>2</sup> surface area with pores ~ 8.0 nm radius. This component can accept 2.36 cc of a dopant second phase in its 70-75 volume percent porosity. Differences between a gel-silica matrix with 1.2 nm pores versus matrix with 8.0 nm are tabulated in Table III. These differences are large and provide a wide range of textural features for use in tailoring multifunctional optics.

For example, consider the fast radiation hard scintillator developed by Nogues, et al.[13]. They utilized a Type VI gel-silica matrix with a 1.2nm average pore radius and 0.35 volume fraction porosity as a host matrix for organic fluors to produce a fast, radiation hard scintillaton detector. The silica matrix provides high radiation resistance compared to the organic plastic scintillators [13] and the organic fluor provides fast scintillation response. Both properties are advantageous for high-speed counting necessary in high-energy physics applications. The primary fluors used by Nogues, B-PBD, P-TP & P-QP (Table II) have good radiation resistance and short decay times of a few nanoseconds, but the fluorescence spectra typically peaks at wavelengths below 400 nm, making it difficult to measure. To overcome this problem Nogues, et al. [13] used another fluor termed a wavelength shifter (WLF) (WLS) 3-HF (Table II) which absorbs the < 400 nm radiation of the primary fluor and re-emits in wavelengths of = 500-600 nm. These wavelengths are advantageous as they are less absorbing in glass than the shorter wavelengths and also result in higher quantum efficiency for silicon photodiodes. When analyzed for scintillation efficiency with  $\alpha$ -,  $\beta$ -, and  $\gamma$ -ray sources, the light output was reported to be only 6-7 times lower than the much more highly developed plastic scintillator [13]. The  $\gamma$ -radiation resistance of the silica matrix was many times greater than the organics. These are very encouraging results for the first generation of multifunctional optical components.

This same type detector with the 3-HF fluor dopant was supplied by Nogues for use as the WLS/detector shown in Figure 10 and was used for the high-temperature UV transmission test in the above mentioned transpiration study. A source emitting 365 nm radiation passes through the heated porous window being tested for transmission and is absorbed and re-emitted by the detector as visible green  $\rightarrow$  yellow-green light from the WLS/detector. Thus, a qualitative and visual method for testing high temperature UV transmission through a porous silica matrix was achieved.

Table III. Property Comparisons Between 800°C Heat Tested Samples of 1.2 nm and 8.0 nm Average Pore Radius.

<u>Property</u>	<u>1.2 nm</u>	<u>8.0 nm</u>
Bulk Density (g/cc)	1.25	0.62
Surface Area per Unit Volume (cm <sup>-1</sup> )	7.63 x 10 <sup>6</sup>	1.81 x 10 <sup>6</sup>
Volume fraction Porosity	0.49	0.73
Vickers Hardness Number	117.3	16.8

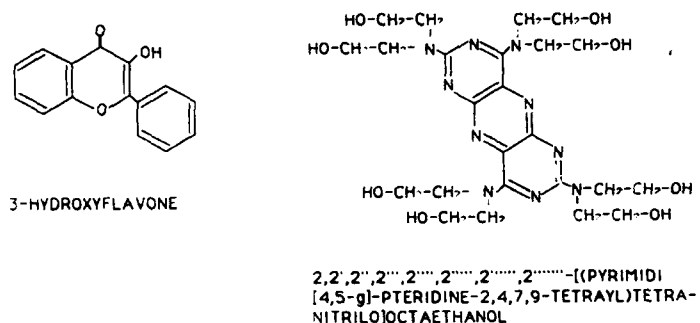


Figure 11. Fluors of different size requiring different pore size matrices.

Organic fluors and dopants come in various sizes, many much larger than the 3-HF fluor used by Nogues (Figure 11). The octaethanol fluor exhibits strong excitation (absorption) bands peaking at 315 and 520 nm while its emission peak is shifted to 590 nm (up 85 nm from 3-HF which is 535 nm max). The strong 315 nm excitation and 590 nm emission band make it better suited for a high temperature UV transmission detector, provided one adds an optical filter to eliminate the oxy-acetylene flame effect on this fluor. With the larger (i.e., 8.0 nm) Type VI matrix it is feasible to use this larger organic molecule which do not fit in the 1.2 nm pore size matrix, or to have a much larger volume fraction of dopant (Table III).

#### ACKNOWLEDGMENTS

The authors are grateful for the financial support of the Air Force Office of Scientific Research under contract #F49620-88-C-0073 and the encouragement of D. R. Ulrich throughout this research. A special thanks is extended to J. L. Nogues for the use of the wavelength shifter/detector.

#### REFERENCES

1. L. L. Hench, S. H. Wang, and J. L. Nogues, in Multifunctional Materials, edited by Robert L. Gunshor, (SPIE: Bellingham, Washington, 1988) Vol. 878, p 76.
2. L. L. Hench and J. K. West, in Chemical Reviews, Main Group Chemistry Thematic Issue, edited by J. Michl, (American Chemical Society, New York, 1990).
3. J. D. Mackenzie and D. R. Ulrich, eds., Ultrastructure Processing of Advanced Ceramics, (J. Wiley and Sons, New York, 1988).
4. M. Prassas, J. Phalippou, and J. Zarzycki, presented at the XIII Int. Conf. on Glasses, Hamburg, Germany, 1985.
5. B. E. Yoldas, Bull. Am. Ceram. Soc. 54, 286 (1975).
6. J. Zarzycki, editor, J. Non-cryst. Solids. 1-3, 1-436 (1986)

7. J. Fricke and R. Caps, in Ultrastructure Processing of Advanced Ceramics edited by J. J. Mackenzie and D. R. Ulrich, (J. Wiley and Sons, New York, 1988) pp. 613-622.
8. J. Zarzycki, M. Prassas and J. Phallipou, *J. Mater. Sci.* 17, 3371-3379 (1982).
9. W. Vasconcelos, Ph.D. Thesis, University of Florida, 1989.
10. J. L. Nogues, C. Balaban, W. V. Moreshead and R. S. Sheu, Advanced Ceramics, edited by W.P.E. Longo, S. N. Monteiro and J. D. Filho (Florida-Brazil Institute, Rio de Janeiro, 1989) pp. 51-60.
11. L. L. Hench, M.J.R. Wilson, C. Balaban, and J. L. Nogues, presented at the 4th International Conference on Ultrastructure Processing of Ceramics, Glasses and Composites, Tucson, Arizona, 1989.
12. S. H. Wang, C. Campbell, and L. L. Hench, in Ultrastructure Processing of Advanced Ceramics, edited by J. D. Mackenzie and D. R. Ulrich, (J. Wiley and Sons, New York, 1988) pp. 145-160.
13. J. L. Nogues, S. Majewski, J. K. Waler, M. Bowen, R. Wojcik, and W. V. Moreshead, *J. Am. Ceram. Soc.* 71 (12), 1159-1163 (1988).
14. L. L. Hench and D. Parsell (personal communication).
15. E. Elias, Masters Thesis, University of Florida, December 1989.
16. V. Ya. Davydov, A. V. Kiselev, and L. T. Zhuravlev, *Trans. Faraday Soc.* 60, 2254 (1964).
17. James E. Huheey, in Inorganic Chemistry, 3rd ed. (Harper & Row, New York, 1983), p. 258.



AD-P007 455



35

# PHOTOACTIVE LIQUID CRYSTALLINE POLYMERS AS MULTIFUNCTIONAL MATERIALS

DAVID CREED<sup>†</sup>, ANSELM C. GRIFFIN<sup>†, \*</sup>, CHARLES E. HOYLE<sup>†, \*</sup> AND KRISHNAN VENKATARAM<sup>†</sup>

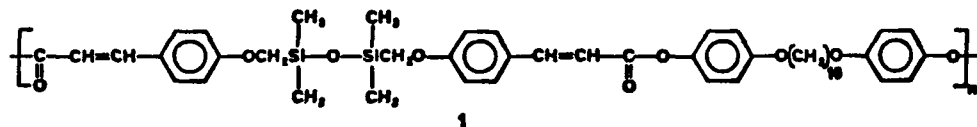
Departments of Chemistry\* and Polymer Science\*, University of Southern Mississippi, Hattiesburg, MS 39406-5043

## ABSTRACT

UV-VIS spectral comparison with model compounds and isolation of the major product from preparative photolysis of one of the models has been used to show that the predominant photochemical reactions in the solid state of an aryl cinnamate polymer are 2+2 cycloaddition and photo-Fries rearrangement.

## INTRODUCTION

Multifunctional macromolecules represent a new concept in polymer materials science. These are organic polymers which combine desirable physical and mechanical properties with one or more functional properties such as novel optical or conductive behavior [1]. Liquid crystalline (LC) polymers have aroused considerable interest owing to their inherent orientational ordering which can be preserved in the solid state and thereby give rise to polymers of high tensile modulus along the direction of orientation. We have been interested in soluble, easily processable photoactive aryl cinnamate LC polymers for some time [2-5], partly because of a fundamental interest in the effect of a liquid crystalline environment on photochemistry and photophysics and partly due to the practical possibility of making biaxially strengthened films or fibers through photocrosslinking. In our earlier work [2] we have investigated the photochemistry of novel main chain thermotropic aryl cinnamate polymers such as 1.



We have also demonstrated that free standing films of a similar polymer could be used as write-once optical recording media [3]. The three principal photochemical pathways available for aryl cinnamate polymers such as **1** are crosslinking and insolubilization via 2+2 cycloaddition leading to the formation of a cyclobutane ring, photo-Fries rearrangement to give the 2'-hydroxy chalcone derivative likely responsible for yellowing of the polymer film and cis-trans isomerization [2]. The photochemistry of polymer **1** has been examined as a function of phase type and temperature and the results indicate that there is pronounced aggregation of the cinnamate chromophores in the LC (nematic) phase, which influences the nature and amount of photoproducts formed [2,6]. In this paper, we shall present evidence from model compound studies to elucidate and substantiate our observations on the photoprocesses in these liquid crystalline polymers.

## EXPERIMENTAL

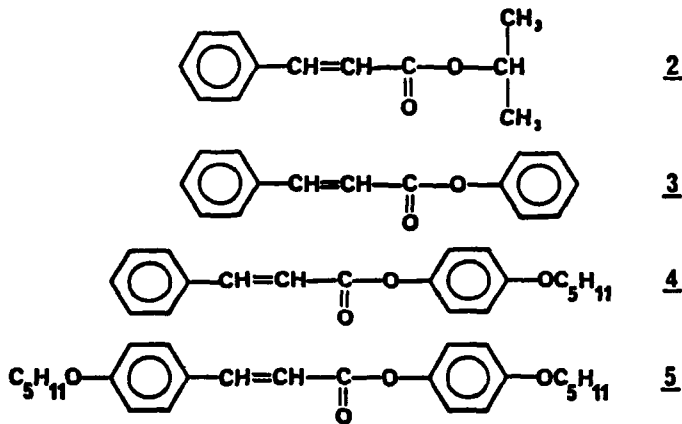
## General

Proton and carbon NMR spectra were recorded on a  $300\text{ MHz}\text{ Bruker NMR}$  spectrometer. Mass spectral data were obtained by direct injection into the ion source of a Hewlett Packard GC-Mass spectrometer. Melting points for all compounds were determined using a Thomas-Hoover capillary melting apparatus. Infrared spectra were recorded on a Mattson Polaris FT-IR spectrophotometer and elemental analyses were performed by Galbraith Laboratories, Knoxville, TN. All UV-VIS spectra were recorded on a Perkin-Elmer Model 552 spectrophotometer. Polarized light microscopy to determine liquid crystalline transitions was conducted using a Reichert-Thermovar microscope equipped with a Mettler FPS/52 heating stage. All temperatures recorded are in degrees Celsius.

Mat. Res. Soc. Symp. Proc. Vol. 175. © 1990 Materials Research Society

Preparation of model cinnamates

The model cinnamates that were examined in this study are shown below.



Isopropyl cinnamate (2)

Model compound **2** was prepared by refluxing trans-cinnamic acid (10 g, 0.07 mol) with isopropyl alcohol (40.5 g, 0.21 mol) in the presence of concentrated sulfuric acid as catalyst (2 ml), for about 15 h. The excess alcohol was removed by a rotary evaporator and the remaining liquid was dissolved in chloroform. The solution was then washed twice with water, once with aqueous sodium bicarbonate (5% w/v) and then once again with water in a separatory funnel. Chloroform was removed from the organic layer under reduced pressure leaving a colorless, sweet smelling liquid, which was dried overnight with anhydrous sodium sulfate and filtered. Distillation under vacuum (90° C/1mm Hg) gave 8.3 g of ester (65%). Infrared and proton NMR spectra were comparable to authentic sample spectra in the literature. UV-VIS (chloroform);  $\lambda_{\text{max}} = 277$  nm. Elemental analysis for  $\text{C}_{12}\text{H}_{14}\text{O}_2$ ; Calculated: C, 75.79%; H, 7.37%. Found: C, 75.46%; H, 7.26%.

Phenyl cinnamate (3)

Trans-cinnamic acid (5 g, 0.03 mol) was refluxed with excess thionyl chloride for 30 minutes. Unreacted thionyl chloride was removed in a rotary evaporator and finally under high vacuum. A 1:1 stoichiometric amount of phenol (3.18 g, 0.03 mol) was dissolved in pyridine (20 ml) and added to the acid chloride. Stirring was maintained for 24 h and then the reaction mixture was poured into 200 ml of aqueous hydrochloric acid (30% v/v). The precipitated solid was filtered, washed repeatedly with water and dried thoroughly in air. It was finally recrystallized from ethanol/water to give 6.05 g (80%) of white crystals. m.p. 75-76° C; lit. [7] 75-76° C. Infrared and proton NMR spectroscopy were consistent with the assigned structure. UV-VIS (chloroform);  $\lambda_{\text{max}} = 285$  nm. Elemental analysis for  $\text{C}_{15}\text{H}_{12}\text{O}_2$ ; Calculated: C, 80.36%; H, 5.36%. Found: C, 80.18%; H, 5.33%.

4-Pentyloxyphenyl Cinnamate (4)

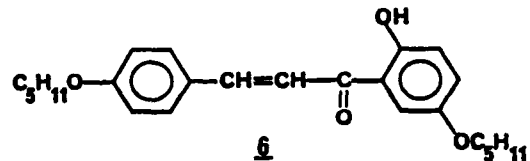
The same procedure as outlined for **3** was used. Trans-cinnamic acid (5 g, 0.03 mol) was converted to the acid chloride using thionyl chloride. It was then reacted with 4-pentyloxyphenol (6.08 g, 0.03 mol) dissolved in pyridine (20 ml) for 24 h and the ester recovered in a similar manner. The ester was recrystallized from ethanol/water to give 8.37 g (80%) of white crystals. m.p. 74-75° C. IR (KBr):  $\text{cm}^{-1}$  2961, 2941, 2871, 1727, 1634, 1504, 1476, 1249, 1190, 1163, 1009, 855, 555.  $^1\text{H}$  NMR (chloroform d),  $\delta$  0.93 (t, 3H),  $\delta$  1.16-2.5 (m, 6H),  $\delta$  3.90 (t, 2H),  $\delta$  6.56-7.86 (m, 11H). UV-VIS (chloroform);  $\lambda_{\text{max}} = 283$  nm. Elemental analysis for  $\text{C}_{20}\text{H}_{22}\text{O}_3$ ; Calculated: C, 77.42%; H, 7.10%. Found: C, 77.77%; H, 7.20%.

4-pentyloxyphenyl 4'-pentyloxy cinnamate (5)

4-Pentyloxy cinnamic acid needed for the synthesis of  $\xi$  was prepared by alkylating methyl 4-hydroxycinnamate (15 g, 0.08 mol) with iodopentane (16.68 g, 0.08 mol) in DMF at 110° for 5 h using potassium carbonate as base, similar to that outlined in literature [8] for an analogous reaction. The mixture was then poured into a large volume of ice water and the resulting solid collected by filtration, air dried and recrystallized from 75% ethanol (m.p. 64-66° C, yield = 47%). The resulting methyl 4-pentyloxy cinnamate (10 g, 0.04 mol) was then hydrolyzed to the acid by refluxing overnight in a solution of potassium hydroxide in ethanol (10% w/v, 150 mol). The acid was then precipitated by acidification of the solution with aqueous HCl (30% v/v, 300 ml), collected by filtration, washed well with water, air dried and recrystallized from 85% ethanol (yield, 64%). K 139 N 179 I (K-crystal, N-nematic, I-isotropic). lit. [9] K 139.5 N 179.5 I. Infrared and proton NMR spectra are consistent with the proposed structure. The cinnamate model compound  $\xi$  was then prepared using the same procedure described above for  $\xi$ . 4-Pentyloxy cinnamic acid (5 g, 0.02 mol) was converted to the acid chloride and then reacted with 4-pentyloxyphenol (3.85 g, 0.02 mol) dissolved in pyridine (20 ml) for 24 h. The workup of the product was the same as for  $\xi$ . Recrystallization was from 95% ethanol and gave 6.6 g of white crystals (78%). K 107 N 124 I. IR (KBr):  $\text{cm}^{-1}$  2957, 2936, 2871, 1721, 1632, 1510, 1395, 1287, 1252, 1196, 1152, 868, 819, 566.  $^1\text{H}$  NMR (chloroform d):  $\delta$  0.92 (t, 6H),  $\delta$  1.16-2.5 (m, 12H),  $\delta$  3.92 (m, 4H),  $\delta$  6.42-7.80 (m, 10H). UV-VIS (chloroform);  $\lambda_{\text{max}}$  = 317 nm. Mass spectrum;  $M^+$  at  $m/e$  = 396, parent peak at  $m/e$  = 217 (loss of p-alkoxyphenoxy radical). Elemental analysis for  $\text{C}_{25}\text{H}_{32}\text{O}_4$ ; Calculated: C, 75.76%; H, 8.08%. Found: C, 75.37%; H, 7.88%.

Preparation of the photo-Fries model (4,5'-dipentyloxy-2'-hydroxychalcone) (6)

The photo-Fries model compound  $\xi$  was obtained by preparative photolysis of 4-pentyloxyphenyl 4'-pentyloxy cinnamate,  $\xi$ .



Compound  $\xi$  (0.5 g) was dissolved in 40 ml of chloroform (concentration =  $3.156 \times 10^{-2}$  moles/liter) and saturated with pre-purified nitrogen for 30 minutes. The solution was then irradiated under a nitrogen atmosphere using a medium pressure mercury lamp with pyrex filter. The solution became yellow almost immediately. Irradiation was continued for 45 h to maximize the yield of the photo-Fries product. Cinnamate starting material was still present in the mixture (by TLC) after this time period. The Fries product was separated from the mixture by preparative TLC on silica gel plates using a 95/5 (v/v) mixture of chloroform/hexane. Repeated recrystallization separately from methanol and then hexane removed starting material contamination. Final recrystallization from 95% EtOH gave an orange crystalline material with a m.p. of 77-78° C. IR (KBr):  $\text{cm}^{-1}$  3442, 2958, 2940, 2867, 1641, 1563, 1424, 1253, 1172, 1020, 832, 580.  $^1\text{H}$  NMR (acetone d<sub>6</sub>):  $\delta$  0.93 (t, 6H),  $\delta$  1.18-2.0 (m, 12H),  $\delta$  4.02 (m, 4H),  $\delta$  6.88-7.88 (m, 9H). UV-VIS (methanol);  $\lambda_{\text{max}}$  = 360 nm. Mass spectrum;  $M^+$  at  $m/e$  = 396, parent peak at  $m/e$  = 136. A UV-VIS spectrum of the Fries model in methanol compares favorably with standard UV-VIS spectra of 2'-hydroxy chalcones in the literature. The IR spectrum shows the loss of ester carbonyl at  $1721 \text{ cm}^{-1}$  and appearance of the keto-carbonyl at  $1641 \text{ cm}^{-1}$  and the weak hydroxyl stretch around  $3400 \text{ cm}^{-1}$ .

Photolysis of cinnamate models

Qualitative photochemical studies were carried out using a Bausch & Lomb SP 200 high pressure mercury lamp source with monochromator [2]. Irradiations were performed in chloroform at model concentrations ranging from 0.7 - 0.9 mg/100 ml chloroform and at wavelengths corresponding to the  $\lambda_{\text{max}}$  values of the appropriate cinnamate. Disappearance of the cinnamate chromophore as a function of irradiation time was monitored using a Perkin-Elmer model 552 UV-VIS spectrophotometer.

## RESULTS AND DISCUSSIONS

Photolysis of a dilute solution of the cinnamate models **2** and **3** are shown in Figs. 1 and 2, respectively.

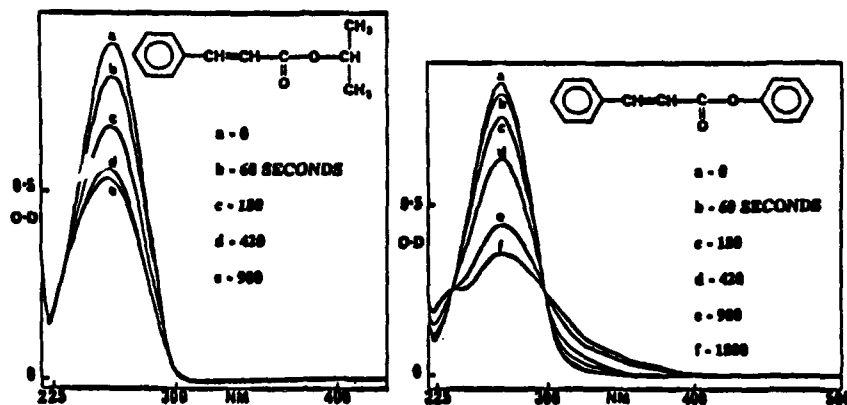


Fig. 1 Solution photolysis of model **2** in chloroform at 277 nm. Times indicated are cumulative irradiation times.

Fig. 2 Solution photolysis of model **3** in chloroform at 285 nm. Times indicated are cumulative irradiation times.

It is immediately obvious that a distinct difference exists between the two spectra in the long wavelength region beyond 300 nm. The predominant reaction occurring in the solution photolysis of isopropyl cinnamate **2** is likely cis-trans isomerization, until a photostationary state is attained (Fig. 1). This has been observed upon irradiation of dilute solutions of other aliphatic cinnamates such as ethyl cinnamate where no dimer is formed [10,11]. Solid state dimerization of cinnamic acid and its derivatives has been long known and the topochemical control of this and other dimerizations has been elegantly established by Schmidt et al [12]. The topochemical postulate essentially states that dimerization takes place with minimum molecular movement and that pre-orientation and an optimum separation distance of interacting chromophores are prerequisites for reaction to occur in the solid state. It can be argued that dimer formation does not take place in dilute solutions due to the low encounter probability for such a bimolecular reaction and the extremely short singlet lifetimes that have been observed for analogous cinnamates [13]. Reiser et al. [14] have, however, observed dimerization in ethyl cinnamate glasses indicating that some pre-organization exists in this rigid matrix due, probably, to a dipolar interaction of the cinnamate chromophores. Hence the major photoreaction in the solution photolysis of aliphatic cinnamates like **2** is the unimolecular cis-trans isomerization. There is no evidence for other unimolecular reactions such as ester cleavage that have been observed for some alkyl cinnamates [15].

Progressive irradiation of the phenyl cinnamate (Fig. 2) in solution results in a continued loss of the absorption due to the cinnamate chromophore and buildup of a new absorption tailing beyond 300 nm. This long wavelength absorption is attributed to a photo-Fries product and has been observed on photolysis of the polymer **1** both in solution and in film [2]. This new band is not seen on photolysis of the aliphatic cinnamate **2** (Fig. 1) as it is not an aryl ester and therefore cannot undergo a photo-Fries rearrangement. Also, analogous polymers in which the aromatic ester linkage has been replaced by an aliphatic ester bond do not show this long wavelength absorption [4]. Models **4** and **5** also exhibit the same general spectral features and photochemical behavior as **3**. Model **5** is a more chemically analogous model for the polymer and this is reflected in the similarity of its solution spectrum and photolysis behavior (Fig. 3) when compared to that of the polymer in solution [2].

Only the ortho photo-Fries product can be formed for the polymer as well as for **5** since the para positions in both cases are blocked by alkoxy substituents. Isolation of the ortho photo-Fries product **6** from the preparative photolysis of **5** and comparison of its spectral shape and long wavelength absorption with that of the photolysis spectrum of **5** further confirms that the ortho photo-Fries product is responsible for the new band at longer wavelengths. The major product in the preparative photolysis of **5** is the photo-Fries product and no dimer could be isolated under these conditions. Similar observations have been made by other groups working with phenyl cinnamates [16,17]. No attempt was

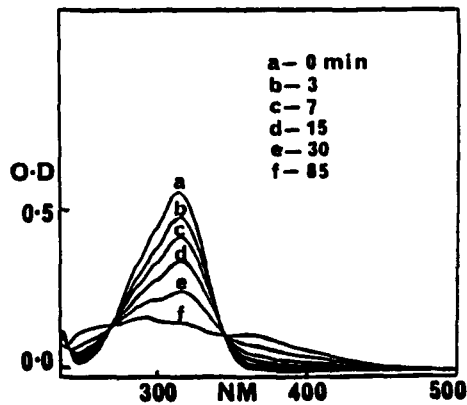


Fig. 3 Solution photolysis of model 5 in chloroform at 317 nm. Times indicated are cumulative irradiation times.

made to isolate any other photo products although their presence could be observed during preparative TLC. The fact that no dimer could be isolated in solution can be rationalized on the basis of the stringent requirements for such a bimolecular reaction and the extremely short singlet lifetimes (ps) that have been observed for a related phenylenediacrylic acid based monomer and polymer [18]. The photo-Fries rearrangement, being a unimolecular process, is more facile in solution, where greater mobility is available for structural reorganization. Such mobility effects have been observed by us upon photolysis of the polymer film as a function of temperature [2,6]. It is also quite probable that other radical additions [19] leading to saturation of the double bond can occur especially in solution where H-atom abstraction from a solvent like chloroform can be envisaged. Preliminary indications of such a possibility could be seen on photolysis of 5 in carbon tetrachloride where no H-atom abstraction can occur. Some qualitative differences in the spectrum can be seen although the Fries product still seems to be the major product. Formation of the dimer in the polymer film has been evidenced by the

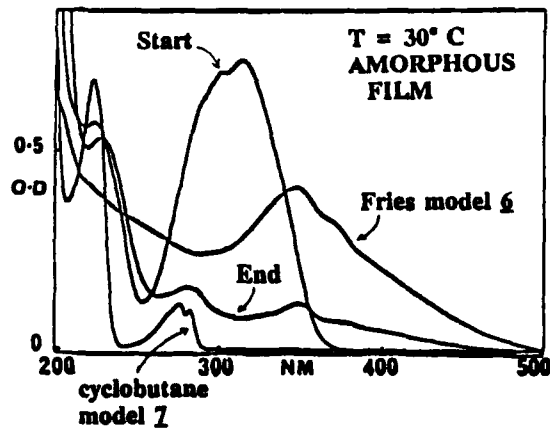


Fig. 4 Composite spectra of the dimer model 7 and the Fries model 6 in PMMA with the initial and exhaustively photolyzed polymer 1 film at 313 nm.

appearance of a peak at 45 ppm in the  $^{13}\text{C}$  solid state NMR spectrum of the photolyzed polymer, detailed infrared analysis [4] and by UV-VIS comparison with a small molecule dimer model 3-(4'-methoxyphenyl) propanoic acid 7 [2]. On overlaying the spectrum of the dimer model 7 and the Fries model, 6 in PMMA, with the exhaustively irradiated polymer film (Fig. 4) it can be seen that the spectral shape of the photolyzed polymer can be approximated reaffirming that 2+2 cycloaddition and photo-Fries reactions are the major contributors in the photochemistry of the aryl cinnamate polymer in the solid state.

### CONCLUSIONS

We have shown through UV-VIS spectral comparison with model compounds and isolation of the major product from preparative photolysis of 5 that the predominant photochemical reactions in the solid state of an aryl cinnamate polymer such as 1 are 2+2 cycloaddition and photo-Fries rearrangement. Although the photo-Fries reaction is usually considered to be an undesirable event because of yellowing of the polymer film, it could have interesting applications in providing effective second harmonic generation for nonlinear optics due to the extended push-pull pi-electronic conjugation in the resulting chalcone chromophore of the photo-Fries product. Some chalcone derivatives have been known to have high second order polarizabilities [20] and this is an avenue we are pursuing.

### ACKNOWLEDGEMENTS

We wish to acknowledge partial support of this work by the National Science Foundation through Grant No. RII-8902064, the State of Mississippi, and the University of Southern Mississippi (DC and CEH), and by the Air Force Office of Scientific Research, F49620-88-C-0068 (ACG). Initial funding was generously provided by Armstrong World Industries.

### REFERENCES

- 1) A. Buckley, G.W. Calundann and A.J. East, SPIE, 878, 94 (1988).
- 2) D. Creed, A.C. Griffin, J.R.D. Gross, C.E. Hoyle and K. Venkataram, Mol. Cryst. Liq. Cryst. 155, 57 (1988).
- 3) A.C. Griffin, C.E. Hoyle, J.R.D. Gross, K. Venkataram, D. Creed and C.B. McArdle, Makromol. Chem. Rapid. Commun. 9, 463 (1988).
- 4) D.M. Haddleton, D. Creed, A.C. Griffin, C.E. Hoyle and K. Venkataram, Makromol. Chem. Rapid. Commun. 10, 391 (1989).
- 5) D.M. Haddleton, K. Venkataram, D. Creed, A.C. Griffin and C.E. Hoyle, Proceedings of the Seventeenth North American Thermal Analysis Society, 2, 430 (1988).
- 6) D. Creed, A.C. Griffin, C.E. Hoyle, K. Venkataram and D.M. Haddleton presented at Macromolecules 89, Oxford, UK, 1989 (unpublished).
- 7) Organic Syntheses, Coll. Vol. III, edited by E.C. Horning (Wiley, New York, N.Y., 1955), p. 714.
- 8) A.C. Griffin and S. Havens, J. Poly. Sci., Polym. Lett. Ed. 19, 951 (1981).
- 9) G.W. Gray and B. Jones, J. Chem. Soc. 1467 (1954).
- 10) J. Rennert, S. Soloway, I. Waltcher and B. Leong, J. Am. Chem. Soc. 94, 7242 (1972).
- 11) R.B. Frings and W. Schnabel, Polymer Photochemistry, 3, 325 (1983).
- 12) G.M.J. Schmidt, M.D. Cohen, J. Chem. Soc. 1996 (1964).
- 13) F.D. Lewis, S.L. Quillen, J.E. Elbert, S. Schneider and P. Geiselhart, J. Photochem. Photobiol. A 47(2), 173 (1989).
- 14) P.L. Egerton, E.M. Hyde, J. Trigg, A. Payne, P. Beynon, M.V. Mijovic and A. Reiser, J. Am. Chem. Soc. 103, 3859 (1981).
- 15) V. Ramesh, R.G. Weiss, J. Org. Chem. 51, 2535 (1986).
- 16) a) H. Obara and H. Takahashi, Bull. Chem. Soc. Jpn. 40(4), 1012 (1967). b) V.T. Ramakrishnan and J. Kagan, J. Org. Chem. 35(9), 2901 (1970).
- 17) A.K. Singh and T.S. Raghuraman, Tetrahedron Lett. 26(34), 4125 (1985).
- 18) M. Graley, A. Reiser, A.J. Roberts and D. Phillips, Macromolecules. 14, 1752 (1981).
- 19) P.L. Egerton, E. Pitts and A. Reiser, Macromolecules, 14, 95 (1981).
- 20) E.M. Ebeid, M.H. Abdel-Kader, R.M. Issa and S.A. El-Daly, Chem. Phys. Lett. 146(3), 331 (1988).



92-18247



AD-P007 456



41

 MULTI-FUNCTIONAL DEVICE APPLICATIONS OF NONLINEAR OPTICAL POLYMER MATERIALS. R. Lytel and G.F. Lipscomb, Lockheed Palo Alto Research Lab. O-9701, B-202, Palo Alto, CA 94304

#### ABSTRACT

Recent developments in the application of electro-optic polymer materials to perform multi-functional roles in integrated optic device applications are summarized and future requirements for practical field operation are discussed.

#### INTRODUCTION

Organic and polymeric materials and devices have been the center of intense scientific and engineering investigation for many years due to the extraordinary nonlinear optical and electro-optic properties of certain conjugated  $\pi$ -electron systems and due to the fundamental success of molecular engineering in creating new materials with appropriate linear and nonlinear optical properties.<sup>[1]</sup> As a result of this fundamental work, materials, in which the microscopic origin of the *nonlinear susceptibility* is well understood and the bulk chemical and mechanical properties are well characterized are now available for implementation in laboratory prototype devices.

Organic electro-optic (E-O) materials offer potentially significant advantages over conventional inorganic electro-optic crystals, such as  $\text{LiNbO}_3$  and  $\text{GaAs}$ , in several key areas of integrated optics technology, as summarized in Table 1, including materials parameters, processing technology and fabrication technology. The most striking advantage, and the reason for the intense interest in these materials, is due to the intrinsic difference in the electro-optic mechanism. Unlike inorganic ferroelectric crystals, where the electro-optic response is dominated by phonon contributions, the electro-optic effect in certain organic materials arises in the electronic structure of the individual molecules, yielding large E-O coefficients with little dispersion from dc to optical frequencies (second harmonic generation) and low dielectric constants. Poled polymer organic materials have been demonstrated which exhibit electro-optic coefficients comparable to that of  $\text{LiNbO}_3$ <sup>[2]</sup> coupled with a dielectric constant nearly an order of magnitude smaller. The low dielectric constant is essential to the success of high bandwidth modulators due to the resulting lower velocity mismatch between the RF and optical waves, and could lead to an improvement of more than a factor of 10 in the bandwidth-length product over current  $\text{LiNbO}_3$  devices. The microscopic molecular origin of the second order nonlinear

susceptibility,  $\chi^{(2)}$ , and linear electro-optic coefficient,  $r$ , in organic NLO materials is now well understood theoretically[3,4] and experimentally[5,6], and the materials are ready for initial exploitation.

The materials research effort in recent years has centered on the inclusion of the nonlinear optical moiety in a guest/host or polymer system with appropriate linear optical, mechanical and processing properties and the artificial creation of the desired symmetry through electric field poling.[7,8] These materials can then be simply and rapidly spun coat into high quality thin films, processed with standard photolithographic techniques and poled quickly and efficiently. A table of the materials and measured electro-optic coefficients from various groups is presented in Table 2. In addition, channel waveguides and integrated optic circuits can be defined by the poling process itself[9] or by a variety of well understood micro-machining techniques. These processes represent a considerable increase in fabrication flexibility and processing simplicity over current Titanium indiffused  $\text{LiNbO}_3$  waveguide technology, which requires processing at temperatures approaching 1000°C after expensive and difficult crystal growth.

Table 1 Current  $\text{LiNbO}_3$  and Projected Organic Integrated Optics Technologies.

<u>PHYSICAL &amp; DEVICE PROPERTIES</u>	<u>Ti:Lithium Niobate</u>	<u>Organic Polymers</u>
Electro-optic coefficient (pm/V)	32	10-50
Dielectric constant	28	4
Loss (dB/cm @ $\lambda=1.3$ mm)	0.1	0.2-0.5
Space-bandwidth product (GHz-cm)	10	120
Crystal Growth Temperature, °C	1000	NA
Waveguide Processing Temperature, °C	1000	150-200
Waveguide Processing Time	10 hr.	10 min.
Multiple Layers Possible	No	Yes
Fabrication & processing	difficult	simpler
Packaging	expensive	UNKNOWN
Maturity	>30 years	<10 years

Table 2 Reported Electro-Optic Coefficients in Poled Polymers

- AT&T BELL LABS. (H.E. Katz et. al, *Mtls. Res. Soc.* **109**, 127 (1987))
  - DCV/PMMA,  $r = 32 \text{ pm/V}$ ,  $\lambda = 1.356 \mu\text{m}$  (guest/host)
  - TCV/PMMA,  $r = 53 \text{ pm/V}$ ,  $\lambda = 1.356 \mu\text{m}$  (guest/host)
- AT&T BELL LABS. (K. Singer et. al, *Appl. Phys. Lett.* **53**, 1800 (1988))
  - DCV-MMA,  $r = 15 \text{ pm/V}$ ,  $\lambda = 0.8 \mu\text{m}$ , corona poled
- AKZO RESEARCH (G. Mohlmann, IGWO/OFC '89, Feb. 89)
  - DANS,  $r = 28 \text{ pm/V}$ ,  $\lambda = 1.3 \mu\text{m}$  (random copolymer)
  - MONS,  $r = 18 \text{ pm/V}$ ,  $\lambda = 1.3 \mu\text{m}$  (random copolymer)
- HOECHST CELANESE (D. Haas, SPIE, San Diego, 1989)
  - $r = 40 \text{ pm/V}$ ,  $\lambda = 1.3 \mu\text{m}$

#### APPLICATIONS TO INTEGRATED OPTIC DEVICES

A serious limitation of  $\text{LiNbO}_3$  modulators is the velocity mismatch between the electrical wave traveling down the electrodes and the optical wave traveling down the optical waveguide. The RF field from the electrodes extends into the dielectric material and thus travels with a velocity  $v = c/\sqrt{\epsilon_{\text{eff}}}$  where  $c$  is the free space velocity of light and  $\epsilon_{\text{eff}}$  is the effective dielectric constant of the waveguide structure.  $\epsilon_{\text{eff}}$  depends on the details of the electrode structure itself.  $\epsilon_{\text{eff}}$  is generally a linear function of  $\epsilon_s$ , the dielectric constant of the electro-optic material. For  $\text{LiNbO}_3$   $\epsilon_s = 38$ , while for the poled polymer films  $\epsilon_s \sim 3.5$ . The light, however, travels down the waveguide with a velocity  $v = c/n$ , where  $n$  is the index of refraction of the waveguide material, which for  $\text{LiNbO}_3$  is  $n = 2.2$  and for the poled polymer films  $n \sim 1.6$ . Thus, the optical and electrical waves traveling down the device structure gradually get out of phase with each other, and for a given device interaction length there is a maximum frequency,  $f_c$ , at which the device can be driven. The high speed modulation limit of the material can be estimated by the bandwidth length product approximately given by:[10]

$$f_c L \approx \frac{c}{(\sqrt{\epsilon_{\text{eff}}} - n)} \quad (1)$$

For  $\text{LiNbO}_3$ ,  $f_c L = 9.6 \text{ GHz-cm}$  for a standard Mach Zehnder configuration[10], while for the organic poled polymer films discussed here  $f_c L \sim$

120 GHz-cm. Thus for this class of materials the primary limitation of LiNbO<sub>3</sub> for high speed modulation in the 20 - 40 GHz range is effectively removed. The limiting factor for the poled polymer films will probably be RF loss in the electrodes, which is increasing as the square root of the drive frequency.

#### Poled Polymer Waveguides

Integrated optic devices have been fabricated at LMSC based on organic polymers by spinning the material into high quality thin films on optical substrates. As spun, the films are isotropic and thus exhibit no linear electro-optic effect,  $r$ . In addition to inducing a non-centrosymmetric structure to achieve a macroscopic electro-optic effect, a second major transformation must be engineered in the material to enable the fabrication of integrated optic circuits. Channel waveguides must be formed to confine and guide the light from one active element of the integrated optic circuit to another. Electric field poling has been extensively studied as a means to partially align nonlinear optical molecules in an inert polymer matrix to induce a macroscopic  $r$ .[7] Figure 1 illustrates a new, powerful method, developed by LMSC, by which channel waveguides can be fabricated by the poling process itself [9]. An electrode structure, defining the channel waveguides, is patterned on an optical substrate, using standard photolithographic techniques, and covered with a buffer layer, to isolate the active waveguide layer from the electrode. The buffer material must be chosen to have an index lower than the guiding layer and to be compatible with the required processing. The electro-optic polymer is spun directly onto the lower buffer layer, and different buffer layers must often be used with different nonlinear polymers. A metal ground plane is then deposited directly onto the nonlinear polymer for poling. The nonlinear layer is then poled by applying an electric field above the polymer glass transition temperature and cooling the sample to room temperature under the influence of the field. The degree of alignment induced, and the resultant electro-optic coefficient, can be calculated based on a statistical average of the molecular susceptibilities.[7] In this case only those regions of the material defined by the electrode pattern on the electro-optic material are poled.

Since most organic nonlinear optical molecules also possess an anisotropic microscopic linear polarizability, the poled region becomes birefringent.[11] The poled regions are uniaxial, with  $n_e$  oriented along the direction of the poling field. Consequently, TM waves propagating along the device structure will experience a greater refractive index in the poled regions than in the unpoled regions, and so can be confined in the lateral dimension. Thus, by applying the

poling fields using electrodes patterned to define the waveguide network, including both active and passive sections, no further patterning of the organic NLO layer is required to form the channel E-O waveguide structures. The devices are then completed by etching off the poling electrode, applying an upper buffer layer and depositing the patterned switching electrodes, as shown in Figure 1. The switching electrodes are positioned to address only the sections of the guide desired to be active. A photograph of a section of poled waveguide is shown in Figure 2. The region on the left is unpoled and the light fans out and is clearly unguided. The region on the right has been poled and the light is clearly guided and confined to the waveguide region. Using this technique, LMSC has fabricated poled polymer channel waveguides, and has demonstrated modulators, couplers, and bends in electro-optic polymer materials.

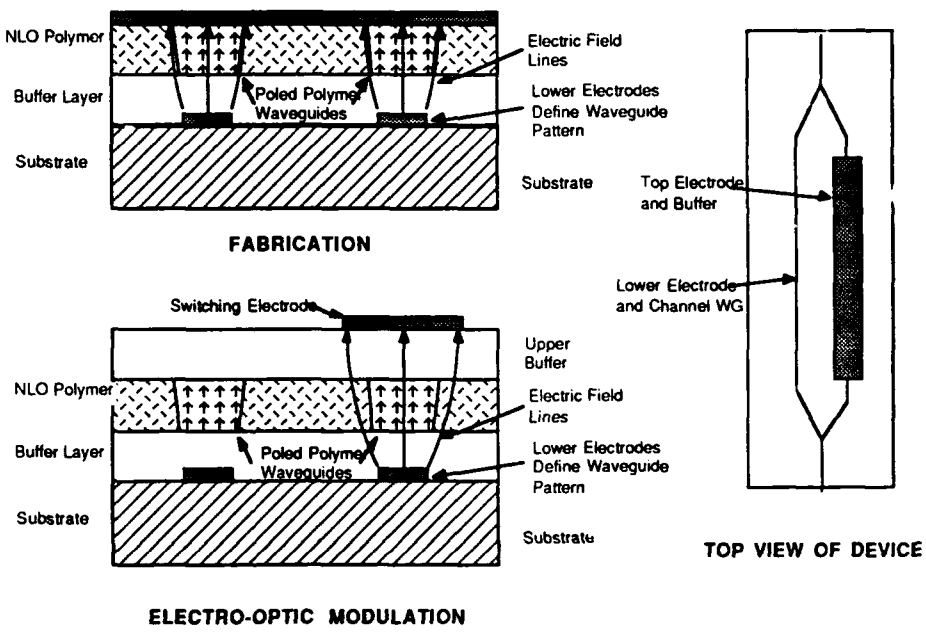


Figure 1. Fabrication of Channel Waveguide by Electric Field Poling.

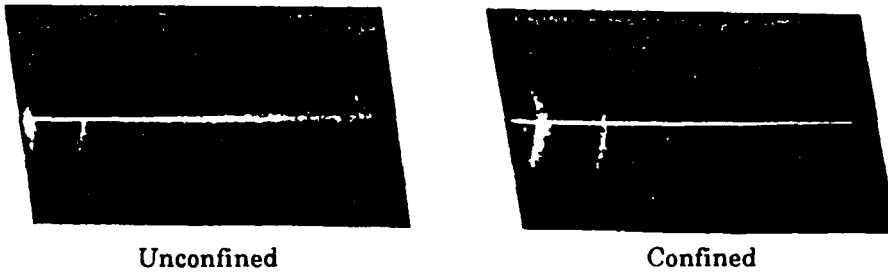


Figure 2. Photograph of a Poled Polymer Waveguide.

### Poled Polymer Phase Modulator

Using the poled polymer waveguide fabrication technique a 1.0 GHz traveling-wave phase modulator was constructed at LMSC and is shown schematically in Figure 3. This device was constructed to investigate the material response at RF frequencies and to verify theoretical performance predictions and was not optimized for optical or electrical performance and was not packaged.

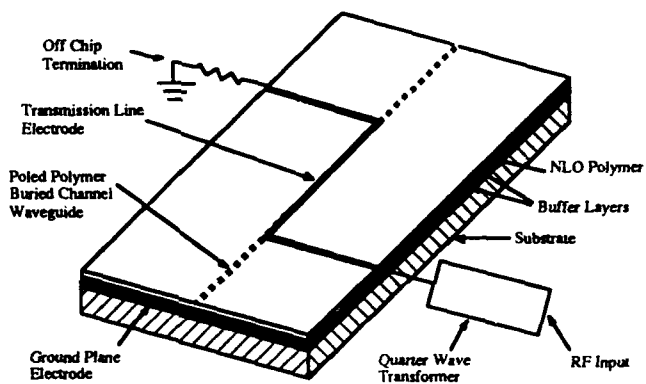


Figure 3 Schematic Diagram of LMSC Traveling Wave Phase Modulator

To fabricate the device a ground plane electrode, buffer layer, E-O polymer and upper buffer layer were deposited on a glass substrate. A straight channel waveguide was fabricated by electric field poling and a 9.5 ohm microstrip electrode was deposited on the upper buffer layer over the active channel. The electrode length over the waveguide was 3 cm. A quarter wave transformer resonant at 260 MHz was used to impedance match the microstrip to the driving electronics and the microstrip was terminated into 9.5 ohms off of the chip. Prism coupling was used to couple light into and out of the device and the resultant phase modulated beam was mixed with an external arm reference beam on the photodetector. Shown in Figure 4 is the signal at 260 MHz for a drive voltage of 8.7 V. This represents a phase modulation of 60% of full wave and yields a value for the electro-optic coefficient,  $r$ , exactly the same as that measured at low frequency. Thus no dispersion is observed in  $r$  out to 260 MHz.

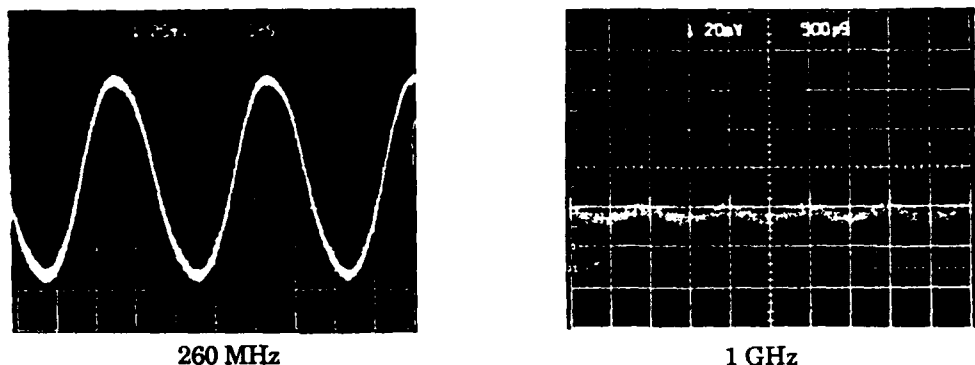


Figure 4 Response of the Phase Modulator at 260 MHz and 1 GHz

Figure 4 also shows the modulated signal at 1.0 GHz. Clear modulation is observed, but the response of the detector, oscilloscope, impedance transformer and electronics were all dropping off rapidly at this point, and therefore, quantitative measurements were not possible.

#### CONSIDERATIONS FOR PRACTICAL APPLICATIONS

Organic electro-optic materials now exhibit very attractive primary properties for integrated optics applications. The ultimate practicality and utility of this new technology, however, will be determined as much by the secondary materials properties as by the primary electro-optic effects. For these applications, primary properties are defined as those that directly affect the optical device function, including electro-optic coefficient, index of refraction, microwave dielectric constant, and propagation loss. Secondary properties are those which indirectly affect the primary device function through altering the processability of the materials, the compatibility of materials and processes with other system components, the stability of materials and structures or the lifetime and reliability of the final device. Some examples of secondary properties include the thermal coefficient of expansion (TCE), thermal stability of the poled state, hydrolytic stability, chemical compatibility and UV sensitivity, as well as a whole host of processing issues. These secondary properties are only now beginning to be addressed by the same molecular engineering techniques that led to the substantial progress in primary properties that has been reported to date.

Before a system designer will select and use a new technology he must have confidence in the long term stability and reliability of the device prototypes. The

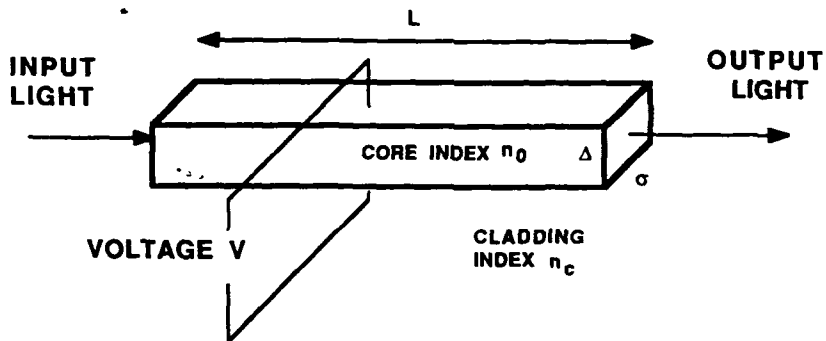


Figure 5 Segment of an Electro-optic Waveguide.

device must form an intrinsically stable package capable of meeting Mil-Spec standards as well as commercial standards. Common temperature requirements are operation up to 125°C and storage up to 200°C. The device should add no additional electrical power requirements and should require no more than normal thermal management. Furthermore, the materials and device structures should be capable of withstanding standard assembly and packaging processes. The finished product must be compatible with subsystem integration, without additional packaging requirements.

As just one example of how secondary properties can affect primary optical device function, we consider the performance of an electro-optic modulator as a function of temperature. Shown in Figure 5 is a single segment of active electro-optic polymer waveguide. The figure of merit for electro-optic phase modulation for this waveguide is the half wave voltage,  $V_\pi$ , and is given by:

$$V_\pi = (\lambda/n_0^2 r)(\Delta/L) \quad (2)$$

$L$  is the length of the waveguide,  $n_0$  is the index of refraction of the waveguide,  $\Delta$  is the cross-sectional dimension,  $r$  is the electro-optic coefficient and  $\lambda$  is the wavelength of the light. The variation in the half-wave voltage as a function of fabrication tolerances and the thermal coefficient of expansion (TCE) is given by:

$$\delta V_\pi/V_\pi = \delta\lambda/\lambda - 3\delta n_0/n_0 - \delta r/r + \delta\Delta/\Delta - \delta L/L \quad (3)$$

For this example it is assumed that a low TCE substrate, such as Silicon, with TCE = 3 ppm/°C is used and effectively pins the polymer waveguide layers in the lateral dimensions. For an electro-optic polymer material with a TCE ~ 100 ppm/°C the half-wave voltage can vary by  $\delta V_\pi/V_\pi \sim 15 - 55\%$  over operating

temperature ranges of -40°C to +125°C. This degree of variation is too severe for normal device operation and efficient device design. For this reason, new polymer backbone materials are now being investigated with TCE ~ 40 ppm/°C and would limit temperature variations to  $\delta V_n/V_n \sim 5\%$ . In this way, the secondary properties of electro-optic polymers can be engineered based on device function and expected operating environment.

## CONCLUSIONS

Organic electro-optic materials with primary properties meeting or exceeding those of standard inorganic electro-optic crystals have now been reported by several groups. The theoretical basis for the nonlinear optical response of organic materials has been well established and molecular engineering techniques have been applied to improve the nonlinear and electro-optic responses achieved. Furthermore, organic electro-optic materials appear to offer significant potential advantages in performance, fabricability, flexibility and cost over conventional inorganic crystalline materials. Electro-optic polymer materials have not yet progressed to the point, however, where full-up field testable proto-type devices can be evaluated in direct competition with inorganic based electro-optic devices and much less to the point where practical devices exhibiting superior performance can be manufactured reproducibly and inexpensively. In order for electro-optic polymers to move from the laboratory into a practical technology, the same molecular engineering techniques that resulted in the exceptional primary electro-optic properties must be applied to optimizing the secondary properties. The next key challenge in the development of electro-optic polymers will be to achieve the long-term reliability and stability required for commercial and defense applications.

---

## REFERENCES

- 1 See for example, Nonlinear Optical Properties of Organic Molecules and Crystals, Vols. 1 and 2, D. Chemla and J. Zyss, ed., Academic Press, NY (1987).
- 2 See for example, "Nonlinear Optical Properties of Polymers," MRS Symposium Proceedings, Vol. 109, A.J. Heeger, J. Orenstein and D.R. Ulrich eds., 1988.
- 3 S.J. Lalama and A.F. Garito, "Origin of the nonlinear second-order optical susceptibilities of organic systems," *Phys. Rev. A*20 1179 (1979).

- 4 D. Pugh and J.O. Morley, "Molecular Hyperpolarizabilities of Organic Materials", in Nonlinear Optical Properties of Organic Molecules and Crystals, Vol. 1, D. Chemla and J. Zyss, ed., Academic Press, NY (1987), p. 193.
- 5 K.D. Singer and A.F. Garito, "Measurements of molecular second-order optical susceptibilities using dc induced second harmonic generation", *J. Chem. Phys.* **75**, 3572 (1981).
- 6 C.C. Teng and A.F. Garito, "Dispersion of the Nonlinear Second-Order Optical Susceptibility of an Organic System: p-nitroaniline", *Phys. Rev. Lett.* **50**, 350 (1983).
- 7 K. D. Singer, J.E. Sohn, and S.J. Lalama, *Appl. Phys. Lett.* **49**, 248 (1986), and K.D. Singer, M.G. Kuzyk and J.E. Sohn, "Second-Order nonlinear-optical processors in orientationally ordered materials: relationship between molecular and macroscopic properties", *J Opt. Soc. Am. B4*, 968 (1987).
- 8 D.J. Williams, "Nonlinear Optical Properties of Guest-Host Polymer Structures", in Nonlinear Optical Properties of Organic Molecules and Crystals, Vol. 1, D. Chemla and J. Zyss, ed., Academic Press, NY (1987), p. 405.
- 9 J.I. Thackara, G. G. Lipscomb, M.A. Stiller, A.J. Ticknor and R. Lytel, *Applied Physics Letters* **52**, 1031 (1988)
- 10 S.K. Krotky and R.C. Alferness, "Ti:LiNbO<sub>3</sub> Integrated Optics Technology", in "Integrated Optical Circuits and Components", L. D. Hutchenson ed., Marcel Dekker Inc., New York, 1987, p.203.
- 11 J.L. Oudar and J. Zyss, "Structural dependence of the nonlinear-optical properties of methyl-(2,4-dinitrophenyl-aminopropanoate crystals", *Phys. Rev. A26*, 2016 (1982).



---

---

**PART II**

**Non-Linear Optics in  
Multifunctional Materials**

92-18248



AD-P007 457



EXPLORATORY STUDIES OF NEW NLO AND PIEZOELECTRIC POLYMERS



H. K. HALL, JR.\*, ANNE B. PADIAS\*, FRANCESCO FUSO\*, ZHENDE NI\*, MICHAEL A. MITCHELL\* AND THOMAS M. LESLIE\*\*

\*Carl S. Marvel Laboratories, Chemistry Department, University of Arizona, Tucson, AZ 85721

\*\*Hoechst-Celanese Co., 86 Morris Avenue, Summit, NJ 07901

ABSTRACT

Synthetic efforts toward novel NLO and piezoelectric polymers are described. NLO-phores are incorporated in the main chain of a polymer with all the dipoles in the same direction by polycondensation of AB-monomers. The polymers containing p-alkoxy- $\alpha$ -cyanocinnamate units in the backbone show cooperative enhancement of SHG in solution. For comparison, p-thio- $\alpha$ -cyanocinnamate is incorporated in the main chain and in the side chain of polymers. Novel potentially piezoelectric polymers synthesized include polymers containing multicyanocyclobutyl or -cyclopropyl groups and acrylonitrile copolymers.

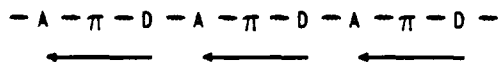
INTRODUCTION

Desirable physical and mechanical properties have always been the major reason why polymers have so many uses. More recently, novel polymers also display one or more functional properties such as piezoelectric or pyroelectric behavior, non linear optical properties ( $\chi^2$  and/or  $\chi^3$ ), electrical conductivity, ferromagnetism. Polymers can thus be used as active parts of electronic and optical devices, while still retaining their typical mechanical properties and their ease of processing. In this paper, our ongoing research in the synthesis of NLO-active and piezoelectric polymers will be reviewed.

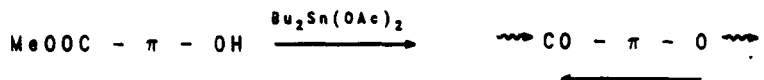
POLYMERS WITH NON-LINEAR OPTICAL PROPERTIES

The use of polymers in NLO materials has many advantages.<sup>1,2</sup> The NLO phores are chemically bound to the polymer molecule and thus no small molecules can leach out. Also, a higher concentration of NLO-phores can be obtained than with guest-host systems. The mechanical properties of the polymers lead to easier and more versatile processing. In polymers containing the NLO-phore in the main chain, cooperative enhancement can possibly be observed by which the total SHG effect of the dipoles is larger than the effect of the sum of the individual dipoles.<sup>3</sup> The aim of this work was to synthesize colorless, optically clear linear polyesters with high concentrations of NLO-phores and high  $t_g$ . The polymers also have to be soluble in common solvents to allow spin-casting.

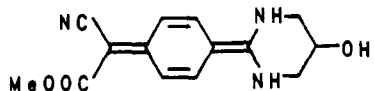
Polymers with NLO-phores in the main chain can be synthesized in which the dipoles of the NLO-phores all line up in the same direction. This is achieved by using an AB monomer, namely a hydroxy-ester monomer with the acceptor groups at the ester terminal and the donor groups at the hydroxyl end, connected by a  $\pi$ -system. Transesterification under standard conditions then leads to a polymer with all the dipoles lined up in the same direction.



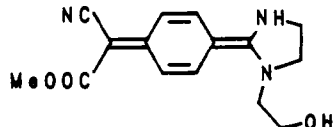
## Transesterification of AB Monomers

Quinodimethane Main Chain Polymers

Quinodimethane monomers with both an ester and a hydroxyl terminal were first investigated.<sup>4</sup> The two following  $\alpha$ -cyano-ester quinodimethanes were prepared:



DAQ



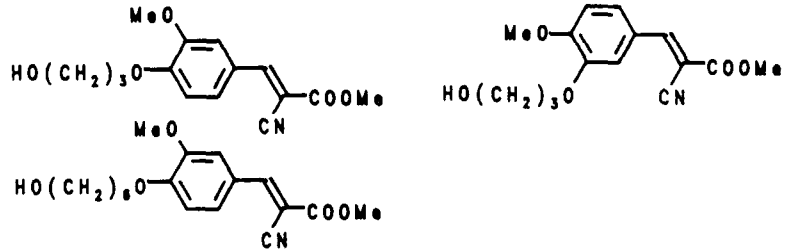
DEQ

the highly symmetric 7,7-(alkanediylidiamino)-8-carbomethoxy-8-cyanoquinodimethane DAQ and the more unsymmetrical DEQ.

Homopolymerization of these two monomers yielded intractable polymers. DAQ and DEQ were copolymerized with 12-hydroxydodecanoic ester to introduce softer segments in the polymer chain, while still maintaining the unidirectional dipoles. However, these copolymers were still too polar, high-melting and too insoluble to permit spin-casting.

Polymers with p-Alkoxy- $\alpha$ -cyano-cinnamate Units in the Main Chain

From the results we obtained with the quinodimethane monomers, it was obvious that the dipole in these monomers was too strong to allow formation of a processable polymer. Therefore a less dipolar, but similar system was selected, namely p-alkoxy- $\alpha$ -cyanocinnamates. Several of these monomers with different length spacer groups at the hydroxy end and slightly different substitution of the phenyl group were synthesized.<sup>5</sup>



Homopolymerization was accomplished by standard two stage polycondensation using dibutyltin diacetate as catalyst. Unfortunately, these homopolymers were still too insoluble in common organic solvent to allow convenient spin casting, even when the six carbon spacer unit was introduced in the monomer. Therefore, we again resorted to copolymerization with 12-hydroxydodecanoic ester. A copolymer containing 33% dodecanoic ester units was easily soluble in dichloromethane, but only 25% resulted again in insolubility. Solution cast films were made of all the soluble copolymers. The yellow transparent films were flexible and amorphous, and could be stretch-oriented.

Electric-field induced second harmonic generation EFISH measurements for model compounds and for the copolymers in solution are summarized in Table I.<sup>3</sup> The  $\mu\beta$  values range from 10 to  $113 \times 10^{-48}$  esu depending on the aromatic substitution pattern. The  $\mu\beta/n$  values, in which  $n$  is the number of NLO monomer units per chain, for the copolymers show considerable enhancement compared to the model compounds:  $G = 15-20$ . The electric field induced SHG signal is therefore considerably larger for these polymer chains than for the individual monomer units. However the enhancement factor is less than the number of monomer units in a chain, which means that the chain conformation is far from extended.

Table I. Electric Field Induced Second Harmonic Generation Results.<sup>3</sup>

Compound	$\mu\beta^a$ ( $\times 10^{-48}$ esu)	
	113	
	57	
	48	
	$\mu\beta/n^b$	$G^c$
copolymer MW 17,000	830	15
copolymer MW 70,000	1140	20

<sup>a</sup> $\mu$  = ground-state dipole moment

<sup>b</sup> $n$  = number of NLO-phore units per chain

<sup>c</sup> $G$  = enhancement factor

Solvent: chloroform

The films of these copolymers were poled above  $t_g$ , and then cooled while the electric field is maintained to lock in the molecular orientations. These polymers have  $t_g$  temperatures below room temperature, so the poling could be done at room temperature. The  $\mu\beta/n$  value for these films was only  $24 \times 10^{-48}$  esu, showing no enhancement whatsoever. We attribute this to excessive entanglement in the polymer chains which do not allow the molecular alignment of the dipole units. Moreover these films lose the SHG signal rapidly and completely at room temperature. This indicates that the dipole

alignment is completely lost above  $t_g$ . This again shows that no rearrangement of the polymeric chains occurred in the poling process, but that only some dipole units in the main chain were aligned with the electric field. This issue of the entanglement versus alignment will be further investigated.

Polymers with p-Thio- $\alpha$ -cyanocinnamate Units in the Main Chain

In this series of polymers we have investigated the effect of using sulfur as the donor unit in a NLO asymmetric AB monomer.<sup>6</sup> S is more polarizable than O, even though the ground state of the sulfide is less polar than the ether analogue.

Different p-thio- $\alpha$ -cyanocinnamates with the following spacer units at the donor end were synthesized: dimethylene, hexamethylene and p-cyclohexane-dimethylene. Different cis/trans ratios of the latter were used.

Table II: Homopolymers with p-thio- $\alpha$ -cyanocinnamate in the Main Chain.

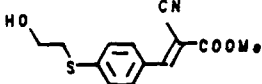
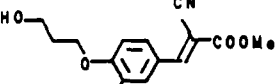
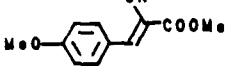
MONOMER	$\eta_{inh}$	$T_g$	$T_m$	SOLUBILITY
	-	82°	200°	HFIP
	-	45°	130°	SWELLS IN CH2CL2
	97% TRANS	.34	113° 240°	PhCl/PhOH
50/50 CIS/TRANS		102°		PhCl/PhOH

Homopolymerizations using the standard two stage polycondensation method and tributyltin acetate as catalyst proceeded satisfactorily, but the obtained polymers were only soluble in highly polar solvents such as a mixture of chlorobenzene and phenol. These homopolymers had  $t_g$  above room temperature as shown in Table II. They crystallized either during polymerization (for the cyclohexane polymers) or upon treatment with methanol at room temperature. An amorphous state was achieved when these polymers were heated above  $t_m$ , followed by rapid cooling. Copolymerizations of the acyclic alkyl chain monomers with 12-hydroxydodecanoic ester led to more soluble and yellow polymers. The crystallinity of these polymers was confirmed by DSC (differential scanning calorimetry) in which all these polymers showed a  $t_m$  between 60 and 110°C, but no glass transition temperature. Copolymers between the acyclic alkyl spacer monomers with the all-trans cyclohexane monomer might lead to less crystalline materials.

As far as the  $\beta$  values of these p-thio- $\alpha$ -cyanocinnamate units are concerned, we have performed calculations of  $\beta$  using the solvatochromic method.<sup>7</sup> The results are summarized in Table III. The p-thio- $\alpha$ -cyanocinnamate has a ground-state dipole moment of 3.84D, which was experimentally measured. We can compare this to a value of 5.37D for p-

methoxy- $\alpha$ -cyanocinnamate, obtained from AM1 calculations. This is in agreement with the expected trend in which the ether analogue would be more polar than the thio-ether in the ground state. The  $\beta$ -values for the thio-ether are considerably larger than for the oxygen analogue. The two  $\beta$ -values of 58 and  $98 \times 10^{-30}$  esu were obtained from solvatochromic measurements in fluorescence and UV, respectively using the Block-Walker method.<sup>7</sup> The  $\beta$ -value for the alkoxy derivative ( $10 \times 10^{-30}$  esu) was calculated from the EFISH measurement and the AM1 value for the dipole moment for the p-methoxy analogue. Within the limitations of the different methods used, we can still conclude that the thio-ether has a higher  $\beta$ -value. This is due to the higher polarizability of the sulfur, which results in a larger dipole moment in the excited state.

Table III.  $\beta$ -values for p-thio- $\alpha$ -cyanocinnamate.

Compound	$\mu_{\text{first}}^a$ (D)	Method	$\beta$ ( $10^{-30}$ esu)	$\mu\beta$ ( $10^{-48}$ esu)
	3.84	exper.	58 <sup>b</sup>	223
			98 <sup>c</sup>	377
			20 <sup>d</sup>	57
	5.37	AM1		

<sup>a</sup>dipole moment in the ground state

<sup>b</sup>from fluorescence

<sup>c</sup>from UV

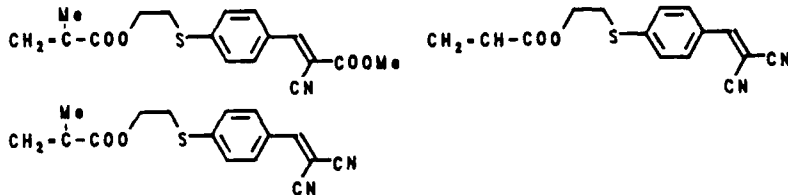
<sup>d</sup> $\beta$ -value obtained from EFISH  $\mu\beta$ -value and AM1 dipole moment for methoxy-derivative

#### Polymers with p-thio- $\alpha$ -cyanocinnamate Units in the Side Chain

In order to investigate the effect of the placement of the NLO phore in the polymer, we prepared acrylate and methacrylate polymers with the same p-thio- $\alpha$ -cyanocinnamate unit in the side chain. The question arises if enhancement of the  $\beta$  value only occurs when the NLO phores are in the main chain, or if this enhancement can also be observed if the NLO phores are attached to the polymer backbone.

p-Thio- $\alpha$ -cyanocinnamate monomers attached to an acrylate or a methacrylate unit were synthesized. The acceptor moiety of the p-thiocinnamate unit was either the  $\alpha$ -cyanoester unit, similar to the unit used above, or the dicyano unit.<sup>8</sup> Polymerizations in bulk consistently led to insoluble polymers, even if the title monomers were copolymerized with methyl methacrylate. Only at a 5/95 field ratio (S-monomer/MMA) was a polymer obtained, yielding optically clear films. Homopolymerizations in benzene led

to soluble polymers with moderately high molecular weights:  $\eta_{inh} = 0.4-0.9$  dL/g. Non-linear properties of these polymers have yet to be investigated.



#### Conclusions Regarding NLO Polymers

To our knowledge, the polymers containing aligned NLO-phores in the main chain are the first ones reported in the literature. From our studies of these polymers, we can conclude that in the p-alkoxy- $\alpha$ -cyanocinnamate polymers, a cooperative enhancement of the SHG can be observed. Unfortunately this enhancement was only found in solution. In films poled above  $t_g$ , no enhancement was detected. Moreover the non-linear properties of these films degraded very rapidly at room temperature, which in this case was above  $t_g$ . What this indicates is that the poling is not able to realign the polymer chain in a film if the NLO-phores are in the backbone and the molecular weight is high.

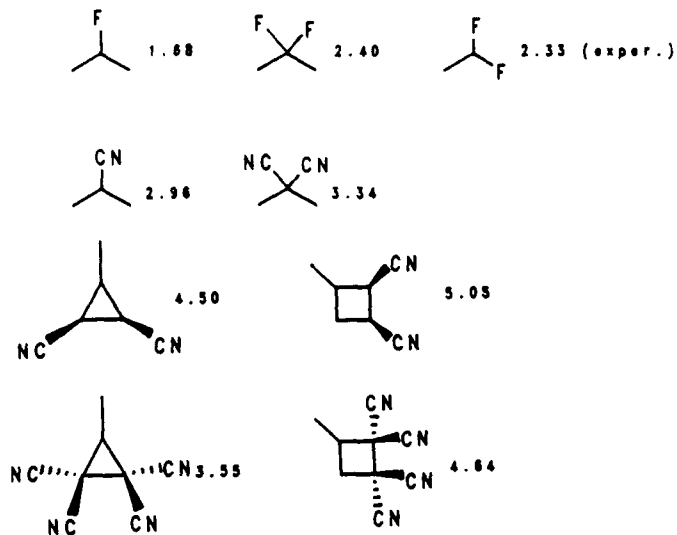
The p-thio- $\alpha$ -cyanocinnamate NLO phores were incorporated in polymers in two different manners, main chain and side chain, to compare the influence of the topology. Surprisingly, the main chain polymers were crystalline, but could be kept in an amorphous state indefinitely. Also, the sulfide polymers had higher  $t_g$ 's than the ether analogs. Within the limitations of the different methods used to compare the  $\beta$ -values, the p-thio- $\alpha$ -cyanocinnamates have a higher potential for second order non-linear optical behavior, due to the higher polarizability of the sulfur atom. Experimental work continues to obtain processable material from both the main chain and side chain polymerizations and to compare their polarizability.

#### CYANO-CONTAINING POLYMERS AS PIEZOELECTRIC MATERIALS

The best known piezoelectric polymer is the  $\beta$ -form of polyvinylidene fluoride, which is crystalline.<sup>9</sup> Among the amorphous polymers, the alternating copolymer of vinylidene cyanide and vinyl acetate is also piezoelectric.<sup>10</sup> A potential piezoelectric polymer has to contain a high concentration of dipoles and also be mechanically very strong. These polymers have to be film-forming and be able to withstand high voltages without breakdown. The dipole moment of a C-F bond is 1.9 D (Debye), while the dipole moment of a cyano group C≡N is 3.9 D.<sup>11</sup> This is an indication why the vinylidene cyanide / vinyl acetate copolymer is piezoelectric.

To synthesize polymers with many dipoles which can be aligned in the same direction, the cyano polymers look very promising. Moreover, if the total dipole moment is the determining factor, one cyano group has a dipole moment comparable to two geminal cyano groups, because of the angle between the two geminal dipoles. To verify this concept, molecular modeling calculations were performed on some aliphatic nitriles and fluorides using AM1.<sup>12</sup> These results are summarized in Table IV. The dipole moments for the fluorides are considerably smaller than for the corresponding nitriles. The calculated dipole moment for 2,2-difluoropropane of 2.40 D is in good agreement with the experimental value of 2.33 D for 1,1-difluoroethane.<sup>11</sup> Moreover the dipole moment of isopropyl cyanide (2.96 D) is only somewhat smaller than the value for 2,2-dicyanopropane (3.34 D).

Table IV: Calculated Dipole Moments (D).

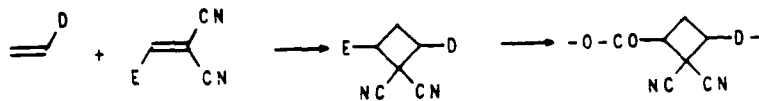


We also calculated dipole moments for small rings, three- and four-membered, containing nitrile substituents. Small rings do not undergo large conformational changes found in the larger rings, most notably in the five- and six-membered rings. The dipole moments for small rings with different substitution patterns with cyano groups were also calculated by AM1. The largest dipole moments were observed for cis-disubstituted rings, both in the three and four-membered series. However synthetically these are not easily accessible. The tetrasubstituted rings had also rather large dipole moments, and are easier to synthesize.

The AM1 calculations support our intuitive ideas that one cyano substituent should be almost as effective as two geminal cyano substituents. This opens up a whole new area of potentially piezoelectric polymers with acrylonitrile as the basic building block. (Polyacrylonitrile itself is not suitable because the polymer forms a helix.) The other possible pathway to piezoelectric polymers is incorporating cyano-substituted cyclopropanes and cyclobutanes in the polymer structure.

#### Polymers Containing Multicyano-substituted Small Rings

Our first approach to the synthesis of polymers containing multicyano cyclobutanes was polycondensation of dicyano-substituted cyclobutanes.<sup>13</sup> The cyclobutanes are obtained from cycloaddition reaction of electron-rich olefins, such as vinyl ethers or p-alkoxystyrenes with methyl  $\beta,\beta$ -dicyanoacrylate.<sup>14</sup>



D = donor substituent such as -OR or -PhOR, E = COOMe

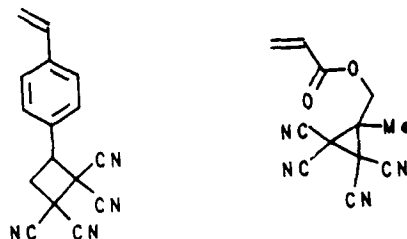
If the donor substituent contains a hydroxy or acetoxy end-group, a conventional polycondensation reaction can lead to a polymer with cyclobutanes substituted by two geminal CN-groups in the main chain. The following cyclobutanes, among others, were synthesized:



R = OH, OAc, E = COOMe

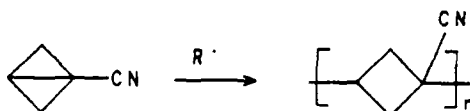
Unfortunately, all attempted polycondensations were unsuccessful due to monomer decomposition. The cycloaddition reaction leading to these cyclobutanes is reversible. Even if the novel polycondensation methods at room temperature pioneered by Ogata were used, did monomer decomposition occur.<sup>15</sup>

In another approach, p-(tetracyanocyclobutyl)styrene was synthesized from p-divinylbenzene and tetracyanoethylene.<sup>16</sup> This styrene monomer could be homopolymerized, but no copolymerization with common monomers such as styrene or acrylonitrile has been observed yet. The polymers are still too low molecular weight to be film-forming, but offer the potential for high concentration of dipoles necessary for piezoelectric behavior.



The tetracyanocyclopropane group has been incorporated in an acrylate and methacrylate monomer, by reaction of acetyl (meth)acrylate with malononitrile.<sup>17</sup> These monomers are also able to homopolymerize by a radical mechanism, but in this case too, no film-forming molecular weights have been obtained yet.

Radical homopolymerization of bicyclobutanecarbonitrile leads to a polymer with cyclobutanes in the main chain and a cyano-substituent at a bridgehead.<sup>18</sup>



NMR studies have determined that this polymer does not have a helical structure, such as a polyacrylonitrile.<sup>19</sup> The polymer is film-forming, and a 25  $\mu$  film could be poled at 50 kV/ $\mu$  at 205°C. A piezoelectric constant  $d_{31}=0.3$  pC/N was observed, which is about 5% of the value obtained for the vinylidene cyanide/vinyl acetate copolymer. This is to date the polymer with the highest  $t_g$ , which shows piezoelectric behavior.<sup>20</sup>

### Acrylonitrile Copolymers

Turning to more common monomers, we are investigating the use of acrylonitrile copolymers as potential piezoelectric materials. As shown from AML calculations, the dipole moment of one cyano group is only slightly lower than the dipole moment of two geminal cyano groups.

Spontaneous copolymerization of acrylonitrile with vinyl acetate has been reported in the presence of zinc chloride at 40°.<sup>21</sup> A perfectly alternating copolymer is obtained. Films can be cast from acetone and a pyroelectric constant  $p = 2 \mu\text{C m}^{-2}\text{K}^{-1}$  has been observed after poling a 40  $\mu\text{m}$  film at 16V/ $\mu$  at 70°. To achieve a higher concentration in dipoles, acrylonitrile was also copolymerized with vinyl formate in the presence of zinc chloride. A clean polymerization was achieved at 0°C, using AIBN as initiator and UV light. The polymer was alternating and also film-forming. The formate groups can be hydrolyzed to yield a copolymer of vinyl alcohol and acrylonitrile. The hydroxyl groups can be used for further functionalization, for example couple with NLO for truly multifunctional polymers.

The alternating copolymers of isobutylvinyl ether and methylvinyl ether with acrylonitrile were also synthesized by using an 85/15 monomer feed ratio. All these polymers also have high inherent viscosities and are film-forming. Their piezo- and pyro-electric properties will be investigated.

### CONCLUSIONS

Synthetic polymer chemists are capable of incorporating appropriate dipoles in polymers in order to achieve the desired functional properties. These dipoles can be placed in the main chain of the polymer or in the side chains. Both second order NLO materials and piezoelectric materials require aligned dipoles in the material. The former require a  $\pi$ -system to allow light interference, while the latter can be observed in materials containing small dipoles.

The physical properties of the polymers are important to allow processing. The physical properties will determine the mechanical properties of the material. The processing can improve both the mechanical properties, but also the functional properties. Better dipole alignment can be obtained by, for example, stretching the material.

In the synthesis of these polymers, there is a continuous struggle between the physical properties and the concentration of dipoles in the material. High dipole concentrations can be achieved, but with a detrimental effect on the physical properties. A balance between maximum effectiveness of the material in the desired functional properties and the mechanical properties has to be sought.

### Acknowledgments

The authors gratefully acknowledge financial support by the Hoechst-Celanese Co., Summit, NJ, Eastman-Kodak Co., Rochester, NY, and the Office of Naval Research. The authors also wish to thank C. S. Willand and D. J. Williams at Eastman-Kodak, I. Kalnin at Hoechst-Celanese, T. Scheinbeim at Rutgers University and P. Carr at the University of Leeds for performing the measurements on the NLO and piezoelectric materials.

References

1. Non-linear Optical and Electroactive Polymers, edited by P.N. Prasad and D.R. Ulrich (Plenum Press, New York, 1988).
2. Non-linear Optical Effects in Organic Polymers, edited by J. Messier, F. Kajzar, P. Prasad and D. Ulrich (Kluwer Academic Publishers, Dordrecht, 1989).
3. C.S. Willand, S.E. Feth, M. Scozzafava, D.J. Williams, G.D. Green, J.I. Weinschenk III, H.K. Hall, Jr. and J.E. Mulvaney, p. 107 in Ref. 1.
4. G.D. Green, H.K. Hall, Jr., J.E. Mulvaney, J. Noonan and D.J. Williams, *Macromolecules* 20, 716 (1987).
5. G.D. Green, J.I. WEinschenk, III, J.E. Mulvaney and H.K. Hall, Jr. *Macromolecules* 20, 722 (1987).
6. F. Fuso and H.K. Hall, Jr. *Macromolecules* (submitted).
7. M.S. Paley, J.M. Harris, H. Loosser, J.C. Baumert, G.C. Borklund, D. Jundt and R.J. Twieg, *J. Org. Chem.* 54, 3774 (1989).
8. Z. Ni, T.M. Leslie and H.K. Hall, Jr. *Macromolecules* (submitted).
9. A. J. Lovinger in Developments in Crystalline Polymers, Vol. 1, edited by D.C. Bassett (Applied Science, London, 1982).
10. S. Miyata, M. Yoshikawa, S. Tasaka, and M. Ko, *Polymer Journal* 12, 857 (1980).
11. V.I. Minkin, O.A. Osipov, and Y.A. Zhdanov, Dipole Moments in Organic Chemistry, translation edited by W.E. Vaughan, (Plenum Press, New York, 1970).
12. M.J.S. Dewar, E.G. Zoebisch, E.F. Healy, and J.J.P. Stewart, *J. Am. Chem. Soc.* 107, 3902 (1985).
13. S. Mori, T. Kakuchi, A.B. Padias and H.K. Hall, Jr. *J. Polym. Sci., Polym. Chem. Ed.* (in press).
14. A.B. Padias and H.K. Hall, Jr. *J. Org. Chem.* 52, 4536 (1987).
15. S. Yasuda, G.C. Wu, H. Tanaka, K. Sanui and N. Ogata, *J. Polym. Sci., Polym. Chem. Ed.* 21, 2609 (1983).
16. A.B. Padias and H.K. Hall, Jr. (manuscript in preparation).
17. J. Y. Lee and H.K. Hall, Jr. (manuscript in preparation).
18. H.K. Hall, Jr., E.P. Blanchard, Jr., S.C. Cherkofsky, J.B. Sieja and W.A. Sheppard, *J. Am. Chem. Soc.* 93, 110 (1971).
19. M. Barfield, R.J.H. Chan, H.K. Hall, Jr. and Y.H. Mou, *Macromolecules* 19, 1350 (1986).
20. J. Oku, H.K. Hall, Jr., J. Scheinbeim and B. Newman, *Polym. Bull.* 17, 135 (1987).
21. C.S.H. Chen, *J. Polym. Sci., Polym. Chem. Ed.* 14, 2109 (1976).



92-18249



AD-P007 458



NATURE OF THE CHEMICAL BONDS IN POLYMER-SALT COMPLEXES:  
RAMAN AND IR STUDIES

Gholamabbas Nazri\* and Donald M. MacArthur, Physical Chemistry Department, GM Research Laboratories Warren, MI 48090 and Ricardo Aroca Department of Chemistry and Biochemistry, University of Windsor, Windsor, Ontario, Canada N9B 3P4

ABSTRACT

Polymer electrolytes are attracting interest because of potential use in "solid state" batteries and electrochromic windows. In this work the nature of the chemical bonds and ion association in polymer-salt complexes were studied. The fundamental vibrational frequencies of  $\text{LiClO}_4$  were calculated using valence force constants which are obtained from the  $\text{ClO}_4^-$  anion. The calculated frequencies and the band assignments agree quite well with the observed frequencies. Raman and IR spectroscopy were used to investigate the interaction of  $\text{Li}^+$  and  $\text{ClO}_4^-$  with the PEO chains. Lithium ion interacted with the negatively charged oxygen of PEO and  $\text{ClO}_4^-$  interacted electro- statically with the positively charged hydrogens. The strong electrostatic interactions induced changes in the intensity of the Raman bands and IR absorption bands of the polymer. The Raman and IR spectra of the polymer-salt complexes clearly show the existence of "free" ions, ion-pairs and salt clusters at various concentrations of the lithium salt. The maximum concentration of "free" ions deduced from the spectroscopy is in excellent agreement with the salt concentration required to obtain maximum ionic conductivity.

INTRODUCTION

Ion conducting polymers have been attracting a great deal of attention due to their softness and ease of fabrication as thin film electrolytes for various solid state devices [1-7]. The major focus has been to develop a solid state battery of the type: alkali metal/polymer electrolyte/intercalation compound. Attaining high ionic conductivity in polymer-alkali metal salt electrolytes is a key to the success of this type of device. A high concentration of "free" ions and a high skeletal mobility of the polymer (low energy barrier of torsional motion) are important factors in achieving high ionic conductivity. In order to dissolve a large amount of salt, a salt with low lattice energy and a polymer with high polarity and low torsional energy are needed. Among various polar polymers the poly ethers are the most promising materials having the required properties. Polyethylene oxide,  $(-\text{CH}_2-\text{CH}_2-\text{O}-)_n$ , and its derivatives are known to dissolve a large amount of salt. In order to reveal the mechanism

of ion transport in polymeric electrolytes and to improve their properties, the energetics of ion-associations in these systems have been studied.

Ionic conductivity, in general, is related to the number of charge carriers (n), the charge of the mobile species (z) and the mobility of the diffusing species ( $\mu$ ) according to;

$$\sigma = nz\mu \quad (1)$$

The mobility of the "free" ion is closely related to the energetics and the degree of interaction with the environment. The number of charge carriers is proportional to the concentration of the dissociated salt.

The classical treatment of liquid electrolytes suggests the formation of ion-pairs at high salt concentration and, above saturation, precipitation of the salt. During ion transport in conventional liquid electrolytes, the ions carry their solvation shell [8]. In glassy inorganic electrolytes, assuming a rigid anion sublattice, ion transport occurs through a hopping mechanism [9-10]. In polymeric electrolytes, ions can carry their solvation shell only for a short distance, dictated by the flexibility of the skeletal motion of the polymer.

In this work we study the vibrational motion of the PEO-LiClO<sub>4</sub> complexes. Raman and IR spectra of the system at various salt/polymer ratios were collected and the threshold of ion-pair formation was determined. A normal mode analysis of LiClO<sub>4</sub> was performed and the vibrational frequencies of free ions and ion-pairs were obtained for comparison. The conductivity of LiClO<sub>4</sub>/PEO at various salt/polymer ratios was measured and compared with the concentration of "free" ions in the polymer.

#### EXPERIMENT

Polyethylene oxide with a molecular weight of 600,000 dalton (Poly Science Inc.) was dissolved in spectroscopic grade methanol. Anhydrous lithium perchlorate (Alfa Products) was also dissolved in methanol. Solutions of LiClO<sub>4</sub>/PEO were made ranging from LiClO<sub>4</sub>/PEO = 1/150 to LiClO<sub>4</sub>/PEO = 1/2. Films of the LiClO<sub>4</sub>/PEO complex were cast on a smooth gold substrate and annealed in a vacuum oven at 75 °C for 10 hours. The spontaneous Raman scattering was excited with the 488 nm or the 514.5 nm line of the Ar<sup>+</sup> ion laser (Spectra Physics model 2000). A polarization rotator (SP model 310-21) mounted on the laser head was used to select TE (S-polarized) or TM (P-polarized) components of the incident beam. Since the sample did not absorb in the visible region, spectra obtained with both excitation lines were identical. For reference and comparison, the Raman scattering of a PEO film on gold, of LiClO<sub>4</sub> in the solid state, and of an aqueous solution of LiClO<sub>4</sub> (where the polarization ratio for each

fundamental was measured) were obtained under similar experimental conditions (resolution and laser power). The resolution for Raman scattering was  $5 \text{ cm}^{-1}$ , and the laser power was ca. 100 mW. A Spex 1403 spectrometer interfaced with an IBM personal computer was used [11]. For backscattering geometry, a Ramanor double monochromator with microscope attachment was used.

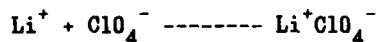
IR spectra of the samples were collected in the diffuse reflection mode with  $2 \text{ cm}^{-1}$  resolution. The IR spectrometer was an IBM-98 FTIR spectrometer operated under vacuum. The sample was isolated from the atmosphere during data collection using a special accessory. A liquid nitrogen cooled, broad band MCT detector was used. The IR spectrum of anhydrous  $\text{LiClO}_4$  powder was also collected in the diffuse reflection mode as a reference spectrum.

The conductivity of  $\text{LiClO}_4/\text{PEO}$  samples at various salt to polymer ratios was measured at room temperature. A uniform film of the polymer-salt complex was formed on Teflon coated stainless steel. The films were annealed at  $50^\circ\text{C}$  under vacuum for two hours. The annealed film was sandwiched between two lithium disks (1.3 cm diameter). A nickel disk was used as current collector on each side of the polymer film. The polymer film was under slight spring load to maintain uniform contact between the lithium disks and the polymer films. The conductivity of the films was measured at 1000 Hz using a GenRad 1689 precision RLC Digibridge.

## RESULTS AND DISCUSSION

### Normal Mode Calculations:

In this work the solid state equilibrium between the "free" ion and the ion-pair according to:



is studied. In order to correlate the observed frequencies in the Raman and the IR spectra, we calculate the fundamental normal mode frequencies for the "free" perchlorate ion ( $\text{ClO}_4^-$ ) and the ion-pair ( $\text{Li}^+\text{ClO}_4^-$ ).

The structural and spectral consequences of ion-pairing have been studied recently for related salts:  $\text{LiClO}_3$  [12] and  $\text{LiNO}_3$  [13]. In these theoretical studies a number of different geometries for each ion-pair were analyzed in order to assign the observed spectra to the irreducible representations of a specific symmetry point group of the molecular system. In the  $\text{LiClO}_4/\text{PEO}$  system, the vibrational fundamentals of  $\text{ClO}_4^-$  are associated with the free ions and those of  $\text{LiClO}_4^-$  with the ion-pair. Changes in the vibrational spectra of the PEO give an indication of the extent and location of the intermolecular interactions.

The  $\text{ClO}_4^-$  anion has a  $T_d$  symmetry, and therefore there are nine fundamentals in  $1a_1 + 1e$  and  $2f_2$  symmetry species. These give rise to a  $1a_1$  mode, a doubly degenerate  $1e$  mode and two triply degenerate  $2f_2$  modes. All four frequencies were observed in the Raman, with a strong and polarized band at  $933 \text{ cm}^{-1}$ , and three depolarized bands at  $462 \text{ cm}^{-1}$  (e),  $627 \text{ cm}^{-1}$  and  $1102 \text{ cm}^{-1}$  ( $f_2$ ). This is in agreement with the values of 935, 462, 628 and  $1102 \text{ cm}^{-1}$  reported by Ross [14].

The most probable structure for the  $\text{LiClO}_4$  ion pair is a  $C_{3v}$  symmetry and, according to correlation tables for descent in symmetry, each  $f$  type will generate an  $a_1$  and an  $e$  symmetry species, while the  $a_1$  and  $e$  of the  $T_d$  will correlate with identical species in the  $C_{3v}$  group. Both symmetry species are infrared and Raman active. There will be a total of 5 stretching vibrations:  $3a_1 + 1e$ . The other 7 vibrations are bending, including one linear bending of the Li-O-Cl in the  $C_{3v}$  molecule. The vibrational modes of the "free"  $\text{ClO}_4^-$  and the ion pair  $\text{LiClO}_4$  are shown in table 1.

Table - 1 Vibrational modes of "free"  $\text{ClO}_4^-$  and ion-pair  $\text{LiClO}_4$

$\text{ClO}_4^-$		$\text{LiClO}_4$		
$a_1$	934 vs	$a_1$	935 vs	Cl-O Stretch
$e$	462 m	$e$	463 m	O-Cl-O bend
$f_2$	627 m	$a_1$	633 m	O-Cl-O bend
	1102 w	$e$	625 m	O-Cl-O bend
		$e$	1104 w	Cl-O stretch
		$a_1$	1130 w	Cl-O stretch
		$a_1$	546 w	Li-O stretch
		$e$	427 w	Li-O-Cl bend

A normal coordinate analysis of the ion-pair was carried out with valence force constants transferred from the perchlorate ion. The analysis gave frequency values to be found in the following regions of the vibrational spectrum; there were two high frequencies, an  $e$  frequency at about  $1104 \text{ cm}^{-1}$ , and an  $a_1$  with a higher value predicted and two bands were observed in the Raman scattering of the  $\text{LiClO}_4$  in the solid state, one at  $1102 \text{ cm}^{-1}$  (probably an  $e$  type), and a second at  $1130 \text{ cm}^{-1}$  that would correspond to the  $a_1$  stretching vibration. A totally symmetric  $a_1$  stretching vibration of the  $\text{ClO}_4^-$  group was observed at  $933 \text{ cm}^{-1}$ . Two frequencies in the  $600-700 \text{ cm}^{-1}$  region, which could be assigned to a pair at  $633$  and  $623 \text{ cm}^{-1}$ , were also observed. A linear bending at about  $350 \text{ cm}^{-1}$ , and the Li-O stretching at about  $500 \text{ cm}^{-1}$  were predicted and observed. The key frequencies that we used for the ion-pair therefore were at  $623$  and  $633 \text{ cm}^{-1}$  and for the "free" ion was at  $623 \text{ cm}^{-1}$ .

Raman and IR Spectra of  $\text{LiClO}_4/\text{PEO}$  Films:

In Fig. 1, the Raman scattering of the PEO film with various concentrations of the  $\text{LiClO}_4$  are shown. It was found that in the range of concentration shown in the figure, there were only minor changes in the frequencies and relative intensities of the PEO Raman bands.

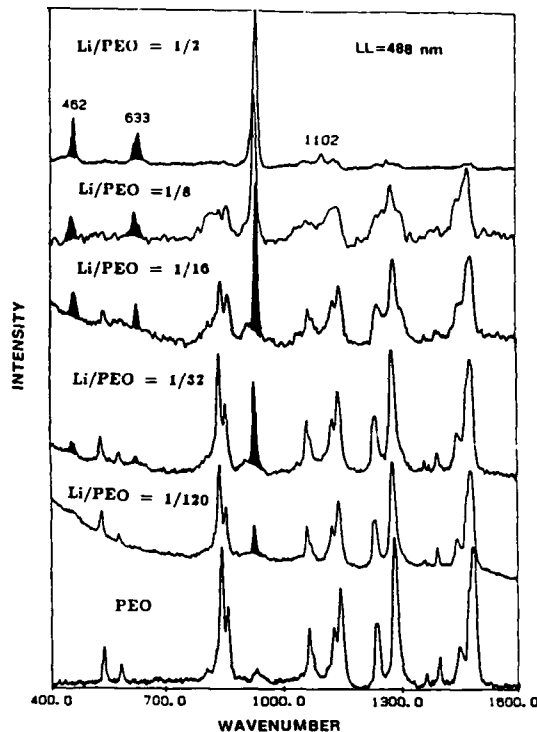


Fig. 1. Raman spectra of  $\text{PEO}-\text{LiClO}_4$  films. The shaded bands and the wavenumbers correspond to the salt

Following the vibrational assignment given by Tadokoro, et al. [15] to PEO, a small red shift of about  $6 \text{ cm}^{-1}$  was observed in the Raman band of the scissoring  $\text{CH}_2$  vibration for low concentrations of the salt up to  $\text{LiClO}_4/\text{PEO} = 1/32$ . A striking reduction in the overall Raman band intensities of the PEO was observed upon further addition of lithium salt to the polymer as shown in Fig. 1. Notice that at the highest salt concentration the PEO Raman bands are barely discernible. This observation clearly indicates that the Raman scattering cross section of the polymer has been drastically reduced. The Raman scattering cross section of a chemical bond is directly related to the change of the bond polarizability. Addition of salt to the polymer apparently gives rise to a significant charge localization in the polymer bonds. Therefore, the covalent nature of the bond involved is altered to a more ionic character. It should be pointed out that infrared intensities may be increased by the localized charge and increased polarity

in the system, since they are proportional to the change of the dipole moment for a particular vibrational mode. We observed that the intensity of the IR bands increased substantially as a result of the addition of salt to the polymer. These observations can be interpreted as the effect of a strong interaction of the dissociated salt with the localized charge on the polymer chain which alters the covalent nature of the chemical bonds in the polymer to a more ionic bond. The involved chemical bonds therefore have a higher dipole moment and lower polarizabilities.

At high concentrations of the salt, typical band broadening due to strong intermolecular interactions were visible. Most notably, in Fig. 1, the broadening of the bending vibration of the CCO group directly involved in the  $\text{Li}^{+} \dots \delta^-$  O-C- interaction is very clearly demonstrated in the frequency range from 1000 to  $1600 \text{ cm}^{-1}$ . A similar band broadening was observed in the infrared spectra shown in Fig. 2. The band broadening is also an indication of the coexistence of the various closely related vibrational energy states. The overlap of the vibrational energy states of the polymer bonds with those bonds which have been modified by the salt gives rise to the observed band broadening. The slight red shift of the band position suggests a lower energy of the vibrational modes, which is the result of a weaker chain-chain interaction.

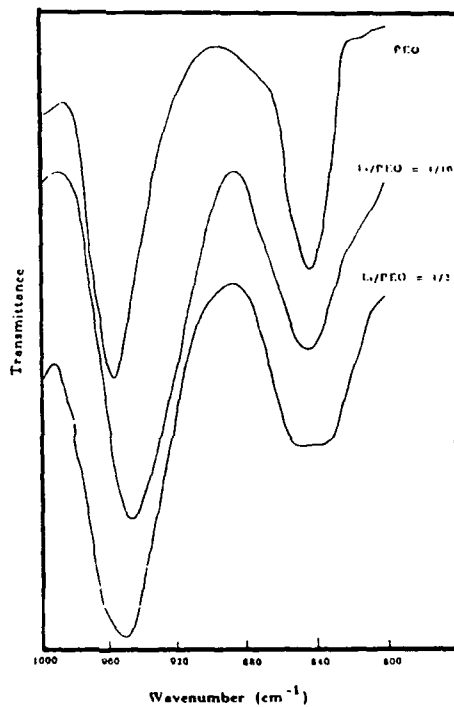


Fig. 2. IR spectra of PEO- $\text{LiClO}_4$  films illustrating the broadening of the  $\text{CH}_2$  bending modes with increasing salt concentration.

Our previous work also shows the reduction of chain-chain interactions due to addition of salt to the polymer [16].

Figure 3 shows the Raman scattering doublet at  $633-623\text{ cm}^{-1}$  for the  $\text{LiClO}_4$  and the change in the intensities of the doublet as the solution of  $\text{LiClO}_4$  in PEO becomes more dilute. The doublet is a valuable qualitative marker for the determination of the existence of ion-pairing. For instance, at high  $\text{LiClO}_4$  concentration ( $\text{LiClO}_4/\text{PEO} = 1/2$ ) both components of the doublet are prominent in the spectrum, but at low concentration only the lower frequency mode is evident.

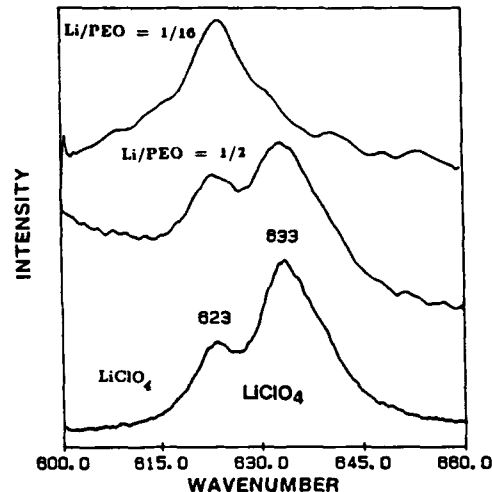


Fig. 3. Raman spectra of PEO- $\text{LiClO}_4$  films in the  $600-660\text{ cm}^{-1}$  region showing concentration dependence of the  $623-633$  pair.

Since both  $a_1$  and  $e$  symmetry species are IR and Raman active, a similar effect with concentration was observed in the infrared spectra as shown in Fig. 4. Clearly, the doublet is associated with the presence of ion-pairs (as seen in the  $\text{LiClO}_4$ ), while the "free" ion shows one single band at  $623\text{ cm}^{-1}$ . At a ratio of  $1/8$ , the relative intensities of the  $623$  and  $633\text{ cm}^{-1}$  bands are reversed compared to the  $\text{LiClO}_4/\text{PEO} = 1/2$  spectrum. At a concentration ratio of  $1/16$  and lower concentrations, the doublet is reduced to a single band with a frequency of  $623\text{ cm}^{-1}$ , close to the value of the  $f_2$  bending of the free ion. At the high  $\text{LiClO}_4$  concentration,  $\text{LiClO}_4/\text{PEO} = 1/2$ , the full Raman spectrum of the ion-pair was observed, including the  $1102\text{ cm}^{-1}$  and the  $1130\text{ cm}^{-1}$  bands. The IR spectrum of  $\text{LiClO}_4/\text{PEO} = 1/2$  shows a band around  $700\text{ cm}^{-1}$  which is a characteristic of the  $\text{LiClO}_4$  salt crystal. This band can be interpreted based on the precipitation of salt clusters in the polymer matrix.

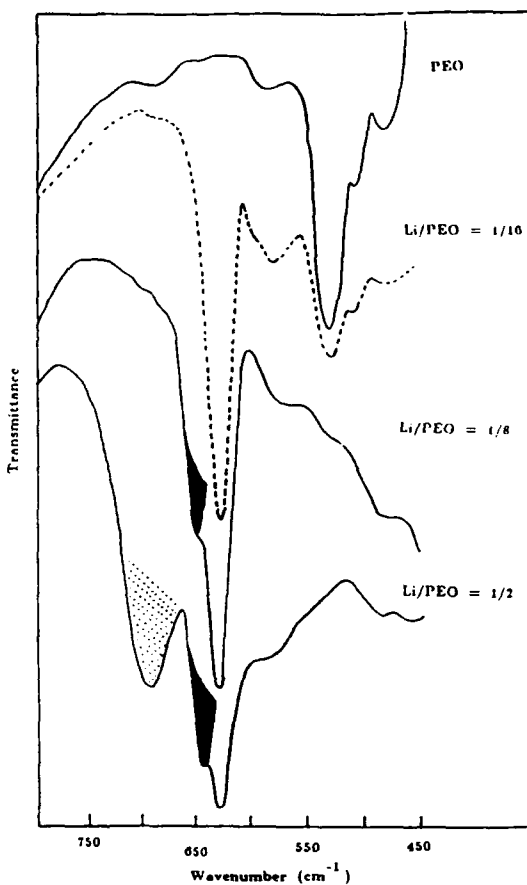


Fig. 4. IR spectra of PEO- $\text{LiClO}_4$  films. Ion-pair formation is illustrated by changes in the  $627 \text{ cm}^{-1}$  band.

It is possible to use some other features in the vibrational spectra to follow the "free" ion/ion-pair equilibrium. For instance, the most intense Raman band of the ion pair is located at  $934 \text{ cm}^{-1}$ . However, both the free ion and the ion pair provide characteristic stretching vibrations of the  $\text{ClO}_4^-$  group at this same frequency, which make the analysis much more involved and adds no more insight.

In conclusion, the bands at  $623$  and  $633 \text{ cm}^{-1}$  indicate that free ions were predominant in the films with  $\text{LiClO}_4/\text{PEO}$  concentration as high as  $1/8$ , while ion-pair and salt aggregates are found at higher concentration ratios.

The conductivity measurements are shown in Fig. 5. The conductivity reaches a maximum at a salt concentration of  $\text{LiClO}_4/\text{PEO} = 1/8$ . Also plotted in Fig. 5 are the integrated intensities of the IR bands at  $623$ ,  $633$  and  $700 \text{ cm}^{-1}$  as a function of the  $\text{LiClO}_4/\text{PEO}$  ratio.

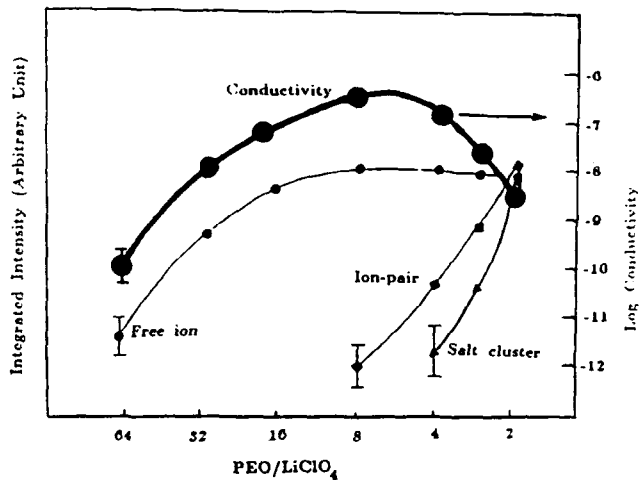


Fig. 5. Conductivity of PEO- $\text{LiClO}_4$  films at various salt concentrations and the dynamics of the "free" ion, ion-pair and salt clusters.

This shows the relationship between the conductivity of the films and the concentration of "free" ions. The maximum ionic conductivity occurs at the threshold of ion-pair formation. It is interesting to note that conductivity decreases with increasing salt concentration after the ion-pair formation is apparent. This property is markedly different from conventional liquid electrolytes. The ion association/dissociation equilibrium has a major role on the mean free path of the ions in the polymeric media. (In the case of polymer electrolytes, the mean free path of an ion refers to the distance in which the "free" ion can travel before being involved with the counter ion to form an ion-pair.) At low salt concentration the free ions are well caged in the polymer and well separated from the counter-ions and the number of available sites for the "free" ion in the polymer matrix is high. Therefore, the "free" ion can travel among several sites before being trapped in the effective coulombic field of the counter-ion. At high salt concentration, however, there is only a limited number of empty sites available for the ions and the probability of ion-pair formation is high. This will reduce the mean free path of the "free" ions and as a result the conductivity decreases.

#### REFERENCES:

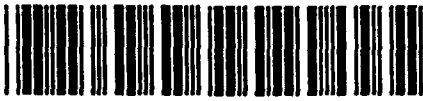
1. B. Scrosati, A. Selvaggi, F. Croce and W. Gang, *J. Power Sources*, **24**, 287, (1988).
2. D. P. Tunstall, A. S. Tomlin, J. R. MacCallum and C. A. Vincent, *J. Phys. C: Solid State Physics*, **21**, 1039 (1988).

3. B. L. Papke, M. A. Ratner and D. F. Shriver, *J. Electrochem. Soc.*, 129, 1694 (1982).
4. J. E. Weston and B. C. H. Steel, *Solid State Ionics*, 7, 75 (1982).
5. V. V. Lontsov, K. S. Kazanskii and N. Shupik, *Doklady Akademii Nauk*, 285, 142 (1985).
6. M. Watanabe, K. Tadano, K. Sanui and N. Ogata, *Chemistry Letters*, 1239, (1987).
7. M. Watanabe, M. Itoh, K. Sanui and N. Ogata, *Macromolecules*, 20, 569 (1987).
8. G. Licheri, in "X-ray Diffraction of Ions in Aqueous Solutions, Hydration and Complex Formation", (Ed. M. Magini) CRC Press Inc. 1988.
9. K. Hughes and J. O. Isard, in *Physics of Electrolytes*, Vol. 1, p. 347 (Ed. J. Hladik), 1972.
10. A. C. Angell, *J. Chem. Phys. Solids* (1989) in press. and A. C. Angell and W. Sichina, *Ann. N. Y. Acad. Sci.* 279, 53, 1976.
11. R. Aroca and P. Cook, *Amm. Lab.*, 16, 122 (1984).
12. J. S. Francisco and I. H. Williams, *Chem. Phys.*, 114, 339 (1987).
13. J. S. Francisco and I. H. Williams, *Chem. Phys.* 120, 389 (1987).
14. S. D. Ross, *Spectrochim. Acta.*, 18, 225 (1962).
15. H. Tadokoro, Y. Chatani, T. Yoshihara, S. Tahara and S. Murahashi, *J. Polymer Sci.*, 48, 109 (1964).



92-18250

AD-P007 459



71

STUDY ON DIOPSIDE WHISKERS PRECIPITATION TYPE HYDROXYAPATITE



TORU NONAMI

TDK Corporation, R & D Center, 2-15-7 Higashi-Owada, Ichikawa-shi, Chiba-ken, 272, Japan

ABSTRACT

A biomedical material for use as artificial bone and dental root is provided which takes the form of a sintered composite body comprising a Hydroxyapatite(HAP) and diopside whisker. The mixed powder of HAP and diopside was heated to make this composite material. The sintering of HAP and the precipitation of diopside whisker were examined, to find a method of making them occur simultaneously. Also, diopside was added to HAP and sintering at 1200°C for 2hr. was done. As a result of these investigations, diopside whisker of aspect ratio 10~15 was formed. Moreover the intermediate layer of CaO-SiO<sub>2</sub>-P<sub>2</sub>O<sub>5</sub>-MgO system was generated at the interface of HAP and whisker. The bending strength of this sintered body was 300MPa and fracture toughness was 3.2 MPa·m<sup>1/2</sup>. These values were higher by about 2times or 3times than those of matrix HAP respectively. The increase in bending strength was attributed to an increase in fracture toughness, caused by an increase in fracture surface energy.

INTRODUCTION

HAP is a biocompatible material and has been used as an artificial bone or teeth material. However, the use range is often limited because of low mechanical strength. We investigated a composite HAP for whisker reinforcement type in which whiskers are simultaneously grown during sintering of HAP in order to overcome this disadvantage. As compared with the addition of pre-formed whiskers it is advantageous to form whiskers simultaneous with crystalline HAP as the matrix because the resulting sintered body has improved toughness and strength due to the increased bond between the whiskers and the matrix. The pre-formed whiskers prevent matrix grain growth upon sintering and tend to induce strain. In order to make this composite, the following technical points were considered.

- (1) The whisker forming materials are preferably selected for biological compatibility.
- (2) Select HAP and whisker forming materials for sintering of HAP and transforming into whiskers simultaneously without causing strain.
- (3) Control the mutual reaction between HAP and whisker forming materials to obtain an intermediate layer, at the interface of HAP and whisker, which has a continuous gradient of concentration between HAP matrix grains and whiskers.
- (4) Keep the matrix grain size fine and density to a specific range by Griffith equation[1].

EXPERIMENT

Fabrication of composite

HAP powder was synthesized by precipitation method. Diopside was prepared by mixing composite powders (of composition SiO<sub>2</sub>, CaCO<sub>3</sub>, MgO). The composition was calcined in air at 1100°C for 2hr. Added 20wt% diopside to HAP and milled in a ball mill for 1hr. The collected cake was dried at 120°C

for 5hr. and a portion of the cake was then molded under a pressure of 30MPa. The compacts were heated in air at 1100~1300°C for 2hr. The obtained composites were sectioned and observed under an electron scanning microscope to determine their whisker amount, matrix grain size, whisker length, and whisker aspect ratio. Crystals precipitated were identified using a powder X-ray diffraction method (XRD). The concentration of Si, Ca, P and Mg was measured using a scanning transmission electron microscope (STEM). HAP disks were fabricated by hot-isostatically pressing at 203MPa and 1000°C for 2hr. in argon.

#### Density of composite

Density of the composite was measured in water using Archimedean technique.

#### Measurement of Mechanical property

Bending strength was measured by three-point bending method on ten test specimens of 3 by 4 by 40mm with a span of 36mm and a crosshead speed of 0.5mm/min. Fracture toughness KIC was measured by three-point bending method on notched-beam specimens of 3 by 2 by 25mm with 15mm span at crosshead speed of 0.5mm/min. Four specimens were tested to get an average of data points. Young's modulus and Poisson's ratio were measured on rectangular bars (80 by 2 by 20mm) using ultrasonic pulse echo method.

## RESULTS AND DISCUSSION

#### Selection of Whisker Forming Material and HAP

Whisker forming materials which can convert into whiskers under sintering condition are selected from the group consisting of calcium silicate, aluminum silicate, aluminum silicate calcium, calcium silicate magnesium, calcium aluminate and magnesium silicate systems which are nontoxic. Then anorthite, diopside, wollastonite, monticellite and mullite were selected on the pretext that they can convert into whisker easily upon sintering. Finally we selected diopside for whisker forming material, which can convert into whisker at about 1000~1300°C, and be simultaneously grown during sintering of HAP. To affect the sintering of HAP and the precipitation of whisker simultaneously, we investigated the sintering temperature of HAP and diopside. The sintering temperature was determined by compacting a material to a density of 1.4g/cm<sup>3</sup>, heating the compact at a rate of 20°C/min. by means of a thermocouple, and measuring the heating temperature at which a shrinkage factor of 5% was reached. The sintering temperature of HAP is variable according to the BET value (Fig.1).

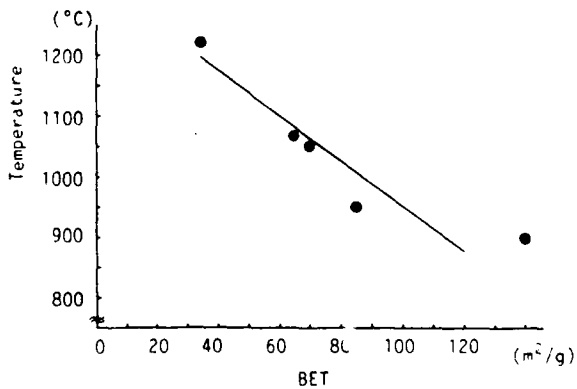


Fig.1 Relation between sintering temperature and BET value of HAP.

The sintering temperature of diopside is variable according to the calcined temperature and composition. Table I. shows the properties of composite body according to the sintering temperature of HAP and diopside. From Table I., diopside preferably has a sintering temperature higher by 100 °C to 300 °C than the sintering temperature of HAP. HAP is sintered in an earlier stage where the whisker component has not been activated. Consequently, the whisker component is unlikely to diffuse into matrix in this stage. If diffusion occurs in this stage, the composition will change and whisker will not form. This is avoided by controlled diffusion of the whisker component in the early stage. There are possibilities that the few matrix is sintered earlier than necessary, and premature sintering of the matrix prevents whisker from precipitating or causes precipitating whisker to be largely stressed. To obtain an intermediate layer between whiskers and matrix, control the chemical reaction between whiskers components and matrix components. Provision of an intermediate layer improves the bond between whiskers and grains also contributing to strength and enables energy control of the interface between whiskers and matrix grains. We investigate the reaction between HAP and diopside. We did the model experiment of diffusion of diopside components to HAP. Table II. shows diffusion constants of Mg and Si from the results of analysis of interface under an electron probe microanalysis (EPMA). The diffusion constant[2] of Mg and Si are increased by an amount of MgO. From these results, mutual reaction between HAP and diopside are controlled by the proportion of MgO in diopside. Table III. shows that Ca/P atom ratios of HAP are effective in the reaction between HAP and diopside. When Ca/P atom ratio is 1.60, HAP changes into tricalcium-phosphate, at the same time diopside changes into wollastonite. These results suggest if the Ca/P atom ratio is less than stoichiometry (Ca/P=1.67), there is some likelihood that part of whisker-forming materials would form a solid solution with HAP, inducing a change in the composition of whisker. As a result, whisker might not fully precipitate. In the case of HAP, part of diopside components might form a solid solution with the HAP to form tricalcium phosphate. When the Ca/P atom ratio is more than 1.67 stoichiometry, there is no change. But in grain boundary it is considered that there are little mutual reaction between HAP and diopside. From these results, we can obtain an ideal intermediate layer if we control the components of diopside and Ca/P atom ratio of HAP. The intermediate layer will contain the common elements of both HAP and diopside, and have a continuous gradient of concentration like Fig.2.

Table I. Sintering temperature of HAP and diopside, and the properties of composite body.

HAP		Diopside		Heated Properties of Composite			
BET Sintering (m <sup>2</sup> /g)	Composition Temp. (°C)	Calcined Temp. (°C)	Sintering Temp. (°C)	Temp. (°C)	Crystal phase *2	Whisker forming	
120	900	A	1100	1330	H D	not formed	
85	950	B	1100	1280	H D	not formed	
85	950	C	1100	1250	H D	formed	
70	1050	C	1000	1050	T W	not formed	
65	1070	C	1100	1250	H D	formed	
35	1220	C	1100	1250	T W	not formed	

\*1 A-SiO<sub>2</sub> 55.2wt% CaO 24.6wt% MgO 20.2wt%  
 B-SiO<sub>2</sub> 55.8wt% CaO 26.0wt% MgO 18.2wt%  
 C-SiO<sub>2</sub> 62.5wt% CaO 23.3wt% MgO 14.2wt%

\*2 D-Diopside  
 H-HAP  
 T-Tricalcium-phosphate  
 W-Wollastonate

Table II. The diffusion constants of Mg and Si.

Diopside components (wt%)			Diffusion constant	
SiO <sub>2</sub>	CaO	MgO	Mg (x10 <sup>-9</sup> cm <sup>2</sup> /s)	Si (x10 <sup>-9</sup> cm <sup>2</sup> /s)
62.5	23.3	14.2	1.2	0.9
52.4	30.3	17.3	1.4	0.9
55.2	24.6	20.2	3.3	2.0

Table III. Ca/P atom ratio of HAP and the properties of composite body.

HAP		Diopside	Heated	Properties of composite			
BET (m <sup>2</sup> /g)	Ca/P	Composition *1	Temp. (°C)	Crystal phase *2	Whisker forming		
65	1.60	C	1250	T H W D	not formed		
65	1.67	C	1250	H D	formed		
65	1.71	C	1250	H D	formed		

\*1 C-SiO<sub>2</sub> 62.5wt% CaO 23.3wt% MgO 14.2wt%

\*2 D-Diopside  
H-HAP  
T-Tricalcium-phosphate  
W-Wollastonite

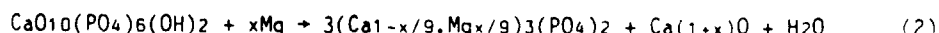
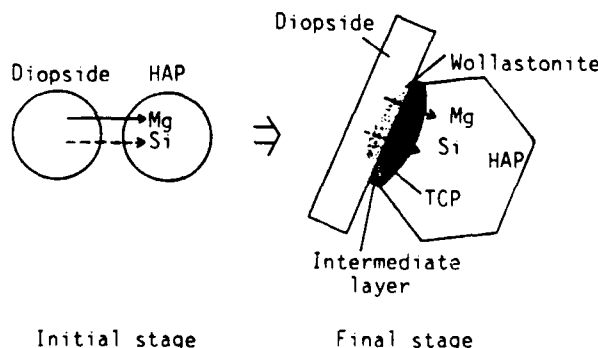


Fig.2 Expectation of mutual reaction between HAP and diopside in grain boundary.

### Fabrication and microstructure of composite

Diopside of composition  $\text{SiO}_2$  62.5%,  $\text{CaO}$  23.3%,  $\text{MgO}$  14.2% in weight percent was used (stoichiometry composition  $\text{SiO}_2$  55.5%,  $\text{CaO}$  25.9%,  $\text{MgO}$  18.6%). HAP of  $\text{Ca}/\text{P}$  atom ratio in 1.67 and BET values of  $65\text{m}^2/\text{g}$  was used. We added diopside powder (20wt%) to the matrix HAP and heated it in air at  $1230^\circ\text{C}$  for 2hr. The microstructure of this composite (HAP-diopside) are shown in Fig.3. Matrix grain size was  $2 \sim 4\mu\text{m}$ , the length of which was  $4 \sim 8\mu\text{m}$ , and the aspect ratio was  $10 \sim 15$ . The result of a transmission electron microscope examination is shown in Fig.4. There are intermediate layers ( $\text{CaO}-\text{SiO}_2-\text{P}_2\text{O}_5-\text{MgO}$  system) in the grain boundary. A little HAP changed into tricalcium phosphate (including Mg), and a little diopside changed into wollastonite. They were generated by mutual reaction between HAP and diopside.



Fig.3 Scanning electron micrographs of HAP-diopside specimens.

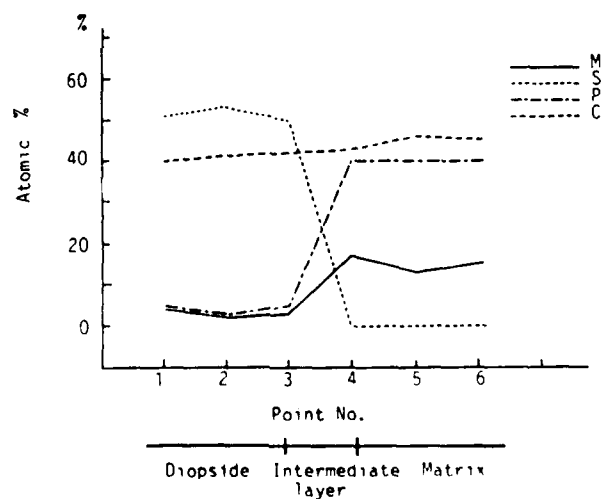


Fig.4 Atomic percents in the grain boundary of Si, P, Ca, Mg detected by transmission electron microscope.

Table IV. Mechanical properties

	$\sigma_f$ (MPa)	E (GPa)	KIC (MPa·m <sup>1/2</sup> )	$\nu$	$\rho$ (g/cm <sup>2</sup> )	c (μm)	$\gamma$ (J/m <sup>2</sup> )
HAP	103	47	1.2	0.26	3.16	22	14
HAP-diopside	300	83	3.2	0.21	3.13	30	59

Mechanical properties

Bending strength ( $\sigma_f$ ), fracture toughness (KIC), Young's modulus (E), Poisson's ratio ( $\nu$ ) are shown in Table IV. It was found that the bending strength and the fracture toughness for the composite (HAP-diopside) were higher by 2times and 3times than those of the HAP. The bending strength is expressed as a function of the fracture toughness and critical flaw size c given by the following equation[3].

$$\sigma_f = KIC / Y \cdot c^{1/2} \quad (1)$$

(Y is a dimensionless crack geometry constant[4].) Using this equation, the critical flaw size c is shown in Table IV. Since the critical flaw size c for HAP-diopside is larger than that of HAP, the increase in bending strength caused by the whisker is attributed to the increase in fracture toughness. The fracture surface energy was calculated by the following equation[5].

$$KIC = [2E\gamma / (1-\nu^2)]^{1/2} \quad (2)$$

The surface energy was calculated by this equation and is shown in Table IV. Young's modulus and fracture surface energy for HAP-diopside are higher by about 2times and 5times than those of HAP. And hence the higher fracture toughness KIC for HAP-diopside is attributed mainly to the increase in the fracture surface energy. We considered it was caused by crack deflecting and pullout of whiskers.

## CONCLUSION

The sintering of HAP and the precipitation of diopside whisker were examined, to find a method for making them occur simultaneously. The BET value of HAP was 65m<sup>2</sup>/g, and the composition of diopside was SiO<sub>2</sub> 62.5%, MgO 14.2%, CaO 23.3%. This was selected to control the reaction of HAP and diopside and obtained diopside whiskers precipitation type HAP composite. There were CaO-SiO<sub>2</sub>-P<sub>2</sub>O<sub>5</sub>-MgO system intermediate layers between HAP and whiskers. Matrix grain size was 2 ~ 4μm, the length of whisker was 4 ~ 8μm, and the aspect ratio was 10 ~ 15. The bending strength 300MPa, and the fracture toughness 3.2MPa·m<sup>1/2</sup> are higher by about 2times or 3times than those of HAP. The increase in bending strength was attributed to the increase in fracture toughness caused by the increase in fracture surface energy. It was considered the increase in fracture surface energy was caused by whisker pullout and crack deflecting.

## REFERENCES

1. A.A.Griffith, Phil. Trans. Roy. Soc. A 221, 163 (1920).
2. Ceram. Soc. Jpn., Ceramic kogaku handbook, (Gihoudo, 1989), P.106.
3. Dabidge, R.W., Mechanical Behavior of Ceramics, (Cambridge Univ. Press London, 1979), P.18.
4. Irwin, G.R., J. Appl. Mech., 29, 651 (1962).
5. Lawn, B.R. and Wilshan, J.R., Fracture of Brittle Solids, (Cambridge Univ. Press London, 1975), P.57.



---

---

**PART II**

**Non-Linear Optics in  
Multifunctional Materials**

92-18251

AD-P007 460



9



MULTIFUNCTIONAL MOLECULAR AND POLYMERIC MATERIALS  
FOR NONLINEAR OPTICS AND PHOTONICS

PARAS N. PRASAD

Photonics Research Laboratory, Department of Chemistry, State University of New York at Buffalo, Buffalo, NY 14214

Molecular units in natural systems are multifunctional in that they exhibit more than one functionalities. This is nature's way of economizing and being efficient. For many technological applications, there is a need for synthetic multifunctional materials which simultaneously exhibit many necessary physical and chemical properties. By appropriate modification of structures both at the molecular and bulk levels, one can incorporate such multifunctionality in molecular and polymeric systems. Our research program focuses on investigations of multifunctional materials for applications in photonics. Photonics describes the emerging new technology in which a photon instead of an electron is used to acquire, process, store and transmit information.

Photonics has many distinct merits over electronics. The most important advantage is the gain in speed; this results from the fact that a photon travels much faster than an electron. Also, in photonic circuitry one can use three-dimensional connectivity to produce smaller integrated optical chips. Other advantages are: that there is no electrical or magnetic interference; that the photonic circuits are fully compatible with existing fiber optic networks; and that remote sensing and space applications are possible. Furthermore, there are new applications of photonics, such as sensor protection against laser threats, that are not achievable from electronics alone.

For optical switching required for optical processing of information one needs to use nonlinear optical effects that allow the manipulation of light propagation by application of an electric field or a laser pulse. In addition, nonlinear optical effects also give rise to a frequency conversion, such as frequency doubling for high density optical data storage and image analysis.

We have developed a very comprehensive research program in the area of nonlinear optical effects in organic materials. This program covers microscopic theory of optical nonlinearity, design and synthesis of novel structures, materials processing for guided waves, measurements of optical nonlinearities and study of device processes. First, we briefly present our accomplishments in each category. Then we describe our research effort in producing heterostructure systems for applications in photonics.

Theory

We have used both classical anharmonic oscillator approach as well as ab-initio calculations to understand the microscopic nature of optical nonlinearities in organic structures. Our ultimate goal is to understand the structure-property relationship so that one may be able to predict structures with enhanced optical nonlinearities. The focus of our work has been on third-order optical nonlinearity.

We developed a simple model of coupled locally anharmonic oscillators which can be used to describe the optical nonlinearities in conjugated organic monomeric, oligomeric and polymeric structures [1]. This method can very readily be used to explain the dependence of the band gap, the linear polarizability,  $\alpha$ , and the second hyperpolarizability (microscopic third-order nonlinear optical coefficient),  $\gamma$ , on the number of repeat units for the oligomers of thiophene and benzene. The results predicted by the coupled anharmonic oscillator model are in good agreement with those of the

experimental studies on thiophene and benzene oligomers recently reported by our group.

Static polarizability and second hyperpolarizability tensors have also been computed for a series of polyenes, polyyynes and cumulenes by *ab initio* SCF theory [2-6] using the finite field (FF) calculations in which a polynomial fit of either energy or induced dipole moment as a function of field strength was conducted. Fully coupled (FF) and uncoupled (SOS) *ab initio* SCF calculations, using identical small basis sets, were found to be in reasonably good agreement for linear polarizabilities but not for the hyperpolarizabilities (nonlinear optical coefficients). Diffuse orbital basis functions are required for qualitatively correct hyperpolarizabilities of small conjugated  $\pi$  systems. We have used a corresponding orbital analysis to separate the  $\sigma$  and  $\pi$  electron contributions to optical nonlinearities. The  $\pi$ -electron contribution dominates the optical nonlinearity. Polarizability and second hyperpolarizability are given by the first and third derivatives, respectively, of charge density with respect to field strength. A contour map of the first derivative density for an acetylenic chain is nearly periodic, corresponding to localized polarization of individual triple bonds. A map of the third derivative density does not exhibit this feature, corresponding to longer range charge shifts induced by the applied electric field.

With a goal to investigate the role of heavy atoms in determining optical nonlinearities, we have conducted [7] *ab-initio* calculations of polarizability,  $\alpha$ , and first and second hyperpolarizabilities,  $\beta$  and  $\gamma$  for the haloform series  $\text{CHX}_3$ , where  $X = \text{F, Cl, Br, and I}$  using the Effective Core Potential (ECP) approach. The microscopic optical nonlinearities  $\alpha$ ,  $\beta$  and  $\gamma$  were calculated as the derivatives of the energy with respect to the electric field, with the energy determined by means of the Self-Consistent-Field approach (SCF), and nonlinearities calculated in the static field limit by means of the Coupled Perturbed Hartree-Fock (CPHF) formalism. To test the usefulness of the ECP method, nonlinear optical responses for the lighter members of the series,  $\text{CHF}_3$  and  $\text{CHCl}_3$ , were computed by using both all electron and ECP calculations. The results are compared, and are found to be in excellent agreement. The effects of various basis sets and inclusion of diffuse and polarization functions are also examined to select a basis set which gives a good description of optical nonlinearities. The ECP technique is, then, used to calculate optical nonlinearities for  $\text{CHBr}_3$  and  $\text{CHI}_3$ . Although a very good agreement was found between the calculated and experimental polarizabilities for the haloform series, a rather poor agreement was obtained for the higher order polarizabilities.

In order to examine the importance of electron correlation, we conducted an *ab-initio* calculation of polarizability and second hyperpolarizability for the benzene molecule including electron-electron correlation [8]. The finite field method was used. For each selected strength of the applied electric field the energy of the benzene molecule was calculated using the Self-Consistent Field method (SCF) as well as with its Moeller-Plesset correction in the second order (MP-2). Then the microscopic optical nonlinear responses were calculated by fitting both the SCF energy and the MP-2 energy to a polynomial in the field strength. We found that electron correlation significantly enhances the second hyperpolarizability. For the polarizability, our computed value showed an excellent agreement with the experimentally measured value. For the second hyperpolarizability, the computed value using MP-2 energy showed a reasonable agreement with that reported by the Electric Field Induced Second Harmonic (EFISH) generation but a poor agreement with the result of Degenerate Four Wave Mixing (DFWM). In conclusion, our theoretical work suggests that current computational studies do not provide a quantitative description of optical nonlinearities, especially the third-order effect.

### Design and Synthesis

Our effort under this topic has been focused on making sequentially built and systematically derivatized structures with an objective that measurements of optical nonlinearities on these compounds will yield an insight into structure-property relationship. To investigate the dependence of the microscopic third-order optical nonlinearity  $\gamma$  on the number of repeat units, we prepared the  $\alpha$ -trimer, tetramer, pentamer and hexamer of thiophene (I):

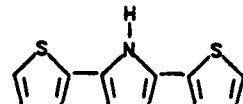
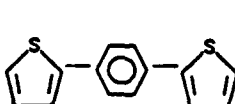


thiophene oligomers  
I

II  $x, y = \text{NO}_2$

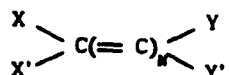
The dependence of both  $\alpha$  and  $\gamma$  on the number of repeat units  $N$  was measured and compared with theoretical predictions [9]. A satisfactory agreement was found.

To examine the effect of systematic derivatization, structures II were prepared and measurements were made. We also prepared the following derivatized structures.



The measurements of  $\alpha$  and  $\gamma$  were made [10]. A comparative study was used to determine the effectiveness of the phenyl, thiophene and pyrrole rings in determining  $\gamma$ .

Another group of compound we have made and are currently investigating is based on rigid cumulene structures III.



III

We have made structures with  $N = 3$  and  $5$ ,  $X = X' = Y = Y' = \text{C}_6\text{H}_5$ .

In order to examine the role of a metal in a conjugated structure we have prepared several higher oligomers of ferrocene and investigated their optical nonlinearities [11]. Our study indicates that the conjugation does not really carry through the metal. The  $\gamma$  value appears to be determined by the  $\pi$ -conjugation through the organic segment.

### Materials Processing

The research under this category has focussed on the preparation of optical quality films and characterization by using structural and

spectroscopic techniques. Ultrathin films with a monolayer resolution have been prepared using both the Langmuir-Blodgett method and the electrochemical polymerization techniques [12-18]. Thin films of optical waveguide dimensions were made by using solution casting techniques such as spin-coating and doctor blading [19,20]. To a very limited extent vacuum deposition has also been used. The objective has been to improve on the optical quality of these films for guided wave or surface-plasmon nonlinear optics.

Molecular assemblies prepared by the Langmuir-Blodgett technique provide useful structures to probe structure-property relationships for nonlinear optical processes. We developed a comprehensive research program in which we studied the Langmuir-Blodgett films of optically nonlinear organic structures. The films were carefully characterized by a variety of surface and spectroscopic techniques. Both second and third order nonlinear optical processes were investigated.

One specific example is that of polythiophene. Monolayer film formation at the air/water interface was investigated for both electrochemically and chemically prepared poly(3-dodecylthiophene) using surface pressure-molecular area isotherms [16]. Only the electrochemically prepared polymer formed a stable monolayer, which was successfully transferred using the horizontal lifting method. The transferred Langmuir-Blodgett films were characterized by u.v.-visible spectroscopy and quartz crystal microbalance measurements. We have also found strong third-order nonlinear optical response from the Langmuir-Blodgett films of poly(3-dodecylthiophene).

#### Experimental Study of Nonlinearity

For experimental study of third-order optical nonlinearity we extensively use the method of femtosecond degenerate four wave mixing. This method has the advantage that one can obtain information on both the magnitude and response time of optical nonlinearity. With a goal to understand the structure-property relationship for third-order microscopic optical nonlinearity, we have investigated the nonlinearities of a number of sequentially built and systematically derivatized  $\pi$ -conjugated structures using degenerate four-wave mixing. An example is the thiophene oligomers. A systematic study of the dependence of the band gap, the linear optical susceptibility, the polarizability  $\alpha$ , and the second hyperpolarizability  $\gamma$ , on the number of repeat unit was conducted for the thiophene series from monomer to hexamer [9]. The experimental values of  $\langle\alpha\rangle$  and  $\langle\gamma\rangle$  for thiophene and  $\langle\alpha\rangle$  for bithiophene are found to be in qualitative agreement with those obtained by a recent ab initio calculation which used the finite field method and included diffuse polarization functions. The experimentally observed dependence of  $\langle\alpha\rangle$  and  $\langle\gamma\rangle$  on the number  $N$  of the thiophene repeat unit is in agreement with that predicted by the ab initio calculations.

We have also investigated the nonlinear response of many conjugated polymers unoriented as well as stretch oriented. The third-order nonlinear optical susceptibility was investigated at wavelengths of 602 and 580 nm for a 10:1 stretch-oriented uniaxial film of poly(p-phenylene vinylene)<sub>3</sub> using femtosecond degenerate four wave mixing [21]. A relatively large  $\chi^{(3)}$  with a subpicosecond response was observed. A large anisotropy in the  $\chi^{(3)}$  value was found, the largest component of  $\chi^{(3)}$  ( $= 5 \times 10^{-10}$  esu) being along the draw direction. This is in agreement with theory which predicts the largest component of  $\gamma$  along the polymer chain.

Electronically resonant third-order optical nonlinearity in several photoresponsive polymers were studied by picosecond and femtosecond degenerate four-wave mixing to investigate the role of photoexcited charge

carriers [22-25]. Both the magnitude and the response time of the observed optical nonlinearities seem to vary over a wide range.

An interesting example is poly(3-dodecylthiophene). The electronically resonance enhanced third-order optical susceptibility of undoped poly(3-dodecylthiophene) was found to be  $\chi^{(3)} \sim 10^{-9}$  esu, large enough to allow the first reported observation of a degenerate four-wave mixing signal from ultrathin Langmuir-Blodgett films of this material [16]. Despite the resonant character, this nonlinearity exhibits femtosecond response. In situ iodine-doping studies of UV-Visible absorption, electrical conductivity and third-order nonlinear optical susceptibility were carried out. Upon doping, the conductivity changed by more than eight orders of magnitude but the  $\chi^{(3)}$  value decreased to within 10 percent of the original value.

We also studied the resonant  $\chi^{(3)}$  behavior of Langmuir-Blodgett films of several phthalocyanines [4,12,13]. Again, the nonlinearity was sufficiently large to observe the degenerate four-wave mixing signal even from a monolayer. The value of  $\chi^{(3)}$  is  $> 10^{-9}$  esu with response being in several picoseconds. Both the magnitude of  $\chi^{(3)}$  and the decay of the signal was found to be dependent on the laser intensity. We assign the intensity dependent decay to the presence of bimolecular processes (exciton-exciton annihilation) [13].

#### Device Processes

Our study under this category focused on the investigation of nonlinear optical processes in waveguides and fibers. We reported the first clear demonstration [26] of intensity-dependent phase shift due to electronic nonlinearity in a nonlinear polymer waveguide in which propagation distances over 5 cm were achieved with total attenuation of  $\sim 1.2$  cm<sup>-1</sup>. Intensity-dependent coupling angle, intensity-dependent coupling efficiency, and limiter action behavior (useful for power limiter sensor protection devices) were observed in the polyamic acid waveguide using grating excitation with 400 fs, 80 ps, and 10 ns pulses. A nonlinear grating coupler analysis identifies the subpicosecond and picosecond processes with electronic nonlinearity, but the dominant effect in the nanosecond experiment is due to thermal nonlinearity derived from weak absorptions. The magnitude and sign of  $n_2$  of electronic nonlinearity were determined from this study.

#### Novel Electroactive and Nonlinear Optical Heterostructures

In this section we discuss some of our very recent accomplishments in producing novel heterostructures for applications in electronics and photonics.

##### (a) Crystalline complexes for efficient frequency doubling.

For high density optical data storage, there is a need for highly efficient frequency doubling materials. Organic molecules in which an electron donor group is separated from an electron acceptor group by a  $\pi$ -electron structure have shown large second-order nonlinearity for frequency doubling. These structures often do not offer wide optical transparency because of the presence of low lying  $\pi-\pi^*$  transition. We have developed new heterostructures which are binary crystalline complexes that show second-order nonlinearity ranking among the highest. These crystalline complexes do not possess the structural features discussed above that have been used in the past for the design of second-order nonlinear material. This new class of material does not rely on  $\pi$ -conjugation and, therefore, offers challenge for developing theoretical models to explain their nonlinearity.

For technological applications we have obtained highly efficient phase-matched frequency doubling in our heterostructures.

(b) Sol-gel silica-polymer composite for integrated optics.

For photonics application, optical waveguides would be an important part of an integrated optical circuit. Conjugated organic polymers constitute an important class of optical materials because they have shown large, nonresonant (non-absorptive), optical nonlinearity with fast response time in the sub-picoseconds regime. In common with most organic polymers however in their pure state, these materials have generally not been found to form good photonic media for optical waveguiding because of typically high optical losses. Conversely, many inorganic glasses, including silica, form excellent photonic media because of the extremely low optical losses achievable. A major problem with such glasses is that their optical nonlinear coefficient e.g.  $\chi^{(3)}$ , the third order nonlinear coefficient, is extremely low. There exists a need for a material combining high nonlinear optical coefficients with high optical quality.

We have prepared to our knowledge the first compatible blend between an inorganic polymer, silica glass, and a  $\pi$ -conjugated optical nonlinear polymer, poly (p-phenylene vinylene), homogeneously mixed over large composition ranges [27,28]. This composite material was prepared by combining sol-gel processing techniques applicable to the silica glass with the preparation of the organic polymer from a water/alcohol soluble sulfonium salt precursor. The organic polymer precursor and the inorganic sol were mixed in a common solvent and converted to the final composite material. The thermal conversion of the organic precursor polymer released HCl which also catalyzed the inorganic sol. The composite material has been characterized by IR, UV-visible spectral analysis and thermogravimetric and differential scanning calorimetric analysis. We have investigated the third-order nonlinearity in this system using femtosecond degenerate four wave mixing and have observed response in less than 100 femtoseconds. The material can be cast into various forms. Thin films cast by the doctor blading technique exhibit good optical quality. We have achieved optical waveguiding at  $1.06 \mu$  in a film of this composite material.

(c) Nonlinear optical processes in a liquid core hollow fiber.

In optical processing, optical amplification and pulse shaping will play important roles. We have observed novel nonlinear optical phenomena in an organic liquid core hollow fiber which can conveniently be used for optical amplification and pulse shaping [29-31]. By using a long interaction length (250 cm) provided by the fiber we have observed novel superbroadening ( $> 200 \text{ cm}^{-1}$ ) of stimulated scattering added on the Stokes side of the pump (Rayleigh) line and the stimulated Raman scattering lines of several anisotropic liquids (eg benzene). To explain these effects, we have proposed a photon scattering model of Rayleigh-Kerr optical effect and Raman-induced optical Kerr effect.

The microscopic picture of the elementary scattering process of optical Kerr effect can be described as follows: a molecule (scattering center) receives an additional energy through the annihilation of an incident photon and simultaneous creation of a red-shifted photon, then the molecule exhausts this additional energy to overcome the rotational viscosity and to do the reorientation work within the liquid. Depending on the initial and final location of the scattering molecule in its eigen-energy levels, the elementary scattering can occur in two possible ways. If the scattering molecule always stays in the same electron-vibrational ground level at the beginning and end of an elementary process, a red-shifted photon will be observed on the Stokes-side of the pump line. This is the Rayleigh-Kerr scattering which corresponds to the ordinary optical Kerr effect. In the

other case, if the induced reorientation is accompanied by a transition of scattering molecule from the initial ground level to a higher electron-vibrational level, a red-shifted photon can be observed on the Stokes-side of a Raman line. This is the Raman-Kerr scattering which corresponds to the so called Raman-induced Kerr (reorientation) effect.

Since molecules in a liquid have a continuous initial orientation angle distribution a great number of elementary scattering processes from different molecules would lead to a continuous red-shifted spectral distribution on the Stokes-side of the pump line and/or Raman lines.

For device applications, we have demonstrated the application of this broadening in high gain amplification of a broad band optical signal [31]. For this purpose a hollow core fiber system filled with liquid benzene was used. Using 4 picosecond dye laser pulses as the pump source, stimulated amplification of the accompanying  $\approx 550 \text{ cm}^{-1}$  broad spontaneous emission was achieved with an amplification factor reaching  $2.3 \times 10^6$ .

#### (d) Langmuir-Blodgett film heterostructure

Poly-n-vinyl carbazole is a photoconductive polymer which has been used for xerography. We have been successful in making Langmuir-Blodgett film heterostructures of poly-n-vinyl carbazole:  $\text{TCNQ-C}_6\text{H}_4\text{C}_6\text{H}_3\text{N}_2^+$  which exhibit charge transfer interaction in monolayer films. These films have the advantage that they provide monolayer and successively deposited multilayer structures. We have successfully transferred such monolayer and multilayer Langmuir-Blodgett films and characterized them by various techniques.

#### Acknowledgements

The author wishes to thank his group members Drs. J. Swiatkiewicz, B. P. Singh, R. Burzynski, J. Pfleger, M. Samoc, A. Samoc, P. Chopra, L. Carlacci, Mr. M. T. Zhao, Mr. Y. Pang, Mr. X. Huang, Mr. P. Logsdon, Mr. M. Casstevens, Mr. M. Carpenter and Mr. He whose works have contributed to this review. The author also thanks Dr. D. Ulrich of AFOSR for his encouragement. This work was supported by the Directorate of Chemical Sciences - Air Force Office of Scientific Research and Air Force Wright Research Development Center - Polymer Branch under contract number F4962087C0042 and by the Office of Innovative Science and Technology - Defense Initiative organization under contract number F4962087C0097.

#### References

1. P.N. Prasad, E. Perrin, and M. Samoc, *J. Chem. Phys.* 91, 2360 (1989).
2. P. Chopra, L. Carlacci, H.F. King, and P.N. Prasad, *J. Phys. Chem.* 93, 7120 (1989).
3. P.N. Prasad, in Nonlinear Optical and Electroactive Polymers, edited by P.N. Prasad and D.R. Ulrich (Plenum Press, New York, 1988), p. 41.
4. P.N. Prasad, in Nonlinear Optical Properties of Polymers, Materials Research Society Symposium Proceedings Vol 109 Eds. A.J. Heeger, J. Orenstein, and D. R. Ulrich (1988) p. 271.
5. P.N. Prasad, in Nonlinear Optical Effects in Organic Polymers, eds. J. Messier, F. Kajzar, P. Prasad, and D. Ulrich, NATO ASI Series E, Vol. 162 (1989) p. 351.

6. P.N. Prasad, in Organic Materials for Non-linear Optics, edited by R.A. Hann and D. Bloor (Royal Society of Chemistry, London, 1989), p. 264.
7. E. Perrin, P.N. Prasad, S.P. Karna and M. Dupuis, submitted to J. Chem. Phys.
8. E. Perrin, P.N. Prasad, P. Mougenot and M. Dupuis, J. Chem. Phys. 91, 4728 (1989).
9. M.T. Zhao, B.P. Singh, and P.N. Prasad, J. Chem. Phys. 89, 5535 (1988).
10. M.T. Zhao, M. Samoc, B.P. Singh, and P.N. Prasad, J. Phys. Chem. 93, 7916 (1989).
11. S. Ghosal, M. Samoc, P.N. Prasad, and J.J. Tufariello, J. Phys. Chem. (in Press).
12. P.N. Prasad, M.K. Casstevens, J. Pfleger, and P. Logsdon, Symposium on Multifunctional Materials - SPIE Proceedings Vol. 878 (1988) p. 106-112.
13. M. Casstevens, M. Samoc, J. Pfleger, and P.N. Prasad, J. Chem. Phys. (in Press).
14. J.E. Biegajski, D.A. Cadenhead, and P.N. Prasad, Langmuir 4, 689-693 (1988).
15. X. Huang, R. Burzynski, and P.N. Prasad, Langmuir 5, 325-329 (1989).
16. P. Logsdon, J. Pfleger, and P.N. Prasad, Synthetic Metals 26, 369 (1988).
17. M.M. Carpenter, P.N. Prasad, and A.C. Griffin, Thin Solid Films 161, 315 (1988).
18. X. Huang, M.T. Zhao, L. Janiszewska, and P.N. Prasad, Synthetic Metals 24, 245 (1988).
19. R. Burzynski, R.J. Zanoni, G. Assanto, G.I. Stegeman, and P.N. Prasad, submitted to J. Appl. Optics.
20. R. Burzynski, P.N. Prasad, and F.E. Karasz, Polymer (in Press).
21. B.P. Singh, P.N. Prasad, and F.E. Karasz, Polymer 29, 1940 (1988).
22. P.N. Prasad, J. Swiatkiewicz and J. Pfleger, Molecular Crystals and Liquid Crystals 160, 53 (1988).
23. S.K. Ghoshal, P. Chopra, B.P. Singh, J. Swiatkiewicz and P.N. Prasad, J. Chem. 90, 5078 (1989).
24. B.P. Singh, M. Samoc, H.S. Nalwa, and P.N. Prasad, J. Chem. Phys. (in Press).
25. M. Samoc and P.N. Prasad, J. Chem. Phys. 91, 6643 (1989).
26. R. Burzynski, B.P. Singh, P.N. Prasad, R. Zanoni, and G.I. Stegeman, Appl. Phys. Lett. 53, 2011 (1988).
27. P.N. Prasad, in Ultrastructure Processing of Ceramics, Glasses and Composites eds. D. Uhlman and D.R. Ulrich, John Wiley (in Press).

28. C.J. Wung, Y. Pang, P.N. Prasad, and F.E. Karasz, submitted for publication to Polymer.
29. G.S. He and P.N. Prasad, Phys. Rev. A (in Press).
30. G.S. He and P.N. Prasad, Optics Commun. 73, 161 (1989).
31. G.S. He, G.C. Xu, R. Burzynski, and P.N. Prasad, Optics Commun. 72, 397 (1989).



92-18252



AD-P007 461



ENHANCEMENT OF THIRD ORDER NONLINEARITY  
ON PHTHALOCYANINE COMPOUNDS



Masahiro Hosoda, Tatsuo Wada, Akira Yamada, Anthony F. Garito<sup>a)</sup>  
and Hiroyuki Sasabe  
Frontier Research Program (RIKEN), Wako, Saitama 351-01, Japan

ABSTRACT

The third order optical susceptibilities  $\chi_{1111}^{(3)}(-3\omega; \omega, \omega, \omega)$  for soluble metallophthalocyanine derivatives were determined by optical third harmonic generation measurements of molecularly doped polymer films at a wavelength of 1907nm. The  $\chi^{(3)}$  value of tetra-tert-butylvanadylphthalocyanine is larger than that of metal-free derivative. We demonstrate experiment on modes of propagating light wave in molecularly doped films which exhibit excellent optical quality. The enhancement of third order optical nonlinear susceptibilities in phthalocyanine compounds are discussed in terms of molecular structure and molecular packing.

INTRODUCTION

Recently it has been recognized that organic materials have extremely large optical nonlinearities and ultrafast responses which are due to delocalized  $\pi$ -electrons. Conjugated linear chains such as polydiacetylenes(PDA) possess very large third order nonlinear optical susceptibility ( $\chi^{(3)}(-3\omega; \omega, \omega, \omega) = 8.5 \times 10^{-10}$  esu) as reported in both theoretical and experimental pioneer works[1][2]. In linear chain structures, the major contribution to the microscopic third order optical susceptibility  $\gamma_{ijkl}(-\omega_4; \omega_1, \omega_2, \omega_3)$  is the dominant chain axis component  $\gamma_{xxxx}(-\omega_4; \omega_1, \omega_2, \omega_3)$  with all electric fields aligned along the chain axis (x-axis). By moving from linear to cyclic conjugated structures, one may open new tensor components such as  $\gamma_{yyyy}$ ,  $\gamma_{xxyy}$ ,  $\gamma_{xyxy}$ ,  $\gamma_{xyyx}$ ,  $\gamma_{yyxx}$ ,  $\gamma_{yxyx}$  and  $\gamma_{yxxy}$  [3]. Furthermore nonlinear optical properties of conjugated cyclic chains are investigated for their secondary properties such as thermal and chemical stabilities and for processabilities.

Among macrocyclic conjugated compounds, metallophthalocyanines are well-known to show various optoelectronic responses [4]. We have already reported that vanadylphthalocyanine(VOPc) has a large third order nonlinear optical susceptibility ( $\chi^{(3)}(-3\omega; \omega, \omega, \omega) = 10^{-10}$  esu at a wavelength of 1907nm) [4][5]. This value is almost the same magnitude of  $\chi^{(3)}$  of PDA. A compound which has excellent solubility in various organic polymers will provide excellent processability to obtain thickness-controlled thin films by conventional spin coating technique. Metallophthalocyanine compounds with pe-

<sup>a)</sup>Permanent address: Department of Physics, University of Pennsylvania, Philadelphia, PA 19104

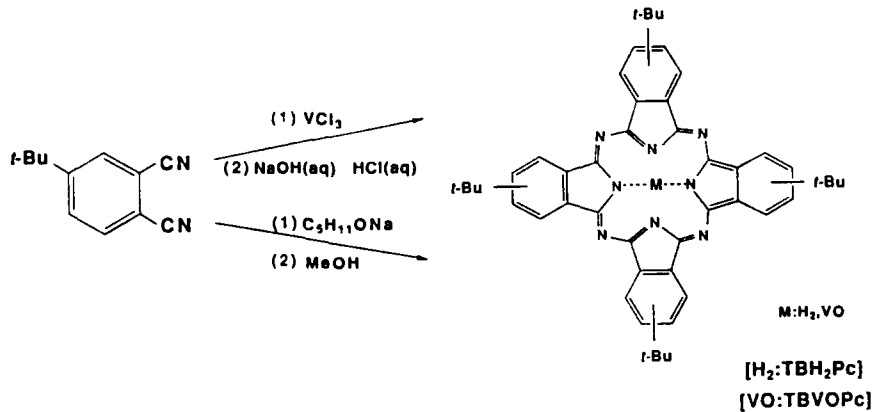
ipheral substitution on each phenyl ring are highly soluble in organic solvents. Among various substituent groups, *tert*-butyl, trimethylsilyl and sulfamide groups seem to give the highest solubilizing effect on phthalocyanine materials[6]. In the present work the *tert*-butyl group is chosen because alkyl groups are well-known to have very little effect on the electronic properties of a chromophore.

In this paper we report optical third harmonic measurements of molecularly doped PMMA films of soluble phthalocyanines and discuss the enhancement of third order optical susceptibilities in phthalocyanine derivatives.

## EXPERIMENTAL

### Materials

Tetra-*tert*-butylphthalocyanines [ M : H<sub>2</sub>(metal-free), VO] (TBH<sub>2</sub>Pc, TBVOPc) were synthesized according to Scheme 1 [6][7]. The materials were thoroughly purified by column chromatography on silica gel using chloroform as an eluent, followed by precipitation from chloroform to methanol. Characterization was made by IR, H-NMR, FD-MS and elemental analysis. Optically transparent films containing TBH<sub>2</sub>Pc or TBVOPc in polymethylmethacrylate (PMMA:Mn=3.1x10<sup>4</sup>) were obtained by spin coating of chloroform solutions onto a fused silica substrate. Refractive indices of thin films are measured by ellipsometry and mode-lines methods.



Scheme 1. Synthesis of tetra-*tert*-butylphthalocyanine compounds

### THG measurement

Optical third harmonic generation measurements were performed at a wavelength of 1907nm under the vacuum of several Torr. in order to eliminate the effect of air. A fundamental wavelength (1064nm) of Q-switched Nd:YAG laser was converted to 1907nm by Stokes-Raman shift through high pressure hydrogen

cell. The transmitted third harmonic (635.7nm) was selected by a monochromator and detected by a photomultiplier tube (PMT). The signal from PMT was integrated by a boxcar triggered in synchronizing with laser. All experimental operations were controlled by a microcomputer.

## RESULTS AND DISCUSSION

### Absorption spectra

TBH<sub>2</sub>Pc or TBVOPc having a peripheral bulky substituent on each phenyl ring showed excellent solbilizing effect and is possible to form thin films by spin coating technique. Those films exhibit electronic transitions in the visible region (Q band at 600-800nm) and in the near UV region (Soret band at 300-400nm), as shown in Figure 1. In the near IR region (1907nm) there is no absorption. The absorption, however, can not be negligible at third harmonic. In general it has been pointed out that Q band attributed to  $\pi-\pi^*$  transition is sensitive to environment of molecules such as orientation and packing of phthalocyanine's ring. Bathochromic or hypsochromic shift in the visible region arising from different morphology is reported on metallophthalocyanines such as H<sub>2</sub>Pc and VOPc [8][9]. Absorption peaks of TBH<sub>2</sub>Pc and TBVOPc films were observed at 612nm and 704nm in Q band, respectively. The correlation between absorption coefficient at each peak wavelength and weight ratio of the phthalocyanines in PMMA is linear as shown in Figure 2. Also no shift of peak position was observed under these conditions.

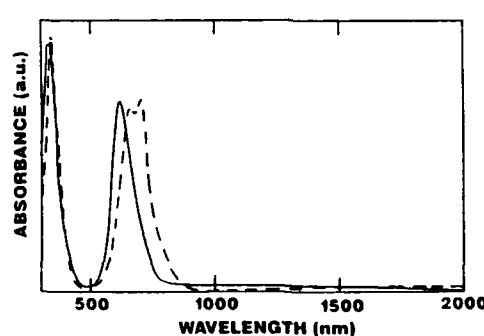


Figure 1. Absorption spectra of tetra-tert-butylphthalocyanine films:  
—, TBH<sub>2</sub>Pc; - - - - -, TBVOPc.

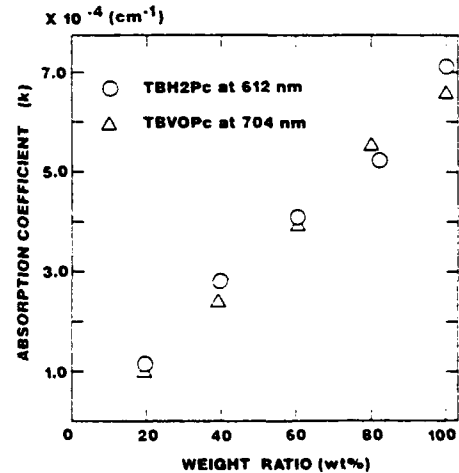


Figure 2. Absorption coefficient and weight ratio of tetra-tert-butylphthalocyanines in PMMA.

### Nonlinear optical properties

The typical results of rotational THG Maker fringes are shown in Figure 3. The interference fringe pattern of a fused silica substrate as reference sample gives a coherence length, which agreed with the value reported in literature [10]. Evaluation of  $\chi^{(3)}$  was carried out with  $\chi^{(3)}$  ( $2.8 \times 10^{-14}$  esu at 1907nm) of a fused silica determined by Meredith *et al* [10]. The obtained patterns were analyzed by the curve fitting method calculated from the equation [11]:

$$J_{3\omega} = \frac{2304\pi^6 J_\omega^3}{C^2} \left| \frac{A\chi^{(3)}}{n_\omega + n_{3\omega}} \right|^2 \left( \frac{1}{\lambda_\omega} \right)^2$$

where  $J_\omega$  is the fundamental beam intensity,  $n_\omega$  and  $n_{3\omega}$  are respectively refractive indices at fundamental and harmonic frequency, and  $A$  is a factor arising from transmission and boundary conditions.

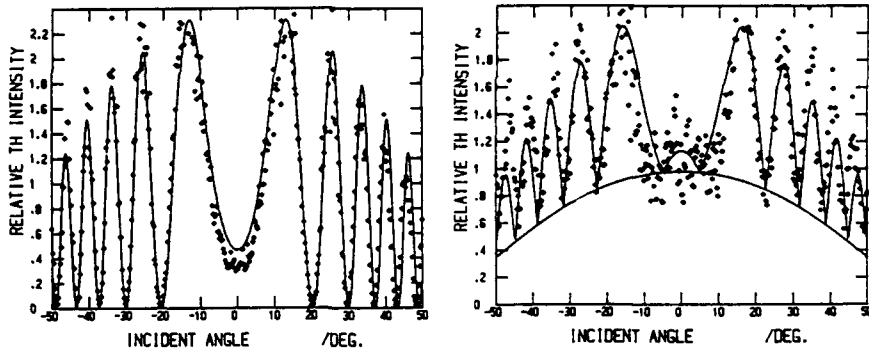


Figure 3. THG Maker fringe patterns of fused silica substrate (thickness 1mm)(left) and  $TBH_2Pc$  (thickness  $0.15 \mu m$ ) on fused silica (right).

The corresponding values of  $\chi^{(3)}$  for  $TBH_2Pc$  and  $TBVOPc$  are  $3.0 \times 10^{-12}$  and  $7.5 \times 10^{-12}$  (esu), respectively.  $\chi^{(3)}$  values of the doped films are proportional to concentration of the phthalocyanine compounds in PMMA as shown in Figure 4.

The measured macroscopic  $\chi_{ijkl}^{(3)}(-3\omega; \omega, \omega, \omega)$  of each molecularly doped films is directly related to the microscopic  $\gamma_{ijkl}(-3\omega; \omega, \omega, \omega)$  of the phthalocyanine molecules through local field factors expressed in terms of the refractive indices  $n_\omega$  and  $n_{3\omega}$ .

Modes of propagating light waves in molecularly doped PMMA thin film of  $TBVOPc$  were clearly observed by using prism-film coupling method. This indicates that these molecularly doped thin films are applicable for nonlinear optical waveguide devices.

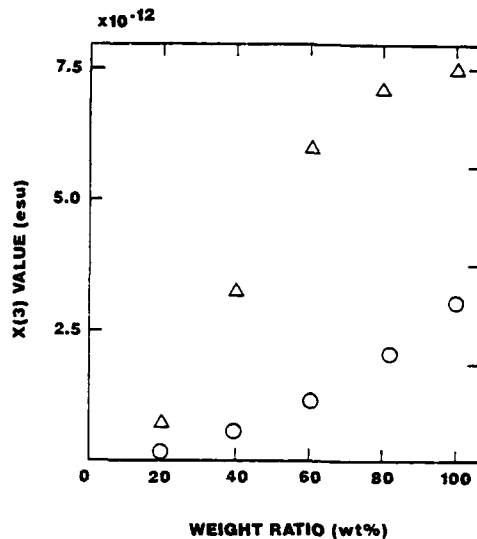


Figure 4.  $X^{(3)}$  value plotted against weight ratio of tert-butylphthalocyanines in PMMA:  
 (○),  $TBH_2Pc$ ; (△),  $TBVOPc$ .

#### Enhancement of third order nonlinearity

As reported previously,  $X^{(3)}$  values of vacuum evaporated thin films of VOPc and  $H_2Pc$  are  $1.85 \times 10^{-10}$  and  $6.0 \times 10^{-12}$  (esu), respectively[4][5]. Difference in  $X^{(3)}$  values of  $TBH_2Pc$  and  $TBVOPc$  indicates that the metal-to-ligand and ligand-to-metal charge transfer states introduced by metal substitution contributes to the enhancement of third order susceptibility, as discussed by Snow *et al* [12]. X-ray analysis showed that thin films of  $TBH_2Pc$  and  $TBVOPc$  on a silica substrate were amorphous. The stacking structure of VOPc is significantly important to increase the third order nonlinearity in condensed states. Introduction of peripheral tert-butyl groups seemed to affect slightly the electronic properties of a chromophore, and reduced about one order of magnitude of  $X^{(3)}$  in VOPc. VOPc possesses distinctly a crystalline form which differs from  $H_2Pc$  [13]. According to Griffith *et al* [10][14], the polymorphism in vacuum-deposited thin films of VOPc is attribute to two crystalline forms of (a) a cofacially stacked arrangement, aligned linearly along the metal-oxo bond and (b) a slipped-stack arrangement, staggered assembly on adjacent molecules in the thin film. The latter unique stacking arrangement leads to bathochromic shift in the visible Q band.

Although detailed investigations are necessary to clarify the changes in packing structure, our preliminary experiments show that these crystalline forms differ each other in the electronic transition of Q band and  $X^{(3)}(-3\omega; \omega, \omega, \omega)$  values[15].

#### ACKNOWLEDGEMENT

The authors wish to thank Mr. M. Kashima of UNITIKA Ltd. for the X-ray analysis of thin films of metallophthalocyanine compounds.

## REFERENCES

- [1] C. Sauteret, J.P. Hermann, R. Fey, F. Pradere, J. Ducuing, R.H. Baughman, and R.R. Chance, *Phys. Rev. Lett.*, 36, 956 (1976).
- [2] G.P. Agrawal, C. Cojan, and C. Flytzanis, *Phys. Rev. B*17, 776 (1978).
- [3] T. Wada, J. Ojima, A. Yamada, A.F. Garito, and H. Sasabe, *Proceedings of SPIE*, 1147, in press.
- [4] T. Wada, Y. Matsuoka, K. Shigehara, A. Yamada, A.F. Garito, and H. Sasabe, *Photoresponsive Materials*, edited by S. Tazuke(*Proceedings of the MRS International Meeting on Advanced Materials*, 12, 1989).
- [5] T. Wada, S. Yamada, Y. Matsuoka, C.H. Grossman, K. Shigehara, H. Sasabe, A. Yamada, and A.F. Garito, *Nonlinear Optics of Organics and Semiconductors*, edited by T. Kobayashi(*Springer Proceedings in Physics*, 36, 1989).
- [6] K-Y. Law, *Inorg. Chem.*, 24, 1778 (1985).
- [7] S.K. Mikhaleenko, S.V. Barkanova, O.L. Lebedev, and E.A. Luk'yanets, *J. Gen. Chem. USSR*, 81, 2770 (1971).
- [8] J.H. Sharp and M. Lardon, *J. Phys. Chem.*, 72, 3230 (1968).
- [9] C.H. Griffiths, M.S. Walker, and P. Goldstein, *Mol. Cryst. Liq. Cryst.*, 33, 149 (1976).
- [10] G.M. Meredith, B. Buchalter, C. Hanzlick, *J. Chem. Phys.*, 78, 553 (1978).
- [11] F. Kajzar and J. Messier, *Thin Solid Films*, 132, 11 (1985).
- [12] J.S. Shirk, J.R. Lindle, F.J. Bartoli, C.A. Hoffman, Z.H. Kafafi, and A.W. Snow, *Appl. Phys. Lett.*, 13, 1287 (1989).
- [13] J.M. Robertson, *J. Chem. Soc.*, 1195 (1936).
- [14] R.Z. Ziolo and C.H. Griffiths, *J. Chem. Soc. Dalton Trans.*, 2300 (1980).
- [15] M. Hosoda, T. Wada, A. Yamada, and H. Sasabe, to be published.



92-18253



AD-P007 462



95

DESIGN, CHARACTERIZATION, AND OPTICAL PROPERTIES  
OF PHOSPHAZENE-BASED POLYMERS

GREGORY J. EXARHOS, AND WILLIAM D. SAMUELS

Pacific Northwest Laboratory, PO Box 999, MSIN K2-44, Richland, WA 99352

ABSTRACT

Physical properties intrinsic to linear inorganic polymer systems can be modified through replacement of chemical groups external to the chain backbone. This substitution also perturbs chemical bonding along the chain which can further influence polymer properties. Several phosphazene polymers deposited as thin dielectric films exhibit extended ultraviolet transmission. Second harmonic generation (SHG) has been observed in these polymers as well as in cyclic polymer precursors. The relative magnitude of SHG is found to correlate both with the nature of the substitutional group and molecular conformation. Influence of these parameters on substrate-film adhesion and measured optical properties is discussed in terms of substitutional group electronegativity, and electronic charge localization in the polymer chain which is probed using molecular spectroscopic techniques.

INTRODUCTION

Polyphosphazenes, having the general formula  $(NPX_2)_n$  where X can be an organic or inorganic substitutional group on the phosphorus atom, belong to a class of linear inorganic polymers which are being used in a variety of technological applications ranging from low temperature elastomers to high temperature thermoplastics. Extreme variations in polymer properties arise from the influence of substituent electronegativity and steric interactions on the chemical bonding within the linear chain. Optical response, substrate adhesion, and stability, are three properties of importance to dielectric film applications. Optimization of these parameters in such materials can be achieved through appropriate derivatization of the reactive polymer.

The nature of phosphorus-nitrogen chemical bonding in these systems has been addressed previously and refined in recent work involving ab initio electronic structure calculations of the phosphonitrilic trimer [1]. This work confirmed the "islands-of-delocalization" model which limits pi-electron delocalization to a three-atom center (N-P-N) owing to the symmetries of the contributing nitrogen 2p and phosphorus 3d atomic orbitals. Electron density is displaced toward the electronegative nitrogen atom centers and generates a partial ionic contribution to the in-chain P-N bond. The magnitude of this effect is controlled by the electron withdrawing power of substituent groups on the phosphorus atom and has been verified in several recent spectroscopic investigations [2,3]. For example, Raman measurements of  $(NPCl_2)_3$  subjected to high hydrostatic pressures show marked intensity increases of the  $A_1$  ring modes with respect to the out of ring  $>PCl_2$  symmetric stretching mode [2]. Results suggest that the observed increase in ring polarizability arises from P-Cl bond contraction which leads to increased electron density on the phosphorus atom sites. Solvent hydrogen bonding influences the distribution of pi electron density in the P-N backbone as demonstrated in work involving Raman measurements of water additions to acetonitrile solutions of the hexamethoxyphosphazene trimer [3]. In addition, a large cross-section for the infrared active P-N stretching mode confirms the predicted polarity of this bond. Variations in mode frequency and relative intensity with the

electronegativity of substituent groups and molecular conformation attest to the marked influence modifying chemical groups exert over localized P-N interactions. Design of multifunctional phosphazene polymers is based upon chemical control of these localized interactions.

The notion of partial ionic bonding in the phosphazene polymer chain suggests an increased basicity of the nitrogen atom centers which can serve as polymer attachment sites to hydroxylated surfaces via a hydrogen bonding mechanism. Such interactions have been identified from  $^{31}\text{P}$  NMR measurements of alumina dispersions in solvents containing dissolved phosphazenes [4], and are important when considering adhesion of polymer films to oxide substrates.

The optical properties of selected phosphazene polymers and polymer precursors are reported in this work. Solution deposition of high quality optical films from homogeneous polymer solutions has been demonstrated using spin casting or dip coating methods. Deposited films adhere strongly to silica substrates and show extended transmission into the ultraviolet region of the spectrum. The wavelength limit for uv transmission and observed non-linear optical response are shown to be perturbed by the nature of functional groups substituted on the phosphorus atom.

## EXPERIMENTAL

### Materials Synthesis

Cyclic dichlorophosphazene trimers or tetramers are convenient starting materials for the preparation of high molecular weight polymers. A thermally induced ring cleavage reaction initiates growth of the linear polyphosphazene chain ( $10^4$  repeat units/chain). Polybisdichlorophosphazene,  $-\text{[NPCl}_2\text{]}_n$ , is readily soluble in nonpolar solvents facilitating purification. The reactive P-Cl bond allows derivatization through a nucleophilic substitution mechanism enabling the preparation of a wide variety of polymers under relatively mild reaction conditions [5]. Derivatization of cyclic polymer precursors is accomplished using analogous techniques and many examples have been reported [6]. Figure 1 summarizes the preparative chemistry and identifies materials used in this investigation. Successive recrystallization insured high purity of the derivatized material which was confirmed from High Performance Liquid Chromatography (HPLC) and  $^{31}\text{P}$  NMR measurements.

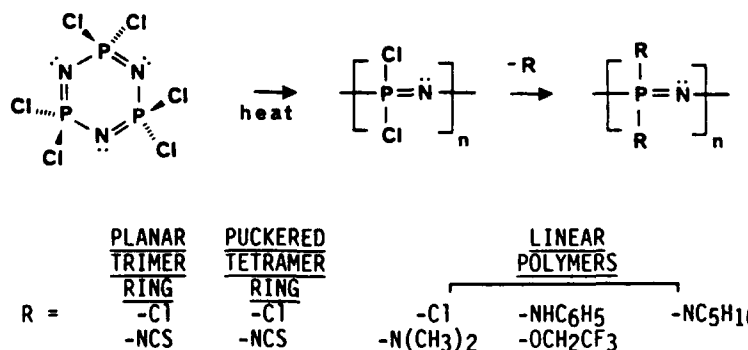


Fig. 1. Thermally-induced polymerization of cyclic phosphazenes and selected derivatives.

Films were deposited onto cleaned silica substrates using dip coating or spin casting techniques. Substrate surfaces were cleaned and hydroxylated by treatment with NaOH/methanol followed by a hydrochloric acid and deionized water rinse to remove residual sodium chloride. Polymer solutions were filtered through 0.2 micrometer Gelman fluoropolymer membranes prior to use. The chlorophosphazene polymer (CP), phenylamine-substituted polymer (PAP), and piperidine-substituted polymer (PP) were dissolved in non-polar solvents (toluene, chloroform, tetrahydrofuran); the trifluoroethoxy polymer (TFEP) was soluble in acetone, and the dimethylamine-substituted phosphazene (DMP) was soluble in trifluoroethanol. Polymer solution concentrations averaged 0.3 N. Standard dip coating or spin casting procedures generated films of 1 micrometer average thickness. While DMA is water soluble at low pH, the other materials show no measurable solubility in or reactivity with water.

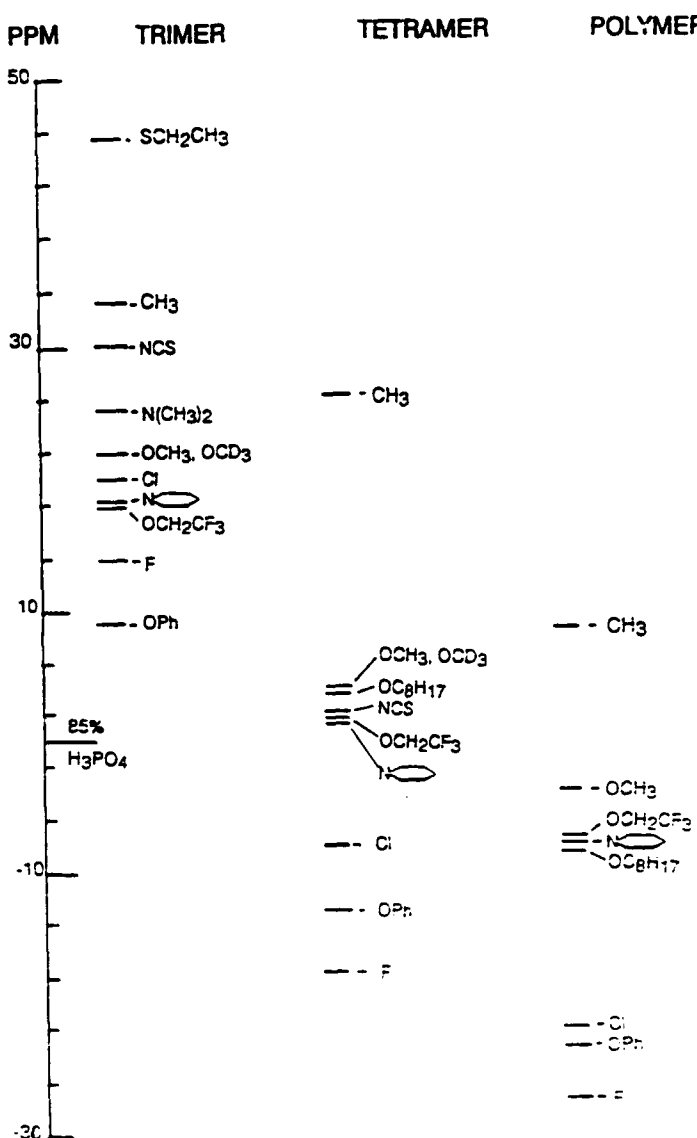
#### Characterization

All materials investigated were fully substituted high molecular weight homopolymers or trimeric (tetrameric) polymer precursors as indicated by a single  $^{31}\text{P}$  line in the magnetic resonance spectrum. Most polymers studied were stable to temperatures approaching 580 K. when heated in air. A summary of the  $^{31}\text{P}$  chemical shift information from magnetic resonance measurements of selected phosphazene polymers and small ring analogues appears in Table I. The chemical shift is a qualitative indication of the electron density at the phosphorus nucleus and it indicates the relative ionicity of the P-N bond.

The existence of a polarized P-N bond in phosphazenes is confirmed by the presence of a strong infrared feature in the 1150-1350  $\text{cm}^{-1}$  region that is very weak in the Raman spectrum. This frequency is dependent on the electron withdrawing tendency of substitutional groups on phosphorus as well as molecular conformation (trimer, tetramer, oligomer, polymer). High frequencies tend to correlate with increasing ionicity in the P-N bond. A ligand ranking based on IR frequencies is in agreement with that shown in Table I which was generated from  $^{31}\text{P}$  NMR chemical shift information.

Transmission spectra of cast polymer films were recorded over the wavelength region from 190 to 900 nm. Analysis of measured spectra using the method described by Manifacier, et. al. [7] allowed determination of film thickness and the complex refractive index. With the exception of the chloropolymer which degraded after several weeks in air, transmission spectra of polymer films were invariant with time suggesting their stability under ambient conditions and absence of trapped carrier solvent in the film.

The observation of green emission during 1064 nm pulsed irradiation of polymer films prompted preliminary measurements of non-linear effects in these materials. Cyclic phosphazene trimers, tetramers, and several polymers were mechanically powdered (<5 micrometer particle size), compressed to 2.0 cm diameter pellets (2 mm thick) under an applied pressure of 0.1 GPa, and evaluated for their ability to generate second harmonic radiation (SHG). The powder technique originally developed by Kurtz and Perry was used [8]. This method has been successfully applied to measurements of the non-linear optical response of organic based polymer materials [9]. A 0.25 m focal length monochromator and diode array detector replaced the photomultiplier and optical filters used in the original experiment.

Table I.  $^{31}\text{P}$  NMR Chemical Frequencies for Phosphazenes

## OPTICAL PROPERTIES OF PHOSPHAZENE POLYMERS

Fringe patterns observed in transmission spectra of two polymer films shown in Fig 2. attest to the uniformity of film thickness over the 1  $\text{cm}^2$  measurement area. Four polymer films, CP, MAP, PP, and TFEP exhibit relatively high transmittance at wavelengths as short as 250 nm; PAP begins to absorb strongly at 300 nm due to the presence of the conjugated phenyl groups in the polymer. The linear index of refraction varies between 1.5 and 1.7 at 500 nm; extinction coefficients average about 5E-4 at 500 nm for most materials. Waveguiding has recently been demonstrated in this laboratory for 425 nm thick PAP films deposited on silica substrates into which shallow surface gratings (.400 micrometer line spacing) have been etched.

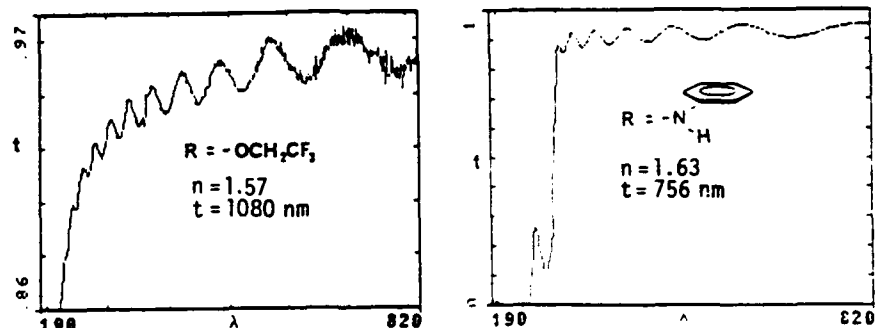


Fig 2. Transmission spectra of trifluoroethoxyphosphazene and phenylaminephosphazene films on silica substrates.

### SECOND HARMONIC GENERATION IN PHOSPHAZENES

Several phosphazene polymers and polymer precursors have been observed to emit green light when irradiated with 1064 nm pulsed radiation at 30 Hz from a Nd:YAG laser. Measurements on the isothiocyanate trimer ( $R=-NCS$ ) are summarized in Fig. 3a and 3b. Emission measured at 532 nm and the observed quadratic power dependence confirm the non-linear optical response (SHG) of this material. Fig. 3c qualitatively ranks the efficiency of SHG for several selected materials. Continuing measurements on derivatized phosphazenes suggest that the magnitude of the SHG effect is controlled by substituent electronegativity and molecular conformation.

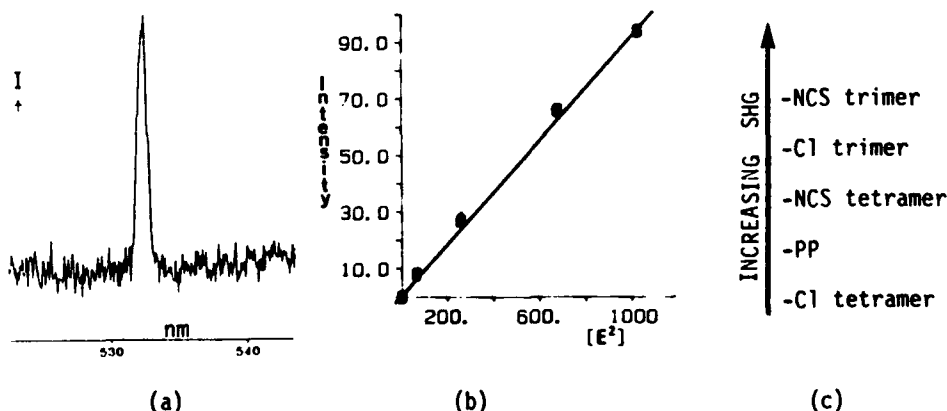


Fig 3. Second Harmonic Generation in phosphazenes. (a) SHG emission from the isothiocyanate trimer. (b) Dependence of SHG intensity on the square of incident pulse energy. (c) Relative SHG efficiency.

### DISCUSSION

Quantum chemical calculations suggest that variations in P-N bond polarity in phosphazenes result from the nature of the substituent group on the phosphorus atom. Restriction of  $\pi$ -electron conjugation to three-atom centers is dictated by the symmetry of the atomic orbitals. Therefore, the polarizability of localized  $-R_2P=N-$  moieties is also perturbed by substituent electronegativity. The model accounts for the observed extension of optical transmission to shorter wavelengths [1]. Here, the

lowest energy allowed electronic transition is between pi-bonding and pi-antibonding states and occurs deep in the ultraviolet owing to the restricted pi-conjugation. Electronic transitions primarily centered on substituent groups will shift the uv edge toward longer wavelengths as observed in PAP.

Substituent electronegativity and molecular geometry are also observed to influence the non-linear optical properties of phosphazenes. Both parameters perturb the electron density at the phosphorus nucleus as seen from  $^{31}\text{P}$  NMR chemical shifts reported in Table I. The relative efficiency of second harmonic generation shown in Fig. 3c mimics the  $^{31}\text{P}$  chemical shift ordering and suggests that such measurements might be appropriate for evaluating new materials with respect to non-linear optical response. On the basis of this argument, alkyl and thiol derivatives appear to be candidate materials for enhanced SHG and are the focus of ongoing work.

The basicity of nitrogen atom centers promotes hydrogen bond formation between phosphazene molecules and hydroxyl groups which exist at oxide surfaces. This bonding mechanism is responsible for film adhesion to glass surfaces and suggests that phosphazene polymers might be candidate adhesives for joining optical components.

Multifunctional behavior in phosphazene materials (adhesion, thermoplasticity, optical response) arises from the unique chemistry of the P-N bond. Optimization of a particular property can be achieved through controlled perturbation of localized pi electron density induced by modifying chemical groups bonded to the phosphorus atom. The bond polarity arguments presented here stress the importance of localized interactions and their influence on physical properties of phosphazenes. Design of polymer systems with mixed functional groups appears to be a feasible route for incorporating multifunctionality in this material.

#### ACKNOWLEDGMENT

Pacific Northwest Laboratory is operated by Battelle Memorial Institute for the U.S. Department of Energy under contract DE-AC06-76RLO 1830. This work has been supported by the Materials Sciences Division of the Office of Basic Energy Sciences, U.S. Department of Energy. We are grateful to Kevin Crosby and Joel Drews for assistance with film deposition and optical measurements.

#### REFERENCES

1. K.F. Ferris, P.M. Friedman, and D.M. Friedrich, *Int. J. Quantum Chem: Quantum Chemistry Symposium* 22, 207 (1988).
2. G.J. Exarhos, and N.J. Hess, *Microbeam Analysis* 1988, 161 (1988).
3. D.M. Friedrich, G.J. Exarhos, W.D. Samuels, K.F. Ferris, N.J. Hess, D.J. Altier, and S.P. Loecker, *Proc. Soc. Photo-Opt. Instrumentation Eng.* 1055, 135 (1989).
4. G.J. Exarhos, K.F. Ferris, D.M. Friedrich, and W.D. Samuels, *J. Am. Ceram. Soc.* 71(9), C406 (1988).
5. H.R. Allcock, *Chem. Eng. News* 63(11), 22 (1985).
6. H.R. Allcock, *Phosphorus-Nitrogen Compounds, Cyclic, Linear, and High Polymeric Systems*, Academic Press, New York, pp.73-87 (1972).
7. J.C. Manificier, J. Gasiot, and J.P. Fillard, *J. Phys.* E9, 4002 (1976).
8. S.K. Kurtz, and T.T. Perry, *J. Appl. Phys.* 39(8), 3798 (1968).
9. D. Chen, N. Okamoto, and R. Matsushima, *Optics Commun.* 69(5,6), 425 (1989).



92-18254

AD-P007 463



101

ORGANIC, ORGANOMETALLIC AND POLYMERIC MATERIALS WITH NONLINEAR  
OPTICAL PROPERTIES

S. R. MARDER,<sup>a</sup> J. W. PERRY,<sup>a</sup> W. F. SCHAEFER,<sup>b</sup> E. J. GINSBURG,<sup>b</sup>  
C. B. GORMAN,<sup>b</sup> R. H. GRUBBS<sup>b</sup>

a: Jet Propulsion Laboratory, California Institute of Technology, Pasadena, CA 91109

b: Division of Chemistry and Chemical Engineering,[1] California Institute of Technology,  
Pasadena, CA 91125

ABSTRACT

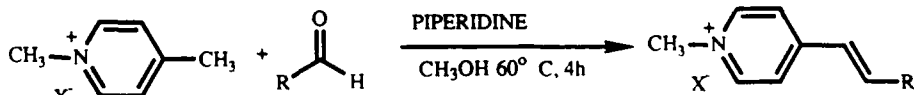
New approaches to both second-order and third-order nonlinear optical materials are presented. A series of organometallic and organic salts, in which the cation has been designed to have a large molecular hyperpolarizability, has been prepared and the SHG efficiencies were measured. Partially substituted derivatives of polyacetylene are synthesized via the ring-opening metathesis polymerization (ROMP) of cyclooctatetraene (COT) and its derivatives. Certain poly-COT derivatives afford soluble, highly conjugated polyacetylenes. These materials exhibit large third-order optical nonlinearities and low scattering losses.

INTRODUCTION

The desire to utilize the nonlinear optical properties of materials in applications such as telecommunications, optical data storage and optical information processing has created a need for new materials with very large nonlinear susceptibilities.[2-4] In the first section of the paper it will be shown that effective polar alignments of ionic, organometallic and organic chromophores, leading to efficient second harmonic generation (SHG) can be found by varying the counterion. In the second section, application of ring opening metathesis polymerization (ROMP) to the synthesis of new substituted polyacetylene derivatives with large third-order nonlinear optical properties and excellent linear optical properties will be demonstrated.

ORGANOMETALLIC AND ORGANIC SALTS WITH SECOND-ORDER OPTICAL  
NONLINEARITIES

It is well established that  $\pi$  donor-acceptor compounds can exhibit large hyperpolarizabilities.[5] The nonlinear chromophore must reside in a noncentrosymmetric environment if the hyperpolarizability ( $\beta$ ) is to lead to an observable bulk effect ( $\chi^{(2)}$ ). Roughly 75% of all known, non-chiral, organic molecules crystallize in centrosymmetric space groups leading to materials with vanishing  $\chi^{(2)}$ .[6] Several strategies have been employed to overcome this major obstacle.[7-12] Meredith demonstrated that  $(\text{CH}_3)_2\text{N}\text{C}_6\text{H}_4\text{-CH=CH-C}_5\text{H}_4\text{N}(\text{CH}_3)^+\text{CH}_3\text{SO}_4^-$  has an SHG efficiency roughly 220 times that of urea [13] which until recently was the largest powder SHG efficiency reported. He suggested that Coulombic interactions in salts could override dipolar interactions which provide a strong driving force for centrosymmetric crystallization in neutral dipolar compounds.[13] We have recently extended this approach and demonstrated that a variety of 4-N-methylstilbazolium salts (Fig. 1) give large powder SHG efficiencies when combined with a suitable counterion (Table I). [14]



X =  $\text{CF}_3\text{SO}_3^-$  and  $\text{CH}_3\text{C}_6\text{H}_4\text{SO}_3^-$ : synthesized directly.

X = Cl: metathesized  $\text{CF}_3\text{SO}_3^-$  salts with  $\text{N}(\text{n-C}_4\text{H}_9)_4\text{Cl}$  in acetone.

X =  $\text{BF}_4^-$ : metathesized Cl salts with  $\text{Na BF}_4^-$  in water.

Figure 1. Synthesis of salts of the form  $\text{R-CH=CH-C}_5\text{H}_4\text{NCH}_3^+\text{X}^-$ .

The yellow compound  $\text{CH}_3\text{OC}_6\text{H}_4\text{-CH=CH-C}_5\text{H}_4\text{N}(\text{CH}_3)^+\text{Cl}^- \cdot 4\text{H}_2\text{O}$  was found to exhibit an efficiency roughly 270 times that of the urea reference standard.  $(\text{CH}_3)_2\text{NC}_6\text{H}_4\text{-CH=CH-CH=CH-C}_5\text{H}_4\text{N}(\text{CH}_3)^+\text{CF}_3\text{SO}_3^-$  gave an efficiency 500 times the urea standard and  $(\text{CH}_3)_2\text{NC}_6\text{H}_4\text{-CH=CH-C}_5\text{H}_4\text{N}(\text{CH}_3)^+\text{CH}_3\text{C}_6\text{H}_4\text{SO}_3^-$  gave a signal 1000 times the urea standard. The data suggest that these ionic chromophores exhibit a higher tendency to crystallize noncentrosymmetrically than do dipolar covalent compounds. The efficacy of the approach is underscored by the observation that more than half of the compounds gave SHG efficiencies greater than urea. Also, of the nine chromophores discussed here, seven could be isolated with a counterion which gave rise to an SHG efficiency greater than 35 times that of urea. Here we present results from our attempt to extend this methodology to organometallic salts and to 2-N-methyl stilbazolium salts.

Table I. Powder SHG efficiencies for salts of the form  $\text{R-CH=CH-C}_5\text{H}_4\text{NCH}_3^+\text{X}^-$ . The left value is for 1064 nm input and the right value is for 1907 nm input (Urea = 1).

R	X =	$\text{CF}_3\text{SO}_3^-$	$\text{BF}_4^-$	$\text{CH}_3\text{C}_6\text{H}_4\text{SO}_3^-$	$\text{Cl}^-$ [15]
$4\text{-CH}_3\text{OC}_6\text{H}_4\text{-}$		54 / 50	0 / 0	100 / 120	270 / 60
$4\text{-CH}_3\text{OC}_6\text{H}_4\text{-CH=CH-}$		0 / 0	2.2 / 1.0	50 / 28	4.3 / 48
$4\text{-CH}_3\text{SC}_6\text{H}_4\text{-}$		0 / 0	0 / 0	1 / -	0 / 0
$2,4\text{-(CH}_3\text{O)}_2\text{C}_6\text{H}_3\text{-}$		67 / 40	2.9 / 5.5	0.08 / 0	0.7 / 0.4
$\text{C}_{16}\text{H}_9\text{- (1-pyrenyl)}$		1.1 / 0.8	- / -	14 / 37	- / -
$4\text{-(CH}_2\text{CH}_2\text{CH}_2\text{CH}_2\text{N)}\text{C}_6\text{H}_4\text{-}$		0.06 / 0.5	0.05 / 5.2	0.03 / 0.2	0 / 1.1
$4\text{-BrC}_6\text{H}_4\text{-}$		0 / 0	0.02 / 0	5.0 / 1.7	100 / 22
$4\text{-(CH}_3)_2\text{NC}_6\text{H}_4\text{-}$		0 / 0	- / 75 [13]	15 / 1000	0 / 0
$4\text{-(CH}_3)_2\text{NC}_6\text{H}_4\text{-CH=CH-}$		5 / 500	4.2 / 350	5 / 115	0 / 0

The observation that the ferrocene complex (Z)-(1-ferrocenyl-2-(4-nitrophenyl) ethylene), has an SHG efficiency 62 times urea demonstrates that organometallic compounds could exhibit large  $\chi^{(2)}$ . [16] Given this observation, we synthesized the compound  $(\text{C}_5\text{H}_5)\text{Fe}(\text{C}_5\text{H}_5)\text{-CH=CH-(4-C}_5\text{H}_4\text{N}(\text{CH}_3)^+\text{I}^-$  and measured its SHG powder efficiency by a modification of the Kurtz powder technique. [17] Powder SHG efficiencies were determined using 1907 nm fundamental radiation (SH at 953.5 nm) to avoid absorption of the SH by the dark colored salts. This new organometallic salt has an SHG efficiency roughly 220 times that of urea, the largest efficiency known for an organometallic compound. [18] Furthermore, the magnitude of the powder SHG signal is sensitive to the nature of the counterion as shown in Table II.

Table II. Powder SHG efficiencies of  $(E)\text{-}(\text{C}_5\text{H}_5)\text{Fe}(\text{C}_5\text{H}_4)\text{-CH=CH-(4-C}_5\text{H}_4\text{N}(\text{CH}_3)^+\text{X}^-$  salts with 1907 nm input (Urea = 1).

X =	$\text{B}(\text{C}_6\text{H}_5)_4$	I	Br	Cl	$\text{CF}_3\text{SO}_3^-$	$\text{BF}_4^-$	$\text{PF}_6^-$	$\text{NO}_3^-$	$\text{CH}_3\text{C}_6\text{H}_4\text{SO}_3^-$
SHG eff.	13	220	170	0	0	50	0.05	120	13

In an attempt to further explore the scope and limitation of the organic salt methodology, we have examined eleven 2-N-methyl stilbazolium compounds. The 2-N-methyl stilbazolium compounds of the form  $\text{R-CH=CH-(2-C}_5\text{H}_4\text{N}(\text{CH}_3)^+\text{X}^-$ , (where  $\text{R}=4\text{-CH}_3\text{OC}_6\text{H}_4$ ,  $\text{X}=\text{CF}_3\text{SO}_3^-$ ;  $\text{R}=4\text{-C}_6\text{H}_4\text{NCH}_2\text{CH}_2\text{CH}_2\text{CH}_2\text{C}_6\text{H}_4$ ,  $\text{X}=\text{CF}_3\text{SO}_3^-$ ;  $\text{R}=4\text{-C}_6\text{H}_4\text{N}(\text{CH}_3)_2$ ,  $\text{X}=\text{CF}_3\text{SO}_3^-$ ,  $\text{BF}_4^-$ ;  $\text{R}=2,4\text{-C}_6\text{H}_3(\text{OCH}_3)_2$ ,  $\text{X}=\text{CF}_3\text{SO}_3^-$ ;  $\text{R}=2\text{-C}_6\text{H}_4\text{OCH}_3$ ,  $\text{X}=\text{CF}_3\text{SO}_3^-$ ;  $\text{R}=(\text{C}_5\text{H}_5)\text{Fe}(\text{C}_5\text{H}_4)$ ,  $\text{X}=\text{CF}_3\text{SO}_3^-$ ,  $\text{CH}_3\text{C}_6\text{H}_4\text{SO}_3^-$ ,  $\text{I}$ ,  $\text{Br}$ ) all gave negligible SHG efficiencies. The exception was  $(3\text{-CH}_3\text{OC}_6\text{H}_4\text{-CH=CH-(2-C}_5\text{H}_4\text{N}(\text{CH}_3)^+\text{CF}_3\text{SO}_3^-}$ , which has an efficiency of 25 times urea. Contrary to conventional wisdom for the design of nonlinear optical chromophores, the donor, the methoxy group, and the acceptor, the cationic alkylated nitrogen atom, are cross conjugated. The cross conjugation, leads to improved transparency ( $\lambda_{\text{max}}$  at 344 nm in methanol,  $\lambda_{\text{cutoff}}$  at 425 nm for  $\sim 100\text{ }\mu\text{m}$  crystal) while maintaining a reasonable bulk optical nonlinearity. [19]

Crystal structures of several salts were determined in order to better understand how the chromophores align in the crystal lattice. In the eight crystal structures we have determined, a recurring structural motif of alternating parallel rows of cations and rows of anions is observed. The compounds shown in figure 2 follow this motif. It is reasonable to suggest that the ions will more likely form linear rows if the chromophore itself is linear; this may explain some of the differences between the 4-stilbazolium series and the 2-stilbazolium series. Whereas molecular asymmetry may tend to favor crystallographic noncentrosymmetry in neutral molecules, it appears from our limited sampling that the opposite is the case for ionic chromophores.

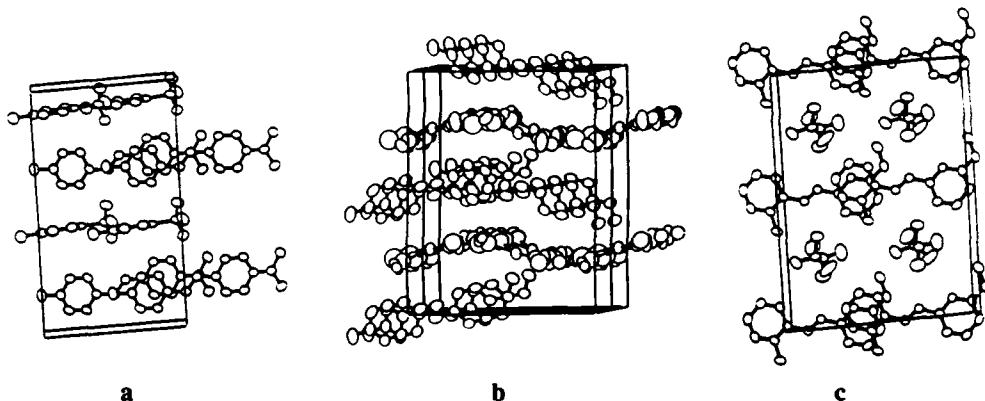


Figure 2. Packing diagrams for a  $(4\text{-}(\text{CH}_3)_2\text{NC}_6\text{H}_4\text{-CH=CH}\text{-}(4\text{-C}_5\text{H}_4\text{N}(\text{CH}_3)^+\text{-p-CH}_3\text{C}_6\text{H}_4\text{S}0_3^-)$ , b  $(4\text{-CH}_3\text{OC}_6\text{H}_4\text{-CH=CH}\text{-}(4\text{-C}_5\text{H}_4\text{N}(\text{CH}_3)^+\text{Cl}^- \cdot 4\text{H}_2\text{O}$  and c  $(3\text{-CH}_3\text{OC}_6\text{H}_4\text{-CH=CH}\text{-}(2\text{-C}_5\text{H}_4\text{N}(\text{CH}_3)^+\text{CF}_3\text{SO}_3^-)$ .

#### NEW POLYMERIC MATERIALS WITH CUBIC OPTICAL NONLINEARITIES DERIVED FROM RING-OPENING METATHESIS POLYMERIZATION.

Ring-opening metathesis polymerization (ROMP) of cyclooctatetraene (COT) produces poly-cyclooctatetraene, a new form of polyacetylene. By extending this method to the ROMP of substituted COTs, we have developed a route into partially substituted polyacetylenes that are soluble in several cases (Fig. 3).<sup>[20-21]</sup> Polymerization is readily accomplished on gram scales in a nitrogen filled drybox. The nascent polymer formed by ROMP has three of the four double bonds from the monomer in a cis configuration. Depending upon the polymer these were converted to the all trans form either thermally or photochemically. The trans poly-RCOT films can be iodine doped to a conductive state.

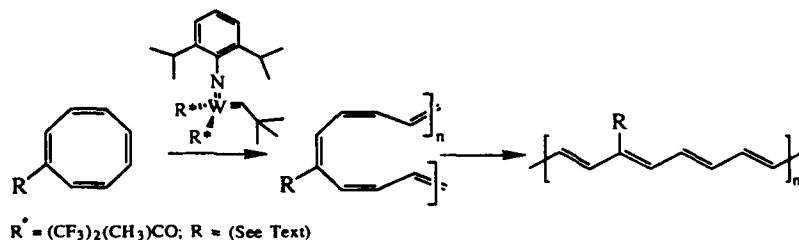


Figure 3. Polymerization of substituted cyclooctatetraenes and isomerization of resulting polymer.

Polymerization of substituted COT derivatives results in partially substituted polymers which are highly conjugated. In contrast, polymerization of substituted acetylenes results in substituted polyacetylenes with low effective conjugation lengths as evidenced by their high-energy visible absorption spectra and comparatively low iodine-doped conductivities.<sup>[22]</sup> This low conjugation

length is presumably due to twisting around the single bonds in the backbone resulting from steric repulsions of the side groups.[23]



Figure 4. Chain Twisting in Substituted Polyacetylene.

Films of poly-RCOT with straight-chain alkyl substituents of at least four carbons are flexible and somewhat soluble in solvents such as tetrahydrofuran (THF) and methylene chloride. Complete solubility is afforded by placing tertiary substituents off of the polyacetylene backbone. Poly-*n*-butylCOT is a freely soluble polymer but is yellow-orange in color indicating a low effective conjugation length. However, poly-trimethylsilylCOT (poly-TMSCOT) is freely soluble and highly conjugated. This polymer is red when formed. However, after photochemical isomerization to the trans form, the polymer is purple, indicative of the increased conjugation length.

Several attempts have been made to correlate the effective conjugation length of a polyene with its absorbance maximum. Based on the extrapolation of polyene absorption data obtained from a variety of workers[24] to the band gap of polyacetylene,[25] an absorption maximum of 630 nm, as seen for poly-*n*-octylCOT, implies an effective conjugation length of at least 25 double bonds.[26] Lower energy absorption maxima are seen in the solid state. A thin film of poly-*n*-octylCOT has a broad absorption centered around 650 nm which is comparable to that observed for a thin film of polyacetylene.[27] Although poly-TMSCOT has a higher energy absorption maximum than poly-*n*-octylCOT, it is still highly conjugated (greater than 15 double bonds). Highly reflective, soluble polymer films can be cast from a photolyzed purple solution and can be iodine doped to conductivities of  $0.2 \Omega^{-1} \text{cm}^{-1}$ .

Recent experimental[27-28] and theoretical[29] studies indicate that extended conjugation leads to large cubic susceptibilities. We have investigated the nonlinear optical properties of a series of random COT-cyclooctadiene copolymers containing 8-32 mole% COT.[30] The  $\chi^{(3)}$  values of the copolymers increase substantially with increasing fraction of COT, reflecting both the increased concentration of conjugated units and the increased conjugation length in the copolymer. The estimated  $\chi^{(3)}$  of a copolymer film with 32% COT is  $\sim 2 \times 10^{-12} \text{ esu}$ .[30] By comparison, a solution measurement of  $\beta$ -carotene (11 conjugated double bonds) gave a value of  $\chi^{(3)} = 9 \times 10^{-11} \text{ esu}$ . Measurements on neat polyacetylene give a value of  $1.3 \times 10^{-9} \text{ esu}$  (enhanced by three-photon resonance) at 1907 nm.[25] Transparent uniform films of the soluble copolymers with low scattering losses can be prepared by spin coating. Thus while the  $\chi^{(3)}$  of the 32% COT copolymer is modest, this work suggested to us that the ROMP synthetic methodology can be used to produce materials with substantial nonlinearities and is flexible enough to allow tailoring of materials properties.

Accordingly, we studied the nonlinear optical properties of some partially substituted polyacetylenes prepared by ROMP. These films were typically prepared by polymerizing the neat monomer and casting the polymerizing mixture either between glass slides, resulting in films of about 20  $\mu\text{m}$  thickness, or between the fused silica windows of a 100  $\mu\text{m}$  path length demountable optical cuvette. Films cast between substrates were easily handled in air and were stable for long periods of time (months). In addition, such assemblies were convenient for examination of the optical properties. THG measurements on poly-*n*-butylCOT films, referenced to a bare fused silica plate, were made using 1064 nm pulses. These measurements showed that the  $|\chi^{(3)}|$  of films of poly-*n*-butylCOT,  $\sim 1 \times 10^{-10} \text{ esu}$ , was comparable to that of unoriented polyacetylene at the same wavelength.[27] However, comparison of the linear transmission spectra of these materials in the near infra-red shows that the partially substituted polyacetylene has greatly improved optical quality.

Absorption spectra of polyCOT films show high optical density (1-3 for 20  $\mu\text{m}$  thick films) even below the true absorption edge[31] in the near IR. The apparent absorption, which decreases

with increasing wavelength but extends out beyond 2000 nm, is actually due to scattering as shown by laser light scattering observations. As an example, we estimate the loss coefficient of such films to be  $> 500 \text{ cm}^{-1}$  at 1500 nm. The origin of this scattering is certainly due to internal optical inhomogeneities in the polymer associated with the semi-crystalline, fibrillar morphology. In contrast, films of poly-*n*-butylCOT show very clean transmission in the near IR. Films 100  $\mu\text{m}$  thick show a sharp absorption edge at  $\sim 900 \text{ nm}$  and very little absorption beyond 1000 nm. For poly-*n*-butylCOT films, we estimate the loss coefficient to be  $< 0.2 \text{ cm}^{-1}$  at 1500 nm. The greatly reduced scattering loss indicates that partial substitution of polyacetylene with *n*-butyl groups has resulted in a more homogeneous morphology, approaching that of an amorphous polymer.

We have also examined films of trans poly-TMSCOT produced from solution by casting or spin-coating. THG measurements at 1064 nm on films of poly-TMSCOT give  $|\chi^{(3)}| = 2 \pm 1 \times 10^{-11} \text{ esu}$ . This value is somewhat lower than that of poly-*n*-butylCOT or polyacetylene, consistent with the reduced effective conjugation length inferred from the energy of the absorption maximum, as discussed earlier. The films of poly-TMSCOT prepared from solution are of good optical quality and show scattering losses at least as low as the poly-*n*-butylCOT films.

### CONCLUSIONS

The results presented here clearly demonstrate that organometallic compounds can give rise to efficient second harmonic generation. The role of organometallic compounds as nonlinear optical materials is only beginning to be realized and further synthetic studies are needed if we are to fully exploit the potential of this class of materials. In addition, we have shown that in many cases the "salt methodology" can be used effectively to find noncentrosymmetric crystalline alignments of highly nonlinear ionic chromophores and thereby achieve large values of  $\chi^{(2)}$ . Further, it has been shown that nonconventional donors such Br- and the pyrenyl moiety can be incorporated into molecules which, in the correct crystallographic environment, exhibit substantial bulk susceptibilities. We believe that this study represents an important step in decoupling the design of desirable molecular properties from the orientational requirements of  $\chi^{(2)}$  materials, although further studies are needed to more clearly define the scope of this approach.

Ring-opening metathesis polymerization of substituted cyclooctatetraene derivatives yields partially substituted polyacetylenes, many of which are soluble and still highly conjugated. Highly conjugated polymers obtained exhibit high optical nonlinearities and low scattering losses. Given the ability to fabricate uniform high, quality films with optical nonlinearities comparable to that of polyacetylene, these polymers may be of interest for nonlinear waveguiding experiments.

### ACKNOWLEDGEMENTS

The research described in this paper was performed, in part, by the Jet Propulsion Laboratory, California Institute of Technology as part of its Center for Space Microelectronics Technology which is supported by the Strategic Defense Initiative Organization, Innovative Science and Technology Office through an agreement with the National Aeronautics and Space Administration (NASA). RHG acknowledges financial support from the Office of Naval Research. The diffractometer used in this study was purchased with a grant from the National Science Foundation #CHE-8219039. SRM thanks the National Research Council and NASA for a Resident Research Associateship at JPL. EJG thanks IBM for a research fellowship. CBG thanks the JPL for a research fellowship. The authors thank Dr. L. Khundkar, B. G. Tiemann and K. J. Perry for technical assistance.

### REFERENCES AND FOOTNOTES

1. Contribution number 8070.
2. D. J. Williams, *Angew. Chem. Int. Ed. Engl.*, **23**, 690, (1984).
3. *Nonlinear Optical Properties of Organic and Polymeric Materials*, ACS Symp. Ser., **233**, edited by, D. J. Williams, (American Chemical Society, Washington, 1983).
4. *Nonlinear Optical Properties of Organic Molecules and Crystals*, edited by D. S. Chemla and J. Zyss, (Academic Press, Orlando, 1987) Volumes 1 and 2.

5. (a) J. L. Oudar and D. S. Chemla, *J. Chem. Phys.*, 66, 2664, (1977). (b) B. F. Levine and C. G. Bethea, *J. Chem. Phys.*, 66, 1070, (1977). (c) S. J. Lalama and A. F. Garito, *Phys. Rev. A*, 20, 1179, (1979).
6. J. F. Nicoud and R. W. Twieg in ref. 3, Vol. 1, p. 242.
7. J. Zyss, J. F. Nicoud and M. Koquillay, *J. Chem. Phys.* 81, 4160, (1984).
8. R. W. Twieg and K. Jain in ref. 2, Page 57.
9. J. S. Zyss, D. S. Chemla and J. F. Nicoud, *J. Chem. Phys.* 74, 4800, (1981).
10. (a) S. Tomaru, S. Zembutsu, M. Kawachi and M. Kobayashi, *J. Chem. Soc., Chem. Comm.*, 1207, (1984), (b) W. Tam, D. F. Eaton, J. C. Calabrese, I. D. Williams, Y. Wang, A. G. Anderson., *Chemistry of Materials*, 1, 128, (1989), (c) I. Weissbuch, M. Lahav, L. Leiserowitz, G. R. Meredith and H. Vanherzeele, *Chemistry of Materials*, 1, 114, (1989).
11. S. D. Cox, T. E. Gier, J. D. Bierlein, and G. D. Stucky, *J. Am. Chem. Soc.*, 110, 2986, (1989)
12. K. D. Singer, J. E. Sohn, and S. J. Lalama, *Appl. Phys. Lett.*, 49, 248, (1986).
13. G.R. Meredith in ref. 2, p. 30.
14. S. R. Marder, J. W. Perry and W. P. Schaefer, *Science*, 245, 626, (1989).
15. The  $\text{Cl}^-$  salts are hygroscopic which is evidenced by both elemental analysis, differential scanning calorimetry, thermogravimetric analysis and X-ray crystallography. [14]
16. M. L. H. Green, S. R. Marder, M. E. Thompson, J. A. Bandy, D. Bloor, P. V. Kolinsky and R. J. Jones, *Nature*, 330, 360, (1987).
17. S. K. Kurtz and T. T. Perry, *J. Appl. Phys.*, 39, 3798, (1968).
18. S. R. Marder, J. W. Perry B. G. Tiemann and W. P. Schaefer, *J. Amer. Chem. Soc.*, submitted.
19. S. R. Marder, J. W. Perry, B. G. Tiemann and W. P. Schaefer, *Chemistry of Materials*, submitted.
20. E. J. Ginsburg, C. B. Gorman, S. R. Marder and R. H. Grubbs, *J. Am. Chem. Soc.*, 111, 7621, (1989).
21. C. B. Gorman, E. J. Ginsburg, S. R. Marder and R. H. Grubbs, *Angew. Chem., In Press*.
22. a) J. M. Zeigler, U.S. Patent Appl. US 760 433 AO, (21 November, 1986); *Chem. Abstr.*, 20, 157042, (1986). (b) J. M. Zeigler, *Polym. Prepr.*, 25, 223, (1984). (c) Y. Okano, T. Masuda and T. Higashimura, *J. Polym. Sci.: Polym. Chem. Ed.*, 22, 1603, (1984). (d) T. Masuda and T. Higashimura, *Adv. in Polymer Science*, 81, 121, (1987).
23. M. Leclerc and R. E. Prud'homme, *J. Polym. Sci: Polym. Phys. Ed.*, 23, 2021, (1985).
24. (a) M. Bohlmann, *Chem. Ber.*, 1952, 85, 387. (b) M. Bohlmann, *Chem. Ber.*, 86, 63, (1953). (c) Bohlmann and Kieslich, *Chem. Ber.*, 87, 1363, (1954). (d) P. Nayler and M. C. Whiting, *J. Chem. Soc. Chem. Comm.*, 3037, (1955). (e) F. Sondheimer, D. Ben-Efriam and R. Wolovsky, *J. Am. Chem. Soc.*, 83, 1675, (1961). (g) Karrer and Eugster, *Helv. Chim. Acta*, 34, 1805, (1951). (h) A. Winston and P. Wichacheewa, *Macromolecules*, 6, 200, (1973).
25. A. O. Patil, A. J. Heeger and F. Wudl, *Chem. Rev.*, 88, 183, (1988).
26. Similar results have been obtained by R. Chance, Exxon Corp. (private communication).
27. F. Kajzar, S. Etemad, J. Messier and G. L. Baker, *Synth. Met.*, 17, 563, (1987).
28. (a) C. Sauteret, J. P. Hermann, R. Frey, F. Predere, J. Ducing, R. H. Baughman and R. R. Chance, *Phys. Rev. Lett.*, 36, 956, (1976). (b) G. M. Carter, Y. J. Chen and S. K. Tripathy, *Appl. Phys. Lett.*, 43, 891, (1983).
29. (a) G. P. Agrawal, C. Cojan and C. Flytzanis, *Phys. Rev. B: Solid State*, 15, 776, (1978). (b) D. N. Beratan, J. N. Onuchic and J. W. Perry, *J. Phys. Chem.*, 91, 2696, (1987). (c) A. F. Garito, J. R. Heflin, K. Y. Wong and O. Zamani-Khamiri, in Nonlinear Optical Properties of Polymers, edited by A. J. Heeger, J. Orenstein and D. R. Ulrich, (Mater.Res. Soc. Proc. 109, Pittsburgh, 1988) p. 91.
30. S. R. Marder J. W. Perry, F. L. Klavetter and R. H. Grubbs, *Chemistry of Materials*, 1, 171, (1989).
31. B. R. Weinberger, C. B. Roxlo, S. Etemad, G. L. Baker and J. Orenstein, *J. Phys. Rev. Lett.*, 53, 86, (1984).





AD-P007 464



107

THIRD-ORDER OPTICAL NONLINEARITY  
IN A POLYMER COMPOSITE

K. M. White<sup>1</sup>, R. E. Harelstad<sup>1</sup>, C. V. Francis<sup>1</sup>, D. J. Gerbi<sup>1</sup>, J. Stevens<sup>2</sup>, and  
P. C. Leung<sup>2</sup>

<sup>1</sup> Science Research Laboratory, 3M Company, St. Paul, MN 55144

<sup>2</sup> Computational Science Center, 3M Company, St. Paul, MN 55144

**ABSTRACT**

Third-order optical nonlinearity in organic materials has generally been sought from molecules and polymers having extended  $\pi$ -electron delocalization in conjugated bonding schemes. In an alternative approach, we have investigated the third-order optical response of a polymeric composite containing charge transfer complexes in which the nonlinearity originates from intermolecular electron delocalization between  $\pi$ -electron clouds in charge transfer stacks. The material, which is composed of a polymer having electron-donating pendant side groups that complex with dopant electron-acceptor molecules, has been processed into an optically clear thin film. Nonlinear characterization of the film by means of third-harmonic generation suggests enhancement of the third-order response arising from charge transfer interactions.

**92-18255**



**INTRODUCTION**

In the development of materials for use in third-order nonlinear optical devices, organic polymers have received significant attention. The versatility that exists for engineering the optical and film forming properties of polymers has made them attractive candidates for integrated optics structures.<sup>1</sup> Incorporation of conjugated  $\pi$ -bonds in polymer backbones, thus facilitating extended electron delocalization which is fundamental to the third-order optical nonlinearity, has produced the largest  $\chi^{(3)}$  values known in organic materials.<sup>2,3</sup>

An alternative means of producing electron delocalization in polymer systems is obtained through intermolecular interactions. Recently, the origin of charge delocalization between molecules in the TTF-TCNQ charge transfer crystal was examined using *ab initio* quantum mechanical calculations.<sup>4</sup> The results showed that an extended, delocalized intermolecular orbital exists between the stacked molecules, suggesting that spatially delocalized intermolecular group orbitals may exist in materials in which face-to-face molecular stacking at short intermolecular distances occurs. Thus, large third-order nonlinearities are also likely to be observed in molecular stacks such as organic charge transfer complexes.

The potential application of several organic charge transfer complexes and complex salts as nonlinear optical materials has been investigated. Large  $\chi^{(3)}$  values have been reported for charge transfer crystals, including the organic conductor  $(BEDT-TTF)_2I_3$ ,<sup>5</sup> and a number of neutral charge transfer complexes,<sup>6</sup> some of which show  $\chi^{(3)}$  values larger than that of the polydiacetylene PTS. Thin films of poly(vinylcarbazole) (PVK) complexed with 2,4,7-trinitrofluoren-9-one (TNF) have also been studied using resonant degenerate four wave mixing to examine the effect that photoinduced electron-hole pairs have on the third-order nonlinear optical response.<sup>7</sup>

Because of the processing advantages of polymers over crystalline materials, incorporation of neutral charge transfer complexes into a polymer film for use as a third-order nonlinear optical material is investigated and reported here. Polymers of 1-vinylpyrene (PVPy), which provide pyrene as the donor entity in the charge transfer complexes, and tetracyanoethylene (TCNE), the electron acceptor, comprised the charge transfer film studied. Third-harmonic generation (THG) was employed to determine the electronic  $\chi^{(3)}$  response of the film without a direct excitation of charge transfer bands. THG of a PVPy film was also measured and the resulting  $\chi^{(3)}$  compared to that of PVPy-TCNE to determine enhancement of third-order nonlinear optical properties displayed by polymeric charge transfer complexes.

## EXPERIMENTAL

### Sample Preparation

Poly(1-vinylpyrene) was synthesized according to published methods,<sup>8</sup> producing a polymer with a weight average molecular weight of 14,500. PVPy-TCNE charge transfer polymer was prepared by mixing equimolar portions of PVPy and TCNE in a suitable solvent and precipitating from a non-solvent.<sup>8</sup> Characterization of PVPy-TCNE by means of EPR, x-ray powder diffraction, visible and near infrared spectroscopy, and elemental analysis indicated that the material was amorphous and contained neutral charge transfer complexes of pyrene and TCNE in a 6:1 molar ratio (pyrene:TCNE).

Spin-coating was found to be the method of choice for processing PVPy and PVPy-TCNE charge transfer complex into films which were uniform and optically clear. Typically, films having thicknesses 0.7-1.0  $\mu\text{m}$  were obtained from 16% (w/w) chlorobenzene solutions that were spin-coated onto fused silica substrates into which gratings (for waveguiding) had been etched.

### Characterization

Waveguiding and transmission spectroscopy were employed to evaluate linear optical properties of the thin films necessary for analysis of THG data. The 633 nm output of a helium-neon laser was waveguided in the films and subsequent analysis of the observed coupling angles yielded the refractive indices and thicknesses of the films at essentially the third-harmonic wavelength. Transmission spectra recorded from 400 to 2000 nm on a UV-Vis-NIR spectrophotometer provided the absorbance of each film at the fundamental and third-harmonic wavelengths and located the charge transfer bands. The spectral interference observed in the thin film spectra also allowed evaluation of refractive indices of the films in the near infrared, given the thicknesses. This method was also used, together with thickness measurements

from a profilometer, to evaluate the refractive index at wavelengths where a film may have been too absorbing to permit determination by a waveguiding measurement.

Third-harmonic generation measurements of the thin film samples were performed using 1907 nm for the fundamental wavelength and 636 nm as the corresponding third-harmonic wavelength. The fundamental was produced by pumping a hydrogen gas cell (300 psig) with the focused, 1064 nm output of a Nd<sup>3+</sup>:YAG laser and isolating the Raman-shifted first Stokes line. The fundamental was weakly focused onto the film sample held in a vacuum chamber to exclude the effects of air on the THG signal. The light was polarized parallel to the axis about which the sample was rotated during the course of the experiment. The third harmonic was isolated using filters and a double monochromator and detected by a photomultiplier tube using boxcar averaging techniques. The third-harmonic intensity data were stored as a function of the angle between the fundamental beam and the normal to the sample surface. To provide reference measurements, THG was also recorded from the fused silica substrates after *in situ* removal of the films.

## RESULTS AND DISCUSSION

Absorption spectra of the purple PVPy-TCNE film displayed two weak peaks at 500 and 800 nm which were assigned as charge transfer bands in the polymer complex film. These wavelengths agree with the corresponding band positions in spectra of pyrene-TCNE charge transfer crystals,<sup>9</sup> indicating the electronic structure in the polymer film is the same as in the crystalline state. Both PVPy and PVPy-TCNE films had refractive indices of  $1.75 \pm .005$  and  $1.72 \pm .01$  at 636 and 1907 nm, respectively.

THG measurements of the thin films enabled determination of their respective  $\chi^{(3)}(-3\omega; \omega, \omega, \omega)$  values, using THG from the fused silica substrates for reference ( $\chi^{(3)}_{\text{ref}} = 2.8 \times 10^{-14}$  esu<sup>10</sup>). The data were fit using the measured linear optical constants and by applying a least squares Simplex<sup>11</sup> algorithm to THG formulas<sup>12</sup> that are appropriate for the sample configuration used. The curve fit of THG from the PVPy-TCNE film and its associated substrate are displayed in Figure 1. Its resultant  $\chi^{(3)}$  value is listed in Table I along with the value determined for PVPy. A comparison of the  $\chi^{(3)}$  magnitudes reveals that the PVPy-TCNE charge transfer polymer film has a third-order susceptibility that is nearly six times greater than that of the PVPy film itself.

**Table I.** Third-order nonlinear optical susceptibilities ( $\chi^{(3)}$ )<sup>\*</sup> of PVPy homopolymer and PVPy-TCNE charge transfer polymer films.

Film	Re[ $\chi^{(3)}$ ]	Im[ $\chi^{(3)}$ ]	$ \chi^{(3)} $
PVPy	.28	.06	.28
PVPy-TCNE	-1.4	-.7	1.6

\* in  $10^{-12}$  esu

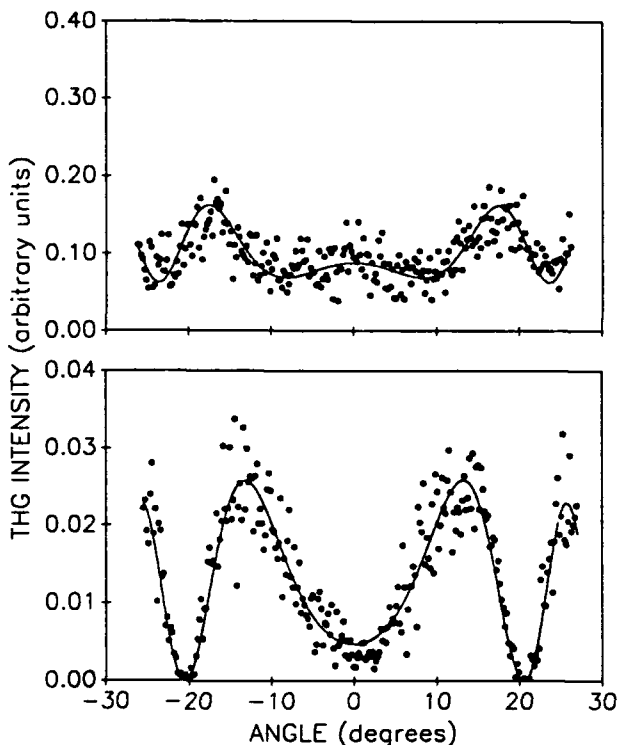


Figure 1. Fit of THG for PVPy-TCNE. The data are from a sample of PVPy-TCNE on fused silica (top) and fused silica substrate alone (bottom).

A THG measurement of TCNE dissolved in poly(methyl methacrylate) (PMMA) was made in order to consider the possibility that the increased  $\chi^{(3)}$  in PVPy-TCNE was due to the added TCNE, rather than the pyrene-TCNE complexes. The PMMA film was prepared so that the TCNE concentration was the same as that found for the PVPy-TCNE film. The TCNE-containing PMMA film had a  $\chi^{(3)}$  only slightly larger than that of PMMA alone, indicating the large  $\chi^{(3)}$  in PVPy-TCNE is due to the presence of charge transfer complexes.

Since the ratio of donor to acceptor molecules in PVPy-TCNE was 6:1, it is expected that the  $\chi^{(3)}$  value of the charge transfer polymer will increase further as the ratio approaches 1:1. The reason for the larger  $\chi^{(3)}$  is two-fold: (1) a higher number density of charge transfer complexes in the nonlinear optical medium, each consisting of one pyrene and one TCNE molecule, and (2) greater association along the polymer chain of these neighboring charge transfer complexes into molecular stacks, enabling extended electron delocalization.

The effect of extended charge transfer complexes on  $\chi^{(3)}$  in PVPy-TCNE was examined by means of a calculation of molecular hyperpolarizabilities,  $\gamma$ , of pyrene and its charge transfer complexes with TCNE. The calculation employed *ab initio* methods and applied finite-field approximations on STO-3G basis sets using GAUSSIAN86.<sup>13</sup> The geometry of the pyrene-TCNE

**Table II.** Comparison of relative experimental  $\chi^{(3)}$  values for polymer films and relative calculated  $\gamma$  values for molecules involving pyrene and its charge transfer complex with TCNE.

	$\chi^{(3)}$ (expt.)		$\gamma$ (calc.)
PVPy	1.0	Pyrene	1.0
PVPy-TCNE (6:1)	5.7	Pyrene-TCNE (1:1 dimer)	10.2
		(2:1 trimer)	286

molecular complex in the crystalline state was assumed. The relative  $\gamma$  values calculated for pyrene and the pyrene-TCNE dimer are consistent with experimental evidence of  $\chi^{(3)}$  enhancement (Table II). The theoretical results imply that mainly pyrene-TCNE dimers were present in the PVPy-TCNE film tested. Furthermore, the pyrene-TCNE-pyrene model suggests that as the complexed species associate into larger stacks,  $\chi^{(3)}$  will continue to increase. This increase is not expected to surpass  $\chi^{(3)}$  values observed for charge transfer crystals<sup>6</sup> in which the charge transfer stacks are "infinite."

## CONCLUSION

Third-order optical nonlinearity ( $\chi^{(3)}$ ), as determined by third-harmonic generation, is found to be greater in a charge transfer polymer film of PVPy-TCNE than in the PVPy homopolymer itself. Experimental and theoretical results suggest that further enhancement of the third-order response will be achieved by adjusting the donor:acceptor ratio in the charge transfer film to be close to 1:1.

## ACKNOWLEDGEMENTS

The authors thank Dong-Wei Zhu and A. R. Katritzky (Chemistry Department, University of Florida) for help in the synthesis of PVPy and R. Moshrefzadeh (3M) for providing gratings for waveguiding studies. We also express our appreciation to 3M Corporate Research Analytical and Properties Laboratory for their continued assistance. This research is sponsored by SDIO/IST and managed by the Air Force Office of Scientific Research (AFSC), under Contract F49620-88-C-0008. The United States Government is authorized to reproduce and distribute reprints for governmental purposes notwithstanding any copyright notice hereon.

## REFERENCES

1. G. I. Stegeman, C. T. Seaton, and R. Zanoni, *Thin Solid Films* **152**, 231 (1987).
2. M. R. Drury, *Solid State Commun.* **68**, 417 (1988).
3. C. Sauteret, J. P. Hermann, R. Frey, F. Pradere, J. Ducuing, R. H. Baughman, and R. R. Chance, *Phys. Rev. Lett.* **36**, 956 (1976).

4. J. Stevens, P. C. Leung, S. H. Chou, A. J. Freeman, and E. Wimmer, in Multifunctional Materials, edited by R. L. Gunshor (Proceedings SPIE 878, Los Angeles, CA, January, 1988) pp. 131-135.
5. P. G. Huggard, W. Blau, and D. Schweitzer, *Appl. Phys. Lett.* 51, 2183 (1987).
6. T. Gotoh, T. Kondoh, K. Egawa, and K. Kubodera, *J. Opt. Soc. Am. B* 6, 703 (1989).
7. P. N. Prasad, J. Swiatkiewicz, and J. Pfleger, *Mol. Cryst. Liq. Cryst.* 160, 53 (1988).
8. K. Tanikawa, T. Ishizuka, K. Suzuki, S. Kusabayashi, and H. Mikawa, *Bull. Chem. Soc. Jpn.* 41, 2719 (1968).
9. H. Kuroda, I. Ikemoto, H. Akamatu, *Bull. Chem. Soc. Jpn.* 39, 1842 (1966).
10. B. Buchalter and G. R. Meredith, *Appl. Opt.* 21, 3221 (1982).
11. J. A. Nedler and R. Mead, *Comput. J.* 7, 308 (1965).
12. F. Kajzar and J. Messier, *Polym. J.* 19, 275 (1987).
13. GAUSSIAN86, M. J. Frisch, J. S. Binkley, H. B. Schlegel, K. Raghavachari, C. F. Melius, R. L. Martin, J. J. P. Stewart, F. W. Bobrowicz, C. M. Rohlfing, L. R. Kahn, D. J. Defrees, R. Seeger, R. A. Whiteside, D. J. Fox, E. M. Fleuder, and J. A. Pople, Carnegie-Mellon Quantum Chemistry Publishing Unit, Pittsburgh, PA, 1984.



92-18256



AD-P007 465



13

SYNTHESIS AND PROPERTIES OF MULTIFUNCTIONAL POLYMERS



H.A. Goldberg, A.J. East, I.L. Kalnin, R.E. Johnson, H.T. Man, R.A. Keosian, and D. Karim  
Robert L. Mitchell Technical Center, Hoechst Celanese, 86 Morris Avenue, Summit, New Jersey

ABSTRACT

Recent work aimed at developing new polymers which exhibit useful optical, electro-optical, and piezoelectric properties is presented. The materials under study are polymers with methacrylate backbones and oxynitrostilbene side chains. The synthesis is outlined, and pyro-electric, electro-optic, and thermal property data are reported and discussed.

INTRODUCTION

In recent years, significant progress has been made in developing polymers with polar side chains that have non-linear optical (NLO or  $\chi^{(2)}$ ) properties [1,2]. To obtain a non-zero  $\chi^{(2)}$ , it is necessary to pole these materials, thus providing some degree of alignment of the polar side groups. The simplest description of the poling process assumes the dipoles can be treated as effectively non-interacting. However, to achieve a significant amount of orientation and a reasonably high  $\chi^{(2)}$ , the molecules studied have had very large dipole moments [3]. Also, the side chain molecules chosen are fairly rigid and elongated. These properties would lead one to expect large interactions between side chains.

Several other properties of rigid side chain polymers will also depend on the interactions of the side chains. For example, since a large fraction of the volume is typically occupied by the side chains, one might expect that these interactions affect the mechanical properties and the glass transition temperature.

In this work we are looking at the polar side chain polymers as multifunctional materials - i.e. materials with not just electro-optic properties but also piezoelectric, pyroelectric, mechanical, optical, and dielectric properties. Our goal is to see if this entire range of properties can be understood and ultimately controlled from a microscopic point of view. By examining a single class of such materials, we hope to begin to understand the relative importance of the molecular properties and intermolecular interactions in determining the utility of these materials.

Concentrating on one polymer system composed of a methyl methacrylate main chain and an oxynitrostilbene NLO segment connected by aliphatic spacer groups containing 3 or 6 carbons, we have synthesized very pure, high molecular weight homopolymers as well as copolymers covering the range of compositions from 5% to 80% oxynitrostilbene. These materials are being used not only in the ongoing work reported in this paper, but also in related studies at Leed's University, Cambridge University, and GEC-Marconi Labs which are being reported in other papers at this meeting. They provide us not only with a range of concentrations of polar side chains, but also with varying degrees of attainable liquid crystalline order [4]. The structure of oxynitrostilbene and its absorption spectrum is shown in Figure 1.

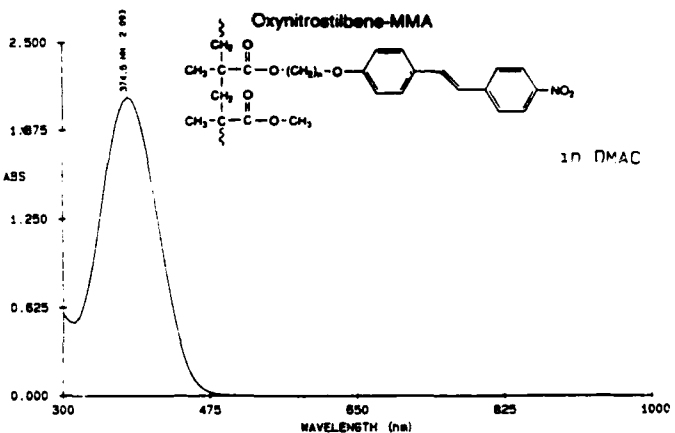


FIGURE 1. ABSORPTION SPECTRUM AND STRUCTURE OF OXYNITROSTILBENE-MMA

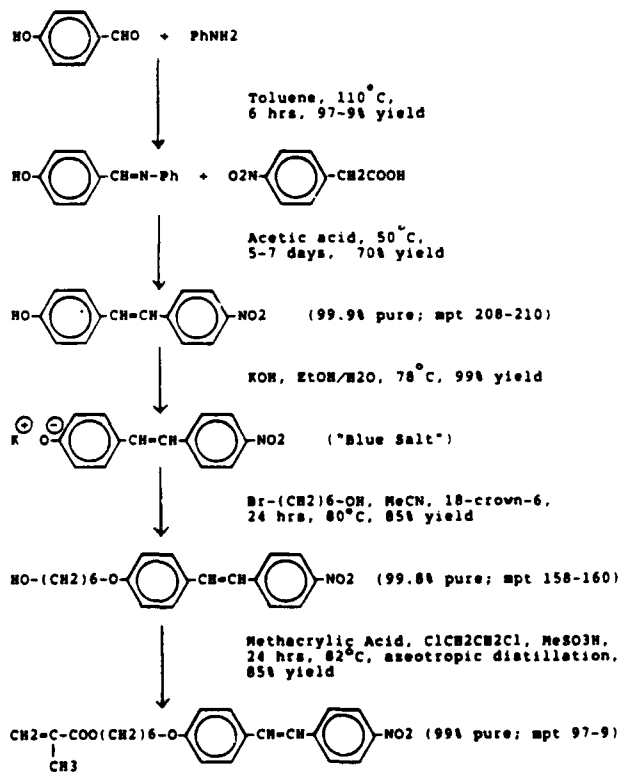


FIGURE 2. OXYNITROSTILBENE MONOMER SYNTHESIS

Our approach is to begin by comparing the pyroelectric response to the electro-optic response in these materials. The pyroelectric response comes from the fact that poled polymer films have a net dipole moment. A temperature change will cause the polarization density to change (from the thermal expansion of the polymer, for example) and thus can generate a current in an external circuit. This same dipolar orientation is responsible for the non-linear optical and electro-optical response of the film. Thus a comparison of these two phenomena should help check our understanding of the microscopic origin of both of these effects. In addition to reporting the first such comparison, we have also determined the thermal expansion coefficient of our material in order to help interpret the pyroelectric data. Some preliminary piezoelectric data is also discussed.

One of the key elements of this work is to study the effect of composition and spacer group on poling and the resulting physical properties. In this paper we can only report some of the preliminary results, since all the necessary characterizations have not yet been completed. Thus, the detailed analysis of the role of composition will be reported at a later time.

#### OXYNITROSTILBENE MONOMER SYNTHESIS

The oxynitrostilbene monomers were synthesized by conventional methods which have already been described by A. Buckley and R. DeMartino [5], and are outlined in Figure 2. We took particular care to make very pure final monomers, and it was found that careful purification of key intermediates made the task of final purification of the monomers much simpler. To check for purity we used HPLC, GC/MS, NMR, and DSC. One interesting example of the importance of having pure intermediates was the hydroxyhexyl ether of nitrostilbene. It was made 99.8% pure, and was found to melt to an isotropic phase at 159°C, contrary to the report by Griffin et al [6] where it was found to form a nematic phase at 137°C. We found that nematic phases in this intermediate were typically due to bis-stilbene impurities.

#### OXYNITROSTILBENE POLYMER SYNTHESIS

Standard radical initiated polymerizations using azo initiators were done for all homopolymers and copolymers. All polymerization solutions were precipitated in methanol using a high shear blender. The solid was then extracted three times with boiling toluene and then partially dissolved in dichloromethane and reprecipitated in methanol twice. Yields were typically better than 80%.

The  $T_g$ 's of the various polymer compositions which have been made are shown in Figure 3. MO6ONS copolymers with more than 50% MO6ONS have liquid crystalline order above  $T_g$  [4]. All other materials are isotropic. We note that the  $T_g$  for the MO6ONS copolymers decreases with increasing MO6ONS content, while the MO3ONS copolymers are relatively insensitive to composition. This is expected since the MO3ONS homopolymer has a  $T_g$  very close to that of pure PMMA.

The representative molecular weights determined by GPC are given in Table I. We note that the number averaged degree of polymerization is greater than 250 in all samples, and thus are clearly much larger than needed to get molecular weight independent properties (such as  $T_g$ ).

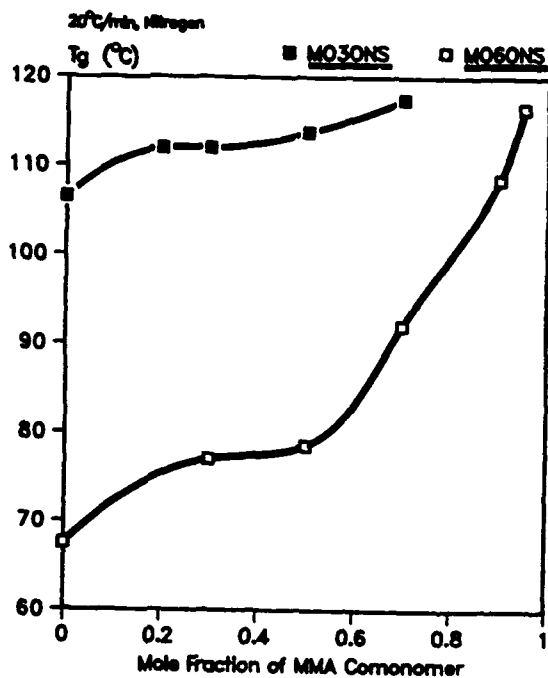
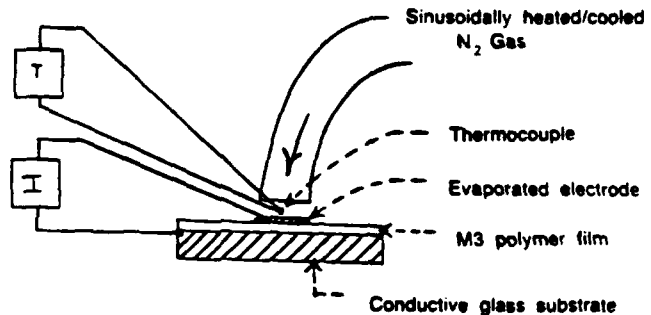


FIGURE 3. GLASS TRANSITION TEMPERATURE vs COPOLYMER COMPOSITION (MOLE % OXYNITROSTILBENE)



$$p = \frac{1}{A} \cdot \frac{dI}{dt} = \frac{1}{A} \cdot \frac{dI}{dt} = \frac{1}{A} \cdot \frac{\Delta I}{\Delta T_0}$$

$p$	- Pyroelectric coefficient	(C/m <sup>2</sup> · °K)
$A$	- Sample area	(m <sup>2</sup> )
$I$	- Current	(amp)
$\omega$	- Cycling frequency	(sec <sup>-1</sup> )
$t$	- Cycling Time	(sec)
$\Delta I$	- Amplitude of current change	(amp)
$\Delta T_0$	- Amplitude of temperature change	(°K)

FIGURE 4. MEASUREMENT OF THE PYROELECTRIC COEFFICIENT  $p$

TABLE I  
OXYNITROSTILBENE-MMA COPOLYMER MOLECULAR WEIGHTS

COMPOSITION	$M_w$	$M_n$
MO3ONS	335,000	126,000
	386,000	196,000
	660,000	210,000
$(MO3ONS)_{0.8} (MMA)_{0.2}$	478,000	235,000
$(MO3ONS)_{0.7} (MMA)_{0.3}$	1,300,000	405,000
$(MO3ONS)_{0.5} (MMA)_{0.5}$	1,200,000	234,000
$(MO3ONS)_{0.3} (MMA)_{0.7}$	731,000	191,000
MO6ONS	990,000	240,000
$(MO6ONS)_{0.1} (MMA)_{0.9}$	720,000	120,000

#### FILM PREPARATION AND POLING

##### Spin Coating from Solution

The purified polymers are dissolved in a suitable solvent, to form viscous solutions, typically containing 13 to 20% polymer. A filtered solution is then spin coated using a Solitec spin coater at speeds of 1000 to 2000 rpm onto a clean electroconductive (ITO coated) glass slide which serves as one electrode. After removal of all solvent by heating above the  $T_g$  of the polymer, a thin gold layer is vacuum evaporated on the film surface as the second electrode. Wire leads are then bonded to the electrodes with a conductive silver-epoxy paste for subsequent poling and characterization.

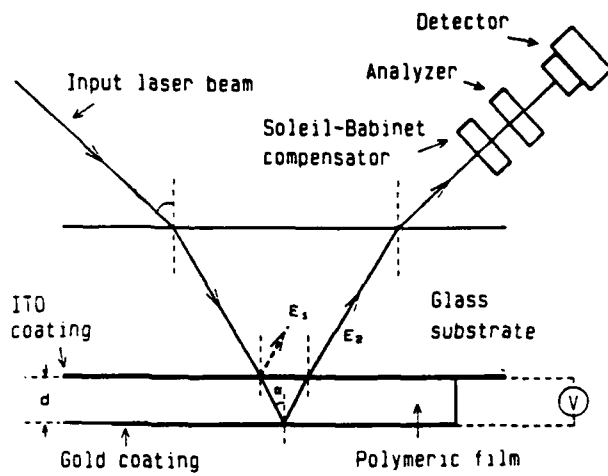
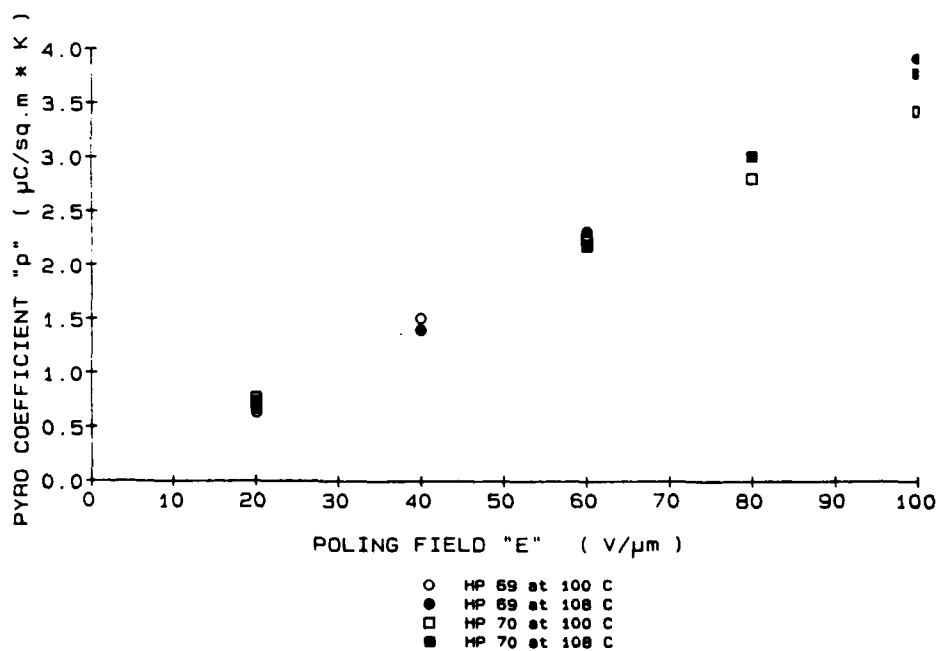
##### Poling of the Spin Coated Films

Poling is done in a d.c. field at a temperature near  $T_g$  so that dipoles have enough mobility to realign with the field. The sample is then cooled down with the field on, thus locking in the induced dipolar orientation. This requires a film having both a high resistivity and high dielectric breakdown strength, since fields of at least  $30 \text{ V}/\mu\text{m}$  are required to orient polymer dipoles effectively. At such high fields imperfections in the film can cause a local breakdown which is likely to short circuit the film and destroy the dipole orientation. We found that our properly prepared polymer films could be poled to about  $100 \text{ V}/\mu\text{m}$  near  $T_g$  without breakdown.

#### MATERIALS CHARACTERIZATIONS

##### Pyroelectric Measurements

A diagram of the apparatus and the equations for obtaining the pyroelectric coefficient 'p' are shown in Figure 4. The apparatus was calibrated against some pyroelectric composite and PVDF specimens measured both here and at Leeds.

FIGURE 5. MEASUREMENT OF THE POCKELS ELECTRO-OPTIC COEFFICIENT  $r$ FIGURE 6. PYROELECTRIC COEFFICIENT  $p$  vs POLING FIELD

### Electro-optic Properties

Figure 5 shows a diagram of the optical configuration of the experimental setup for measuring the electro-optic coefficient of poled polymer films. The same samples prepared for pyroelectric measurements were used here. A laser beam is incident on the back of the glass substrate at an angle  $\phi$ . It propagates through the substrate, the ITO, the polymer layer, and is then reflected back out into the air by the top gold electrode. The polarization of the input beam is set at 45 degrees to the plane of incidence so that the parallel (p-wave) and perpendicular (s-wave) components of the optical field are equal in amplitude. The reflected beam propagates through a Soleil-Babinet compensator, an analyzer and into a detector. The modulation in the beam is measured using a lock-in amplifier.

When a modulating voltage is applied across the electrodes, a change in the phase angle  $\delta\psi$  in both the s and p waves is induced by the change in refractive index  $\delta n$  due to the electro-optic effect, and also a change in path length  $\delta l$  due to the change in the refraction angle  $\alpha$ . Hence

$$\delta\psi = \frac{2\pi}{\lambda} (1 \delta n + n \delta l) \quad (1)$$

This change in phase angle is converted to intensity modulation of the laser beam by the output analyzer, and the purpose of the Babinet-compensator is to bias the output light intensity at the most linear region, or at the half-intensity point  $I_0$ . With the use of the approximations  $n_3 = n_1 \approx n$  and  $r_{33} = 3r_{11}$  where  $r$  is the electro-optic tensor and 3 and 1 represent directions perpendicular and parallel to the film, respectively, the electro-optic coefficient can be obtained by the following expression

$$r_{33} = \frac{3 I_m}{4\pi V_m I_c n^2} \frac{(n^2 - \sin 2\omega)^{3/2}}{(n^2 - 2 \sin 2\omega)} \frac{1}{\sin 2\omega} \quad (2)$$

where  $I_m$  is the amplitude of the modulation, and  $\omega$  and  $V_m$  are the modulation frequency and voltage respectively.

### Relationships Between the Pyro and Electro-optic Properties and the Poling Conditions

Electroded MO3ONS homopolymer ( $T_g \sim 115^\circ C$ ) films were prepared on ITO glass as described above and poled at  $100 V/\mu m$  and  $108^\circ C$ . Two of these were first characterized by measuring the 'p' and 'r' and then sent together with two earlier films to I.M. Ward at Leeds University who measured the hydrostatic piezoelectric charge coefficient " $d_33$ ". Its average value is given in Table 4. Two other MO3ONS films were poled at different fields and temperatures - 20, 40, 60, 80, and  $100 V/\mu m$ , and  $108$  or  $100^\circ C$ , respectively. After each poling the "p" and the "r" coefficients were measured. Thereafter the film was depoled by heating and holding at  $108^\circ C$ , then poled again, and so on. The 'p' and 'r' values vs. the poling field at two temperatures near the  $T_g$  are shown in Figures 6 and 7, respectively. Both the 'p' and 'r' increase fairly linearly with poling field, at least

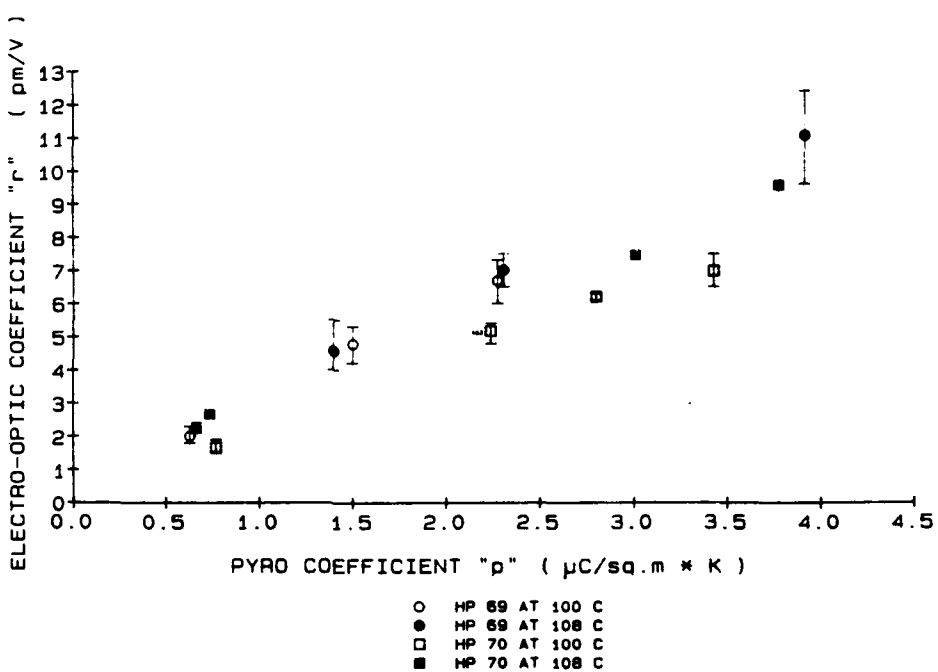
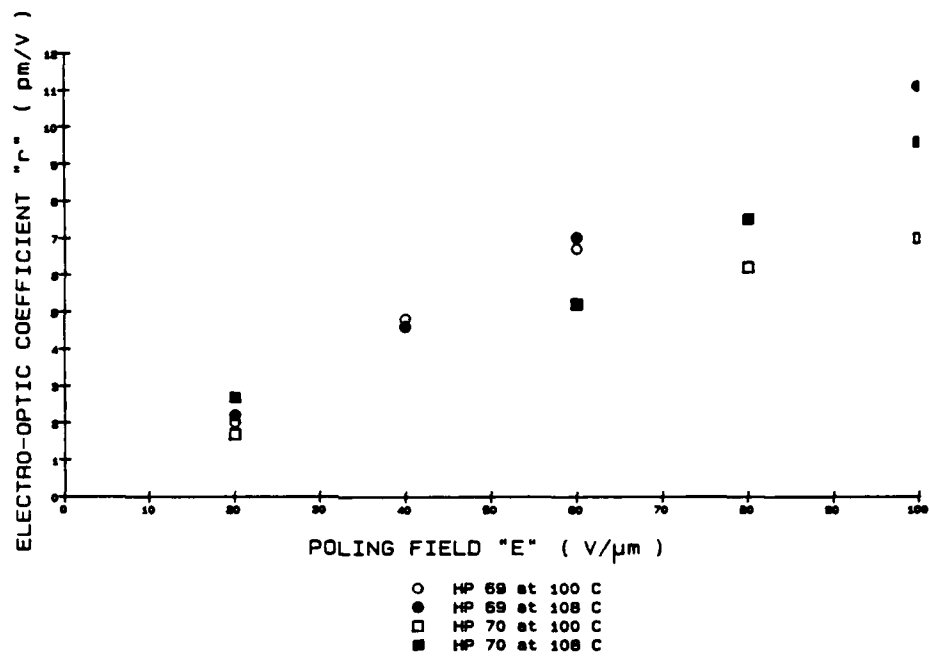


FIGURE 8. PYROELECTRIC COEFFICIENT vs POCKELS COEFFICIENT

up to 100 V/ $\mu$ m, and are only slightly affected by the temperature. The plot of the 'p' vs. the 'r' coefficients given in Figure 8 also depicts the range in the 'r' values resulting from three individual 'r' measurements in different locations of the film. It is seen that for reasons not yet understood the scatter varies irregularly. In view of the observed linearity one may conclude that if the MO3ONS homopolymer films could be improved so as to withstand higher poling fields, the 'p' and 'r' coefficients would be substantially higher.

MO6ONS homopolymer films are liquid crystalline up to a temperature of 155°C [4]. Upon spin coating, they form opaque films during room temperature evaporation of solvent. This is probably due to formation of a liquid crystalline phase and its associated microstructure. However, after heating in vacuum at 115°C for several hours (to remove any residual solvent) the films become transparent. We have not yet completed the characterizations of these films and thus do not know the nature of any liquid crystalline order. These films were subsequently poled at 70°C, and characterized for their electro-optic and pyroelectric properties.

MO6ONS-MMA 50-50 copolymers do not have any liquid crystalline states above  $T_g$ , and remain transparent after spin coating as do the MO3ONS polymers and copolymers.

#### Dielectric Properties

The capacitance and the loss tangent,  $\tan \delta$ , of many spin coated films fabricated from a number of lots of the MO3ONS and MO6ONS homo- and 50/50 copolymers have been measured over the frequency range of 0.1 to 100 kHz prior to the poling (see Table II). The low frequency (100 Hz) values were used in Table 3. Although the values for the nitrostilbene polymers are close together ranging from 3.3 to 3.6 over the whole frequency range, the homopolymers have somewhat higher  $\epsilon$  values and are also significantly less lossy above 10 kHz than their copolymer counterparts which have additional MMA in the main chain.

TABLE II

MEAN RELATIVE PERMITTIVITY ( $\epsilon$ ) AND DIELECTRIC LOSS ( $\tan \delta$ ) OF THE MO3ONS AND MO6ONS HOMO- AND CO-POLYMERS.

Polymers:	p-MO3ONS	p-MO3ONS-MMA	p-MO6ONS	p-MO6ONS-MMA
Frequency (kHz)	" $\epsilon$ "			
0.1	3.61	3.54	3.67	3.48
1.0	3.55	3.48	3.625	3.43
10	3.50	3.43	3.595	3.38
100	3.45	3.34	3.555	3.30
" $\tan \delta$ " (%)				
0.1	0.94	1.15	0.845	1.0
1.0	0.90	1.13	0.62	1.0
10	1.03	1.85	0.89	1.7
100	4.1	8.5	3.37	10

### Bulk Density and Thermal Expansion

To get some idea of the thermal expansion behavior of our NLO polymers, one inch diameter disks, 2-3 mm thick, were vacuum hot pressed from an MO3ONS homopolymer powder at ca. 140°C. The bulk densities of the disks ranged from 1.26 to 1.31 Mg/m<sup>3</sup>. The thermal expansion coefficients ( $\alpha_t$ ) were calculated from the dilation curves obtained by means of a DuPont 1090 TMA Analyzer. The curves were slightly nonlinear, giving an  $\alpha_t$  value of 60  $\mu\text{m}/\text{m}^\circ\text{C}$  at room temperature and 80  $\mu\text{m}/\text{m}^\circ\text{C}$  at 90°. These are fairly close to the handbook value of neat PMMA which is listed as 70  $\mu\text{m}/\text{m}^\circ\text{C}$ .

### **THEORY AND DISCUSSION**

#### Polarization Density

The electro-optic, piezoelectric, and pyroelectric effects all depend on the polarization density which is developed upon poling. Following Mopsik and Broadhurst [7] one can write:

$$P = (N/V)[(n^2+2)/3]\mu\langle\cos\theta\rangle \quad (3)$$

where:

$N/V$  is the number of dipolar molecules per unit volume

$(n^2+2)/3$  describes the increase in macroscopic polarization due to the electronic polarizability of the polymer

$\mu$  is the dipole moment of the dipolar molecule

$\langle\cos\theta\rangle$  is the thermodynamic average of the cosine of the angle between the molecular dipole and the direction of the polarization (the initial poling field).

If one assumes that the dipoles act independently during poling and that the unpoled distribution is isotropic, one finds that [8]

$$\langle\cos\theta\rangle = (a/3) - a^3/45 + \dots \quad (4)$$

where:  $a = \mu E_t / (k_b T_p)$

and where:  $E_t$  = local poling field =  $\{\epsilon(n^2+2)/(n^2+2\epsilon)\}E$   
 $T_p$  = poling temperature.

If the system is in a completely ordered liquid crystalline state (with the director parallel to the poling field) before poling, then one would expect

$$\langle\cos\theta\rangle = \tanh(a). \quad (5)$$

These results will be valid only when the poling temperature is enough high to insure that the dipoles reach thermal equilibrium with the poling field. In addition, this treatment completely neglects any correlations between the motion of dipoles. In this type of model, changes in the copolymer ratio change the polarization density primarily through changes in  $N/V$ .

### Dielectric Constant and Mechanical Properties

The room temperature dielectric constant differs from the index of refraction squared primarily because of the orientational motion of dipolar species in the polymer. Thus, one might be surprised that the low frequency dielectric constant of MO3ONS homopolymer is essentially the same as pure PMMA. This is probably due to two competing effects: the increase in the density of dipoles upon going from PMMA to MO3ONS, and the decrease in their mobility. This decrease in mobility may well be related to the brittleness of oxynitrostilbene films, and might arise from the strong dipolar interaction between oxynitrostilbenes. Although temperature dependent data is certainly needed, this speculation is qualitatively consistent with the dielectric data shown in Table II.

### Pyroelectric and Piezoelectric Effects

In this paper we will restrict ourselves to considering thin films on rigid substrates. We therefore do not have to worry about changes in electrode and sample area [9]. The macroscopic polarization density is equal to the charge per unit area on the electrodes placed on either side of a thin film, and thus the piezoelectric coefficient is

$$d_h = dP/d\sigma \quad (6)$$

where  $\sigma$  is just the hydrostatic stress (i.e. the pressure).

The pyroelectric coefficient can simply be written as

$$p = dP/dT. \quad (7)$$

There are three terms in  $P$  which could vary in principal with either the stress or the temperature:

1.  $N/V$  will change because of changes in the density with  $T$  or stress. The relationship between changes in stress and  $T$  will be given by the thermal expansion coefficient.
2.  $(n^2+2)/3$  will change with  $T$  and stress, but those changes will be predominantly due to density (and thus  $N/V$ ) changes. If one writes  $n^2$  in terms of molecular polarizabilities and the number density of molecules [10]

$$n^2 = [1+8\pi(N/V)\alpha/3]/[1-4\pi(N/V)\alpha/3]. \quad (8)$$

where  $\alpha$  is the electronic polarizability, and  $N/V$  is the number density as before, it is straightforward to calculate the derivative with respect to density changes.

3.  $\langle \cos\theta \rangle$  will change only to the extent that the orientation induced during poling is not completely frozen in. This is usually referred to as the primary effect in pyroelectrics, while the phenomena described in 1 and 2 are referred to as secondary effects [9]. We will discuss the importance of primary effect ( $\langle \cos\theta \rangle$ ) changes later.

For now, we will concentrate on changes in polarization due to changes in the volume of the sample. We note that for thin films on a rigid substrate

$$-(1/V)dV/d\sigma = (K/3)\{(1+v)/(1-v)\} \quad (9)$$

and

$$(1/V)dV/dT = \alpha_p(1+v)/(1-v) \quad (10)$$

where  $K$  = compressibility  
 $v$  = Poisson ratio.

If we denote the piezoelectric coefficient and pyroelectric coefficient calculated as described here, but neglecting changes in orientation (i.e.  $\langle \cos\theta \rangle$ ) at constant volume with a superscript s (for secondary) then we get

$$d_h^s = [(n^2+2)/3]^2 (N/V) \mu \langle \cos\theta \rangle (K/3) \{(1+v)/(1-v)\} \quad (11)$$

and

$$p^s = [(n^2+2)/3]^2 (N/V) \mu \langle \cos\theta \rangle \alpha_p \{(1+v)/(1-v)\}. \quad (12)$$

Note that the term  $(n^2+2)/3$  is now squared. One power of this term comes from the need to include the effect of electronic polarizability on the charge density, and the second power comes from including the changes in that polarizability with changes in density (i.e. volume).

The above equations were used with the values of the relevant variable s shown in Table III to give the results shown in Table IV. Since many of the important parameters have not yet been measured, we have used estimates based on the measurements which have been performed and the known properties of PMMA. We note first, that the calculated value of the piezoelectric constant is significantly higher than the experimentally determined value. One possible explanation is that the sample does not pole to the level expected. This idea is however inconsistent with the close agreement between the theoretical and experimental results for the pyroelectric coefficient. In addition, the linear electro-optic coefficient,  $r$ , calculated with the same independent dipole poling model used here is much lower than the experimental value. Another possibility is that the sample depoled before the piezo measurement was made. Although this cannot be ruled out, there is significant evidence that these samples have very good polarization stability [11]. Some of the discrepancy could be because oxynitrostilbene polymers are much stiffer than PMMA, and thus the value of  $K$  used in the calculation was much too large. This would be consistent with the qualitative result that all of these oxynitrostilbene films are extremely brittle. Work is presently under way to measure the elastic properties of these materials directly.

TABLE III  
VARIABLES USED IN THEORY

MATERIALS:	MO3ONS	MO3ONS-MMA 50-50 COP.	MO6ONS	MO6ONS-MMA 50-50-COP.
$d(\text{gm/cm}^3)$	1.31	1.25 <sup>c</sup>	1.31 <sup>c</sup>	1.25 <sup>c</sup>
$n$	1.6	1.6	1.6	1.6
$\epsilon(0)$	3.6	3.5	3.6	3.5
$N/V(10^{27}/\text{m}^3)$	2.1	1.6	1.9	1.5
$\mu(\text{debyes})^b$	7	7	7	7
$\langle \cos\theta \rangle$	0.23	0.23	0.23(0.6)	0.23
$\langle \cos^3\theta \rangle$	0.14	0.14	0.14(0.6)	0.14
$\alpha_p(10^{-6}/\text{C})$	60	65 <sup>c</sup>	60 <sup>c</sup>	65 <sup>c</sup>
$K(10^{-10}/\text{Pa})^a$	2.5	2.5	2.5	2.5
$v^s$	0.37	0.37	0.37	0.37
$\beta(10^{-40}\text{m}^4/\text{volt})$	80	80	80	80

a: PMMA value [17]  
 c: Estimate based on MO3ONS and PMMA data

b: Theoretical estimate

The values of  $\langle \cos\theta \rangle$  and  $\langle \cos^3\theta \rangle$  were calculated assuming an isotropic glass, except for the values in parenthesis which are those expected for an Ising (liquid crystalline) like model. The applied field was  $100V/\mu m$ .

TABLE IV  
 COMPARISON OF MEASURED AND CALCULATED COEFICIENTS

MATERIAL:	MO3ONS	MO3ONS-MMA 50-50 COP.	MO6ONS	MO6ONS-MMA 50-50 COP.
$d_3$ (measured) ( $10^{-12} C/N$ )	1.4			
$d_3$ (calculated) ( $10^{-12} C/N$ )	4.8	3.6	4.3(11)	3.2
$p$ (measured) ( $10^{-6} C/km^2$ )	3.9	3.0	3.4	3.5
$p$ (calculated) ( $10^{-6} C/km^2$ )	3.4	2.6	3.1(8.2)	2.4
$r$ (measured) ( $10^{-12} m/Volt$ )	11	13	9.4	14
$r$ (calculated) ( $10^{-12} m/Volt$ )	5.2	4.0	4.7(21)	4.0

All measurements and calculations are for films poled at  $100V/\mu m$ . The variability in the data from sample to sample is about 20% for all measurements.

The experimental pyroelectric coefficients are in remarkably good agreement with the measured values given the numerous uncertainties in both the measurement and the calculations. However, we can still not rule out other potential contributions to  $p$ . First of all, we have neglected any contribution to the pyroelectric effect from the methacrylate backbone. This is clearly an oversimplification given the fact that PMMA has a pyroelectric effect [11]. Another effect which must be considered is a significant primary contribution to the pyroelectric coefficient; i.e.  $\langle \cos\theta \rangle$  variation with  $T$  even at constant volume. There are two likely causes for this: a significant thermal motion of the dipoles around their equilibrium configuration, and a changing environment for the dipoles with temperature. The first has been discussed by Mopsik and Broadhurst [7], and should contribute significantly to the low frequency dielectric constant as well as to any d.c. induced second harmonic generation (DCSHG) observable in unpoled films. The second effect would also have consequences for the temperature dependence of both of these measurements. Further dielectric measurements as well as DCSHG experiments are planned. It is important to remember that more careful measurements of all the parameters that go into the calculation, as well as further pyroelectric measurements will be required in order to fully understand the role of dipolar motion in determining these material properties.

### Electro-optic Properties

The linear electro-optic coefficient,  $r$ , determines the size of the index change one can achieve in an electro-optic material through the application of an external field  $E$  through the relationship [12]

$$\Delta n = n^3 r E/2 \quad (13)$$

For simplicity, we will only be concerned with the coefficients associated with electric fields normal to the film surface (i.e.  $r_{33}$ ). We can then write [13]:

$$r = 2f^2(\omega)f(0)F(\omega, \omega')(\mathcal{N}/V)\beta \langle \cos^3 \theta \rangle / (n^2 \epsilon) \quad (14)$$

where:  $f(\omega) = (n^2 + 2)/3$   
 $f(0) = \epsilon(n^2 + 2)/(n^2 + 2\epsilon)$

are the local field corrections;

$$F(\omega, \omega') = 2(3\omega_0^2 - \omega^2)(\omega_0^2 - \omega'^2)(\omega_0^2 - 4\omega^2) / \{3\omega_0^2(\omega_0^2 - \omega^2)^2\} \quad (15)$$

is the two level system correction for resonant enhancement effects [12], where  $\omega_0$  is the eigenfrequency of the two level system,  $\omega'$  is the fundamental frequency in a DCSHG experiments, and  $\omega$  is the optical frequency in an electro-optic measurement. In our case the wavelengths, related to  $\omega$  by

$$\lambda = 2\pi c/\omega \quad (16)$$

corresponding to  $\omega_0$ ,  $\omega$ , and  $\omega'$  are  $0.38 \mu\text{m}$ ,  $0.633 \mu\text{m}$ , and  $1.3 \mu\text{m}$  respectively. The value of  $\mu\beta$  found was  $130 \times 10^{-30} \text{ D-cm}^5/\text{esu}$ . The electro-optic measurements were done as described above using  $0.633 \mu\text{m}$  radiation. Table IV shows that this model underestimates all the measured values of the electro-optic coefficient. The calculations were done using the data presented in Table III. The value of  $\langle \cos^3 \theta \rangle$  was calculated assuming an initially isotropic system [8]. The value of  $\beta$  was determined from an DCSHG measurement [14] of  $\mu\beta$  (which was  $130 \times 10^{-30} \text{ D-cm}^5/\text{esu}$ ) on the polymers in cyclohexanone (using  $1.3 \mu\text{m}$  as the fundamental). This is somewhat lower than other reported values on similar materials [13], although the differences are not large enough to account for the large values of  $r$  measured here. The  $\chi^{(2)}$  of the MO3ONS film was also measured directly, using a maker fringe analysis as described by Jerphagnon and Kurtz [15] in the thin film limit [16], and was found to be  $14 \text{ pm/V}$ . The value calculated using this model is  $9.1 \text{ pm/V}$ , in better agreement than the  $r$  values. At this time, we do not know if this disagreement is due to uncertainties in the measurements (which are often large [12]). We note that the closer agreement between the calculated and measured values of  $\chi^{(2)}$  may be due to the fact that one does not need to make corrections for resonant enhancement in that calculation. Both the  $\mu\beta$  measurement and the  $\chi^{(2)}$  measurement involve doubling double  $1.3 \mu\text{m}$  light.

### SUMMARY AND CONCLUSIONS

The synthesis of methacrylate backbone, oxynitrostilbene polymers has been described. These materials have been reproducibly made in 30-50 gm batches of high purity and molecular weight with varying MMA copolymer and two aliphatic carbon spacer lengths (3 and 6). The materials described here are being used as a model system with which to understand the entire range

of electro-optic, pyroelectric, piezoelectric, optical, and mechanical properties of polar side chain polymers.

Although this ambitious program is still in progress, we have reported here on the first detailed comparison of electro-optic, piezoelectric, and pyroelectric measurements on a single side chain polymer system. All of the electro-optic measurements give higher activity than expected using a simple model. The pyroelectric measurements are in reasonable agreement with this model as long as the changes in dipolar motion and coupling do not dominate the pyroelectric effect. This same poling model leads to an overestimate of the piezoelectric coefficient. Part of this disagreement may be due to the oxynitrostilbene being less compressible than PMMA, consistent with the observed brittleness of these films. However, it is clear that more work is needed in order to fully understand the nature of poling and the importance of interactions between dipolar species in these materials.

#### REFERENCES

- [1] D. Ulrich, in Nonlinear Optical Effects in Organic Polymers, ed by Messier, Kajzar, Prasad and Ulrich, klumer Academic Publishers, Dordrecht, p299, (1989).
- [2] A. Buckley and J.B. Stamatoff, in Nonlinear Optical Effects in Organic Polymers, ed by Messier, Kajzar, Prasad and Ulrich, klumer Academic Publishers, Dordrecht, p327, (1989).
- [3] K.D. Singer, J.E. Sohn, L.A. King, and H.M. Gordon; J. Optical Soc. Am. B 6, 1339, (1989).
- [4] T. Lemmon and A.H. Windle, proceedings of 1989 MRS meeting symposium on Multifunctional Materials.
- [5] A. Buckley, R N Demartino et alia, "Organo-Optics: Nonlinear Properties of Polymers", AFOSR Contract # F49620-85-C-0047, (1986).
- [6] A.C. Griffin, A.M. Bhatti, and R.S.L. Hung, to appear in Nonlinear Optical and Electroactive Polymers, Plenum, New York, (1989).
- [7] F.I. Mopsik and M.G. Broadhurst, J. of Applied Physics 46, p4204, (1975).
- [8] D.J. Williams, in Nonlinear Optical Properties of Organic Molecules and Crystals; D.S. Chemla and J. Zyss ed., Academic Press, Orlando, p 405, (1987).
- [9] E.L. Nix, J. Namayakhara, G.R. Davies, and I.M. Ward, J. Polymer Science: B: Polymer Physics 26, p 127, (1988).
- [10] M. Born and E. Wolf, Principals of Optics, Pergamon Press, Oxford, (1988).
- [11] P.L. Carr, G.R. Davies, and I.M. Ward proceedings of 1989 MRS meeting symposium on Multifunctional Materials.
- [12] K.D. Singer, S.L. Lalama, J.E. Sohn, and R.D. Small, in Nonlinear Optical Properties of Organic Molecules and Crystals; D.S. Chemla and J. Zyss ed., Academic Press, Orlando, p 437, (1987).

- [13] D. Haas, H. Yoon, H.T. Man, G. Gross, S. Mann, and N. Parsons, Proceedings of the SPIE symposium on Organic Non-linear Optical Materials, San Diego, August 1989.
- [14] C. Teng, Molecular Optics: Disperison of the Nonlinear Second Order Optical Susceptibilty, University Microfilms, (1983).
- [15] J. Jerphagnon, S.K.Kurtz; J. of Applied Physics, vol 41, number 4, p 1667-81, (1970).
- [16] K.D.Singer, J.E.Sohn, S.J.Lalama ; Applied Physics Letters 49 p 248-50 (1986).
- [17] J. Brandrup and E.H. Immergut ed., Polymer Handbook 2nd edition, Wiley, New York (1975).

#### ACKNOWLEDGEMENTS

We would like to thank Alan Buckley, Jim Stamatoff, and Don Ulrich for their encouragement and guidance throughout this work. Special acknowledgements are due to Frank Battito, George Breckenridge and Ray Carney. In addition, we would like to thank Joe Menczel and Nancy Platner for the thermal analysis, Rose Peterson and Ho-nan Sung for determining the molecular weights, Jens Gaeda and Lynn Isaacson for NMR characterizations and Mark Sebastian for helping with the determination of molecular purity. We gratefully acknowledge the financial support of the SDIO/AFOSR through contract # F49620-87-C-0109.



92-18257

AD-P007 466



129



## MOLECULAR DESIGN OF SYNTHETIC POLYPEPTIDES FOR NONLINEAR OPTICS

T. ISHII, T. WADA, A. F. GARITO,\* H. SASABE, A. YAMADA  
FRONTIER RESEARCH PROGRAM (RIKEN)  
2-1, Hirosawa, Wako-shi, Saitama 351-01, Japan

### ABSTRACT

Second order molecular susceptibilities  $\beta$  of poly( $\gamma$ -benzyl L-glutamate) (PBLG) and poly( $\gamma$ -p-nitrobenzyl L-glutamate) (PNBLG) were determined by means of dc-induced second harmonic generation (dc-SHG) technique in solutions at a wavelength of 1064nm as  $1.5 \times 10^{-29}$  esu and  $-4.9 \times 10^{-29}$  esu, respectively. Among PBLG, PNBLG and nitrobenzene, it was found that only PNBLG has negative value of  $\beta$ . It follows that the effect of nitrophenyl groups in side chains is dominant for  $\beta$  whereas the contribution of carbonyl groups in main chain is dominant for the permanent dipole moment  $\mu$  in PNBLG.

### INTRODUCTION

Recently remarkable progress has been made on polymeric optoelectronic devices, such as electro-optic modulators based on second order nonlinear responses. Although poled host-guest systems attract much interest in this field[1-3], several problems have been pointed out : (1)the concentration of guest is not sufficient, (2)very strong electric field is required for the highly oriented structure, (3)due to the molecular motions and/or dipole-dipole repulsion, the nonlinear optical effect tends to decay. In order to overcome these problems, the second order susceptibility  $\beta$  should be enhanced and the permanent dipole moment  $\mu$  should be optimized.

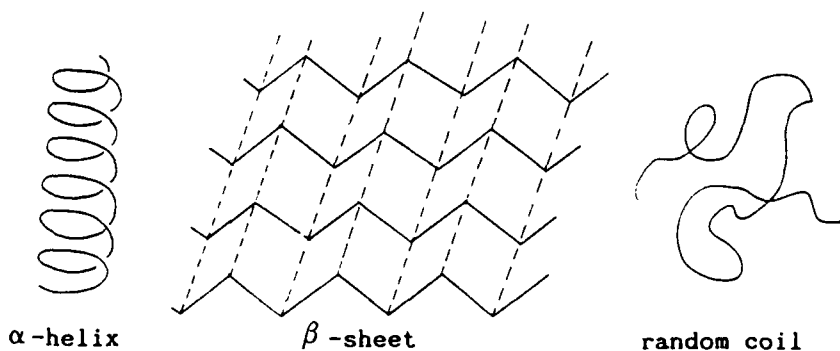


Figure 1. Secondary structures of polypeptides

Several attempts have been made to align chromophores using higher order structures of polymers[3,4]. One is to utilize liquid crystalline polymers as a matrix and the other

\*) Permanent address: Department of Physics, University of Pennsylvania, PA. 19104

is to use polymer itself with higher order conformation, e.g.,  $\alpha$ -helix or  $\beta$ -sheet in polypeptides. Typical conformation of polypeptides is illustrated in Figure 1. Poly( $\gamma$ -benzyl L-glutamate) (PBLG), a typical  $\alpha$ -helical synthetic polypeptide, is known to have large dipole moment proportional to degree of polymerization, because all carbonyl groups in the main chain are almost parallel to helical axis. In fact, highly polymerized PBLG (DP=2500) is reported to have very large  $\mu$  (8000 Debye)[6] and  $\beta$  ( $2 \times 10^{-28}$  esu)[7]. This value of  $\beta$ , however, is not large enough for practical use because of the large molecular weight.

If side chains of PBLG are not perpendicular to the helical axis,  $\beta$  and  $\mu$  of side chains may contribute to those of an entire molecule. In this system the dipole moment of a polymer chain can be controlled by proper choice of molecular weight and/or by adjusting the  $\mu$  value of side chains. In order to determine whether side chains contribute to molecular susceptibility  $\beta$  or not, we introduced nitro groups into *p*-position of benzyl groups of PBLG, and measured  $\beta$  by means of dc-SHG technique.

## EXPERIMENTAL

### Synthesis

PBLG was synthesized by the usual NCA (N-carboxy anhydride) method as described in Figure 2. Molecular weight was determined to be 44,000 from the viscosity after to Doty *et al.* [8]. Poly( $\gamma$ -*p*-nitrobenzyl L-glutamate) (PNBLG) was obtained by transesterification of PBLG with *p*-nitrobenzylalcohol. Substitution was found to be perfect from  $^1\text{H-NMR}$  spectrum. During transesterification, the degree of polymerization was not changed, since PBLG obtained by transesterification of PNBLG had same viscosity as original PBLG.

CP/MAS  $^{13}\text{C-NMR}$  spectrum of solid PNBLG showed a peak at 57 ppm., which corresponds to a chemical shift of  $\alpha$ -carbon of  $\alpha$ -helical polypeptides in the solid state.  $\alpha$ -Helical conformation in solution is confirmed from the dipole moment and molecular susceptibility measured in solutions for PBLG and PNBLG.

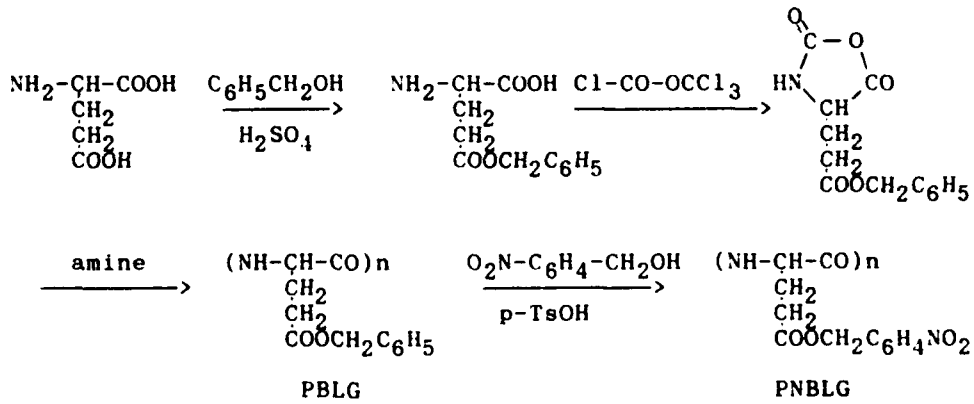


Figure 2. Synthesis of PBLG and PNBLG

### Measurement

PBLG has no absorption from 300 to 1500 nm, while PNBLG has absorption edge at around 400 nm.

Measurements of  $\beta$  were carried out in solutions after the method described by Singer et al. [9-11]. For PBLG  $\beta$  was determined both in dichloroethane(DCE) and in DMF, while for PNBLG the measurement was performed only in DMF. In order to calculate  $\mu$ , linear polarizability  $\alpha$ , and  $\beta$  of polymer, refractive index  $n$ , dielectric constant  $\epsilon$ , and macroscopic third order susceptibility  $\Gamma(-2\omega; \omega, \omega, 0)$  of the solution were plotted against concentration of polymers.

Refractive indices were measured at a wavelength of 1064 nm and dielectric constants were measured at 30 kHz. The dc-SHG experiment was performed by a wedge Maker fringe technique [12-16] using  $\alpha$ -quartz as a reference. A 10-Hz pulser triggers a Q-switched Nd:YAG laser operating at 1064nm and a high voltage (2-8kV) pulser through a delay generator. From the amplitude of Maker fringe patterns and refractive indices, third order hyperpolarizability  $\Gamma$  of the solutions were calculated. Figure 3 shows a Maker fringe pattern of dc-SHG of PBLG/DCE solution. In Figure 4, dependence of  $\Gamma$  on concentration of polymers is shown for PBLG/DCE, PBLG/DMF, and PNBLG/DMF. Dipole moment  $\mu$  and linear molecular polarizability  $\alpha$  were calculated from refractive indices  $n$  and dielectric constants  $\epsilon$  after Singer et al. [9].

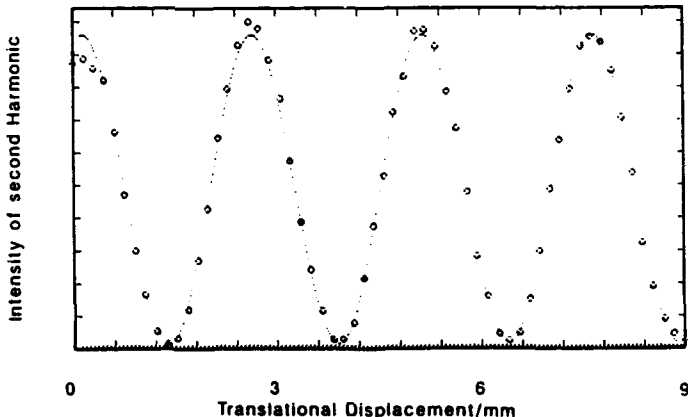
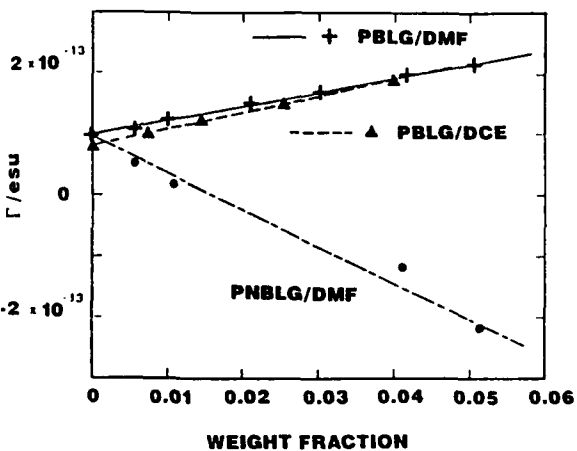


Figure 3. Maker fringe pattern of PBLG/DCE

(Dotted line indicates the calculated curve)

### RESULTS AND DISCUSSION

Values of  $\mu$ ,  $\alpha$ , and  $\beta$  of polypeptides are summarized in Table I. Nonlinear susceptibility  $\beta$  of PBLG and PNBLG showed opposite sign. That is, the nonlinear polarization and the permanent dipole moment align in the same direction in PBLG, whereas opposite in PNBLG. Since nitrobenzene and PBLG to possess positive values of  $\beta$ , in PNBLG both  $\mu$  and second order nonlinear polarization are opposite between main chains and side chains.

Figure 4.  $\Gamma$  vs weight fraction of polymerTable I.  $\mu$ ,  $\alpha$ , and  $\beta$  of polypeptides

sample	$\mu$ /esu	$\alpha$ /esu	$\beta$ /esu
PBLG/DCE	$3.8 \times 10^{-16}$	$4.6 \times 10^{-21}$	$1.3 \times 10^{-29}$
PBLG/DMF	$4.8 \times 10^{-16}$	$4.6 \times 10^{-21}$	$1.5 \times 10^{-29}$
PNBLG/DMF	$4.3 \times 10^{-16}$	$5.5 \times 10^{-21}$	$-4.9 \times 10^{-29}$

It is obvious that in PNBLG main chains contribute to the permanent dipole moment dominantly, whereas side chains to second order nonlinear susceptibility. Let  $\mu$  be along z axis (helical axis of a molecule) and the angle between z axis and a side chain be  $\theta$  (Figure 5). Then it follows the Equation (1):

$$\mu_{\text{eff}} = \mu_{\text{side}} \cos(\theta) , \quad (1)$$

where  $\mu_{\text{eff}}$  is the contribution of a side chain to  $\mu$ , and  $\mu_{\text{side}}$  is the dipole moment of a side chain. From the dc-SHG measurement the nonlinear susceptibility of z-direction  $\beta_z$  is given by Equation (2):

$$\beta_z = \beta_{zzz} + (\beta_{zyy} + \beta_{zxx} + 2\beta_{yyz} + 2\beta_{xxz})/3 . \quad (2)$$

Since PBLG and PNBLG have no absorption at both fundamental and harmonic wavelengths, Equation (2) can be simplified as Equation (3) from Kleinman symmetry [17].

$$\beta_z = \beta_{zzz} + \beta_{zxx} + \beta_{zyy} . \quad (3)$$

The contribution of a side chain to molecular nonlinear susceptibility is given by Equation (4):

$$\beta_{\text{eff}} = \beta_{\text{side}} \cos(\theta) \quad , \quad (4)$$

where  $\beta_{\text{side}}$  is the second order susceptibility of a side chain. Since  $\beta$  of nitrobenzene is more than twenty times larger than that of benzyl glutamate (of PBLG), while  $\mu$  of nitrobenzene is only twice as large as that of benzyl glutamate (see Table II), and (1) and (4) have identical form, it is obvious that the side chain is dominant for  $\beta$  while the main chain is dominant for  $\mu$ .

Assuming that nonlinear optical susceptibility of side chains of PNBLG is the same as that of nitrobenzene and that in PBLG the side chains don't contribute to  $\beta$ , we can estimate  $\cos(\theta)$  in Equations (1) and (4) from  $\beta$  of PBLG, PNBLG, and nitrobenzene( $\text{NO}_2$ ). The factors of  $\beta$ ,  $\alpha$ , and  $\mu$  of nitrobenzene are measured in DMF by the same method as PBLG and PNBLG. Results are summarized in Table II with those of repeating unit of PBLG and PNBLG. By using  $\beta$  in Table II,  $\cos(\theta)$  is roughly estimated as 0.2. This result indicates that about 1/5 of nonlinearity and dipole moment of side chain effectively contribute to the dipole moment and the molecular nonlinear susceptibility.

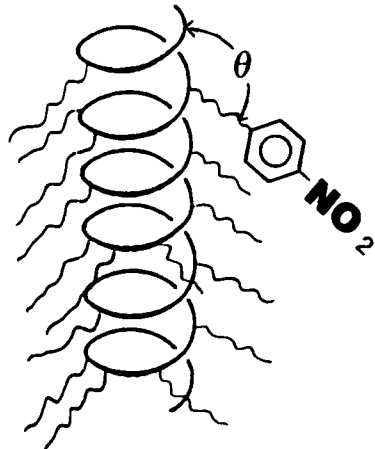


Figure 5.  
Conformation of PNBLG

Table II.  $\mu$ ,  $\alpha$ , and  $\beta$  (per repeating unit)

sample	$\mu/\text{esu}$	$\alpha/\text{esu}$	$\beta/\text{esu}$
$\phi\text{-NO}_2/\text{DMF}$	$4.2 \times 10^{-18}$	$1.4 \times 10^{-23}$	$1.9 \times 10^{-30}$
PBLG/DMF	$2.1 \times 10^{-18}$	$2.3 \times 10^{-23}$	$7.6 \times 10^{-32}$
PNBLG/DMF	$2.1 \times 10^{-18}$	$2.7 \times 10^{-23}$	$-2.5 \times 10^{-31}$

From the  $\beta$  measurement of PBLG and PNBLG, it is concluded that  $\beta$  of PBLG can be changed by introducing nitro groups to side chains of PBLG. This result suggests the chemical modification of  $\alpha$ -helical polypeptides is a new method for obtaining nonlinear optically active materials.

#### ACKNOWLEDGMENT

The authors thank Mr. H. Iwatani in Nippon Oil Company, LTD. for taking solid state  $^{13}\text{C}$ -NMR spectra.

## REFERENCES

- [1] G. R. Meredith, J. G. Van Dusen, and D. J. Williams, *Macromolecules* 15, 1385 (1982).
- [2] G. R. Meredith, J. G. Van Dusen, and D. J. Williams, *ACS Symp. Ser.* 233, 109-134 (1983).
- [3] K. D. Singer, J. E. Sohn, and S. J. Lalama, *Appl. Phys. Lett.*, 49, 248 (1986).
- [4] R. Oshima, T. Wada and J. Kumamoto, *J. Polym. Sci. Polym. Chem. Ed.*, 22, 2047 (1984).
- [5] R. Oshima, T. Wada and J. Kumamoto, *J. Polym. Sci. Polym. Chem. Ed.*, 22, 3135 (1984).
- [6] H. Watanabe, and K. Yoshioka, *Biopolymers* 2, 91 (1964).
- [7] B. F. Levine, and C. G. Bethea, *J. Chem. Phys.*, 65, 1989 (1976).
- [8] P. Doty, J. H. Bradbury, and A. M. Holtzer, *J. Am. Chem. Soc.*, 78, 947 (1956).
- [9] K. D. Singer, and A. F. Garito, *J. Chem. Phys.*, 75, 3572 (1981).
- [10] C. C. Teng, and A. F. Garito, *Phys. Rev. B*, 28, 6766 (1983).
- [11] S. J. Lalama, K. D. Singer, A. F. Garito, and K. N. Desai, *Appl. Phys. Lett.*, 39, 940 (1981).
- [12] P. D. Maker, R. W. Terhune, M. Nisenoff, and C. M. Savage, *Phys. Rev. Lett.*, 8, 21 (1962).
- [13] G. D. Boyd, H. Kasper, and J. H. McFee, *IEEE J. Quantum Electron. QE-7*, 563, (1971).
- [14] C. G. Bethea, *Appl. Opt.*, 14, 1447 (1975).
- [15] B. F. Levine, and C. G. Bethea, *J. Chem. Phys.*, 63, 2666 (1975).
- [16] J. L. Oudar, and D. S. Chemla, *J. Chem. Phys.*, 66, 2664 (1977).
- [17] D. A. Kleinman, *Phys. Rev.* 126, 1977 (1962).



92-18258

AD-P007 467



135

MULTIFUNCTIONAL MACROMOLECULES  
- SOME DEVICE OPTIONS



MICHAEL R. WORBOYS, MICHAEL S. GRIFFITH, NICHOLAS A. DAVIES  
GEC-Marconi Research Centre, West Hanningfield Road, Great Baddow, Chelmsford,  
Essex, CM2 8HN, UK.

#### ABSTRACT

Multifunctional macromolecules can, in principle, combine a number of active material functions such as optical nonlinearity and photoconductivity in one material. Multifunctionality may offer new options for device fabrication and implementation. However, in practice the implementation of a device which uses a range of material properties such as piezoelectricity and photoconductivity in a single layer of active material is some distance away. This is in part due to the difficulty of optimising a material simultaneously for two separate properties. Therefore the approach we have taken is to identify device configurations which rely on multilayers, each separate layer providing one of the active device functions. Initial results on the fabrication and characterisation of two such proof of principle devices, a light modulated deformable mirror and a light modulated electro-optic layer, are described.

#### INTRODUCTION

The use of polymeric materials in optical devices can lead to a simplification of the device fabrication requirements. In thin film optical devices the polishing of inorganic materials to obtain uniform layers of a few microns thickness is both time consuming and expensive. This is greatly simplified if polymer films are used as they can be prepared as large area thin film samples by spin coating (as used, for example, with photoresists). Polymers are available which exhibit active functions such as photoconduction, piezoelectricity and optical nonlinearity. The latter class of materials have experienced particularly rapid development in recent years, with the aim of exploiting the high optical nonlinearity exhibited by some organic molecules in device applications.

Recently, the feasibility of obtaining macromolecular materials which exhibit a range of active functions has been considered. An example of such a material is polyvinylidene difluoride (PVDF) which is both piezoelectric and pyroelectric. However, more complex multifunctional macromolecular materials are being considered which exhibit functions such as photoconduction and piezoelectricity. This paper describes our approach at GEC-Marconi on identifying devices to which the multifunctional macromolecular concept might be applied. Progress with the fabrication and characterisation of two proof-of-principle devices, a light modulated deformable mirror (LMDM) and a light modulated electro-optic layer, (LMEOL) are described. It is expected that these devices will help to suggest ways in which multifunctional macromolecules can be more fully utilised.

#### DEVICE OPTIONS

In selecting appropriate devices for study, the approach taken was to consider how a device might be fabricated with conventional components. Initially this could be achieved by considering multilayers, in which each layer provided a required device function, for example, polarisation, photoconduction, or electro-optic modulation. Such devices offer potential for the exploitation of multifunctionality in that two or more device functions might be combined in the one material so that fewer discrete layers would be required. However, it is not clear at this stage exactly how this might be achieved as, in many of the devices, successful operation requires that the function of one layer is used to control that of another. Using this approach, at least two active layers will always be required.

It is also important to consider the 'non-functional' physical properties of the various layers. For example, the electro-optic layer must be electro-optic but it must also have a good optical transparency. Likewise, the processability of a material is important if the functionality of the material is to be exploited in device applications. In terms of the devices considered here, processability could refer to the ability to prepare large area films of a controlled uniformity and thickness.

An alternative approach to multifunctionality is to incorporate all the required multifunctionality in a single layer. In principle, this can be achieved by including functions like those of our multilayers within one molecule. For example by bonding both NLO moieties and photoconducting groups to the same backbone.

Both of the proof-of-principle devices selected for study were through plane 2D optical devices, namely (i) a light modulated deformable mirror (LMDM) and (ii) a light modulated electro-optic layer (LMEOL). Although the basic operation performed by each of the devices is simple, each is capable of use in more complex device designs for a range of advanced applications.

#### LIGHT MODULATED DEFORMABLE MIRROR

A schematic diagram of the light modulated deformable mirror (LMDM) is shown in Figure 1. It should be noted that this is just one example of this class of device, in other types the glass support need not be used and the active layers could be either sufficiently thick to be self supporting or a thin membrane stretched over an aperture. Deformable mirrors have been widely discussed in the literature but these have all been either mechanically or electrically addressed. The operation of this optically addressed device is simple in principle. A voltage is applied across both the photoconductor and the piezoelectric layer. With no light incident on the photoconductor its impedance remains high and very little voltage is applied to the piezoelectric layer. At higher incident light intensities the impedance of the photoconductor is reduced so that more of the voltage falls over the piezoelectric layer. This results in the piezoelectric layer deforming, the magnitude of the deformation being proportional to the incident light intensity.

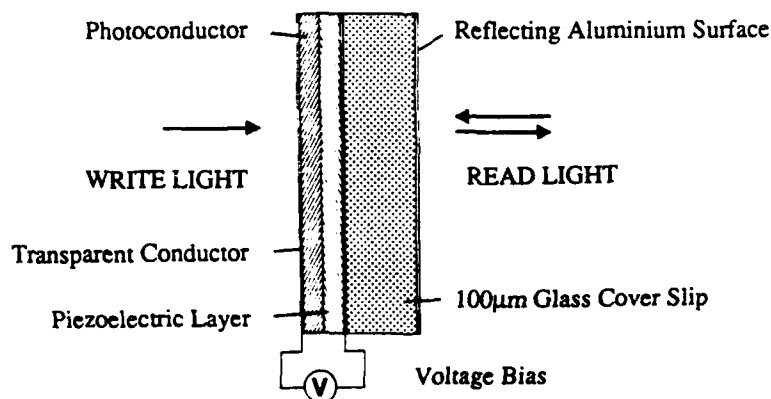


Figure 1: The Light Modulated Deformable Mirror

### Materials Characterisation

Poly vinyl carbazole (PVK) doped with 5% trinitro fluorenone (TNF) was chosen as the photoconductor in the LMDM. There were a number of reasons for this. Firstly, it enabled the LMDM to be constructed entirely with active layers which were macromolecular in character. Secondly, the polymer has a higher dark resistivity than that of a semiconductor so that impedance matching to the piezo polymer could be achieved.

A single layer of PVK-TNF (5%) was used to determine the response characteristics of the photoconductor. This was prepared by dip coating the polymer onto ITO glass. A top electrode of evaporated gold was deposited on the surface of the PVK-TNF, with an active area of  $2.0\text{ cm}^2$ . Response times were measured for rise times on illumination ( $5\text{ mW.cm}^{-2}$ ) and fall times when the illumination was removed. The rise and fall times, as determined by the voltage dropped across a resistor ( $2\text{ M}\Omega$ ) in series with the photoconductor, were recorded on a digital storage scope for analysis. No measurable change in response speed was observed on replacing the  $2\text{ M}\Omega$  resistor with a  $15\text{ k}\Omega$  resistor.

The times taken for the photoconductor to come to equilibrium were quite long. Table I summarises the results for both a positive and a negative bias voltage of  $100\text{ V}$ . The times are given for the signal to rise from 0% to 90% and from 0% to 64% ( $\tau$ ) of the equilibrium illuminated state value and for the signal to fall from 100% to 10% and from 100% to 36% ( $\tau$ ) of the equilibrium light state value (i.e. return to the dark state).

Table I: Response Measurements of Single Layer PVK-TNF (5%)

Applied Voltage	Rise time (secs)		Fall time (secs)	
	0-90%	0-64% ( $\tau$ )	100-10%	100-36% ( $\tau$ )
+100 V	150	1.65	390	23
-100 V	150	2.5	420	45

As can be seen, the response times are very slow and would limit the range of possible applications for a device. Typical values for carrier mobilities in PVK are  $10^4\text{ cm}^2.\text{V}^{-1}.\text{s}^{-1}$  for holes (majority carriers) and  $10^9\text{ cm}^2.\text{V}^{-1}.\text{s}^{-1}$  for electrons [1]. This compares with a mobility of  $10\text{ cm}^2.\text{V}^{-1}.\text{s}^{-1}$  for electrons in amorphous silicon. However, the low carrier mobility in the PVK system is not the limiting factor on the response time. Instead this is believed to result from charge trapping in the polymer which causes dispersive transport. This effect is notably worse in systems which have only a low doping level, as was required here to achieve impedance matching to the PVDF.

The piezoelectric polymer used in the construction of the LMDM was poly vinylidene difluoride. The film ( $9\text{ }\mu\text{m}$  thick) was used as supplied (Kynar) and had a quoted piezoelectric constant  $d_{31}$  of  $25\text{ pm.V}^{-1}$ .

### Fabrication of Light Modulated Deformable Mirror

The structure of the LMDM is shown in Figure 1. An aluminium layer was evaporated onto a  $100\text{ }\mu\text{m}$  thick glass slide to provide the mirror surface. The PVDF film (coated on one side with aluminium) was bonded to the other face of the glass slide and a layer of photoconductor dip-coated onto the surface. A semitransparent film of gold was evaporated over the photoconductor to form the top electrode. Finally, electrical connections were made to the piezo film electrode and the semitransparent gold electrode.

### Measurement of LMDM Deformation

To characterise the optical modulation of the mirror, the device was incorporated into a Michelson interferometer (Figure 2). Although the surface of the glass cover slip was not optically flat it formed a good reflecting surface and a clear interference pattern could be formed. The movement of the centre of the fringe pattern was monitored using a photodetector. Thus, as the mirror moved, the fringe pattern alternated between light and dark and this was recorded on a digital storage oscilloscope.

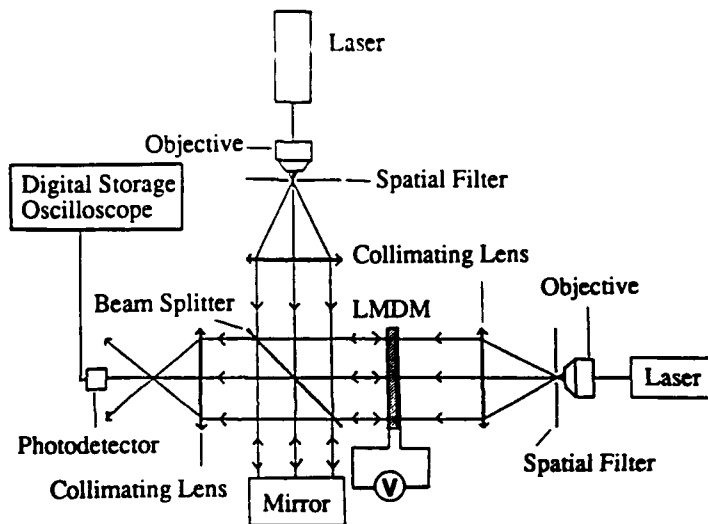


Figure 2: Optical Arrangement used to Measure the LMDM Response

Measurement of the mirror deformation was achieved as follows. With the write light off, 100 Volts was applied to the device. This resulted in some deformation of the device, the magnitude of which was monitored by measuring the number of fringes passing a photodetector. The photoconductor was then illuminated with a uniform write-light beam of  $\sim 5\text{mW.cm}^2$  and the additional deformation of the mirror determined by noting the fringe movement as before. The measurement wavelength was 633 nm and one fringe represents  $\lambda/2$ . Typical results for two different mirrors are given in Table II.

Table II: Number of Fringes of Movement Observed as a Result of Applied Field and Illumination

	Mirror 1	Mirror 2
100 volts bias voltage (no illumination)	7	10
Full write light (with voltage applied)	14	20
Available modulation	7	10

The available modulation exhibited by the two mirrors with the write light on and the write light off was found to be seven and ten fringes respectively. As can be seen, the mirror deformed when a voltage was applied with no write light. Ideally, this should not occur and indicates that the impedance of the photopolymer was not sufficiently high in the dark state so that when the voltage was applied a significant portion fell across the piezo polymer.

The magnitude of the mirror deformation was found to be dependent on the intensity of the incident write beam. This is shown in Figure 3 where the deformation of the mirror as a function of write light intensity is shown. It can be seen that the mirror is most sensitive to low light intensities ( $< 50 \mu\text{W.cm}^{-2}$ ). This is a direct result of the impedance matching of the photoconductor in the dark state to the piezopolymer. At low light intensities the impedance of the photoconductor rapidly falls to a value below that of the piezopolymer. In principle it is possible to change the sensitivity of the device by appropriate choice of impedance for each of the layers.

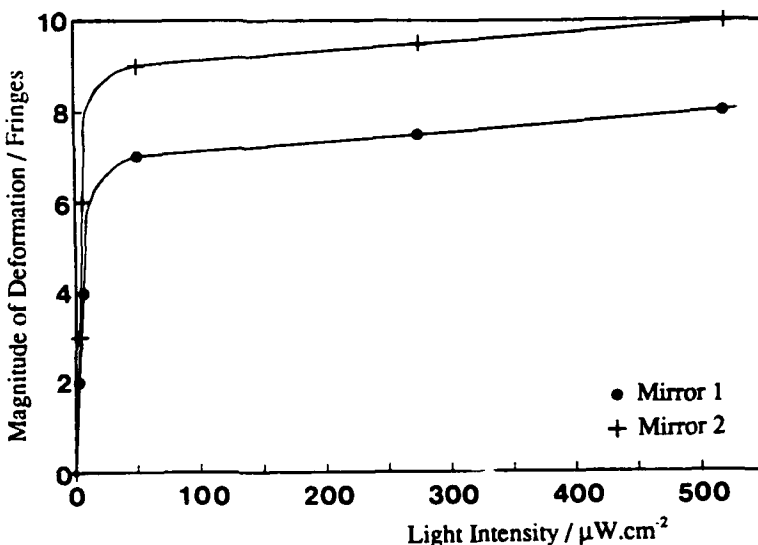


Figure 3: Variation of LMDM Deformation with Write Beam Intensity

#### Response Time

The response time of the LMDM is governed by three main factors; the mechanical response, the photoconductor response and the RC time response. The contributions of each of these is considered below.

If there were no limitations from any other aspects of the device, the maximum controllable frequency of operation would be limited by the mechanical response of the mirror. For a plate supported only at one end, as used here, the angular frequency of the resonant mechanical response is given by [2];

$$\omega_o = 2\pi f_o = \frac{1.015h}{l^2} \sqrt{\frac{Y}{\rho}} \quad \dots (1)$$

where  $h$  is the total thickness,  $l$  is the active length,  $Y$  is Youngs modulus and  $\rho$  is the material density. Since the thickness of the glass is very much greater than that of the PVDF or PVK and the Youngs modulus of the glass is greater than that of the PVDF or PVK, then the resonance can be estimated from the glass cover slip parameters alone. Using  $h = 100 \mu\text{m}$ ,  $Y = 6.6 \times 10^{10} \text{ N.m}^{-2}$ ,  $l = 3 \times 10^{-2} \text{ m}$  and  $\rho = 2.5 \text{ g.cm}^{-3}$ , a value of  $1/f_o$  of 0.35 ms is obtained as the mechanical response time for the device.

The response time of the PVK-TNF photoconductor was experimentally determined above. The main influence on the response speed is the carrier mobility and the charge trapping which occurs in the photopolymer.

The electrical switching time of the mirror can be modelled as an ac equivalent circuit, the characteristic response time  $\tau$  of which is given by

$$\tau = \frac{(C_1 + C_2)R_1R_2}{R_1 + R_2} \quad \dots \dots (2)$$

where  $C_1$  and  $C_2$  are respectively the PVK-TNF and the PVDF layer capacitances and  $R_1$  and  $R_2$  are respectively the PVK-TNF light or dark resistance and the PVDF layer resistance. Substituting suitable values for these parameters yields  $\tau_{\text{ON}} \sim 0.9$  sec and  $\tau_{\text{OFF}} \sim 185$  sec.

The deformation time of a LMDM was experimentally determined using the interferometric method described in Section 4.3. The response of the mirror to the write beam being turned on and then off is shown in Figure 4. Values of  $\tau$  were obtained from these graphs and these are compared in Table III with the response times calculated from each contributing source. It was not possible to extract the times for 0-90% rise and 100-10% fall from the graphs in Figure 4 as the signals at these long times became lost in noise.

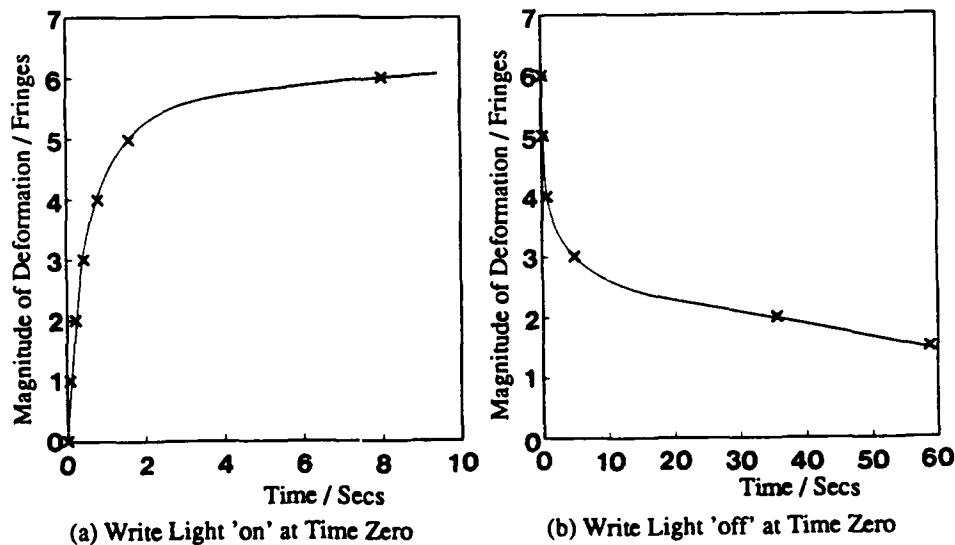


Figure 4: Time Response of LMDM with (a) Write Light Turned 'on' at Time Zero, and (b) Write Light Turned 'off' at Time Zero

Table III: Summary of Time Response for LMDM

Response	Time on (Seconds)		Time off (Seconds)	
	0-90%	0-64% ( $\tau$ )	100-10%	100-36% ( $\tau$ )
Experimentally measured		0.75		25
Photoconductor limit	150	1.65/2.5	390/420	23/45
Mechanical limit		$3.5 \times 10^{-4}$		$3.5 \times 10^{-4}$
R.C. limit		0.9		183

The values in Table III, although widely varying in magnitude, can be compared to gain information on the origin of the limiting time response of the LMDM. From the table, the  $\tau_{ON}$  would appear to be limited by the photoconductor and the  $\tau_{OFF}$  by RC response. However, this approach is somewhat naive and other factors must be considered. The experimentally measured value of  $\tau_{ON}$  is less than the value of  $\tau_{ON}$  derived for both the RC and photoconductor responses. This is because the impedance of the photoconductor in the light state  $R_L$  is very much less than the impedance of the piezofilm  $R_{PF}$ . With an incident light pulse, the decrease in the impedance of the photoconductor from its dark state  $R_D$  to a value such that ~99% of the voltage is applied across the piezofilm takes only ~0.1 sec. After this point, the continued fall in impedance of the photopolymer to its value  $R_L$  does not significantly increase the voltage applied across the piezofilm. The measured  $\tau_{ON}$  is therefore limited by the RC response of the device.

From the table, the limiting time response for achieving the 'off' state would appear to result from the RC response of the mirror. However, the value of  $\tau_{OFF} \sim 183$  seconds which was calculated assumed that the change in resistance of the photoconductor from  $R_D$  to  $R_L$  upon illumination was instantaneous. Since the value of the photoconductor impedance changes relatively slowly the calculation of an RC time constant is not strictly valid as it assumes a constant impedance. It can be shown that at any point on the photoconductor impedance curve the RC time constant is significantly less than the time it has taken for the photoconductor impedance to reach that point. Therefore, it can be seen that  $\tau_{OFF}$  is limited by the photoconductor response.

#### LIGHT MODULATED ELECTRO-OPTIC LAYER

The electro-optic dual layer is at an early stage of fabrication as a proof-of-principle device. A schematic diagram of the device is shown in Figure 5. The device consists of an electro-optic layer and a photoconductor which are separated by a light blocking conducting layer. A voltage bias is applied across the whole device. The impedance of the photoconductor in the dark state is greater than that of the electro-optic layer and so most of the applied potential falls across the photoconductor. On illumination, the impedance of the photoconductor becomes lower than that of the electro-optic layer and so most of the potential falls across the electro-optic layer, resulting in a change in the birefringence or phase retardation. Thus in principle the operation of the dual layer is simple. However, if the optimum operating conditions are to be achieved, the correct impedance matching of the photoconductor and electro-optic layer is essential.

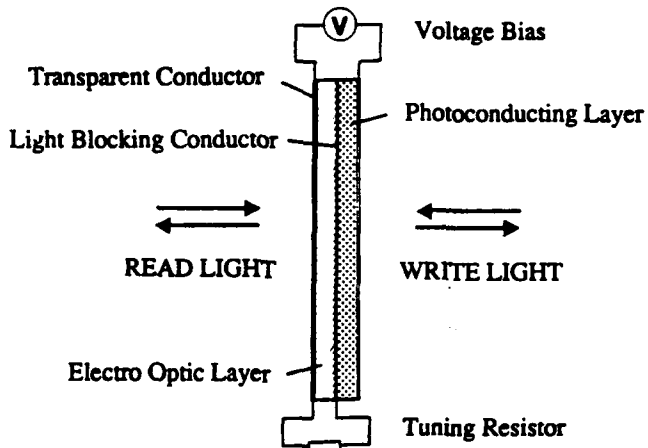


Figure 5: Light Modulated Electro-Optic Layer

To aid in the impedance matching of the two layers, a tuning resistor can be placed in parallel with the electro-optic layer. This tuning resistor is necessary because the impedance of the electro-optic layer  $R_{EO}$  is very much greater than either the light or dark impedance ( $R_L$  and  $R_D$  respectively) of the photoconductor used. Although the impedance of PVK doped with 5% TNF would have an impedance similar to that of the electro-optic layer, the slow response time would make the operation of the device too slow to characterise using the required lock-in amplifier.

The value of the tuning resistor  $R_T$  is chosen so as to obtain the maximum voltage swing across the EO layer. The optimum impedance  $R_Z$  for the parallel combination of the electro-optic layer and tuning resistor is given by

$$R_Z = R_L R_D \quad \dots \dots (3)$$

In practice,  $R_{EO} \gg R_L, R_D$ , and the value of  $R_Z$  will effectively be equivalent to the value of the tuning resistor,  $R_T$ .

#### Materials Characterisation

Poly vinyl carbazole doped with an equal proportion of TNF was used as the photoconductor. The response times of this material were fully characterised using the methods previously described for the LMDM.

The electro-optic polymer was a 50:50 side chain copolymer of methyl methacrylate and an electro-optic monomer. The co-monomer had an oxy nitro stilbene attached to the methacrylate backbone via a three carbon flexible spacer linkage. Films of this polymer were prepared by spin coating onto an ITO coated substrate. The solvent was removed by vacuum baking at 165°C for ~ 16 hours. Films were typically ~ 3  $\mu\text{m}$  in thickness. Previous experimentation had shown that the maximum electro-optic coefficient was obtained by poling the polymer at ~ 20°C below its glass transition temperature (117°C). Using a poling field of 140 V  $\mu\text{m}^{-1}$  a value of  $r_{33}$  of ~ 10 pm.V $^{-1}$  was obtained.

The technique used to measure the electro-optic coefficient is based on the fact that the birefringence of the polymer can be changed by applying a voltage. The optical arrangement used is shown in Figure 6. A square wave generator is used to modulate the birefringence of the polymer. This results in a modulation of the light passing through the analyser and arriving at the photodetector. The signal from the photodetector is measured using a lock-in amplifier whose reference signal is obtained from the square wave generator. A Soleil-Babinet compensator is used to ensure that light emerging from the sample is circularly polarised. Using this configuration maximises the change in transmission for a given change in birefringence.

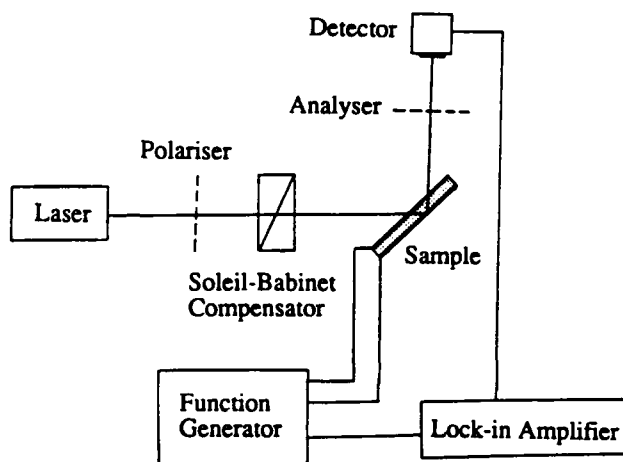


Figure 6: Optical Arrangement Used for Measuring Electro-Optic Coefficients

#### Fabrication of Light Modulated Electro-Optic Layer

The structure of the light modulated electro-optic layer is shown in Figure 5. A  $3\text{ }\mu\text{m}$  electro-optic layer was spin coated onto a glass substrate with appropriately patterned ITO electrodes. A thin layer of chrome-gold was thermally deposited onto the top surface of the polymer and the polymer poled at  $115^\circ\text{C}$  using a poling field of  $100\text{ V.}\mu\text{m}^{-1}$ . An electro-optic coefficient of  $4.6\text{ pm.}\text{V}^{-1}$  was measured. A layer of PVK : TNF (1:1) was dipcoated over the chrome-gold electrode and a further layer of chrome-gold was thermally deposited onto the PVK : TNF surface. Electrical contact was made to each of the three electrodes. It should be noted that, in the configuration used here, the light modulated electro-optic layer is essentially a single pixel device.

#### Characterisation of the Light Modulated Electro-Optic Layer

The characterisation of the light modulated electro-optic layer was undertaken using the optical arrangement shown in Figure 7. The device was operated at 3.6, 4.2 and 5 Hz with a bias voltage of 100 V and a tuning resistor of  $70\text{ M}\Omega$  in parallel with the electro-optic layer. The response of the electro-optic layer to the modulated write light incident on the photoconductor was measured using a lock-in amplifier.

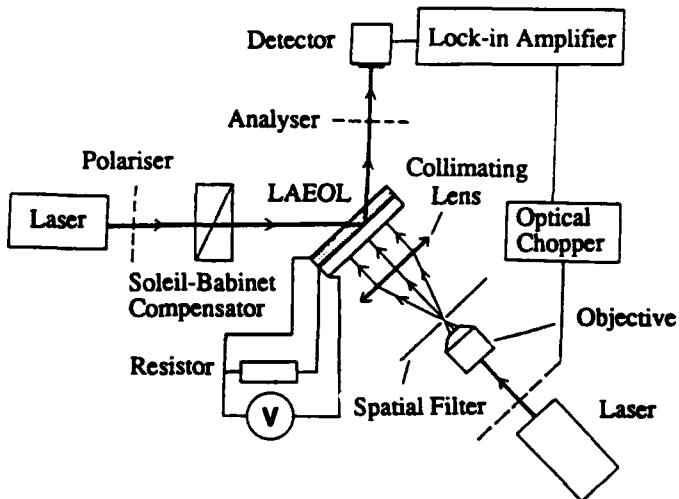


Figure 7: Optical Arrangement Used to Measure the Response of the Light Modulated Electro-Optic Layer

It should be noted that the device was fabricated purely as a proof-of-principle and at this stage the factor limiting the time response of the device are still under consideration. Among these factors are the speed of response of the photoconductor (which determines rate of bias voltage transfer), the value of the tuning resistor (which determines impedance matching of the layers) and the RC time constant for the two layers. It has also been found that the impedance of the photoconductor is field dependent. Using the previously determined value of  $r_{33}$  for the electro-optic layer and the measured response of the electro-optic layer in the device, it was possible to calculate the actual voltage swing which was occurring across the electro-optic layer and this is shown in Figure 8.

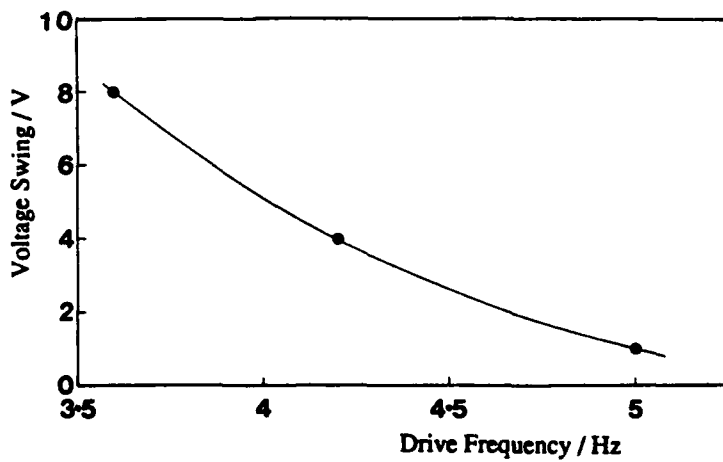


Figure 8: Response of the Electro-Optic Dual Layer

## DISCUSSION

The proof-of-principle devices fabricated here have used the materials currently available. It is clear that whilst large improvements in device performance can be envisaged, the realisation of these depends critically on the availability of improved materials. In particular, our work has highlighted the limitations imposed on device efficiency by the current generation of polymer photoconductors. Clearly photopolymers with faster responses are required. In particular, the recovery speed to the dark resistance after illumination would limit the use of a device containing a polymer photoconductor to applications in which fast signal correction was not required. For example, correction of aberrations due to thermal effects can be envisaged.

The experimental performance of the LMDM has been analysed in some detail. It was found that the turn-on speed was limited by the RC response whilst the turn-off speed was limited by the response of the photoconductor. It is clear that in multilayer devices the large d.c. resistivities of polymers can result in large RC time constants. The type of response exhibited by the LMDM, where the turn-on and turn-off speeds are significantly different, will restrict the use of the device to systems in which the signal is changing relatively slowly.

An initial assessment of the light modulated electro-optic layer has been made. Clearly the device was not fully optimised and had a very slow response time because the impedance of the photoconductor was very high. Ways in which the response time can be improved are currently under study. All the characterisation of the electro-optic polymer used in this work has required the use of a lock-in amplifier to observe optical modulation. This increases experimental complexity and again limits the use of these materials in practical devices. It is clear that the search for polymers with higher electro-optic coefficients must be continued if credibility in these materials is to be maintained.

Whilst improvements to currently available materials such as electro-optic polymers and photopolymers can be identified, there may also be possibilities for designing organic materials with 'new' properties. For example, there appear to be no transparent organic conductors. The organic equivalent of ITO would open up new possibilities in device design in that multilayer stacks with electrodes between could be fabricated. Advantages such as matched expansion coefficients between layers and compatible fabrication techniques would be expected from the use of such a material.

## CONCLUSIONS

We have successfully fabricated and demonstrated a proof-of-principle light modulated deformable mirror and a light modulated electro-optic layer. Both the control and active functions in these devices were achieved using macromolecular layers, in keeping with our stated approach to achieving multifunctionality. Work is continuing to improve the response time and efficiency of these devices.

Fabrication of these proof-of-principle devices has demonstrated the potential of macromolecules for use in novel devices. However, it has also highlighted some of the improvements required to current generation materials if practical devices are to be realised. The use of truly multifunctional materials, for example, materials in which a photoconductivity property is combined with either a piezo electric or an electro-optic response, has yet to be addressed. This remains a challenge to be met in the future by both materials scientists and device engineers.

## REFERENCES

- [1] *Electronic Properties of Polymers*, edited by J. Mort and G. Pfister (J. Wiley and Sons Publishers, New York, 1982), p. 224.
- [2] M. Toda and S. Osaka, *Trans IECE of Japan*, E61 (7), 507 (1978).

#### ACKNOWLEDGEMENTS

This work was funded by SDIO/IST through AFOSR under subcontract from the Hoechst Celanese Corporation (F49620-87-C-0109). The support and direction given to the programme by Dr. D. Ulrich is gratefully acknowledged. The electro-optic polymer used in this work was supplied by the Hoechst Celanese Corporation.



---

---

**PART III**

---

**Multifunctional  
Inorganic Materials**

92-18259



AD-P007 468

49



## MULTIFUNCTIONAL CERAMIC MATERIALS--REVIEW AND PROJECTIONS

JOHN D. MACKENZIE

University of California, Department of Materials Science and Engineering,  
Los Angeles, CA 90024-1595

### ABSTRACT

Multifunctional engineering systems made up of different material components each providing primarily a single function are well known. Frequently, even for a monofunctional application, the material component must already have an optimum set of secondary properties to fulfill that function. It would be desirable to have multifunctional material components. In this paper some known multifunctional ceramic materials, mainly crystalline and glassy oxide systems, are reviewed. These are conveniently divided into molecular, ultrastructural and integrated materials systems. Projections are made regarding the future developments of multifunctional ceramics as well as nanocomposites with both inorganic and organic components based on the sol-gel technique.

### INTRODUCTION

The function of an engineering material such as a polymer, a metal or a ceramic, can be defined as the specific purpose for which that material is used in an application. Frequently, an engineering material is only functional not because of one specific primary property alone but because of a number of other secondary properties as well. Buckley, et al., for instance, considered that specific functional polymeric materials can be prepared by the attachment of active side-chains to a polymer backbone [1]. One example given was the "Side-Chain Liquid Crystal Polymers" for nonlinear optical (NLO) applications. The logic is that although many organic crystals have desirable NLO activity, they lack acceptable mechanical properties and are difficult for fabrication into various shapes. The attachment of the NLO group to a stable and easily fabricable polymeric host would lead to a "functional" polymer. Other specific functional polymers mentioned were the electronically conductive polymers and the piezoelectric polymers. Since these individual functionalities are readily achieved, it should be possible to incorporate two or more functionalities into one macromolecular structure. This can be achieved by attaching the different side-chains onto one polymer backbone or by the blending of two functional polymers. If the primary property of each of these side-chains is utilized in the same device, then an useful "multifunctional" material will have been developed. Further, through the interactions between the different side-chains, new and useful properties may result.

The superficial reaction to the innovative concept of Buckley, et al is whether multifunctional ceramic materials can be developed with the same approach. Ceramics, be they crystalline or glassy, are principally ionic oxides. One is primarily concerned with ions and their coordinations rather than polymer backbones and side-chains. The processing of ceramics and polymers is also markedly different. Thus, the initial reaction is that the preparation of multifunctional ceramics are perhaps unachievable. However, further considerations reveal that not only are multifunctional ceramics possible but that many have already been prepared. The objectives of this paper are to present a review on some of these multifunctional ceramics, especially oxides, and to offer some suggestions for future developments. This review is mainly concerned with optical and electrical properties.

### FUNCTIONAL ENTITIES IN CERAMICS

Perhaps the most common and oldest example of a functional ceramic is a silicate glass. A silicate glass is easily fabricable into various shapes, mechanically strong and environmentally stable. It is thus an analogue of Buckley's organic polymer. It functions as a window material because of the above-mentioned secondary properties and its primary property of optical transparency. Here, the structure of the rigid liquid with its absence of porosity and grain-

boundaries can perhaps be considered as the cause of its transparency and hence a functionality. However, even if optical transparency is included as a secondary property, then the selective absorption of visible light because of the presence of certain transition metal ions as part of the glassy network must be accepted as a functionality of the silicate glass. The transition metal ions such as  $\text{Fe}^{2+}$ ,  $\text{Fe}^{3+}$ ,  $\text{Mn}^{2+}$ ,  $\text{Co}^{2+}$ , etc. are now analogues of Buckley's side-chains. Similar to transition and rare-earth metal ions, defects in oxide structures such as ionic vacancies are well-known to induce optical absorption in oxides. They too are therefore functionalities. A ferroelectric ceramic such as  $\text{BaTiO}_3$  is spontaneously polarized because of the cooperative alignment of dipoles due to the off-set of the  $\text{Ti}^{4+}$  ions in the octahedral hole formed by six oxygen ions. The assembly of oriented dipoles in a ferroelectric domain can thus be considered as a functionality of the  $\text{BaTiO}_3$  crystal. Ions, defects and cation-anion assemblies, the analogues of side-chains in organic polymers can be considered as "molecular" functionalities. The simultaneous presence of such molecular functionalities in a ceramic crystal or glass can lead to a multifunctional ceramic. In addition to molecular functionalities, the presence of microcrystalline second phases in a ceramic matrix can constitute another type of functionality. One such example is silver chloride microcrystals with dimensions of less than  $200\text{\AA}$  within a silicate glass matrix. They cause phototropic behavior. These are arbitrarily termed "ultrastructure" functionalities. Examples of some of these ceramic materials are now presented.

#### MOLECULAR MULTIFUNCTIONAL CERAMICS

Some examples of molecular multifunctional ceramics are presented in Table I. The most common examples are those in which the functional entities are both ions.

##### a. Energy transfer between ions

The phenomena of fluorescence quenching in silicate glasses are well known [2]. Energy absorbed by a  $\text{Mn}^{2+}$  ion, for instance, is transferred to a  $\text{Fe}^{3+}$ . This negative effect is rendered into good use in the development of phosphors. Thus  $\text{Sb}^{3+}$  ion in a  $3\text{Ca}_3(\text{PO}_4)_2\text{-CaF}_2$  host enhances the absorption of UV radiation and efficient emission in the blue part of the spectrum is achieved through energy transfer between the  $\text{Sb}^{3+}$  and the  $\text{Mn}^{2+}$  [3]. Another example is the energy transfer from  $\text{Ce}^{3+}$  to  $\text{Nd}^{3+}$  ions in a single crystal of  $\beta$ -alumina [4]. The role of the  $\text{Ce}^{3+}$  ion is to absorb pumping radiation. The role of the  $\text{Nd}^{3+}$  ion is to produce stimulated emission. Such energy transfer between ions has been used to increase the absorption cross-section of laser materials containing weakly absorbing trivalent lanthanide ions [5]. Similarly, energy transfer from  $\text{Mn}^{2+}$  ion to  $\text{Nd}^{3+}$  ion in a fluoride glass was recently reported by Reisfeld [6]. At low concentration of Nd, the Mn serves as an efficient storage of energy which results in a significant lengthening of the lifetime of the Nd ion.

##### b. Superionic Conducting and laser-active oxide

$\beta$ -alumina crystals containing  $\text{Na}^+$  are well-known superionic conductors.  $\beta''$ -aluminas containing rare earth ions such as  $\text{Nd}^{3+}$  are laser materials [7]. The two structures can be combined to produce single  $\beta$ -magnetoplumbite crystals which contain both superionic conducting  $\text{Na}^+$  ions as well as lasing  $\text{Nd}^{3+}$  ions [8]. These crystals are truly multifunctional ceramics although their applications are still unclear at present.

TABLE I. Examples of Molecular Multifunctional Ceramics

No.	Functionality		Host	Interactions/ Applications	Ref
	A	B			
1	Ion A (Sb <sup>3+</sup> )	Ion B (Mn <sup>2+</sup> )	Halophosphate	Energy transfer phosphors	3
2	Ion A (Ce <sup>3+</sup> )	Ion B (Nd <sup>3+</sup> )	$\beta$ -Alumina	Energy transfer, lasers	4
3	Ion A (Mn <sup>3+</sup> )	Ion B (Nd <sup>3+</sup> )	Fluoride glass	Energy transfer, lasers	6
4	Ion A (Na <sup>+</sup> )	Ion B (Nd <sup>3+</sup> )	$\beta$ -Magneto-plumbite	Superionic cond., lasers	8
5	Ion A (Cu <sup>+</sup> )	Ferroelectric B	Sr <sub>0.5</sub> Ba <sub>0.5</sub> Nb <sub>2</sub> O <sub>6</sub>	Photorefractivity	9
6	Ion A (Sm <sup>3+</sup> )	Ferroelectric B	BaTiO <sub>3</sub>	Ferroelectric grain boundary, PTC	13
7	Defect A	Gradient Index B	SiO <sub>2</sub> fiber	Frequency doubling	18
8	Ferromag. A	Ferroelectric B	BTF 2	Magnetoelectric effect	20

c. Photorefraction [9]

The origin of ferroelectricity in oxides such as BaTiO<sub>3</sub> and Sr<sub>0.5</sub>Ba<sub>0.5</sub>Nb<sub>2</sub>O<sub>6</sub> (SBN) is well-understood. Here, the off-set of the Ti<sup>4+</sup> or Nb<sup>5+</sup> ions in the octahedral holes of the oxygen polyhedra results in electric dipoles. Spontaneous polarization occurs when these dipoles are cooperatively aligned to give domains. A ferroelectric oxide can be considered as a functional ceramic. The oxide can also be doped to cause photoconductivity. Thus, if Cu<sup>+</sup> ions are present in the lattice, electrons are generated by the reaction:



If a transparent doped ferroelectric crystal is first masked and external radiation is incident perpendicular to the optic axis, photoelectrons generated in the exposed regions will tend to migrate towards the unexposed regions. A schematic representation of this effect is shown in Fig. 1. This results in a change in refractive index  $\Delta n$  such that [10]

$$\Delta n = (1/2)n_0^3 r_{\text{eff}} \delta E \quad (2)$$

where  $n_0$  is the original index,  
 $r_{\text{eff}}$  is the effective electro-optic coeff, and  
 $\delta E$  is the variation of the electric field.

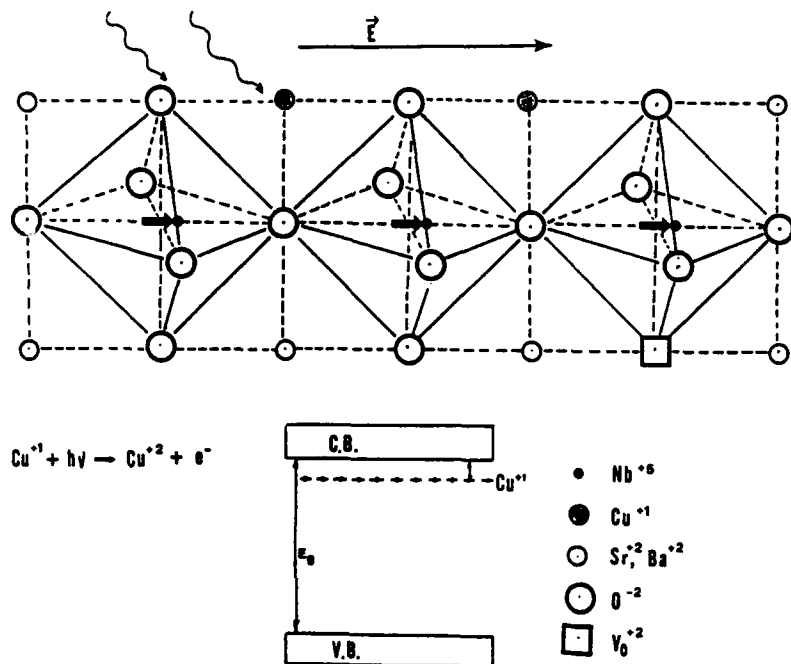


Fig. 1. Schematic representation of photorefractive effect in doped SBN ceramic.  $\vec{E}$  is the direction of the optic axis and the thick arrows within the distorted octahedra represent the oriented dipoles.

The photoconductive ceramic can also be separately considered as a functional material. The combination of ferroelectricity and photoconductivity in a doped ferroelectric thus results in a multifunctional ceramic. The applications of such photorefractive ceramic single crystals as display and memory devices have been demonstrated by Xu Yuhan [11]. Recently, the successful preparation of transparent SBN and PZT thin films on glass substrates by the sol-gel method in the author's laboratory should enhance the application of photorefractivity and extend its use to large flat display systems [12]. The ferroelectric behavior of such a transparent SBN film is shown in Fig. 2.

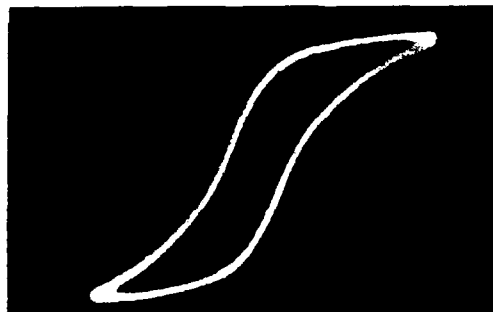


Fig. 2 P-E hysteresis loop of transparent SBN thin film of  $0.8 \mu\text{m}$  thickness on silica glass substrate prepared by sol-gel method [12].

d. The PTC Effect:

Ferroelectrics such as  $\text{BaTiO}_3$  are normally very good electrical insulators. The incorporation of small amounts of dopants such as rare-earth ions can cause a large increase of electrical conductivity. For instance, if  $\text{Sm}^{3+}$  ions are placed in  $\text{Ba}^{2+}$  positions in the lattice, the material now becomes  $\text{Ba}_{2-x} \text{Sm}^{3+} (\text{Ti}^{4+}_{1-x} \text{Ti}^{3+}_x) \text{O}_3$ . Electronic hopping conduction can take place between the  $\text{Ti}^{3+}$  and  $\text{Ti}^{4+}$  ions. This semiconducting ferroelectric can now be considered as a functional ceramic. Many rare earth and other ions have been used as dopants. When the electrical resistivity of these doped polycrystalline ceramics was measured, very large increases of the resistivity was observed at or near the Curie temperature,  $T_c$ , as exemplified by a  $\text{Sm}^{3+}$  doped sample of  $\text{BaTiO}_3$  in Fig. 3 [13]. This is known as the "PTC" effect and has been widely applied in electrical switching devices. Some dopants such as  $\text{Mn}^{2+}$  can produce a resistivity increase at  $T_c$  of more than six orders of magnitude [14]. The most interesting discovery was that the PTC effect was absent in doped single crystals of ferroelectrics as shown in Fig. 3 [15]. The grain boundary of the doped ferroelectric single crystal grains can now be considered as another functionality. The PTC polycrystalline ferroelectric semiconductor is thus a multifunctional ceramic.

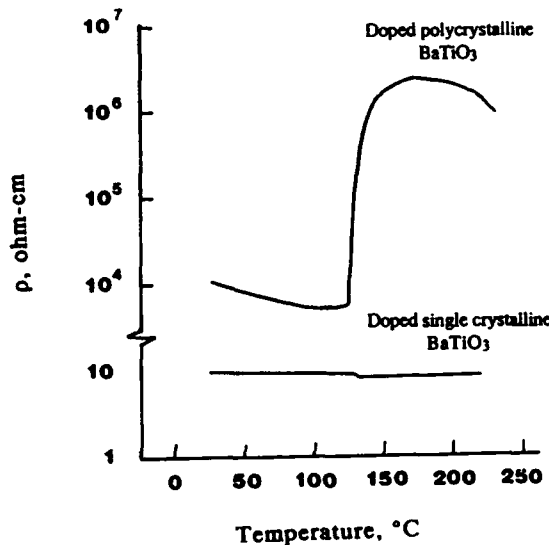


Fig. 3 Electrical resistivity of single crystal and polycrystalline  $\text{Ba}_{0.9995} \text{Sm}_{0.0005} \text{TiO}_3$  [15].

e. Frequency doubling in doped silica optical fibers

High purity silica glass fibers with a refractive index gradient to confine and guide an incident ray over long distances are obviously a molecular functional ceramic since the core and the cladding are both silica with no phase boundary between them. The refractive index gradient is caused by the type or concentration of dopant ions in the glassy network. Because the silica glass is centrosymmetric all the second-order dipole nonlinear coefficients should be zero. Nevertheless, weak sum-frequency and second-harmonic generation were observed with a  $\text{GeO}_2$ -dope  $\text{SiO}_2$  fiber [16]. Later work was able to produce efficient frequency doubling in the conversion of the  $1.06 \mu\text{m}$  red light from a Nd:YAG laser into green light of  $0.53 \mu\text{m}$  with different commercially available Ge-doped silica fibers [17]. Green light was only observed after the fiber was steadily illuminated with the red light for periods in excess of an hour. More recently, second-harmonic green light was generated after only a few minutes of seeding with a  $0.53 \mu\text{m}$  harmonic light together with the  $1.06 \mu\text{m}$  radiation [18]. It has been postulated that photoinduced defects are responsible for second-harmonic generation [18]. These photoinduced defects in the Ge-doped silica glass can thus also be considered as another functionality of the material. A multifunctional material is thus fabricated by the creation of such defects within a waveguide having a refractive index gradient.

f. Magnetoelectric crystals

In the foregoing, a ferroelectric ceramic was considered to be a functional material. Similarly, one can also consider a ferromagnetic oxide to be another functional ceramic. A crystal exhibiting both ferroelectricity and ferromagnetism is thus a multifunctional solid. Many transition metal boracites,  $\text{Me}_3\text{B}_7\text{O}_{13}\text{X}$ , in which Me is a divalent 3d transition metal (Cr, Mn, Fe, Co, Ni and Cr), and X is Cl, Br or I, are apparently both ferroelectric as well as anti-ferromagnetic at temperatures well below  $20^\circ\text{C}$  [19]. The only exception within this group is the Ni-I-boracite which exhibits onsets of ferroelectricity as well as weak ferromagnetism at about  $60^\circ\text{K}$ . The compound  $\text{Bi}_2\text{Bi}_4\text{Fe}_2\text{Ti}_3\text{O}_{18}$  (known as BTF 2) is ferroelectric at temperatures below  $752^\circ\text{C}$  and is apparently weakly ferromagnetic at temperatures below about  $400^\circ\text{C}$  [20]. The coupling of these two properties gives rise to a magnetoelectric effect. Although the applications of magnetoelectric solids are not yet known, these multifunctional oxides are worthy of further research.

## ULTRASTRUCTURAL MULTIFUNCTIONAL CERAMICS

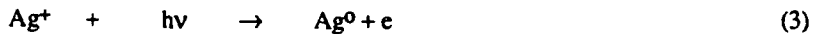
The term "ultrastructure" is presently interpreted to be applicable to solid phases with dimensions from ten to a few hundred Angstroms when such ultrafine particles are found within a matrix of much larger dimensions. Such two-phase or multiphase solids can be termed "nanocomposites." Many unusual and interesting properties can be derived via ultrastructural processing of ceramics [21]. In Table II, some examples of multifunctional ceramics prepared by ultrastructural processing are presented. In each of the four examples given, the very small dimension of one of the solid phases in the nanocomposite is the direct cause of an unusual property of the material. As such, it has created a functionality. It may also be the cause of another unrelated property of the composite and thus resulting in a multifunctional ceramic.

TABLE II. Examples of Ultrastructural Multifunctional Ceramics

No.	Functionality A	Functionality B	Host	Interactions/ Applications	Ref
1	AgCl	Opt. trans- parency	Silicate glass	Photochromism	22
2	CdS	Opt. trans- parency	Silicate glass	Quantum confinement NLO	25
3	Pb crystal- lites	Second elec. em.	Silicate glass	Light amplifn. MCP	26
4	Polymer filaments	Organic dye molecules	Silica gel	NLO prop. lasers	27

a. Photochromic glass

Photochromic materials change color on exposure to some radiation and revert to the original color when the incident radiation is removed or if they are irradiated with a radiation of different wavelength. Of these, perhaps the most interesting, and certainly most useful, are the photochromic silicate glasses containing microcrystallites of silver halides. An excellent review has been published by Araujo [22]. Briefly, when  $\text{Ag}^+$  and  $\text{Cl}^-$  ions are both present in some molten glass, controlled cooling and heat-treatment can lead to the formation of  $\text{AgCl}$  crystallites of about  $100\text{\AA}$  in dimensions. Qualitatively, darkening can be represented by the reactions



The colloidal silver  $(\text{Ag})_n$  is assumed to be the cause of darkening. The  $\text{Cl}_2$  molecules do not react with the silicate glass host at room temperature and its diffusion coefficient is extremely low. Thus on removal of the incident light, the reverse reactions occur to reform the  $\text{AgCl}$ . The presence of sensitizing agents such as  $\text{Cu}$  and  $\text{Cd}$  ions can have significant effects on the photochromic process. The small dimensions of the  $\text{AgCl}$  crystals within a silicate glass permits optical transparency for the composite. The  $\text{AgCl}$  dissociation within an inert and impermeable glassy matrix permits the reversibility of color. We can therefore consider such a photochromic glass to be a multifunctional solid since a lens, for example, can be reversibly darkened in sunlight and cleared in the shade.

b. Quantum confinement of CdS-CdSe crystals in glass

The preparation of colored silicate glasses containing ultrafine crystallites of  $\text{CdS}$  was first achieved more than a hundred years ago [2]. Orange and red glass filters containing  $\text{CdS}$  and  $\text{CdSe}$  crystallites have also been commercially available for many years. Recently, however, these glasses have received a great deal of new attention because of their nonlinear optical property [23,24]. Single crystals of  $\text{CdS}$  are known to have extremely high values of nonlinear refractive index at temperatures around  $2^\circ\text{K}$  and should be highly desirable as an

optical switching material but for the very low temperature necessary for their utility. Although the figure of merit,  $F$ , for nonlinear optical switching applications is given by

$$F = n_2/t\alpha \quad (6)$$

where  $n_2$  is the nonlinear index,  $t$  is the switch-off time and  $\alpha$  is the absorption coefficient, for practical applications, the temperature at which the nonlinear process operates is also important [25]. The bound exciton level in CdS responsible for its high nonlinear coefficient is saturated at around 2°K, but is annihilated at higher temperatures. As the size of the crystal decreases until it approaches that of the exciton dimension, the effect of "quantum confinement" occurs. Quantum confinement can be interpreted as a size-dependent change in the band structure of a crystal. Quantum confinement in extremely small crystallites of CdS should now permit the use of these semiconductor crystals as a NLO material at room temperature. Indeed, commercial CdS/CdSe glass filters were shown to have third-order susceptibilities at  $10^{-8} - 10^{-9}$  esu at ambient temperatures [23]. These very high values of  $x^{(3)}$  should now make the CdS-containing nanocomposites to have practical values. Similar to the logic developed for the photochromic glasses, these CdS-based glasses can be regarded as multifunctional ceramics.

c. Secondary electron emission from reduced lead silicate glasses [26]

When electrons of some energy  $E$  are allowed to impinge on a solid surface in a vacuum, secondary electrons may be generated. The yield of secondary electrons,  $d$  is given by

$$d = \int n(x) f(x) dx \quad (7)$$

where  $n(x)$  is the number of secondaries produced by one primary at a depth between  $x$  and  $x + dx$ , and  $f(x)$  is the probability that a secondary produced at  $x$  reaches the surface and is emitted. The yield is a function of  $E$  and the maximum yield  $d_{max}$  is a measure of the usefulness of the material. Lead silicate glasses can be partially reduced in  $H_2$  and rendered into a semiconducting material of high electrical resistivity. Conductivity occurs by electron migration between "strings" of loosely connected lead crystallites. Such reduced lead glasses in the form of small tubes are used in light amplification devices known as microchannel plates (MCP). A primary electron emitted from phosphor impinges on the inner surface of the tube and if  $d_{max}$  is 3, would generate 3 secondaries. If the two ends of the tube are subjected to an electric field, the secondaries would be propelled down the tube, each now in turn producing secondaries. The lead crystallites would replenish secondaries lost in the process. Thus one primary electron originating from a photon can produce a million electrons at the exit end of the tube which in turn would generate photons. Such lead glasses are thus multifunctional materials, with the lead crystallites in loose contact and its accompanying semiconduction as one functional entity and the secondary emitter of the glass surface as a second functionality. The material is indeed a nanocomposite.

d. Organic dyes in Silica/Polymer composites

The sol-gel technique has led to the preparation of many new materials with interesting properties. One such family of material is the transparent composites made by the impregnation of organic polymers into the micropores of silica gel [27]. The pore dimensions are typically around 100Å and the porosity can be controlled with wide limits. The refractive indices of the transparent composite can thus be controlled accurately through the porosity. The brittleness of the pure ceramic is lowered and the hardness of the pure polymer is increased. Such a nanocomposite is thus a functional material. In the gelation process of the silica, organic dye molecules with useful NLO properties can be added to the solution. After gelation, the dye molecules are trapped within the inert oxide cage. After impregnation with organic polymers, a "triphasic" nanocomposite is formed. A variety dyes have been entrapped this way [28]. The

protected NLO-active dye molecules in the oxide cage formed by the silica network constitutes another functionality. Another variant of the process is to disperse the dyes in the organic monomer prior to impregnation and polymerization. These organic-inorganic nanocomposites are truly new multifunctional materials although the word ceramics can no longer be applied.

### MULTIFUNCTIONAL INTEGRATED SYSTEMS

The physical combination of functional materials, for example by the vapor deposition of thin films on to a functional substrate can obviously create numerous multifunctional integrated systems. These would include such devices as electrochromic windows [29,30], thermochromic windows [31], and the so-called "Head-Up-Displays" (HUD) [32]. The latter is particularly interesting in that it uses sol-gel technology to deposit a high index film over a small selected area of an automobile window. This does not interfere with driving and yet permits the driver to follow the speed of the vehicle through green light reflected from the sol-gel derived film. Many of the afore-mentioned functional materials can be integrated into multifunctional integrated materials systems. A discussion of such new systems is beyond the scope of the present paper.

### PROJECTIONS

The above considerations are based on a somewhat new approach towards the recognition of functionalities in ceramic materials and how such functionalities are created via innovative processing methods. The adoption of such an approach will no doubt uncover many new functional ceramics and thus enable the preparation of new multifunctional ceramics. The combination of functional organic entities and functional ceramics will probably be a fruitful area of research in the near future. The use of the sol-gel technique to achieve such goals has already been discussed above. Another obvious approach is through intercalation [33]. The modified sol-gel process to prepare "ceramers" or "ormosils" (organically modified silicates) through the chemical combination of organic and inorganic groups is another promising approach to new multifunctional materials [34].

### ACKNOWLEDGEMENTS

I am much grateful to the Directorate of Chemical and Atmospheric Sciences, Air Force Office of Scientific Research, for the support of this work. I am particularly grateful to Dr. D.R. Ulrich and Dr. G. Gallagher-Daggitt for offering me the challenge to prepare this publication. This paper could not have been written without the many helpful discussions I have had with Professor Xu Yuhan and the assistance of my students C.J. Chen, Ren Xu and Haixing Zheng.

### REFERENCES

1. A. Buckley, G.W. Calundann, J.A. East, Proc. SPIE, 878, 94 (1988).
2. W.A. Weyl, Coloured Glasses, (The Society of Glass Technology, Sheffield, England, 1950), pp. 440-452.
3. C.G.A. Hill, Chem. in Brit. Sept. 723 (1983).
4. L.A. Momoda, J.D. Barrie, B. Dunn, Mat. Res. Bull. 24, 859 (1989).

5. R. Reisfeld, C.K. Jorgensen, Lasers and Excited States of Rare Earths, (Springer-Verlag, Berlin, 1977).
6. R. Reisfeld, in Halide Glasses for Infrared Fiberoptics, edited by R.M. Almeida (Martinus Nijhoff Publishers, Boston, 1987), pp. 237-251.
7. B. Dunn, G.C. Farrington and J.O. Thomas, MRS Bull. XIV, 22 (1989).
8. G. Aka and R. Collongues, to be published.
9. G.A. Rakuljic, A. Yariv, R. Neurgaonkar, Opt. Eng. 25, 1212 (1986).
10. A. Yariv, P. Yeh, Optical Waves in Crystals (Wiley & Sons, New York, 1984), p. 338.
11. Xu Yuhan, to be published.
12. C.J. Chen, Xu Yuhan, R. Xu, J.D. Mackenzie, Proc. 1st Int. Ceramic Sci. and Tech. Congress, Anaheim, CA, October 31-November 3, 1989 (in press).
13. O. Saburi, J. Phys. Soc. Japan 14, 1159 (1959).
14. K. Okazaki, Ceramic Engineering for Dielectrics (Gakkensha Co., Ltd., Tokyo, 1969), p. 378.
15. G. Goodman, J. Am. Ceram. Soc. 46, 48 (1963).
16. Y. Sasaki, Y. Ohmori, Appl. Phys. Lett. 39, 468 (1981).
17. U. Osterberg, W. Margulis, Opt. Lett. 11, 516 (1986).
18. R.H. Stolen and H.W. K. Tom, Opt. Lett. 12, 585 (1987).
19. H. Schmid, H. Rieder, E. Ascher, Solid State Comm. 3, 327 (1965).
20. J.A. Deverin, Ferroelectrics 19, 9 (1978).
21. J.D. Mackenzie, D.R. Ulrich, Ultrastructure Processing of Advanced Ceramics (Wiley & Sons, New York 1988).
22. R. Araujo, in Treatise on Materials Science and Technology, Vol. 12, edited by M. Tomozawa and R.H. Doremus (Academic Press, New York 1977) pp. 91-155.
23. R.K. Jain, R.C. Lind, J. Opt. Soc. Am. 73, 647 (1983).
24. S.S. Yao, et al, Appl. Phys. Lett. 46, 801 (1985).
25. J.H. Simmons, E.M. Clausen, Jr., B.G. Potter, Jr. in Ultrastructure Processing of Advanced Ceramics, edited by J.D. Mackenzie and D.R. Ulrich (Wiley & Sons, New York 1988) pp. 661-669.
26. K. Ooka, B. Dunn, J.D. Mackenzie, J. Non-Cryst. Solids 12, 1 (1973).
27. E.J. A. Pope, J.D. Mackenzie, J. Mater. Res. 4, 1018 (1989).
28. E.J.A. Pope, J.D. Mackenzie, MRS Bull. XII, 29 (1987).
29. C.B. Greenberg, D.E. Singleton, U.S. Patent No. 4,768,865 (September 6, 1988).
30. F.G.K. Baucke and J.A. Duffy, Chem. in Brit. July, 643 (1985).

31. C.B. Greenberg, D.E. Singleton, Solar Energy Mat. 16, 501 (1987).
32. K. Makita, Central Glass Co., ltd., Japan, to be published.
33. M.S. Whittenham, A.J. Jacobson, Intercalation Chemistry (Acad. Press, New York 1982).
34. H. Schmidt in Better Ceramics Through Chemistry, Edited by C.J. Brinker, D.E. Clark, D.R. Ulrich (North-Holland, New York 1984) pp. 327-336.





AD-P007 469



161

## MULTIFUNCTIONAL FERROIC NANOCOMPOSITES

R.E. NEWNHAM, S. E. MCKINSTRY, and H. IKAWA  
Materials Research Laboratory, the Pennsylvania State University, University Park, PA  
16802

### ABSTRACT

As trends towards miniaturized components and systems continue in many fields, there has been a rapid development in similarly scaled-down composites. In the electronics industry, these nanocomposites (and especially active nanocomposites based on ferroic elements) form a basis for many of the recent advances in both information and charge storage. While the overall properties of some of these composites can be explained as straightforward extrapolations from the bulk properties, in other instances the small size of the ferroic phase has important consequences on the macroscopic behavior of the composite. This paper reviews some of the recent developments in small-scale ferroic nanocomposites and details the relation between component size and the resultant properties.

### INTRODUCTION

The study of composite electroceramics has resulted in several new families of devices with properties superior to those obtainable from single phase materials [1]. Typically, the success of such composites can be traced to well-designed phase connectivity patterns, which can, for example, force desirable field concentrations in a single phase, enhance the anisotropy of property coefficients, and control the transport of heat or charge. Engineering of this type accounts for the rapid growth in composite biomedical transducers, thermistors, hydrophones, and chemical sensors.

However, the drive towards small-scale components has resulted in a new generation of composites in which not only the connectivity, but the scale of the components also plays a remarkable role in the overall properties. This is especially important in the case of ferroic materials, where both the presence of domain walls and indeed, the ferroic transition itself, is controlled by the crystallite size. In order to predict what properties to expect from ferroic nanocomposites, then, it is necessary to understand how size affects the behavior of single phase ferroics. This is easiest to illustrate with the family of ferromagnetic materials, as they are by far the best studied of the ferroics, but new experimental evidence is accumulating that small ferroelectric, ferroelastic, and secondary ferroic particles will show similar behavior.

Beginning from the larger end of the size spectrum, it is well known that large grained ferroic ceramics exhibit complex domain structures which are often bounded by several different types of domain walls. As the size of the system decreases, however, the volume free energy necessarily decreases as well, and it becomes increasingly difficult to support the energy term associated with domain walls [2]. Consequently, the number of domains is projected to decrease as first one and then the other types of walls are eliminated.

At still smaller sizes (~20nm for many magnets), ferroic particles undergo a phase change to the high temperature symmetry group. In the case of ferromagnetic particles (and more recently relaxor ferroelectrics as well) this has been correlated with the size at which the decrease in volume free energy accompanying magnetization is on the order of the thermal energy[3,4]. As a result, the spin direction is randomized with time, leading to an unmagnetized but highly orientable single domain crystal. Thus a magnet in this size regime is characterized by a zero net magnetization, the disappearance of a magnetic hysteresis loop, and extremely high magnetic susceptibilities. Materials displaying this type of enhanced responsiveness are termed superparamagnetic, superparaelectric, or superparaelastic solids.

Because ferroic properties are caused by cooperative phenomena, it is intuitively appealing to suppose that the system will be forced to revert to the para-state at some size where there are simply too few atoms to sustain the cooperative interactions. Thus, at sizes approaching atomic dimensions, superparamagnetic materials should revert to ordinary paramagnetism in which the magnetic susceptibility follows a Curie law with temperature.



In summary, then, we expect four regions in the size dependence of ferroic properties (Fig. 1). In large crystallites, multidomain effects accompanied by hysteresis take place. Reductions in size lead to single domain particles, and at yet smaller sizes to destabilized ferroics with large property coefficients, and finally to normal behavior as the particle size approaches the atomic scale. Similar transitions with size are expected in secondary ferroics. Typical sizes at which ferromagnetic, ferroelectric, and ferroelastic materials undergo these transitions and the effect of size on the transformations temperatures have been reviewed previously [5].

#### MAGNETIC NANOCOMPOSITES

Magnetic nanocomposites based on either small particles or thin films are by far the most extensively studied of the ferroic nanocomposites. Fundamental research on the properties of fine magnets has, in recent years, been spurred by the burgeoning market in technological applications of nanoscale devices. One of the obvious benefits to be reaped from the use of smaller magnetic particles (especially in the magnetic recording industry) is that smaller storage units lead to the possibility of storing information at a higher density. There are also some applications, however, where the small size of the ferroic component results in properties considerably different from those of a bulk magnet. Composites designed to exploit this effect include some thin film ferromagnetic/paramagnetic sandwiches and the magnetic fluids used in clean seals.

The magnetic recording industry has played a substantial role in the development of fine ferroic powders. Magnetic disks and tapes for recording and computer memories are prepared by coating a substrate, typically a smooth nylon film, with a layer of ferromagnetic powder dispersed in a binder. Powders are chosen for their retentivity, coercivity, low noise, and the density of information they can store [6]. As the last two characteristics are strongly correlated to the particle size, preparation of high quality fine particles is of considerable importance to the industry. For most applications acicular  $\gamma$ - $\text{Fe}_2\text{O}_3$  particles about  $.2 \mu\text{m}$  long and  $0.02 \mu\text{m}$  in diameter are aligned parallel to both the film plane and the tape play direction. These materials qualify as composites through the use of a polymeric backing layers and a permanent binder to fix the magnetic particles to the backing.

In a number of instances, however, even higher storage densities are desired, and finer particles for both parallel and perpendicular recording are being investigated. In pioneering studies with the perpendicular recording technique, Iwasaki and coworkers developed an rf sputtered Co-Cr composition (thickness  $\sim 1 \mu\text{m}$ ) which can store up to 15,000 bits/in [6]. This demonstration of feasibility, coupled with projected upper limits on the linear recording density topping 100,000 bits/inch (by contrast, current technology for parallel recording is limited to 15,000 bits of information/in, although 25,000 may eventually be possible [7]) has generated tremendous interest in this field. As of 1983, disks for perpendicular recording with densities on the order of 40,000 bits/in had been reported by several different firms [8]. Principal among the materials systems being investigated for perpendicular recording are Co-doped iron oxide powders, Co films, and hexagonal barium ferrite platelets  $< 500 \text{ nm}$  in diameter [9]. Because of the comparative fragility of the metallic films used in perpendicular recording, they are most typically utilized in hard disk drives or other "flying head" applications where there is no contact between the recording head and the magnetic medium. The development of more durable, corrosion resistant oxide films may lessen these restrictions somewhat, opening perpendicular recording to more and more applications.

One promising example of what is possible with ingenious processing is the 1-3 composite developed by Tsuya et al for uniform, high density magnetic components [10]. In their experiments, an aluminum alloy substrate is oxidized under conditions which result in the generation of a regular network of honeycomb cells on the surface. The columnar pores formed during oxidation can subsequently be etched to increase the diameter to  $>400\text{\AA}$  and backfilled with iron to create a high density of magnetic elements with practical values for the coercive force (See Fig. 2).

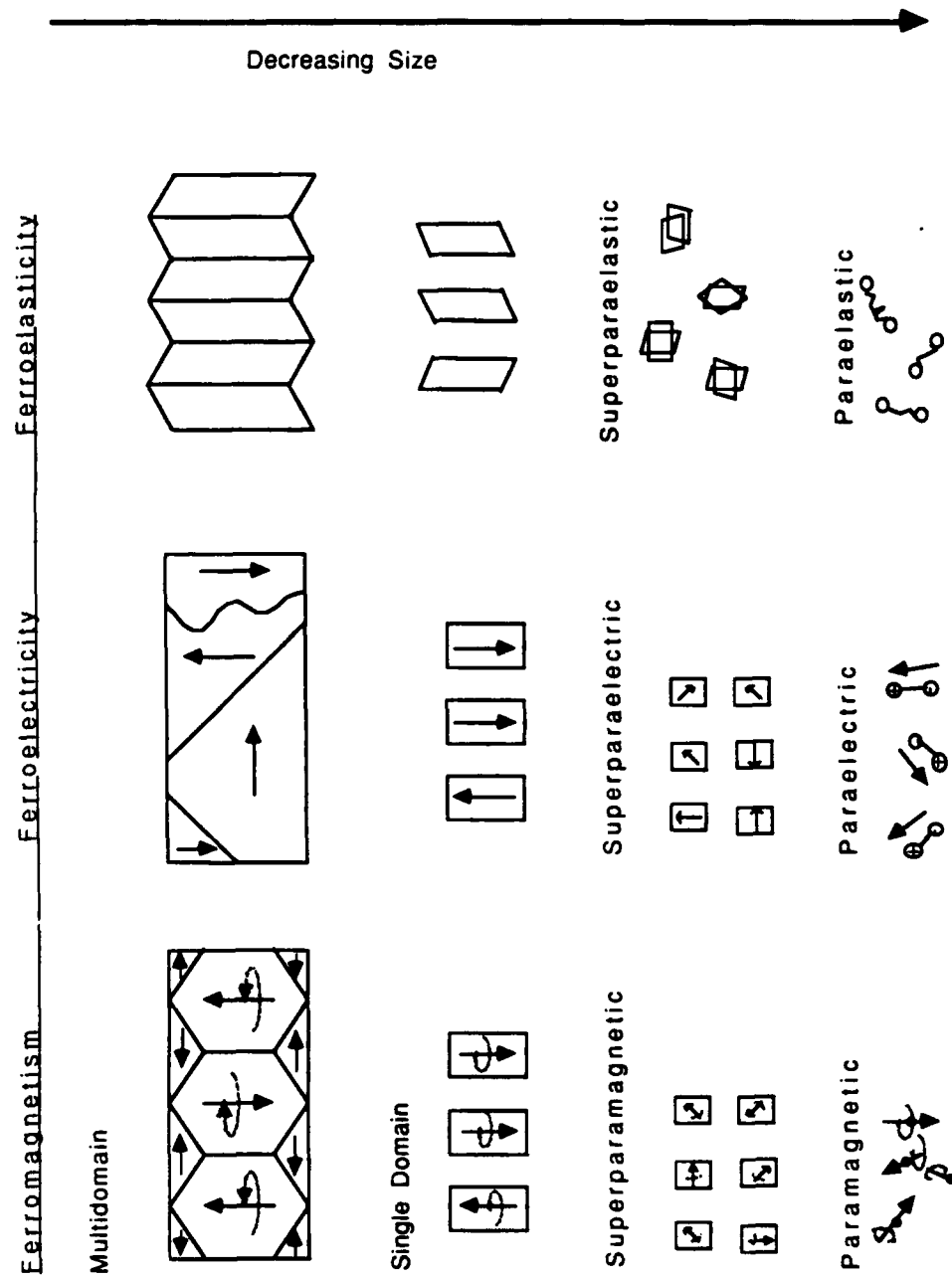


Fig. 1: Changes in the domain configurations of ferroics as a function of size

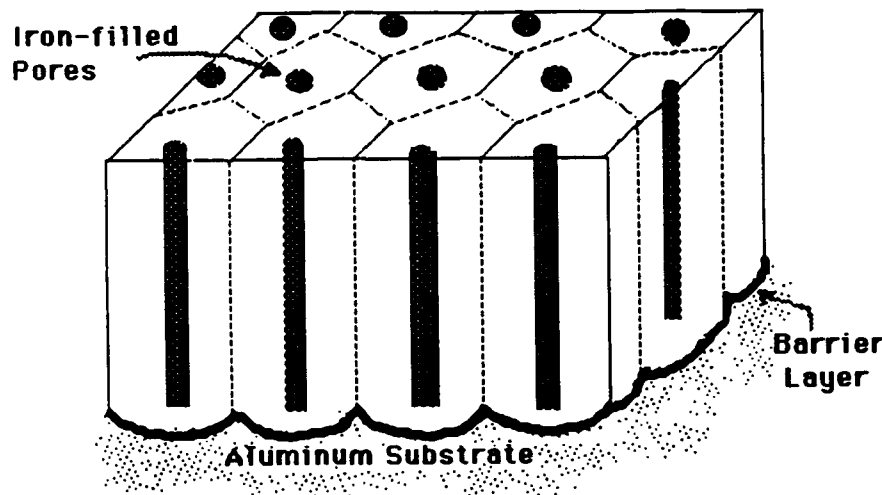


Fig. 2: 1-3 nanocomposite used for perpendicular recording. To produce this structure a honeycomb network of cells is created by oxidizing an aluminum alloy. The pores are then etched and backfilled with iron [10].

Another 2-2 composite which has been favored by the progress in vertical recording is the thin film lamellae structure used in magneto-optical recording. In this type of device, polarized light is either reflected from or transmitted through a thin magnetic layer. The ellipticity of the resulting light is affected by the magnetization state, leading to the possibility of storing and reading digital information. In order to eliminate noise which could otherwise interfere with the comparatively weak signal, a multilayer structure similar to that shown in Fig. 3 and designed to effectively magnify the desired signal through interference effects is sometimes incorporated [10].

Another growing field in magnetic recording is the use of ultrathin sandwiches of ferroic and non-magnetic layers. Using sophisticated deposition techniques, magnetic layers on the order of 5 - 20 Å can be separated by buffering films thin enough to permit magnetic coupling through the intermediate layer. This type of film will constitute a new type of magnetic recording media with exceptional storage properties. Currently under study are a variety of transition metal or rare earth multilayers which, when deposited under appropriate conditions, display an innate perpendicular magnetic anisotropy over limited thickness ranges [11-15]. Especially exciting are some of the Co-based composites which couple the preferential alignment with an enhanced Kerr rotation angle, an excellent combination for magneto-optical recording applications [12]. Moreover, the Co/Pd and Co/Pt composites under scrutiny are more corrosion resistant than the rare earth-containing alloys currently in use.

Work on this type of structure has also been extended to oxide superlattice systems. Bando has prepared CoO/NiO superlattices on sapphire and CoO/Fe<sub>3</sub>O<sub>4</sub> on rocksalt, obtaining highly crystalline products in which the in-plane lattice spacings of each layer differed from the bulk values to provide a better match to other layers. In order to minimize concurrent changes in the unit cell volume, this was accompanied by variations in the out-of-plane spacings. Neutron diffraction results for the CoO/NiO modulated structures show a strong magnetic correlation between the layers and a well-defined Neel temperature for each composition. The transition temperature for the films all lie on the line joining the Neel temperatures of NiO and CoO [16, 17].

In contrast to the case of magnetic memory elements where a permanent magnet is essential for long-term storage, ferrofluids rely on the enhancement of magnetic properties that can be achieved through the use of superparamagnetic particles with no lasting moments.

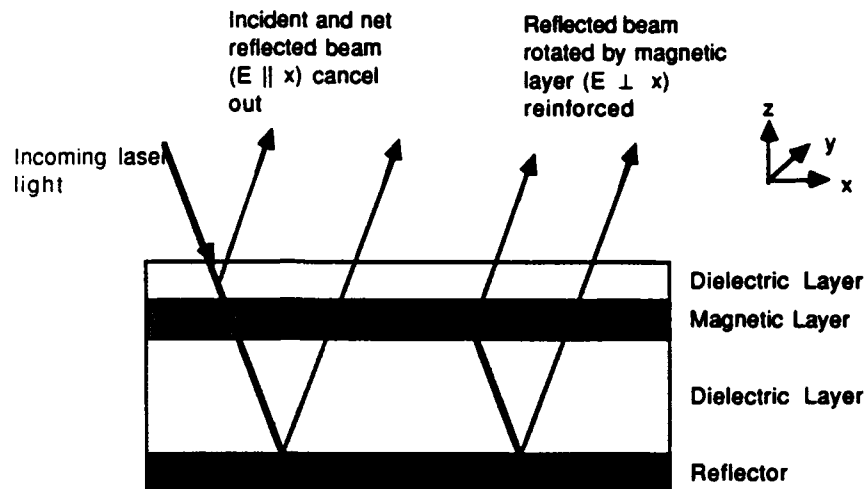


Fig. 3: 2-2 composite utilized in magnetooptic memories. This arrangement cancels out components of the light wave which are not rotated by the magnetic layer while amplifying the rotated signal [8]

Typically, a ferrofluid consists of a suspension of magnetic particles small enough ( $\sim 10\text{nm}$ ) so that Brownian motion is sufficient to prevent settling. As superparamagnets, each particle behaves as a paramagnet, but one in which the magnetic moment is hundreds or thousands of times higher than that of a single unit cell. Consequently, the use of exceptionally fine particles, mandated by the need for colloid stability, leads to the added benefit of magnetic properties superior to those which could be achieved with larger ferromagnetic particles.

Long term stability of such suspensions, however, also requires that individual particles be shielded from each other by a buffer layer thick enough to prevent agglomeration due to van der Waals forces. This has been approached primarily by two different routes, a) coating the particles with a polymer to insure mechanical separation and b) endowing all of the particles with a like surface charge so that Coulombic repulsion maintains the necessary distance [18,19].

The first approach most often utilizes organic solvents and surfactants to realize a well-dispersed colloid. As discussed below, dispersions of this type have found widespread use as non-contaminating seals. In the second means of suspending the powders, however, the particles are charged in the same way so that each behaves as a macro-ion. One of the distinct advantages of this system is the ease with which the ferrofluid can be dispersed in water-based solutions. This could prove extremely beneficial in medical technology as a ferrofluid with a pH and salinity comparable to blood could be introduced into the circulatory system and manipulated throughout the body by external magnetic fields. Once located in position, it could then serve as an aid in diagnostic imaging, a temporary means of blocking blood flow, a drug dispenser, or as a means of selectively concentrating high doses of X-rays in diseased tissue while minimizing damage to neighboring areas [19,20].

Several of the more conventional uses of ferrofluids also entail controlling the position of the fluid with an external magnetic field. A magnetic fluid separating two gaseous phases, for example, can be pinned in place by an encircling magnetic field, even if there is a pressure differential across the seal. Seals and bearings of this type, being non-abrasive, have received wide acceptance in industries where the dust created through ordinary wear on solid-solid seals can be catastrophic. Consequently, this type of seal is regularly used in computer hard disks to prevent dust from entering and "crashing" a head. Similarly, ferrofluid seals have been incorporated into cleanroom design, crystal growth units, gas lasers, motors, blowers,

cryogenic units, and cleanroom robotics [10,21].

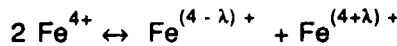
Other applications in which the liquid position is controlled by a magnetic field include loudspeakers and inkjet printers. Loudspeaker designs of this type incorporate magnetic fluids to fill the gap between the voice coil and the permanent magnet. The fluid is retained in the gap by the existing magnetic field; its presence dissipates heat which would otherwise limit the power handling, and flattens the frequency response. Ferromagnetic inks for inkjet printers have also been studied at the Matsushita Electric company in Japan. The use of magnetic ink aids in the formation and resorption of the jet, leading to output with quality comparable to the lower end of available laser printers [19,21].

Other prototype ferrofluid-based devices are aimed at the detection of magnetically-induced anisotropy in composite properties (i.e. birefringence in the refractive index). Thus, for example, a viscometer suitable for small samples has been constructed on the principle that as a magnetic field is removed from a liquid to which a small amount of ferrofluid has been mixed, the observed birefringence will decay exponentially at a rate proportional to the host fluid viscosity. In principle, the induced birefringence could also be utilized in magneto-optic devices for manipulating polarized light [22].

Ferrofluids have also found application in a number of different fields, including levitation systems for separating materials of differing density, vibration dampers, engines for converting low grade heat to useable energy, and devices to measure very small inclination angles [19,21].

#### Self Assembling Nanocomposites

The definition of nanocomposite can also be extended to encompass macroscopically "single phase" materials displaying inhomogeneities in structure or properties on a fine scale. Examples of this behavior found among ferromagnetic composites include solid solutions of magnetic and nonmagnetic materials (i.e. Fe in Cu) in which the interactions between isolated magnetic dipoles (iron atoms) can be either ferromagnetic or antiferromagnetic [23]. As a consequence of the complicated magnetic interactions that occur, the lowest energy state in such spin glasses consists of islands of aligned spins. Recent studies suggest that a few magnetic perovskites also behave like spin glasses (See Fig. 4). In this latter case, the formation of nanodomains in an essentially disordered matrix has been coupled to a charge disproportionation:



and the appearance of a combination of ferromagnetic and antiferromagnetic ordering [24,25]. The resultant picture bears many qualitative similarities to a relaxor ferroelectric. Although few, if any, practical applications for spin glasses are under development, the attempts to mathematically model such complicated, "dirty" systems has had interesting implications on problems as diverse as finding optimized solutions for large sets of variables and constraints and determining if polymer sequencing could have affected the process of evolution [23].

#### **FERROELECTRIC NANOCOMPOSITES**

In contrast to the case of ferromagnetic nanocomposites, ferroelectric nanocomposites are largely unstudied. This is due, in part, to the concentration on the larger scale composites currently utilized as pressure sensors, vibration dampers, and transducers. However, there are an increasing number of applications in which a small component size is mandated by the need for optical transparency or low driving voltages, prompting a growing interest in the field of fine ferroelectrics. While much of this work is in its preliminary stages, current results promise properties which cannot currently be achieved with bulk ferroelectrics.

One interesting example of this is the family of relaxor ferroelectrics, which although prepared as bulk materials, display inhomogeneities in both composition and ordering on a nanometer scale [4,26-29]. In TEM studies on compositions including many of the

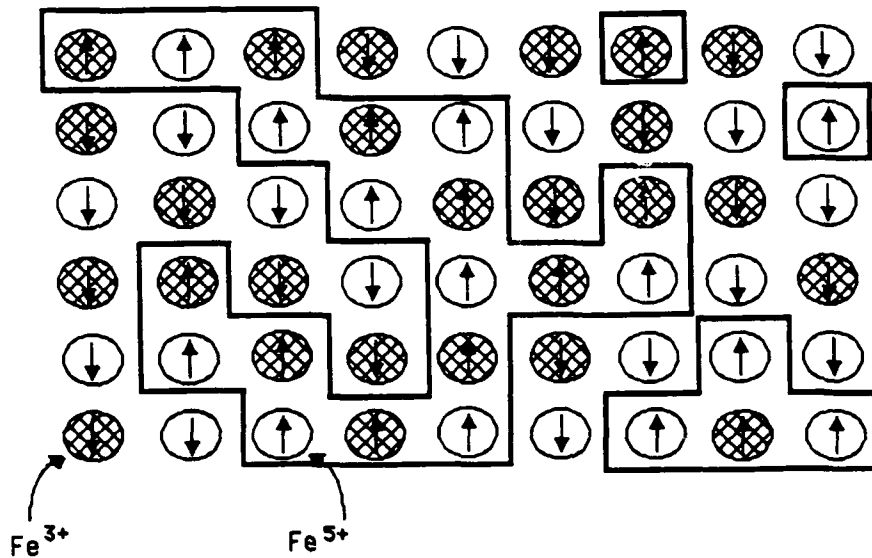


Fig. 4: Schematic of a spin glass showing the regions of aligned domains [24,25] caused by antiferromagnetic coupling between like ions and ferromagnetic coupling between unlike ions.

$A(B'_{1/2}, B''_{1/2})O_3$  and  $A(B'_{2/3}, B''_{1/3})O_3$  perovskites, it has been found that such materials exhibit microdomains (typically 20 - 300 Å in size) of 1:1 ordering on the B sublattice dispersed in a disordered matrix [27-29]. It has been suggested that as a result of this local nonstoichiometry the spontaneous polarization in these materials is also disordered on a very fine scale [4,28]. Thus a lead magnesium niobate ceramic can be regarded as a collection of disordered, but highly orientable, dipoles. Moreover, these incongruities in the lattice lead to different regions of a crystallite having different Curie temperatures. The result, much like the case of superparamagnetism, is a high dielectric permittivity over a broad temperature range even though the net spontaneous polarization is zero. The low temperature coefficient of capacitance (TCC) of these materials coupled with the high dielectric constant (a marked contrast to homogeneous ferroelectrics where the well-defined Curie temperature results in a large TCC in those regions where the dielectric constant is also high) makes relaxors attractive as capacitors. The comparatively low firing temperatures of these materials is also eliciting interest from the electronic component packaging industry as it should permit co-firing of capacitors with high conductivity, low-cost electrodes.

In many of the relaxor compositions, the small-scale heterogeneities present on quenching can be controlled by annealing at high temperatures to produce larger ordered regions. Once the ordered microdomains in a relaxor grow beyond a certain size, however, the material reverts to ordinary ferroelectric (or antiferroelectric) behavior with a well defined transition temperature and a non-dispersive dielectric response. This, in turn, raises the TCC, minimizing its potential use as a capacitor composition. For lead indium niobate the critical domain size at which antiferroelectric ordering appears is 80 nm [28].

Another example of the effect of nano-scale heterogeneities on macroscopic properties is the recent discovery of exceptional optical properties in the incommensurate phase of  $[N(CH_3)_4]_2ZnCl_4$  [30]. Here, the deviation from the crystal periodicity is accompanied by a peak in the electrooptic coefficient to a value  $10^5$  times higher than has been reported for any other material. When the temperature is raised to the point that this material returns to a commensurate lattice, effectively regaining its small scale periodicity, the electro-optic coefficient returns to more common value.

In addition to such nanocomposites where the pertinent inhomogeneity is caused by a small-scale restructuring of the lattice, there are ferroelectric nanocomposites produced by

mixing two or more different phases together. Among these more conventional two-phase ferroelectric nanocomposites is the electronic analog to the ferromagnetic fluid. Using fine BaTiO<sub>3</sub> particles suspended in an organic carrier liquid, Miller et al have shown that the resulting liquid displays a maximum in the dielectric constant at the tetragonal-cubic phase transition of the perovskite [31]. Similarly, Bachmann and Bärner have determined that milled particles (average diameter = 10nm) dispersed in a mixture of heptane and oleic acid have permanent polar moments [32]. Hopefully as work in this area proceeds, these liquids will find applications in areas as diverse as those employing ferromagnetic fluids. In particular, ferroelectric fluids could be used as an alternative to liquid crystals in display panels.

These goals do not seem unreasonable in light of the some of the recent successes in preparing solid 0-3 ferroelectric nanocomposites with ferroic properties. Indicative of the advances in this area is the work of Lee et al with coprecipitated PbTiO<sub>3</sub> powders dispersed in a polymeric matrix. In a series of poling studies they demonstrated that the polarization vectors of powders <~20 nm in diameter could be aligned under strong electric fields, leading to a net polar moment and piezoelectricity in the composite [33]. 0-3 composites of this type have traditionally been used as vibration sensors and dampers. It is hoped that by miniaturizing the ferroic component such materials can be integrated into optical applications (see below).

Another area where small particulate ferroelectrics may be useful is in the preparation of materials for frequency doubling high intensity IR lasers down to a wavelength at which SiO<sub>2</sub> optical fibers transmit light well. In order to accomplish this, it is necessary to use a material which is both an efficient second harmonic generator and for which the refractive index can be matched at the primary and secondary frequencies. While ferroelectrics fulfill the first requirement, the refractive indices of ferroelectrics undergo ordinary dispersion, so index matching is not possible in an unpoled ceramic. However, it should be possible to compensate for the dispersion by using a crystal's birefringence to slow the frequency doubled wave [34]. Unfortunately, no single material couples the necessary magnitude for the optical anisotropy and efficient conversion of the primary to the secondary frequency with resistance to optical damage. One of the schemes proposed to overcome this difficulty entails preparing a composite of non-spherical ferroelectric particles embedded in a transparent matrix. If all of the particles could be aligned, the resulting material should display form birefringence (due to the particle shape anisotropy) of a magnitude large enough for index matching. To insure transparency of such a composite, though, the dispersed phase must be considerably smaller than the wavelength of light (~500nm) to avoid scattering losses.

#### FERROELASTIC NANOCOMPOSITES

Although ferroelastic materials were first described by Aizu in 1969, there are still very few devices utilizing the ferroic nature of these materials. Instead, the gadolinium molybdate crystals proposed for use in optical shutters, read only memories, and electronically variable SAW/bulk delay lines [35] most often possess few domain walls. Part of the reason that comparatively little is known about ferroelastics with artificially generated fine domain structures is that there are a limited number of materials for which the coercive stress is low enough to move the domain walls without affecting either the crystal's structural state or its mechanical integrity. Indeed, the amount of energy it would take to induce controlled, closely spaced twins is often too large to be sustained.

This may be the reason that the ferroic properties of zirconia, an additive widely used for toughening ceramics, are largely unstudied. Although one would expect domain wall movement to permit stress relaxation and so increase the fracture toughness of zirconia ceramics, available experimental data are contradictory and do not completely support this hypothesis. Studies by Virkar and Matsumoto, for example, indicate that the toughness of tetragonal zirconia is related to ferroelastic contributions [36]. Although these results have been called into question [37], similar conclusions can be inferred from the careful studies of Michel et al [38]. In contrast, Ingel et al [39] concluded on the basis of mechanical property measurements on pure zirconia as a function of temperature that the major contribution to the

toughness in zirconia is the tetragonal to monoclinic phase transition. The exceptionally large fracture toughnesses of partially stabilized zirconia ceramics are also explained as stemming from the same stress-induced phase transformation [40,41]. At temperatures above 900° C, Ingel's data does contain a slight upward trend in fracture strength which may be related to ferroelasticity. However, if this indicates the magnitude of energy (temperature) necessary to free the domain walls, it clearly precludes using ferroelasticity as the sole toughening mechanism at room temperature for zirconia ceramics. Consequently, it can be concluded that the coercive stress of many ferroelastics is too high for practical manipulation at low temperatures.

One notable exception to this is neodymium pentaphosphate (NPP), a pure ferroelastic crystal first discovered in 1972 by Danielmeyer and Weber. The high temperature, prototype form of NPP is orthorhombic while the ferroelastic low temperature form is monoclinic (point group 2/m). There are two types of domain structures in NPP; those separated by a (001) twin plane (a-type domain wall) and others bounded by (100) twin planes (b-type domain wall). Interesting from a practical point of view is the fact that in NPP the domain walls can be moved by a shear stress of only 0.014 N/mm<sup>2</sup>.

Meeks and Auld have made outstanding progress in controlling the domain structure in NPP by using a mechanical stress in conjunction with a laser beam [42]. Several types of domain structures can be generated in this fashion, including tunable arrays with domain wall periods between 100 and 3  $\mu$ m. This lower value agrees with an estimate based on theoretical considerations of the minimum achievable domain size. However, it was also shown that periods down to 0.5  $\mu$ m could be obtained with arrays trapped between two types of domain walls (See Fig. 5). Periodic structures like this interact with both optical and acoustic waves, leading to potential applications as a new functional material for tunable active gratings for lasers, tunable diffraction gratings, tunable Bragg reflection gratings, tunable acoustic filters, optical modulators, and optical domain wall memories. As their lowest periodicity is just at the border where a structure can be considered nanoscale, this work offers the possibility that true nanocomposites based on pure ferroelastics may eventually be possible.

One approach designed to overcome the difficulties associated with producing nanoscale domains is to utilize ferroics in which the ferroelasticity arises only as a consequence of the primary order parameter. In the perovskite ferroelectrics, for example, the 90° domains are both ferroelectric and ferroelastic due to the spontaneous strain. Thus, in relaxor ferroelectrics, where the regions of coherent polarization can be on the order of 100 nm, ferroelastic domains with similar scales should also be present. Lead lanthanum zirconate titanate (PLZT) ceramics fulfilling these requirements have been shown to demonstrate shape memory effects [43], a property closely tied with ferroelasticity. This is a particularly exciting result as ferroelastics with very small domains might become superparaelastic. The high mechanical compliance that should accompany such a transition would be extremely useful in preparing ceramics with high fracture toughnesses.

## CONCLUSIONS

The study of composite electroceramics has been a fruitful source of new properties and new functional materials. As these components are miniaturized, however, the focus of composite design has broadened from engineering of advantageous connectivity patterns to include the utilization of size effects to control the macroscopic behavior of nanocomposites. This has proved to be especially important for ferroic nanocomposites, where a reduction in size profoundly affects the number and type of domain walls present in the material. The role of this type of behavior on several functional ferromagnetic, ferroelectric, and ferroelastic nanocomposites has been discussed.

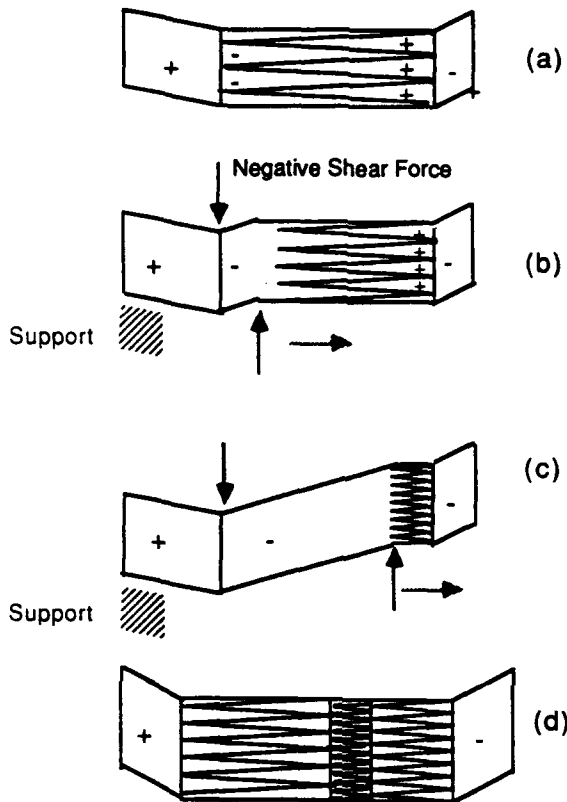


Fig. 5: One method of obtaining tunable twins. The initial state shown in (a) is stressed in (b). As the bottom stress point is moved to the right, the domains become much smaller (c). (d) shows the configuration with which the 500nm periodic domains were created [42].

#### ACKNOWLEDGEMENTS

The authors would like to thank DARPA, Alcoa, and Corning Glass for their financial support of this project.

#### REFERENCES

1. R. E. Newnham, *Ann. Rev. Mater. Sci.* **16** 47 (1986).
2. C. Kittel, *Phys. Rev.* **70**(11,12) 965 (1946).
3. C.P. Bean and I.S. Jacobs, *J. Appl. Phys.* **27**(12) 1448 (1956).
4. L.E. Cross *Ferroelectrics* **76**(3-4) 241 (1987).
5. R. E. Newnham and S.E. McKinstry, Indianapolis Meeting of the American Ceramic Society 1989.
6. Marvin Camras, *Magnetic Recording Handbook*, (Van Nostrand Reinhold Company, New York, 1988)
7. Robert M. White, *Sci. Amer.* **243** 138 (1980).
8. Robert M. White, *IEEE Spectrum* **20** 32 (1983).
9. O. Kubo, T. Ido, H. Yokoyama, and Y. Koike, *J. Appl. Phys.* **57**(1) 4280 (1985).

10. N. Tsuya, Y. Saito, H. Nakamura, S. Hayano, A. Furugohri, K. Ohta, Y. Wakui, and T. Tokushima, J. Mag. Mag. Mat. 54-57 1681-1682 (1986).
11. Noboru Sato, J. Appl. Phys. 59(7) 2514 (1986).
12. Y. Ochiai, S. Hashimoto, and K. Aso, IEEE Trans. Mag. 25(5) 3755 (1989).
13. W.B. Zeper, F.J.A.M. Greidanus and P.F. Garcia, IEEE Trans. Mag. 25(5) 3764 (1989).
14. S. Honda, S. Nishimura, and T. Kusuda, IEEE Trans. Mag. 25(5) 4027 (1989).
15. P.J. Grundy, S.S. Babkair, and M. Ohkoshi, IEEE Trans. Mag. 25(5) 3626 (1989).
16. Y. Bando, Proc. Seventh Seminar on Frontier Technology - Nano-Hybridization and Creation of New Functions Feb. 7-10, 1989 Oiso, Japan.
17. M. Takano, T. Terashima, Y. Bando, and H. Ikeda, "Neutron diffraction study of artificial CoO-NiO superlattices," Appl. Phys. Lett. 51(3) 205 (1987).
18. B. Berkovsky, ed., Thermomechanics of Magnetic Fluids, (Hemisphere Publishing Corporation, Washington, 1978)
19. Jean-Claude Bacri, Regine Perzynski, and Dominique Salin, Endeavor. New Series 12(2) 76 (1988).
20. M.P. Perry, in Thermomechanics of Magnetic Fluids, edited by B. Berkovsky (Hemisphere Publishing Corporation, Washington 1978)
21. Ronald E. Rosenweig, Scientific American Oct. 1982, 136.
22. R.V. Mehta, in Thermomechanics of Magnetic Fluids, edited by B. Berkovsky (Hemisphere Publishing Corporation, Washington 1978).
23. Daniel L. Stein, Scientific American July 1989, 52.
24. P.D. Battle, T.C. Gibb, P. Lightfoot, and M. Matsui, submitted to J. Solid State Chem. (1989).
25. T.C. Gibb and M. Matsuo, J. Solid State Chem. 81 83 (1989).
26. G.A. Smolensky, J. Phys. Soc. Jpn. 28 suppl. 26-37 (1970).
27. J. Chen, H. M. Chan, and M.P. Harmer, J. Am. Ceram. Soc. 72(4) 593 (1989).
28. C.A. Randall, D.J. Barber, P. Groves, and R.W. Whatmore, J. Mat. Sci. 23(10) 3678 (1988).
29. C.A. Randall and A.S. Bhalla, submitted to Jap. J. Appl. Phys. (1989).
30. K. Saito, T. Watanabe, and J. Kobayashi, Ferroelectrics 75 153 (1987).
31. D. Miller, unpublished work
32. R. Bachmann and K. Barner, Sol. State Comm. 68(9) 865 (1988).
33. M. Lee, A. Halliyal, and R. E. Newnham, Ferroelectrics 87 71 (1988).
34. Frits Zernicke and John E. Midwinter, Applied Nonlinear Optics (John Wiley and Sons, New York 1973).
35. L.A. Coldren, R.A. Lemons, A.M. Glass, and W.A. Bonner, Appl. Phys. Lett. 30(10) 506 (1977).
36. A.V. Virkar and R.L.K. Matsumoto J. Am. Ceram. Soc. 69(10) C224 (1986).
37. M.V. Swain in Science and Technology of Zirconia III edited by S. Somiya, N. Yamamoto, and H. Yanagida (The American Ceramic Soc. Inc., Columbus, Ohio 1988) p. 439.
38. D. Michel, L. Mazerolles, and M.P. Jorba in Science and Technology of Zirconia II, edited by N. Clausen, M. Ruhle, and A. Heuer (The American Ceramic Society Inc., Columbus, Ohio 1983) p. 131.
39. R.P. Ingel, P.A. Willging, and B.A. Bender in Science and Technology of Zirconia III edited by S. Somiya, N. Yamamoto, and H. Yanagida (The American Ceramic Soc. Inc., Columbus, Ohio 1988) p. 459.
40. A.G. Evans and R.M. Cannon Acta Metall. 34(5) 761 (1986).
41. K. Urabe, A. Nakajima, H. Ikawa, and S. Udagawa in Science and Technology of Zirconia III edited by S. Somiya, N. Yamamoto, and H. Yanagida (The American Ceramic Soc. Inc., Columbus, Ohio 1988) p. 345.
42. S.W. Meeks and B.A. Auld, Adv. Electron. Electron. Phys. 71 251 (1988).
43. T. Kimura, R.E. Newnham, and L.E. Cross, Phase Trans. 2 113 (1981).



92-18261

AD--P007 470



## CONTROL OF $\text{YBa}_2\text{Cu}_3\text{O}_y$ SOL-GEL SOLUTION STRUCTURE BY CHEMICAL MODIFICATION OF ORGANIC ACID AND ITS EFFECTS

Haixing Zheng and J.D.Mackenzie  
 Department of Materials Science and Engineering, University of California-Los Angeles, Los Angeles, CA 90024

2-ethylhexanoic acid (2EHA) has been applied to control the  $\text{YBa}_2\text{Cu}_3\text{O}_{7-x}$  sol-gel solution. The experimental results prove that 2EHA functions as a sol-gel solution structure controlling and precipitation-prevention agent. The structure of the solution can be one, two or three dimensions of the network by using different concentration of 2EHA to modify the metal alkoxides. With decreasing 2EHA concentration, the homogeneity is improved due to increasing the network connectivity. This results in: (1) ease of the formation of  $\text{YBa}_2\text{Cu}_3\text{O}_{7-x}$ ; (2) denser microstructure with fine grains; and (3) narrower but lower superconducting transition.

### I. INTRODUCTION

Since the discovery of the high temperature superconducting ceramics, numerous techniques have been tested in order to overcome the difficulties in the fabrication (e.g. porosity, preparation of specific shapes). The sol-gel process has been demonstrated to be ideal for the fabrication of high Tc superconducting ceramic fibers or wires [1]. In the sol-gel process, the metal alkoxides in organic solvents are hydrolyzed and polymerized [2]. These low temperature solution reactions yield the ultrahomogeneity of materials and low final phase-forming and densification temperature [3]. By controlling the hydrolysis and polycondensation reactions a homogeneous solution with proper viscosity can be made for the fiber drawing and film coating [4]. Water content, modification of sol-gel solution are two common techniques to control a solution reaction [1,5]. Here we have studied the structure change induced by the modification of the metal alkoxide solution by 2EHA. Further effects of 2EHA on the formation of  $\text{YBa}_2\text{Cu}_3\text{O}_{7-x}$ , microstructure and superconductivity of final products have been investigated.

### II. EXPERIMENTAL

Barium, yttrium and copper isopropoxides were synthesized by reacting the metal with isopropanol or metal chlorides in isopropanol with sodium isopropoxide. The starting solutions were prepared by mixing these metal alkoxide solutions in stoichiometry of Y: Ba: Cu = 1: 2: 3 while different amount of 2-ethylhexanoic acid (2EHA/Alkoxides = 0, 1.5, 3.5, 5.5, 7.5, and 9.5) were added. Then these solutions were refluxed for one hour to make the modifying reaction completely. After being concentrated by distilling off the excess isopropanol, the solution were exposed to atmosphere. With exposing time increasing, the viscosities of the solutions increased, and the fibers could be drawn or the rigid gels formed. All concentrated solutions should be prepared in  $\text{N}_2$  atmosphere.

All TGA measurements were carried out on samples aged for one day in room temperature with a heating rate of 10°C/min using PERKIN-ELMER Model TGS-2 Thermogravimetric Systems. The superconducting transition temperature (Tc) of the samples were tested using the standard four-probe technique.

### 3. EXPERIMENTAL RESULTS

#### 3.1. The Properties Of The Sol-Gel Solutions

Table 1 show the effects of 2EHA on gelling behaviors. If no 2EHA is added into yttrium, barium and copper isopropoxide solution the precipitation will occur. Again, if the molar ratio of 2EHA to  $\text{YBa}_2\text{Cu}_3$  isopropoxide is higher than 7.5 (i.e. more than 7.5 of 13 OPri groups in  $\text{YBa}_2\text{Cu}_3(\text{OPri})$  are replace with 2EHA) the precipitation also takes place. At low amount of 2EHA, the metal isopropoxide solutions form dark blue amorphous gels, and there is no point

Table 1 The Effects of 2EHA and Oxide Contents of Samples

2EHA/Alkoxides (mole)	Characteristics	Oxide Content (wt%) <sup>a</sup>	
		Predicted	Observed
0.0	precipitate	100.00	-
(a) 1.5	gel	76.44	73.13
(b) 3.5	gel	58.17	56.46
(c) 5.5	fiber	46.95	46.59
(d) 7.5	fiber	39.36	42.13
9.5	precipitate	33.88	-

<sup>a</sup>) oxide content is that of compound after hydrolysis and polymerization at room temperature.

for fiber drawing. With amount of 2EHA increasing (2EHA/alkoxides = 5.5 and 7.5), the solution becomes spinnable and fibers can be drawn. Fig.1 shows  $\text{YBa}_2\text{Cu}_3\text{O}_{7-x}$  as drawn fibers.

Fig.2 is TGA curves of gelling samples with the 2EHA/alkoxides ratio = 1.5 (a), 3.5 (b), 5.5 (c) and 7.5(d). The weight loss at low temperature (<600°C) is due to the burning off the organic salts. The weight loss increases with the ratio increasing. The oxide content (wt% at 800°C) in these samples are tabulated in Table 1. The maximum oxide content is about 80 wt% for sample a. Fig.2 also shows that the decomposition of the samples is different, namely two steps decomposition of the sample d, but one step decomposition for sample a,b and c. This implies the structure difference in dry gelling samples, which is illustrated more obviously by infrared spectra (Fig. 3). In the range of 1200  $\text{cm}^{-1}$  to 1800  $\text{cm}^{-1}$ , there are many discrete peaks for sample d, but all these peaks become more indistinct from sample d to sample a.

### 3.2. The Formation Of $\text{YBa}_2\text{Cu}_3\text{O}_{7-x}$ Phase

Fig.4 is x-ray diffraction patterns of sample a and sample d fired at 750°C and 800°C for one hour. If samples are heat treated at 750°C for one hour  $\text{YBa}_2\text{Cu}_3\text{O}_{7-x}$  phase is formed. The main phase of sample a is  $\text{YBa}_2\text{Cu}_3\text{O}_{7-x}$  phase. In contrast the most of sample d are still  $\text{BaCO}_3$ ,  $\text{CuO}$ , etc. At 800°C for one hour, sample a consists of nearly pure  $\text{YBa}_2\text{Cu}_3\text{O}_{7-x}$  phase, however impurities such as  $\text{Y}_2\text{BaCuO}_5$ ,  $\text{BaCO}_3$  exist in sample d.

### 3.3. The Microstructure Of $\text{YBa}_2\text{Cu}_3\text{O}_{7-x}$ Ceramics



Fig.1  $\text{YBa}_2\text{Cu}_3\text{O}_{7-x}$  as drawn fibers

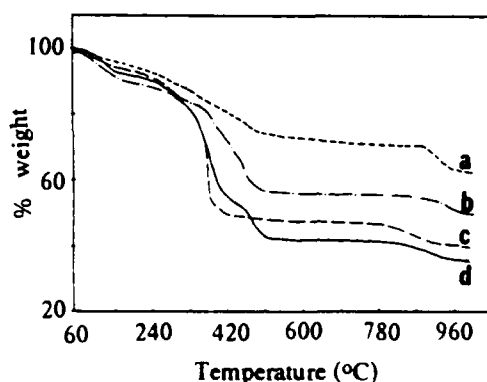


Fig.2 The effect of 2EHA content on the weight loss of  $\text{YBa}_2\text{Cu}_3\text{O}_{7-x}$  dry gels

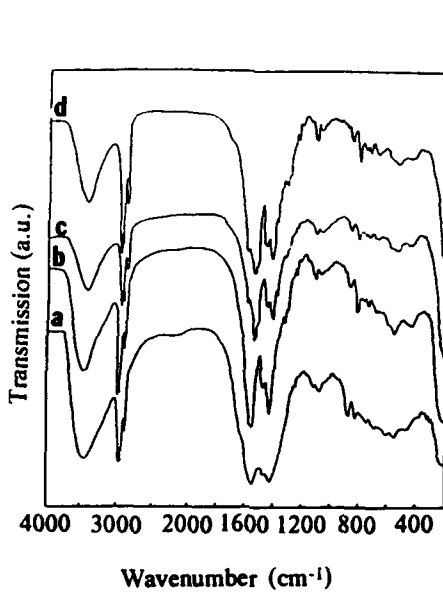


Fig.3 Infrared spectra of the  $\text{YBa}_2\text{Cu}_3\text{O}_{7-x}$  dry gels

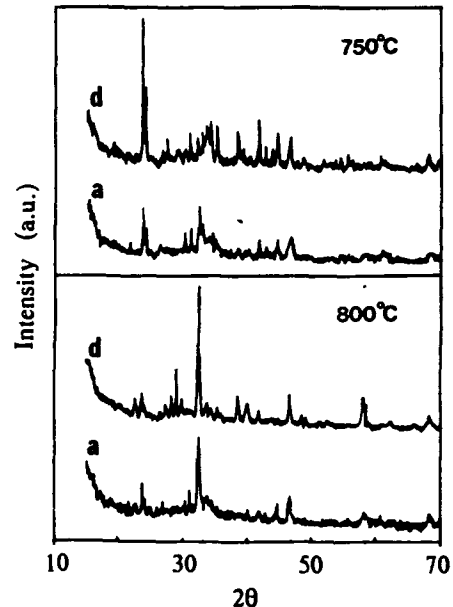


Fig.4 X-ray diffraction patterns of the  $\text{YBa}_2\text{Cu}_3\text{O}_{7-x}$  dry gels heat treated at different temperature for one hour

Fig.5 is the scanning electron micrographs of fractured surfaces of sample a, c and d fired at 800°C for one hour. SEM shows that sample d is porous, but both of samples a and c are almost completely dense and the surface areas are  $0.27\text{m}^2/\text{g}$  and  $0.32\text{m}^2/\text{g}$ , respectively. The sample c consists of homogeneous grains (a few  $\mu\text{m}$ ) sintered together. As the amount of 2EHA decreases the grains of sample a becomes much finer.

#### 3.4. The Superconducting Properties

The dependence of electrical voltage across the sample (a, c and d) bars of the same size fired at 800°C for one hour were shown in Fig.6. All samples showed semiconducting behavior above the onset  $T_c$  temperature, i.e. the resistivity increased with decreasing temperature. But the resistivity of sample c began to drop at 90K and reach zero at 57K, and that of sample a started at 60K and vanished at 38K. So with increasing the acid, the onset  $T_c$  increased, but



(a) 2EHA/alkoxides = 1.5      (c) 2EHA/alkoxides = 5.5      (d) 2EHA/alkoxides = 7.5

Fig.5 The scanning electrical micrographs of the fractured surfaces of  $\text{YBa}_2\text{Cu}_3\text{O}_{7-x}$  dry gels

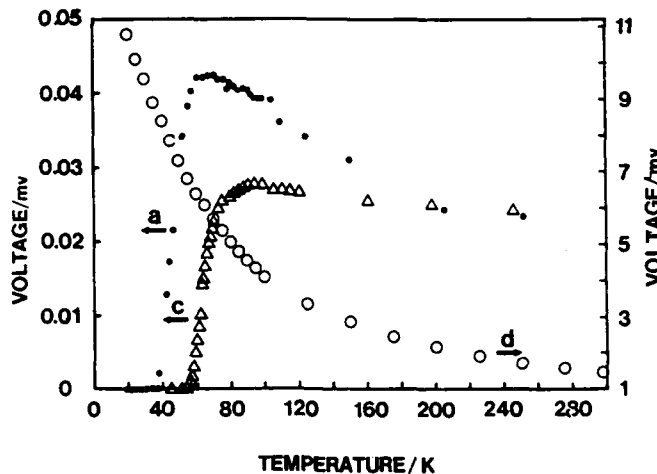
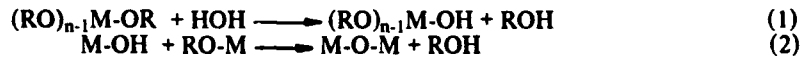


Fig.6 The dependence of electrical voltage across the samples (fired at 800°C for one hour) on temperature

superconducting transition width  $\Delta T$  ( $T_c(\text{onset}) - T_c(\text{zero resistance})$ ) also increased. These results agreed with P. Barboux's results, which showed that the samples prepared by the solution technique have lower  $T_c$  but sharper superconducting transition than the samples prepared by the solid state reaction. Sample d is not superconducting at all. All these three samples heat treated at 950°C and properly annealing have zero resistance  $T_c$  around 85K.

#### 4. DISCUSSIONS

In sol-gel process, when metal alkoxides,  $M(OR)_n$  react with water, two simultaneous reactions take place: hydrolysis (1) and polymerization (2):



The hydrolysis reaction will go so rapidly that the hydroxides precipitate out for the hygroscopic metal alkoxides such as yttrium, copper, or barium alkoxide [5]. However the precipitate could be prevented and the sol-gel solution becomes controllable if modifying the metal alkoxides using nonhydrolysis organic groups (OA) such as  $(RCOO)^-$  since OA groups could not be hydrolyzed. Fig. 7 illustrates the possible mechanism of 2EHA controlling the structure of the sol-gel solution. Obviously, nonhydrolysis organic group not only can prevent the hydroxide formation but also can change the structure of the sol-gel solution or network connectivity since it prevent certain degree of polymerization. This mechanism is qualitatively proved by experimental results shown in Table 1. Table 1 shows that the solutions with low ratio of 2EHA/alkoxides (1.5 and 3.5) is not spinnable and only forms the gels rapidly -implying a structure with high network connectivity (maybe three dimension structure of the inorganic polymers), and the solutions with high 2EHA/alkoxides ratio (5.5 and 7.5) become spinnable indicating one dimensional structure or one with partial two dimensional structure of the inorganic polymers. Further experimental supports come from the oxide contents of the inorganic polymers. The chemical makeup for yttrium, barium and copper polymer modified by 2EHA is:  $YBa_2Cu_3O_{(13-m)/2}(OOC_8H_{15})_m$ . The calculated oxide content as well as the experimental values (from Fig. 2) for  $m = 1.5, 3.5, 5.5, \text{ and } 7.5$  of the  $YBa_2Cu_3O_{(13-m)/2}(OOC_8H_{15})_m$  polymer on the 2EHA amount ( $m$ ) is listed in Table 1. The experimental oxide contents agree well with predicated values. The network connectivity change with 2EHA ratio is also confirmed by the IR spectra (Fig.3). As the yttrium, copper and barium alkoxides hydrolyze and polycondense more completely, the resultant inorganic polymers are more homogeneous, i.e. the difference among the each units is less distinct. The difference in the homogeneity of the  $YBa_2Cu_3O_{(13-m)/2}(OOC_8H_{15})_m$  polymers will be reflected in infrared

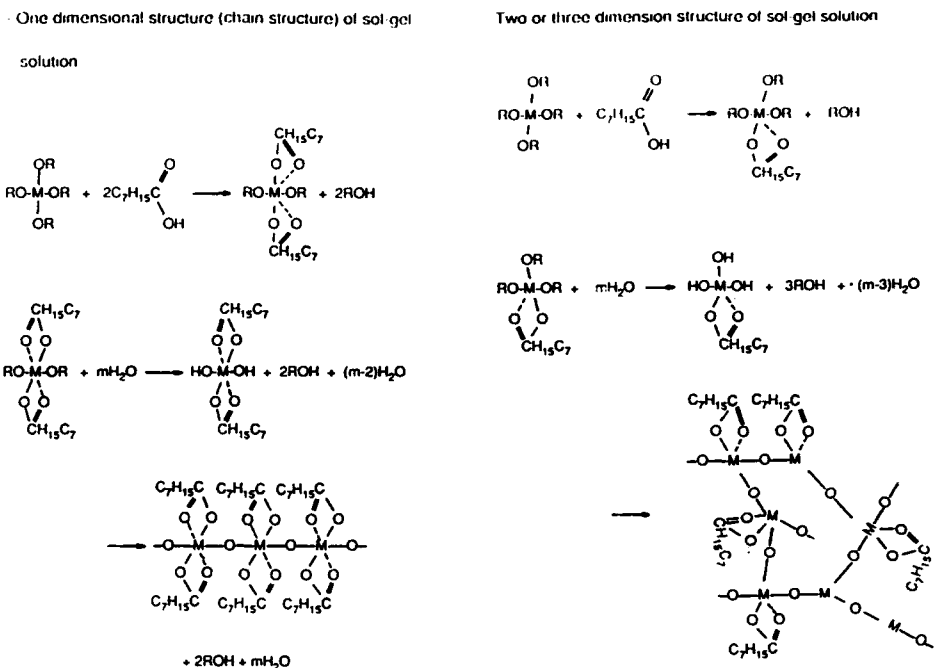


Fig.7 The possible mechanism of 2EHA controlling the structure of the inorganic polymers

spectra by the different resolution of the infrared absorption peaks. Fig.3 shows that the peaks in sample a (2EHA ratio = 1.5) are more indistinct than in sample d (2EHA ratio = 7.5). This says that there is a higher network connectivity or more homogeneity in sample a.

The lower the 2EHA ratio is the higher connectivity the structure of a sample is. As the 2EHA ratio increase from 1.5 to 7.5, the solution changes from nonspinnable one (forming gels) to spinnable one (forming fibers). This change will affect properties related to the homogeneity of gels. The higher network connectivity means more complete polymerization, and more homogeneity in the sample. This certainly will make the formation of  $\text{YBa}_2\text{Cu}_3\text{O}_{7-x}$  phase easier, i.e. the formation of more  $\text{YBa}_2\text{Cu}_3\text{O}_{7-x}$  phase for the samples with low 2EHA ratio. The experimental results confirm this inference. At 750°C much more  $\text{YBa}_2\text{Cu}_3\text{O}_{7-x}$  phase forms in the sample a than in sample d; at 800°C sample a mainly consists of  $\text{YBa}_2\text{Cu}_3\text{O}_{7-x}$  while sample d consists of  $\text{YBa}_2\text{Cu}_3\text{O}_{7-x}$ ,  $\text{Y}_2\text{BaCuO}_5$ ,  $\text{BaCO}_3$ , et al.

It is the same that the network connectivity i.e. homogeneity of the solutions affecting crystallization or phase transformation also affects the microstructure of fired samples. As known, the crystallization of a desired compound from a homogeneous amorphous matrix will result in microstructure with fine and uniform grains because of the homogeneous nucleation and uniform crystal growth process. However, the crystallization of the desired compound from a heterogeneous matrix must undergo the recrystallization and grain growth. This process generally produces the more porous microstructure with non-uniform grains due to the heterogeneous nucleation and different driving force between large and small grains. A reduction in the overall connectivity of an inorganic polymer means decreasing in the chemical homogeneity. This causes the change in the nucleation and crystal growth from homogeneous mechanism to heterogeneous mechanism. The microstructures of sample a, c and d in Fig. 5 show this change.

The superconducting behaviors of sample a, c and d shown in Fig.6 further reflect the difference in the overall connectivity, i.e. the homogeneity. The general agreement has been reached that purer and larger  $\text{YBa}_2\text{Cu}_3\text{O}_{7-x}$  grains (e.g. the extreme case: single crystal) possess a higher onset  $T_c$  and a narrower superconducting transition, and vis-a-vis lower onset  $T_c$  and a wider superconducting transition [6]. As discussed above, the sample with a lower 2EHA content (sample a) produce more  $\text{YBa}_2\text{Cu}_3\text{O}_{7-x}$  phase with fine grains. Therefore the

onset  $T_c$  will be lower ( $T_{c(onset)} = 60K$ ) due to the fine grains and the transition will be narrow ( $\Delta T = 22K$ ); In contrast, the sample with high 2EHA content (sample c) gives impurer materials with larger grains, which gives the higher onset  $T_c$  ( $T_{c(onset)} = 90K$ ) and the wider transition ( $\Delta T = 33K$ ). The porosity and the existence of non-superconducting phase result in no superconductivity in sample d when heat treated at 800°C for one hour.

## 5. CONCLUSIONS

2-ethylhexanoic acid (2EHA) in the fabrication of  $YBa_2Cu_3O_{7-x}$  materials by sol-gel process acts as a precipitation-prevention and solution structure-change agent. By controlling the amount of 2-ethylhexanoic acid the structure of solution can changed from one dimension to three dimensions. The higher network connectivity (or more homogeneous) the solution the easier the formation of  $YBa_2Cu_3O_{7-x}$  phase, and the lower the onset  $T_c$  and the narrower the superconducting transition.

**ACKNOWLEDGEMENT:** The financial supports of the Air Force Office of Scientific Research, Directorate of Chemical and Atmospheric Science and the Strategic Defence Initiative Organization are greatly appreciated.

## REFERENCE

1. Haixing Zheng, K.C.Chen and J.D.Mackenzie, in Extended Abstract: High Temperature Superconductors II, edited by D.W.Capone, W.H.Butler, B.Batlogg and C.W.Chu, (Materials Research Society, Pittsburg, 1988), EA-14, pp.93
2. J.E.Mcgrath, J.P.Pullockaren, J.S.Riffle, S.Killic and C.S.Elsbernd, Ultrastructure Processing of Advanced Ceramics, edited by J.D.Mackenzie and D.R.Ulrich (A Wiley-Interscience Publication, 1988), pp.55
3. J.D.Mackenzie, J.Non-Cryst.Solids, 48, 1(1982)
4. L.C.Klein (ed.), Sol-Gel Technology for Thin Films, Fibers, Preforms, Electrons, and Specialty Shapes, (Noyes Publications, 1988)
5. Haixing Zheng, M.W.Colby and J.D.Mackenzie, in Better Ceramics Through Chemistry III, edited by C.J.Brinker, D.E.Clark and D.R.Ulrich, (Materials Research Society, Pittsburg, 1988)
6. P.Barbous, Presentation in 90th Annual American Ceramic Society Meeting, May, 1988, Cincinnati, (unpublished work)



92-18262

AD-P007 471



79

SYNTHESIS OF POLYIMIDE-SILICATE HYBRIDS VIA SOL-GEL  
ULTRASTRUCTURE PROCESSING



M. SPINU, A. BRENNAN, J. RANCOURT, G. L. WILKES, AND J. E. McGRATH\*

Departments of Chemistry, Chemical Engineering and NSF Science and  
Technology Center: High Performance Polymeric Adhesives and Composites  
Virginia Polytechnic Institute and State University, Blacksburg, VA 24061

\*To whom correspondence should be addressed

ABSTRACT

New organic/inorganic hybrid materials were prepared by hydrolysis and co-condensation of tetramethylorthosilicate (TMOS) with trimethoxysilane functionalized polyimide oligomers via sol-gel ultrastructure processing. In the first reaction step, amine terminated, fully imidized, soluble, high Tg polyimides were prepared from appropriate diamines and dianhydrides by solution imidization techniques. The amine end-groups were then quantitatively derivatized to nadimide structures through reaction with *cis*-norbornene 2,3 dicarboxylic anhydride. Subsequently, the nadimides were quantitatively derivatized to trimethoxysilane functionalities via hydrosilylation reactions in the presence of chloroplatinic acid catalyst. The resulting hexamethoxy functionalized polyimide oligomers were hydrolyzed and co-condensed at elevated temperatures under mild pressure with TMOS via sol-gel processing to generate thermally stable polyimide-silicate hybrids. The synthesis and characterization of these materials is discussed.

INTRODUCTION

Organic/inorganic hybrids represent a new class of polymeric materials which have the potential to combine the desired properties of both inorganic and organic systems, e.g. the outstanding thermal and dimensional stability, high modulus and hardness associated with the inorganic materials and the high flexibility in property design inherent to organic polymers. The sol-gel process is one possible route to achieve the above combination of properties. A general scheme for the synthesis of organic/inorganic hybrids through a sol-gel process is shown in Figure 1 below. It has been reported in earlier publications [1-3] that novel materials can be prepared by incorporation of PDMS and PTMO oligomers into the sol-gel silicate glasses. These materials possess some characteristics of inorganic glasses and also display some flexibility due to the elastomeric organic component. The present paper describes the synthesis and characterization of organic silicate hybrids containing well-defined, functionalized high performance polyimide precursors as the organic component and TMOS as the inorganic component.

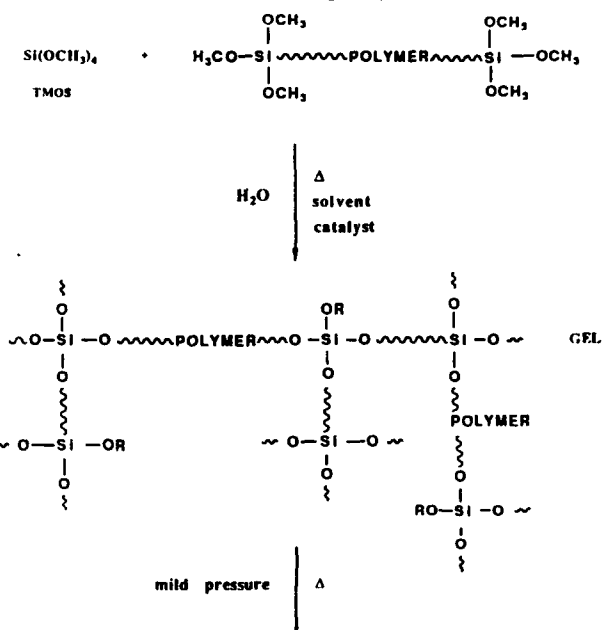
EXPERIMENTAL

Materials

Chemical grade (99%) tetramethylorthosilicate (TMOS) from Petrarch, *cis*-norbornene 2,3 dicarboxylic anhydride and HPLC grade water from Aldrich were used without further purification. Trimethoxysilane from Petrarch was distilled and stored under inert atmosphere until use. Hydrogen hexachloroplatinate IV pentahydrate ( $H_2PtCl_6 \cdot 5H_2O$ ) from Aldrich was stored under inert atmosphere and used as received. Tetrahydrofuran (THF) was

distilled from sodium metal and dimethylformamide (DMF) was distilled from calcium hydride.

Figure 1. General scheme for the synthesis of organic silicate hybrids via sol-gel processes



### Synthesis

## MODIFIED SOL-GEL SILICATE NETWORKS

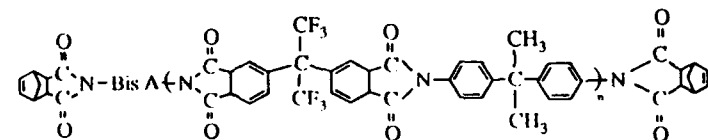
## Functionalized polyimides

In the first step of this synthesis, amine terminated, fully imidized polyimide oligomers of controlled molecular weight were prepared by the solution imidization techniques [4, 5]. For the present study a polyimide structure based on 6F dianhydride and Bis A diamine monomers was employed (for monomer nomenclature see [6]). The resulting polyimide structures are characterized by a low dielectric constant [6, 7], high Tg and high thermo-oxidative stability. The amine terminated oligomers were subsequently reacted with *cis*-norbornene 2,3 dicarboxylic anhydride to generate nadimide end-groups in quantitative yields, using previously described techniques [8]. Finally, methoxy functionalized polyimide oligomers were obtained by hydrosilylation at the norbornene double bond in the presence of trimethoxysilane as the hydrosilylation agent and chloroplatinic acid catalyst, as shown in Figure 2. The hydrosilylation reaction was carried out under anhydrous conditions to avoid premature hydrolysis and subsequent self-condensation of the methoxy functionalized oligomers. The conditions for complete oligomer functionalization were determined with a suitable model reaction. The hydrosilylation was completed in about 24 hours at the refluxing temperature of THF (65°) utilizing a catalyst level of  $5 \times 10^{-3}$  moles catalyst/mole double bond.

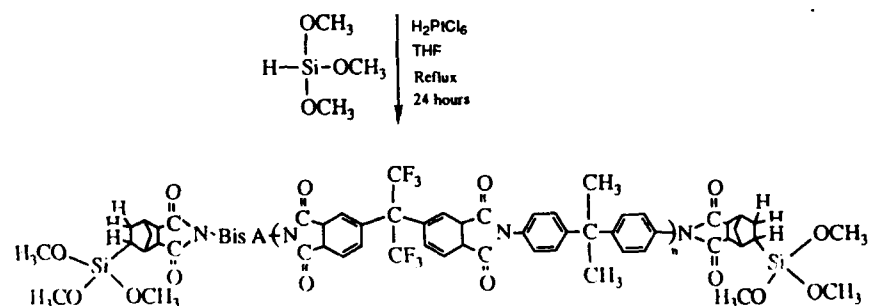
### Polyimide-Silicate hybrids

Methoxy functionalized polyimide oligomers (with number average molecular weight  $\langle M_n \rangle = 3,000$  g/mole) were used as the organic component and TMOS was used as the inorganic component for the synthesis of polyimide-silicate hybrids, according to the general reaction scheme

Figure 2. Synthesis of methoxy functionalized polyimides



NADIMIDE TERMINATED POLYIMIDES



outlined in Figure 1. DMF was used as the reaction solvent and a stoichiometric amount of water was added for the initial hydrolysis step. A catalyst free system was employed for these preliminary studies, however, the reaction rate can be considerably increased by the use of catalysts. The initial reaction mixtures were homogeneous for all compositions investigated (from 20/80 to 80/20 PI/SiO<sub>2</sub> hybrids) at a 20% solids content. Two series of experiments were performed for the above compositions. In the first series, the reactions were carried out under mild pressure conditions [3], up to a maximum temperature of 165°C, according to the time-temperature profile in Figure 3a. All compositions investigated gelled shortly after the reaction temperature reached 100°C. In the second series, the gels were additionally reacted up to 315°C, (above the glass transition temperature of the polyimide component), according to the time-temperature profile in Figure 3b.

Figure 3. Time-Temperature profile for the synthesis of PI-silicate hybrids

Figure 3 a

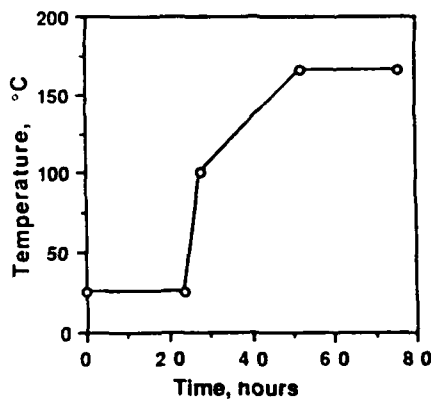
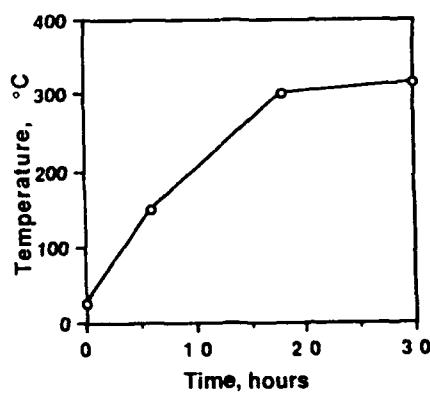


Figure 3b



Analytical TechniquesSpectral analysis

<sup>1</sup>H NMR spectra were measured at room temperature on a Bruker WP 270 spectrometer operating at 270 MHz. <sup>13</sup>C NMR spectra were measured at room temperature on a Bruker WP 270 spectrometer operating at 67.93 MHz. Solid state <sup>29</sup>Si MAS NMR spectra were obtained at room temperature on a Bruker spectrometer operating at 59.61 MHz. Samples were spun at the magic angle at about 7 kHz.

Thermal analysis

TGA-MS was performed using a Perkin-Elmer thermogravimetric analyzer and a Hewlett-Packard 5970 series mass selective detector. A two meter long, 10  $\mu$ m ID deactivated capillary column was used to convey the volatile products from the TGA to the mass spectrometer. The samples were heated in a helium atmosphere from 30°C to 800°C at a heating rate of 30 deg./min. Selected ion chromatograms were obtained at the mass to charge ratio for the components of interest.

## RESULTS AND DISCUSSION

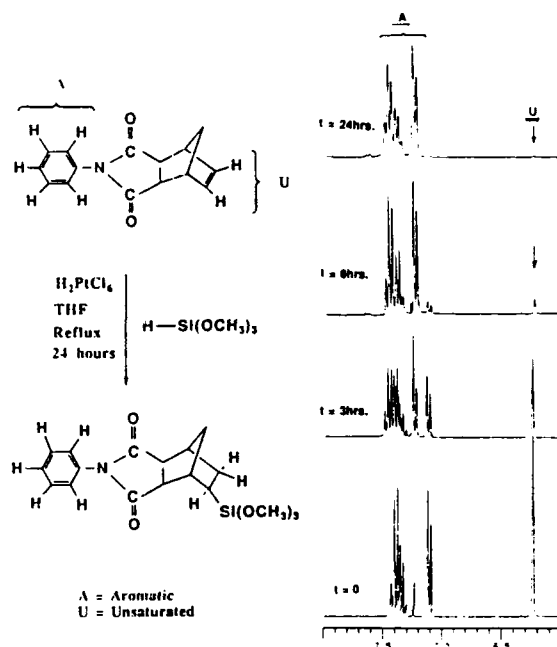
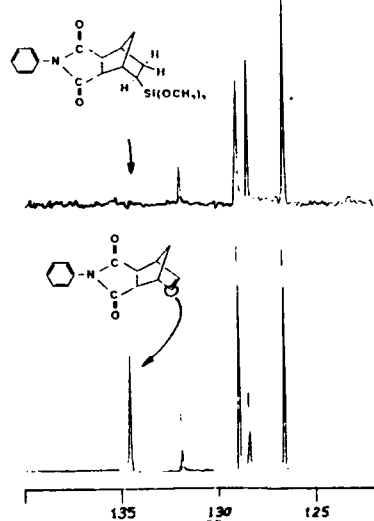
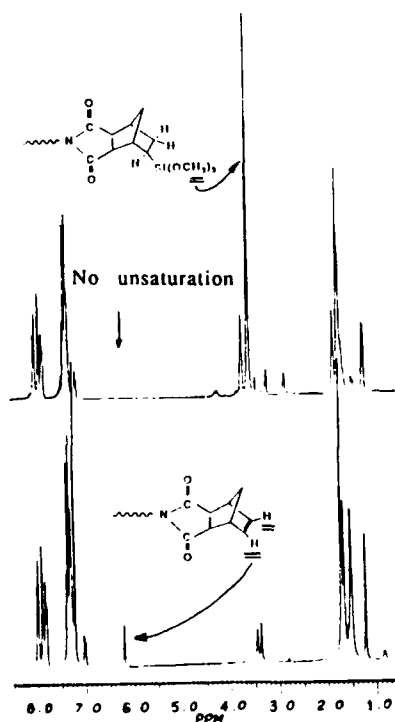
Characterization of methoxy functionalized polyimide oligomersSpectral data

The reaction conditions for complete hydrosilylation at the norbornene double bond have been investigated on a suitable model compound, using <sup>1</sup>H and <sup>13</sup>C NMR techniques. Quantitative reaction occurred after 24 hours at 65°C, as indicated by the complete disappearance of the unsaturation in both <sup>1</sup>H and <sup>13</sup>C NMR (Figure 4 and Figure 5 respectively). An excess of the hydrosilylating agent was required in order to complete the reaction. The same reaction conditions were employed to perform hydrosilylation of the nadimide functionalized polyimide oligomers. A typical <sup>1</sup>H NMR spectra of a polyimide oligomer before and after hydrosilylation is shown in Figure 6. The complete loss of unsaturated norbornene protons (at ~ 6.2 ppm) and the appearance of the methoxy protons (at ~ 3.5 ppm) indicated that quantitative hydrosilylation was achieved.

Thermal data

TGA-MS was employed to study the behavior of the polyimide networks during hydrolysis and condensation reactions under sol-gel conditions. This analysis was performed using a polyimide previously reacted at a maximum temperature of 165°C and ion chromatograms were constructed for molecular species of interest, e.g. CH<sub>3</sub>OH (or CH<sub>3</sub>) and H<sub>2</sub>O (possible by-products of the condensation reactions). Typical ion chromatograms are shown in Figure 7a and 7b for CH<sub>3</sub> and H<sub>2</sub>O respectively. The evolution of both CH<sub>3</sub>OH and H<sub>2</sub>O in the temperature range of 200-370°C can be attributed to condensation reactions taking place during heating. This evolution reaches a maximum at temperatures just above the glass transition of the polyimide (about 250°C for a polyimide oligomer with  $\langle Mn \rangle = 3K$ , as determined by DSC at a heating rate of 10 deg/min), suggesting that faster condensation reactions occur under these conditions. These observations are in agreement with solubility experiments which indicated that the polyimide oligomers became highly insoluble after reaction at 300°C for 30 minutes. Further evolution of the two species (CH<sub>3</sub> and H<sub>2</sub>O) at temperatures above 500°C can be attributed to decomposition processes.

## Model reaction for hydrosilylation at the nadimide double bond

Figure 4.  $^1\text{H}$  NMRFigure 5.  $^{13}\text{C}$  NMRFigure 6. Nadimide and methoxy functionalized polyimide oligomer -  $^1\text{H}$  NMR

TGA-MS for a reference polyimide network. Ion chromatograms for  $\text{CH}_3\text{OH}$  (Figure 7a) and  $\text{H}_2\text{O}$  (Figure 7b) evolution during heating (heating rate 30.0 deg/min).

Figure 7a

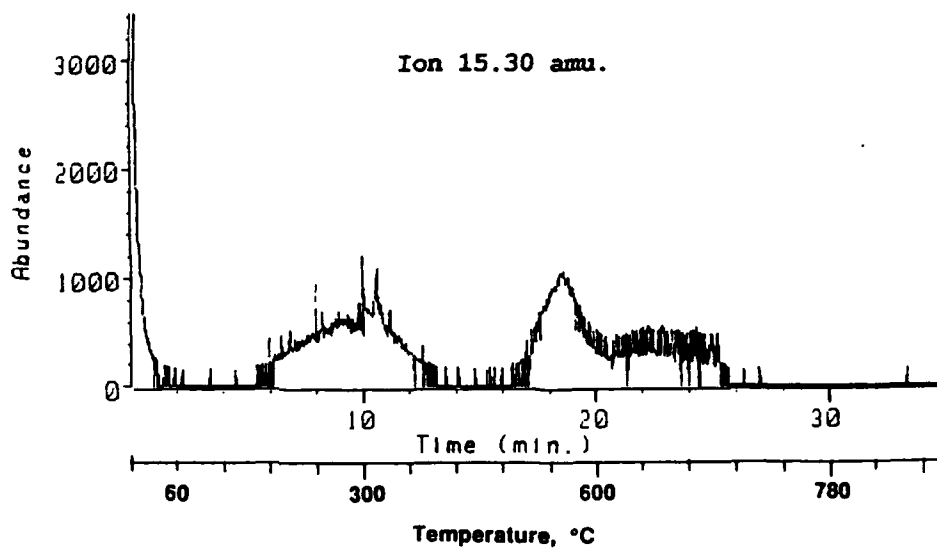
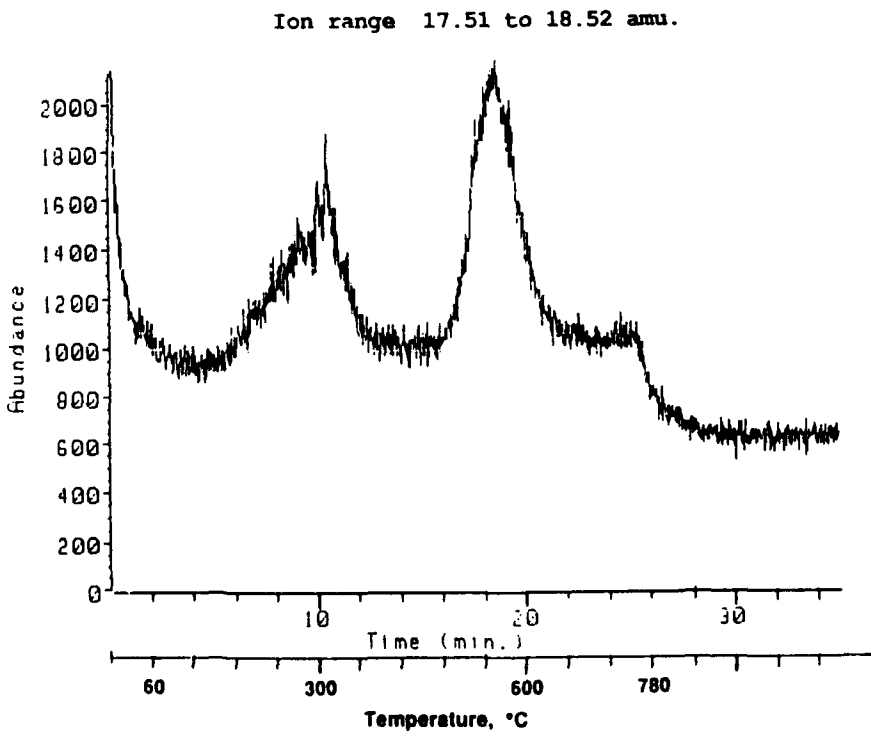


Figure 7b



Characterization of polyimide-silicate hybrids

The extent of conversion with respect to network formation was investigated as a function of hybrid composition and processing temperature using solid state  $^{29}\text{Si}$  MAS NMR. Two main silicon species resonating at about -100 ppm and -110 ppm (with respect to the TMS standard) were observed for all hybrid compositions and both reaction temperatures investigated. These two resonances correspond to branching (T) and network (Q) points respectively, as shown by Kelts et al. [9]. As the reaction temperature increased (from 165°C to 315°C) the percentage of T species decreased and the percentage of Q species increased accordingly, resulting in a higher extent of conversion of the three dimensional networks. The results are summarized in Table I below.

Table I

Effect of hybrid composition and processing temperature on conversion

Max. Processing temp. °C	Hybrid PI/ $\text{SiO}_2$ comp.	% T (mole %)	% Q (mole %)	% Conversion $^{29}\text{Si}$ NMR
165	20/80	40	60	90
	80/20	40	60	90
315	20/80	33	67	92
	80/20	17	83	96

**CONCLUSIONS**

Methoxy functionalized polyimide oligomers were synthesized and successfully co-reacted with TMOS to generate polyimide-silicate hybrids. The extent of conversion of the silicate networks was slightly dependent on both hybrid composition and reaction temperature. The diffusion controlled reaction in the gel state resulted in higher conversions when processing temperatures exceeding the glass transition of the organic polyimide component were employed. Further investigations are necessary in order to determine the optimum processing conditions for the generation of homogeneous, highly consolidated polyimide-silicate hybrids.

Acknowledgments

This work was supported by the AFOSR under Contract No. 86-0133 and by the ONR under Contract No. N00014-88-K-0007. The authors would like to thank T. Glass for his help with the solid state  $^{29}\text{Si}$  MAS NMR. The use of facilities made possible by the NSF Science and technology Center for High Performance Polymeric Adhesives and Composites is also gratefully acknowledged.

## REFERENCES

1. G. L. Wilkes, B. Orler and H. Huang, *Polym. Prep.* **26(2)**, 300, (1985).
2. H. Huang, B. Orler and G. L. Wilkes, *Polym. Bull.* **14(6)**, 557, (1985); *Macromolecules* **20(6)**, 1322, (1987).
3. M. Spinu and J. E. McGrath, *Mater. Res. Soc. Proc.*, April 1989, San Diego, in press.
4. J. D. Summers, Ph.D. Thesis, VPI & SU, (1988).
5. C. A. Arnold, et. al., *Polym. (London)*, **30(6)**, 986, (1989).
6. C. A. Arnold, Y. P. Chen, M. E. Rogers, J. D. Graybeal and J. E. McGrath, 3rd International SAMPE Electronics Conference, Los Angeles, CA, June 20-22, 1989, (1989).
7. C. A. Arnold, J. D. Summers, Y. P. Chen, T. H. Yoon, B. E. McGrath, D. Chen and J. E. McGrath, "Polyimides: Materials, Chemistry and Characterization"; C. Feger, M. M. Khojasteh and J. E. McGrath editors, Elsevier, 69, (1989).
8. S. D. Wu, J. S. Senger, J. C. Hedrick, G. D. Lyle, M. Chen, D. H. Chen, V. Crump and J. E. McGrath, *SAMPE Symposium*, **34(1)**, 139, (1989).
9. L. W. Kelts, N. J. Effinger and S. M. Melpolder, *J. Non-Cryst. Solids*, **83**, 353 (1986).



92-18263



AD-P007 472



187

PROTECTIVE COATINGS FOR HIGH TEMPERATURE, LIGHT WEIGHT,  
STRUCTURAL APPLICATIONS

J. Covino, K. Klemm, and J. Dykema  
Research Department, Naval Weapons Center, China Lake, California 93555-6001

ABSTRACT

Protective coatings for both titanium-aluminum (Ti-Al) alloys and for carbon-carbon (C-C) composites have been synthesized and characterized for high temperature, light weight, structural applications. Coatings of choice must show protection against oxygen and hydrogen in severe environments. Aluminum-silicate glass ceramics were chosen as coating candidates because they are stable to temperatures of 1500°C, are nonreactive to oxygen, and have minimal reactivity with respect to hot hydrogen.

INTRODUCTION

Today there are many novel applications which require temperature resistant, light weight and durable coatings with properties far above presently available materials. Thus much effort is going into the development and characterization of coatings. Coatings of choice are expected to be light weight, have good mechanical properties and show protection against oxygen and hydrogen both at cryogenic conditions and at high temperatures and pressures.

Protective coatings for both titanium-aluminum (Ti-Al) alloys and for carbon-carbon (C-C) composites have been synthesized and characterized with respect to protection against oxygen and hydrogen under both mild environments of low flows and low temperatures and severe environments of high flows and high temperatures. Mixed oxide glass ceramics were chosen as coating candidates because they are stable to temperatures of 1500°C, are nonreactive to oxygen, and are minimally reactive to hot hydrogen. [1] Depending on the chemical composition, these materials have fairly low thermal expansion coefficients ( $\pm 10^{-8}$  to  $10^{-6}$  in the 0 to 600K temperature range). [2] Mixed oxycarbides are also coating materials being investigated. For example SiC is the most oxidation resistant (up to 1640°C) of all carbides.[3] This paper will discuss the chemistry of the coating synthesis and its applications, as well as the characterization of such coatings. The synthetic processes discussed include the Sol-Gel process, Slurry Impregnation, and Chemical Vapor Deposition (CVD). The coatings were characterized using elemental analysis, X-ray diffraction, scanning electron microscopy (SEM), Auger spectroscopy, heat treatments in both hydrogen and oxygen, and some hydrogen permeation measurements.

COATING SYNTHESIS AND CHARACTERIZATION

Coating Synthesis

In our work, we have addressed three different synthetic methods for coating development. These are: (1) the Sol-Gel process; (2) the lacquer-slurry process; and (3) the CVD method.

The Sol-Gel process involves controlled hydrolysis of metal alkoxides, metal salts, or metal organics, followed by controlled dehydration. The Sol-Gel process for coatings is affordable and scalable. Coating composition can be tailored by the solution composition. Coating thickness and uniformity are controllable by solution viscosity, method and rate of application, and sintering conditions. In this work, the Sol-Gel method was used to develop coatings for Ti-Al alloys. The Ti-Al alloys used were the  $\alpha$ -2 Ti-Al and a variety of  $\gamma$  Ti-Al alloys. The coatings applied using the Sol-Gel method are  $\text{Al}_2\text{O}_3$ , Si-Al-Oxide and Si-Al-Ti-Oxide.

The lacquer-slurry process involves the dispersion of powders into an organic lacquer, application of this slurry on the substrate, and sintering of the coated substrate to achieve densification. Coating composition can be controlled by both materials and lacquer selection.

Coating thickness and uniformity is controllable by particle size of dispersing materials, choice of lacquer, and method of application. Coatings using the lacquer-slurry method were only applied on C-C composites and were mixtures of  $\alpha$  or  $\beta$  SiC, Al<sub>2</sub>O<sub>3</sub>, Al<sub>4</sub>C<sub>3</sub> and Y<sub>2</sub>O<sub>3</sub>.

The last type of coating application method investigated was the CVD method. SiC, Si<sub>3</sub>N<sub>4</sub>, ZrC, and Ni coatings were applied to C-C using the CVD method, and characterization of these coatings was performed.

### Coating Characterization

In order to understand processing parameters and coating effectiveness all coatings were thoroughly characterized. The characterization tools used were: elemental analysis, X-ray diffraction, scanning electron microscopy (SEM), Auger spectroscopy, heat treatments in both hydrogen and oxygen, and some hydrogen permeation measurements.

The effectiveness of a coating for hydrogen/oxygen protection is a strong function of its thickness and effective density (determined by application method). But thick coatings can be detrimental in light weight structural applications due to weight and performance. Coating thicknesses were evaluated by the sputter depth profiling technique available with an Auger spectrometer. Table I summarizes the measured coating thickness for many of the coatings characterized in this study.

**Table I. Measured Coating Thickness for a Variety of Coatings.**

Coating material/Substrate	Method of application	Coating thickness
Al <sub>2</sub> O <sub>3</sub> / $\alpha$ -2 Ti-Al	Sol-Gel	1.5 $\mu$ m
Si-Al-Oxide / $\alpha$ -2 and $\gamma$ TiAl	Sol-Gel	1.5-6.0 $\mu$ m
C-C coatings	Lacquer Slurry	0.5 mm
SiC / C-C	CVD	0.3 mm
Si <sub>3</sub> N <sub>4</sub> / C-C	CVD	0.3 (0.17-0.59) mm
Ni / C-C	CVD	0.3 mm
ZrC / C-C	CVD	0.14 mm

Elemental analysis was performed on the Sol-Gel produced Al<sub>2</sub>O<sub>3</sub> and Si-Al-oxide coatings for the Ti-Al alloys. The two coatings produced analyzed as Al<sub>2</sub>O<sub>3</sub> (Al:O ratio of 2:3) and a Si-Al-oxide having a 48-49 mole % of aluminum oxide and 52-51 mole % of silicon oxide.

Micrographs of the Si-Al-oxide coatings on  $\alpha$ -2 Ti-Al alloy show that the coatings are noncrystalline, and of uniform thickness and density even at temperatures as high as 850°C. The measured coating thickness for these samples was 2  $\mu$ m. SEMs were also taken on a variety of slurry coatings containing SiC, Al<sub>2</sub>O<sub>3</sub>, Y<sub>2</sub>O<sub>3</sub> and Al<sub>2</sub>O<sub>3</sub> on graphite and on C-C. The best coating examined for the C-C composite to date has a composition of 50 wt %  $\alpha$ -SiC + 50 wt % YAG (Y<sub>6</sub>Al<sub>10</sub>O<sub>24</sub>). The 50 wt %  $\alpha$ -SiC + 50 wt % YAG coating has good uniformity; it can, however, be chipped. Further research is needed to improve coating properties. Such parameters as soak temperatures, times, atmospheric conditions during soak, and chemical composition need to be adjusted.

Annealing experiments were performed on the Si-Al-oxide (Si (50 mole %) - Al (50 mole %)) and Si-Al-Ti-oxide (Si (50 mole %) - Al (50 mole %) - Ti (2.3 mole %)) coatings to evaluate what happens to the coating morphology as it is heated. The coatings were heated in air for 4 hours at different temperatures. X-ray analyses as a function of temperature for the Si-Al-oxide and the Si-Al-Ti-oxide coatings are reported in Figure 1 and 2 respectively. It can be seen in Figure 1 that the Si-Al-oxide coating does not start to crystallize until 950°C. At temperatures below 950°C this material is amorphous (glass-like). Maintaining the coating in this amorphous state can be used to control coating damage during thermal cycling and service life of the substrate and coating material. Figure 2 shows that 2.3 mole % of Ti shifts the temperature at which crystallization takes place to 1000°C, as compared to 950°C for the Si-Al-oxide coating. The addition of such small amounts of Ti in the coating might improve the thermal, chemical, and mechanical stability of the coating during the lifetime of the coated structure.

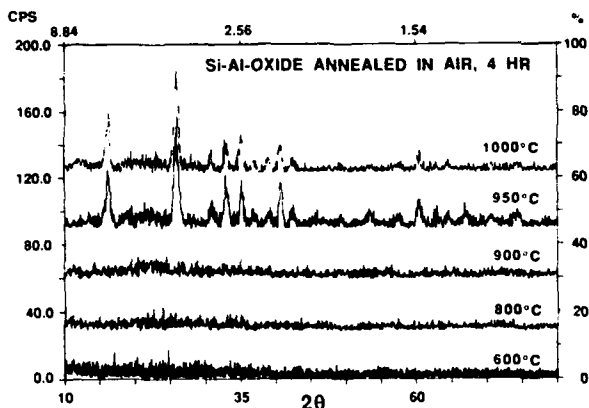


Fig. 1. X-Ray Data as a Function of Temperature for the Sol-Gel Produced Si-Al-Oxide Coating.

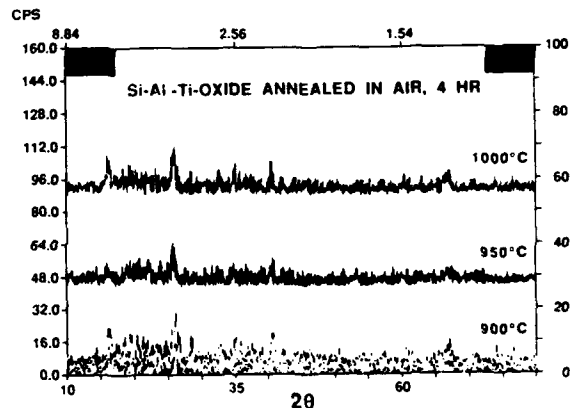


Fig. 2. X-Ray Data as a Function of Temperature for the Sol-Gel Produced Si-Al-Ti-Oxide Coating.

To evaluate  $\text{Al}_2\text{O}_3$  (fig. 3) and Si-Al-oxide (fig. 4) coatings stability on both  $\alpha$ -2 and  $\gamma$  Ti-Al alloy, Thermal Gravimetric Analyses (TGA) were performed in oxygen and in hydrogen/inert gas (either Argon or Nitrogen). TGA data for  $\text{Al}_2\text{O}_3$  coated  $\alpha$ -2 Ti-Al alloy and the  $\text{Al}_2\text{O}_3$  coated  $\gamma$  Ti-Al alloy is shown in Figure 3. While, Figure 4 contains the TGA data for Si-Al-oxide coated and uncoated  $\alpha$ -2 Ti-Al alloys. All TGA data were taken from room temperature to 1000°C at a rate of 2°C per minute.

As reflected in Figure 3, very little weight gain was observed for the  $\text{Al}_2\text{O}_3$  coated  $\alpha$ -2 Ti-Al alloy either in oxygen (1% weight gain) or in 10%  $\text{H}_2$ /90%  $\text{N}_2$  (0.6% weight gain). However, the data show a significant increase in the rate of weight gain from 600 to 1000°C. Furthermore, when the coated  $\alpha$ -2 Ti-Al alloy was removed from the TGA, coating flake-off was apparent. The TGA's show the  $\text{Al}_2\text{O}_3$  coated  $\gamma$  Ti-Al system to be more stable in both oxygen (0.6% weight gain) and 10%  $\text{H}_2$ /90%  $\text{N}_2$  (4% weight gain) than the coated  $\alpha$ -2 Ti-Al alloy. The TGA residue for the  $\text{Al}_2\text{O}_3$  coating showed no signs of separation from the  $\gamma$  Ti-Al alloy. This is consistent with the  $\gamma$  Ti-Al being more oxygen resistant than  $\alpha$ -2 Ti-Al.

Figure 4 clearly shows that the coated  $\alpha$ -2 Ti-Al alloy behaves better than the uncoated alloy in both pure oxygen and in 50%  $\text{H}_2$ /50% Ar (argon). In oxygen, the coated  $\alpha$ -2 Ti-Al alloy gains less than 0.1 wt % as compared to a 6 to 10 wt % for the uncoated material. These data also show that the oxide coating significantly improves the reactivity of the  $\alpha$ -2 Ti-Al alloy in 50%  $\text{H}_2$ /50% Ar. In hydrogen the uncoated  $\alpha$ -2 Ti-Al alloy gains 10 wt % and turns black, while the coated  $\alpha$ -2 Ti-Al alloy gains only 0.6 wt % and has no apparent color change. It should be noted that both in oxygen and in 50%  $\text{H}_2$ /50% Ar, the coated material gains the majority of its weight by 300°C. After 500°C, the weight gain levels off.

The study confirms that the Si-Al oxide coating is more thermally stable than the  $\text{Al}_2\text{O}_3$  coating. For example, in the case of Si-Al-oxide coated  $\alpha$ -2 in oxygen a total weight gain of 0.1% was observed, while for the  $\text{Al}_2\text{O}_3$  coated  $\alpha$ -2 a weight gain of 1% was seen.

Comparison of the H<sub>2</sub> data for the two coating systems is somewhat questionable because the Al<sub>2</sub>O<sub>3</sub> coated  $\alpha$ -2 was heated in H<sub>2</sub>/N<sub>2</sub>, and N<sub>2</sub> is known to passivate Ti-Al alloys, thus making the data appear better than they would in pure H<sub>2</sub>. Ar is basically inert to the Ti-Al alloys.

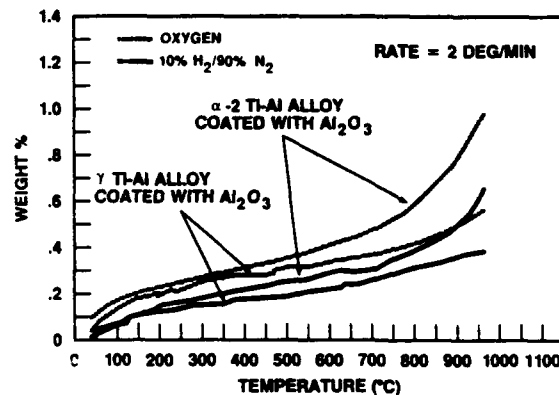


Fig. 3. Thermal Gravimetric Analysis of  $\alpha$ -2 and  $\gamma$  Ti-Al Alloy Coated with Al<sub>2</sub>O<sub>3</sub>.

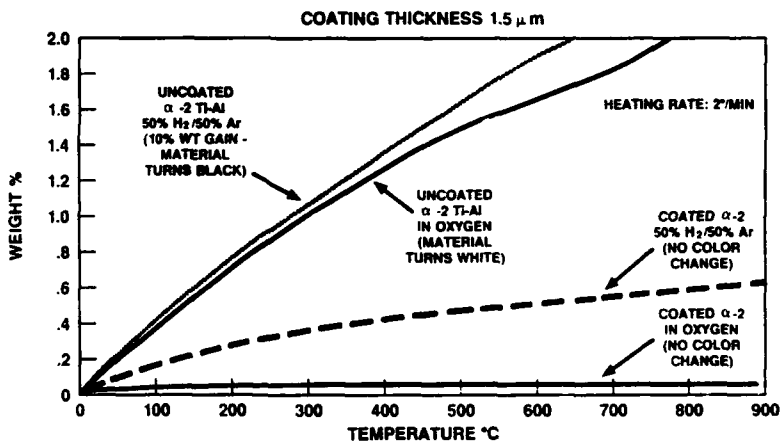


Fig. 4. Thermal Gravimetric Analysis of Uncoated and Si-Al-Oxide Coated  $\alpha$ -2 Ti-Al Alloy.

Knoop Hardness measurements were performed on the coating/substrate materials. Table II summarizes the data. The table can be used to evaluate coating uniformity and relative adhesion to the substrate. The hardness data suggest that the Al<sub>2</sub>O<sub>3</sub> coated  $\alpha$ -2 Ti-Al alloy is not uniform nor well adhered. This is seen by the large interval and standard deviation. On the other hand, the coating for the  $\gamma$  Ti-Al alloy is much more uniform.

TABLE II. Hardness Measurements for Coated and Uncoated Ti-Al Alloys made using a Knoop Indenter with a 500-gram load and 15-s. Dwell Time.

STATISTICAL VALUES	COATING SYSTEM				
	$\alpha$ -2 Ti-Al Alloy Uncoated	$\alpha$ -2 Ti-Al Alloy Coated with Al <sub>2</sub> O <sub>3</sub>	$\alpha$ -2 Ti-Al Alloy Coated with Si-Al-Oxide	$\gamma$ Ti-Al Alloy Uncoated	$\gamma$ Ti-Al Alloy Coated with Al <sub>2</sub> O <sub>3</sub>
MEAN	613.1	578.5	441.3	373.0	377.9
INTERVAL	294.2	658.0	182.5	108.0	140.0
STAND.DEV.	82.9	189.0	64.0	31.7	51.0

Both the coated and uncoated gamma Ti-Al alloys have very similar values for the mean, interval, and standard deviation. The Knoop hardness data for the Si-Al-oxide coated  $\alpha$ -2 Ti-Al alloy suggest that this coating, although softer than the  $\text{Al}_2\text{O}_3$  coating, is better adhered and more uniform than the  $\text{Al}_2\text{O}_3$  coated  $\alpha$ -2 Ti-Al alloy.

Hydrogen permeation experiments were performed as a function of temperature (from 25°C to 300°C) using the "membrane permeation" technique. Details of the permeation method and theory are described by Lynch [3] and Doremus [4]. Data obtained for coated and uncoated C-C composites and for Si-Al-oxide coated and uncoated Ti-Al alloys are illustrated in Fig. 5-7. These data were calculated by subtraction of the measured background level. When the sample achieved a desired temperature it was saturated with deuterium for a 24-hour period to assure equilibrium. To verify equilibrium, three flow rate measurements were made over an eight hour period. If the flow rate was equivalent all three times the value was reported.

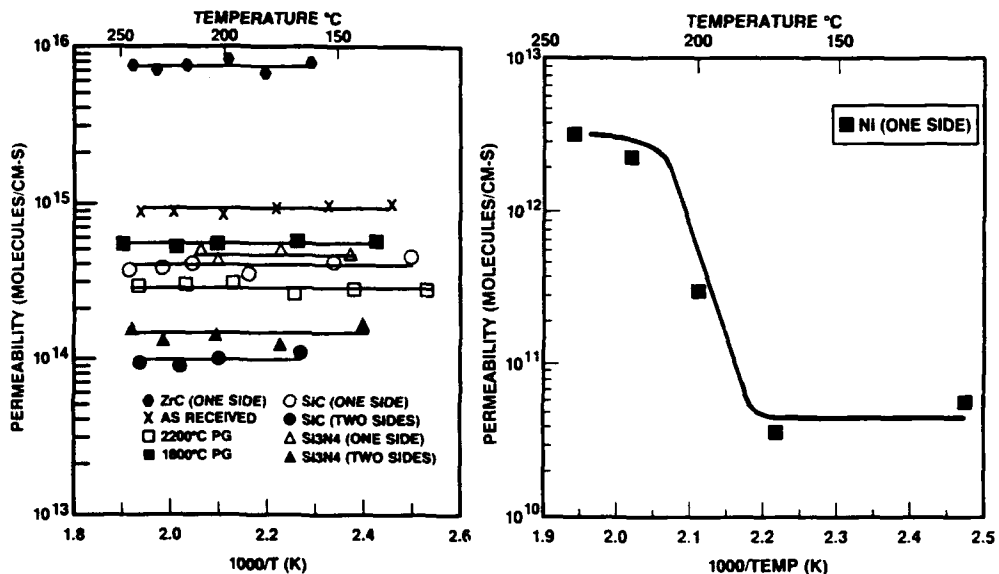


Fig. 5.  $\text{H}_2$  Permeability Vs Temperature for Coated and Uncoated C-C Composites.

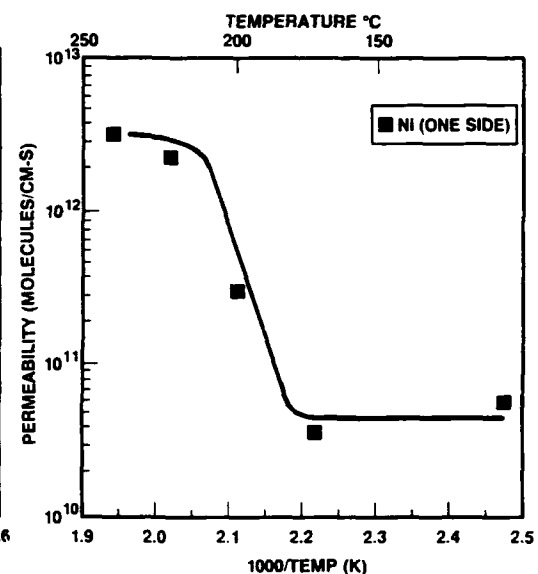


Fig. 6.  $\text{H}_2$  Permeability Vs Temperature for Ni Coated C-C Composite.

Figure 5 shows the permeability vs. temperature data for SiC,  $\text{Si}_3\text{N}_4$ , and ZrC coated C-C composite and for uncoated C-C. The figure key notes whether the C-C composite was coated on a single side or on both sides. The data shows no temperature dependence. This is usually an indication of the samples' having high porosity. The SiC (2 sides) is the least hydrogen permeable coating for the C-C composite measured to date. The permeation data for ZrC coated C-C composite illustrate that out of the coatings evaluated, the ZrC coated by the CVD method tends to degrade the C-C substrate. The permeation data for ZrC coated C-C are higher than even the uncoated C-C composite. Further characterization of the ZrC C-C coating system is continuing in order to better identify changes that are taking place that can cause an increase in the permeation with respect to uncoated C-C.

Figure 6 illustrates permeation as a function of temperature for Ni coated C-C composite. At low temperatures, the permeation of the Ni coated C-C is  $5 \times 10^{10}$  molecules/cm-s; at approximately 200°C the permeation is  $2 \times 10^{13}$  molecules/cm-s. The drastic increase in permeation at approximately 200°C was caused by spalling off of the Ni coating. This was verified by post test visual inspection.

Two Ti-Al alloy having a nominal compositions of Ti-33Al-5Nb-1Ta ( $\gamma$  alloy) and Ti-14Al-20Nb-3.2V-2.0Mo ( $\alpha$ -2 alloy) were coated with a Si-Al-oxide by the Sol-Gel process. The coated samples were annealed to 850°C before any measurements were made. Hydrogen permeation measurements were performed on the coated and uncoated Ti-Al alloys and the data is reported in Fig. 7. The data shows that the hydrogen permeability of

the  $\gamma$  Ti-Al alloy is not very much affected by the 1.5  $\mu\text{m}$  coating while it is drastically reduced for the  $\alpha$ -2 Ti-Al alloy.

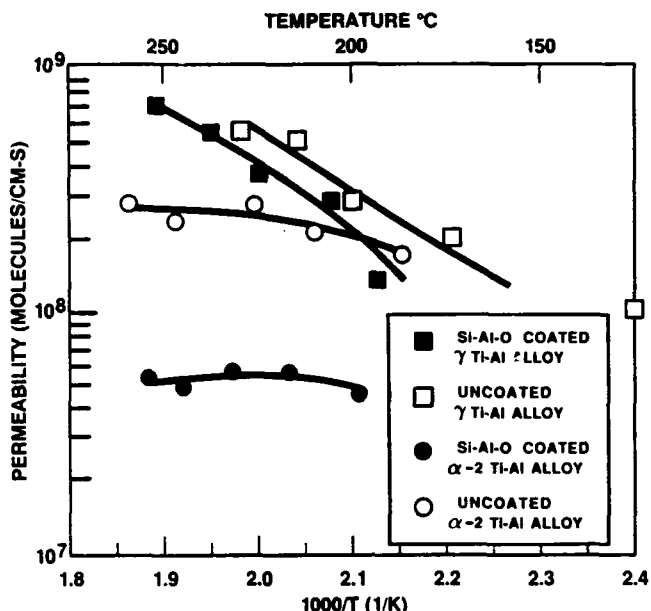


Fig. 7. H<sub>2</sub> Permeability Vs Temperature for Si-Al-Oxide Coated  $\alpha$ -2 and  $\gamma$  Ti-Al Alloys.

## CONCLUSIONS

Coatings made by three synthetic methods, the Sol-Gel, the lacquer-slurry process, and Chemical Vapor Deposition, have been characterized in terms of their survivability in high temperature and hydrogen/oxygen environments. Oxide coatings made by the Sol-Gel process show some improvement in thermal stability and in hydrogen/oxygen environments for the Ti-Al alloys. While the 1.5- $\mu\text{m}$  thick coating of Si-Al-oxide causes a drastic change in the permeability for the  $\alpha$ -2 Ti-Al alloy, it does not change the hydrogen permeability for the  $\gamma$  Ti-Al alloy. A thicker coating may be required for the reduction of permeability for the  $\gamma$  Ti-Al alloy.

The lacquer-slurry coatings applied on C-C composite appear to be the best coatings for C-C known to date. However, much more improvement in the area of stabilizing the adhesion on C-C still remains.

From the coating applied using CVD techniques on C-C composite, all coatings characterized to date have a high hydrogen permeation. The SiC (2 sides) is the least hydrogen permeable coating for the C-C composite measured to date. The permeation data for ZrC coated C-C show that the ZrC coating applied by CVD tends to degrade the stability of the C-C when exposed to hydrogen. For the Ni coated C-C, the permeation started out fairly low ( $5 \times 10^{10}$  molecules/cm-s), and at approximately 200°C it increased sharply to  $2 \times 10^{13}$  molecules/cm-s. Such increase in permeation was caused by spalling off of the Ni coatings.

## REFERENCES

1. A. F. Wells, *Structural Inorganic Chemistry*, Chapter 13, 4th ed. (Clarendon Press, Oxford, England, 1975), p. 1075.
2. J. Covino and J. M. Bennett, *Laser-Gyro Materials Studies*, Naval Weapons Center, China Lake, CA, (NWC TP 6705, March 1986).
3. J. F. Lynch, C.G. Ruderer, & W. H. Duckworth, *Engineering Properties Of Selected Ceramic Materials*, Am. Ceram. Soc., Columbus, OH (1966).
4. R. H. Doremus, *Modern Aspects of the Vitreous State*, Vol. 2, (Butterworths Scientific Publications, London, 1962).





AD-P007 473



193

HIGH COMPRESSIVE STRENGTH ORDERED POLYMER FIBERS AND FILMS  
VIA SOL GEL MICROCOMPOSITE PROCESSING

ROBERT F. KOVAR, RICHARD W. LUSIGNEA, R. ROSS HAGHIGHAT\*,  
CARLO PANTANO\*\* AND EDWIN L. THOMAS\*\*\*  
\*Foster-Miller, Inc.  
350 Second Avenue  
Waltham, MA 02154-1196

\*\*Materials Science & Engineering  
Pennsylvania State University  
University Park, PA

\*\*\*Materials Science & Engineering  
Massachusetts Institute of Technology  
Cambridge, MA 02139

92-18264



ABSTRACT

Sol-gel glass microcomposite processing of polybenzobisthiazole (PBZT) films increased the compressive strength of PBZT/PEEK film laminates by more than four times. The presence of glass within microfibrillar regions of PBZT/sol-gel glass microcomposite films inhibited microbuckling during compression and greatly increased resistance to compressive failure.

Studies of PBZT/sol-gel glass microcomposite film morphology conducted at UMass by E.L. Thomas and at Penn State by C. Pantano indicated sol-gel glass precursor solutions had condensed within PBZT to produce a fine-scale (100 to 300Å) granular structure, homogeneously distributed throughout PBZT lamellae of microfibrils.

In a parallel effort, we have successfully extended sol-gel microcomposite processing technology for the improvement of compressive strength in ordered polymer fibers. Details concerning our results will be discussed.

INTRODUCTION

The purpose of this Small Business Innovative Research (SBIR) program was to develop a new class of microcomposite materials that would exhibit the high tensile strength and toughness of ordered polymers and the excellent compressive strength of glass. During Phase I, we demonstrated the feasibility of improving PBZT ordered polymer film compressive properties by infiltration with sol-gel glass reagents. The Phase II program addressed the following: analysis of PBZT/sol-gel glass morphology, development of sol-gel reagent infiltration processes, lamination of PBZT/sol-gel films and microcomposite of prototype parts to demonstrate improved compressive strength performance over other materials.

In a parallel study, we applied sol-gel technology to the processing of polybenzobisoxazole (PBO) fibers, thereby dramatically increasing their compressive strength from 60 Ksi to 168 Ksi.

PBZT and PBO

PBZT and PBO are members of a new class of polymeric materials collectively referred to as ordered polymers. As a result of their rigid-rod-like molecular structures, these materials form liquid crystalline solutions from which extremely strong, stiff fibers and films have been processed. The U.S. Air Force Materials Laboratory (AFML) has developed rod-like polymers with the best combination of strength, stiffness, thermal capability, and environmental resistance [1-3]. Figure 1 illustrates the molecular structures of PBZT and PBO.

The fiber and film-forming processes involve several operations in which a polymer solution undergoes a succession of structural changes leading to the final solid. In the coagulation stage, a liquid to solid phase transition is induced, either by diffusion of a nonsolvent or by a decrease in temperature. It is reasonable to assume that the structure formed by this phase transition is the basis for the structure of the final solid.

On the basis of electron-microscopic observation, Professors Farris and Thomas from the University of Massachusetts concluded that the structure formed during the coagulation stage of PBZT fiber spinning was an interconnected network of highly oriented microfibrils of 80 to 100 $\text{\AA}$  diam. Figure 2a shows the structural model for a wet coagulated PBZT film [4,5].

The rod-like (fibrillar) microstructure of PBZT and PBO is key to forming a microcomposite, and is the result of processing liquid crystalline solutions of PBZT as outlined below:

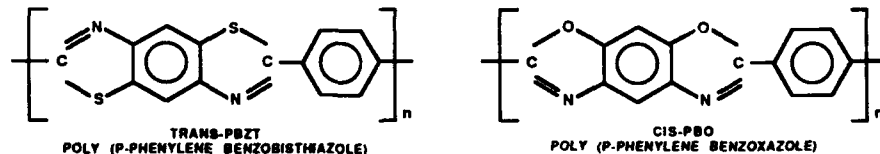


Figure 1. Molecular Structure of PBZT and PBO.

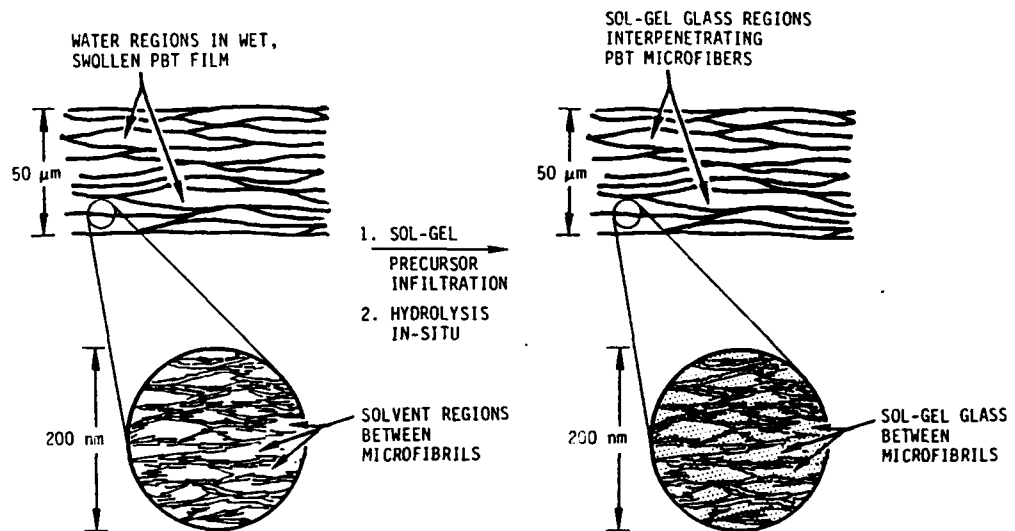


Figure 2. Structure of PBZT and PBO/Sol-Gel Glass IPN Microcomposite Films

- Oriented films are extruded, stretched, sheared, etc., from a nematic (liquid crystalline) low concentration polymer solution, or spinning dope, of PBZT or PBO
- The oriented dope is coagulated with water, causing deprotonation of the rod-like molecules, giving rise to an interlocked PBZT network filled with water and acid
- After a period of time, the acid is washed out by diffusion, leaving a water-swollen PBZT fibrillar microstructure
- Water is removed by evaporation, and under proper constraint the PBZT and PBO will densify to form a high quality film.

It is possible, however, to infiltrate the interior of the swollen fibrillar structure with a variety of materials such as sol-gel glass or organic adhesive binder resins and thus form a microcomposite network. These microcomposites combined the excellent strength properties of PBZT with some unique contributions from the ultrafine network of the infiltrant [6,7]. A structural model for a PBZT or PBO/sol-gel glass microcomposite was illustrated in Figure 2(b).

#### Microcomposite Processing of PBZT Films

The major limitations of ordered polymers were low compressive strength and poor interlaminar adhesion. The low compressive strength is caused by the buckling of the microfibrillar network during compression.

One way to prevent the buckling of ordered polymers is to fill the interior of a PBZT film with a material of high compressive strength, such as glass. Sol-gel glass technology presented an ideal means of producing such a network. Since the glass reagent and the PBZT were both solution-processed, a molecular scale interaction was imminent and an ultrafine ( $<0.1\mu$ ) microstructure was formed.

As a result of their inherent microporosity in the water-swollen state, PBZT films were uniquely suited for development into novel microcomposites, where regions between microfibrils became infiltrated with sol-gel glass. Organic silicon alkoxides were chosen as candidate glass precursors because they hydrolyzed in the presence of water to produce rigid silica glasses of high compressive strength and thermal stability.

Sol-gel processing of glasses and ceramics involved hydrolysis of low molecular-weight monomeric precursors in solution. First, the precursor was reacted with water to form a coherent gel. This resulting gel was then converted to a dense glass or crystalline ceramic under the influence of heat and pressure. During this process, volatiles were evaporated and the porous structure was densified by sintering. Figure 2 illustrates the formation and structure of PBZT and PBO/sol-gel of microcomposite films.

Initially, a wet coagulated PBZT film was infiltrated with sol-gel precursor reagent in an effort to fill the microporous interior of the PBZT with a glass network. Next, a slow drying cycle (devolatilization step) was followed where the microcomposite was dried under tension in order to enhance the high tensile and compressive properties of the ordered polymer microcomposite. Post-heat treatment to 350°C was used to further remove high temperature solvents, while hot-pressing at 400°C/200 psi - the final step of processing - completed the densification and substantially decreased the void volume within the microcomposite.

#### Phase I Results

During the program, we successfully infiltrated a variety of sol-gel reagents into PBZT films, significantly changing their properties. The extent of infiltration was readily controlled by adjusting reagent concentration and film immersion times. PBZT films containing rigid glass and soft elastomer were prepared using selected sol-gel reagents. Certain sol-gel formulations were used to infiltrate, then bind multiple PBZT films together into transparent, consolidated laminates.

#### Phase II Results

In Phase II we improved the compressive strength of PBZT films in laminate form more than fourfold by microcomposite processing the films with sol-gel silica precursor reagents. This process filled the microfibrillar network formed during coagulation of PBZT ordered polymer film with high compressive

strength sol-gel derived silica glass, which prevented microbuckling during compressive loading.

The glass also provided a means for bonding films into laminates, since it became mechanically interlocked with the PBZT structure during formation. Since PBZT/sol-gel glass were both processed from solution, their combination formed an interpenetrating, two-phase material with homogeneity on a very fine scale (less than  $0.1\mu$ ). Such a material is known as a microcomposite. Ceramics and glasses exhibit high compressive strength, low tensile strength and brittle fracture. PBZT, on the other hand, has exceptional tensile strength and high toughness, but suffers from low compressive strength. Formation of a PBZT/sol-gel glass microcomposite combined the desirable properties of each component into a new material with greatly improved properties. Sol-gel glass processing was used to introduce glass into the microfibrillar network of PBZT films.

#### PBZT/Sol-Gel Film Laminate Compression Test Specimens

Multi-ply laminates of PBZT/sol-gel glass microcomposite were prepared for direct compressive strength measurements by Rohr Industries. The study marked the first time that direct compressive strength of an ordered polymer reinforced by a sol-gel glass had been evaluated.

$\text{SiO}_2$  was selected as the standard infiltrant to produce two types of PBZT/sol-gel specimens since pertinent data regarding infiltrant diffusion rate and infiltrant concentration versus infiltration time had been already established as reported previously.

The two PBZT/ $\text{SiO}_2$  laminates varied in that one specimen, the microcomposite was staged-dried and heat-treated to  $250^\circ\text{C}$  without pressure prior to lamination. In the second sample, the microcomposite was hot-pressed at 1,500 psi at  $350^\circ\text{C}$  prior to lamination. This additional processing step densified the films and increased their observed stiffness. The densified microcomposite film also exhibited a greater degree of brittleness, probably due to the presence of brittle sol-gel glass domains between microfibrils of PBZT.

Poly (ether-ether ketone) (PEEK) was chosen as the adhesive matrix to bond the individual microcomposite films into a laminate because this resin has been shown to readily bond to PBZT. We have since demonstrated its suitability for use with PBZT/sol-gel films. PEEK was thermally stable to  $400^\circ\text{C}$  and was readily available in film form, making its processing into laminates rapid and convenient. This combination of properties qualified PEEK resin as a suitable adhesive for PBZT/sol-gel microcomposites.

A third PBZT microcomposite film compression test laminate was prepared from IP-600-infiltrated PBZT films and PEEK adhesive resin to demonstrate that organic resin infiltrants could be used to improve compressive strength as well. Infiltrated films were stage-dried and B-staged according to the manufacturer's directions. The films were then hot-pressed under 200 psi pressure at  $300^\circ\text{C}$  to cure the resin and densify the microcomposite. PEEK

adhesive resin was used to bond multiple plies of hot-pressed PBZT/IP-600 film into composite test specimens.

#### Direct Compressive Strength Measurements

PBZT/sol-gel glass microcomposite laminates were tested to determine their compressive strengths. Since an ASTM acceptable test fixture was initially not available at Foster-Miller, Rohr Industries agreed to conduct complementary compressive strength testing on our laminates. Subsequent specimens were tested using a test systems fixture purchased for in-house evaluation of the composites.

#### Rohr Industries Direct Compression Testing

PBZT/sol-gel film laminates bonded with PEEK organic resin were tested at Rohr Industries (courtesy of Mr. Robert Greer). These studies were conducted to demonstrate improvements in the compressive strength of PBZT films by sol-gel processing.

Table 1 illustrates the compression test results for PBZT/sol-gel film composites tested at Rohr Industries. The test results indicated that sol-gel processing of PBZT ordered polymer film using silica sol-gel reagents had significantly improved (84-240%) the compressive strength of film laminates derived from the material, and that predensification of the PBZT/silica microcomposite films at elevated temperature and pressure was necessary to realize the optimum benefit.

Table 1. Compressive Strengths of PBZT/Sol-Gel Glass Microcomposite Film/PEEK Film Laminates (Isotropic Layup)

Sample	Identification	Vol. % PBZT	Isotropic Compressive Strength* (psi)	Isotropic Compressive Modulus (Msi)	Percent Change
FMI-1	PBZT/PEEK Control (0.019 in. thick)	86	9,400	3.69	-
FMI-3	PBZT/SiO <sub>2</sub> /PEEK Not fully densified	51	17,300	2.80	+84
FMI-2	PBZT/SiO <sub>2</sub> /PEEK Densified at 400°C/1,200 psi (0.30 in. thick)	65	23,700	2.60	+150
FMI-4	PBZT/IP-600/PEEK Not fully densified	50	32,000		+240

\*Compressive strengths measured by Bob Greer, Rohr Industries, Chula Vista, CA.

### Foster-Miller Direct Compression Test Experiment

To facilitate timely improvements in PBZT film laminate compressive strength, a Test Systems Technology direct compressive strength measurement fixture was set up at Foster-Miller. This allowed us to quickly evaluate the effects of various microcomposite process changes on the compressive strength of PBZT/sol-gel glass microcomposite film laminates prepared by hot-pressing

PBZT microcomposite films with PEEK thermoplastic film adhesive. A total of 50 composite compressive test specimens were prepared and tested in a series of controlled experiments where individual microcomposite processing parameters were varied. Besides providing valuable information concerning the effects of various process changes upon compressive strength, the above test matrix eventually led to the fourfold improvement of PBZT film compressive strength in laminate form. Table 2 illustrates the results of Foster-Miller compression tests involving PBZT/sol-gel microcomposite film laminates.

### Compressive Strength Versus Glass Content

The maximum compressive strength was realized when the "high draw" PBZT ( $\pm 12$  deg of orientation) network was combined with  $\text{SiO}_2$  sol-gel glass and laminated with PEEK as the adhesive. Figure 3 plots the compressive strength versus the glass content for the PBZT/ $\text{SiO}_2$  sol-gel microcomposites tested. The straight line illustrates the expected rule-of-mixtures values.

The maximum compressive strength,  $K_c = 49$  Kpsi, was realized for a sample containing 40 percent by volume  $\text{SiO}_2$  glass. This laminate was processed from a highly oriented biaxial film of PBZT ( $\pm 12$  deg), and was laminated using PEEK as the adhesive. Cutting the films along the fibril direction improved the compressive strength by increasing the total available load-bearing fibrils as the composite was subjected to compressive loading.

Considering Figure 3 again, it is apparent that at low glass loadings, the compressive strength values deviate from the rule-of-mixtures and a noticeable gain in the compressive strength is realized for minute glass addition. Introducing 1.5 volume fraction of glass into the PBZT matrix increased the compressive strength by more than twofold. Therefore, one may initially conclude that it is the introduction of glass into the PBZT matrix and not necessarily the glass volume fraction which improves the compressive strength. It is likely that glass alters the compressive failure mechanism in such a way as to increase the compressive strength by greater than 300 to 400 percent.

### MORPHOLOGICAL STUDY OF PBZT/SOL-GEL MICROCOMPOSITES

Information concerning the molecular arrangement of PBZT and sol-gel glass components within PBZT/sol-gel glass microcomposite films was important to our

Table 2. Foster-Miller Compressive Strength Test Results for  
PBZT/Sol-Gel Glass Microcomposite Film Laminates

Description	Film Orientation Angle with Respect to Machine Direction	Sol-Gel Content (Vol %)	Average Compressive Strength (Kpsi)	Comments
PBZT/PEEK $\pm 12$	0	13.2 (2.4)*		
PBZT/SiO <sub>2</sub> /PEEK	$\pm 12$	1.5	25.0 (3.6)	
PBZT/SiO <sub>2</sub> $\pm 12$	3	35.0 (2)		
PBZT/SiO <sub>2</sub> $\pm 12$	5	28.0 (4.2)		
PBZT/SiO <sub>2</sub> /PEEK	$\pm 12$	7	29.0 (4.6)	
PBZT/SiO <sub>2</sub> $\pm 12$	18	25.9 (1.2)		
PBZT/SiO <sub>2</sub> /PEEK	$\pm 12$	20	32.4 (4.10)	
PBZT/SiO <sub>2</sub> /PEEK	$\pm 12$	40	32.9 (4.4)	
PBZT/SiO <sub>2</sub> /PEEK	$\pm 12$	40	10.4 (3.2)	Dicromate acid etch
BZT/SiO <sub>2</sub> /PEEK	$\pm 12$	40	0.5 (4.0)	Thin PBZT film
PBZT/SiO <sub>2</sub> /epoxy 1-2-3	$\pm 12$	11	13.0	
PBZT/SiO <sub>2</sub> /epoxy structure	$\pm 12$	40	23.2 (8.8)	
BZT/SiO <sub>2</sub> /PEEK	$\pm 12$	40 49 (max)	43.5 (3.5)	Film cut along primary orientation direction
PBZT/lead borate/PEEK	$\pm 12$	40	3.0 (-)	Lead borate decomposition
PBZT/lead borate/epoxy	$\pm 12$	40	10.5	
PBZT/PEEK $\pm 34$	0	8.6		
PBZT/SiO <sub>2</sub> /PEEK	$\pm 34$	18	16.5 (6.6)	
PBZT/SiO <sub>2</sub> /glass adhesive	$\pm 34$	18	15.0 (0.5)	

\*Standard deviation in Kpsi

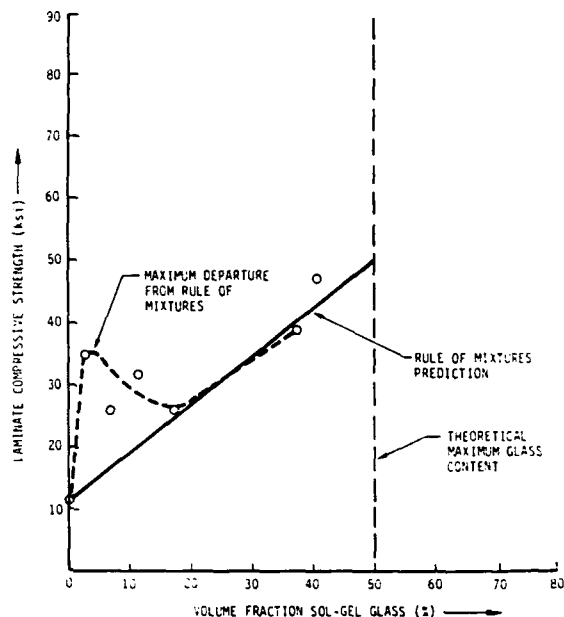


Figure 3. Variation of PBZT/Sol-Gel Microcomposite Film Laminate Compressive Strength with Sol-Gel Glass Content

understanding the mechanism for compressive strength improvement. Techniques for further extending compressive strength were revealed by the morphology of microcomposite films that had exhibited the highest increases.

Complementary morphological studies were conducted by Professor Edwin L. Thomas at the University of Massachusetts, Amherst, and Professor Carlo Pantano at Pennsylvania State University. The studies were undertaken to elucidate the morphology of PBZT/sol-gel glass microcomposite films and the mechanism for compressive strength improvement imparted to PBZT films during the microcomposite process. Details concerning the results of each study are presented in the appendices attached to the Phase II final report [9]. The studies are summarized here to familiarize the reader with the significance of their findings and to report that they verified the formation of a true microcomposite, with domain sizes smaller than  $0.1\mu$ , during sol-gel processing of PBZT film. Figure 4 shows a TEM micrograph of PBZT/sol-gel  $\text{SiO}_2$  film with domain size smaller than  $0.1\mu$ .

The results of the University of Massachusetts and Pennsylvania State University morphological studies confirmed that sol-gel processing of PBZT films had produced microcomposite structure, with dimensions smaller than  $0.1\mu$ , where the spaces between PBZT microfibrils had become filled with a matrix of sol-gel glass. Support of the PBZT microfibrillar network against buckling by the sol-gel glass matrix was manifested by an observed fourfold



Figure 4. TEM Micrograph Showing Sol-Gel Silica within a PBZT/Silica Microcomposite Film. The Domain Size is Smaller than  $0.1\mu$  (100 nm).  
(Courtesy of Professor Carlo Pantano, Penn State)

improvement in compressive strength of PBZT/sol-gel silica microcomposite film/PEEK film laminates versus untreated control laminates. However, microscopic analysis of failed film laminate compression test specimens indicated that improved adhesion between sol-gel glass-modified PBZT film surfaces and PEEK matrix resin might have played a part as well. The importance of hot-pressing to the densification and subsequent improved compressive performance of PBZT/sol-gel microcomposite films was verified.

#### PBO/Sol-Gel Microcomposite Fibers

During this interim, two opportunities for direct compression testing of sol-gel processed PBO fibers were presented by Dr. Wade Adams and Dr. Ivan Goldfarb of WRDC, Wright-Patterson AFB, OH. In the first method, PBO/sol-gel glass microcomposite fibers, sol-gel processed at Foster-Miller, were tested at WRDC for compression strength by the fiber recoil method. This test method (illustrated in Figure 5) involved tensioning the fiber to a specified load below its breaking point, then quickly cutting the fiber, causing each end to snap into compression. The broken fibers were then examined under a microscope for the presence of kink bands indicating evidence for compressive failure of the fiber. The load placed upon each new fiber specimen was

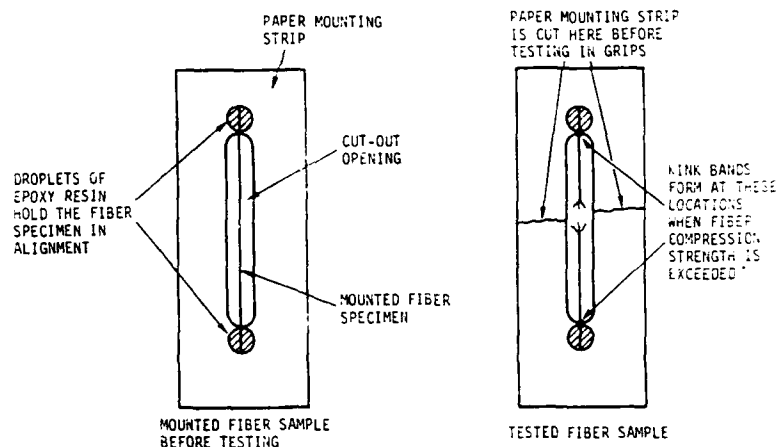


Figure 5. Configuration of Mounted Fiber Compression Test Specimens

increased until repeated compressive failure (kinking) was observed. The compressive strength of the fiber was then calculated.

Table 3 presents the results of preliminary PBO/sol-gel glass microcomposite fiber recoil testing conducted at WRDC. The test results indicated that sol-gel silica infiltration had improved the compressive strength of PBO fiber by 25 percent and the Thermid IP-600 infiltration improved the same property by more than 40 percent. However, extensive damage had occurred to the fibers during handling, as evidenced by their fibrillar appearance and the presence of kink bands before testing. Further testing of PBO/sol-gel glass microcomposite fibers at WRDC was planned for the future, using modified processing and handling techniques to minimize fiber damage and maximize compressive strength improvement.

In a separate series of tests, water-swollen PBO fiber tow, generously supply by Dow, was processed into PBO/sol-gel silica microcomposite fibers at Foster-Miller, then submitted for measurement of compressive strength by a novel technique [8]. This method involved the embedding of single PBO/sol-gel silica microcomposite fibers within dogbone-shaped castings of transparent epoxy resin, as illustrated in Figure 6. The vertically mounted epoxy castings were then compressed, and the fibers were observed carefully for the onset of kink band formation, an indication that compressive failure of the fiber had occurred. Table 4 presents the results of this preliminary study on sixteen batch-processed PBO fibers, which indicated more than threefold improvement in compressive strength. Although this degree of relative improvement in compressive strength had already been achieved with PBZT films during this program, these results were more significant because the untreated control compressive strengths of PBO fiber were so much higher. The high

Table 3. Compressive Strengths of Preliminary PBO/Sol-Gel Microcomposite Fibers

Sample	Compressive* Strength Ksi
PBO control fiber	30
PBO/silica	40
PBO/sodium borosilicate	26 to 30
PBO/5 percent Thermid IP-600	45 to 56

\*Compressive strengths of fiber samples were determined at WRDC using the fiber recoil method.

value of compressive strength for PBO/sol-gel silica microcomposite fibers suggests application of these unique materials as advanced aircraft and spacecraft structures.

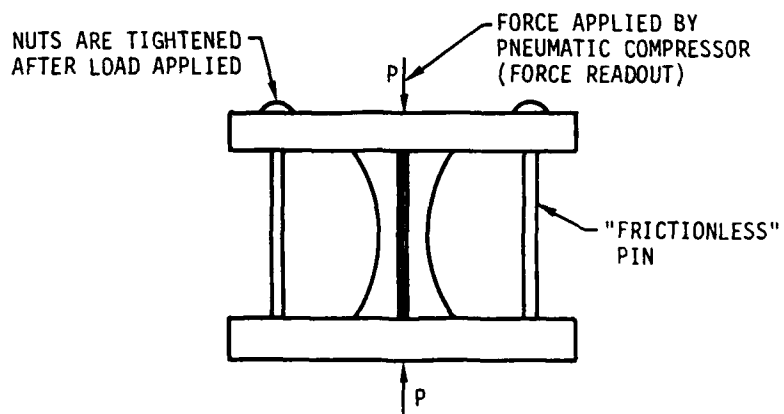


Figure 6. Illustration of Epoxy Resin-Embedded Fiber Sample under Compression

Table 4. Mechanical Properties of Foster-Miller PBO/Sol-Gel Silica Microcomposite Fibers\*

Sample	Compressive Strength (Ksi)	Fiber Diameter ( $\mu$ )	Tensile Strength (Ksi)	Fiber Modulus (Msi)
PBO fiber as-received	45 $\pm$ 11 (27)	20 $\pm$ 2 (39)	488 $\pm$ 79 (29)	26 $\pm$ 24 (20)
Foster-Miller PBO control**	60 $\pm$ 15 (12)	19 $\pm$ 2.7 (20)	424 $\pm$ 74 (16)	28 $\pm$ 2.4 (13)
PBO/sol-gel silica	168 $\pm$ 31 (16)	21 $\pm$ 2.6 (19)	358 $\pm$ 41 (15)	19 $\pm$ 2.1 (11)

\* Tests were conducted by Professor Lawrence Drzal at Michigan State University.

\*\* Foster-Miller PBO control fiber was stage-dried to 350°C.

\*\*\* Tests conducted according to ASTM 03379.

Note: This compressive strength test procedure assumed that PBO fibers remained strongly bonded to the epoxy resin matrix during compressive loading. The numbers in parenthesis represent the number of samples tested.

#### SUMMARY

Our efforts on the ordered polymer sol-gel microcomposite processing program enabled us to achieve four major goals. First, we improved the compressive strength of PBO fibers from 60 to 168 ksi, with only 15 percent loss in tensile strength by sol-gel processing the water-swollen PBO fiber tow. A study of the morphology in PBO/sol-gel glass microcomposite fibers exhibiting such high compressive strength values will be the subject of a future report. Second, we increased the compressive strength of PBZT/sol-gel glass microcomposite film/PEEK film laminates from 8 to 49 ksi by application of similar treatments to water-swollen PBZT films. Third, we developed methods for laminating multiple plies of PBZT/sol-gel glass microcomposite film into thick, rigid composite structures through the use of PEEK thermoplastic resin adhesive. Fourth, working with the University of Massachusetts and Pennsylvania State University, we elucidated the mechanism for compressive strength improvement in these novel materials by studying their morphology and microstructure. These successful results were obtained by applying technology developed during the Phases I and II microcomposite programs.

The attainment of such high compressive strength values for PBO/sol-gel silica microcomposite fibers has helped to solve the major problem inhibiting the application of these materials as advanced spacecraft and aerospace structures; namely, poor compressive strength. The pathway to their immediate development is now open. Foster-Miller will team with Dow and major aircraft manufacturing companies to exploit this novel technology during Phase III of this SBIR program.

## REFERENCES

1. Allen, S.R., A.G. Filippov, R.J. Farris, E.L. Thomas, C.P. Wong, G.C. Barry, and E.C. Chenevey, Macromolecules, **14**, 1135 (1981).
2. Allen, S.R., A.G. Filippov, R.J. Farris, and E.L. Thomas, "The Strength and Stiffness of Polymers," A.E. Zachariades and R.S. Porter, eds., Marcel Dekker, New York (1983).
3. Wolfe, J.F., B.M. Loo, and F.E. Arnold, Macromolecules, **14**, 915 (1981); Mark, J.E., and S.J. Pan, Macromolecules, Rapid Comm. **3**, 681-685 (1982); Ning, Y.P., M.Y. Tang, C.Y. Jiang, and J.E. Mark, Journal App. Poly. Sci., **29**, 3209-3212 (1984).
4. Pottick, and R.J. Farris, "Alterations in the Structure and Mechanics of PBT Fibers due to the Collapse Process During Drying,: Nonwovens Symposium (April 1985).
5. Cohen, Y. and E.L. Thomas, Macromolecules **21**, 433 (1988).
6. Lusignea, R.W., Research in Progress, "Processing Rod-Like Polymers," Contract No. F33615-84-C-5120. "Ordered Polymers for Large Mirror Substrates," Contract No. F33615-85-C-5009.
7. Proceedings of the First International Workshop on Glasses and Glass Ceramics from Gels, J. Non-Crystalline Solids, **48**, 1-2 (1982).
8. Drzal, L.T., "The Interfacial and Compressive Properties of Polybenzothiazole Fibers," AFWAL-TR-86-4003 (1986).
9. Kovar, R.F., R. Haghigat and R.W. Lusignea, "Microcomposite Processing and Applications," AFOSR Phase II Final Report No. AFB-0022-FM-8689-93.

## ACKNOWLEDGEMENTS

We thank Dr. Donald Ulrich and AFOSR for the Phase I and Phase II SBIR funding that led to the development of sol-gel microcomposite processing. We also gratefully acknowledge the assistance and cooperation of Drs. Wade Adams and Ivan Goldfarb of WRDC in fiber-recoil compression testing and of Michigan State University in epoxy resin-embedded compression testing of PBO/sol-gel fibers. The generous supply of high quality, water-swollen PBO fibers from Dow is greatly appreciated.



AD-P007 474

207



## The Influence of Sol-gel Glass Technology on Coherent and Partially Coherent Optical Imaging Systems

NICHOLAS J. PHILLIPS

Reader in Physics

Loughborough University of Technology

Loughborough

Leicestershire

LE11 3TU

92-18265



### Abstract

This paper addresses developments in the understanding of intra-cavity elements in ion lasers using sol-gel prepared silica. Growing interest centres around the generation of coherent light in the near u.v. spectrum. Sol-gel silica offers unprecedented levels of purity and homogeneity for critical intra-cavity applications and may well solve the problem of creating colour-centre free Brewster windows for use in the u.v.

We also report new work which makes use of the porous phase of such material and show how it is directed at one of the early bastions of photographic science - Lippmann's photography.

### 1. Introduction.

Sol-gel derived silica is assuming considerable importance for a variety of physical reasons. Firstly the use of low-temperature processes in manufacture means that unprecedented levels of purity can be achieved. Secondly, the various phases of manufacture mean that different types of physical structure are available from the one material.

The fully densified phase of gel-silica is of great interest in optics because it offers the prospect of optical elements with unusually good transmissivity ranging from the infra red (including the difficult water absorption bands) through to the ultra violet (near to the u.v. band gap).

When the material is only partially densified then it exhibits voiding which itself is of interest because it can lead to modification of the refractive index of the material and hence to the generation of graded index optical elements.

Our interest is twofold. Firstly, we are interested in the application of gel-silica to intra-cavity optical elements for lasers. Secondly, as a result of a worldwide interest in the integration of polymers into porous silica matrices we have embarked on a programme of study of optical elements recorded in imaging polymer which is itself embedded in porous silica.

We choose two topics for discussion. The first of these is related to the performance of the argon-ion laser at the 363.8 nm line in the ultra violet. We shall report on fundamental studies related to laser output and applications to non-contact lithography in the u.v. for the production of micro-circuits. Our second topic relates to the porous phase of the material and an interesting application in partially coherent optical imaging related to the colour photographic process of Lippmann (c 1896).

## 2. Basic Intra-cavity Studies Related to Sol-gel Elements in Ion Lasers.

Our interest has centred on the improvement of ion lasers by the utilisation of low loss elements in the optical cavity. The two critical areas here are (a) the intra-cavity etalon and (b) the Brewster windows at the ends of the plasma tube.

For the study (a), we have devised a novel form of interferometry which analyzes the thermal expansion and the change of refractive index which occurs on expansion. The two interferometric regimes are shown below.

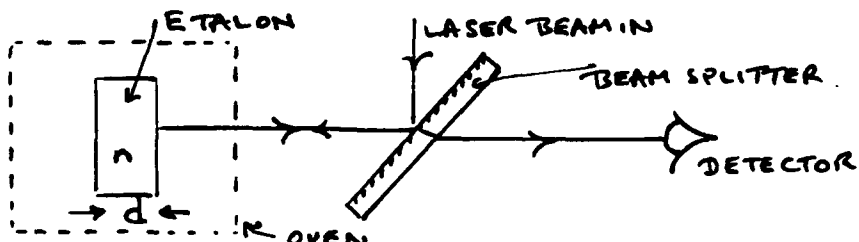


Figure 1. Thermal ramp experiment.

In this experiment an etalon is heated in a thermally ramped oven and a detector measures the light reflected off the etalon. Such reflection includes both the Fresnel component of the front surface and the coherent addition of partial waves reflected off the second face and subject to multiple internal reflection. Typical results are shown below:

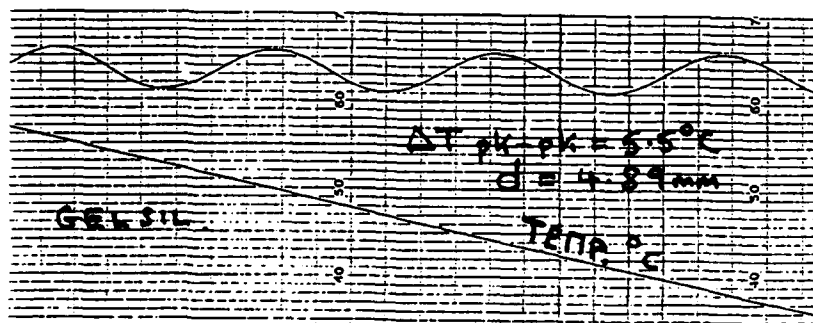


Figure 2. Typical reflection results for light reflected off a thermally ramped etalon.

Great care has to be taken with the accuracy of the thermal ramp and our system uses a 12 bit resolution digital driver to ensure the necessary accuracy.

The thermal ramp experiment in fact provides a measure of the quantity  $\phi = \frac{4\pi n d}{\lambda_a}$  where  $n$  is the refractive index of the etalon and  $d$  its thickness. Thus the important optical phase shift parameter

$$\phi = \frac{4\pi n d}{\lambda_a} \quad (2.1)$$

where  $\lambda_a$  is the interrogation wavelength in air, is subject to change as the temperature of the etalon is changed. We note that increments of  $\phi$  are generated thus

$$\Delta\phi = \frac{4\pi}{\lambda_a} (n d + d \Delta n) \quad (2.2)$$

The reflectivity peaks in the thermal ramp experiment are incrementally separated by the condition  $\Delta\phi = 2\pi$ . Unfortunately, the measurement of  $\Delta\phi$  itself is not sufficient to measure  $\Delta d$  and  $\Delta n$  separately. The experiment measures their sum according to equation (2.2).

A second experiment is now under way which measures  $\Delta d$  directly:

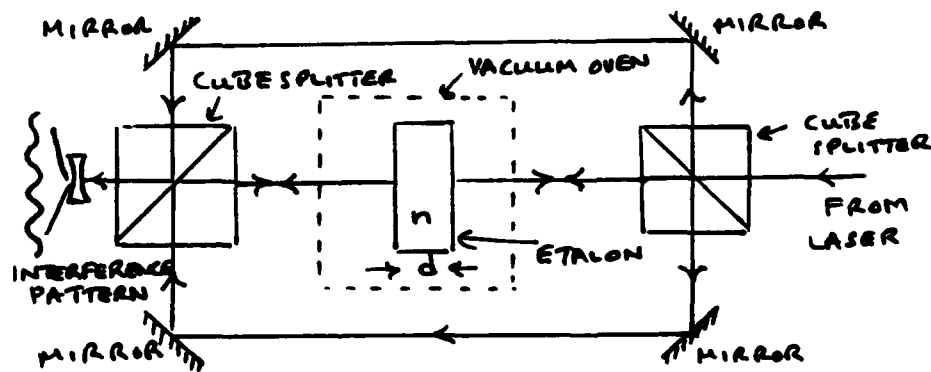


Figure 3. Measurement of  $\Delta d$  using direct interferometry.

The complexity of this experiment is brought about by the need to avoid errors due to displacement of the optical sample. The two beam paths permit interrogation of the two faces of the etalon simultaneously and the interferometer is only sensitive to relative movement of the two faces.

Whereas the simple thermal ramp experiment is insensitive to its laboratory environment (except within the oven) this second experiment is

much more demanding. This is due to the fact that air path changes outside the etalon contribute phase shift errors in excess of the phase shift under measurement. For this reason, a vacuum oven is under construction in order to remove the air path effect. Evidently, the whole experiment needs to be designed wisely in order to provide results commensurate with its potential accuracy. We note that the first measurement (thermal ramping and reflectance) is externally incoherent since the detector measures the intensity of the reflected light. The interference takes place **within** the etalon itself. The second experiment has a much more complex structure and it is an **external** view of the etalon that is being observed.

In the second experiment, we measure  $\Delta d$  directly using the condition

$$\frac{2\Delta d}{\lambda_a} = 1 \quad (2.3)$$

for the separation of the interference maxima and noting that

$$\alpha = \frac{1}{d} \frac{\Delta d}{\Delta T} = \frac{1}{d} \frac{\lambda_a}{2} \frac{1}{\Delta T} \quad (2.4)$$

where  $\alpha$  is the thermal expansion coefficient and  $\Delta T$  is the temperature increment required to produce a shift of one fringe.

It should, with a little ingenuity, be possible to amalgamate the two experiments to read out  $\Delta d$  and  $\Delta n$  in an elegant fashion.

Quoted values for  $\alpha$  are very small for silica and our aim is to confirm or otherwise these numerical values. In the future, the precision of measurement will have to increase if titania-silica mixtures exhibit their promise of virtually zero expansion.

#### **Brewster windows:**

Advances in plasma tube technology have been considerable but the bottom-line problem for ion laser tubes is the quality of the windows at the end of the tube. Such windows must be impeccably flat, free of strain and have exceptionally low levels of scatter and absorption.

Windows can exhibit poor performance from the outset but often degrade during the lifetime of the laser due to colour centre formation. Working in the near u.v., windows have a tendency to become cloudy with the passage of time and the precise damage mechanisms are not yet understood. It is clear that organic contaminants in the neighbourhood of a window can 'crack' under the influence of ozone liberated by the local laser beam interaction with air. Thus it is advisable to run windows in an external atmosphere of nitrogen for

serious u.v. applications. When nitrogen is not used, it is customary to clean windows regularly with silica solvents such as ammonium difluoride.

Advances in plasma tube design have created conditions in which the deposition of particles on the inside of the window due to bore erosion has greatly reduced. Thus the advent of ultra pure and ultra stable windows may make a timely contribution to increased laser performance.

### 3. An Application of Coherent U.V. Recording Based on Ion Laser Technology.

Recent developments in holography have lead to the creation of micro circuit images on the surface of silicon slices:

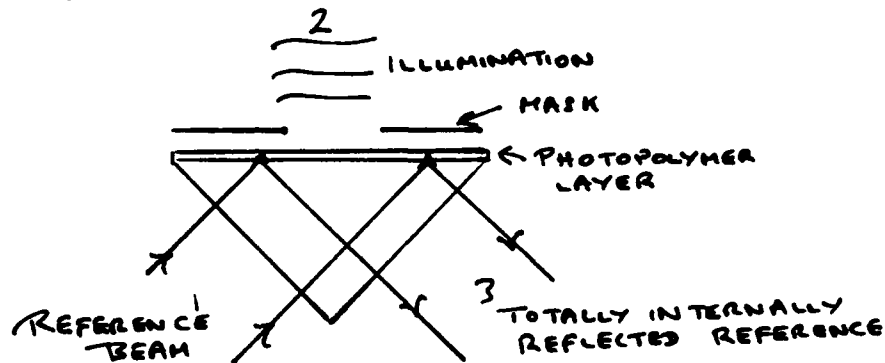


Figure 4. Total internal reflection method for the creation of holograms of precision masks for lithography.

Holograms can now be formed in a thin photopolymeric layer at the surface of a prism. The illumination 2 impinges on the mask at which it diffracts and then interferes with the totally internally reflected reference wave 3. Such holograms can be replayed backwards thus:

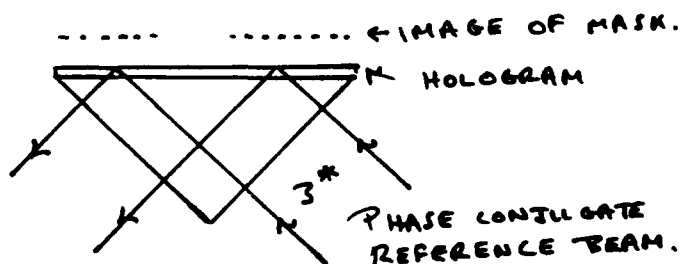


Figure 5. Creation of a projected image from a polymer hologram.

On replay of the hologram, an image of the mask is projected into the air typically some 50 - 100  $\mu\text{m}$  above the hologram surface. The importance of such work is that it can create images with sub-micron resolution and over a large page size. Such technology illustrates the growing importance of coherent optical imaging using ion lasers working in the u.v. part of the spectrum. The cheap polymer layer replaces the normally used and extremely costly imaging lens. Such a lens can account for a significant fraction of the \$1.5 M often encountered in the cost of a conventional stepper apparatus.

The polymer (a product of DuPont) is an example of a medium in which precision images can be formed without any external process procedure. The mechanism of image formation in such a medium is important and can be seen from the diagram below.

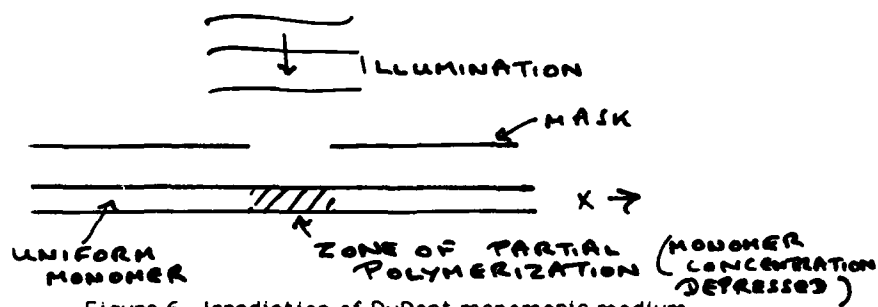


Figure 6. Irradiation of DuPont monomeric medium.

FINALLY  $n = n(x)$  .

$\xrightarrow{\quad} \xrightarrow{\quad} \xleftarrow{\quad} \rightarrow n$  .  
 MONOMER DIFFUSES TO RELIEVE CONCENTRATION GRADIENTS .

Figure 7. A non-uniform refractive index field is formed by diffusion of the monomer.

Such a material can be used in all regimes in which a self processing medium is required. It obviously lends itself to regimes in which embedment is required in a porous medium and we shall discuss such matters in the next section.

#### 4. Porous Silica and Its Role in Imaging Science.

As we have illustrated above, monomeric imaging materials exist that require no local process technology. They are sensitive to the u.v. and once the image is formed (image implying a variable refractive index field) then the result can be made permanent merely by flooding the recording with a blanket of incoherent u.v. thus using up all the available monomer.

Porous gel-silica is a natural product of the stages of formation of gel-silica. Pore sizes can range from the 90 nm bracket of the Swedish Air Glass A.B. product which is an extremely fragile but very light (density  $\approx 1.2$  gm/cc) material used for thermal insulation, down to virtually nothing.

The products of GELTECH have been aimed at a sophisticated market and the densification technology is not in the public domain. GEL-SIL can be obtained in a variety of densified forms and appears a little opalescent at a pore size of some 50 Å.

In most of the porous gel-silica media, it is thought that the pores are interconnected and it is the interconnection that gives rise to the bulk of the Rayleigh scatter which causes the opalescence.

In fact, if scatter is caused by small spherical inclusions of refractive index  $n_s$  in a medium of refractive index  $n_m$ , then scattering theory shows that the inclusions exhibit a Rayleigh scatter cross section  $\sigma_{RS}$  given by

$$\sigma_{RS} = \frac{\pi}{12} \left( \frac{2\pi}{\lambda_a} \right)^4 \frac{n_m^4 (n_s^2 - n_m^2)^2 \Delta^6}{(n_s^2 + 2n_m^2)^2} \quad (4.1)$$

where  $\lambda_a$  is the scattered wavelength in air and  $\Delta$  is the diameter of the scattering centre.

Note that the origin of the scattering can be seen as caused by the difference of refractive index between the medium and the scattering centre. Thus if  $n_s \rightarrow n_m$  the scatter vanishes as it obviously must.

It is this property of index matching that gives so much promise to porous silica optical elements which are filled with imaging or other polymer. For example, the DuPont monomer has a refractive index of approximately 1.5. The silica matrix has a refractive index of value 1.48. The relative scattering of a filled porous matrix as compared to one with air in the voids will then be given by the factor

$$R = \frac{(n_s^2 - n_m^2)^2 (1 + 2n_m^2)^2}{(n_s^2 + 2n_m^2)^2 (1 - n_m^2)^2} \quad (4.2)$$

Choosing the values for  $n_s = 1.5$  and  $n_m = 1.48$ , we have

$$R = 1.65 \cdot 10^{-3} \quad (4.3)$$

and a major reduction of scattering results.

Evidently, the slight opalescence of a porous gel-silica matrix can be killed by void filling with an index matching monomer. This gives great credence to the validity of porous matrix-polymer composite optics.

In fact the author has already seen samples of Soviet work (Popov *et al.* - State Optics Institute of Leningrad) showing clear evidence of the validity of the above arguments and also evidence of some high efficiency diffraction gratings recorded in such media.

### 5. A Novel Use of Porous Silica Media in the Partially Coherent Imaging Method of Lippmann (c 1895).

The author revisited the work of Lippmann in an article in the Journal of Photographic Science Vol.32 1984. (On Lippmann's photography). The central issue is the reproduction of colour using the reflection of quasi-monochromatic light off a mirror:

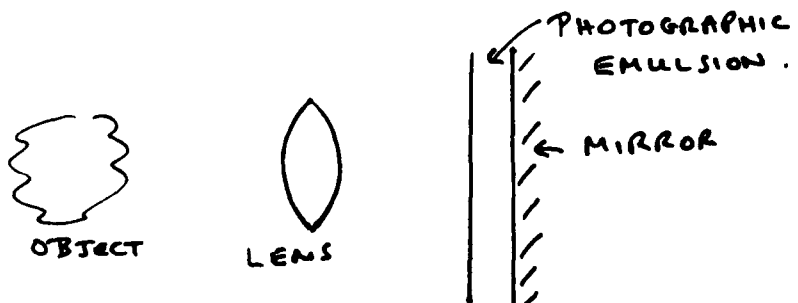


Figure 8. Lippmann's photographic regime.

Here the incoming waves of light reflect off the mirror and an optical standing wave pattern is created in the photographic emulsion. For any elemental wave entering the emulsion from the left, its reflection contains the phase history of the incoming wave. Let us represent the incoming wave amplitude by

$$A_i e^{i\psi - ikx}$$

where  $x$  is a coordinate as shown and  $k = 2\pi/\lambda_a$  where  $\lambda_a$  is the wavelength in air. Then the reflected amplitude is given by

$$A_r = e^{i\psi + ikx + i\phi_r}$$

where  $\phi_r$  is the phase shift on reflection. The addition of amplitudes gives a total amplitude  $A_{\text{tot}}$  (assuming  $A_i \approx A_r \approx A_0$  say)

$$A_{\text{tot}} = A_0 e^{i\psi} [e^{-ikx} + e^{+ikx + i\phi_r}] \quad (5.1)$$

The intensity is given by  $|A_{\text{tot}}|^2$  and is hence

$$I = A_0^2 4 \cos^2 \left( \frac{kx + \phi_r}{2} \right) \quad (5.2)$$

and is independent of  $\psi$ . Essentially, so long as the light is sufficiently monochromatic, a pattern is formed and it is stationary independent of the phase disturbance  $\psi$  of the incoming light.

The practical difficulty of the problem is the process of contacting the emulsion against the mirror in a way that provides good optical matching and at the same time permits disassembly of the system to allow processing of the emulsion. Historically, mercury used to be used. Nowadays, its toxicity rules it out for serious use.

Our early approach has been to use a film layer and a metallised mylar mirror. They are contacted together and hold on to each other by Van der Waals contact using a contact fluid. We established that one has to wait until surplus fluid has disappeared from the contact interface. At that point, an extremely tough bond between the emulsion and the mirror results:

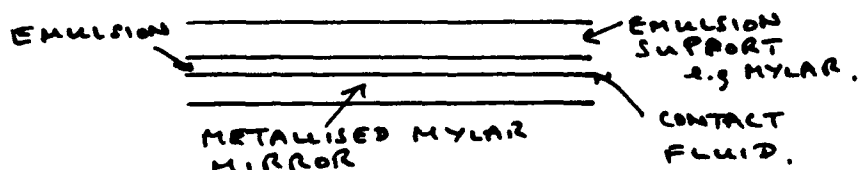


Figure 9. Contact technology for Lippmann photography.

We found that the method depends crucially on evaporation or loss of surplus contact fluid thus requiring that a minimal - (probably a few molecular layers) thickness of fluid be achieved by whatever loss mechanisms are present.

We are now clear that it is the leaking of contact fluid - probably in vapour form through the film layer and through the metallised base that permits this necessary loss mechanism. It is clear that this permits the establishment of what we might call 'hyper contact' between the sensitive film and metallised mirror.

A new approach is now under investigation. This is made possible by the advent of porous glass. The mirror is replaced by porous glass overcoated with aluminium. Clearly the pore sizes and thickness of aluminium overcoat must be considered so that the pores are not blocked.

Such a regime permits capillary and evaporative loss of surplus contact fluid and this is now under investigation:

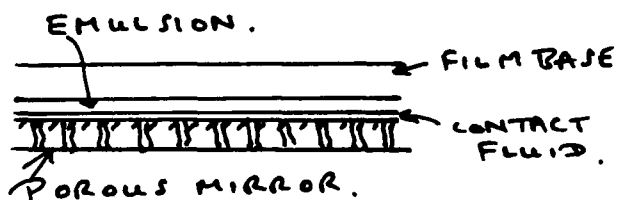


Figure 10. Lippmann contact process using porous mirror support.

Solving this problem will permit generation of archivally permanent colour photographs often unsuccessfully achieved in Lippmann's time. Our brief is to produce modern versions in full colour and using robust and healthy technology.

## 6. Conclusions

This paper has touched on areas of physical interest that link to the emerging sol-gel glass technology.

Evaluation of optical elements in laser cavities is a subject still in its infancy. However the prognostication for sol-gel silica is very good. It is too early to comment on the competitiveness with high temperature prepared silica but the ground rules are now established and the definitive expansion measurements will be available soon.

The porous phase of the material offers exciting prospects and in combination with novel imaging polymers, we should see significant progress in the formation of polymer-silica complexes for optical element production.

The inclusion of Lippmann's photographic process in our discussion serves to make the point that there are areas of classical physics which can take new shape as a result of emergent materials technology



92-18266

AD-P007 475



DESIGNING PORE-SIZE IN SILICA GELS: [H<sub>2</sub>O] - [TMOS] SYSTEM

H. KIDO, P. B. MALLA, AND S. KOMARNENI

Materials Research Laboratory, The Pennsylvania State University, University Park, PA 16802.

ABSTRACT

A series of microporous silica gels were synthesized by hydrolyzing tetramethyl-orthosilicate (TMOS) with varying amounts of water. No catalyst or alcohol was added. The gels were characterized by water sorption isotherms, the BET nitrogen surface area measurements, and differential thermal analysis. Although the gelation time for all H<sub>2</sub>O/TMOS molar ratios (R) was approximately the same (about 3 hr), the pore-size (pore diameter) and sorption capacity were found to be minimum in the R range 4.96-5.37 but increased with both increasing and decreasing R. Water sorption isotherms measured at 25°C after degassing at 200°C of gels prepared with R = 4.96-5.37 exhibited moderate Type I (Brunauer classification) isotherm which changed to intermediate between Type I and Type IV with decreasing or increasing R. These results indicated that the amount of organic or water which was not utilized in the reaction and the degree of cross-linking apparently played a role for the observed variations in pore-size or shape of water isotherms.

INTRODUCTION

Porous solids are known to be ideal candidates for catalytic activities and for the study of the effect of confined space on the properties of fluids. An ability to design pores of varying size and uniform distributions in solids is very important to delineate the effect of varying degree of restrictive geometry on fluid properties. Pore-size in gels is also important from the view point of making glasses and monoliths, since the gels with small pores tend to fracture during sintering.

Recently Shafer et al.<sup>1</sup> Chan et al.<sup>2</sup> synthesized gels (and porous glasses) of varying pore-size (>20 Å), surface area and pore volume by sol-gel route. They indicated that the sol-gel glasses could serve as a host for numerous physical experiments. Nitrogen adsorption and mercury porosimetry were used to characterize the pore structures. We were, however, interested in designing the pore-size (pore diameter) in the region <20 Å. For a comprehensive characterization of pores, water adsorption measurements were carried out, since water molecules can penetrate into the micropores whereas nitrogen molecules do not have access due to steric hindrance. Moreover, if we consider the application of gels as desiccation materials, data on water adsorption behavior is indispensable. The objective of this study was to develop a new class of desiccation materials for gas-fired dehumidification and cooling system applications. The ideal desiccation material for this purpose should have moderate Type I isotherm rather than an extreme Type I, Type II or Type IV<sup>3</sup>. In this paper, we report the control of pore-size in silica gel in the region of <20 Å. To make the system simple, we used TMOS and water only, and the use of alcohol or catalyst was avoided.

EXPERIMENTAL

Silica gels were prepared at room temperature by mixing 10 ml of tetramethyl-orthosilicate (TMOS) with various amounts of deionized water in conical flasks. The conical flasks were sealed with glass stoppers. Conditions for gel synthesis are given in Table I. The mixed solution was stirred until gelation occurred. After gelation, gels were further left in the conical flasks for about 12 hr, and dried at 65-70°C for 2 days. Following drying, gels were heated at 200-600°C in air before further characterization.

Water sorption isotherms were measured at 25°C by a volumetric sorption apparatus interfaced with a computer<sup>4</sup>. All samples were evacuated at 200°C for 4 hr before sorption measurements. Using the BET equation, water surface areas of these gels were also determined. Approximate pore sizes were estimated from t-plots<sup>5,6</sup>. The BET nitrogen surface areas were measured by one-point method using Monosorb, Quanta Chrome apparatus. Samples were evacuated at 200°C for 2 hr prior to nitrogen surface area measurements.

Differential thermal analysis (DTA) was performed using a Perkin Elmer DTA 1700 system. Samples were heated in air (40 cc/min) at the rate of 10°/min.

## RESULTS

The mixture of TMOS and water became clear within 30 min of stirring. The gelation time for all  $[H_2O]/[TMOS]$  was about three hours. This time is considerably lower compared to the system involving tetraethylorthosilicate (TEOS). As reported first by Avnir and Kaufman<sup>7</sup>, there was no need of addition of alcohol to form a clear gel.

Water sorption isotherms of various gels are given in Figure 1. From the figure, it is evident that the shape of isotherms can be varied by varying the  $[H_2O]/[TMOS]$  ratio (R). Samples with R close to 5 (4.13-5.37) exhibited moderate type I isotherm which slowly converted to isotherm intermediate between Type I and Type IV with increasing and decreasing R. In all cases, the isotherms were saturated at  $P/P_0 \approx 0.5$  indicating the microporous nature of gels. The sorption capacities measured at  $P/P_0 = 0.96 \pm 0.01$  are presented in Table I. Again the sorption was minimum for  $R = 4.96-5.37$  which increased with increasing and decreasing R. The BET nitrogen surface areas, like sorption capacities, also passed through a minimum (Figure 2). The BET water surface areas, however, increased steadily with increasing R (Figure 2). Although the validity of the BET equation is limited to multilayer sorption, surface areas measured using BET fit in the range of  $P/P_0 = 0.05-3.0$  for these microporous system yielded reasonable values. The surface areas calculated from t-plot (Figure 3) are also in good agreement with those obtained from BET equation (Figure 2). The average pore sizes as determined from t-plots of water are given in Table I. The pores were distributed over a range of sizes. The largest pore-size in all cases was about 18 Å, however the smallest pore-size first decreased and then increased with increasing amount of water. In the determination of pore-size by t-plots, the BET "C" constant, of 5.6 was used, since our samples had the constant of  $5 \pm 1$  and the value of 5.6 is the smallest BET "C" constant given by Hagymassy et al<sup>5</sup>. The water isotherms of gel prepared at  $[H_2O]/[TMOS] = 4.96$  and calcined at various temperatures are given in Figure 4. The increased calcination temperature suppressed the sorption at lower relative pressure and converted the isotherm shape to Type V (Figures 4, 5).

Differential thermal analysis (DTA) was performed to study the mechanism which controlled the pore-size in silica gels. The thermograms of various gels are given in Figures 6-7. The endothermic peak near 150°C is due to the evaporation of water. The exothermic peaks at 300-500°C correspond to the combustion of organic materials. Various peaks at this temperature range may be attributed to organic substance of various molecular weights. The

Table I. Conditions of gel synthesis in relation to water sorption capacity and pore-size.

Gel No.	$H_2O$ (ml)	$[H_2O]/[Si(OCH_3)_4]$	Sorption capacity (ml/g, $P/P_0 = 0.96 \pm 0.01$ )	Average pore-size (Å)
1	4.0	3.31	0.328	11.0
2	5.0	4.13	0.285	9.0
3	6.0	4.96	0.276	8.7
4	6.5	5.37	0.278	8.4
5	7.0	5.79	0.316	9.2
6	8.0	6.61	0.321	9.0
7	9.0	7.44	0.373	10.0

**Figure 1.** Water adsorption isotherms of silica gels prepared with various R and heated at 200°C: (○) 5.37, (●) 4.96, (▽) 5.79, (▲) 7.44, and (■) 3.31. The solid curve is an ideal isotherm shape required for cooling system application.

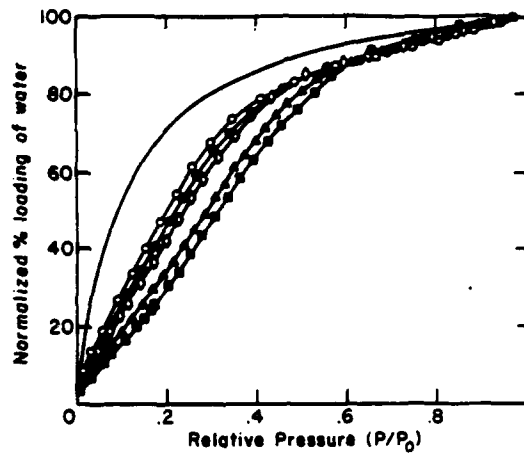


**Figure 2.** Surface areas of silica gels as a function of R: BET nitrogen (●), BET water (□), and from t-plots of water (○).

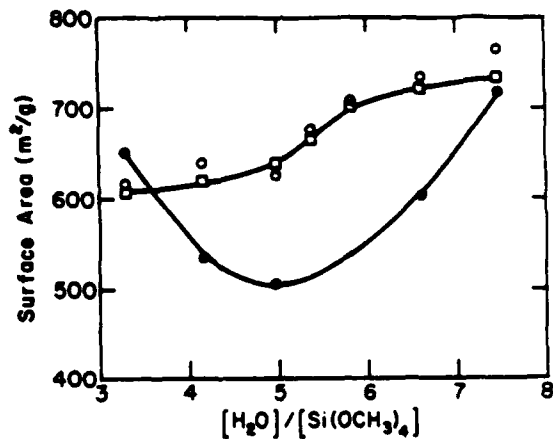
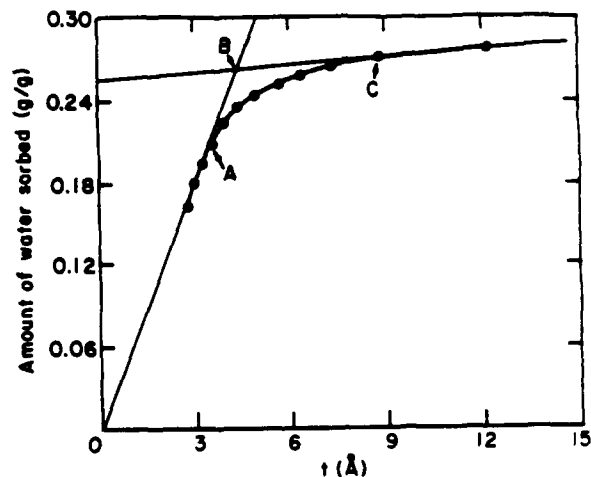


**Figure 3.** t-plot of water (for gel with R = 4.96) illustrating the method for estimation of surface area (slope of the straight line passing through the origin), smallest (A), average (B) and largest (C) pore radii (t). The pore-size (pore diameter) is twice the value of t.



number of exothermic peaks decreased with increasing amount of water indicating the increased amount of consumption of organic molecules by hydrolysis.

## DISCUSSION

Pore-size, its structure and the affinity between adsorbate and adsorbent are some of the important parameters that govern the amount and the rate of vapor adsorption on the surfaces of solids, and consequently determine the shape of the adsorption isotherm. For example, large pores facilitate multilayer adsorption of vapors such as water and nitrogen and exhibit type II or Type IV isotherm, whereas multilayer adsorption is physically not possible in small pores and therefore the adsorption follows Type I isotherm. In addition there are two other types of isotherms, Types III and V which are exhibited by nonporous and microporous hydrophobic (or weak interaction between adsorbate and adsorbent) solids, respectively. In these solids, there will be very small or no adsorption of adsorbate molecules at lower relative vapor pressure, and the adsorption will be enhanced only after adsorbate-adsorbate interaction becomes important. The effect of pore-size and affinity between adsorbent and adsorbate molecules on the shape of isotherm has been previously discussed by Malla et al.<sup>8</sup>

As seen in Figure 1, water isotherms of various shapes have been achieved by changing the water to TMOS ratio. The variation in isotherm shapes must have resulted from the difference in pore-size and the affinity towards water in these gels. In fact, the tendency of gels to exhibit Type I isotherm was increased as the pore-size decreased (Table I). As the pore-size decreases, the adsorbate molecules experience stronger field from the neighboring pore walls, hence the enhanced adsorption (volume filling) at low relative pressure and Type I isotherm<sup>9-11</sup>. The small BET "C" constants (4-6) of all gels studied indicated that the gels had low affinity for water molecules. Normally, molecular sieve zeolites (type X and type Y) which have pore-size similar to the gels reported in this study (8-12 Å) exhibit extreme Type I isotherms due to very high affinity of zeolite surface for water. The moderate Type I isotherm exhibited by some of these gels instead of extreme Type I may be attributed to their low affinity for water. The affinity of gels for water molecules was further reduced by thermal treatment higher than 200°C as a result of loss of silanol groups from the pore and external surfaces (Figure 4). At 500-600°C, the Type I isotherm changed to a typical Type V (Figure 4). At 600°C, the total water sorption capacity and the BET nitrogen surface area were severely reduced due to the collapse of considerable amount of micropores (Figure 5).

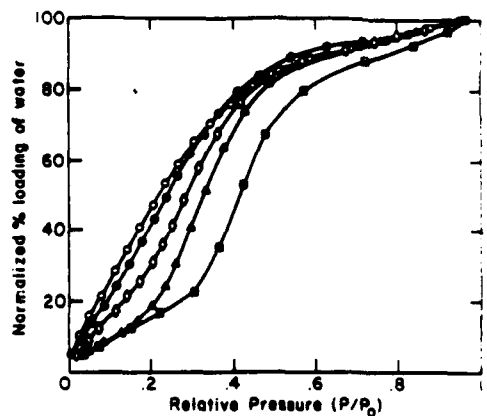


Figure 4. Water adsorption isotherms of gel with  $R = 4.96$  as a function of calcination temperature: (○) 200°C, (●) 300°C, (◊) 400°C, (▲) 500°C, and (■) 600°C.

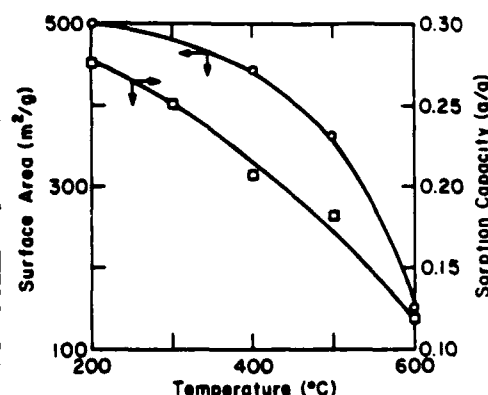


Figure 5. Surface area (○) and Sorption capacity at  $P/P_0 = 0.96 \pm 0.01$  (□) of gel with  $R = 4.96$  as a function of calcination temperature.

Both water sorption capacities and nitrogen surface areas decreased with the decrease in pore-size (Table I, Figure 2). Water surface areas were higher than nitrogen surface areas except for sample,  $R = 3.31$ . The increase in water surface areas compared to nitrogen may be attributed to the inability of nitrogen to penetrate some of the micropores due to steric hindrance but are accessible to water molecules. The decrease in water surface area of sample,  $R = 3.31$  compared to nitrogen may be attributed to the presence of some unreacted organic groups which made the pore surface somewhat more hydrophobic than other samples, hence reduction in water surface area. In fact this sample had much more unreacted organic groups as indicated by thermogram (discussed later). Thus water molecules may serve as a better probe than nitrogen molecules in the investigation of pore-structure and the nature of surface of microporous solids such as gels. For  $R = 7.44$ , both nitrogen and water surface areas are practically the same indicating that both nitrogen and water molecules are accessible to all pores.

Analysis of DTA peaks between 300 and 500°C indicated the presence of various amounts of both low and high molecular weight organic molecules, respectively in the gels. Gel with  $R = 3.31$  contained large amount of organic substances with relatively low molecular weights (Figure 6). In this sample, the amount of water used was not sufficient to hydrolyze all the organic molecules. With increasing amount of water, peaks due to the combustion of organic material disappeared from the lower temperature side. Sample with  $R = 6.61$  indicated a small but broad peak only due to organic molecules (Figure 7). Thus the gel with  $R = 3.31$  contained a large amount of organic molecules, whereas  $R = 6.61$  had excess of water.

Many studies concerning the effect of water/Alkoxide in the structure of gels have been reported, especially in acid or base catalyzed systems. A high  $H_2O$ /alkoxide ratio was found to lead to complete hydrolysis and the formation of highly cross-linked products, whereas a low water content would promote the polymerization of only partially hydrolyzed alkoxide molecules leading to less cross-linked polymers<sup>12,13</sup>. Klein and Garvey<sup>14</sup> studied the effect of water on acid- and base catalyzed systems and found that the increase of water content in acid catalyzed system produced gels of high surface area and the gels from base catalyzed system produced low surface area. In the present study, water/TMOS ratio was found to affect the pore-size and the affinity of surface for water molecules which eventually affect the water sorption properties of dried gels. The increase of pore-size in gels of low and high water content may be attributed to the amount of organic molecules and water, respectively, remained in the gels, which after evaporation left behind larger pores as compared to the gels that had low amount of both organic and water molecules. In addition, formation of a highly cross-linked product in the sample with high water content might also have contributed to its larger pore-size. Further design in pore-size and water isotherm shapes of gels may be achieved by the addition of catalysts (e.g., HCl, HF) or addition of ions that can form part of  $SiO_2$  network (e.g.,  $Al^{3+}$ ). These studies are underway.

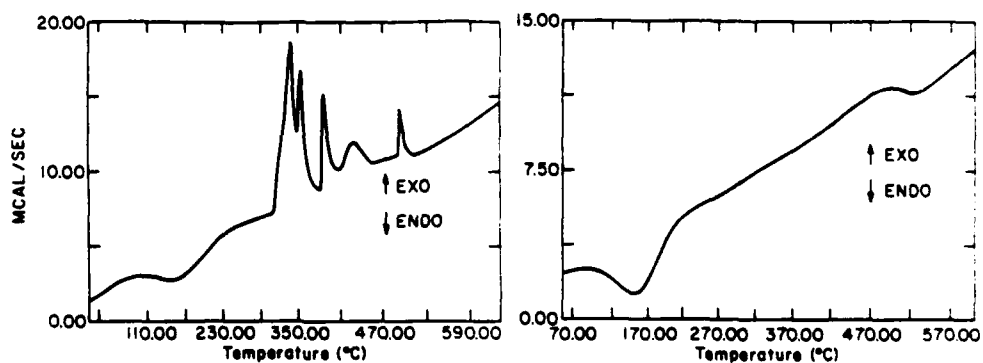


Figure 6. Thermogram (DTA) of gel with  $R = 3.31$ .

Figure 7. Thermogram (DTA) of gel with  $R = 6.61$ .

## ACKNOWLEDGMENTS

This study was supported by the Gas Research Institute under Contract 5087-260-1473. We thank Dr. H. Taguchi for the determination of BET nitrogen surface areas and Mr. G. Zimmerman for DTA analysis.

## REFERENCES

1. M.W. Shafer, D.D. Awschalom, and J. Warnock, *J. Appl. Phys.* **61** (12), 5438 (1987).
2. J-B. Chan, D-W. Hua, R. Winter, and J. Jonas, *J. Mater. Res. Soc.* **4** (3), 693 (1989).
3. R.K. Colier, T.S. Cole, and Z. Lavan, "Advanced Desiccation Materials Assessment-Final Report." Gas Research Institute, Contract 5084-243-1089 (1986).
4. S. Yamanaka and S. Komarneni, U.S. Patent (filed) (1988).
5. J. Hagymassy, Jr., S. Brunauer, and R. Sh. Mikhail, *J. colloid & Interface Sci.* **29** (3) 485 (1969).
6. J. Hagymassy and S. Brunauer, *J. Colloid & Interface Sci.* **33** (2), 317 (1970).
7. D. Avnir and V.R. Kaufman, *J. Non-Cryst. Solids* **192**, 180 (1987).
8. P. B. Malla, S. Yamanaka and S. Komarneni, *Solid State Ionics* **32/33**, 354 (1989).
9. M.M. Dubinin, in *Progress in Surface & Membrane Sci.*, edited by J.F. Danielli, M.D. Rosenberg, and D.A. Cadenhead (Academic Press, New York, 1975) **9**, 1-70.
10. K.S.W. Sing, in *Colloid Science*, edited by D.H. Everett (The Chemical Society, London, 1973) **1**, 1-48.
11. D.H. Everett and J.C. Powl, *J. Chem. Soc. Faraday Trans. I*, **72**, 619 (1976).
12. S. Sakka and K. Komiya, *J. Non-Cryst. Solids* **48**, 31 (1982).
13. K.D. Keefer, in *Better Ceramics Through Chemistry*, edited by C. J. Brinker, D.E. Clark, and D.R. Ulrich (Mater. Res. Soc. Proc. **32**, Pittsburg, PA 1984) pp. 15-24.
14. L. C. Klein and G.J. Garvey, in *Better Ceramics Through Chemistry*, edited by C. J. Brinker, D.E. Clark, and D.R. Ulrich (Mater. Res. Soc. Proc. **32**, Pittsburg, PA 1984) pp. 33-39.



---

---

**PART IV**

---

**Polymers for  
Untrastructures**

92-18267

AD-P007 476



227



## DIELECTRIC RELAXATION PROPERTIES AND ALIGNMENT BEHAVIOUR OF LIQUID-CRYSTALLINE SIDE-CHAIN POLYMERS

GRAHAM WILLIAMS AND ALI NAZEMI

University College of Swansea, Department of Chemistry,  
Singleton Park, Swansea SA2 8PP, United Kingdom

FRANK E KARASZ

University of Massachusetts, Department of Polymer Science and  
Engineering, Amherst, MA01003, USA.

### ABSTRACT

We describe the alignment behaviour of different liquid-crystalline (LC) side-chain polymers when they are subjected to electrical/thermal treatments. It is shown that the alignment behaviour is determined by several variables for a given polymer, including the amplitude and frequency of the applied electric field and both the thermal and electrical history of the sample and its low-field dielectric relaxation properties. It is shown that the dielectric relaxation spectra vary systematically with the degree of macroscopic alignment of the sample and its temperature. The anisotropy of dielectric properties may be understood in terms of the anisotropic reorientational motions of the dipolar mesogenic groups. The permittivity data allow the degree of macroscopic alignment to be determined, via a director order parameter  $S_d$  for samples prepared in different ways and also for samples being realigned, as a function of time, by directing electric fields. We illustrate these principles through data we have obtained for a copolymer having the mesogenic groups attached longitudinally and transversely to the main chain.

### INTRODUCTION

Liquid crystalline side-chain polymers are currently of interest due to their electroactive, magnetoactive and photoactive properties. When macroscopically-aligned they exhibit anisotropic optical properties and such materials in film-form (1-100  $\mu\text{m}$  thickness) show promise as media for optical data storage, optical wave-guiding and non-linear optical processing [1-3]. Most applications require a material to be aligned (by directing electric or magnetic fields or by surface forces). It is therefore important to establish quantitatively-reproducible methods for the alignment of LC side-chain polymers in film-form, and to provide simple quantitative methods for determining the nature and extent of macroscopic alignment present in a sample.

In earlier publications we have shown that LC side chain polymers of different chemical structures may be aligned macroscopically using carefully-controlled combinations of electrical and thermal treatments (see refs. 4-10 and refs. therein). The nature and extent of macroscopic alignment achieved may be determined quantitatively using dielectric relaxation spectroscopy in the medium frequency range 10-10<sup>5</sup> Hz [7,11]. Also the dielectric relaxation spectra for homeotropically-aligned, planarly-aligned, unaligned and inter-

mediately-aligned samples may be analysed, in favourable cases, in terms of relaxation modes which arise due to the anisotropic motions of the dipole moment  $\mu$  of the mesogenic head group [5,7,8,11,12]. It is important to note that the mechanism of macroscopic realignment of a LC phase involves the dielectric anisotropy term  $\Delta\epsilon'(\omega) = \epsilon_{||}(\omega) - \epsilon_{\perp}(\omega)$  where  $||$  and  $\perp$  refer to measurements made parallel with and perpendicular to, respectively, the local director  $n$ , and  $\epsilon'(\omega)$  is the real part of the dielectric permittivity measured at the angular frequency  $\omega = 2\pi f/\text{Hz}$ . For  $\Delta\epsilon'(\omega) > 0$ , H-alignment is favoured while for  $\Delta\epsilon'(\omega) < 0$ , P-alignment is favoured. The condition  $\Delta\epsilon'(\omega) = 0$  occurs at the crossover frequency  $\omega_c$  [13,14] whose value varies rapidly with sample temperature for LC side-chain polymers [6].

In the present paper we summarize briefly some of the theoretical and practical aspects of the dielectric relaxation properties and alignment behaviour of siloxane-chain LC side-chain polymers. We illustrate such properties and behaviour using data we have obtained for a copolymer which contains mesogenic groups attached longitudinally and laterally to the main chain.

#### THEORETICAL

The dielectric permittivity tensor  $\epsilon(\omega)$  for a uniaxial liquid crystal contains the principal permittivities  $\epsilon_{||}(\omega)$  and  $\epsilon_{\perp}(\omega)$  which are measured  $||$  and  $\perp$  to the director axis  $n$  respectively. These permittivities are complex quantities whose real part  $\epsilon_i'(\omega)$  is the 'permittivity' and imaginary part  $\epsilon_i''(\omega)$  is the 'loss factor'. Here  $i = ||$  or  $\perp$ .

For a sample having uniaxial symmetry, as is the case for smectic or nematic liquid crystals which have been aligned with an electric field applied normal to the electrodes, then a simple macroscopic theory gives the measured complex permittivity  $\epsilon(\omega)$  as [7,8]

$$\epsilon(\omega) = \frac{(1+2S_d)}{3} \cdot \epsilon_{||}(\omega) + \frac{2(1-S_d)}{3} \cdot \epsilon_{\perp}(\omega) \quad (1)$$

where the director order parameter  $S_d$  lies in the range  $-0.5 \leq S_d \leq 1$ , and  $S_d = 1$  corresponds to H-alignment,  $S_d = 0$  corresponds to unaligned (U) and  $S_d = -0.5$  corresponds to P-alignment. If  $\epsilon_{||}(\omega)$ ,  $\epsilon_{\perp}(\omega)$ ,  $\epsilon_u(\omega)$  (any two of three) are known at a given frequency then measurement of  $\epsilon(\omega)$  (either  $\epsilon'(\omega)$  or  $\epsilon''(\omega)$ ) gives, from eqn. (1), the value of  $S_d$  for the sample. The applicability of eqn. (1) to experimental data can be checked by determining  $S_d$  from permittivity or loss data at different values of  $\omega$  in the relaxation range. We have shown that eqn. (1) gives very satisfactory results for siloxane-chain LC polymers. Note that at the crossover frequency  $\omega = \omega_c$ , for the

permittivity curves, then  $\epsilon_{||}'(\omega_c) = \epsilon_{\perp}'(\omega_c)$  so from eqn. (1) all curves for  $\epsilon'(\omega)$  (i.e., for different values of  $S_d$ ) cross at  $\omega_c$  at that sample temperature. The crossover frequency is an isosbestic point (or frequency). Similarly, all curves for  $\epsilon''(\omega)$  cross at a (different) isosbestic frequency,  $\omega_c'$  say, and this occurs for  $\epsilon_{||}''(\omega_c') = \epsilon_{\perp}''(\omega_c')$ . The experimental observation of isosbestic frequencies for samples having different  $S_d$  values provides a test of eqn. (1) and a test of the quality of the experimental data. If a directing a.c. electric field is applied to a sample (at a fixed sample temperature) then if its frequency  $f < \omega_c/2\pi$ , H-alignment is favoured while if  $f > \omega_c/2\pi$ , P-alignment is favoured [13,14] (see also ref. 8 for a discussion of two-frequency addressing).

The principal permittivities  $\epsilon_{||}(\omega)$  and  $\epsilon_{\perp}(\omega)$  may be related to molecular quantities as follows [7] for the simple case of a uniaxial LC phase in which dipole moment orientational correlations are absent.

$$\epsilon_{||}(\omega) = \epsilon_{||}^{\infty} + \frac{G}{3kT} [\mu_t^2 \cdot (1+2S) \cdot F_{||}^f(\omega) + \mu_t^2 \cdot (1-S) \cdot F_{||}^t(\omega)] \quad (2a)$$

$$\epsilon_{\perp}(\omega) = \epsilon_{\perp}^{\infty} + \frac{G}{3kT} [\mu_t^2 \cdot (1-S) \cdot F_{\perp}^f(\omega) + \mu_t^2 \cdot (1+S/2) \cdot F_{\perp}^t(\omega)] \quad (2b)$$

where  $G$  is a factor involving the concentrations of dipolar groups,  $\mu_t = \mu \cdot \cos\beta$  and  $\mu_t = \mu \cdot \sin\beta$ , where  $\beta$  is the angle between  $\mu$  and the z-axis of the dipolar mesogenic group.  $S$  is the local order parameter of the LC phase and the  $F_j^i(\omega)$  are relaxation functions which are related to functions  $f_j^i(t)$ , which are themselves linear combinations of time correlation functions  $\Phi_{mn}^1(t)$  for the orientational motions of the molecular axes of the mesogenic group. We have [12]

$$F_j^i(\omega) = 1 - i\omega \cdot F[f_j^i(t)] \quad (3)$$

$$\Phi_{mn}^1(t) = \langle D_{mn}^{1*}(\Omega(0)) D_{mn}^1(\Omega(t)) \rangle \quad (4)$$

where the  $D_{mn}^1(\Omega)$  are elements of the Wigner rotation matrix. The forms of the different  $f_j^i(t)$  have been specified [12]. The relaxation functions in eqns. (2) correspond to four orthogonal relaxation modes the simplest of which corresponds to the following relaxation function in the time domain

$$f_{||}^f(t) = \Phi_{00}^1(t) = \langle \cos\theta_{zn}(t) \rangle \quad (5)$$

where  $\theta_{zn}$  is the angle between the molecular z-axis and the local director  $n$ .

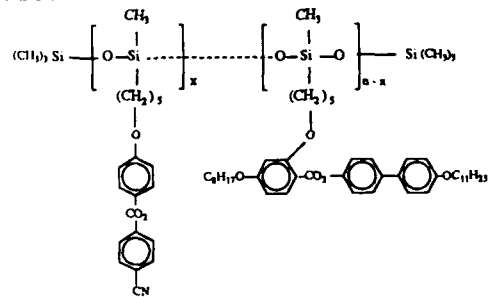
Thus the dielectric relaxation behaviour arises from four relaxation modes, two for  $\epsilon_{||}(\omega)$  and two for  $\epsilon_{\perp}(\omega)$  in which a

portion of  $\mu_r^2$  and  $\mu_t^2$  is relaxed in each case. For an unaligned sample  $\epsilon(\omega)$  will correspond to a weighted sum of all four relaxation modes, as required by eqns. (1) and (2).

If an unaligned or partially-aligned material is subjected to a strong aligning a.c. electric field, then realignment will occur towards H- or P-alignment, depending on the frequency, as we have discussed. The origin of realignment lies in the dielectric torque produced which is proportional to  $\Delta\epsilon'(\omega)$  (see ref. 7 for a discussion). The high viscosity of the LC phase may prevent realignment occurring especially for  $T \ll T_c$ , as we have found for siloxane homopolymers [4-7], but realignment in the LC phase has been observed for a siloxane copolymer [15], where the packing of mesogenic groups along and between chains is less perfect than that for the homopolymer, and for a malonate polymer [10] in which the mesogenic groups are spaced out more extensively along the chain. The realignment process in the LC phase may be considered in terms of a continuum theory of liquid crystals as has been described recently by Martins and coworkers [16] and applied by them to their time-dependent NMR data for a main chain LC polymer which was subjected to a strong magnetic field. The rate of realignment depends upon the dynamic viscosities and the different elastic constants in addition to the magnitude of the applied field and the anisotropy of susceptibility (electric, magnetic). We have applied their theory in order to rationalize our experimental results for the electric-field-induced realignment of a malonate polymer in its LC state [9]. However, we shall see that it appears that surface forces may play an important role in determining the rate of realignment of a material in its LC state.

#### MATERIAL AND EXPERIMENTAL

The copolymer studied was provided by Professor G.W. Gray, Dr. D. Lacey and Dr. J.S. Hill of Hull University. It had the following structure.



$n = 50$ ,  $x = 16.7$ , the clearing temperature  $T_c \sim 110^\circ\text{C}$  and the glass transition temperature  $T_g$  was  $\sim 7^\circ\text{C}$  by DSC.

The dielectric measurements were made using methods described previously [4,5] and the sample (1 cm diameter, 100  $\mu\text{m}$  in thickness) was subjected to a.c. voltages at chosen frequencies and at different sample temperatures.

## RESULTS

Aspects of the dielectric properties and optical properties of this copolymer have been reported previously [17]. It was shown that H-aligned material could be prepared by cooling from the melt in the presence of a strong low frequency voltage. Also it was shown that realignment could be achieved in the LC state, allowing H-aligned or P-aligned specimens to be made using low or high frequency applied voltages, respectively. In the present work we consider the effects of both the thermal and electrical histories on the alignment processes and we give results for the time-dependence of the electric-field-induced realignment in the LC state.

Figure 1 shows, as one example of our data, the plots of the dielectric absorption factor  $G_p/\omega$  ( $= \epsilon''(\omega)C_a$ ) against  $\log_{10}(f/\text{Hz})$  for a H-aligned sample at different temperatures. This sample was made homeotropic by applying 300V at 200Hz for one hour at 70°C. Here  $G_p$  is the equivalent parallel conductance of the sample at  $\omega = 2\pi f/\text{Hz}$  and  $C_a$  is the inter-electrode capacitance. For  $T > 90^\circ\text{C}$  there is a marked fall in the height of the loss curves, in anticipation of the final clearing temperature  $T_c \sim 110^\circ\text{C}$ . The loss curves in the LC range are slightly broader than those observed previously for the  $\delta$ -process (00-relaxation mode) in the H-aligned form of siloxane homopolymers containing longitudinally attached cyano-aromatic ester mesogenic groups [5,7,8]. The apparent skewness to lower

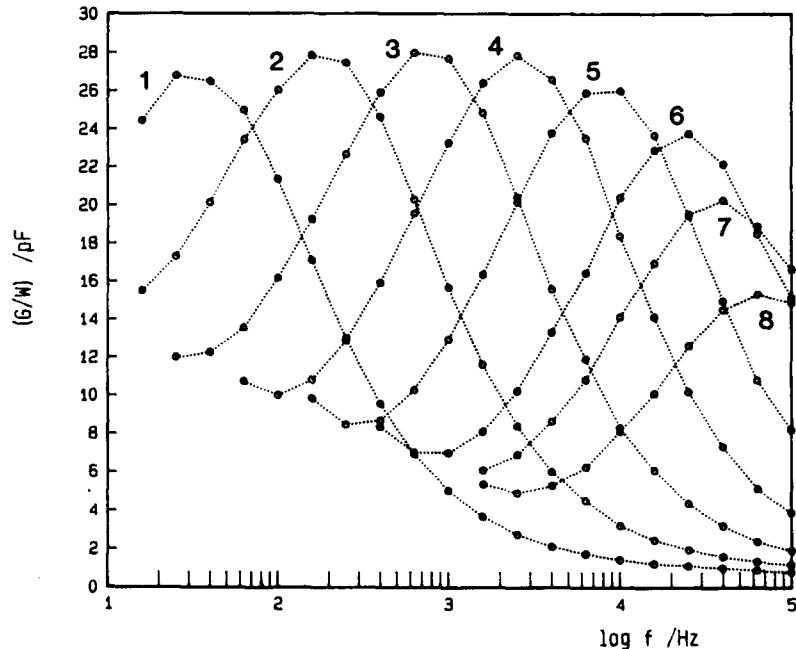


Figure 1.  $G_p/\omega$  against  $\log_{10}(f/\text{Hz})$  for a H-aligned sample at different temperatures. Curves 1-8 correspond to 40, 50, 60, 70, 80, 90, 95 and  $100.5^\circ\text{C}$ , respectively.

frequencies for the loss peaks is due to the overlapping tail of the d.c. conductivity process. P-aligned material was formed from the H-aligned material by applying 300V at 20 kHz for several hours at 70°C. Figure 2 compares the loss curves of a sample at 50°C in its H-aligned, P-aligned and unaligned states. Note the crossover at  $\sim 10^4$  Hz for 50°C. The  $\delta$ -peak is essentially eliminated on going to P-aligned material. The rising loss at higher frequencies for the P-aligned material shows that the peaks for the 10 and 11 relaxation modes occur at still higher frequencies. For siloxane homopolymers having the cyano-aromatic ester groups attached longitudinally to the chain we found previously [4-8] that  $\delta$ - and  $\alpha$ -processes were observed, where the  $\alpha$ -process had a magnitude which was at least comparable with that of the  $\delta$ -process. The present results are very different, with no evidence for an  $\alpha$ -process of any substantial magnitude. This implies that  $\mu_t \ll \mu_\delta$  for the copolymer, so that the relaxation strengths of the 01 and 11 relaxation modes (eqns. 2,  $F_1 f(\omega)$  and  $F_{11}^t(\omega)$ , respectively) are rather smaller than those we have observed in other polymers.

We now turn to the alignment behaviour. In figure 3 we plot the heights of the loss peaks for H-aligned, P-aligned and unaligned forms of a sample as a function of temperature. The three loci meet in the region of 110°C (final  $T_c$ ) beyond which the sample is a normal isotropic melt. We note that the fall in the peak-height of the  $\delta$ -process for the H-aligned sample in the range 90-110°C is accompanied by a complementary increase in the peak-height of the process (10-mode) seen for the P-aligned

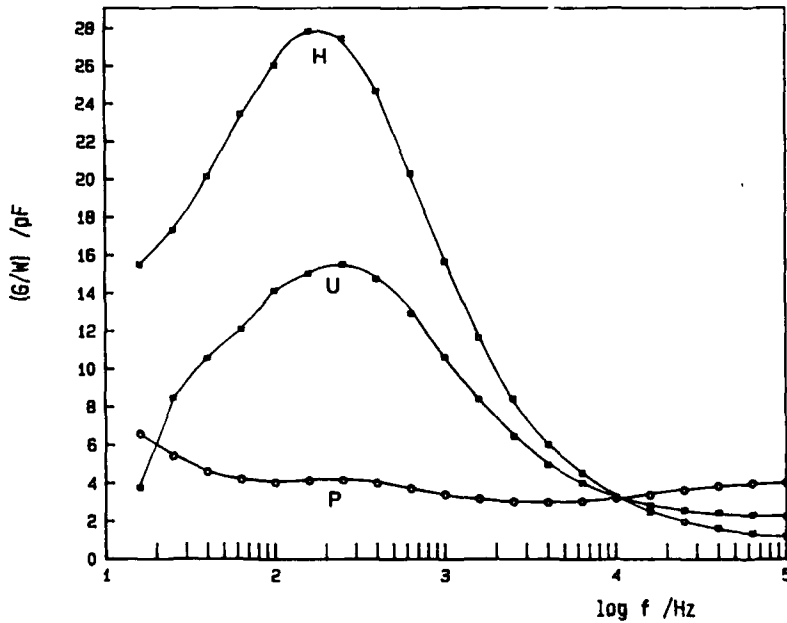


Figure 2.  $G_p/\omega$  against  $\log_{10}(f/\text{Hz})$  for unaligned, H-aligned and P-aligned states of the sample at 50°C

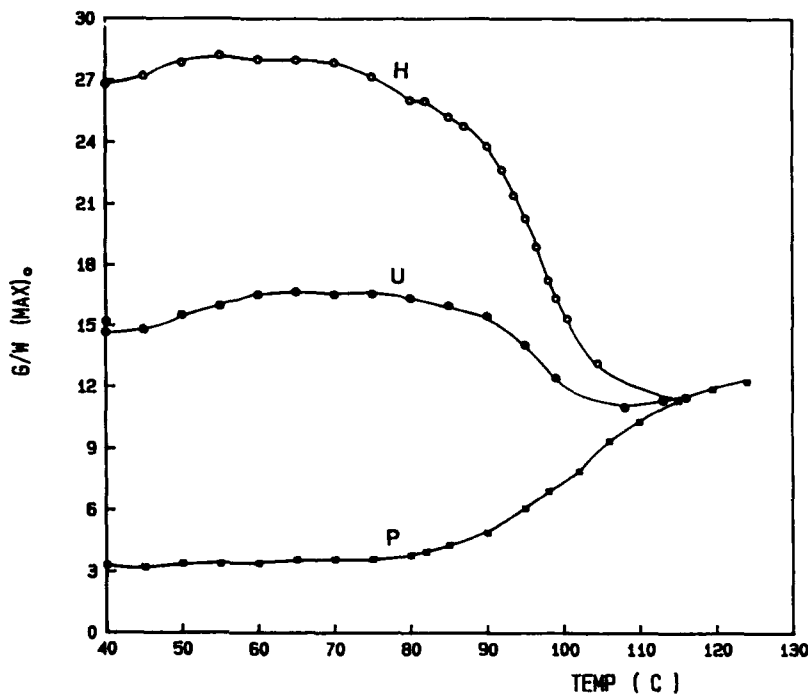


Figure 3. The peak heights,  $(G_p/\omega)_{\text{MAX}}$  against temperature for the loss spectra of unaligned, H-aligned and P-aligned states of the sample.

sample in the same range of temperature. Two explanations are possible for such behaviour: (i) that the range 90–110°C is a biphasic range in which LC phase and isotropic phase coexist or, (ii) that this is a pre-transitional region in which the order parameter  $S$  for the LC phase decreases steadily with temperature. Our optical studies [17] do not suggest case (i) and we presently consider that case (ii) applies to this copolymer. Note that we are able to realign a sample from  $H \rightarrow P \rightarrow H$ , etc., using the two-frequency addressing principle for  $T = 70^\circ\text{C}$  and below, i.e., well under  $T_c$ . This was not found possible for siloxane homopolymers with similar cyano-aromatic ester groups [4–8], so it appears that the disruption of the LC packing of the longitudinally-attached groups by the laterally-attached mesogenic groups enhances realignment in the LC phase and, allows P-material to be formed. (To form P-aligned material by cooling from the melt would require directing fields of high frequencies beyond our practical range.) Note also that the 'unaligned' material shows a decrease in the height of the loss peak in the range 90–110°C which indicates that this material is aligned homeotropically to some extent. A calculation of  $S_d$  from the data of figure 3 gives  $S_d = 0.22$  for the 'unaligned' sample. Thus on cooling from the melt into the LC state in the absence of the electric field the sample was formed in a partially H-aligned state. As we shall see, this

affects the realignment behaviour when the 'unaligned' sample is subjected to directing a.c. electric fields.

In one experiment the sample was cooled from the melt in the absence of an applied a.c. voltage. Then, at 70°C, 300V at 200Hz was applied for one hour to render the sample fully homeotropic, as judged by its loss spectrum. This sample was converted into the P-aligned state at 70°C using 300V at 20 kHz and its loss spectrum was recorded. This P-aligned sample was studied as a function of time at 70°C. Figure 4 shows that on standing at this temperature, the loss curves grow back towards that of the original H-aligned sample in the absence of any applied voltage. The sample 'remembers' that it had been aligned homeotropically before it was aligned planarly and it seeks to return to that H-aligned condition.  $S_d$  grows from -0.5 to ~ 0.27 in 16 hours. The desire to return to H-alignment may be associated with the fact that the 'unaligned' material was slightly H-aligned, as we have discussed, and therefore forming H-aligned material at 70°C, using a low frequency a.c. voltage, gave the most stable (or favoured) state for this sample in the absence of an applied field. As a test of this suggestion, the sample was returned to the fully H-aligned state using 300V at 200Hz and its stability was monitored at 70°C. It was found that no detectable change was observed in the loss spectrum of this fully H-aligned sample over 17 hours showing that the H-aligned material was completely stable in the absence of the

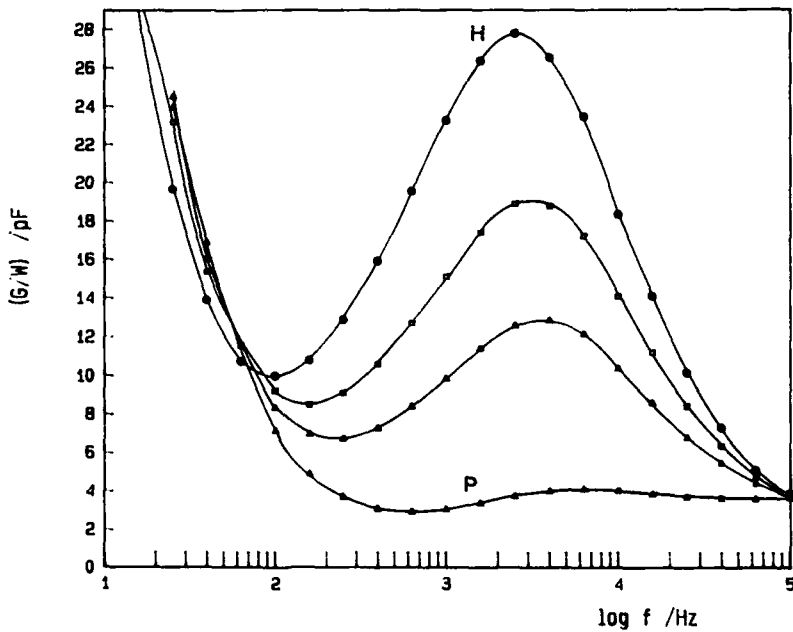


Figure 4. The loss curves for a sample:- freshly prepared in the P-aligned state ( $\Delta$ ), after 3 hours following removal of the directing field ( $\blacktriangle$ ), after 16 hours following removal of the directing field ( $\blacksquare$ ). The curve ( $\bullet$ ) is that for the fully H-aligned sample. All measurements were made at 70°C.

field. The rate of return towards H-alignment was found to depend on the path used initially to achieve P-alignment. In one experiment a sample was prepared using the following sequence;

melt  $\rightarrow$  unaligned  $\rightarrow$  P-aligned  
sample at 70°C sample at 70°C

Figure 5 shows the recovery curve (measured as loss at  $\log_{10} f = 3.7$ ) for this sample together with the recovery curve for a sample subjected to the following sequence

melt  $\rightarrow$  unaligned  $\rightarrow$  H-aligned  $\rightarrow$  P-aligned  
sample at 70°C sample at 70°C sample at 70°C

Although both samples are nominally planar at  $t = 0$ , the sample which had previously been homeotropic shows a marked recovery while that which had not shows only a small recovery. An obvious interpretation of this behaviour is that the 'unaligned' material is H-aligned to some extent at the polymer-metal surface so when this material is forced to become fully H-aligned, the surface and bulk alignments match to form a continuous monodomain. Subsequent realignment into the planar condition requires the mesogenic groups to reorientate and produces strain in the polymer backbone and spacer groups.

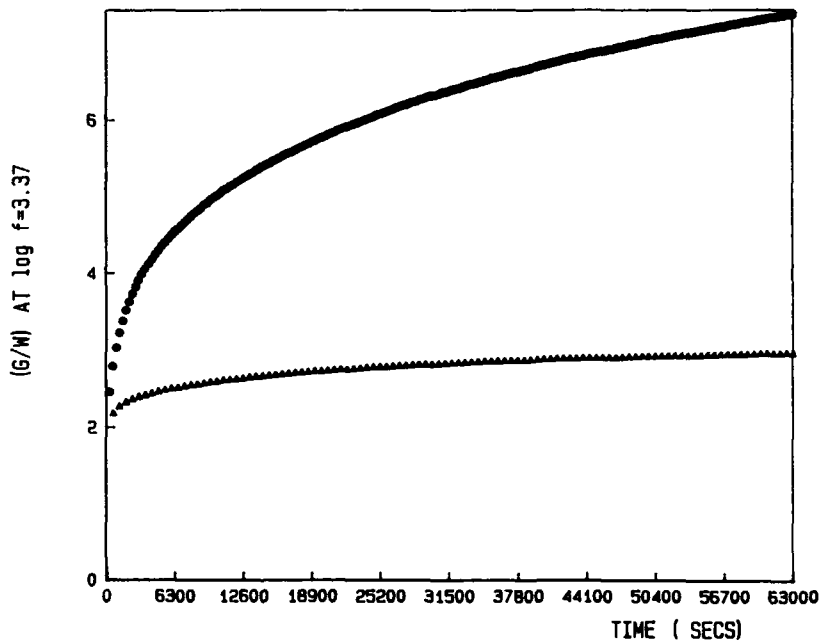


Figure 5. The recovery of alignment for two samples which have P-alignment at  $t = 0$ . Curves denoted by ● and Δ correspond to samples which were or were not, respectively, previously aligned homeotropically. Loss measured at  $\log_{10} f = 3.7$ .

Removal of the high frequency field removes the torque holding the strained LC phase so realignment occurs towards H-alignment as the strain is released. On the other hand, if a sample is driven from U  $\rightarrow$  P alignment, the bulk material is P-aligned while the surface regions are H-aligned. On removal of the high frequency aligning voltage there is a loss of strain only in the interface region between surface (H-aligned) and bulk (P-aligned). Thus, only a small recovery effect is observed (figure 5).

We have also studied the kinetics of the voltage-induced transformations for the following sequences: U  $\rightarrow$  H  $\rightarrow$  P  $\rightarrow$  H and U  $\rightarrow$  P  $\rightarrow$  H at 70°C. In the first sequence the H  $\rightarrow$  P transformation has an induction period and is very slow, overall, giving a time to completion  $\sim 7 \times 10^3$  seconds. The reverse transformation P  $\rightarrow$  H is much faster, with a time to completion of  $\sim 2 \times 10^3$  seconds, and this has been confirmed by optical microscopy [17]. We also find that P  $\rightarrow$  H in the second sequence described above is  $\sim 10$  times slower than that for P  $\rightarrow$  H in the first sequence. The sample in the second sequence had not been H-aligned previously so had no 'memory' of such a condition whereas the sample prepared in the P-aligned state in the first sequence had such a memory (as for field-free recovery, figure 5).

Thus although it is possible to achieve the conversions H  $\leftrightarrow$  P in the LC state for this copolymer, using the two-frequency addressing principle, the stability of the H- or P-aligned materials obtained depends on the thermal/electrical history of the sample.

We note that the recovery experiments and field-induced transformations were conducted at 70°C. Lowering the sample temperature to room temperature for H- or P-aligned samples (prepared in different ways) has the effect of stabilizing the given alignment of the material due to the increase in effective viscosity of the polymer as T<sub>g</sub> is approached.

#### CONCLUSIONS

It has been shown that dielectric relaxation spectroscopy provides a convenient, direct and quantitative method for monitoring the macroscopic alignment of LC side chain polymers. Using this method we have shown that the alignment behaviour of a siloxane-chain copolymer may be studied in detail. It is found that H- or P-aligned or intermediately-aligned materials may be prepared using the two-frequency-addressing method and that although the H-aligned material is stable, P-aligned material may have different stabilities, depending on the thermal/electrical history of the sample. Clearly surface factors are important in this case for the stability and kinetic response to applied fields for H-aligned and P-aligned material.

## ACKNOWLEDGEMENTS

The authors thank Prof. Gray, Dr. Lacey and Dr. Hill for the provision of the sample and they wish to thank Dr. Donald R. Ulrich for discussions during the course of this work. The research was sponsored by the Air Force Office of Scientific Research (research programme sponsored by SDIO/IST and managed by AFOSR) under Contract F49620-87-C-0111. The United States Government is authorized to reproduce and distribute reprints for governmental purposes notwithstanding any copyright notation hereon.

## REFERENCES

1. H. Finkelmann and G. Rehage, *Adv. Polym. Sci.*, 60/61, 99 (1984).
2. V.P. Shibaev and N.A. Plate, *Adv. Polym. Sci.*, 60/61, 173 (1984).
3. C.B. McArdle (Ed.), Side Chain Liquid Crystal Polymers, Blackie, Glasgow and London, 1989.
4. G.S. Attard and G. Williams, *Polymer*, 27, 2 (1986).
5. G.S. Attard and G. Williams, *Liquid Crystals*, 1, 253 (1986).
6. G.S. Attard, K. Araki and G. Williams, *J. Molec. Electronics*, 3, 1 (1987).
7. G.S. Attard, K. Araki and G. Williams, *Brit. Polym. J.*, 19, 119 (1987).
8. G.S. Attard, K. Araki, J.J. Moura-Ramos and G. Williams, *Liquid Crystals*, 2, 1 (1987).
9. A. Kozak, G.P. Simon and G. Williams, *Polymer Commun.*, 30, 102 (1989).
10. G.S. Attard, K. Araki, J.J. Moura-Ramos, G. Williams, A.C. Griffin, A.M. Bhatti and R.S.L. Hung, in Polymer Association Structures, Liquid Crystals and Microemulsions, M.A. El Nokaly (Ed.), ACS Symposium Series No. 384, 1989, p. 255.
11. G.S. Attard, *Mol. Phys.*, 58, 1087 (1986).
12. K. Araki, G.S. Attard, A. Kozak, G. Williams, G.W. Gray, D. Lacey and G. Nestor, *J. Chem. Soc., Faraday Trans. 2*, 84, 1067 (1988).
13. M.G. Clark, K.J. Harrison and E.P. Raynes, *Phys. Technol.*, 11, 232 (1980).
14. M.G. Clark, *Displays*, January, 169 (1981).
15. A. Kozak, J.J. Moura-Ramos, G.P. Simon and G. Williams, *Makromol. Chem.*, 190, (1989), in press.
16. A.F. Martins, P. Esnault and F. Volino, *Phys. Rev. Lett.*, 57, 1745 (1986).
17. A. Nazemi, E.J. Kellar, G. Williams, F.E. Karasz, G.W. Gray, D. Lacey and J.S. Hill, submitted for publication.



92-18268

AD-P007 477



239



LIQUID CRYSTALLINE MATERIALS FOR POLYMERS WITH  
ANISOTROPIC ULTRASTRUCTURES

GEORGE S. ATTARD

Department of Chemistry, The University, Southampton SO9 5NH, UK.

ABSTRACT

The in-situ polymerisation of reactive thermotropic and lyotropic liquid crystals affords a method of processing new polymers with anisotropic ultrastructures.

INTRODUCTION

In solid state physics the concept of ultrastructure is used to describe a well defined arrangement of complex periodic structures with characteristic length-scales of a few hundred Å. When applied to liquid crystalline phases it describes structures with length-scales from a few tens of Å to a few thousand Å. The ultrastructure of thermotropic liquid crystalline phases results from a combination of long-range orientational order coupled with varying degrees of spatial order. Three examples of mesophase ultrastructures for rod-like and disc-like molecules are illustrated in Figures 1a and 1b.

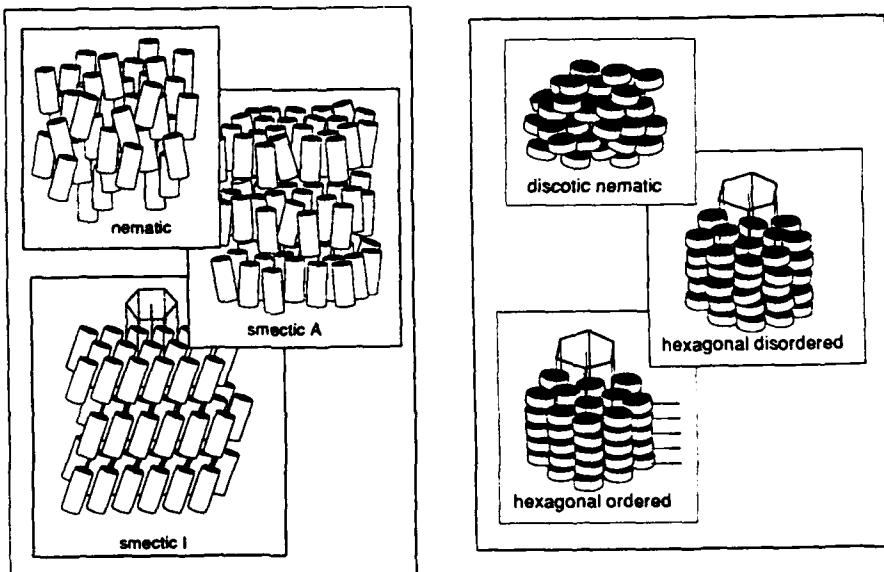


FIGURE 1

By contrast with the case of thermotropic liquid crystals, the ultrastructure of lyotropic liquid crystals results from the supramolecular arrangement of aggregates of amphiphilic molecules and in this case characteristic length-scales in excess of 500Å are in principle possible.

In polymeric materials anisotropic ultrastructures can occur either because the materials are liquid crystalline or because they are processed from the liquid crystalline phase. The overwhelming majority of polymers with anisotropic ultrastructures reported to date belong to the former class of compounds, and are mostly thermotropic mesogens.

Thermotropic liquid crystalline polymers are usually described as being of the main-chain or of the side-chain variety, depending on whether the rigid anisometric units (ie. rod- or disc-like units) are an integral part of the backbone or whether they are present as pendant side-chains. Mixed main-chain and side-chain systems have also been reported. A great diversity in polymer and copolymer architecture is thus possible as illustrated schematically in Figure 2.

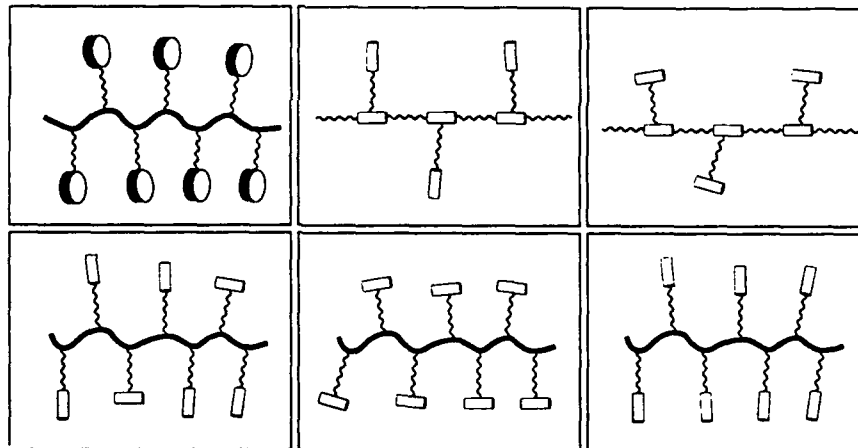


FIGURE 2

Typical synthetic routes to such polymers involve reactions performed in isotropic solution. Furthermore, the use of cross-linking agents during or after the polymerisation reaction results in the formation of elastomers and depending on the concentration of cross-links per polymer chain the side-chains may adopt an orientationally ordered ultrastructure as illustrated in Figure 3. Stretching films of these elastomers changes their optical properties and their use as acousto-optical transducers has been suggested. Note that because the polymerisation/cross-linking reactions are carried out in isotropic solution the polymer network is orientationally disordered (i.e. isotropic).

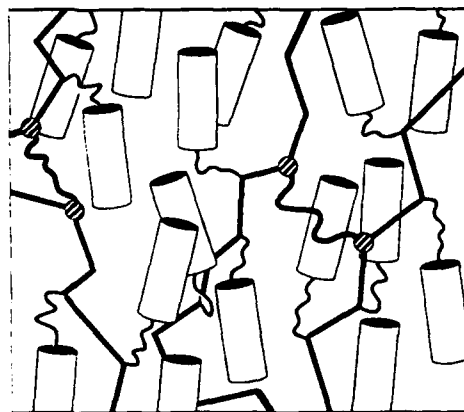
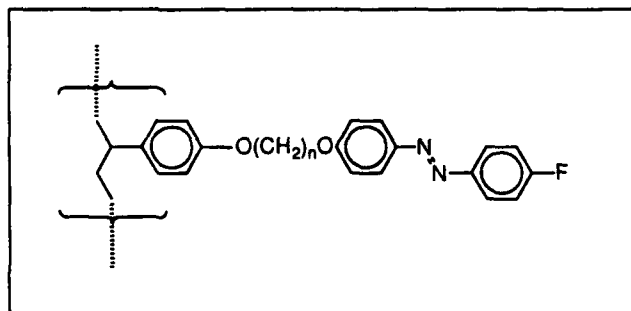


FIGURE 3

#### LIQUID CRYSTALLINE SIDE-CHAIN POLYMERS

The orientational anisotropy encountered in liquid crystalline polymers, particularly those of the side-chain variety, is of relevance to a number of technologies, e.g. laser-addressed optical information storage, and optical information and image processing based on non-linear optical (n.l.o.) effects. Of central importance to these applications is the ability of liquid crystalline phases to respond to electric fields. Accordingly, considerable effort is currently directed at the molecular engineering of materials whose dielectric, ultrastructural, and transitional properties are optimised to give fast response times, and, in the case of materials for  $\chi^{(2)}$  applications, a durable non-centrosymmetric distribution of dipole orientations when in the glassy state. As an illustration of the sophistication of the molecular engineering approach to new functional materials with anisotropic ultrastructure we consider the case of a homologous series of poly(styrene) derivatives synthesised at Southampton:



The motivation behind the design of these materials was the requirement to achieve liquid crystalline polymers with a high glass-transition temperature. Such materials were to be used in a study of the ageing of poling at various temperatures below  $T_g$  in order to obtain insights into the possible causes of loss of performance commonly observed in poled l.c. films for second harmonic generation. In addition to the primary requirement of high  $T_g$ , the high field strengths routinely employed in aligning and poling the polymers imposed the requirement for low clearing temperatures, ideally in the range 80-110°C, in order to minimise dielectric breakdown due to conductivity effects. By a careful consideration of the extensive structure-property relationships elucidated for low molar mass liquid crystals, we were able to design compounds with the required combination of properties. Furthermore we found that the parity of the alkyl spacer chain which links the mesogenic cores to the poly(styrene) backbone leads to an odd-even effect in the clearing temperatures. This provides a further design tool with which to fine-tune the physical properties of these materials. The transitional behaviour of the homologous series is shown in Figure 4. Note that the transition from liquid crystal to isotropic proceeds via a biphasic region which typically spans a 4 degree range. Studies of the dielectric, and poling properties of these materials are being carried out by Professor G. Williams at Swansea University.

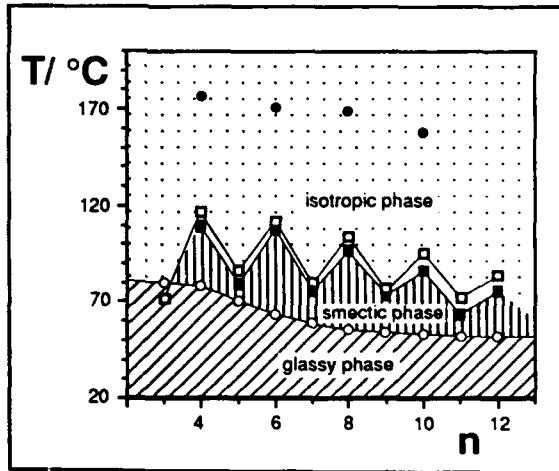


FIGURE 4

#### ANISOTROPIC MACROMOLECULAR ULTRASTRUCTURES FROM POLYMERSISABLE L.C. MONOMERS

After a decade of research in side-chain polymers it is becoming apparent that as a class of compounds they exhibit a much more limited polymorphism than the analogous low molar mass

liquid crystals. In principle polymers exhibiting the orientational and spatial anisotropy found in some of the more ordered smectic phases should have unusual mechanical and optical properties. One way of achieving polymers with this type of ultrastructure involves the polymerisation of reactive liquid crystalline monomers in the mesomorphic state. The resulting polymers, though not themselves liquid crystalline, would still have the anisotropic ultrastructure of the parent mesophase locked-in. However, because of the success in making new materials from reactions carried out in isotropic solution, and because of the structural and functional sophistication that is achievable using this approach, there has been little interest in attempting polymerisation directly in liquid crystalline phases. Ironically in-situ polymerisation was used in the first reported syntheses of liquid crystalline side-chain polymers<sup>1</sup>.

Clearly, the choice of polymerisable unit, and its location in the monomer are very important considerations in determining the success of in situ polymerisation. The ground rules for selecting suitable polymerisable units emerge from the following considerations. The polymerisable unit chosen must be such that the polymerisation process proceeds with a uniform release of heat. This requires effective dissipation of thermal energy to avoid creation of hot-spots which would lead to disruption of the ultrastructure. Furthermore it is essential that the heating caused by the polymerisation reaction does not lead to a phase transition. This problem can partly be overcome by designing materials in which the mesophase of interest is stable over a wide temperature range. The polymerisable unit and its location in the monomer must be such as to be conducive (or at least not disruptive) to the formation of orientationally ordered phases. Finally, it is essential that the nascent polymer does not lead to phase separation of the system into a monomer-rich phase with one ultrastructure and a polymer-rich phase with a different ultrastructure. This would require the polymerisation to proceed at a faster rate than the kinetics of phase separation.

Considerable research is required to acquire the thermodynamic and kinetic data that will enable the intelligent design of polymerisable units. However, our experiments have shown that the use of diacetylenic units as the polymerisable groups in liquid crystalline monomers meets most of the criteria set out above. It is well known from the work of Wegner<sup>2</sup> and others that in the solid state diacetylene monomers undergo a topochemical polymerisation with little distortion of the lattice structure. Our work together with the work of Hardy et al.<sup>3</sup> and Schen et al.<sup>4</sup> seems to suggest that this situation applies in highly ordered smectic phases too. By a suitable choice of anisometric unit it is possible, at least in principle, to prepare polymer networks of the types shown in Figures 5a and 5b. Depending on whether the diacetylenic monomers form interdigitated or bilayer smectic phases, two-dimensional or three-dimensional polymer networks can result. These can be regarded as the two- or three-dimensional analogues of conventional ladder polymers, since they consist of two sheets of unbranched polymer chains cross-linked through the anisometric groups of the parent monomer.

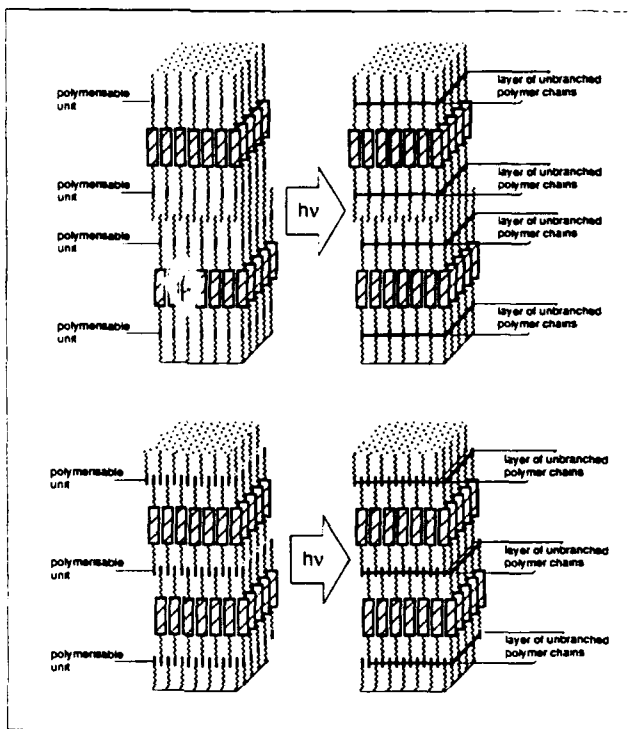
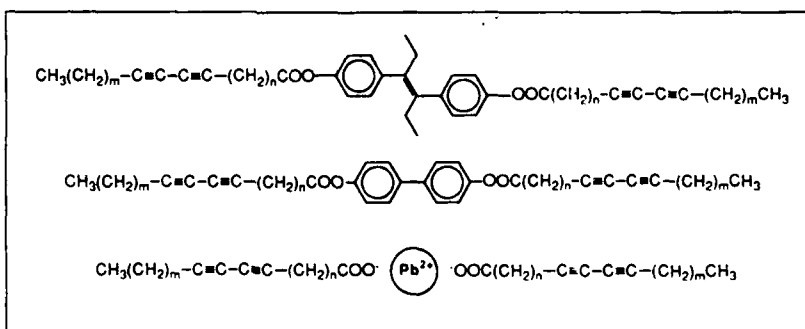


FIGURE 5

Over the past year we have synthesised a number of monomeric liquid crystals bearing one or more diacetylenic sequences which we found to polymerise readily when in the highly ordered smectic phases to yield sandwich polymers of the type shown in Figure 5a:



Work is currently in progress to achieve the 3-D type networks. By designing materials which can be readily aligned by electric/magnetic fields or by flow, uniform thick elastomeric

films with multiple or sandwich-like layer ultrastructures can be prepared.

The versatility of the liquid crystalline state of matter in processing new polymer materials is further illustrated by a system we developed which can be processed from the mesophase into highly oriented fibres of diameters ranging from  $6\mu$ - $100\mu$ . The polymerisable monomers in these materials consist of disc-like molecules with a diacetylene unit in each of four alkyl chains radiating from the discotic core. These systems form thermotropic discotic mesophases with an ultrastructure similar to those shown in Figure 1b. Fibres can be drawn easily from the discotic melt. As a fibre is drawn it cools to form a lamellar crystal so that at room temperature the fibre (which can be several metres long) is essentially a single crystal. From X-ray diffraction studies we conclude that the molecular arrangement in the fibres is as shown in Figure 6, a structure that clearly owes much to the ultrastructure of the parent mesophase. Exposing the fibres to uv light results in optic fibres of high optical quality and with good third order optical non linearities due to the presence of the poly(diacetylene) network. The excellent surface quality of the fibres produced using this method is shown in the scanning electron micrograph in Figure 7.

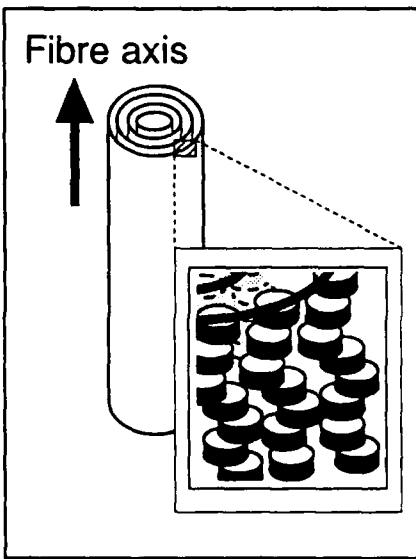


FIGURE 6

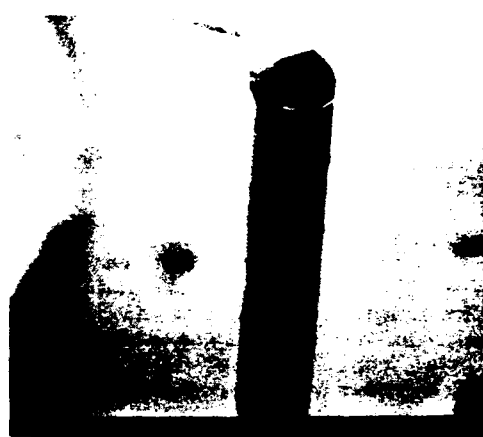


FIGURE 7

Lyotropic polymerisable monomers can also be used as a route to polymers with unusual ultrastructures. As in the case of thermotropic monomers, lyotropic systems exhibit a rich variety of ultrastructures with the amphiphilic molecules being arranged for example in layers, spherical, cylindrical, or discotic micelles, or in lattices with cubic symmetry. The latter family of mesophases is particularly interesting from the technological point of view. The ultrastructure of these intriguing mesophases consists of a bicontinuous network of water pores/channels and aliphatic sheets, as illustrated by the example shown in Figure 8. Such materials can be considered as the organic analogues of zeolites. The channel dimensions and connectivities can be controlled by the conditions under which the cubic phases are formed. Such phases are of great biological importance being involved in processes such as fat digestion; the intimate association of the water and aliphatic regions coupled with the fast diffusion within each of the bicontinuous regions providing a method for catalysing lipid hydrolysis. It has been shown that incorporation of polymerisable monomers in such cubic phases followed by polymerisation leads to microporous polymeric networks which are self-supporting when dried<sup>5</sup>. We are currently investigating the use of polymerisable amphiphiles to produce such microporous networks with improved mechanical and optical properties. The monodispersity of the pore size coupled with the controllable pore/channel sizes makes these materials of interest for ultrafiltration applications and as novel supports for enzymatic catalysis. In addition, the high surface area and the

intimate association of the water channels with the aliphatic sheets can be exploited to produce redox polymer networks.

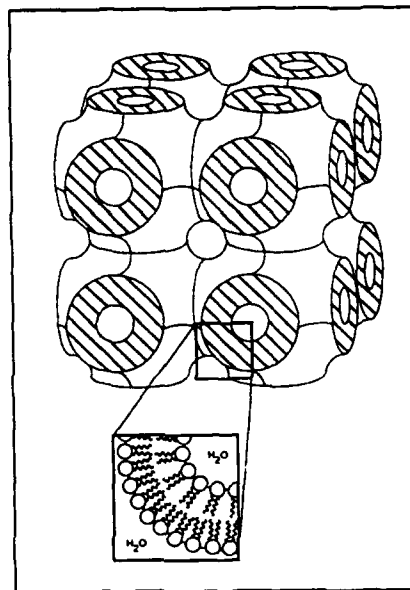


FIGURE 8

#### CONCLUSION

We have shown that by a careful choice of polymerisable unit reactive liquid crystalline monomers can be designed to exhibit a range of thermotropic and lyotropic structures which can be locked-in on polymerisation to yield multifunctional macromolecular networks with controlled and unusual anisotropic ultrastructures. This development represents a significant departure from the anisotropy conventionally encountered in liquid crystalline polymers and illustrates the versatility of the liquid crystalline state of matter as a route to novel polymeric materials.

#### REFERENCES

1. Y. Bouligand, P.E. Cladis, L. Liebert, and L. Strzelecki, *Mol.Cryst. Liq. Cryst.* **25**, 233 (1974).

2. B. Tieke, G. Lieser, and G. Wegner, *J. Polym. Sci., Polym. Chem. Edn.* 17, 1631 (1979).
3. G. Hardy, G.H.W. Milburn, K. Nyitrai, J. Horvath, G. Balazs, J. Varga, and A.J. Shand, *New Polymeric Mater.* 1, 209 (1989).
4. M.A. Schen, *Proc. SPIE Int. Soc. Opt. Eng.* 824, 93 (1987).
5. D.M. Anderson and P. Strom in Polymer Association Structures, edited by M.A. El-Nokaly (ACS Symposium Series 384, New Orleans, LO 1987) pp. 204-224.



92-18269

AD-P007 478



249

MAGNETIC PROPERTIES OF LIQUID CRYSTALS  
INCORPORATING METAL CENTRES



WOLFGANG HAASE, STEFAN GEHRING, AND BETTINA BORCHERS

Institut für Physikalische Chemie, Technische Hochschule Darmstadt, Peter-  
senstraße 20, D-6100 Darmstadt, Federal Republic of Germany

ABSTRACT

Magnetic susceptibility data (300-520 K) of monomeric and dimeric mesogenic copper(II) compounds are presented. Different magnetic effects arising from the paramagnetic Cu(II)-centres and the diamagnetic anisotropy of the mesogenic groups are observed and discussed with respect to possible *intermolecular interactions*.

INTRODUCTION

The increasing number of studies in metal containing liquid crystalline compounds (metallo-mesogens) is based on their new physical and chemical properties [1-3]. Interesting technical applications on the magnetic and optical field are expected from the combination of the magnetic and optical properties of transition metal complexes with the well-known properties of liquid crystals (l.c.'s) like optical, magnetic, and dielectrical anisotropy or thermal behavior. Up to now, the research has been concentrated on chemical syntheses and phase characterizations [1-3], whereas the investigations of other physical data, especially magnetic ones, are limited [4-7].

In this paper we report on magnetic susceptibility measurements in the crystalline and liquid crystalline state of different thermotropic metallo-mesogens with dimeric and monomeric copper(II)-centres. Some basic problems concerning the interpretation of the magnetic data obtained from these systems are discussed concerning possible *intermolecular magnetic interactions* in the l.c. state.

EXPERIMENTAL

The investigated compounds 1-5 are shown in figure 1. They were prepared according to procedures described in the literature (1-3 [8], 4 [9], 5 [10]), the elemental analyses agree with the calculated data.

Thermal behavior and phase characterizations were investigated using DSC, polarizing microscopy, and X-ray techniques. These data as far as reported were confirmed; they are included in figures 2-6.

The magnetic susceptibilities were measured in the heating mode with a Faraday-system [11] modified for the temperature range 300-520 K. Except 4 no data in the isotropic phase could be obtained because of thermal decomposition. The molar susceptibilities (per mole Cu) were corrected for

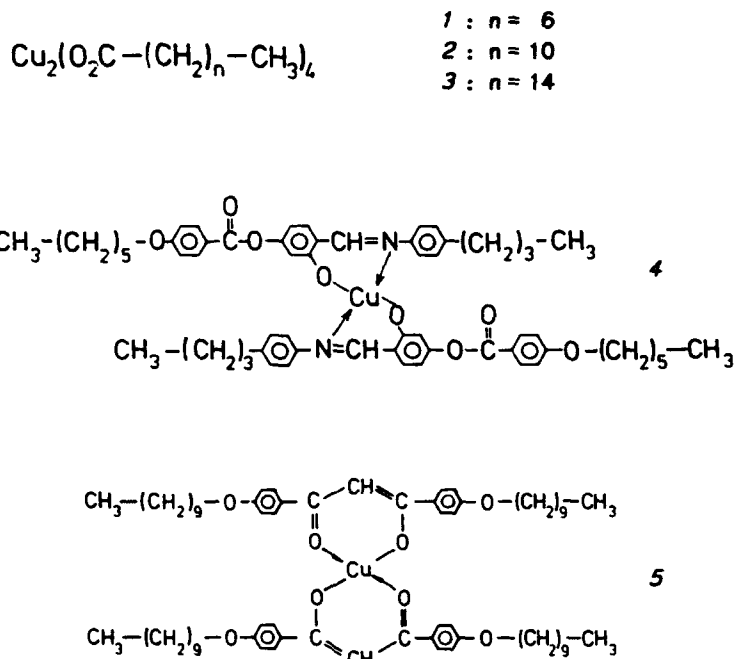


Figure 1: Investigated compounds

Isotropic diamagnetism ( $-\chi_{\text{dia}} / 10^{-6} \text{ cm}^3 \text{ mol}^{-1} = 206.0$  (1), 296.9 (2), 387.8 (3), 623.4 (4), 746.6 (5)).

## RESULTS

The experimental and calculated  $\chi(T)$ -data are presented together with the phase transition temperatures in figures 2-6 for 1-5 (C: crystalline, D: discotic, N: nematic, I: isotropic).

The three copper(II)-carboxylates exhibit a similar magnetic behavior at the phase transition C  $\rightarrow$  D ( $D_h$ ) with  $\Delta\chi = \chi^D - \chi^C < 0$ . For 1 and 3 comparable  $\chi(T)$ -dependences were observed, whereas the  $\chi(T)$ -data of 2 are characterized by an additional jump with  $\Delta\chi = \chi^{C_2} - \chi^{C_1} > 0$  at the phase transition  $C_1 \rightarrow C_2$ . The unusual magnetic behavior of 2 agrees with results reported previously by other authors, as well as the corresponding low temperature data which are not presented here [4].

In case of the Cu(II)-Schiff's Base 4 a  $\Delta\chi > 0$  jump occurs at the phase transition C  $\rightarrow$  N.

For the Cu(II)-diketonato compound 5 the observed magnetism was not influenced by the phase transitions C  $\rightarrow$  D  $\rightarrow$  I.

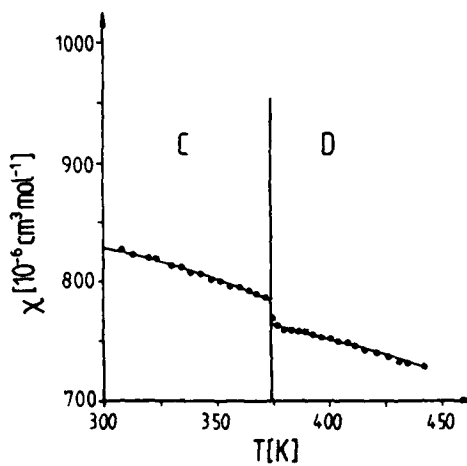


Figure 2: Experimental (●) and calculated (—) magnetic susceptibilities vs. temperature and phase transition  $T_{C \rightarrow D}$  for 1

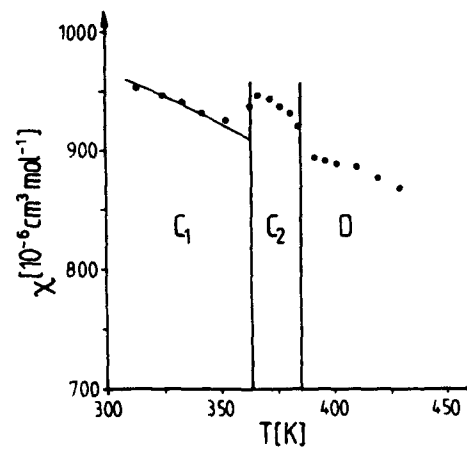


Figure 3: Experimental (●) and calculated (—) magnetic susceptibilities vs. temperature and phase transitions for 2

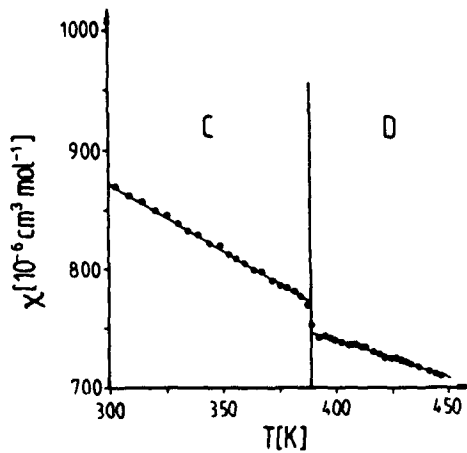


Figure 4: Experimental (●) and calculated (—) magnetic susceptibilities vs. temperature and phase transition  $T_{C \rightarrow D}$  for 3

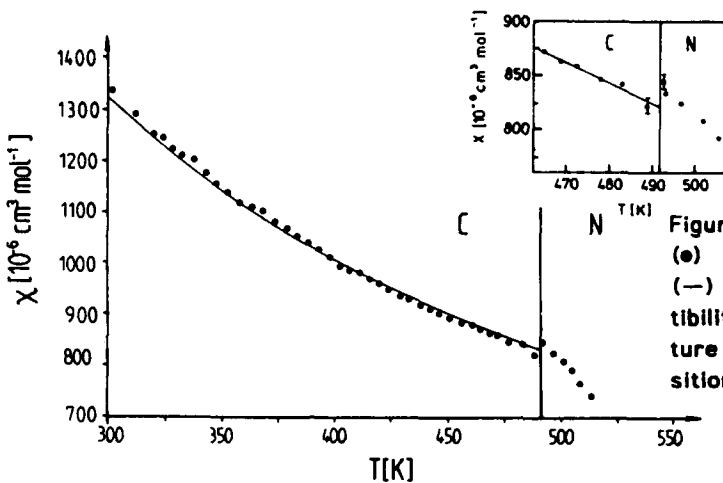


Figure 5: Experimental (●) and calculated (—) magnetic susceptibilities vs. temperature and phase transition  $T_{C-N}$  for 4

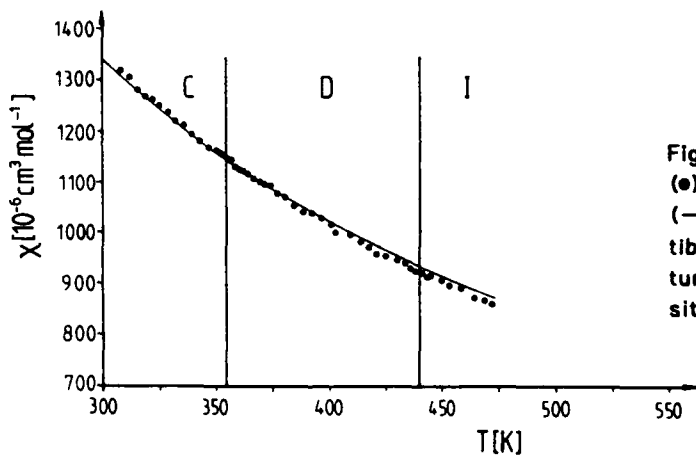


Figure 6: Experimental (●) and calculated (—) magnetic susceptibilities vs. temperature and phase transitions for 5

## DISCUSSION

To deduce an *intermolecular* magnetic coupling from susceptibility measurements in the liquid crystalline phase of these new metallo-mesogenic systems two different magnetic phenomena arising from the combination of paramagnetism and anisotropy of l.c. properties have to be regarded in principle:

- The leading term for e.g. mononuclear Cu(II) compounds is expected from the paramagnetism of the unpaired electron obeying the Curie-law. In case of dimeric Cu(II) systems intramolecular exchange interaction leads to e.g. diamagnetic ground-states for antiferromagnetic coupling.
- Well aligned mesogenic compounds with phenyl- or cyano-groups show diamagnetic anisotropy in the l.c. phase with  $\Delta\chi > 0$  ( $\Delta\chi = \chi_{\parallel} - \chi_{\perp}$ ) in general [12]. The size of  $\Delta\chi$  depends on the number of phenyl-groups.

### Copper(II)-Carboxylates 1-3

The  $\chi(T)$ -data of 1-3 which are reduced in comparison with those for isolated paramagnetic  $S=1/2$ -centres confirm the existence of exchange coupled Cu(II)-centres. In the solid state, some anhydrous Cu(II)-carboxylates consist of the well-known fourfold  $\text{CO}_2$ -bridged dimeric Cu(II)-units linked together to alternating chains [13,14, and ref. given in 4]. However, for the magnetic description the model of discrete antiferromagnetically exchange coupled dimeric Cu(II)-units is in excellent agreement with the experimental  $\chi(T)$ -data. This was also previously reported for 2. [4]. The exchange coupling constant  $J$  and the isotropic electron g-factor obtained from a least-squares-fit of the Bleaney-Bowers equation (eq. (1),  $\Theta=0$  K; from  $H=-2J\hat{S}_1\hat{S}_2$ ) to the experimental susceptibility data are given in table 1. The fits were performed separately for the crystalline state and mesophase.

$$\chi_{\text{calc.}} = \frac{N_A g^2 \mu_B^2}{k(T-\Theta)} \frac{1}{3 + \exp\{-2J/kT\}} \quad (1)$$

Table 1: Magnetic exchange parameters for 1-3 in the crystalline and l.c. phase (models A, B)

	1	2	3
crystalline phase ( $\Theta=0$ K, fixed); 2: $C_1$			
$J/\text{cm}^{-1}$	-153(2)	-139(2)	-120(2)
g	2.12(2)	2.22(2)	2.00(2)
discotic phase, model A (best fit, $\Theta=0$ K, fixed)			
$J/\text{cm}^{-1}$	-180(2)	-	-172(2)
g	2.21(2)	-	2.16(2)
discotic phase, model B (( $J, g$ ) <sub>C-phase</sub> , fixed)			
$J/\text{cm}^{-1}$	-153	-	-120
g	2.12	-	2.00
$\Theta/\text{K}$	-5.1(5)	-	5.0(5)

For 1-3 the observed spontaneous  $\chi$ -decrease at  $T_{C \rightarrow D}$  can be explained with two models based on the assumption, that the Cu(II)-magnetism dominates over the diamagnetic anisotropy because of the lack of phenyl-groups. With two solid phases 2 differs from 1 and 3. The changed magnetic susceptibilities in the  $C_1$ - and  $C_2$ -phase may indicate changes in the molecular geometry.

The best fits for the I.c.-phase of 1 and 3 were obtained varying J and g simultaneously (table I, model A; figures 2 and 4). The effects on J and g - comparing the C- and D-phases - are greater than reported in previous investigations on comparable systems [4]. As a consequence of these changes in the exchange parameters, the molecular ordering in the I.c.-phase should be associated with essential modifications within the dimeric Cu(II)-unit and/or the local Cu(II)-coordination geometry.

Assuming model B the solid state structure of the dimeric  $\text{Cu}_2(\text{O}_2\text{C}-)_4$ -core is not supposed to be modified by the phase transition C  $\rightarrow$  D. Therefore, the fit parameters J and g were fixed at the values of the crystalline phase. The reduced  $\chi$ -values are explained with an additional *intermolecular* magnetic coupling expressed by a Weiss-constant  $\Theta$  in equation (1). For both, 1 and 3,  $\Theta = -5$  K was obtained indicating *intermolecular* antiferromagnetic interactions. The fits were of sufficient quality. Further studies based on alternating chain behavior are under investigation.

To summarize, the temperature dependence of the magnetic susceptibilities in mesogenic Cu(II)-carboxylates like 1-3 is clearly affected by the I.c. ordering. However, an unequivocal proof for *intermolecular* magnetic coupling is not possible on the basis of  $\chi(T)$ -data only.

#### Cu(II)-Schiff's Base 4

The orientation of the rod-like Cu(II)-Schiff's Base 4 parallel to the magnetic field leads to a diamagnetic anisotropy of  $\chi$  comparable to that observed for usual diamagnetic liquid crystals [12]. X-ray experiments in H-fields confirmed the orientation of 4 which is caused by the six phenyl-groups within the molecule. Therefore, the jump  $\Delta\chi > 0$  at  $T_{\text{C} \rightarrow \text{N}}$  can be explained by a dominating diamagnetic anisotropy. A magnetic long range order effect cannot be separated. The solid phase magnetism ( $\mu_{\text{eff}}^{\text{exp.}} = 1.797(6)$   $\mu_B$ ) obeys the Curie-law with  $g = 2.01(2)$ .

#### Cu(II)-Diketonate 5

In contrast to 4 compound 5 shows a Curie-behavior over the whole temperature range under investigation ( $\mu_{\text{eff}}^{\text{exp.}} = 1.801(6)$   $\mu_B$ ;  $g = 2.02(2)$ ). An influence on  $\chi$  of the different phases (C  $\rightarrow$  D  $\rightarrow$  I) as well as a magnetic long range effect could not be observed. The missing alignment in the I.c. phase - also observed in X-ray experiments - seems to be responsible for this behavior. Nevertheless, we have to point out, that there is still the possibility of a compensation of diamagnetic anisotropy and antiferromagnetic long range effects on  $\chi$ .

#### ACKNOWLEDGEMENT

This work was supported by the Deutsche Forschungsgemeinschaft.

References

1. H. Adams, N.A. Bailey, D.W. Bruce, R. Dhillon, D.A. Dunmur, S.E. Hunt, E. Lalinde, A.A. Maggs, R. Orr, P. Styring, M.S. Wragg, and P.M. Maitlis, *Polyhedron* **7**, 1861 (1988).
2. B. Mühlberger and W. Haase, *Liq. Cryst.* **5**, 251 (1989).
3. Proceedings of the 1<sup>st</sup> International Symposium on Metal-Containing Liquid Crystals ("Metallo-Mesogens"), University of Sheffield, United Kingdom, 12.-13.4.1989.
4. A.-M. Giroud-Godquin, J.-M. Latour, and J.-C. Marchon, *Inorg. Chem.* **24**, 4452 (1985).
5. I.G. Bikchantaev, Y.G. Galyametdinov, and I.V. Ovchinnikov, *Zhurnal Strukt. Khimii* **28**, 61 (1987) [*J. Struct. Chem. (USSR)* **28**, 685 (1988)].
6. M.P. Eastman, M.-L. Horng, B. Freiha, and K.W. Sheu, *Liq. Cryst.* **2**, 223 (1987).
7. J.-J. André, M. Bernard, C. Piechocki, and J. Simon, *J. Phys. Chem.* **90**, 1327 (1986).
8. H. Abied, D. Guillon, A. Skoulios, P. Weber, A.-M. Giroud-Godquin, and J.C. Marchon, *Liq. Cryst.* **2**, 269 (1987).
9. W. Haase und B. Borchers, presented at the Symposium "Metallo-Mesogens", 1989 [cf. ref. 3].
10. K. Ohta, H. Muroki, A. Takagi, K.-I. Hatada, H. Ema, I. Yamamoto, and K. Matsuzaki, *Mol. Cryst. Liq. Cryst.* **140**, 131 (1986).
11. L. Merz and W. Haase, *J. Chem. Soc., Dalton Trans.* **1980**, 875.
12. H.J. Müller and W. Haase, *J. Physique* **44**, 1209 (1983).
13. Y.A. Simonov and T.I. Mallinovskii, *Sov. Phys. Crystallogr.* **15**, 310 (1970).
14. T.R. Lomer and K. Perera, *Acta Crystallogr.* **B30**, 2913 (1974).





AD-P007 479



257

DIELECTRIC PROPERTIES OF POLYMERIC LIQUID CRYSTALS  
WITH STRONG LATERAL DIPOLE GROUPS

WOLFGANG HAASE AND MATTHIAS PFEIFFER

Institut für Physikalische Chemie, Technische Hochschule Darmstadt, Petersenstr.  
20, D-6100 Darmstadt, Federal Republic of Germany.

ABSTRACT

Using broad band dielectric spectroscopy on well oriented microdomains of mesogenic polymethacrylates the influence of strong lateral dipole groups on the dielectric parameters could be verified. The mesogenic groups investigated were phenylbenzoates with fluorine substituents at the phenyl ring. The orientation of the samples was maintained in a superconducting magnet with field strength of 7.2 T. The results are compared with those obtained for non-substituted compounds.

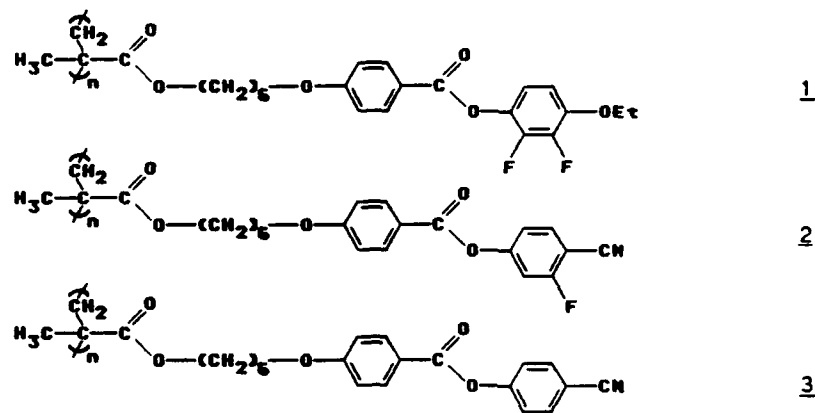
INTRODUCTION

Since their first synthesis in 1978 [1,2], many experimental and theoretical works have been done on the subject of liquid crystalline side chain polymers [3]. They have attracted considerable interest as materials e. g. for data storage and for non linear optics. Broad band dielectric spectroscopy starting from Hz up to some MHz is a very useful and direct method to detect the molecular dynamics of these compounds since different polar groups are involved in various motions. Recently some data have been published [4-10], which show at least three different relaxation processes, two of them are molecular processes ( $\delta$ ,  $\alpha$ ) and one is a local process ( $\beta$ ). As far as we know, no measurements have been done on samples with strong lateral dipole groups. Anisotropic data of such substances should lead to a better understanding of the relaxation processes. Because of the higher frequency of the relaxation around the long axis such mesogenic polymers are of interest for application too.

In this paper we report on two polymethacrylates (shown on the next page) with mesogenic phenylbenzoate groups in the side chain. The phenyl group of compound 1 has fluorine atoms in 2- and 3-positions and an ethyloxy group in 4-position. Compound 2 contains only one fluorine in 3-position. The 4-position is substituted by a cyano group. Measurements on compound 3 are already published [9,10]. We discuss for comparison also data of 3.

92-18270





## EXPERIMENTAL

The phase transition temperatures ( $^{\circ}\text{C}$ ) were measured by DSC and polarizing microscope (1: g 27  $\text{S}_\text{A}$  72.5 l; 2: g 30  $\text{S}_\text{A}$  80.5 l; 3, g 27  $\text{S}_\text{A}$  94 N 102 l). The structures of phases were identified by X-ray investigations, too.

The dielectric spectra are measured in a frequency range from 10 Hz up to  $10^7$  Hz using an impedance analyzer (HP 4192 A). The measurements were done under computer control. The sample was put into a parallel plane plate capacitor, consisting of two gold-coated glass plates separated by 75  $\mu\text{m}$  spacers, by means of capillary forces. The active area of the capacitor is  $0.78 \text{ cm}^2$ . To obtain a good alignment of the samples, the measurement cell was located in an electromagnet of 1.2 T field strength [11,12].

Sample 1 could be oriented only by using a superconducting magnet of a field strength of 7.2 T applying the following procedure: The cooling and heating process was repeated several times in the vicinity of the clearing point with a rate of 3 K per hour. After holding the temperature for 10-12 hours at 3 K below the clearing point the sample was cooled down just below the glass transition point. The aligned samples obtained by this procedure are completely transparent. Cooling down further to about 15 K below the glass temperature some small cracks in the polymer glass appeared. This effect was observed only in completely transparent samples. However, uncompletely oriented samples which appeared slightly opac showed the same dielectric anisotropy in the dielectric spectra. Besides the quality of orientation was checked by means of polarizing microscopy and by X-ray diffraction on an equally treated sample. During the measurements it was not possible to keep the high quality of orientation in the 1.2 T field when the temperature approached the clearing point. On a time scale of several hours a reorientation process took place depending on temperature.

## RESULTS AND DISCUSSION

Based on a model developed by Nordio and Segre [13] we describe [8-10] the molecular relaxation processes using a modified function:

$$\epsilon_{||}(v) - \epsilon_{||}^{\infty} = F^2 \frac{4 \pi N}{3 k T} \left( \mu_l^2 (1 + 2 S) A_{00}(v) + \mu_t^2 (1 - S) A_{01}(v) \right) + A_h(\mu, S, v) \quad (1)$$

$\overbrace{\hspace{10em}}^{A_{00}}$     $\overbrace{\hspace{10em}}^{A_{01}}$

$$\epsilon_{\perp}(v) - \epsilon_{\perp}^{\infty} = F^2 \frac{4 \pi N}{3 k T} \left( \mu_l^2 (1 - S) A_{10}(v) + \mu_t^2 (1 + 1/2 S) A_{11}(v) \right) + A_h(\mu, S, v) \quad (2)$$

$\overbrace{\hspace{10em}}^{A_{10}}$     $\overbrace{\hspace{10em}}^{A_{11}}$

$\mu_l$  and  $\mu_t$  are the longitudinal and transversal components of the dipole moment with respect to the mesogen's long axis,  $||$ - and  $\perp$ - denotes the orientation of the measuring field with respect to the director of the sample.  $A_{ij}(v)$  are the Fourier-transforms of correlation functions of the Wigner rotational matrix.  $A_h(\mu, S, v)$  takes into account the contribution of dipole movement due to the dynamics of the main chain. The term  $A_{00}$  describes the  $\delta$ -relaxation, whereas all other terms contribute to the  $\alpha$ -relaxation. Anisotropic measurements with strong lateral dipole groups should enable a separation of the  $\alpha$ -relaxation because of the different orientation and temperature dependence of the processes  $A_{01}$ ,  $A_{10}$  and  $A_{11}$ .

For a comparative analysis estimated values of the longitudinal and transversal dipole components using dipole moments [14-16] are listed in table I. X-ray structure analysis [17] and theoretical calculations [18] give evidence to assume all-trans conformation of the mesogen and an angle of torsion between the benzoate- and the phenyl group of 60 or 120 degrees.

Tab. I.: Estimated longitudinal and transversal components of the dipole moment.  $\mu_{t60}$  transversal component, 60 degree conformation;  $\mu_{t120}$  transversal component, 120 degree conformation;  $\mu_t$  transversal component, both conformations equally distributed;  $\mu_l$  longitudinal component. All values are given in Debye. (1 D =  $3.343 \cdot 10^{-29}$  Cm).

Compound	$\mu_{t60}$	$\mu_{t120}$	$\mu_t$	$\mu_l$
1	5.6	3.3	4.4	1
2	4.3	2.5	3.3	6.6
3	2.6	2.6	2.6	5.8

The absorption spectra of compound 1 in parallel orientation (fig. 1) show three relaxation processes. At low frequencies the absorption peak of the  $\gamma$ -relaxation appears. The spectrum is dominated by the large absorption in the kHz region and by an also strong relaxation in the MHz region. The first one is caused by the  $\alpha$ -process, the latter one by the  $\beta$ -process, which is interpreted as a local flipping process of the benzoate's carboxylate group.

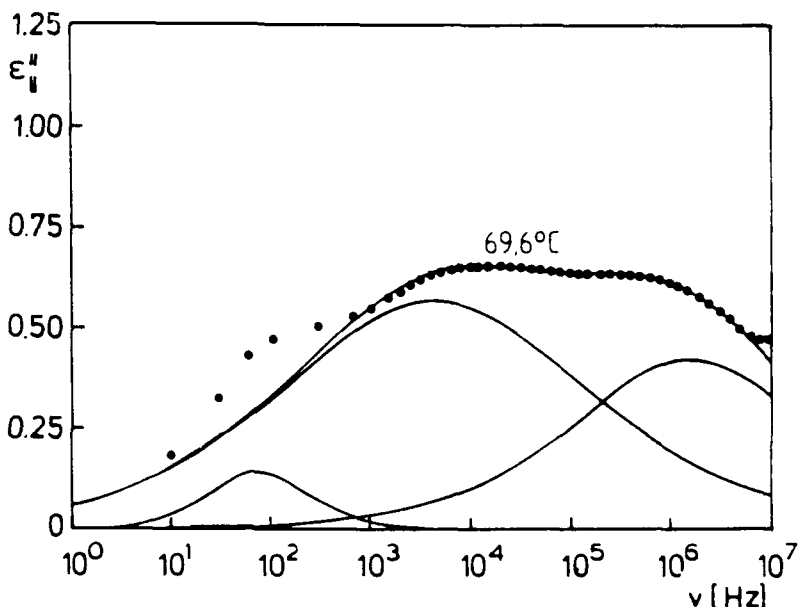


Fig. 1.: Absorption spectrum of compound 1 in  $\parallel$ -direction, showing  $\gamma$ ,  $\alpha$  and  $\beta$ -relaxation. The lines are fits using a sum of two Cole-Cole functions. The line of the  $\gamma$ -relaxation (ca. 100 Hz) is estimated from the deviation.

Figure 2 shows a spectrum of the same substance in perpendicular orientation. The  $\gamma$ -relaxation cannot be observed anymore whereas the relaxation strength of the  $\alpha$ - and  $\beta$ -relaxation is quite stronger.

By introducing two fluorine atoms and substituting the cyano group of 3 by an ethyloxy group the longitudinal dipole moment as well as the relaxation strength of the  $\gamma$ -relaxation were reduced very drastically. However, the expected increase of the  $\alpha$ -relaxation strength for 1 could not be verified. The relaxation strengths are weaker than the respective processes of 2, but stronger than the corresponding processes of 3. This unexpected behaviour can be explained by assuming generally a 120 degree conformation of the difluorinated compound (see tab. 1).

In figure 3 the absorption spectra of compound 2 in parallel and perpendicular orientation are presented. The large absorption in  $\parallel$ -orientation is due to the  $\gamma$ -relaxation. The  $\alpha$ - and probably the  $\beta$ -relaxation are indicated only by a weak

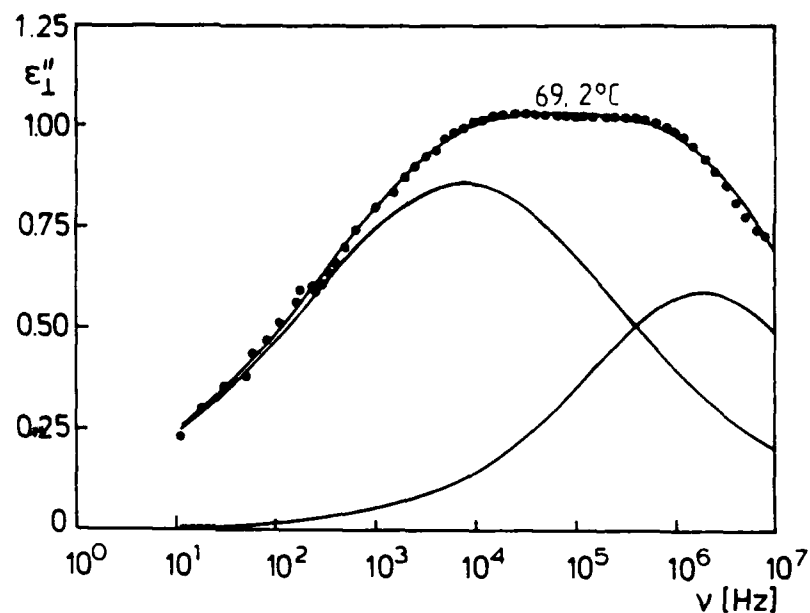


Fig. 2.: Absorption spectrum of compound 1 in L-direction, showing  $\alpha$  and  $\beta$ -relaxation. The lines are fits using a sum of two Cole-Cole functions.

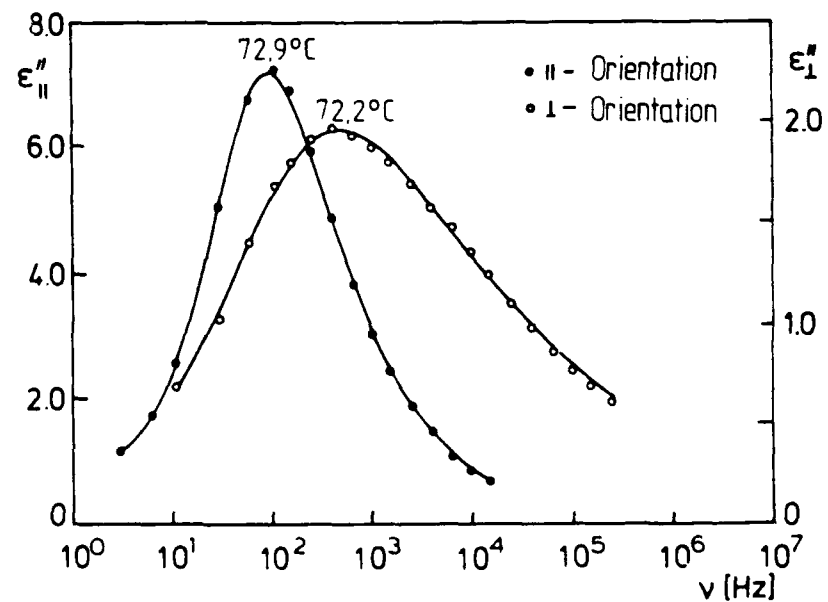


Fig. 3.: Absorption spectra of compound 2 in II and L-direction, showing the  $\alpha$ - and  $\beta$ -relaxation.

asymmetry of the absorption peak. The broad and weaker absorption in the spectra of  $\perp$ -orientation is caused by the  $\alpha$ -relaxation. The  $\beta$ -relaxation is not separated from the  $\alpha$ -relaxation but it causes the flat high frequency part of the absorption peak. It could not be analyzed independently. So, an analysis was made by means of the asymmetric Havriliak-Negami function [19]. At low temperatures the influence of the  $\beta$ -relaxation rises and shifts the maximum of the absorption peak to higher frequencies. The additional fluorine atom in 2 compared with 3 leads to an increase of both components of the dipole moment. This should lead to an enhancement of the relaxation processes. Assuming the proportionality between the square of the dipole moment and the relaxation strength, sample 2 shows for the  $\delta$ -relaxation the expected increase of the relaxation strength. Assuming equal distribution between the 60 and 120 degree conformation, the  $\alpha$ -relaxation is also intensified by the expected amount.

Figure 4 presents the plot of the relaxation frequencies versus reciprocal temperature for the compounds 1 and 2. The  $\alpha$ -relaxation of 1 exhibits a strongly nonlinear behaviour, which may be described by a WLF-equation [20]. It vanishes at the glass transition. The  $\beta$ -relaxation shows Arrhenius-like behaviour in the investigated range and is still observed in the glassy state. The activation energy is calculated equal to  $(80 \pm 5)$  kJ/mol. The  $\delta$ -relaxation of 2 also shows in the range of measuring Arrhenius-like behaviour with an activation energy of  $(230 \pm 10)$  kJ/mol. Due to the low relaxation frequencies the process could not be traced to the glass transition. The temperature dependence of the  $\alpha$ -relaxation exhibits WLF-behaviour at higher frequencies. At lower frequencies the non separated contribution of the  $\beta$ -relaxation is clearly observed

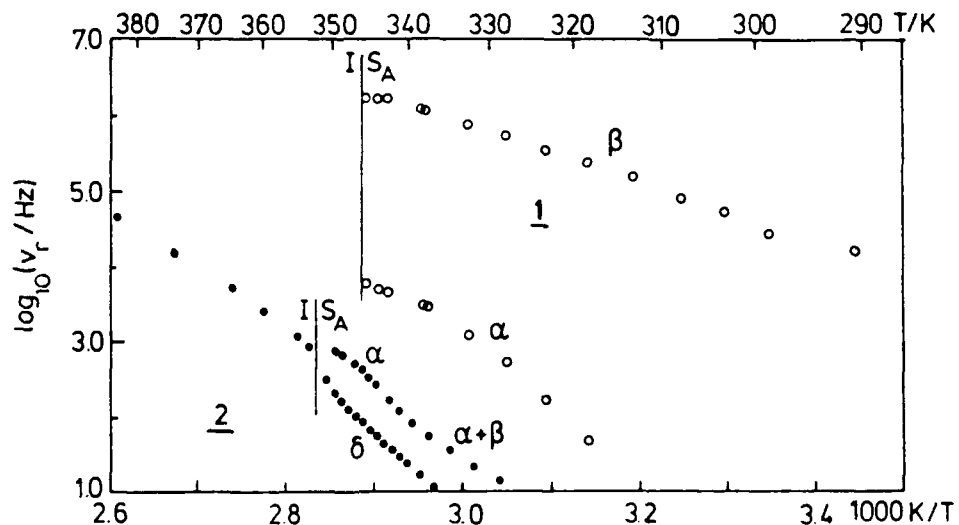


Fig. 4.: Activation diagram for compounds 1 and 2.

## ACKNOWLEDGEMENT

We thank Dr. Dorsch and Dr. Rieger from E. Merck Company, Darmstadt, for providing us with samples 1 and 2. Financial support by the Deutsche Forschungsgemeinschaft is greatly acknowledged.

## REFERENCES

1. H. Finkelmann, H. Ringsdorf and J.H. Wendorff, *Macromol. Chem.* 179, 273 (1978).
2. V. P. Shibaev, N.A. Plate and Y. S. Freidzon, *J. Polym. Sci. Polym. Chem. Ed.* 17, 1655 (1979).
3. C. B. McArdle ed., Side Chain Liquid Crystal Polymers, (Blackie and Son Ltd., Glasgow, 1989)
4. G.S. Attard G. Williams, W.G. Gray, D. Lacey and P.A. Gemmel, *Polymer* 27, 185 (1986).
5. S. U. Vallerien, F. Kremer and C. Boeffel, *Liq. Cryst.* 4, 79 (1989).
6. W. Kresse, S. Kostromin and V.P. Shibaev, *Macromol. Chem. Rap. Commun.* 3, 509 (1982).
7. J.D. Parnaix, R. Njeumo, L. Legrand, P. Le Barney and J.C. Dubois, *Liq. Cryst.* 2, 167 (1987).
8. F.J. Bormuth and W. Haase, *Liq. Cryst.* 3, 881 (1988).
9. F.J. Bormuth and W. Haase, *Liq. Cryst.* 5, (1989), in print.
10. F.J. Bormuth, PhD thesis, Darmstadt (1988).
11. W. Haase, H. Pranoto and F.J. Bormuth, *Ber. Bunsenges. Phys. Chem.* 89, 1229 (1985).
12. H. Pranoto, PhD thesis, Darmstadt (1984).
13. P.L. Nordio, G. Rigatti and U. Segre, *Mol. Phys.* 25, 129 (1973).
14. R.T. Klingblad, *J. Am. Chem. Soc.* 96, 7651 (1974).
15. V.I. Mikin, O.A. Osipov and Y.A. Zhanov, Dipolmoments in Organic Chemistry, (Plenum Press, 1970).
16. Handbook of Chemistry and Physics, (Chemical Rubber Press, 1984).
17. W. Haase, H. Paulus and R. Pendzialek, *Mol. Cryst. Liq. Cryst.* 101, 291 (1983).
18. Z.X. Fan, S. Buchner, W. Haase and H.G. Zachmann, *J. Chem. Phys.*, in print.
19. S. Havriliak and S. Negami, *J. Polym. Sci. C14*, 99 (1966).
20. M.L. Williams, R.F. Landel and J.D. Ferry, *J. Am. Chem. Soc.* 77, 370 (1955).



92-18271



AD-P007 480



5



## SYNTHESIS AND PROPERTIES OF COMB-LIKE LIQUID CRYSTALLINE POLYMERS WITH ELECTROOPTICALLY ACTIVE MESOGENIC SIDE GROUPS

M. MAEDA\*, R.S. KUMAR, A. BLUMSTEIN, S.K. TRIPATHY,  
P. SIXOU\*\* and F. FAUBERT\*\*

University of Lowell, Lowell, MA 01854

\*\*Laboratoire de Physique de la Matière Condensée

Université de Nice, Nice, France

\* on leave from Asahi Chemical Industry, Tokyo, Japan

### ABSTRACT

In an attempt to synthesize side chain liquid crystalline polymers containing NLO active moieties, a number of *p*-substituted aromatic azomethine phenols with donor-acceptor substituents such as  $\text{N}^{\text{+}}\text{C}$  and  $\text{NO}_2$ , were prepared and incorporated into a polymer chain as side groups.

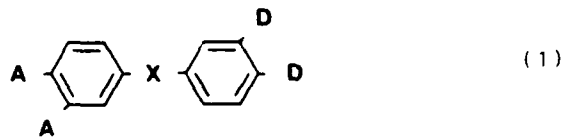
Liquid crystalline properties of intermediate compounds composed of such moieties were explored separately and in mixtures. Phase diagrams were established. These intermediate compounds of M2C8 and M5C8 show interesting mesogenic properties.

Methacrylic esters with such moieties were also synthesized. Homopolymer and copolymer systems with donor-acceptor substituents were obtained. Such copolymers also display liquid crystalline properties.

### INTRODUCTION

Many types of side chain liquid crystalline polymers which can form mesophases with smectic, nematic, or cholesteric molecular organizations have been reported.[1] Acrylic, methacrylic, siloxane and other structures are available as main chains. Various rigid aromatic moieties(such as biphenyl) can be chosen as mesogenic groups.

In this work we have synthesized moieties combining a potential for liquid crystallinity with a potential for NLO properties.[2] Such moieties are characterized by the presence of donor (D) and acceptor (A) substituents with a conjugate bond (V) on the mesogenic moieties, such as (1).[3]



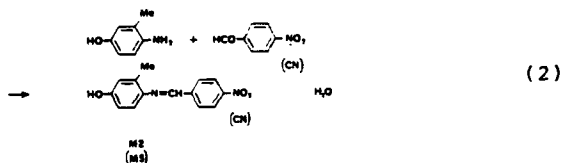
Such moieties can be introduced into the side chain or the main chain of liquid crystalline polymers.

Second order nonlinear optical properties are enhanced by spontaneous molecular orientation.[4] Orientation of a mesogenic group with a strong dipole in a LCP can be performed by an external force field in the anisotropic phase.[5]

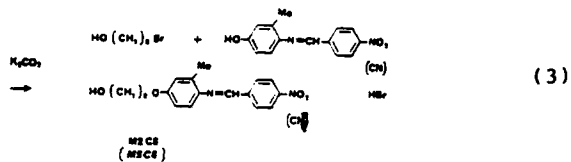
In this paper, synthetic, structural and thermal studies of such side chain LCP containing NLO moieties are described.

## EXPERIMENTAL

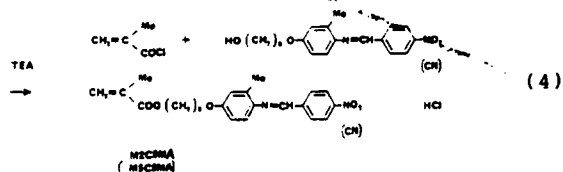
Two types of p-substituted aromatic azomethine phenols M2 and M5 were synthesized and used for further steps. Moieties M2 (or M5) were synthesized by condensation of p-nitro-benzaldehyde (or p-cyano-benzaldehyde) and 4-amino-m-cresol. [2]



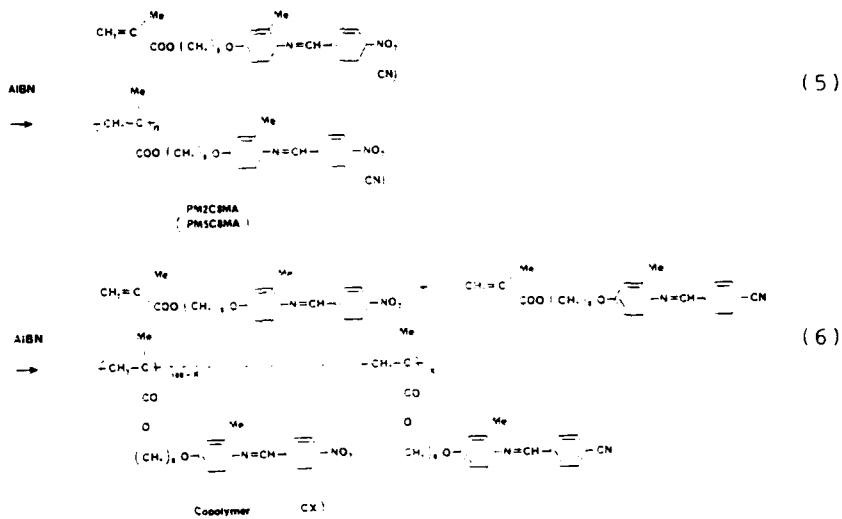
Polymethylene chain was attached to M2 and M5 to increase the mobility of the mesogenic groups when incorporated into a polymer chain as a side group. Intermediate compounds (M2C8 and M5C8) were synthesized by condensation of M2 or M5 and 8-bromo-1-octanol in the presence of  $K_2CO_3$ .



Finally, methacrylates of intermediate compounds (M2C8MA and M5C8MA) were synthesized from M2C8 or M5C8 and methacryloyl chloride in distilled THF solution in presence of triethylamine. Purification of M2, M5, intermediates and monomers was performed by recrystallization from concentrated solutions. Purity was checked by elemental analysis and was found satisfactory.



Polymerization and co-polymerization of M2C8MA, M5C8MA and of their mixtures were performed radically. Distilled benzene was used as the solvent and AIBN was used as the initiator. Polymerization tubes were sealed under high vacuum and the polymerization was conducted at 60 °C for 30-70 hours.[3] Polymers were precipitated repeatedly in a methylene chloride-methanol mixture.



## RESULTS

### Molecular weight of polymers

Molecular weight of polymers were determined by GPC. Polystyrene standards were used as molecular weight references. Both homopolymers and copolymers were characterized by relatively narrow GPC distributions indicating a good compositional homogeneity (in the case of copolymers) and relatively narrow molecular mass distributions. Occassionally, the chromatograms displayed a shoulder.

In addition, viscosity measurements of polymer solutions (1,1,2,2,-tetrachloroethane) were done. The average molecular weights and the inherent viscosities of polymers are listed in Table I.

Table I Molecular weight and inherent viscosity of polymers

	Elution Volume(ml)	M peak	Inherent Viscosity(dl/g)
C 00	17.8	72,800	0.085
C 20	18.6	49,400	0.068
C 30	18.6	49,400	0.062
C 50	18.5	51,900	0.084
C 60	18.3	57,100	0.070
C 70	18.6	49,400	0.059
C 80	18.2	60,000	0.081
C 90	18.4	54,500	0.052
C100	18.8	44,900	0.041

### Structural study of polymers

In order to check the composition of copolymers, quantitative FT-IR analysis was performed.[7] Fig.1 shows FT-IR spectra of copolymers with  $x = 0, 30, 60, 100$  respectively ( $x$  corresponds to M2C5MA content expressed in mole percent). C-NO<sub>2</sub> (1522 and 1342 cm<sup>-1</sup>) and C≡N (2228 cm<sup>-1</sup>) were taken as the frequencies corresponding to the characteristic peaks of M2C8MA and M5C8MA respectively. C=O (1726 cm<sup>-1</sup>) was taken as the internal reference frequency.

In Fig.2 the ratio of these intensities was plotted against the composition and shows a linear dependence.

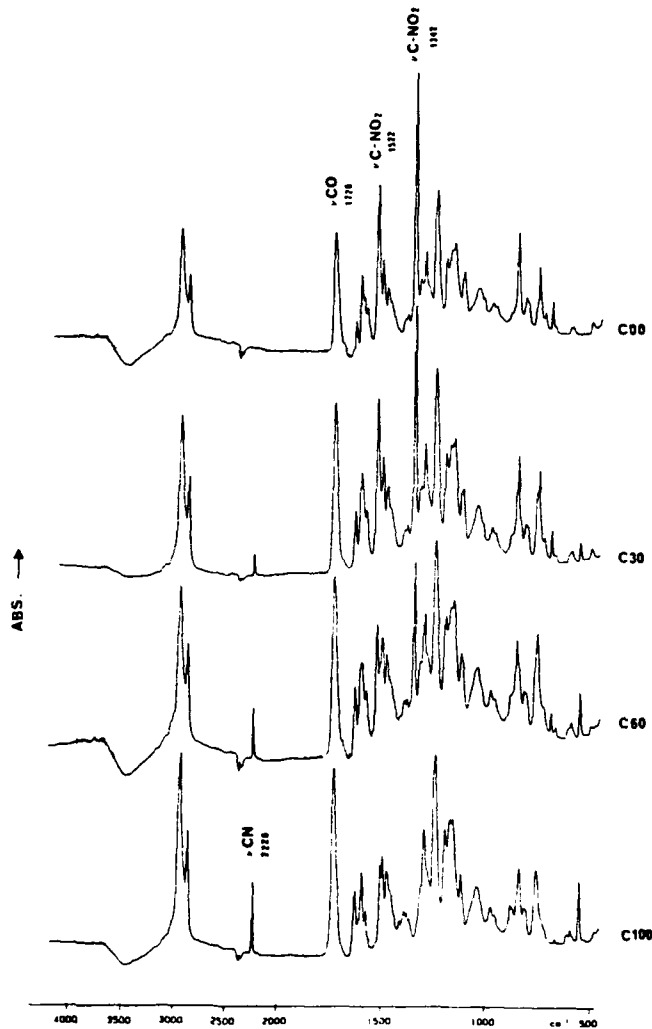


Fig.1 FT-IR spectra of copolymers ( $X = 0, 30, 60, 100$ )

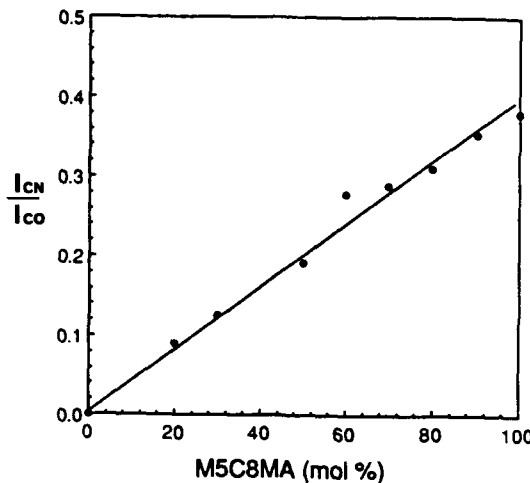


Fig.2 Copolymer composition vs. the FT-IR ratio

Thermal properties of polymers and of their intermediates

Thermal properties were determined by DSC. The phase diagram of the mixture of monomer intermediates, M2C8 and M5C8 is given in Fig.3. An eutectic composition is apparent at 30% of M5C8. At this composition the nematic interval is the largest. The nematic mesophase for all compositions is monotropic.

The phase diagram of the copolymer system is given in Fig.4. In contrast, to the low molecular mass intermediates no crystallization of polymers and copolymers takes place. While the polymer of M2C8MA does not display any liquid crystallinity, poly(M5C8MA) is clearly an enantiotropic nematic. The copolymers display in the interval (between 20 and 90% M5C8MA composition) a wide enantiotropic nematic mesophase and the nematic phase of polymers and copolymers can be quenched by cooling.

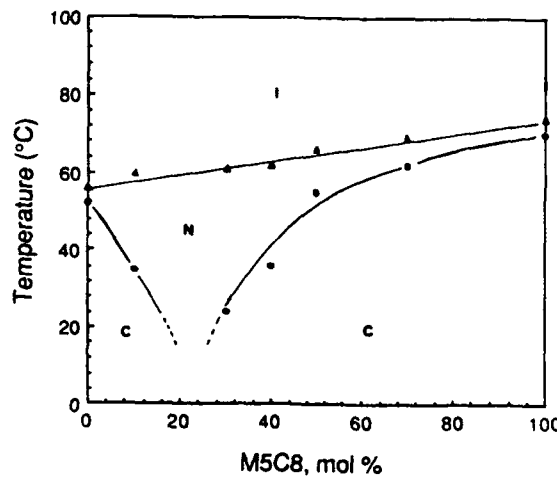


Fig.3 Phase diagram of mixture of M2C8 and M5C8

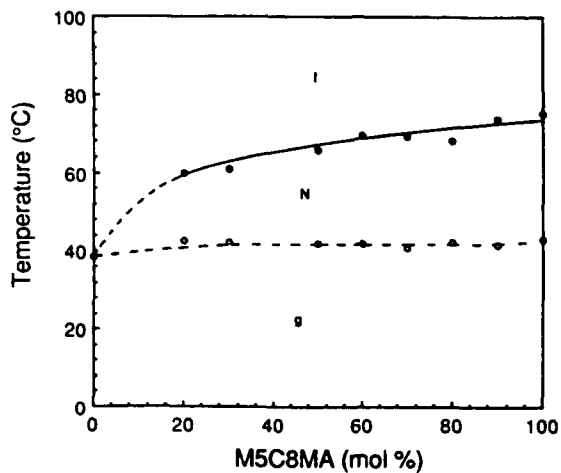


Fig.4 Phase Diagram of Copolymer System

#### CONCLUSIONS

Side chain liquid crystalline polymers and copolymers containing moieties with potential mesogenic and NLO properties were synthesized and characterized.

Phase diagrams of low molecular mass intermediates and of the corresponding copolymers were established. While the low molecular mass intermediates displayed monotropic nematic mesophases the corresponding copolymers displayed large enantiotropic nematic intervals. Both types of liquid crystalline polymers can be studied for their NLO properties in their nematic state.

#### ACKNOWLEDGEMENT

Partial support for this work from Asahi Chemical Co. and from NSF Polymers Program (grant DMR 8823084) is gratefully acknowledged.

#### REFERENCES

- [1] for example V.P. Shibaev and N.A. Plate, *Adv. Polym. Sci.*, 60/61, 173 (1984)
- [2] R.S. Kumar, J. Kumar, S.S. Kumar, A. Blumstein and S.K. Tripathy, *Proceeding of international symposium of macromolecules*. Kyoto (1988)
- [3] J.L. Oudar, *J. Chem. Phys.*, 67, 446 (1977)
- [4] K.D. Singer, M.G. Kuzyk and J.E. Sohn, *J. Opt. Soc. Am. B4*, 969 (1987)
- [5] Z.A. Roganava et.al. *Eur. Polym. J.*, 21, 645 (1985)
- [6] S.G. Kostromin, V.P. Shibaev and N.A. Plate, *Liq. Crysts.*, 2, 195 (1987)
- [7] C.H. Lin, M. Maeda and A. Blumstein, *J. Appl. Polym. Sci.* to be published.

THERMOTROPIC CHIRAL NEMATIC POLYMERS  
AS OPTICAL MATERIALS

S.H. Chen\*, M.L. Tsai and S.D. Jacobs

Department of Chemical Engineering and Laboratory for Laser Energetics  
206 Gavett Hall, University of Rochester, Rochester, 14627

\*To whom correspondence should be addressed.

Abstract

Chiral nematic copolymers based on optically active cholesterol, dihydrocholesterol, (R)-(+)- and (S)-(-)-1-phenylethylamine, and (+)- and (-)- isopinocampheol were synthesized and characterized for the investigations of thermotropic and optical properties. Although helical sense does not appear to correlate with the sign of  $[\alpha]_D$  of the precursor chiral compound as suggested by the observations of cholesteryl and dihydrocholesteryl copolymers, the inversion of chirality in the pendant group, (R)-(+)- vs (S)-(-)-1-phenylethylamine, does lead to the opposite handedness in the resultant helical structure. To better understand the structure-property relationships involving helical sense and twisting power, systematic studies of the roles played by both nematogenic and chiral structures as well as other structural features of the comonomers should be conducted.

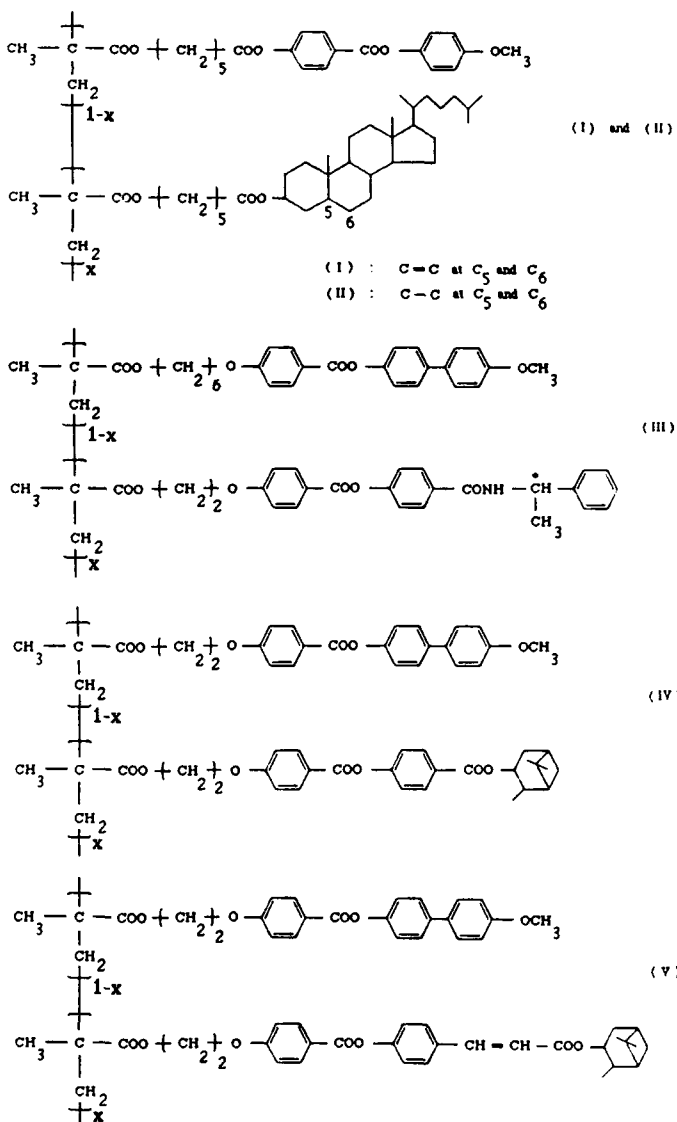
Introduction

Because of the unique property of selective wavelength reflection, chiral nematic polymers have recently been demonstrated to be capable of forming optical notch filters[1,2]. This class of polymers are also potentially useful for the fabrication of such optical devices as isolators, beamsplitters and beam apodizers[3]. Moreover, they are ideal candidates for optical information storage based on mesomorphic transitions and the accompanying changes in the index of refraction and optical birefringence[4-6]. Most of these applications require polymers capable of forming both right- and left-handed helical structures upon proper thermal annealing.

Although there exist a number of polymers reported to form left-handed helical structures[7-10], there is a paucity of right-handed polymers, the only known examples being chemically modified poly( $\gamma$ -benzyl D- or L-glutamate)[11] and (hydroxypropyl)cellulose[12]. In these two series of right-handed polymers, chiral centers reside in the polymer backbone. In the case of glutamate copolymers the inversion of chirality has been shown to lead to opposite handedness in the helical structure[10,13]. The key issue to be addressed in the present communication is whether or not the same observation is applicable to polymers in which chiral centers reside in side groups. Methacrylate copolymers incorporating optically active cholesterol, dihydrocholesterol, and two pairs of enantiomers, (R)-(+)- and (S)-(-)-1-phenylethylamine and (+)- and (-)-isopinocampheol, were synthesized and characterized to examine the possible correlation between the absolute configuration of a pendant chiral group and helical sense at the supramolecular level.

Polymer Structures

Copolymers synthesized for the present study include the following:



The details of the synthesis and characterization of both monomers and polymers have been described elsewhere[14] and hence will not be repeated here.

### Results and Discussion

The thermotropic and optical properties of the five copolymer series under present investigation are summarized in Table 1. In the comparison of (I) to (II) involving cholesteryl and dihydrocholesteryl groups, respectively, we make two observations: a) While copolymer (I) did not show smectic mesophase under hot-stage polarizing optical microscope, the smectic to cholesteric transition was clearly identifiable with both optical microscopy and differential scanning calorimetry for copolymer (II). b). Cholesterol has a helical twisting power 80% higher than dihydrocholesterol in identical macromolecular structural settings. The intriguing point is that cholesterol and dihydrocholesterol possess about the same overall absolute configurations[15], while they show opposite signs in their specific optical rotations:  $[\alpha]_D^{24} - 40^\circ$  (C-2,  $\text{CHCl}_3$ ), cholesterol;  $[\alpha]_D^{21} +23.8^\circ$  (C-1.3,  $\text{CHCl}_3$ ), dihydrocholesterol. Using a low molar mass nematic host and a chiral dopant mixed at a ratio that gives rise to the desired  $\lambda_R$  with known handedness, it was determined that both (I) and (II) present left-handed helical structures. Thus, other structural features being identical, the sign of the specific optical rotation of the pendant chiral group does not seem to affect helical sense in thermotropic copolymers. This observation leaves the absolute configuration of the pendant chiral group to be further examined. One of the approaches to achieve this task is to use a pair of optically pure enantiomers as the pendant group, (R)-(+)- and (S)-(-)-1-phenylethylamine being the examples to be pursued in what follows.

Results for the two series of copolymer (III) are also presented in Table 1. There exists a wide temperature range for the existence of the cholesteric mesophase, and the selective reflection wavelength was found to be practically independent of temperature within an experimental uncertainty of  $\pm 3\%$  associated with the determination of  $\lambda_R$  at annealing temperatures up to  $433^\circ\text{K}$ . It was also found that the inversion of chirality of the pendant group leads to the opposite handedness in the resultant helical structure; the (R)-(+)- and (S)-(-)-enantiomer were found to give rise to a right- and left-handed helix, respectively. Both copolymer (IV) and (V) showed the cholesteric mesophase; however, isopinocampheol has a lower helical twisting power than all the other chiral moieties. The enhanced rigidity associated with the chiral comonomer has an increased helical twisting power as one compares copolymer (IV) to (V).

Finally,  $\lambda_R^{-1}$  as a function of  $x$  is plotted up in Fig. 1 for the three copolymer series. Since the temperature dependences of  $\lambda_R$  were found to be insignificant, the helical twisting power can be determined from the slope,  $(d\lambda_R^{-1}/dx)$  as  $x \rightarrow 0$ , in light of the fact that the average refractive index  $n$  is not expected to differ by more than 3% from one copolymer to the other as estimated via group contribution methods[16]. It is clear that 1-phenylethylamine possesses a helical twisting power intermediate between cholesterol and dihydrocholesterol. It thus appears that the helical twisting power is a function of the structures of both nematogenic and chiral comonomers.

Table 1. Thermotropic property and selective reflection wavelength for copolymers (I), (II), (III), (IV) and (V)<sup>a,b</sup>

mole fraction of chiral moiety, x	glass transition, T <sub>g</sub> (°K)	mesomorphic transition (°K) smectic cholesteric isotropic	λ <sub>s</sub> , nm	10 <sup>-3</sup> M <sub>w</sub>	M <sub>w</sub> /M <sub>n</sub>
<b>Copolymer (I)</b>					
0.08	313	---	379	1244	16.7 1.13
0.17	323	---	393	642	33.6 1.18
0.21	314	---	386	534	17.7 1.13
<b>Copolymer (II)</b>					
0.20	316	351	386	954	29.0 1.12
0.29	310	363	387	680	26.6 1.13
0.40	311	363	382	560	19.8 1.16
<b>Copolymer (III) with (R)-(+)-1-phenylethylamine</b>					
0.13	346	---	487	1105	20.9 1.62
0.18	344	---	477	842	25.4 1.60
0.23	355	---	467	675	25.6 1.64
0.28	351	---	455	550	28.1 1.65
<b>Copolymer (III) with (S)-(-)-1-phenylethylamine</b>					
0.16	343	---	491	1088	24.2 1.72
0.19	345	---	476	785	20.8 1.54
0.26	354	---	459	575	22.2 1.47
<b>Copolymer (IV) with (1S,2S,3S,5R)-(+)-isopinocampheol<sup>c</sup></b>					
0.17	363	---	514	---	12.5 1.44
0.28	345	---	475	---	13.6 1.65
0.38	366	---	460	---	22.2 2.74
0.45	367	---	443	---	37.2 2.62
0.59	362	---	424	---	36.3 2.50
0.70	374	---	417	---	41.8 2.09
0.75	364	---	380	---	32.1 1.92
<b>Copolymer (V) with (1S,2S,3S,5R)-(+)-isopinocampheol</b>					
0.16	360	---	504	---	11.0 1.45
0.26	357	---	488	2817	15.3 1.84
0.38	364	---	463	2176	26.2 2.38
0.46	353	---	351	1735	19.4 1.76
0.49	380	---	---	---	29.1 2.44

a. x values were determined with integration on proton NMR spectra.

b. M<sub>w</sub> varies from one batch to the other because of the difference in initiator to monomer ratio.

c. λ<sub>s</sub> outside of the wavelength range on Lambda-9 spectrophotometer although the cholesteric mesophase was observed under polarising optical microscope.

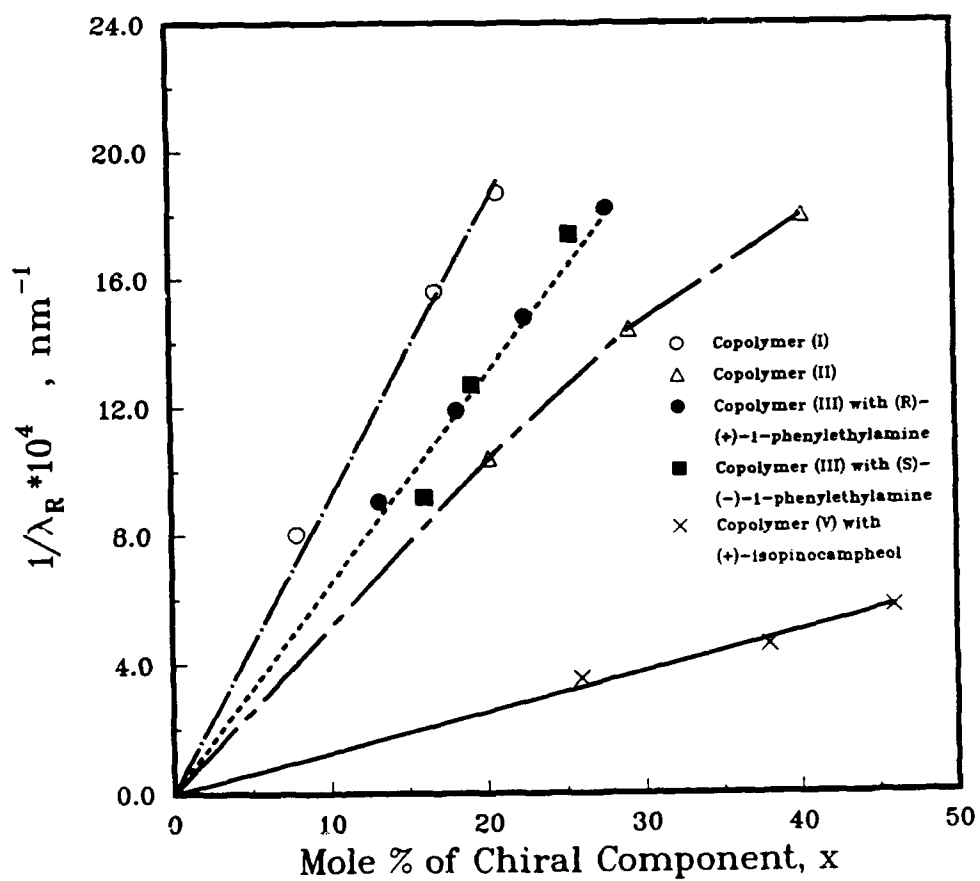


Fig. 1.  $1/\lambda_R$  vs x for chiral nematic copolymers.

Acknowledgement

The authors wish to acknowledge helpful discussions with K. L. Marshall of the Laboratory for Laser Energetics, University of Rochester. This work was supported by Kaiser Electronics and the National Science Foundation under Grant CBT-8714924. Partial support was also provided by the U.S. Army Research Office under contract DAAL03-86-K-0173, the U.S. Department of Energy Division of Inertial Fusion under agreement No. DE-FC03-85DP40200, and by the Laser Fusion Feasibility Project at the Laboratory for Laser Energetics which has the following sponsors: Empire State Electric Energy Research Corporation, New York State Energy Research and Development Authority, Ontario Hydro, and the University of Rochester. Such support does not imply endorsement of the content by any of the above parties.

REFERENCES

1. Ishihara, S.; Yokotani, F.; Matsuo, Y.; Moritomo, K.; *Polymer*, 1988, 29, 2141.
2. Tsai, M. L.; Chen, S. H.; Jacobs, S. D.; *Appl. Phys. Lett.*, 1989, 54, 2395.
3. Jacobs, S. D.; Cerqua, K. A.; Marshall, K. L.; Schmid, A.; Guardalben, M. J.; Skerrett, K. J.; *J. Opt. Soc. Am. B*, 1988, 5, 1962.
4. Ortler, R.; Bräuchle, C.; Miller, A.; Piepli, G.; *Makromol. Chem., Rapid Commun.* 1989, 10, 189.
5. Eich, M.; Wendorff, J. H.; *Makromol. Chem., Rapid Commun.* 1987, 8, 467.
6. Nakamura, T.; Ueno, T.; Tani, C.; *Mol. Cryst. Liq. Cryst.* 1989, 169, 167.
7. Krigbaum, W.R.; Ciferri, A.; Asrar, J.; Toriumi, H.; *Mol. Cryst. Liq. Cryst.*, 1981, 76, 79.
8. Fink, H.; Rehage, G.; *Makromol. Chem., Rapid Commun.*, 1982, 3, 859.
9. Freidzon, Ya. S.; Boiko, N. I.; Shibaev, V. P.; Platé, N. A.; *Eur. Polym. J.* 1986, 22, 13.
10. Watanabe, J.; Fukuda, Y.; Gehani, R.; Umematsu, I.; *Macromolecules*, 1984, 17, 1004.
11. Watanabe, J.; Nagase, T.; *Macromolecules*, 1988, 21, 171.
12. Tseng, S. L.; Laivins, G. V.; Gray, D. G.; *Macromolecules*, 1982, 15, 1262; Bhadani, S. N.; Gray, D. G.; *Mol. Cryst. Liq. Cryst.* 1983, 99, 29.
13. Watanabe, J.; Goto, M.; Nagase, T.; *Macromolecules*, 1987, 20, 298.
14. Tsai, M.L.; Chen, S.H.; *Macromolecules*, 1989 (in press); Tsai, M.L.; Chen, S.H.; *Macromolecules*, 1989 (in preparation).
15. Daux, W. L.; Norton, D. A.; "Atlas of Steroid Structure," Vol. 1 Plenum, New York, 1975.
16. Van Krevelen, D. W.; Hoftyzer, P. J.; Chapter 10 in "Properties of Polymers," Elsevier Scientific Publishing Company, Amsterdam, 1976.

92-18273

AD-P007 481



277

MULTI-LAYERS THIN FILMS OF ACETALIZED POLY(VINYL ALCOHOL)  
DERIVATIVES OBTAINED BY THE LB METHOD AND THEIR  
OPTO-ELECTRONIC PROPERTIES

KIYOSHI OGUCHI\*, YASUHIKO YOKOH\*\*, KOHEI SANUI AND NAOYA OGATA\*\*\*  
\*Central Research Institute, Dai Nippon Printing Co.,Ltd., 1-1,  
Ichigaya-Kagacho 1-Chome, Shinjuku-ku, Tokyo 162 Japan  
\*\*Chiba Laboratory, UBE Industries, Ltd., 8-1,Goi-minamikaigan,  
Ichihara City, Chiba 290 Japan  
\*\*\*Department of Chemistry, Sophia University, 7-1 Kioi-cho,  
Chiyoda-ku, Tokyo 102 Japan

ABSTRACT

The formation of surface films of acetalized poly(vinyl alcohol)s at the air/water interface has been investigated in terms of the structure of the transferred films, after transfer of these surface films to solid substrates by means of the Langmuir-Blodgett technique. Furthermore, their electron beam exposure characteristics and non-linear optical properties were measured. It was found that the monolayers of acetalized poly(vinyl alcohol)s having aliphatic side chains gave stable surface films with a limiting area of ca.  $0.3\text{nm}^2/\text{average repeat unit}$ , irrespective of the side-chain length and the degree of polymerization of the starting poly(vinyl alcohol). The surface films could be deposited onto various substrates with deposition ratios of 1.0. The resulting multilayers were Y type. The thickness of the multilayers was proportional to the number of layers, and the single-layer thickness increased with increasing sidechain length. The surface wettability of the multilayers changed alternatingly, depending on whether the number of layers was even or odd. These results indicated that the surface films were monolayers of polymers, with hydrophilic main chains spread over the air/water interface and hydrophobic side chains directed approximately normal to the interface. The transferred films maintained the oriented structure of the monolayers at the interface. The acetalized poly(vinyl alcohol)s prepared by the LB technique is adaptable as a high resolution negative-type EB resist. And the second harmonic generation (SHG) of some acetalized poly(vinyl alcohol)s was observed by LB method and by electric field poling method.

INTRODUCTION

The Langmuir-Blodgett(LB) method is one of the important techniques for producing very thin and uniform films that can be controlled to molecular dimensions[1,2]. Many kinds of amphiphilic molecules such as long-chain fatty acids are being investigated. Recently, applications of LB films are being anticipated in many fields and discussed. For example, LB films as dielectronic devices[3-5], as electron beam resists[6,7] or as non-linear optical materials[8-10] have been investigated. Furthermore, the application of the LB films in molecular electronic devices is anticipated[11]. However, the current LB films have poor thermal and mechanical stability. This is a problem with respect to practical applications.

Polymeric multilayers are expected to form stable thin films and two ideas have been proposed. One is to form

monolayers or multilayers having polymerizable functional groups and then to initiate polymerization by some appropriate treatments such as heating, UV or electron beam(EB) irradiation[12-16]. The other is to form monolayers using suitable amphiphilic polymers and deposit them onto substrates by the LB method[17-23]. If amphiphilic polymers, spread at the air/water interface, form monolayers which have oriented structures reflecting their amphiphilic nature, and the monolayers are transferred to solid substrates without disrupting the oriented structures, it may be expected that the LB films have unique properties in comparison with the usual bulk film of the same polymer.

Our interest has been focused on the possibility of creating oriented LB films from synthetic polymers. Acetalized poly(vinyl alcohol)s (PVA) having various side chains were selected as a model of amphiphilic polymers. This paper describes in detail the formation of surface films of acetalized PVAs and the characterization of the built-up multilayers. Furthermore, their EB exposure characteristics as resists and non-linear optical properties as second harmonic generation are also examined.

#### (1) ACETALIZED POLY(VINYL ALCOHOLS) AS LB-FILMS AND ELECTRON BEAM EXPOSURE CHARACTERISTICS

##### Materials Syntheses

Fig.1 shows the structures of various acetalized PVAs. Acetalized PVA having linear aliphatic side chains were synthesized from the corresponding aldehyde using hydrochloric acid as a catalyst[24,25]. A typical synthesis was as follows. 1.0g of PVA having a degree of polymerization of 2000 and 8.0g of octyl aldehyde were dissolved in 16ml of benzene and 4ml of ethanol, and two drops of hydrochloric acid (35% aqueous) added. The reaction was carried out with stirring at 40°C for 15h. The solution was poured into excess methanol containing an equimolar amount of sodium hydroxide and acetalized polymer was separated by filtration. It was further purified by reprecipitation from chloroform into methanol and finally dried under vacuum.

##### Preparation of LB Films

Water used was ion-exchanged, filtered(activated charcoal and membrane filter), and distilled twice in dual quartz still. Benzene was purified by distillation. Glass apparatus was etched by concentrated KOH-ethanol solution and thoroughly rinsed with purified water. The LB equipment used in this study was a LAUDA film balance. It consists of a Teflon-coated through, a Langmuir-type surface pressure measurement unit, and a moving barrier. The acetalized PVAs were dissolved in benzene in about 0.01wt% and were dropped on the surface of water. After evaporation of the solvent, surface pressure-area curves were recorded with a compression speed in the range of 0.5-2.5cm/min.

The surface films of acetalized PVAs were transferred to the substrates by the following methods. The surface films of acetalized PVAs were firstly compressed to appropriate pressure. While keeping the pressure constant, the substrates were vertically taken up and down with a speed of 0.5-2.5cm/min across the surface films(vertical method), or the substrates were horizontally lowered until they were in contact with the monolayers on the water and then were lifted(horizontal method).

Table I  
Properties of Acetalized PVA

Polymer	x <sup>a)</sup>	Tg(°C) <sup>b)</sup>	Td(°C) <sup>c)</sup>
AA-PVA(2000)	0.61	116	340
BuA-PVA(2000)	0.72	60	320
OA-PVA(300)	0.75	22	340
OA-PVA(1400)	0.79	24	330
OA-PVA(2000)	0.70	22	330
OA-PVA(2600)	0.79	28	330
OA-PVA(2000)	0.74	22	340
DDA-PVA(2000)	0.73	13	350
TrDA-PVA(2000)	0.78	3	340
TeDA-PVA(2000)	0.76	5	350

a) Mole fraction of acetalized unit determined by elemental analysis.

b) Glass transition temperature determined by DSC.

c) Decomposition temperature determined by TG-DTA.

Figure 1 Structure of acetalized PVAs

Multilayers of various numbers were obtained by repeating the procedures. The substrates used were cleaned by appropriate method.

#### Electron Beam Exposure

Electron beam exposure characteristics of the LB films of acetalized PVAs were evaluated as EB resists. The films were exposed electron beam resist evaluation apparatus, ERE-301 (ELIONIX Co.), at the accelerating voltage of 10KV. The exposed films were developed in a solution of monochlorobenzene for 60s and rinsed with isopropyl alcohol for 30s. After development and post-baking, wet etching was performed. A film prepared by conventional spin coating was also investigated in order to compare it with the LB film of the same polymer.

#### RESULTS AND DISCUSSION

##### Monolayers of Acetalized PVA

The properties of acetalized PVAs are summarized in Table I. The acetalized content was about 60-80mol%. In the case of acetalized PVA having aliphatic side chain, the glass transition temperatures Tg decreased with increasing length of the methylene side chain.

Figure 2 shows the surface pressure-area curves of acetalized PVA on distilled water. As the area was compressed, the surface pressure firstly increased steeply, reached a plateau region, and then increased again, for all of the curves. With increasing the side chain length, the surface pressure which gave the plateau region increased and the slope of the curves became steeper. It was found that the monolayer of acetalized PVA was more stable on water when the length of alkyl side chain was longer than it was short. In order to examine the plateau region, a compression-expansion recycle test was performed and it was found that collapse did not occur at the plateau region. It's plateau region might be due to a conformational change, owing to the balance between the hydrophilic and hydrophobic parts of the polymer.

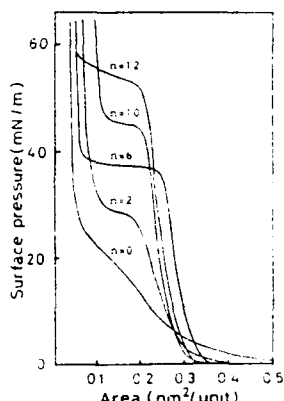


Figure 2 Surface pressure-area curves of acetalized PVA on distilled water

Limiting area per repeat unit was determined from the surface pressure-area curves in Fig. 2 as extrapolated area at zero pressure for the condensed region below the shoulder. In order to eliminate the influence of the different acetal group content on limiting areas, limiting areas per acetal unit were estimated by assuming that the limiting area of PVA was  $0.12\text{nm}^2/\text{unit}$  [26]. The calculation method was as follows;

$$\text{Area per acetal unit} = [A - 0.12(1-X)]/X$$

A=Area per unit determined from Fig. 2  
X=Mole fraction of acetal group content

Limiting areas of acetalized PVAs are summarized in Table II and the effect of side chain length on the limiting area is shown in Fig. 3. It was found from Fig. 3 that the limiting area of acetalized PVA tended to a constant area with increasing length of the methylene side chain. The constant value of  $0.34\text{nm}^2/\text{acetal unit}$  is rather in agreement with the molecular model of acetalized PVA, assuming that the main chain lies flat on the water and the side chain is above the main chain. It should be noted that the limiting areas were constant independent of the molecular weight (Table II).

#### Multilayers of Acetalized PVA

Table III shows the conditions for depositing acetalized PVA onto various substrates. With the exception of AA-PVA, monolayers of acetalized PVA were easily deposited onto various substrates. It was noteworthy that the first layer was only transferred in a down-mode for Si and Ge substrates which are hydrophobic surfaces, and in an up-mode for the Cr, Al and glass substrates which are hydrophilic surfaces. After the second layer, the surface films could be transferred both in an up-mode and a down-mode to form Y-type layers.

Fig. 4 shows the relationship between number of layers and the thickness of the multilayers as measured by ellipsometry. It was clear that each case gave a linear relationship, showing the thickness of multilayers to be proportional to the number of layers. The thickness of the multilayers increased with increasing length of the methylene side chain for a given number of layers. This result was also found to be the case when a Talystep mechanical stylus was used. Fig. 5 shows the effect of the number of methylene groups in the side chain on the

Table II  
Limiting Areas of Acetalized PVA

Polymer	Limiting area		
	$\text{m}^2/\text{mg}$	$\text{nm}^2/\text{unit}$	$\text{nm}^2/\text{acetal unit}^a$
AA-PVA(2000)	2.30	0.33	0.47
Bu-PVA(2000)	1.58	0.30	0.37
CA-PVA(300)	1.16	0.31	0.37
DA-PVA(1400)	1.15	0.32	0.37
DA-PVA(2000)	1.16	0.31	0.37
DA-PVA(2600)	1.15	0.32	0.37
DA-PVA(2900)	1.00	0.30	0.36
DDA-PVA(2000)	0.86	0.28	0.34
TrDA-PVA(2000)	0.82	0.30	0.35
TeDA-PVA(2000)	0.76	0.29	0.34

<sup>a</sup>) Estimated assuming limiting area of PVA being  $0.12\text{nm}^2/\text{unit}$ .

Table III Deposition Conditions of Acetylated PVA <sup>a)</sup>						
Polymer <sup>b)</sup>	Subphase temp. (°C)	Surfa- ce pressure (mN/m)	Deposition			
			Substrate	Method	No. of layers	Ratio
AA-PVA	11.8	10	Si	V <sup>c)</sup>	60	-
BuA-PVA	11.0	25	Si	V	50	0.98
OA-PVA	10.5	30	Si	V	40	0.99
OA-PVA	7.4	30	Si	V	20	1.01
OA-PVA	24.4	30	Si	V	-	-
DDA-PVA	10.8	32	Si	V	50	0.98
TEDA-PVA	10.6	36	Si	V	40	1.00
OA-PVA	13.1	10	Cr	V	100	0.68
OA-PVA	13.5	20	Cr	V	70	0.87
OA-PVA	13.5	30	Cr	V	70	0.94
OA-PVA	10.3	15	Cr <sup>d)</sup>	H	110	0.85
OA-PVA	10.0	30	Cr	H	20	0.93
OA-PVA	10.5	10	Cr	V	20	1.01
OA-PVA	10.5	30	A1	V	20	1.00
OA-PVA	10.8	30	Glass	V	20	0.94

a) Subphase, distilled water; deposition speed, 1.25-2.50 cm/min.

b) Degree of polymerization of the starting PVA is 2000.

c) Vertical method.

d) Horizontal method.

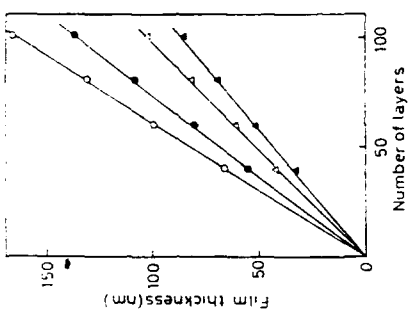


Figure 4 Relationship between number of layers and the thickness of the multilayers as measured by ellipsometry (○) TeDA-PVA; (○) DDA-PVA; (△) OA-PVA; (▲) BuA-PVA

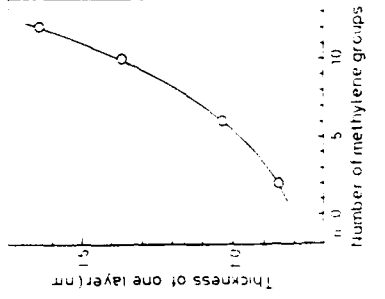


Figure 5 Effect of methylene length of acetal side chain on the thickness per layer

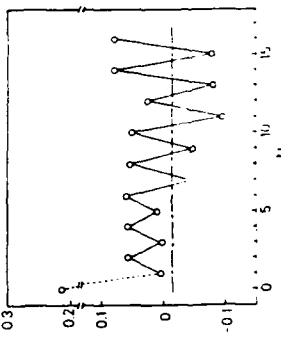


Figure 6 Relationship between wetability and N for OA-PVA  
N Number of superimposed monolayers// Wetability of film surface by spin coating

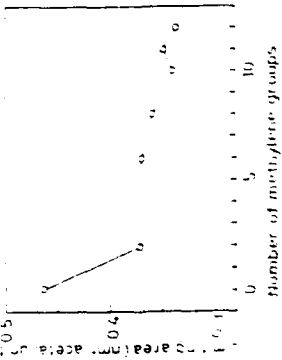


Figure 3 Effect of methylene length of acetal side chain on limiting area

thickness per layer calculated from the results shown in Fig. 4. The thickness per layer increased dramatically with the length of the side chain. The slope between  $n=10$  and  $n=12$  gave  $0.14\text{nm}$  per methylene unit. This value was close to the value for long-chain fatty acids ( $0.145\text{nm}$  per methylene unit) determined by Blodgett[1]. The thickness per layer may increase linearly with the number of the methylene units in the side chain when  $n$  is larger than 10.

When the LB film from the acetalized PVA is Y-type layer, it is expected that the surface wettability would be alternatively changed by odd and even numbers of the LB layers. Fig. 6 shows the wettability of the LB film of OA-PVA onto an Al substrate as a function of the number of layers ( $N$ ). The wettability was estimated by measuring the contact angle of water at 1min after dropping distilled water on the surface. The wettability changed according to the odd or even numbers of layers. The wettability of the surface prepared by spin-coating lay between the values of even and odd  $N$ s, when  $N$  was larger than 6. This indicates that in the case of an even number of layers, the surface is hydrophilic, and in the case of an odd number of layers, the surface is hydrophobic.

From the results mentioned above, it was found that LB films of acetalized PVA having long alkyl side chaines were rather well-ordered with the side chain directed normal to the main chain.

#### Characteristics of Electron Beam Exposure

It has previously been reported that acetalized PVAs were easily crosslinked by EB exposure and the cross-linking reaction might occur at the acetal groups[27].

Fig.7 shows the sensitive curve of OA-PVA prepared by LB method and by spin-coating. It was found that the sensitive curve changed depending on the film thickness and the sensitivity of OA-PVA prepared by the LB method was lower than that of the same polymer prepared by spin-coating. The difference between the films prepared by LB method and spin-coating is the stereostructure. Fig.8 shows the relationship between electron sensitivity and methylene length of acetal side chain. The sensitivity was higher with increasing the length of the methylene side chains and at almost the same thickness, the sensitivity of films prepared by the LB and spin-coating methods was different with increasing the numbers of methylene units.

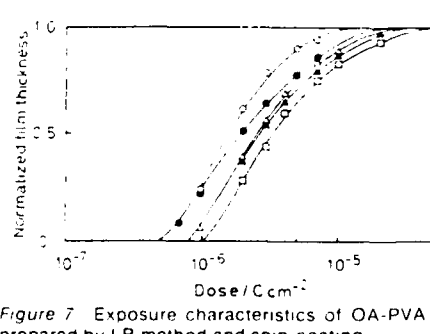


Figure 7 Exposure characteristics of OA-PVA prepared by LB method and spin-coating  
(○) (●) Spin-coating film. (□) (△) LB film  
Film thickness: (○) 660nm; (●) 120nm;  
(△) 150nm. (□) 100nm.  
(□) 62nm  
Development Chlorobenzene, 60s

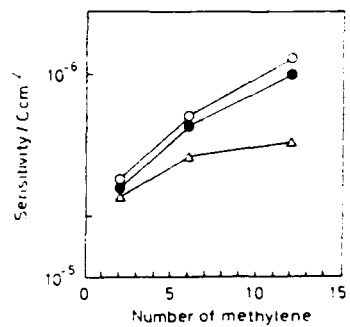


Figure 8 Relationship between electron sensitivity and methylene length of acetal side chain  
(○) (●) Spin-coating film. (□) (△) LB film  
Film thickness (○) 610-660 nm; (●) 120-130nm  
(△) 100-120nm

This difference of the sensitivity may be ascribed to the stereostructure of the film. In case of the LB method, the multilayer crosslinked by EB exposure may consist two dimensional networks rather than three dimensional networks due to the oriented structure with the side chain directed normal to the main chain, and this tendency may become remarkable when the number of methylene units increase.

As very thin, defect-free and uniform films could be obtained by the LB method in comparison with the spin coating method, the resolution of the acetalized PVA was higher in LB films than in films of the same polymer prepared by spin coating. Thus the LB method is useful in achieving high resolution in microlithography.

#### (2) ACETALIZED POLY(VINYLALCOHOL) AS NONLINEAR OPTICAL MATERIALS

Recently, organic nonlinear optical (NLO) materials are becoming very important in the field of opto electronic devices because they have a potential for developing highly efficient functions as photonic devices. Organic polymers are one of major materials for NLO applications because of their ability to design their molecular structures and their processability to design their photonic devices. Main characteristics of NLO polymers are summarized as follows compared with those of inorganic compounds.

- 1) Large optical nonlinearities.
- 2) Ultrafast response times.
- 3) Large induced damage thresholds.
- 4) Good processability.
- 5) Orientation process is necessary.

To study NLO polymers, there would be two approaches. One is the molecularly doped system which is a physical mixture of polymer and NLO organic compounds.[28,29] The other is the side chain-attached polymer which contains the NLO moiety as a part of the chain via chemical linkage.[30-32] This study aims at the synthesis of side chain-attached polymer.

#### Acetalized Poly(vinylalcohol) as SHG active polymers

It is known that the monolayers of LB films are highly oriented on the water surface. If the monolayers were transferred onto the substrate smoothly, SHG active LB films would be obtained. In the field of opto-electric devices, the processability of the polymers is important. For example optical IC fabrication is supported by submicron patterning technology. EB resistable polymers are very suitable for electron-beam patterning. If the polymers were coated, oriented, and patterned onto the substrate, SHG active wave guide would be obtained. Besides these two unique properties, acetalized PVA has good properties. It's film is very uniform and transparent, and easy to synthesis. Many SHG moiety can be introduced as side chains into PVA main chain.

#### Orientation Method

In case of the SHG of NLO polymers, orientation process is necessary. This study aims at the synthesis of SHG active polymers, using two types of poling method, that is electric field (EF) poling and LB orientation.

## 1) Electric Field Poling

This method is used widely [33] for NLO polymers because polymers are insulator. High electric field (ca. 200kV/cm) is applied at near  $T_g$ . In this method, uniformity and relaxation are important problems. When the doped polymers are EF poled, the SHG efficiency decreases to ca.30% in 24 hours.

## 2) LB Orientation

This orientation method is limited to the material which has both hydrophilic and hydrophobic moieties. In this report we have found the acetalized PVAs, which have long alkyl side chaines, form stable LB-film on the water surface. They are deposited onto a substrate, and deposited film is Y-type film. In order to make a SHG active LB film, we need to deposite Z- or X-type film because Z- or X-type film has a noncentrosymmetric structure which is absolutely necessary for SHG material.

Also we have investigated two deposition method, one is vertical method and other is horizontal method. When we use the acetalized PVAs, which have long alkyl side chains, both methods are effective to deposite LB films onto both hydrophilic and hydrophobic substrates. To make a optical wave guide onto the substrate, the width of the wave guide needs to be ca.1 $\mu$ m thickness. In order to make 1 $\mu$ m width polymer, it is necessary to deposite ca.500 layers onto the substrate. Vertical method is more preferable than horizontal method, because vertical method is continuous process. So we tried to deposite LB film onto the substrate by a vertical method.

## RESULTS AND DISCUSSION

Fig.9 shows synthetic route of acetalized PVA which had p-nitroaniline moiety in the side chain. The p-nitroaniline structure is a typical SHG structure. 2-Methyl-4-nitroaniline (MNA) crystal has been known as a SHG active crystal, because it has p-nitroaniline structure. p-Nitroaniline acetal as a starting material was obtained by substitution reaction of fluorine with methylaminoacetal in DMSO. Hydrofluoric acid generated from the reaction was quenched by sodium bicarbonate.

The polymer of p-NAn-PVA was prepared by the acetal exchange reaction of p-nitroaniline acetal with PVA in water using hydrochloric acid as a catalyst. The crude polymer was purified by reprecipitation method. The introduction ratio ( $x$ ) of the side chains (Table IV) were calculated using the elemental analysis data. The obtained acetalized PVAs and analytical data were summarized in Table IV.

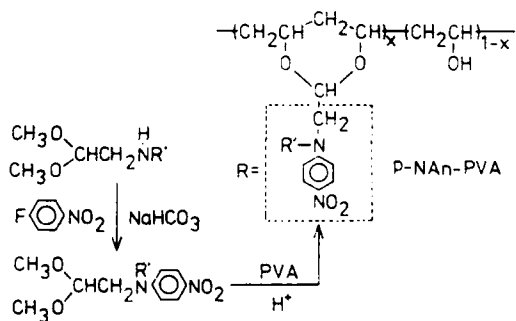


Figure 9 Synthetic route of Acetalized PVA

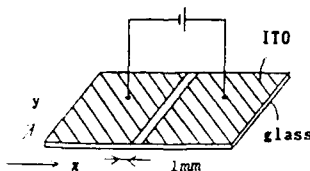


Figure 10 Electric Field Poling condition  
80°C ( $T_g = 73.8^\circ C$ )  
20KV/cm 1 hr

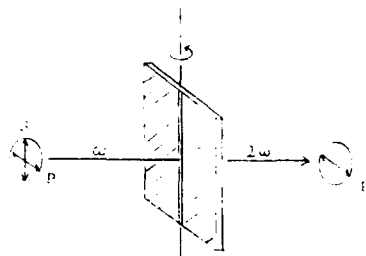


Figure 11 Measurement of SHG of  
Poled Polymer  
 $\omega = 1.064 \mu m$

Table IV Properties of Acetalized PVA

	Side chain	$\eta_{sp}/c$	Limiting oxygen index	Adiabatic deposition ratio of CA-PVA/Z
CA-PVA	$-CH_2-CH_2-$	0.819	33.61	
DA-PVA	$-CH_2-$	0.775	30	
<i>m</i> -NBA-PVA	$-CH_2-CH(NH_2)-$	0.419	5wt%	1.62
<i>p</i> -NBA-PVA	$-CH_2-CH_2-NH_2-$	0.526	11.47	15wt%
<i>p</i> -NAn-PVA	$-CH_2-CH_2-N_3-$	0.66	1.41	1wt%
<i>m</i> -N-PVA	$-CH_2-CH_2-NH-$	0.591	0.79	1wt%

\*1 Reported Value

\*2 Z-type deposition ratio =  $\frac{\text{deposition ratio during down process}}{\text{deposition ratio during up-lift process}}$

#### ELECTRIC FIELD POLING

This process had two steps. The first step was polymer coating on the substrate, and the second step was voltage application to the coated polymer. The synthesized acetalized PVAs were spin coated on the glass substrate. The concentration of acetalized PVAs were ca.10wt% in DMF, and the rotation speed of the substrate was 4000 r.p.m. The transparency of the spin coated films depended on temperature. When spin coated at 20°C-50°C then micro crystals deposited on the substrate. It would be due to the rapid lowering of the substrate temperature. When spin coated at 60°C-100°C then no micro crystals deposited and film was very transparent and uniform. The cut off wave length of *p*-NAn-PVA film is 480 nm.

This means  $0.532 \mu m$  SHG of Nd:YAG laser can be exposed from the polymer without absorption. Ellipsometry technique was used for the measurement of the film thickness and refractive index. The coated film on the ITO electrode was heated near  $T_g$ , and cooled to room temperature under the electric field. Slit type substrate shown in fig.10 was studied.

The slit type was convenient for microscopic observation of the polymer orientation, but insulation broke down easily under the high electric field. The applied voltage was 2-3KV and the slit width was 1mm, so as to be 20-30KV/cm.

SHG coefficient was measured with Maker-fringe method using Q-switched Nd:YAG laser operating at  $1.064 \mu m$ . (Fig.11) We introduced P- or S-polarized laser beam and detected S-polarized SH beam. Fig.12 shows fringe pattern from *p*-NAn-PVA using slit type substrate. "ps" means S-polarized beam was introduced and detected P-polarized SH-beam. "pp" beam was 7 times larger than "ps" beam. This implies that SHG was dependent on the orientation of the side chains of the polymer. We observed SHG on *p*-NAn-PVA and DN-PVA but not on *p*-NBA-PVA and *m*-NBA-PVA. Only *p*-nitro aniline structure of the side chain was effective for SHG.

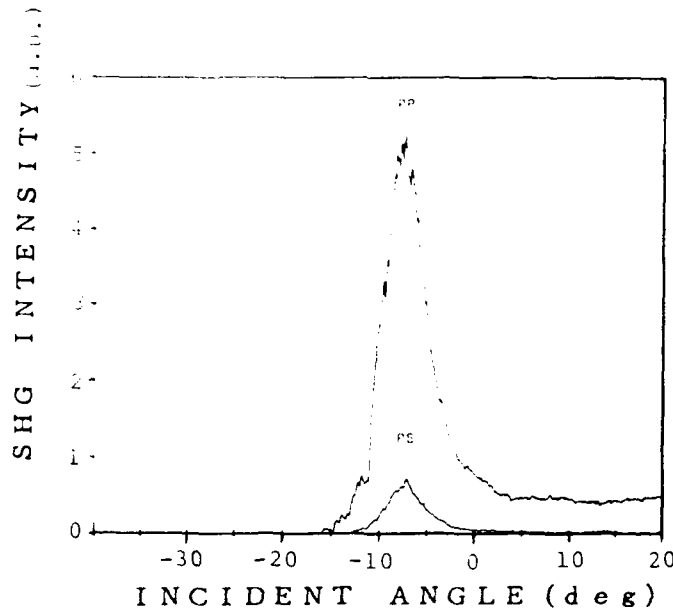


Figure 12 SHG of p-NAn-PVA (slit type substrate)

#### LB ORIENTATION

The limiting area calculated from the surface pressure-area isotherm of p-NAn-PVA was  $4.41\text{\AA}^2/\text{unit}$ , which was extremely small value compared to that of OA-PVA ( $33.61\text{\AA}^2/\text{unit}$ ) (Table IV). The aggregate structure of p-NAn-PVA might reduce the limiting area of it because p-nitro aniline structure had large dipolemoment and made aggregate structure easily [34].

We tried to deposite this p-NAn-PVA only on the glass substrate by a vertical method, but the film was too hard to deposite. In case of OA-PVA, the film on water was very soft and formed Y-type film on the glass. So we mixed p-NAn-PVA with OA-PVA. Only with a 1wt% addition of OA-PVA, it could be deposited on the glass, and formed Z-type film. We defined Z-type deposition ratio shown in Table IV, footnote \*2. If this value was 0 then ideal Z-film was formed, while was 1 then ideal Y- was formed. Table IV shows minimum value of Z-type deposition ratio. Only with 1wt% addition of OA-PVA, p-NAn-PVA made best Z-type film. If more than 1wt% was added then Z-type deposition ratio increased and made Y-type film. However this Z-type film showed no SHG. The aggregate structure of the p-NAn-PVA film on water would cancel the SHG ability of the polymer.

Monomer type supports were examined instead of OA-PVA. 33wt% addition of stearamide gave uniform LB-film on water, and deposited on the glass to form Z-type film. The Z-type deposition ratio was -0.236. The negative value due to the small expansion of the LB film on water during down process. The LB-film was deposited on both side of the substrate by 14X2 layers. This sample gave SHG fringe pattern shown in Fig 13,

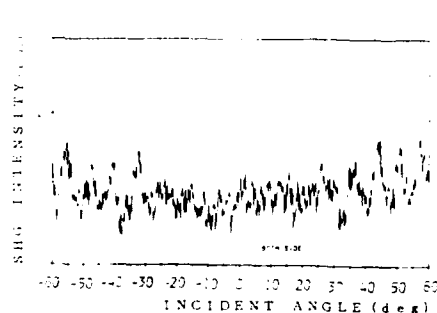


Figure 13 SHG of p-NAn-PVA  
(LB orientation)

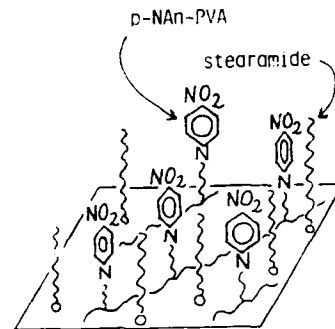


Figure 14 LB structure of p-NAn-PVA  
mixed with stearamide

which exhibited vertical orientation of the side chains. The role of the stearamide summarized as follows.

1) The appropriate softener of the polymer.

When we used OA-PVA as a support, the LB-film on water was too soft. So more than 1wt% addition of OA-PVA, the deposited film became Y-type film. On the other hand, stearamide as a support ( 0-33wt% ) gave Z-type film. It would be due to the structure of LB-film in Fig.14. The stearamide would fill the side chain space of polymer and would make full-packed system. This structure would not make the LB-film too soft, and make Z-film not Y-film.

2) The support of side chain of the polymer.

The side chain of the p-NAn-PVA made aggregate structure due to the strong dipole moment of p-nitroaniline moiety of the side chain. The alkyl chains of stearamide would cancel the dipole moments and make vertical orientation of the side chains.

#### CONCLUSION

The p-NAn-PVA was synthesized, and two types of orientation methods were examined. SHG activity was observed by both method. Electric field poling was more effective than LB-method.

References

- [ 1 ] K.B.Blodgett, J. Amer. Soc., 57, 1007(1935)
- [ 2 ] K.B.Blodgett and I.Langmuir, Phys. Rev., 51, 964(1937)
- [ 3 ] V.K.Agarwal, Thin Solid Films, 24, 55(1974)
- [ 4 ] R.M.Handv et al., J.Electrochem. Soc., 113, 109(1966)
- [ 5 ] M.Sugi et al., Appl. Phys. Lett., 27, 559(1975)
- [ 6 ] A.Barraud et al., Solid State Technol., 22, 120(1979)
- [ 7 ] G.Fariss et al., J.Materials Sci., 18, 2603(1983)
- [ 8 ] O.A.Aktsipetrov, N.N.Akhmediev, E.D.Mishina, V.R.Novak, JETP Lett., 37, 207(1983)
- [ 9 ] I.R.Girling, N.A.Cade, P.V.Kolinsky, C.M.Montgomery, Electron. Lett., 21, 169(1985)
- [10] C.W.Pitt, L.M.Walpita, Thin Solid Films, 68, 101(1980)
- [11] Int. Symp. on Future Electron Devices, Bioelectronic and Molecular Electronic Devices, Edited by M.Aizawa (Tokyo, Japan, 1985, Preprint)
- [12] V.Enkelmann and J.B.Lando, J. Polym. Sci., 62, 509(1977)
- [13] G.L.LLarkis, Jr.C.W.Burknart, E.D.Thompson, J.B.Lando and E.Ortiz, Thin Solid Films, 99, 277(1983)
- [14] K.Fukuda, Y.Shibasaki and H.Nakahara, ibid., 99, 87(1983)
- [15] G.Lieser, B.Tieke and G.Wegner, ibid., 68, 77(1980)
- [16] A.Barraud, C.Rosilio and A.Ruaudel-Teixier, ibid., 68, 91(1980)
- [17] A.K.Engel, T.Yoden, K.Sanui and N.Ogata, J. Amer.Chem. Soc., 107, 8308(1985)
- [18] A.Vickers, R.H.Tredgold, P.Hodge, E.Khoshdel and I.Girling, ibid., 134, 43(1985)
- [19] T.Kawaguchi, H.Nakahara and K.Fukuda, Thin Solid Films, 133, 29(1985)
- [20] C.S.Winter, R.H.Tredgold, A.J.Vickers, E.Koshdel and P.Hodge, ibid., 134, 75(1985)
- [21] M.Kamimoto, M.Suzuki, T.Konishi, Y.Imai, M.Iwamoto and T.Hino, Chem. Lett., 823(1986)
- [22] K.Oguchi, T.Yoden, K.Sanui and N.Ogata, Polym.J., 18, 887(1986)
- [23] M.Watanabe, Y.Kosaka, K.Sanui, N.Ogata, K.Oguchi and T.Yoden, Macromolecules, 20, 452(1987)
- [24] H.Noma and T.Koh, Kobunshi Kagaku, 4, 123(1943)
- [25] H.Noma, T.Koh and T.Tsuneta, ibid., 6, 439(1949)
- [26] D.J.Crisp, J.Colloid Sci., 1, 49(1946)
- [27] K.Oguchi, K.Sanui, N.Ogata, Y.Takahashi and T.Nakada, Polm. Eng. Sci., 29, 353(1989)
- [28] G.R.Meredith, J.G.VanDusen and D.J.Williams, Macromolecules, 15, 1385(1982)
- [29] K.D.Singer, J.E.Sohn, S.J.Lalama, Appl.Phys.Lett., 49, 248(1986)
- [30] S.Matsumoto, K.Kubodera, T.Kurihara and T.Kaino, Appl.Phys.Lett., 51, 1(1987)
- [31] C.Ye, T.J.Marks, J.Yang and G.K.Wang, Macromolecules, 20, 2322(1987)
- [32] A.C.Griffin, A.M.Bhatti and R.S.L.Hung, SPIE, 682, 65(1986)
- [33] Hoechist Celanese, U.S.Patent 854,282, U.S.933,425, U.S.822,094  
Y.Sudo, M.Amano, H.Yamamoto, T.Kaino, Jpn.Kokai Tokkyo Koho JP63/26,639  
Y.Sudo, M.Amano, Y.Takeuchi, Jpn.Kokai Tokkyo Koho JP63/204,235
- [34] T.Inoue, K.Yase, M.Okada, H.Matsuda et al., Jpn.J.Appl.Phys., 27, 1635(1988)

92-18274



AD-P007 482



DIELECTRIC, TSC AND ELECTROMECHANICAL MEASUREMENTS  
ON SOME PROSPECTIVE NLO POLYMERS

PAUL L. CARR, GEOFF R. DAVIES, AND IAN M. WARD  
Physics Department, University of Leeds, Woodhouse Lane, Leeds LS2 9JT, UK

ABSTRACT

The pyroelectric coefficients of a range of polymers with a methacrylate backbone and nitrostilbene or nitrobiphenyl mesogens attached by a 3 or 6 carbon spacer have been measured in order to assess the efficiency of the poling process. It is found that the response is much lower than the guest-host system MNA in PMMA, suggesting that the polar mesogens pack anti-parallel and that this alignment is not broken by the applied field.

These strong interactions also provide an explanation for the absence of the  $\beta$  relaxation process in the experimental polymers and therefore the brittle nature of the films. They may also explain the stability of the polarisation achieved.

INTRODUCTION

The long term objective of this work is to produce polymers with useful multifunctional properties. Ideally, easily fabricated, transparent films are required which have useful non-linear optical properties and which also show piezo and pyro electric responses.

For materials to exhibit piezoelectricity pyroelectricity or second harmonic generation, they must be macroscopically non-centrosymmetric. In the case of polymeric materials, the macroscopic centre of symmetry arising from the random arrangement of molecules is destroyed by the application of a static electric field which produces a preferential polar alignment. The field is usually applied at high temperatures and removed at low temperatures when the polarisation is "frozen in".

The effectiveness of this operation, known as poling, will determine the subsequent activity of the sample. We have therefore been investigating the poling process in a variety of polymeric systems. We originally used the thermally stimulated current (TSC) technique to characterise the degree of polarisation produced but since this technique has to destroy the polarisation in order to measure it, we now use the pyroelectric coefficient as an alternative indicator of the degree of poling. The measurement of the pyroelectric coefficient is non-destructive, simple and rapidly performed.

A limitation of pyro-electric measurements is that the contribution from the polymer backbone and the side chain mesogen are not distinguishable. Some NLO measurements have therefore been carried out in the Hoechst Celanese laboratory, but ageing problems contribute a degree of uncertainty to these measurements. A limited number of piezo-electric measurements have also been undertaken in our own laboratories.

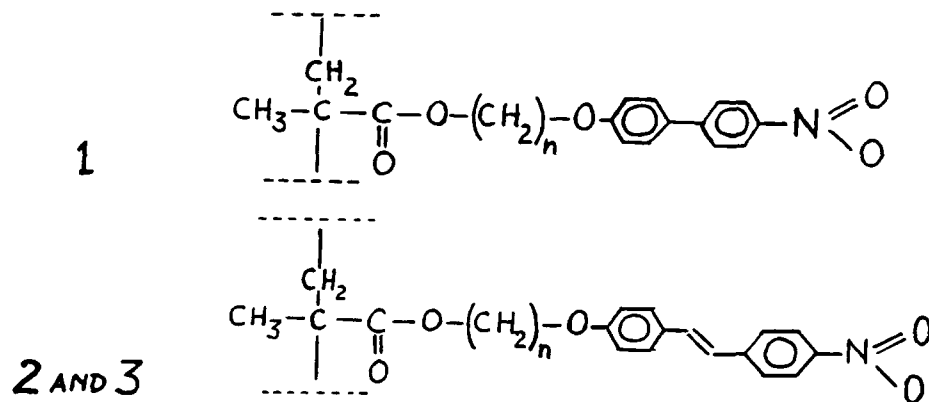
Some of the polymers studied exhibit liquid crystalline behavior and it was hoped to exploit this property in aligning the side chain mesogen groups.

## EXPERIMENTAL

Materials Studied

The materials studied were

- (1) a polymethacrylate of 4-(6-Methacryloyloxyhexyloxy)-4'-nitro biphenyl (MO6ONBP) with a 6 carbon spacer,[1]
- (2) Poly(4-(3-oxypropane)-oxy-4'-nitrostilbene methacrylate (MO3ONS)
- (3) the same mesogen with a 6 carbon spacer (MO6ONS)[2]



The compositions of the materials studied, all of which were synthesised by Hoechst Celanese, are summarised in Table I, together with their glass transition temperatures and clearing temperatures if any. Liquid crystalline behavior was shown by the 6 spacer polymers but not by the 3 spacer material.

TABLE I Samples Studied

Sample Composition	Sample Code	T <sub>g</sub> °C	T <sub>cl</sub> °C
MO6ONBP	1	57	76
MO3ONS	2	114	—
MO6ONS	3	71	155
10% MNA in PMMA	4	51	—
PMMA	5	119	—
MO3ONS Melt Pressed	6	114	—
MO6ONS A/C Aligned	7	71	155

### Sample Preparation

When studying side-chain liquid crystalline polymers supplied by Hoechst Celanese we found that they made extremely brittle films which could not be handled unless they were left upon the substrate on which they were cast. Initially, it was thought that this might be due to too low a molecular weight but after much chemical effort by Hoechst Celanese high molecular weight samples were also found to be brittle.

Samples were generally prepared as thin films (10-20  $\mu\text{m}$  thick) on aluminised glass slides by solvent casting. Solutions were made up in dimethyl sulphoxide, cyclopentanone or benzonitrile and filtered through 0.2 $\mu\text{m}$  filters. Films were cast by dip coating one or two layers onto microscope slides. They were allowed to solidify at room temperature for 10 minutes then heated for four hours in a vacuum oven at 20°C above  $T_g$ .

Some samples were prepared by melt pressing the polymer between pre-electroded glass slides. Even at temperatures 70-80°C above  $T_g$ , samples of thickness less than 50  $\mu\text{m}$  were difficult to prepare.

Gold, platinum and aluminium electrodes have been used and thermally stimulated current data showed that there were small differences in the charge injected during poling. However, these differences did not affect the pyroelectric results obtained.

Poling was generally performed by the application of an electric field (10 to 100 MV/m) to evaporated aluminium electrodes on the surface of the sample at temperatures around  $T_g$ . Best results were often obtained by poling a few degrees below  $T_g$  as measured by DSC or the peak in a TSC spectrum. Above this temperature large increases in ionic conductivity occurred and film breakdown became increasingly frequent.

We have also used corona poling but the lowest voltages which we could use (~ 3 kV), if applied to thin films above  $T_g$ , frequently produced break-up of the films into isolated droplets! Corona poling at or below  $T_g$  allowed such voltages to be applied and produced the highest pyroelectric coefficients but it often produced local breakdown in the films, reducing their effective poled area. This, together with the uncertainty in the effective poling field, makes the analysis of corona poling data somewhat uncertain and no such data are discussed in this paper.

### Measurements Performed

The primary measurement consists of the determination of the pyroelectric coefficient as a function of poling voltage for solvent cast films. This has been shown to correlate with the Pockels Coefficient measured at Hoechst Celanese (see Fig. 1). Some hydrostatic piezo-electric coefficients have been measured which also correlate with the pyro-electric measurements, Fig. 2. These correlations show that the pyroelectric coefficient provides a good indication of multifunctional behavior in the range of poling voltages used.

Thermally stimulated current data were obtained by heating samples at a rate of 10°C/minute to  $T_g + 20$ . Trapped charges are also released in this process which can sometimes be identified as a separate peak in the TSC spectra. Unfortunately, in some cases the charge and dipolar peaks overlap making it difficult to determine the dipolar polarisation.

Some samples were subjected to an AC director aligning field in the liquid crystal phase prior to DC poling.[3,4] An RMS voltage of 5V/mm at 200 Hz was applied while cooling the sample at 0.1°C/minute through the liquid crystal phase. The DC poling voltage was then applied from room temperature and maintained throughout the poling temperature cycle.

To measure the pyroelectric coefficient the sample is placed in a rapid stream of temperature controlled dry nitrogen the temperature of which is then ramped up and down to create a triangular wave of peak-peak amplitude 3°C and period 100 s. (the thermal delay for thin film samples is less than 1 s) The sample is effectively short circuited by connecting it to an electrometer in the fast feedback mode and the resultant current is logged by computer at about 3 readings/sec. The fundamentals of the temperature wave and the current wave are then calculated by Fourier analysis.

This technique yields the phase of the response, which can help to distinguish a reversible pyroelectric response from an irreversible change in thermally stimulated current with temperature. A genuine pyroelectric current from a thin sample will be essentially 90° out of phase with the temperature wave but the change in the irreversible depolarisation current will be in phase with the temperature wave.

If  $A$  is the area of the sample,  $T$  the amplitude of the temperature wave of period  $\tau$  and  $I$  is the component of the current wave 90° out of phase with the temperature wave, then the pyroelectric coefficient  $\gamma$  is given by  $\gamma = (I \times \tau) / (\pi \times T \times A)$ .

#### RESULTS

In view of the range of  $T_g$ 's exhibited by the copolymers, maintaining a set poling temperature for all samples is neither possible nor sensible. We have therefore chosen to compare data for different samples poled at their  $T_g$  for 2 minutes and cooled to room temperature at 10°C/min..

Figure 3 shows that the effects of small changes in poling temperature near  $T_g$  are small. Results have been illustrated by plotting the pyroelectric coefficient as a function of poling voltage. Taking the slope of this graph as an indication of activity averages out the scatter in individual data points. The correlations are in all cases linear, with no sign of saturation in the response, showing that high dipole orientations have not been reached, and the slope relates to the combined dipole moment of the molecule and the mobility of the mesogenic groups at the poling temperature.

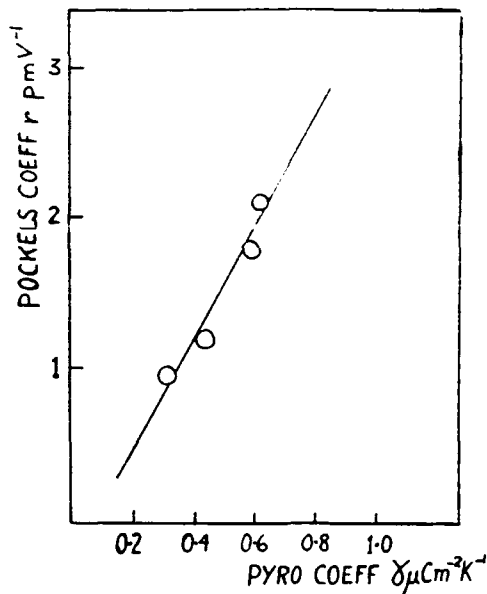


FIG 1. POCKELS COEFF VS PYRO COEFF  
M060NS HOMOPOLYMER

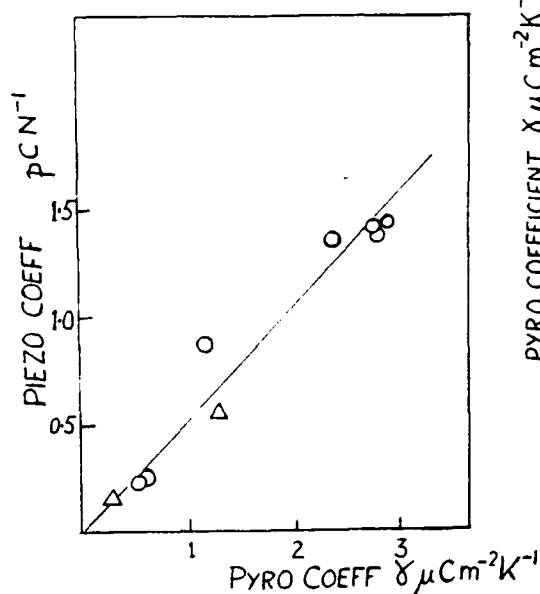


FIG 2. PIEZO COEFF vs PYRO COEFF  
KEY. O 2,  $\Delta$  1.

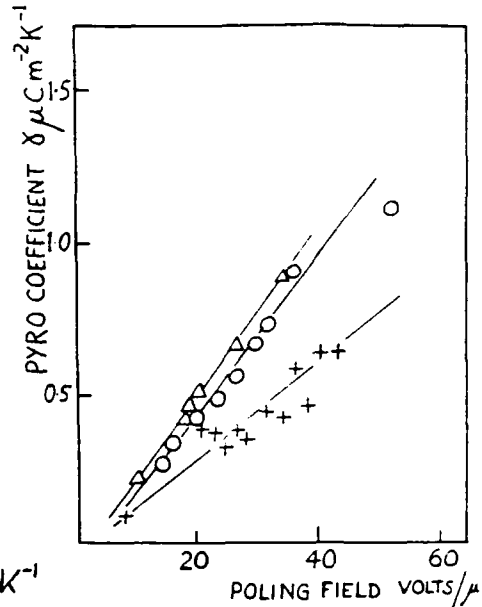


FIG 3. PYRO COEFF vs POLING FIELD  
KEY. 2 POLED AT  $\Delta$  110°C,  
O 105°C, + 95°C.

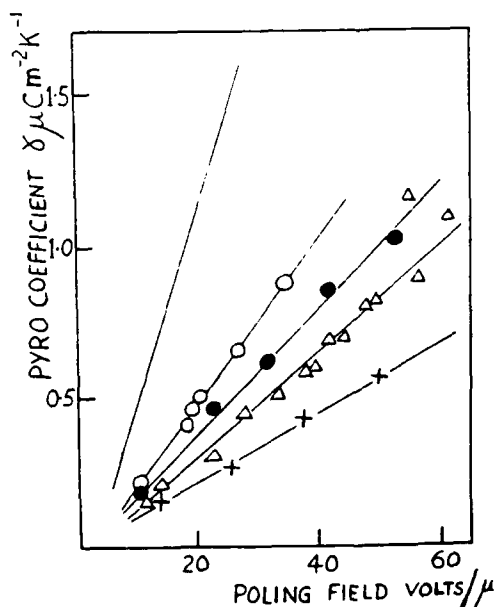


FIG 4. PYRO COEFF vs POLING FIELD  
KEY. — 4, O 2, ● 3,  $\Delta$  1,  
+ 5.

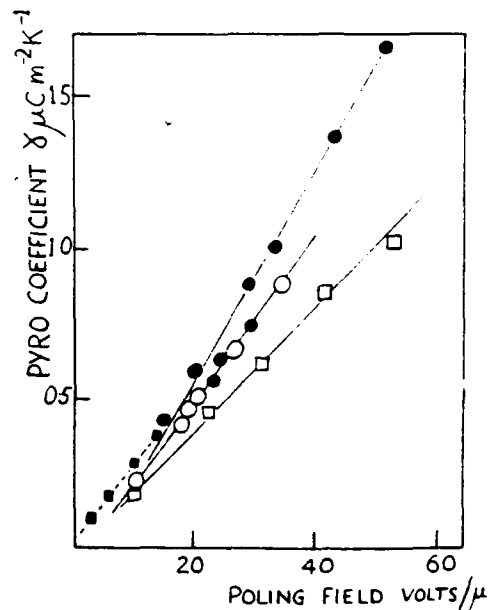


FIG 5. PYRO COEFF vs POLING FIELD  
KEY. ● 6, O 2, ■ 7, □ 3.

The nitro-biphenyl, the long and short spacer nitrostilbenes, the guest-host material and PMMA itself are compared in Fig. 4. Significantly, despite the quite large dipole moment of the respective mesogens, the results for the experimental polymers lie well below those for the guest host material, and the nitro biphenyl in particular is not much more active than the backbone PMMA itself. The nitrostilbene is more active than the biphenyl and it is also interesting to note that the 3 spacer stilbene is more active than the 6 spacer stilbene. The structural implication of this finding will be discussed later.

Fig. 5 compares melt-pressed and solvent cast samples (MO3ONS) and AC pre-aligned samples with normally poled samples (MO6ONS). This figure shows that melt-pressed MO3ONS yield higher coefficients than solvent cast MO3ONS. The reason for this is not yet clear. Since melt-pressed samples are about  $40\mu\text{m}$  thick whereas the solvent cast samples are  $10-20\mu\text{m}$  thick it may be due to a difference in molecular orientation between the surface and the bulk material. Alternatively, the flow pattern produced by melt-pressing may have induced a different orientation to that in the solvent cast films.

The few results from AC director pre-alignment indicate that the expected advantages of this technique [5] have not been achieved. Again this may have structural implications.

Some limited stability measurements have been made which show the decay in pyroelectric response with storage at room temperature over a period of hours to days. The data for materials 1, 2, 3, and 5 are shown in Fig. 6 where the relative pyroelectric coefficient (ratio to first measurement) is plotted as a function of the logarithm of the time after removal of the poling field.

Materials 2 and 3 show a surprisingly similar decay despite their different  $T_g$ 's. A further indication that the  $T_g$  is not the important parameter controlling the decay rate is given by a comparison of the data for sample 1 with that for PMMA which shows an extremely rapid decay despite its much higher  $T_g$ .

The decay in response should obviously be related to relaxation within the polymers. Examining the dielectric loss, Fig. 7, it is immediately clear that the PMMA  $\beta$  process is eliminated by the addition of the side chain mesogens. It is therefore highly probable that the higher stability of the experimental polymers is in general due the absence of a relaxation process near room temperature. The data of Fig. 7 are also relevant when considering the mechanical properties of the films. The extremely brittle nature of the side chain polymers may also be related to the lack of a relaxation process near room temperature.[6]

Partial poling to isolate charge peaks and identify optimum poling conditions is illustrated in Fig. 8. Curve 1 shows the data for a nitrobiphenyl sample which was poled at  $10\text{V}/\mu\text{m}$  while cooling from  $70-60^\circ\text{C}$ . The associated pyrocoefficient, prior to the polarisation min was  $0.005 \mu\text{Cm}^{-2}\text{K}^{-1}$ . The same sample, also poled at  $10\text{V}/\mu\text{m}$ , while cooling from  $60-35^\circ\text{C}$ , curve 2 and had a pyroelectric coefficient of  $0.1 \mu\text{Cm}^{-2}\text{K}^{-1}$ .

The absence of a  $\beta$  relaxation is again shown in the TSC spectra illustrated in Fig. 9, where the liquid crystal side chain polymers are seen to exhibit sharp depolarisation peaks at  $T_g$ , with no discernable low temperature loss while PMMA shows a broader  $T_g$  peak and also a broad low temperature peak. The drop below  $40^\circ\text{C}$  is presumably due to decay prior to the measurement.

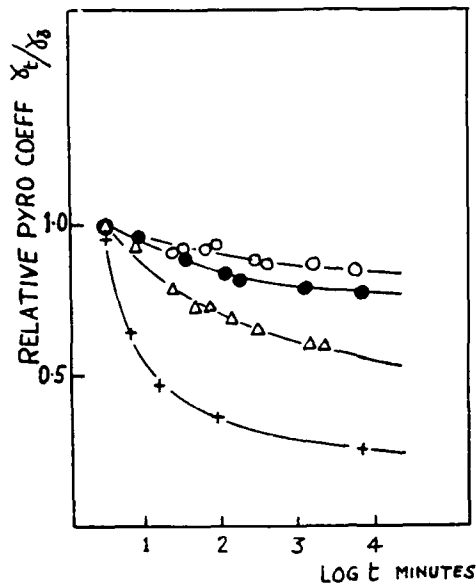


FIG 6. PYRO COEFF DECAY vs TIME  
KEY.  $\circ$  2,  $\bullet$  3,  $\triangle$  1,  $+$  5.

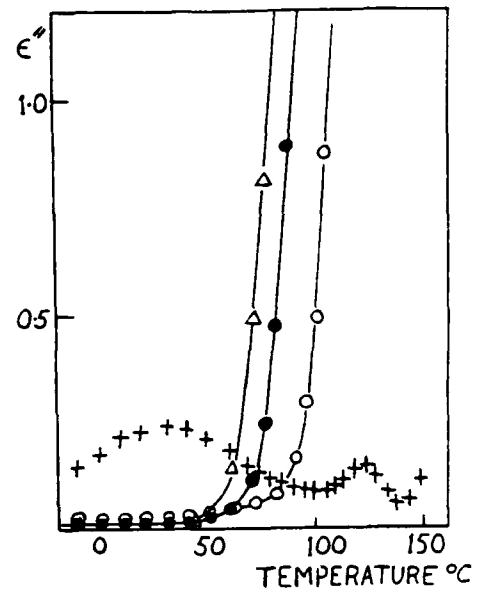


FIG 7. DIELECTRIC LOSS FACTOR  
vs TEMPERATURE  
KEY.  $\triangle$  1,  $\circ$  2,  $\bullet$  3,  $+$  5.

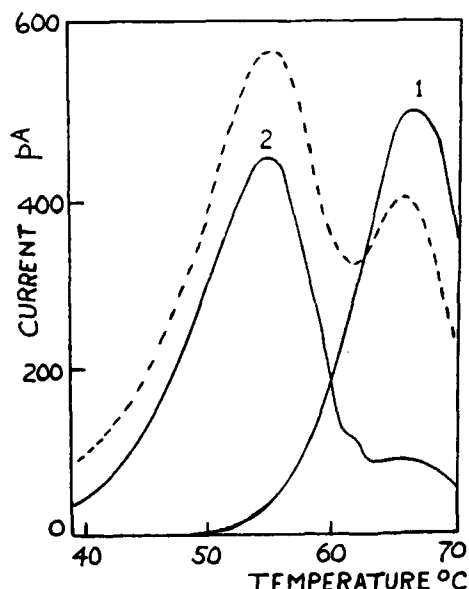


FIG 8. T.S.C. RESULTS FOR FULL  
AND PARTIAL POLING

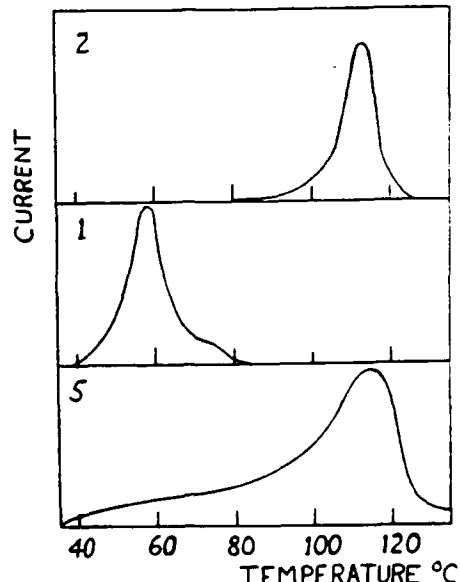


FIG 9. TSC DATA FOR SAMPLES  
1, 2, 5.

## DISCUSSION

These data indicate that the poling process used is not achieving high polar alignment. The plots of pyroelectric response against poling field show no incipient saturation and the coefficients are small by comparison with 10% MNA in PMMA.

We believe that this is due to strong anti-polar pairing of the side-groups which persists in the highest poling fields.[7] Indeed the data in Fig. 4 suggest that increased side chain mobility derived from a longer spacer group results in more pronounced pairing with a consequent reduction in poling efficiency.

Moreover, these strong electrostatic interactions produced what is effectively a tightly cross-linked structure. This high degree of cross-linking provides an explanation for the extremely brittle nature of the materials, even at high molecular weight. It also immobilises the dipoles so that they do not show a dielectric dispersion below the glass transition and makes the materials difficult to pole.

After poling, sufficient cross link pairs still exist to eliminate the  $\beta$  relaxation and improve the stability of such orientation as is produced.

## CONCLUSIONS

It is gratifying to find that piezoelectric, pyroelectric and NLO responses can be detected from the same material, though not at the highest levels attainable in other materials. Since the poling has not achieved saturation, there is obvious room for improvement in response by more effective poling and possibly by pre-orientation of the molecules.

The electrostatic interactions between the mesogens 'cross-link' the chains, leading a brittleness even at high molecular weights, and limit the polarisation which can be produced. They may, however, help stabilize the polarisation.

In the future mesogens which pack parallel, rather than anti-parallel should be sought which, if capable of forming a liquid crystalline state, could be readily oriented in relatively weak electric fields.

## REFERENCES

1. R.N. Martino et. al. Nonlinear Optical and Electroactive Polymers, edited by P.N. Prasad and D.R. Ulrich (Plenum Press, New York, 1988) pp-169-187.
2. A. Griffin. A.M. Bhatti, R.S.L. Hung, *ibid*, p.375-390.
3. G.S. Attard, K. Araki, and G. Williams. *Brit. Poly. J.* 19 119-127. (1987).
4. G.S. Attard, and G. Williams. *J. Mol Electronics* 2. (1986).
5. R. Simon, and H.J. Coles, *Polymer* 27, 811 (1986).
6. E.A. Hoff and S. Turner. *Bull. Amer. Soc. Test. Mater.* 225, TP 208, (1957).
7. N.A Plate, R.V. Talrose, Ya.S. Freidzon, and V.P. Shibaev. *Poly J.* 19 p.135. (1987)

AD-P007 483



297

SILICONE CONTAINING LIQUID CRYSTALLINE  
POLYURETHANES AND POLYESTERS

Robert Kosfeld, F. Braun, L. Willner, M. Heß  
University of Duisburg, Department of Physical Chemistry  
D-4100 Duisburg, FRG

92-18275



ABSTRACT

Series of poly(urethanes) were prepared in which the spacer groups between the rigid segments contained siloxanes. The conditions for the appearance of liquid crystallinity and a fair thermal stability were investigated and compared to those of corresponding esters.

INTRODUCTION

In linear, semiflexible poly(esters) – class  $\alpha$  according to [1,2] – relationships between chemical structure, liquid crystallinity and thermal properties have been investigated intensively [3,4]. In spite of their technical importance there is much less known on structure–properties relationships and mesomorphic potential of poly(urethanes).

In non-polymeric material it had been found that the urethane linkage has not the high potential to maintain the linear and rigid character of the mesogenic group as in most of the structures investigated liquid crystallinity was lost if the ester linkage had been replaced by the urethane [5,7]. In polymeric material a few thermotropic poly(urethanes) have been synthesized during the past 8 years, basing on different synthetic concepts [8–16].

In most of the cases high thermal transition temperatures and low thermal stability were observed. These facts reduce the certainty with which mesophases can be found and analyzed.

Recent synthesis of diurethanes with thermotropic behaviour [17] led to a new series of poly(urethanes) which show mesophases. Incorporation of siloxane groups into the spacer sequences was shown to decrease thermal transitions in a series of poly(esters) [18]. This concept now has been applied to poly(urethanes) [19] with some success.

EXPERIMENTAL

**Diisocyanates** were prepared by the phosgene method or using the diacylchlorides [20] and diazides with a subsequent Curtius–degradation [21].

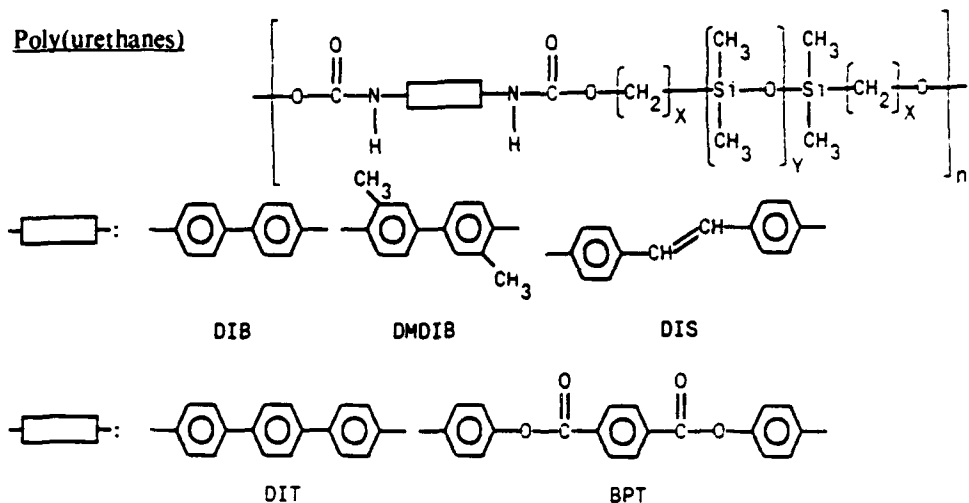
**Hydroxi-terminated alkyl-oligosiloxanes** were prepared according to [22,23].

**Poly(urethanes)** were synthesized by addition of excess diol to the diisocyanate in N,N-diacetamid at 100 °C in the presence of a catalyst.

**Poly(esters)** were synthesized by common procedures from the diole and the diacylchlorid in tetrahydrofuran.

For thermal analysis a DSC-2 and a TGS-2 (Fa. Perkin-Elmer) and a Leitz Orthoplan (trade name) pol microscope equipped with a hot stage were used.

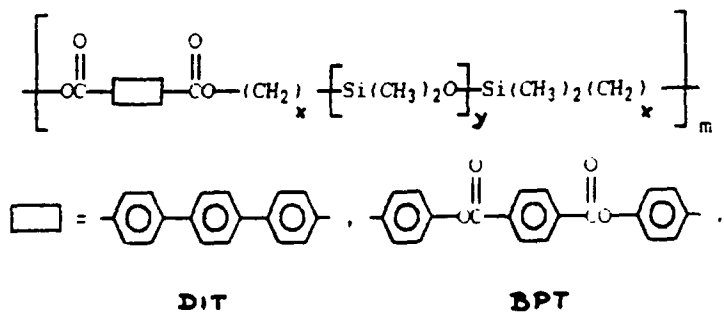
## RESULTS AND DISCUSSION

Poly(urethanes)

The spacers used were  $x = 3, 5, 6, 11$  and  $y = 1$   
 and  $x = 3$   $y = 2, 3$

The limiting viscosities were about 0,2 dL/g.

It turned out that only the long rigid segments DIT and BPT generated thermotropicity, which was strongly depending on the structure of the spacer.

Poly(esters)

The limiting viscosities were about 0,2 dL/g.

All poly(esters) which were prepared showed thermotropicity. In several cases also polymorphism in the liquid state was observed.

Transition temperatures and thermal stability are summarized in table 1.

Table I Thermal properties of Poly(urethanes) and Poly(esters)

		Transition temperat. °C	Begin of decomp. <sup>b</sup> °C	weight loss <sup>b</sup> °C
<b>Poly(urethanes)<sup>d</sup></b>				
DIT	y=1 x=3	k <sup>a</sup> 247 lc dec.	200	3,7 (260 °C/0,5h)
	1 5	k 250 lc 265i	270	3,9 (260 °C/0,5h)
	1 6	k <sup>a</sup> 241 lc 267i	270	4,0 (260 °C/0,5h)
	1 11	k <sup>a</sup> 227 lc 254i	281	2,4 (260 °C/0,5h)
BPT	1 3	k <sup>a</sup> 231 lc 260-i 270i	190	22,5 (260 °C/0,5h)
<b>Poly(esters)<sup>c,e</sup></b>				
DIT	y=1 x=3	k 78 s 177i k 106 s 168i	220 210	1,0 (150 °C/2h) 0,3 (130 °C/1h)
	1 5	k 108 s <sub>1</sub> 160 s <sub>2</sub> 172i	270	0,8 (170 °C/2h)
	1 6	k 109 s <sub>1</sub> 134 s <sub>2</sub> 157i	290	0,0 (150 °C/2h)
BPT	1 3	k 116 s 155 n 171i	230	1,0 (160 °C/2h)

k: crystalline, lc: Liquid crystalline, phase type unidentified s<sub>1</sub>: smectic phase s<sub>2</sub>: smectic phase, type different from s<sub>1</sub>; n: nematic phase i: isotropic phase a: from DSC measurements a glass transition at about -115 °C may be derived.

b: from TGS under nitrogen atmosphere. c: more detailed information about the properties of the whole series of esters will be given in subsequent papers of the authors [24,25]. d: the melting processes are typically polymodal, the transition into the liquid crystalline state was detected microscopically. Increasing aliphatic chain length promotes crystallization. e: In the solid state different types of crystalline phases were identified.

### Thermal stability

With respect to investigations in the molten state and possible technical applications including melt-processing stability of the polymers is important.

In poly(urethanes) below 280 °C back reaction and degradation into amine, CO<sub>2</sub>, and olefin is observed. Increasing siloxane content decreases thermal stability which is at y>1 independent on the type of rigid segment and begins at about 200 °C. An increasing number of methylene groups on the contrary also increases thermal stability. In this case beginning decomposition is markedly influenced by the nature of the mesogenic group. The DIT derivatives are more stable than the BPT. The urethane-linkage seems to be destabilized in the vicinity of the siloxane group as an increasing number of methylene groups results in a positive influence on thermal stability.

This is just in contrast to what is observed in corresponding ester derivatives, where increasing siloxane content increases thermal stability [27,28]. It is not the siloxane bond which is splitted but it is the urethane which breaks down at higher temperatures. In general it was found, that the comparable poly(esters) show a uniform decomposition pattern which is almost independent of the structure of the rigid part and the spacer. In all poly(ester) samples decomposition did not start in the unisotropic state but several decades in temperature above the transition into the isotropic phase.

### Thermotropicity

In poly(urethanes) the DIT unit shows a greater tendency to build mesophases than the less planar and more flexible BPT unit although the BPT unit is longer. Longer alkyl chains with a central disiloxane group stabilize the mesophase and decrease phase transitions.

Compared to the corresponding esters the presence of urethane groups decreased the tendency to form mesophases. The hydrogen bonds, which are present in the urethanes should not only hinder the process of mesophase formation because they increase the melting points, but they should also act as a stabilizer if a mesophase is present as they support a parallel arrangement of the mesogenic elements. Of course this stabilization must not be so strong that the limit of thermal stability of the urethane linkage is reached. This kind of stabilization of the mesophase in fact is present if one takes the clearing temperature as a measure of mesophase stability. The small range within which the phases are stable is due to a high degree of stabilization in the solid state which effects a larger increase in melting points than in clearing points. There is a sensitive balance between destabilizing effects in the solid phase and stabilizing mechanisms in the melt necessary. Substituted disiloxanes in the spacer are suitable for this purpose. They flexibilize due to their high chain mobility and disturb a further linear arrangement along the chain due to the different bond angles at Si and O. Chain packing decreases so that a lower crystallization tendency and a higher solubility is observed.

### CONCLUSION

It has been proved that liquid crystalline poly(urethanes) basing on aromatic diisocyanates can be prepared in combination with bis-hydroxialkyl-disiloxanes. A careful balance between the local density of the hydrogen bonds, the rigidity of the hard segment and the destabilizing interactions is necessary to obtain poly(urethanes) with a remarkable thermal stability. Further developments basing on the concept may lead to broader mesophases. The study of mechanical and rheological properties as well as microdomain morphology and blending will be of interest in future.

### ACKNOWLEDGEMENT

We are grateful to the Deutsche Forschungsgemeinschaft for support of this research.

### REFERENCES

- [1] W. Brostow, *Kunststoffe* – German Plastics **78**, 795 (1988)
- [2] W. Brostow, *Polymer* (1989) in press
- [3] A. Blumstein, J. Asrar, R.B. Blumstein  
in: *Liquid Crystals and Ordered Fluids*, Vol. 4,  
edited by J.F. Johnson (Plenum Press, New York 1985) p. 311
- [4] R.W. Lenz, *Pure & Appl. Chem.* **57**, 1537 (1985)
- [5] G.A. Lorenzo, L. Verbit, *Mol. Cryst. Liq. Cryst.* **30**, 87 (1975)
- [6] A. Bloom, P.L.K. Hung, *Mol. Cryst. Liq. Cryst.* **44**, 323 (1978)
- [7] P.M. Agocs, G. Motika, J.A. Szabo, A.I. Zoltai, *Acta Phys. Chem.* **27**, 81 (1981)
- [8] K. Iimura, N. Koide, H. Tanabe, M. Takeda, *Makromol. Chem.* **182**, 2569 (1981)
- [9] W. Mormann, M. Brahm, *Makromol. Chem.* **190**, 631 (1989)
- [10] M. Tanaka, T. Nakaya, *Kobunshi Ronbunshi* **42**, 529 (1985)
- [11] M. Tanaka, T. Nakaya, *Kobunshi Ronbunshi* **43**, 311 (1986)
- [12] M. Tanaka, T. Nakaya, *Makromol. Chem.* **187**, 2345 (1987)
- [13] M. Tanaka, T. Nakaya, *J. Macromol. Sci., Chem.* **A24**, 777 (1987)
- [14] M. Sato, S.W. Kantor, *Polymer Preprints Japan* **34**, 262 (1985)
- [15] P.J. Stenhouse, E.M. Valles, S.W. Kantor, W.J. McKnight, *Macromol.* **22**, 1467 (1989)

- [16] H. R. Kricheldorf, J. Awe, *Makromol. Chem. Rapid Commun.* **2**, 681 (1988)
- [17] R. Kosfeld, F. Braun, M. Heß, L. Willner, *Liquid Crystals*, **51**, 217 (1989)
- [18] H.R. Ringsdorf, A. Schneller, *Brit. Polym. J.* **13**, 43 (1981)
- [19] L. Willner, F. Braun, M. Heß, R. Kosfeld  
in: *Integration of Fundamental Polymer Science and Technology*, Vol 4,  
edited by P. Lemstra, L. Kleintjens (Elsevier Applied Science Publishers, London  
1989/90) in press
- [20] T.W. Campbell, *J. Am. Chem. Soc.* **82**, 3126 (1960)
- [21] H. R. Kricheldorf, *Synthesis*, 551 (1972)
- [22] R. Kosfeld, F. Braun, L. Willner, M. Heß, *J. Organomet. Chem.* **332**, 63 (1987)
- [23] F. Braun, L. Willner, M. Heß, R. Kosfeld, *J. Organomet. Chem.* **360**, 53 (1989)
- [24] F. Braun, L. Willner, M. Heß, R. Kosfeld, *Makromol. Chem.*, to be published
- [25] F. Braun, L. Willner, M. Heß, R. Kosfeld, *Makromol. Chem., Rapid Comm.* **10**,  
51 (1989)
- [26] R. Braun, PhD thesis, University of Duisburg, 1989
- [27] C. Aguilera, PhD thesis, University of Mainz, 1981

---

---

**PART V**

---

**Multifunctional Design**

92-18276

AD-P007 484



05

## MICROSTRUCTURAL CONTROL IN SIDE CHAIN POLYMERS FOR OPTICAL APPLICATIONS

ROB FINDLAY, TIM LEMMON AND ALAN WINDLE

Department of Materials Science and Metallurgy, University of Cambridge,  
Pembroke Street, Cambridge CB2 3QZ, UK.

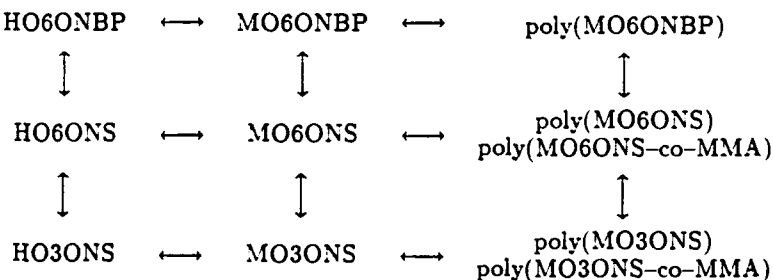
### ABSTRACT

Characterisations of side chain liquid crystalline polymers point towards chemical structures and processing techniques which optimise their suitability for non-linear optical (NLO) applications. Techniques used are thermal analysis, X-ray and hotstage polarised light microscopy (orthoscopic and conoscopic).

### INTRODUCTION

Interest in NLO materials is fed by the promise of optical computers. Organic materials are interesting because their chemistry can be tailored to suit the application, and because they are easily processed. In particular, liquid crystals show strong anisotropy and may have strong dipoles. The molecules can be reoriented by a poling field to produce a noncentrosymmetric structure, which is a necessary condition for high  $\chi^{(2)}$  materials.

Much research has recently focussed on side chain liquid crystalline polymers<sup>1,2,3</sup> because of their ease of poling, optical clarity, and reasonable mechanical properties. In this work, we look at a number of materials which were synthesised by Dr. L.F. Charbonneau and colleagues at Hoechst-Celanese, who provided details of composition and M.Wt., and are related as follows:



### NOTATION

HO6ONBP monomer is a nitrobiphenyl mesogenic group connected by oxygen to an alkyl spacer 6 units long, with a hydroxyl terminator.

MO6ONBP monomer is the same but with a methyl substituted vinyl terminator.

poly(MO6ONBP) is the polymer of the same, with a methacrylate backbone.

poly(MO6ONS) is the same, but with a nitrostilbene mesogenic group.

poly(MO3ONS) is the same, but with an alkyl spacer 3 units long.

poly(MO3ONS-co-MMA) is a random copolymer of MO3ONS and methylmethacrylate.

poly(MO3ONS<sub>0.3</sub> MMA<sub>0.7</sub>) is the same, but specifically it is composed of 30% MO3ONS units. The other designations follow the same scheme.

## TECHNIQUES

Temperatures in tables are in °C, and heating rates standardised at 20°C/min.  $T_g$  is the glass transition measured from the extrapolated onset using DSC;  $T_{endo}$  is the endotherm peak temperature measured using DSC, which usually coincides with the clearing point (mesophase to isotropic transition) seen in the optical microscope.

DSC (differential scanning calorimetry) is performed on a Perkin-Elmer DSC7, and samples are first held for 10 minutes well above the melting point to erase the thermal history; hotstage optical microscopy uses a Swift microscope with a Linkam programmable hotstage, and conoscopy uses a Zeiss Jena microscope; optical microscopy samples are pressed well above the melting point between clean glass slides or cover slips.

$T_{deg}$  is the degradation onset temperature measured using a Pergin-Elmer TGA (thermogravimetric analyser). M.Wt. is the molecular weight, and D.P. the degree of polymerisation (number of monomer units in the chain).

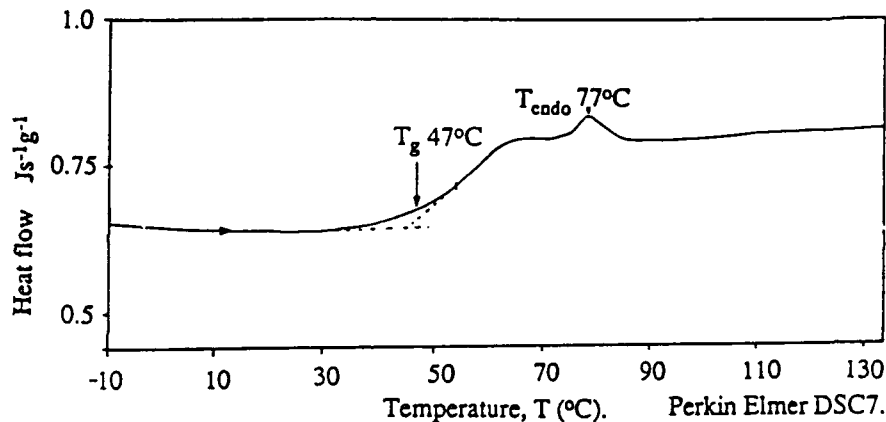


Figure 1: Typical DSC trace (poly(MO6ONBP) M.Wt. 849 800)

## HO6ONBP, MO6ONBP, HO6ONS, MO6ONS MONOMERS

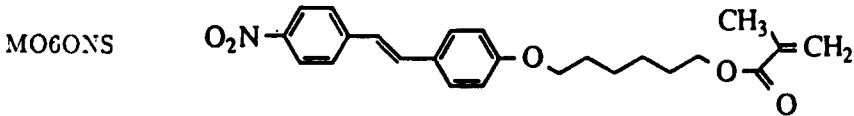
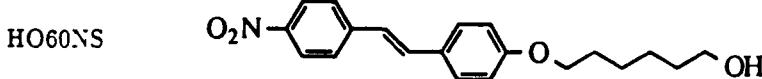
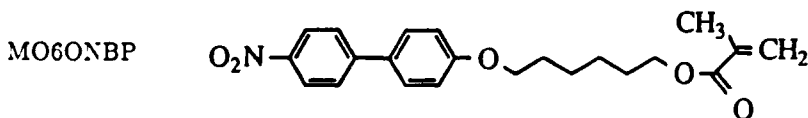


Table (i)

Material	M.Wt.	$T_m$	$T_{deg}$
HO6ONBP	339	124	?
MO6ONBP	383	61	?
HO6ONS	341	163	368
MO6ONS	409	101	324

All form lath-like birefringent solid crystals, and melt to form isotropic liquids which display no liquid crystallinity.

Comparison

Both the melting point and crystallinity of HO6ONBP are much reduced when a methyl substituted vinyl terminator is used (X-ray studies show that HO6ONBP is ~ 40% crystalline, MO6ONBP is ~ 20%).

Replacing the nitrobiphenyl group of HO6ONBP with nitrostilbene forms the higher melting point material HO6ONS, and does not introduce liquid crystallinity. Similarly, replacing the nitrobiphenyl group of the vinyl substituted MO6ONBP with nitrostilbene to form MO6ONS also raises the melting point, without introducing liquid crystallinity. The melting point of MO6ONS is, however, lower than that of HO6ONS due to the bulkier vinyl group.

**POLY(MO6ONBP) HOMOPOLYMER**

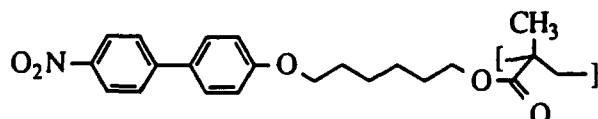


Table (ii)

Material	M.Wt.	D.P.	$T_g$	$T_{endo}$
poly(MO6ONBP)	147 000	380	51	75
poly(MO6ONBP)	777 500	2 030	47	77
poly(MO6ONBP)	849 800	2 220	47	77
poly(MO6ONBP)	1 241 000	3 240	54	79

X-ray studies show no orientation in a freshly drawn (quenched) fibre, but after annealing between  $T_g$  and  $T_{endo}$  some small-angle peaks appear, indicating a smectic phase (fibre of m. wt. 1 241 000 annealed at 65°C for 4 hrs). This result was confirmed in a plot of diffracted intensity from a pressed film which had been annealed for 24 hours at 64°C and quenched. Peaks were observed which corresponded to ~21 Å (first order side chain), 12.2 Å (second order), 7.9 Å (third order), and 4.6 Å (interchain). There is no evidence of solid crystallinity. Molecular modelling studies show that the length of the side chain, in the fully extended conformation, is 22.6 Å.

Transmission optical microscopy using a hotstage shows a clear, isotropic phase above ~ 110°C. Below this temperature, the material shows a birefringence flash when sheared, and has a uniaxial conoscopic figure centred on the microscope axis. A truly isotropic phase would give a totally black conoscopic image, and we provisionally interpret this observation as due to some degree of homeotropic surface alignment, which indicates that surface fields have a strong effect on this material. There is no corresponding endotherm at 110°C on the DSC trace.

On further cooling, a highly scattering texture appears at  $T_{endo}$ , and conoscopy reveals an increasingly biaxial figure whose melatopes rotate 90° between the onset of this texture and its full development. It is not clear whether the biaxiality is the consequence of some degree of alignment of the backbone breaking the uniaxial optical symmetry of the sidegroups, or whether it represents some rotation correlation of the mesogenic sidegroups about their long axes. The sudden rotation of the optic axial plane as the smectic phase begins to form, may indicate that the structure is a smectic C.

Experiments on the material of M.Wt. 849 800 show that the scattering intensity (reduction in brightness of the straight-through beam as measured using a photodiode) is reduced at faster cooling rates, and quenching onto a cold aluminium block avoids formation of the smectic phase altogether (see Fig. 2). This agrees with the quenched fibre results.

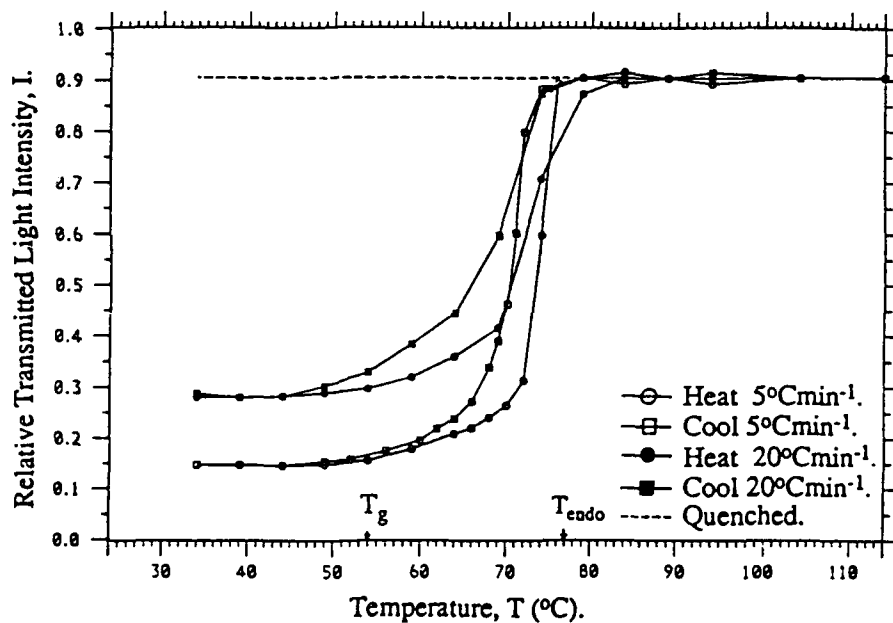


Figure 2: Graphs of transmitted light intensity for the M.Wt. 849 800 poly(MO6ONBP) material.

### Comparison

Changing the molecular weight of poly(MO6ONBP) has little effect on the thermal properties, although we would expect the longer chains to yield better mechanical properties.

Polymerisation of MO6ONBP monomer, which is not liquid crystalline, produces a smectic liquid crystalline polymer poly(MO6ONBP).

## POLY(MO6ONS) HOMOPOLYMER

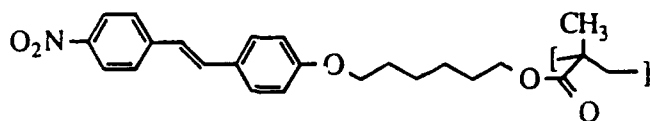


Table (iii)

Material	$T_g$	$T_{endo}$	$T_{deg}$
poly(MO6ONS)	61	156	385

Optical microscopy using a hotstage shows that the poly(MO6ONS) material is isotropic above  $T_{endo}$ . On slow cooling ( $0.1^\circ\text{C}/\text{min}$ ) a highly scattering texture forms over the range  $152.5^\circ\text{C}$  to  $150.6^\circ\text{C}$ . The scattering texture starts at the edge of the sample and grows towards the middle, an observation which can be explained by air cooling of the top of the sample.

The scattering mesophase texture is very insistent, and some even manages to form when a thin sheared film, on one side of a  $120\text{ }\mu\text{m}$  thick cover slip, is quenched into liquid nitrogen.

X-ray studies of fibres drawn from the isotropic melt reveal a partially oriented phase, with the mesogenic groups lying perpendicular to the fibre axis. This phase is provisionally classified as smectic. The alignment is more pronounced after annealing above  $T_g$  (4 hrs at  $100^\circ\text{C}$ ). There is no evidence of solid crystallinity.

Comparison

On replacing the nitrobiphenyl groups in poly(MO6ONBP) with nitrostilbene groups to form poly(MO6ONS), the glass transition temperature is slightly raised. The clearing point at  $T_{endo}$  is considerably raised from  $77^\circ\text{C}$  to  $156^\circ\text{C}$ , indicating a large increase in the stability of the liquid crystalline phase. The strong tendency to form the mesophase, even on quenching, is further evidence for this.

As with the MO6ONBP material, polymerising MO6ONS, which is not itself liquid crystalline, produces a smectic liquid crystalline polymer.

## POLY(MO6ONS-co-MMA) RANDOM COPOLYMER

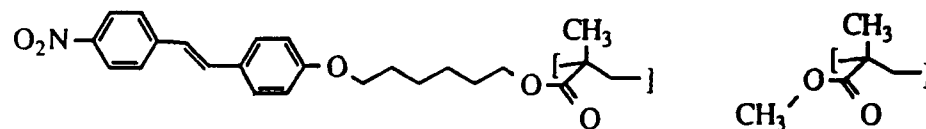


Table (iv): see also Fig. 3

Material	$T_g$	$T_{endo}$	$T_{deg}$
poly(MO6ONS)	61	156	385
poly(MO6ONS <sub>0.7</sub> MMA <sub>0.3</sub> )	54	119	366
poly(MO6ONS <sub>0.5</sub> MMA <sub>0.5</sub> )	69	—	376
poly(MO6ONS <sub>0.3</sub> MMA <sub>0.7</sub> )	87	—	355
poly(MO6ONS <sub>0.05</sub> MMA <sub>0.95</sub> )	110	—	353

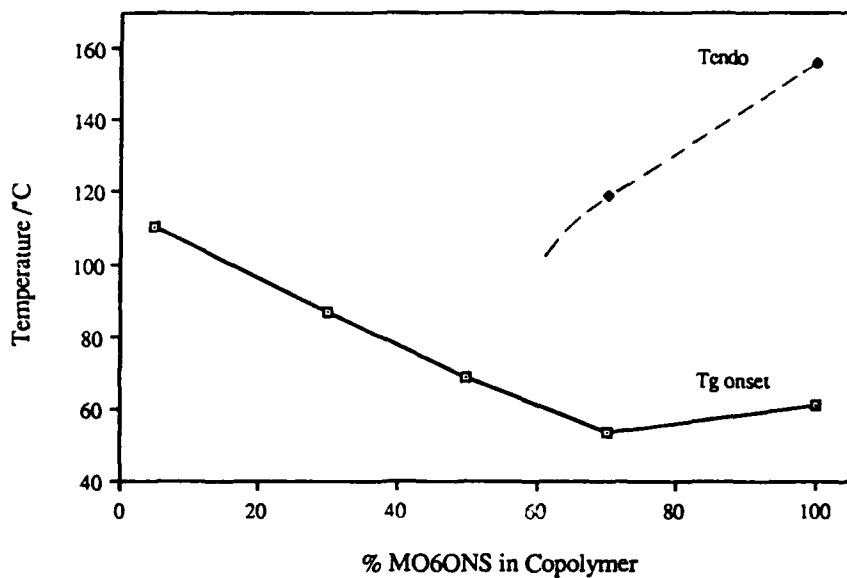


Figure 3: Variation of  $T_g$  and  $T_{endo}$  with composition  
(remember that  $T_g$  is an onset at  $20^\circ\text{C}/\text{min}$ , and will vary with heating rate)

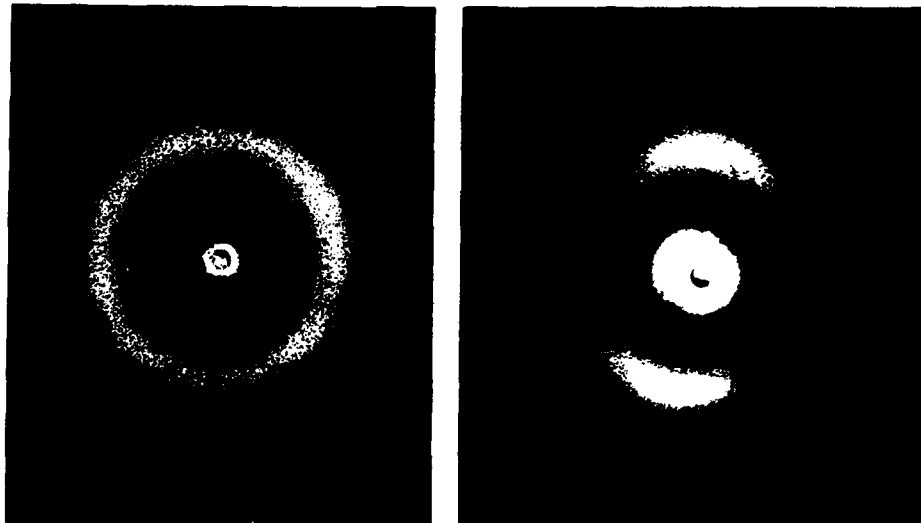


Figure 4: Microbeam X-ray patterns of the poly(MO6ONS<sub>0.7</sub> MMA<sub>0.3</sub>) material before and after annealing for 2 hours at  $100^\circ\text{C}$  (fibre axis  $\uparrow$ )

X-ray studies show no orientation in freshly drawn fibres, but show smectic peaks in annealed ones (see Fig. 4). The peaks visible in the photograph correspond to  $8.7\text{\AA}$  (third order side chain) and  $4.8\text{\AA}$  (interchain).

#### Comparison

The X-ray studies confirm the previously noted similarities between the MO6ONS

and the MO6ONBP materials.

The behaviour of the homopolymer was discussed in the previous section. Optical microscopy using a hotstage confirms that the liquid crystallinity is reduced by increasing the proportion of MMA groups in the chain, to the extent that the smectic scattering texture observed in the homopolymer and the poly(MO6ONS<sub>0.7</sub> MMA<sub>0.3</sub>) material is not seen at all in the others.

There is a suspicion (see Fig. 3) that the poly(MO6ONS<sub>0.5</sub> MMA<sub>0.5</sub>) material may have a  $T_{\text{endo}}$  close to and just below  $T_g$ .

### HO3ONS MONOMER

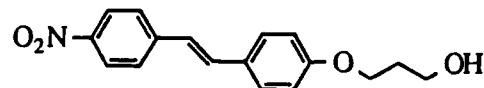


Table (v)

Material	M.Wt.	$T_m$	$T_{\text{endo}}$	$T_{\text{deg}}$
HO3ONS	299	119	145	375

On cooling from the isotropic phase, a classic Schlieren texture appears, indicating a nematic phase. Disclinations of strength  $\pm \frac{1}{2}$ , which occur at the ends of surface defects, annihilate to leave only  $\pm 1$  disclinations normal to the surface. In small drops of the sample, only +1 defects are found. The nematic goes on to solidify to birefringent lath crystals, which radiate out from nucleation points.

#### Comparison

Shortening the alkyl chain in HO6ONS to three units long in HO3ONS has allowed a mesophase to form, by reducing the mesogenic dilution of the flexible tail.

### MO3ONS MONOMER

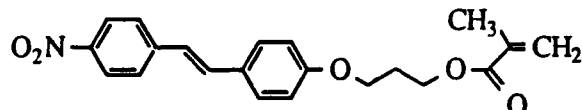


Table (vi)

Material	M.Wt.	$T_m$	$T_{\text{deg}}$
MO3ONS	367	141	340

Forms lath-like birefringent solid crystals. It melts to form an isotropic liquid and displays no liquid crystallinity.

#### Comparison

Replacing the hydroxyl group in liquid crystalline HO3ONS with a vinyl group has produced non-liquid crystalline MO3ONS, which also has a slightly higher melting point. This is analogous to the loss of liquid crystallinity when the alkyl chain of HO6ONS is lengthened to form HO6ONS.

The melting point of MO3ONS is dramatically higher than MO6ONS, because MO6ONS has a longer alkyl chain which causes a loss of rigidity in the crystal.

## POLY(MO3ONS-co-MMA) RANDOM COPOLYMER

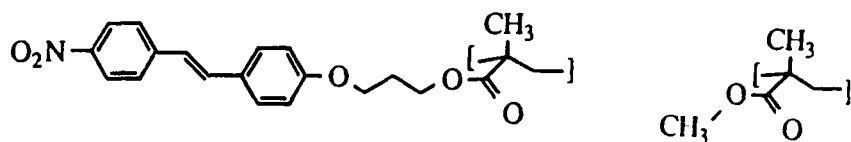


Table (vii)

Material	$T_g$	$T_{deg}$
poly(MO3ONS)	95	378
poly(MO3ONS <sub>0.7</sub> MMA <sub>0.3</sub> )	107	376
poly(MO3ONS <sub>0.5</sub> MMA <sub>0.5</sub> )	105	372
poly(MO3ONS <sub>0.3</sub> MMA <sub>0.7</sub> )	114	360

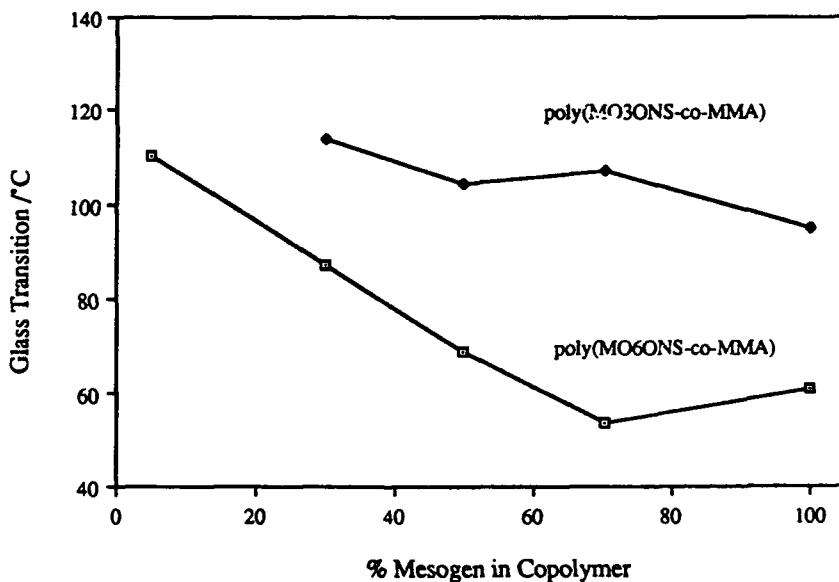


Figure 5: Variation of glass transition onset against composition for poly(MO3ONS-co-MMA) and poly(MO6ONS-co-MMA)

Optical microscopy with a hotstage showed that they are isotropic liquids and solids with no evidence of a mesophase or crystallinity.

Comparison

Reducing the decoupling in the poly(MO6ONS-co-MMA) materials by shortening the spacer to form the poly(MO3ONS-co-MMA) materials has removed the liquid crystallinity and raised the  $T_g$ . This is in contrast with the behaviour of flexible chains in monomers (e.g. HO3ONS and HO6ONS) where long alkyl chains oppose liquid crystallinity.

Polymerisation of the non-liquid crystalline monomer MO3ONS has not induced liquid crystallinity, in contrast with MO6ONS, due to strong coupling with the backbone.

## CONCLUSIONS

The smectic phases formed by some of the polymers may be avoided by fast cooling from the isotropic phase (as confirmed by conoscopy of quenched samples, and by scattered light measurements), although in the case of the poly(MO<sub>6</sub>ONS) homopolymer the cooling rate required is prohibitively fast. In any case, the smectic phase would form during the poling near  $T_g$  that is required for  $\chi^{(2)}$  NLO applications (as confirmed by X-ray studies on annealed fibres).

The optically clear homeotropic phases, as observed in the poly(MO<sub>6</sub>ONBP) homopolymer, promise to be useful and well aligned, although electric field poling above  $T_g$  is often difficult due to the low dielectric breakdown strength.<sup>4</sup>

More interesting is the indication that the poly(MO<sub>6</sub>ONS<sub>0.5</sub> MMA<sub>0.5</sub>) material has a  $T_{endo}$  just below the measured  $T_g$ . This is a molecular solution to the scattering texture problem; a material which is almost, but not quite, liquid crystalline at its glass transition will tend to align readily under the influence of a field. Such a phase may be particularly appropriate for poling in external electric fields. The question also arises as to whether intermediate spacer lengths, 4 or 5 units long, would yield similarly borderline liquid crystalline materials.

## ACKNOWLEDGEMENTS

We are indebted to the following: Don Ulrich from the Department of the Air Force, Washington, DC, USA, for funding the project; Hoechst Celanese, Summit, New Jersey, USA for providing the excellent and very pure materials, and for much support; Professor Derek Hull, Department of Materials Science and Metallurgy, Cambridge, UK for provision of laboratory facilities.

## REFERENCES

1. Thomas M. Leslie, Ronald N. DeMartino, E. Won Choe, Garo Khanarian, David Haas, Greg Nelson, James B. Stamatoff, Dago E. Stuetz, Chia-Chi Teng and Hyun-Nam Yoon, *Mol. Cryst. Liq. Cryst.*, **153**, 451-477 (1987)
2. J.B. Stamatoff, A. Buckley, G. Calundann, E.W. Choe, R. DeMartino, G. Khanarian, T. Leslie, G. Nelson, D. Stuetz, C.C. Teng and H.N. Yoon, *SPIE Molecular and Polymeric Optoelectronic Materials: Fundamentals and Applications*, **682**, 85-92 (1986)
3. H. Finkelmann, in *Polymer Liquid Crystals*, edited by A. Ciferri, W.R. Krigbaum and Robert B. Meyer (Academic Press Inc., New York, 1982, ISBN 0-12-174680-1), ch. 2.
4. H.J. Coles, Physics Department, University of Manchester, UK. (private communication).

92-18277

AD-P007 485



315

## PERIODIC AREA MINIMIZATION SURFACES IN MICROSTRUCTURAL SCIENCE

EDWIN L. THOMAS and SAMUEL P. GIDO

Department of Materials Science and Engineering, and Program in Polymer Science and Technology, Massachusetts Institute of Technology, Cambridge, MA 02139

### Abstract

An A/B block copolymer consists of two macromolecules bonded together. In forming an equilibrium structure, such a material may separate into distinct phases, creating domains of component A and of component B. A dominant factor in the determination of the domain morphology is area-minimization of the intermaterial surface, subject to fixed volume fractions. Surfaces that satisfy this mathematical condition are said to have constant mean curvature. The geometry of such surfaces strongly influences material physical properties. We have discovered domain structures in microphase-separated diblock copolymers that closely approximate periodic surfaces of constant mean curvature. Transmission electron microscopy and computer-simulation are used to deduce the three dimensional microstructure by comparison of tilt series with two-dimensional image projection simulations of three-dimensional mathematical models. Two structures are discussed: First is the double diamond microdomain morphology, associated with a newly discovered family of triply periodic constant mean curvature surfaces. Second, a doubly periodic boundary between lamellar microdomains, corresponding to a classically known minimal surface (Scherk's First Surface), is described.

### Introduction

Most multifunctional materials are multiphased: comprised of two or more phases whose simultaneous presence and mutual arrangement lead to unique properties. Emphasis in multiphased materials research in recent years has been concerned with the production of microphase textures of ever finer scale, since novel macroscopic properties can arise from materials with nanoscale structure. As the size scale of the phase domains decreases, an increasing percentage of the material is at or near an intermaterial interface. Surface phenomena which are absent or negligible in the bulk materials then begin to dominate the physics. Materials which have extremely high interphase surface area per unit volume can exhibit entirely new physical properties.

In order to exploit such materials we need to learn how to control the size and mutual arrangement of the microphases. A commonly used route to such ordered micro and nanocomposites involves directly building up the structure via microlithographic processes. With this approach process control is critical. An alternative approach is that of self assembly — the ability of amphiphilic molecules to organize themselves into nanoscale patterns in response to thermodynamic driving forces[1,2,3]. In our work we employ very large amphiphiles: diblock copolymers consisting of two chemically different polymer segments. The mutual repulsion of these segments leads to the formation of periodic nanoscale structure. This self repulsion arises due to the positive enthalpy of interaction between the different block monomer units, and is not significantly resisted by the loss of entropy because of the long chain nature of the molecules. The local segregation of the A and B segments into microphases occurs in spatially periodic patterns, due to the covalent link between the two types of segments.

Area-minimization of the A-B intermaterial interface is a dominant factor in determining the specific microdomain geometry which forms for a particular ratio of A and B block lengths. Area minimization subject to fixed volume fraction (fixed composition) is the mathematical

condition for interfacial surfaces of constant mean curvature. In differential geometry, the mean curvature ( $H$ ) at a point on a surface is defined as the average of the two principal curvatures or alternatively as the average of the reciprocals of the two principal radii of curvature[4]. The well known spherical, cylindrical and lamellar block copolymer microdomain structures are all examples of intermaterial interfaces of constant mean curvature. A fourth microdomain geometry, the so called ordered bicontinuous double diamond (OBDD) structure is a recently discovered[5,6] example of a triply periodic microdomain partitioning surface of constant mean curvature. Here we examine some structure-property relationships (transport and mechanical) for the OBDD structure.

An additional intermaterial surface which we have discovered in block copolymers is at the boundary between two grains of lamellar microdomains. This doubly periodic interface has zero mean curvature and corresponds to a classical area minimizing surface discovered by H. F. Scherk[7]. This surface allows the maintenance of microphase continuity through a twist grain boundary, and thus is likely to have profound effects on transport and mechanical properties.

### Experimental Methods

Block copolymers used in this work were highly monodisperse polystyrene-*b*-polybutadiene (SB) or polystyrene-*b*-polysisoprene (SI) diblocks and starblocks of various compositions synthesized by L. J. Fetters of Exxon. Microphase separated samples were prepared by slow casting ~1 mm thick films from ~8 wt/vol % solutions of a neutral solvent (toluene). Solvent was evaporated at room temperature for one week, and then to ensure development of the equilibrium microstructure, samples were annealed under high vacuum at 115°C for another week. This annealing temperature is significantly below the microphase separation temperature, but ~10°C above the glass transition of the more rigid component, polystyrene. Dynamic mechanical and stress-strain experiments were then performed on these microphase separated materials. Gas absorption studies were also conducted. In order to correlate microstructure with the observed properties, morphological investigations were conducted utilizing SAXS and TEM. Although X-ray scattering allows determination of the lattice parameters and symmetry, it cannot determine whether or not the actual material interfaces are coincident with or even systematically related to the predicted constant mean curvature surfaces with the same periodicity. To demonstrate the presence of these surfaces, 400-1000Å sections were obtained using cryo-ultramicrotomy. The sections were stained with osmium tetroxide and observed with TEM. These images were interpreted by comparison to computer generated projections based on the interface minimizing model surfaces. Computer projections were produced by passing rays through a hypothetical space simulating separate microphases partitioned by the appropriate model surface. Each such ray corresponded to a pixel on the video monitor. The gray level of the pixel was determined as a weighted average of the gray levels assigned to the two component materials. The weight given to each component was determined by the distance the ray traveled through each respective component. This corresponds to the linear approximation of Beer's law for mass thickness contrast in thin specimens. By varying the direction of the rays, different simulated projections were generated and compared to TEM tilt series images.

### Constant Mean Curvature Model for the OBDD Microstructure

Anderson and Thomas[8] have shown that the constant mean curvature (CMC or  $H$ ) surface used to model the OBDD structure is part of a family of surfaces that includes a classically known minimal surface. A minimal surface is a CMC surface with  $H = 0$ . It is the solution to the problem of area minimization without volume constraints. A soap film on a wire frame assumes a minimal surface geometry. This soap film minimal surface occurs when there is zero pressure difference across the film, since both sides are exposed to the

atmosphere. This observation suggests that one might possibly observe minimal surface interfaces in real materials if the volume fractions happen to be 50/50. In fact, the solution to the area minimization problem for 0.5 volume fraction happens to be the same as the minimization with no volume constraints at all. In diblock copolymers for 0.5 volume fraction a lamellar morphology is observed with planar interfaces. Planes are CMC surfaces with  $H = 0$ , and thus are also minimal. It is interesting to extend the analogy between the pressure difference across a soap film and volume fractions on either side of a material interface one step further. Note that a soap bubble does have a pressure difference across its interface (given by the Young-Laplace equation). Its surface is a CMC surface, the sphere, which, of course, is also one of the interface geometries observed in block copolymers for unequal volume fractions.

A family of CMC surfaces computed by Anderson[9] was used to define the interface for the OBDD morphology. To construct a surface of this family, begin with diamond cubic-close packed spheres of one material a matrix of another. The interfacial surface, which is discontinuous in this case, has constant mean curvature and space group  $F\bar{4}3m$ . Now imagine joining each sphere to each of four adjacent neighbors with a small "neck", after first shrinking the spheres slightly in order to create gaps for the necks. A computer generated perspective view of the resulting triply periodic structure is shown in Figure 1. The fusing of the spheres can be done in such a way that the new intermaterial dividing surface is also of constant mean curvature, although slightly greater than that of the original spheres. The interfacial area, however, is decreased from that of the packed spheres, and the space group is unchanged.

A family of such structures can be generated where every structure has space group  $F\bar{4}3m$ , is topologically equivalent to the bicontinuous structure shown in the figure, and is characterized by a continuous dividing surface of constant mean curvature. This family exists for minority phase ("channel phase") volume fractions from about 0.131 to 0.5. Above 0.5 the channel material becomes the matrix and *vice versa*; thus symmetrical results are obtained. The family member at exactly 0.5 volume fraction, corresponds to the Schwarz diamond or "D" surface[10], which is minimal. The D surface exhibits additional symmetries, which combine with those common to all members of the family, to give space group  $Pn3m$ . If the D minimal surface and any other member of the CMC diamond surface family are placed on the same lattice, and the CMC surface is reflected through the minimal surface, a copy of the CMC surface is generated which is displaced from the original by half a body diagonal of the  $F\bar{4}3m$  unit cell. Close examination of Figure 1 will reveal two diamond lattices. One lattice is surrounded by the CMC surface. The second lattice, which is intertwined with but does not intersect the first, indicates the position of the the copy of the surface after the reflection process just described. The space group of the original CMC surface together with its copy is  $Pn3m$  because the reflection is now a symmetry. Two distinct but mutually intertwined diamond networks of a channel phase in a matrix phase, with space group  $Pn3m$  is, of course, the set of structural characteristics observed[5,6] in block copolymer materials with the OBDD morphology.

The OBDD structure with two diamond networks has a lattice parameter of one half that of the original single diamond structure. The effects of a smaller unit cell, rescaling, and the factor of two for the double diamond as opposed to the single diamond all cancel out so that the surface area per unit cell is unchanged by the addition of the second diamond network. The minimum volume fraction for which this interface can occur, however, is doubled from 0.131 (single diamond) to 0.262 (double diamond). At the volume fraction 0.262, a plot of interfacial area vs. volume fraction exhibits a very sharp minimum[8]. This minimum represents a surface area that is smaller than for any other known triply periodic CMC surface. This may be an important reason why the OBDD structure is observed in block copolymers as opposed to other types of triply periodic CMC surfaces, such as those based on Schwarz' P surface[1,10,11]. Table I is a compilation of some SI and SB block copolymer compositions that have been observed to exhibit the OBDD morphology. These typically have channel phase volume fractions in or near the 0.30 to 0.33 range. These volume fractions are very close to the volume fraction of the calculated, sharp, surface area minimum.

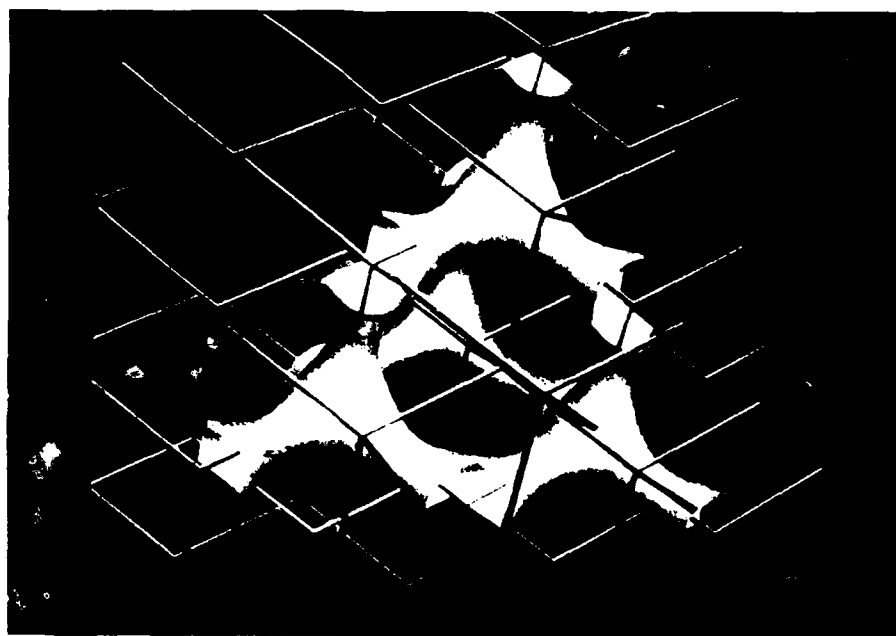


**Figure 1:** Computer Graphic of Two Interpenetrating Diamond Lattices with a CMC Surface of the Schwarz D Family Shown on One Lattice, *Ref. 9.*

**TABLE I:** Some SI and SB Copolymers With OBDD Microstructure (not an exhaustive compilation)

Description	$M_n$ (per arm for star)	Wt. frac. PS	Vol. frac. PS	Channel Phase	Ref
SI diblock	95,600	0.65	0.62	I	6
SI diblock	186,000	0.69	0.66	I	6
SI diblock	207,000	0.66	0.63	I	6
SB diblock	31,800	0.682	0.651	B	18
18 arm SI star, S outer block	23,000	0.30	0.29	S	14
8-18 arm SI star, S outer block	33,000	0.30	0.29	S	14
12-18 arm SI star, S outer block	100,000	0.30	0.29	S	14
6-18 arm SI star, S outer block	33,000	0.28	0.27	S	20

### OBDD Structure-Property Relationships

The blending of two or more components to form a multiphased solid has long been utilized as a means of tailoring physical properties, typically by employing rather different blend components. Depending on component volume fractions, relative viscosities, relative surface tensions and processing history, bicomponent blends often exhibit a microstructure consisting of a matrix phase surrounding a dispersed, discontinuous phase. Recently researchers at Shell[12] have pioneered the concept of interpenetrating polymer phase network blends. For example they produced blends of 30 vol% polycarbonate (PC) with 70 vol% styrene-ethylene butylene rubber-styrene (S-EB-S) triblock copolymer. When careful processing techniques were used to produce a continuous PC minor phase the modulus of the material increased nearly 100 fold over the discontinuous case. Instead of processing to achieve a co-continuous interspersion with chaotic geometry and highly variable phase size, the self-assembling nature of block copolymers may be utilized to achieve thermodynamic equilibrium microstructures with precisely controlled phase size and long range ordered connectivity patterns.

Newnham[13] has classified ordered biphasic solids into 10 possible connectivity microstructural classes. He denotes 0 for a discontinuous phase, and 1, 2 and 3 for a 1, 2 or 3 dimensionally continuous phase respectively. Four of his classes are of relevance to block copolymer microstructures, and are shown in Figure 2. The 0-3 microstructure consists of a discontinuous phase in a continuous matrix. In the block copolymer case this corresponds to a BCC packing of spherical domains. The 1-3 microstructure consists of 1 dimensional, rod-like, domains in a matrix. This corresponds to a hexagonal packing of cylindrical block copolymer microdomains. The 2-2 microstructure consists of alternating layers, which corresponds to lamellar block copolymer domains. Finally, the 3-3 microstructure consists of two interpenetrating bicontinuous phases, for which the block copolymer example is the OBDD structure.

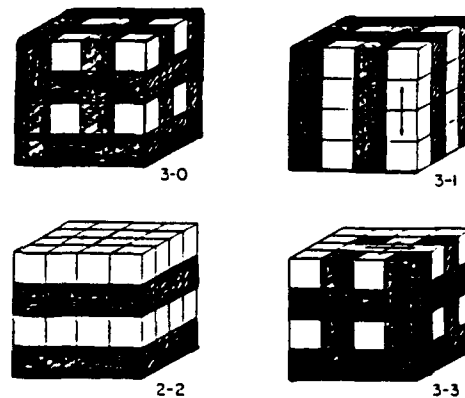


**Figure 2:** Four of Newnham's Biphasic Classifications, that are relevant to block copolymer microstructures: 3-0, 3-1, 2-2 and 3-3 continuity, Ref. 13.

Mechanical properties benefit substantially from the bicontinuous, triply periodic nature of the OBDD structure. Figure 3 is a modulus-temperature plot for microphase separated SI block copolymers [14]. At a polystyrene volume fraction of 0.27 the 3-3 double diamond sample exhibits an order of magnitude increase in room temperature storage modulus over that of the sample with a 1-3 cylindrical microstructure. Figure 4 shows the large strain mechanical behavior of the double diamond and the cylindrical microstructures with PS channel phases in PI matrices. Young's modulus and yield stress are enhanced by an order of magnitude for the OBDD over the cylindrical microdomain morphology. Clearly the dimensional connectivity of a phase strongly influences the macroscopic properties of the composite.

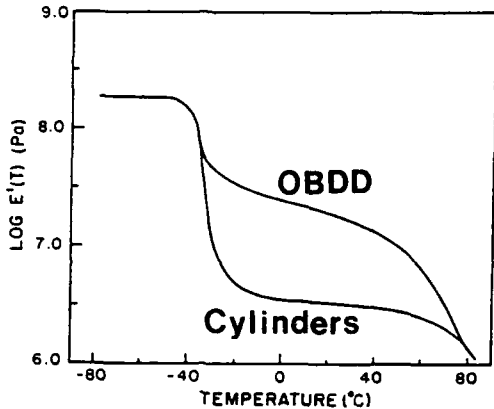


Figure 3: Dynamic Mechanical Storage Modulus vs. Temperature for SI Diblock Copolymers with Cylindrical and OBDD Polystyrene Microphases, Ref. 14.

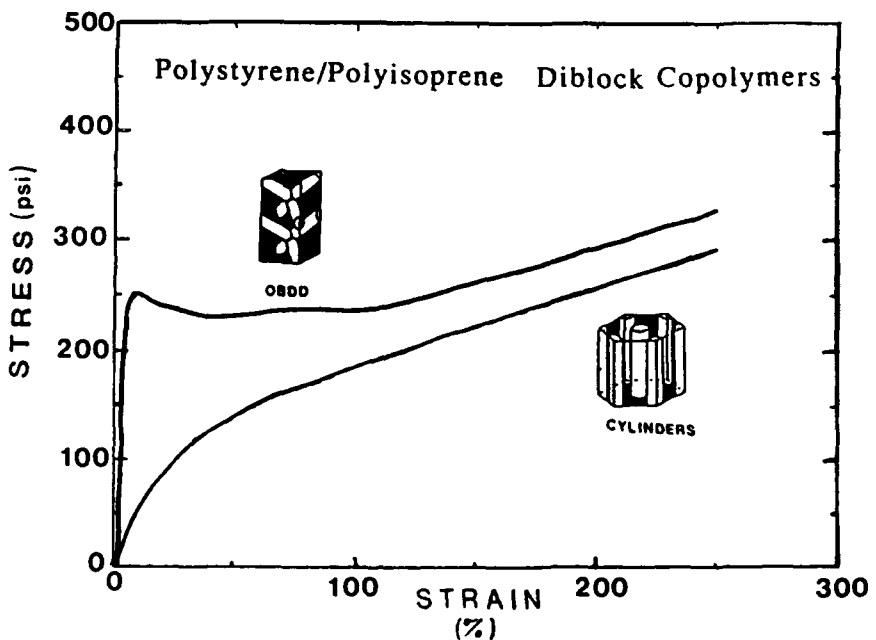
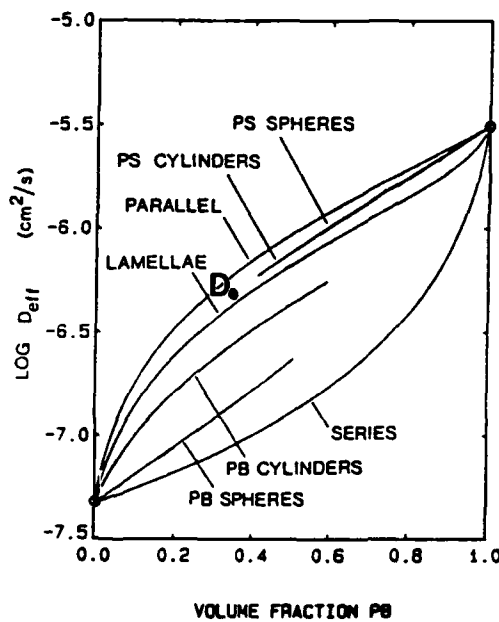


Figure 4: Stress vs. Strain Comparison of SI Diblock copolymers with Cylindrical and OBDD Polystyrene Microphases, Dale Handlin Jr. (previously unpublished).

We have established that the double diamond microstructure is a sensitive function of composition, molecular weight and arm number, in the case of star block copolymers[5,15,16]. The double diamond microstructure has also been recently discovered in binary and ternary blends of diblocks and homopolymers[17]. Channel dimensions can be tailored since they scale as the 2/3rds power of the minority component molecular weight. For practical molecular weights in, for example, SI block copolymers, channel diameters from 2 to

100 nm are possible. These dimensions are orders of magnitude below the micron scale of phase separation typically observed in polymer blends. The nanophase scale and high degree of order indicate that one should expect novel properties which are strongly effected by very high interfacial area per unit volume. One very important category of such properties are gas transport / separation properties. Certainly the regularity and tailorability of dimensions of continuous microphases is of great utility to the designers of membranes for gas separations. The contribution of the material in the interfacial regions to the transport properties is not well understood but is likely to be important, since the concentration of the interfacial energy in this narrow region may lead to increased free volume. Figure 5 shows a comparison of the effective  $\text{CO}_2$  diffusion coefficient in the different types of SB block copolymer microstructures[18]. Transport of  $\text{CO}_2$  is much better in the polybutadiene phase than in the polystyrene phase. When polybutadiene is restricted to the channel phase, the effective diffusion coefficient is highest for the OBDD microstructure (sample D). In fact, the PB OBDD material even gave better transport than PB lamellae, and nearly as good as that observed for PB matrix materials. An OBDD membrane with PB diamond networks in a PS matrix has the significant advantage of mechanical rigidity and toughness over the PB matrix materials, which only have a modest advantage in  $\text{CO}_2$  transport properties.



**Figure 5: Effective  $\text{CO}_2$  Diffusion Coefficient in Different SB block Copolymer Morphologies, Ref. 18.**

#### Lamellar Grain Boundaries — Scherk's First Surface

Although the detailed arrangement of the microdomains in block copolymer systems has been well studied, the corresponding study of the superstructure of grains of such ordered domains has not. The specific structure of the boundary region between grains is of great importance for physical properties such as modulus and diffusivity that depend on the continuity of the phases across grain boundaries. Thermodynamic considerations, as well as macroscopic properties, strongly suggest that phase continuity of the lamellar microdomain morphology is maintained across phase boundaries[18]. For two neighboring grains

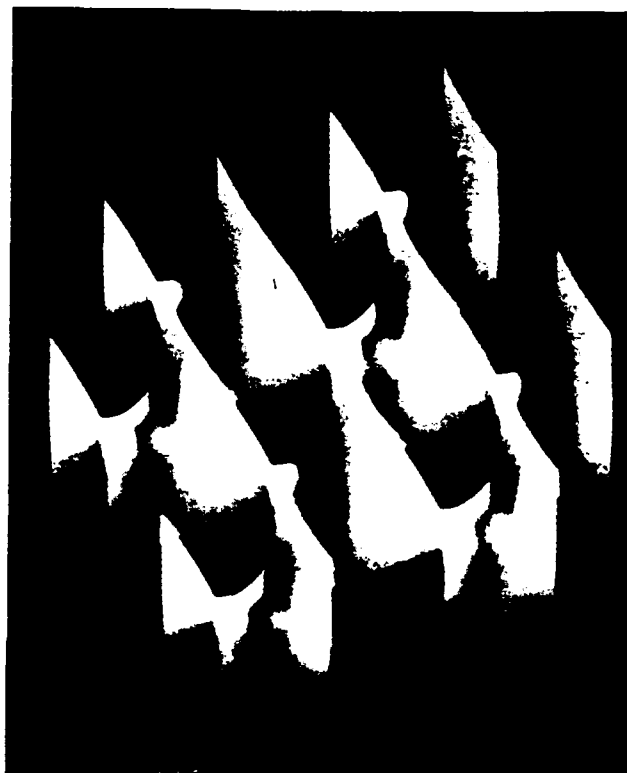


**Figure 6:** Scherk's First Surface 90 Degree Twist Grain Boundary  
*Computer Graphic by James T. Hoffman, Ref 16.*

consisting of parallel stacks of alternating A and B lamellae, the boundary will depend on the orientation of each grain. Thomas, Anderson, Henkee and Hoffman[19] have discussed the situation analogous to a 90-degree twist boundary in crystals. In this case the normals to each set of lamellae are orthogonal, and the model is a minimal surface discovered in the 1830's by H. Scherk[7]. Essentially, the problem is to smoothly join two sets of evenly spaced planes that meet orthogonally. The solution to this problem, called Scherk's First Surface, is shown in three dimensional perspective in Figure 6. The portion of the surface where the two sets of lamellae come into contact consists of a doubly periodic array of saddle regions. Figure 7 shows (a) a TEM image of a SB block copolymer film in a region where the lamellae undergo a twist reorientation of 90 degrees, and (b) the corresponding computer projection of Scherk's first surface. The TEM and computer images both view down one of the lamellar normals, since this is the best direction from which to observe the characteristic saddle shape of the interface. The detailed agreement between the experimental micrograph and the projection of the surface suggests that the actual boundary interface between the two grains approximates Scherk's First Surface. This allows phase continuity and minimizes unfavorable A/B contact between phases.

Since lamellar twist grain boundaries occur at angles of other than 90 degrees, and since they may also involve tilt, it proposed to extend the model based on Scherk's First Surface to cover these cases also. In fact, it turns out that in his original paper Scherk himself presented a relatively simple analytical representation for a whole family of these minimal surfaces corresponding to lamellae meeting at any twist angle. Scherk presented his findings more as a

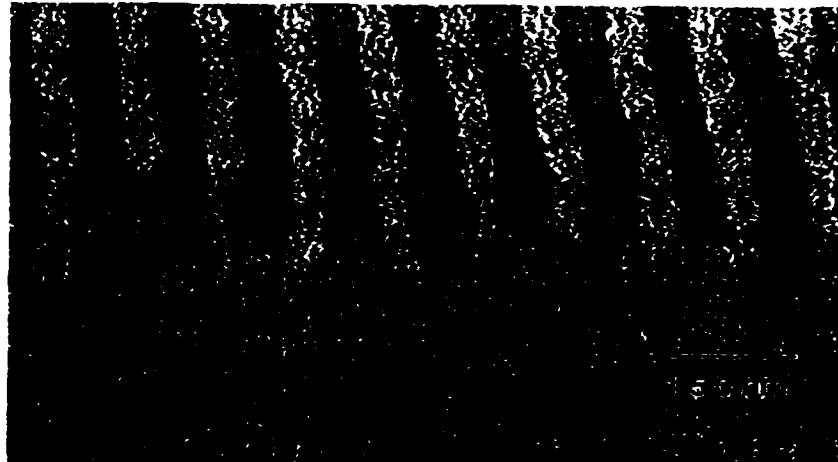


**Figure 7a:** TEM Image of SB block copolymer 90 Degree Twist Boundary Normal To One of the Sets of Lamellae. *Chris S. Henkee in Ref. 16.*

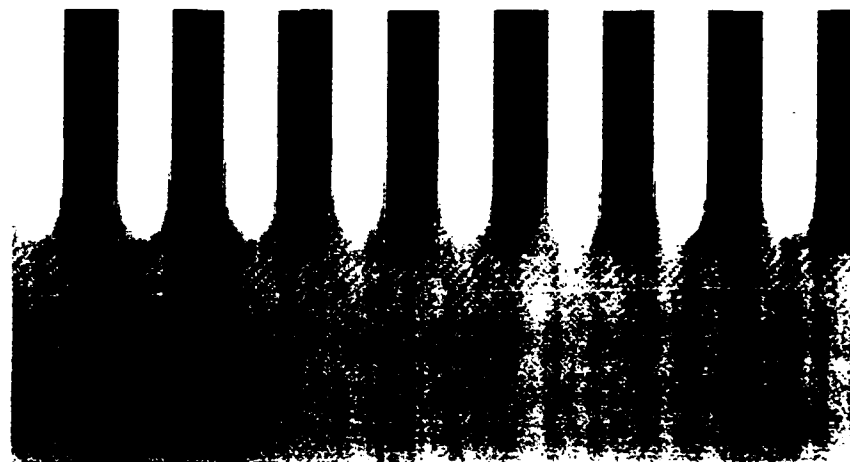


**Figure 7b:** Computer Generated Projection of Scherk's First Surface Normal To One of the Sets of Planes. *David M. Anderson in Ref. 16.*

solution to a differential equation corresponding to  $H = 0$  over all space, than as a surface. He provided no illustrations, and it is quite certain that he was not thinking of lamellar grain boundaries. However, to visualize a twisted Scherk surface one simply needs to imagine rotating the lamellae from the 90-degree orientation shown in the figure. The saddle regions distort appropriately to maintain zero mean curvature and the connection across the boundary.

Karcher has given an illustration of Scherk's First Surface at a twist other than 90-degrees [19]. Current work in our group involves modeling lamellar grain boundaries with twisted and tilted variations of Scherk's First Surface. Again computer projections of the surfaces are compared with TEM micrographs. Grain boundary energy calculations and applications to modeling mechanical and transport properties across grain boundaries are areas of ongoing research.

### Acknowledgements

Many people have contributed to the work discussed in this paper. The authors wish to thank: David M. Anderson, David B. Alward, David J. Kinning, David C. Martin, Dale L. Handlin Jr., Chris S. Henkee, Lewis J. Fetter and Karen I. Winey. We are also very grateful for the support provided by AFOSR grant 88001.

### References

1. L. E. Scriven, *Nature* **263**, 123 (1976).
2. W. Longley and T. J. McIntosh, *Nature* **303**, 612 (1983).
3. S. T. Hyde, S. Andersson, B. Ericsson and K. Larsson, *Z. Krist.* **168**, 213 (1984).
4. D. J. Struik, *Lectures on Classical Differential Geometry*. 2nd ed. (Dover, New York, 1961).
5. E. L. Thomas, D. B. Alward, D. J. Kinning, D. C. Martin, D. L. Handlin Jr. and L. J. Fetter, *Macromolecules* **19**, 2197 (1986).
6. H. Hasegawa, H. Tanaka, K. Yamasaki and T. Hashimoto, *Macromolecules* **20**, 1651 (1987).
7. H.F. Scherk, *Journal fur die Reine und Angewandte Mathematik*. **13**, 185 (1835).
8. D. M. Anderson and E. L. Thomas, *Macromolecules* **21**, 3221 (1988).
9. D. M. Anderson, Ph.D Dissertation, University of Minnesota, Minneapolis, MN, 1986.
10. H. A. Schwarz, *Gesammelte Mathematische Abhandlungen* Springer: Berlin, 1890.
11. J. Charvolin and J. F. Sadoc, *J. Physique* **48**, 1559 (1987).
12. W. P. Gergen, R. G. Lutz, and S. Davidson, in *Themoplastic Elastomers* (ed) N. Legge, G. Holden and H. Schoeder, (Hanser Publ., Munich, 1978).
13. R. E. Newnham, D. P. Skinner and L. E. Cross, *Mat. Res. Soc. Bull.* **13**, 525, (1978).
14. D. B. Alward, D. J. Kinning, E. L. Thomas and L. J. Fetter, *Macromolecules* **19**, 215 (1986).
15. D. S. Herman, D. J. Kinning, E. L. Thomas and L. J. Fetter, *Macromolecules* **20**, 2940 (1987).
16. E. L. Thomas, D. M. Anderson, C. S. Henkee and D. Hoffman, *Nature* **334**, 598 (1988).
17. K. I. Winey, L. J. Fetter, and L. E. Thomas, to be submitted.
18. D. J. Kinning, E. L. Thomas and J. M. Ottino, *Macromolecules* **20**, 1129 (1987).
19. H. Karcher *Construction of Minimal Surfaces. Preprint, Sonderforschungsbereich 256*, U. Bonn, Germany, Nov. 1989.
20. D. Herman, D. J. Kinning, L. J. Fetter and E. L. Thomas, *Macromolecules* **20**, 2940 (1987).

92-18278



AD-P007 486



BEHAVIOR OF SUPERCONDUCTING  
CERAMIC-POLYMER COMPOSITE

C. VIPULANANDAN AND S. SALIB

Texas Center for Superconductivity at the University of Houston, University  
of Houston, Houston, Texas 77204-5506

ABSTRACT

Poly (methyl methacrylate) (PMMA) was used to improve the flexural properties of the high temperature superconducting ceramics ( $YBa_2Cu_3O_{7-x}$ ). The organic polymer was impregnated into the porous ceramic at room temperature. The flexural properties were evaluated using disk specimens. The interaction between the PMMA and ceramic was studied using electron probe microanalysis (EPMA). Poly (methyl methacrylate) polymer increased the flexural strength of the superconducting ceramic without affecting its electrical properties. Flexural strength relationships have been developed for the superconducting ceramic with and without polymer. Performance of the ceramic-polymer composite was also evaluated by thermocycling between 77k and 300k.

INTRODUCTION

Since it is difficult to grow large crystals of the high temperature superconducting phase Yttrium-Barium-Copper oxide ( $YBa_2Cu_3O_{7-x}$ ), fabrication of bulk components from sintered polycrystalline aggregates of the superconducting material by various means are being investigated [3]. The performance of the high temperature superconducting ceramics (HTSC) is sensitive to the preparation condition and could be totally or partially responsible for the many discrepancies in the reported results. The low strength, low fracture toughness and brittleness of the superconducting ceramic provides a challenge, namely how to improve the mechanical and fracture properties of this material without diluting the bulk superconducting properties. The limited compatibility of HTSC with other materials also has restricted the available additives to enhance the mechanical properties, probably to the noble metals. In potential applications, superconductors will be subjected to large stresses caused by high magnetic fields. Hence the main emphasis of most of the studies have been directed towards manufacturing stronger superconductors.

Using various methods of processing, an upper limit of relative density, defined as bulk density/ theoretical density of the superconductor ( $6.35 \text{ gm/cm}^3$ ), between 85 and 95% has been achieved. In the dry compaction-sintering process, the uniaxial compaction pressure has been varied up to 300 MPa [3]. Investigating the pore distribution within the ceramic, Blendell et al. [3] have identified three kinds of pores: pores trapped inside grains, pores on two or more grain junctions and larger pores due to poor packing. The pores on the boundary are small and are mostly due to grain junctions. Bruce et al. [1] have noted that the HTSC is susceptible to the phenomena of moisture enhanced slow crack growth. Barns et al. [2] have noted that epoxy (thermosetting polymer) coating greatly inhibits the reaction of HTSC with water. Hence isolating the HTSC from moist environment is important and polymer coating can be used to protect it. The strength and modulus values reported in the literature for HTSC have large variation and there has been no effort to systematically characterize them in terms of their porosity. In the majority of applications foreseen for the new ceramic superconductor it is likely that they will be subjected to very high mechanical stresses at low temperatures. Hence enhancing the mechanical properties of the superconducting ceramic using PMMA is of primary interest. Although the ceramic superconductor will be used at 77 K to take advantage of their electrical properties they will be inevitably subjected to thermocycling during installation and routine maintenance. Since the thermal properties of PMMA and HTSC are different, it is of importance to understand the performance of the ceramic-polymer composite repeated after temperature cycles.

## EXPERIMENTAL PROGRAM

The powder mix was prepared by mixing yttrium oxide, cupric oxide and barium carbonate in appropriate proportions. The constituent powders were mechanically mixed in using a mortar and pestle. The calcination of the powder has proven to be critical in the preparation of such ceramic. The dry powder was calcined at 900°C for 6 hrs., dry ground using a mortar and pestle and then finally calcined at 900°C for another 12 hrs. After calcination the powder was reground and mixed with methyl cellulose binder (2% by weight) before compacting in a 12.5 mm diameter double sided metal die to a maximum pressure of 350 MPa. The load was applied at a rate of 2 kN/min. and the maximum load was held for 10 minutes before unloading. The density of the dry compacted specimens were determined using gravimetric method and the dimensions of the specimen were measured using a shadowgraph. The compacted pellets were placed in platinum boats and sintered at 940°C in flowing oxygen environment for 24 hours and then annealed at 600°C for 5 hours.

The electrical resistivity was measured from room temperature to 77 K using a four point dc-probe method. The electrical contacts were made with fine aluminum wire and indium paste. A constant current of 100 mA was used for resistance measurements. The voltage difference was measured accurate to 0.1  $\mu$ V. The change in resistivity with temperature was monitored continuously using a X-Y recorder. All the samples were investigated for Meissner effect before the temperature test.

The disk and beam HTSC specimens were impregnated with Poly (methyl methacrylate at room temperature. Clear colorless MMA monomer had a viscosity of 0.53 cps and a specific gravity of 0.94. The MMA monomer was mixed with a promoter, dimethyl aniline (2% by monomer weight) and catalyzed using benzoyl peroxide powder (2% by weight of monomer). Both the promoter and catalyst were mixed well with the monomer and the disk specimens were allowed to soak in the polymerizing mixture. The polymerization is exothermal and the reaction is a free radical chain polymerization. The HTSC specimens were soaked in the polymer and removed as soon as the polymer starts to gel, which allows about 10 minutes for impregnation. The soaked specimens were cured at 60°C for 24 hours to ensure polymerization within the ceramic pores.

Studies have shown that carbon dioxide can hinder the superconducting properties. Since the polymer is made up of carbon, oxygen and hydrogen, and carbon dioxide is released during polymerization the effect of polymer on the superconducting properties was studied. The reaction between the superconductor and the PMMA polymer was studied to investigate any changes in the stoichiometry of the  $\text{YBa}_2\text{Cu}_3\text{O}_{7-x}$ , especially near the interface. The method selected for this study is the electron probe microanalysis (EPMA).

The mechanical properties of the HTSC specimens were evaluated by concentrically loading the simply supported disk (5). The tests were done at a constant machine displacement of 0.5 mm/min. The deflection at the center of the specimen was measured using a photonic sensor accurate to 0.00025 mm. The disk specimens were thinly coated with a reflective material and calibrated before the test. During the test the load versus center deflection was monitored continuously using a X-Y recorder. In order to characterize the polymer, few polymer disk specimens were also tested. At room temperature the PMMA had a mean flexural strength of 54 MPa. Based on gravimetric measurements, the method of impregnation adopted in this study resulted in filling up to about 40% of voids and an increase in relative density (ratio of composite density to density of solid HTSC) of about 4%.

Thermocycling tests were done on 12.5 mm diameter and 1.78 mm thick disk specimens individually. The pellet was tied to a piece of steel wire and then lowered into liquid nitrogen for one minute and hence the specimen was subjected to excessive temperature gradient. Each time the specimen was taken out of liquid nitrogen, hot air was blown on it using a low drier to bring it to room temperature. Every effort was taken to avoid any condensation of moisture on the specimens. The specimens were tested after 1, 10, and 100 cycles. The mechanical tests were done on the disk specimens soon after the completion of thermocycling.

## ANALYSIS OF RESULTS

The effect of polymer impregnation on the strength, modulus and temperature-resistance relationship and thermocycling properties have been analyzed. The possible change in chemical composition at the interface have been discussed. All specimens with and without polymer modification showed Meissner effect and no change in the critical transition temperature ( $T_c$ ).

### Interaction Study

The microprobe was used to investigate possible reaction between the superconductor and PMMA at the interface a wave dispersive spectroscopic (WDS) analysis was performed at 1,900 magnification. Eight points on the sample scanning across the pore, interface and HTSC were selected as shown in Figure 1a to investigate the percentage distribution of such elements as C, Y, Ba, Cu and O. C was selected to represent the PMMA. Figure 2 shows the distribution of each element along the investigated path and as expected in the pore carbon concentration was very high. At the interface and within HTSC the stoichiometry of  $\text{YBa}_2\text{Cu}_3\text{O}_{7-x}$  is maintained indicating that polymer did not react with the HTSC under the processing conditions adopted in this study.

### Strength-Porosity Relationship

The load-displacement responses are linear up to very near the failure load for HTSC with and without polymer. The strength and modulus were determined from peak load and displacement using the relationships suggested by S. Timoshenko (4). Impregnation of PMMA polymer increases the strength and stiffness of the superconducting ceramic and the change in properties depend on the porosity as shown in Figure 3. The flexural strength (determined from disk specimens) of porous ceramic can be represented as

$$\sigma_c = \sigma_0 F_\sigma(n) \quad (1)$$

where  $F_\sigma(n)$  is a function of porosity ( $n$ ) and satisfying the condition when  $n=0$ ,  $F_\sigma(n)=1$ . Several linear and nonlinear representations for  $F_\sigma(n)$  were investigated to fit the test data and the best and simple representation for  $F_\sigma(n)$  (where  $0 < n < 0.35$ ) is given as

$$F_\sigma(n) = (1 - A_\sigma n) \quad (2)$$

Least square fit of the test data gives a value of 1.83 for  $A_\sigma$  and 74 MPa for  $\sigma_0$ . The polymer composite strength ( $\sigma_{pc}$ ) can be represented as  $\sigma_c + \Delta\sigma_p$ , where increase in flexural strength ( $\Delta\sigma_p$ ) due to polymer impregnation can be represented as

$$\Delta\sigma_p = B_\sigma n \quad (3)$$

Least square fit of the test data gives a value of 139 MPa for  $B_\sigma$ . The predictions using Equations (2) and (3) are compared to the experimental data in Figure 3.

### Thermocycling Properties

Figure 4 shows the variation of normalized strength (normalized with respect to the strength at the same porosity with no thermocycling) with number of thermocycles. The HTSC flexural strength remains almost unchanged up to 100 thermocycles. The flexural strength of the superconductor-polymer composites tend to decrease with the increasing number of thermocycles. This may be due to the degradation of the polymer within the ceramic

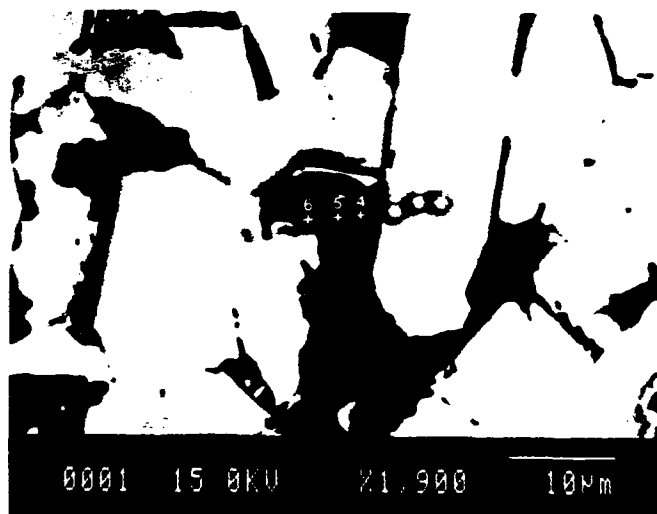


Figure 1. SEM Micrograph (1900X) of HTSC-Polymer Composite with Points Chosen for WDS Analysis (Dark-Polymer: Light - HTSC).

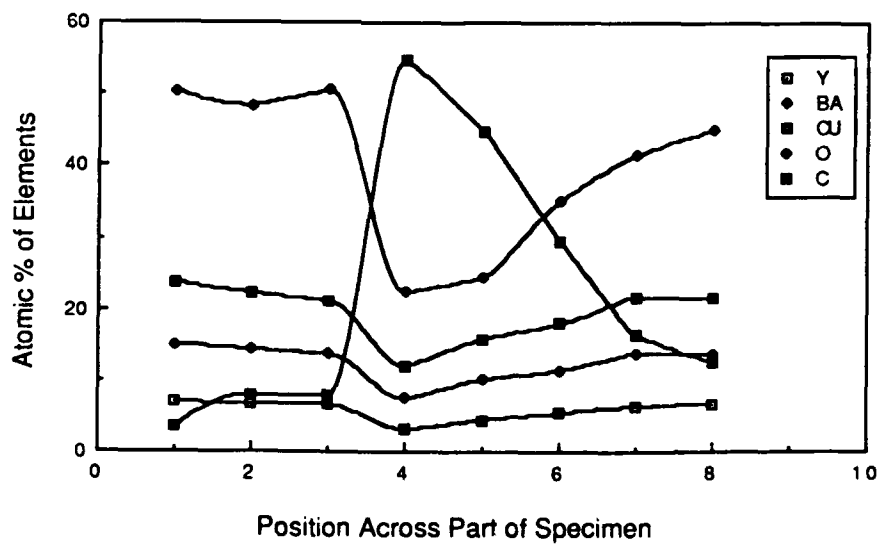


Figure 2. Wave Dispersive Spectrometer (WDS) Analysis Across HTSC-Polymer Interface.

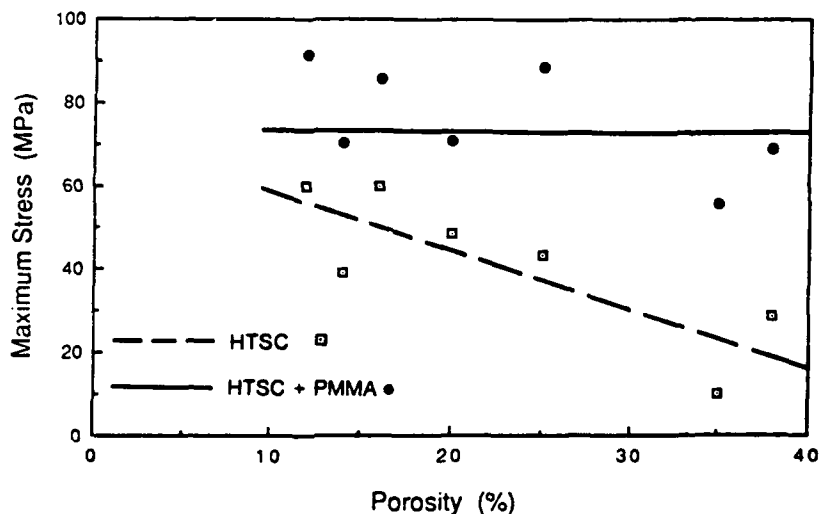


Figure 3. Strength-Porosity Relationship for the Superconducting Ceramic with and without Polymer.

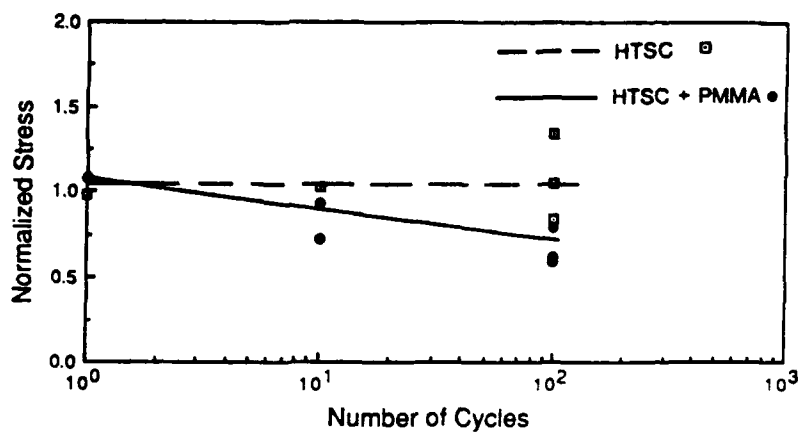


Figure 4. Variation of Normalized Flexural Strength with Number of Thermocycles for the Superconducting Ceramic with and without Polymer.

pores. But, even after 100 cycles the ceramic-polymer composite has higher strength than the HTSC ceramic.

### CONCLUSIONS

Based on this study Poly (methyl methacrylate) (PMMA) can be used effectively to increase the flexural strength of the superconducting ceramic without affecting its electrical properties. The polymer impregnation can be done at room temperature. Electron probe microanalysis show no reaction between the HTSC and PMMA under the processing conditions adopted in this study. The increase in strength due to polymer impregnation depends on the porosity of the ceramic. The flexural strength of the superconducting ceramic with and without polymer have been related to the porosity using linear functional relationships. During thermocycling between 77 K and 300 K, the flexural strength of HTSC-polymer composite is reduced, but even after 100 cycles it is still greater than HTSC strength.

### ACKNOWLEDGEMENT

This work was supported by the Texas Center for Superconductivity at the University of Houston under Prime grant MDA 972-80A-G-0002 from the Defence Advanced Research Projects Agency. The authors also thank Professors K. Salama and K. Ravi-Chandar for their continued encouragement and very valuable suggestions during this study.

### REFERENCES

- (1) R. L. Barnes and R. A. Laudise, *Applied Physics Letter* 51(17), pp. 1373 -1375, October 26, 1987.
- (2) A. J. Bruce, M. Eibschutz, W. H. Grodkiewicz, T. R. Kyle, L. G. Van Urt and G. J. Zydzik, *Material Research Bulletin*, Vol. 23, No.3, pp. 349 -355, 1988.
- (3) W. J. Smothers, Editor, *Ceramic Superconductors*, American Ceramic Materials (ACEME8), American Ceramic Society, Vol. 2, No. 3B, pp. 267 - 738, 1987.
- (4) S. Timoshenko and S. Woinowsky-Krieger, *Theory of Plates and Shells*, McGraw-Hill Book Company, New York, 580 pp., 1959.
- (5) C. Vipulanandan, K. Ravi-Chandar, S. Salib, and N. Dharmarajan, *Superconductivity Applications and Developments*, American Society of Mechanical Engineers, pp.51-60, 1988.

92-18279

AD-P007 487



331

MICROSTRUCTURE AND ELECTRICAL PROPERTIES OF  
KEVLAR/POLYPYRROLE COMPOSITE FIBERS

I.P. RECTOR<sup>a</sup>, D. DEGROOT<sup>b</sup>, T.J. MARKS<sup>a,c,d</sup>, AND S.H. CARR<sup>a,d</sup>  
Northwestern University, <sup>a</sup>Department of Materials Science and  
Engineering, <sup>b</sup>Department of Electrical Engineering and Computer  
Science, <sup>c</sup>Department of Chemistry, and the <sup>d</sup>Materials Research  
Center, 2145 Sheridan Road, Evanston, IL 60208.

ABSTRACT

Electrically conducting composite polypyrrrole/poly(p-phenylene-terephthalamide) (PPTA or KEVLAR) fibers have been prepared by chemical polymerization of pyrrole within the interstices of the hydrogen-bonded gel structure of never-dried PPTA fibers. The resultant fibers contain a uniform dispersion of polypyrrrole, as evidenced by scanning electron microscopy. The temperature dependence of the electrical conductivity of these hybrid fibers is presented. The conductivity is well described by the fluctuation-induced charge transport model over the entire temperature range of interest. However, the low temperature electrical conductivity also exhibits a hopping-like temperature dependence, and an Arrhenius-like temperature dependence is observed in the high temperature limit. Measurements of the temperature-dependent thermopower are indicative of a p-type carrier.

INTRODUCTION

Electrically conductive polymeric materials have a number of important potential application, including EMI shielding, antistatic agents, and conductive coatings. Due to its high conductivity and ease of preparation, the electrical properties of polypyrrrole have been particularly well studied. However the inherent insolubility of polypyrrrole has limited its application. In an effort to overcome this processing limitation, the preparation of electrically conductive composite films by electropolymerization of pyrrole on an electrode covered with a suitable matrix polymer has attracted a great deal of attention in recent years. As examples, the matrix polymers poly(vinyl alcohol) [1], poly(vinyl chloride) [2], and poly(p-phenyleneterephthalamide) (PPTA) [3] have been utilized in this approach, resulting in composite films with improved mechanical properties and thermal stabilities over the corresponding pure polypyrrrole films. Recently a method of composite fiber preparation has also been reported in which a surface coating of polypyrrrole is applied to a substrate fiber [4,5].

Work in this laboratory has centered on the production of electrically conductive composite fibers based on phthalocyanine materials in combination with the rod-like polymers PPTA or poly(p-phenylenebenzobisthiazole) (see, for example, reference [6]). We present here a new approach of hybrid polypyrrrole/PPTA fiber preparation which results in a dispersion of polypyrrrole throughout the matrix (PPTA) phase, in contrast with previously reported methods [4,5]. The temperature dependence of the electrical properties of these fibers will also be surveyed.

EXPERIMENTAL

PPTA fibers were produced by the conventional dry-jet wet spinning method. The fibers were stored on the take-up drum in the precipitation medium (tap water) to retain the never-dried structure. Pyrrole monomer (Sigma Chemical) was distilled and stored under dry nitrogen in a desiccator

at 5 C prior to usage.  $\text{FeCl}_3 \cdot 6\text{H}_2\text{O}$  (Mallinckrodt) was used as received and was stored in a desiccator before use.

The infiltration step was effected by wrapping a never-dried PPTA fiber section around a small glass rack and exposing it to an aqueous  $\text{FeCl}_3$  solution (35.0%). The infiltration was typically conducted for 24 hours with stirring under ambient conditions. Subsequently the glass rack was briefly immersed in distilled water (1-2 seconds) to remove excess  $\text{FeCl}_3$  and placed in a saturated pyrrole atmosphere at 100 C for 1-3 hours. The composite fibers were then washed with copious amounts of distilled water and dried at ambient temperature. The resultant flexible fibers are a metallic dark blue in color.

Room temperature conductivity measurements were obtained on a standard four probe DC apparatus, utilizing a Keithley constant current source and voltage comparator electrometer. Variable temperature measurements were carried out on the automated charge transport system described previously. Morphology was examined by SEM utilizing a Hitachi S-570. To reveal internal structural detail, the fibers were etched with trifluoromethane sulfonic acid (triflic acid) or sulfuric acid.

#### RESULTS AND DISCUSSION

Electrically conductive polypyrroles have been demonstrated to exhibit a DC conductivity  $\sigma$  which scales with temperature  $T$  as

$$\ln \sigma \sim T^{-1/4} \quad (1)$$

over limited temperature ranges [7-9]. Mott has proposed a variable-range hopping charge transport mechanism [10], which predicts the observed functional dependence of electrical conductivity on temperature:

$$\sigma = \sigma_0 \exp[-(B/T)^{1/4}] \quad (2)$$

where

$$\sigma_0 = e^2 R^2 N(E_F) \quad (3)$$

$$R = 3/4 [3/(2\pi\hbar k T N(E_F))]^{1/4} \quad (4)$$

$$B = (24a^3/\pi k N(E_F))^{1/4} \quad (5)$$

Here  $e$  is the electron charge,  $R$  is the average hopping distance,  $N(E_F)$  is the density of states at the Fermi level,  $a$  is the inverse of the wave function localization length, and  $k$  is Boltzmann's constant. In this model the transport process is dominated by electrons that tunnel between localized states which exist near the Fermi level. These localized electronic states are a result of system disorder, the conduction electrons now being described as bound states. Since the states involved in a hopping process are generally of different energy, transport is accomplished with the assistance of phonons. Hopping charge transport has also been shown to be in reasonable agreement with experimental results on amorphous semiconductors such as Ge or Si [10].

The temperature dependence of the electrical conductivity in carbon black-polymer composite materials has been shown to follow the fluctuation-induced tunneling model of Sheng [11]. At low temperature the electrical conductivity is dominated by elastic tunneling between conductive domains. The junctions of closest approach between these conductive grains are modeled as elementary capacitors; the temperature dependence of the conductivity is then dominated by thermally activated voltage fluctuations across these insulating regions. In the high temperature regime, the electrical conductivity is characterized by thermally activated transport

through the insulating barriers. The temperature dependent conductivity is given by

$$\sigma = \sigma_0 \exp[-T_1/(T + T_0)] \quad (6)$$

where  $\sigma$ ,  $T_1$ , and  $T_0$  are model parameters. This model may also prove to be a useful framework in which to examine the temperature dependence of the charge transport data of the polypyrrole/PPTA fibers.

Figures 1(a) and 1(b) show micrographs of composite fibers etched with triflic acid or sulfuric acid. In Figure 1(a) the collapsed polypyrrole skin as well as the internal polypyrrole domains, both remaining after the selective dissolution of the PPTA, are readily observed. From Figure 1(b) is seen that the polypyrrole exists as flattened particles dispersed throughout the PPTA matrix. In addition a light surface coating of polypyrrole is again noted to exist. The internal morphology of Figure 1(b) is similar to the "pancake-like" morphology observed by Koga et al. [3] in electrochemically prepared polypyrrole/PPTA composite films. Thus, the method of creating these fibers is established as being effective in producing composite materials, whose dispersed phase exists throughout the bulk.



Figure 1(a) Scanning electron micrograph of polypyrrole/PPTA fiber etched with triflic acid.



Figure 1(b) Scanning electron micrograph of polypyrrole/PPTA fiber etched with sulfuric acid.

The temperature dependence of the fiber electrical properties were investigated to provide information regarding the dominant charge transport mechanism. The temperature dependence of the thermopower of the hybrid fibers was measured and is indicative of a p-type carrier, in agreement with other measurements of charge transport in pure polypyrrole [7-9]. The predictions of hopping theory are tested in Figure 2 for composite fibers of nominal composition 41% (w/w) polypyrrole and shown to be in reasonable accord with the predictions of hopping conductivity at temperatures below  $\sim 106$  K. In the case of these composite fibers electron transport is complicated by the presence of insulating PPTA regions between the conductive polypyrrole domains. Hence it should not be anticipated that one conduction mechanism is operative over the entire temperature range of interest. At high temperature a simple thermally activated process may be dominant. An Arrhenius plot of the experimental data (Figure 3) shows this assumption to be plausible for temperatures higher than  $\sim 242$  K.

The experimental conductivities may also be used to test the predictions of fluctuation-induced tunneling (Figure 4). The agreement appears to be quite reasonable over the entire measured temperature range. The parameter  $T_1$  is a measure of the effective tunneling barrier height;  $T_1$  may be viewed as the temperature below which fluctuation enhancements of the tunneling process

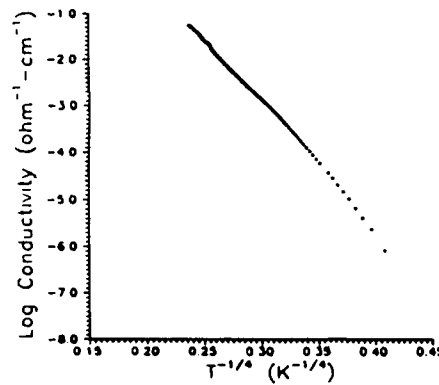


Figure 2 Fit of experimental conductivities to Mott's variable-range hopping.

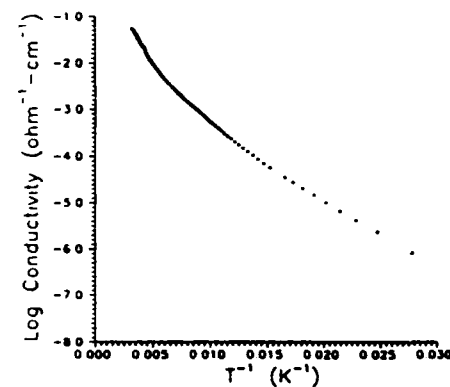


Figure 3 Arrhenius plot of experimental conductivities.

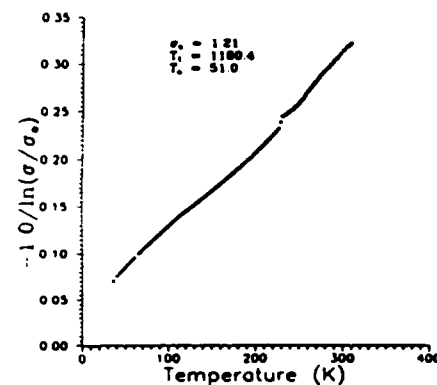


Figure 4 Fluctuation-induced tunneling fit of experimental conductivities.

begin to decrease [11]. The experimental conductivities, whether viewed in terms of Arrhenius-like behavior at high temperatures and hopping-like behavior at low temperatures, or in the context of fluctuation-induced tunneling, indicate that a single charge transport mechanism is not operative over the entire temperature range of interest. Further charge transport measurements as a function of fiber composition and preparation conditions are in progress and will further elucidate the mechanism of electrical conduction.

## CONCLUSION

Composite polypyrrole/PPTA fibers have been prepared by polymerization of pyrrole within the gel structure of never-dried PPTA fibers. Scanning electron microscopy results indicate the formation of a two-phase dispersion of polypyrrole throughout the PPTA matrix. The temperature dependence of the electrical conductivity supports analysis in terms of either hopping charge transport at low temperature and Arrhenius-like behavior in the high temperature limit or a fluctuation-induced tunneling charge transport over the entire measured temperature range. Measurements of the temperature dependent thermopower indicate that the dominant charge carrier is p-type.

## ACKNOWLEDGEMENTS

The authors would like to express their appreciation to H.O. Marcy and Dr. C.R. Kannewurf of the Electrical Engineering and Computer Science Department at Northwestern University for helpful discussions. Financial assistance was provided by the Air Force Office of Scientific Research; use of the Central Facilities of the Materials Research Center (NSF MRL-funded) is greatly appreciated.

## REFERENCES

1. S.E. Linsey and G.B. Street, *Synth. Met.*, 10, 67 (1984/1985).
2. O. Niva, M. Hikita, and T. Tamamura, *Makromol. Chem., Rapid Commun.*, 6, 375 (1985).
3. K. Koga, T. Iino, S. Ueta, M. Takayanagi, *Polym. J.*, 21, 303 (1989).
4. R.V. Gregory, W.C. Kimbrell, and H.B. Kuhn, *Synth. Met.*, 28, C823 (1989).
5. S. Chen and Y. Tsai, *Angew. Makromol. Chem.*, 169, 153 (1989).
6. J.M.C. Redman, J.M. Giesler, W.R. Romanko, S.H. Carr, P.A. Depra, T.J. Marks, H.O. Marcy, C.R. Kannewurf, *Synth. Met.*, 29, F25 (1989).
7. Y. Shen, K. Carneiro, C. Jacobson, R. Qian, and J. Qiu, *Synth. Met.*, 18, 77 (1987).
8. K. Bender, E. Gogu, I. Hennig, D. Schweitzer, and H. Mienstedt, *Synth. Met.*, 18, 85 (1987).
9. D.S. Maddison, J. Unsworth, and R.R. Roberts, *Synth. Met.*, 26, 99 (1988).
10. N.F. Mott and E.A. Davis, Electronic Processes in Non-Crystalline Materials, (Clarendon Press, 1979), pp. 32-34, 52-55.
11. P. Sheng, *Phys. Rev. B*, 21, 2180, 1980.

AD-P007 488



337

New Synthesis/Processing Routes to Materials Exhibiting Large Optical Nonlinearity

L. R. Dalton and L. P. Yu  
Department of Chemistry  
University of Southern California  
Los Angeles, California 90089-0482

92-18280



Abstract

Synthesis/processing schemes for the preparation of optical quality thin films of  $\pi$ -electron containing organic and organometallic materials are discussed. Fabrication approaches range from preparation of molecular/polymer composites, to preparation of copolymers containing pendant electroactive moieties, to preparation of copolymers with electroactive units incorporated into the polymer backbone, to the preparation of polymer/polymer composites. Such fabrication methodologies (particularly the latter three approaches) have the advantage of facilitating control over polymer solubility and of avoiding aggregation of electroactive units. The synthetic schemes discussed here yield materials with well-defined electroactive units; thus, diffuse bandedges associated with a distribution of  $\pi$ -electron conjugation lengths are avoided. Degenerate four wave mixing (DFWM) measurements at 532, 579-600, and 1064 nm are used to determine third order susceptibilities. Investigation of the frequency dependence of  $\chi^{(3)}/\alpha$  established that resonance contributions dominate non-linear optical activity near the  $\pi-\pi^*$  bandedge. A variety of electroactive moieties have been investigated with the largest values of  $\chi^{(3)}/\alpha$  ( $= 10^{-12}$  esu cm) being observed for triphenodioxazine, metal phthalocyanine, metal tetraazaannulene, 6,6'-dimethoxy-quinolidine cyanine units.

**Introduction**

Molecular hyperpolarizabilities are frequently measured employing solutions of electroactive molecules dissolved in appropriate solvents. The solution concentrations are varied to permit the contributions of solute and solvent optical nonlinearities to be measured and susceptibilities to be determined. Such studies are particularly useful for investigation of the dependence of optical nonlinearity upon molecular structure, e.g., length of  $\pi$ -electron conjugation<sup>1</sup>, electron donating or withdrawing substituents, etc. Measurements on solution samples are difficult for molecules exhibiting poor solubility or prone to molecular aggregation. Moreover, potential applications of optical nonlinearity may require a particular

morphology such as an optical quality thin film. In this communication, we focus upon preparation of solid state materials (thin films) and upon measurement of third order susceptibility for these materials.

Fabrication of thin film devices have been pursued for some time for second order materials; for these materials resultant lattices must exhibit non-centrosymmetric symmetry. The required molecular order is often achieved by poling molecular/polymer composites or polymer with electroactive units attached as pendants to a non-active polymer backbone<sup>2,3</sup>. Third order activity does not require non-centrosymmetric structures but solubility is useful in achieving versatile processing (and even characterization) of materials.

At the other extreme from the investigation of optical nonlinearity of molecules is the study of homopolymers. Delocalized  $\pi$ -electron interactions in electroactive polymers lead to enhanced intermolecular attraction and reduced flexibility which in turn leads to reduced solubility. For polymers prepared by polycondensation, poor solubility can lead to a distribution of low molecular weight oligomers. If oligomer lengths are less than the intrinsic self-localization length of the  $\pi$ -electron system, then a distribution of optical bandgaps will exist. Yu and Dalton<sup>4</sup> have demonstrated that bandedge smearing can be avoided by the incorporation of electroactive units of defined length into block copolymers. A more sharply defined bandedge is of utility in separating resonant from non-resonant contributions to optical nonlinearity when investigating the frequency dependence of optical nonlinearity. Improved solubility facilitates the utilization of conventional analytical characterization techniques (NMR, chromatography, UV-Vis, etc.) for defining structure to be used in structure/function correlations. In the present work, we have attempted to examine a number of potential electroactive structures incorporated into material matrices in ways that permit the variation of concentration of electroactive units and control of intermolecular interactions. Investigation of the ratio of third order susceptibility to optical absorption (loss) as a function of concentration of electroactive moiety may provide insight into intermolecular contributions to optical nonlinearity or if these are absent into the relative contributions of resonant and non-resonant processes to measured third order susceptibility.

### Results and Discussion

Characterization of optical nonlinearity is effected employing degenerate four wave (DFWM); the protocol employed in these measurements and the analysis of data is discussed elsewhere<sup>5,6</sup>.

As is shown in Figs. 1 and 2, several potentially interesting electroactive molecules can be synthesized by varying the stoichiometry of monomers in the reaction of dichloroquinones with

substituted 2-aminophenols. We have prepared composites of molecule I in polycarbonate and have recorded strong DFWM signals (see Fig. 3). The value of  $\chi^{(3)}/\alpha$  ( $= 4 \times 10^{-13}$  esu cm) obtained at 532 nm is very close to that ( $= 2.5 \times 10^{-13}$  esu cm) obtained for a composite of nickel tetraazaannulene (5,7,12,14-tetramethyl-dibenzo[b,i][1,4,8,11]tetraazacyclotetradecaahexaenatonickel(II)). A strong DFWM signal is also observed for the polycarbonate composite containing dinitrotriphenodioxazine; however, this signal is observed to decay with time suggesting a photochemical reaction.

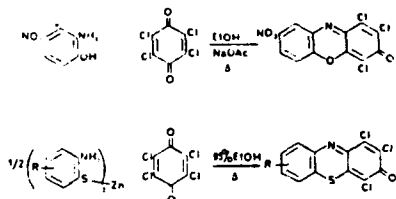


Fig. 1. Reaction scheme for three fused ring compounds.

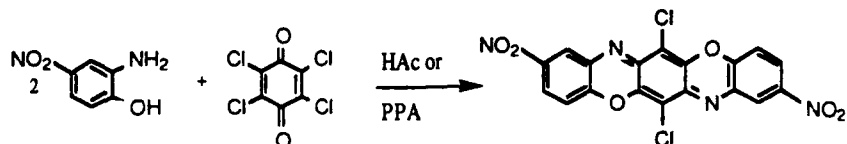


Fig. 2. Reaction scheme for five fused ring compound.

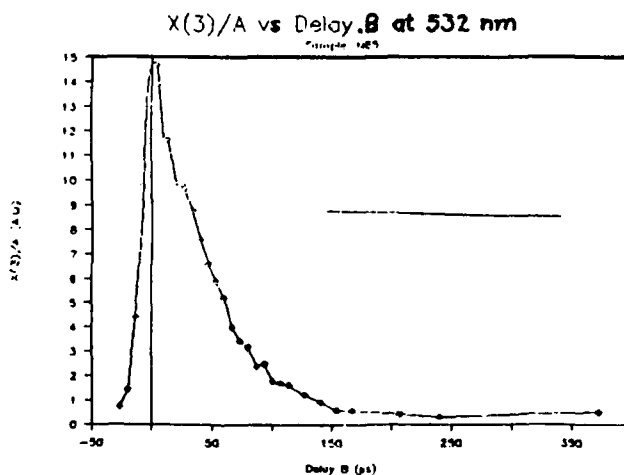


Fig. 3. Plot of DFWM signal as function of delay time of three fused ring.

Copolymers containing various electroactive units can be prepared by reacting appropriate monomers with 1,5-bis(4-aminophenyleneoxy)-pentane as discussed in reference 4. The synthesis of an oxypentane with a reactive aldehyde (denoted A) is shown in Fig. 4. This material can be reacted as shown in Fig. 5 to produce copolymers containing phenylpolyene segments. In Fig. 6, the reaction with diaminoacridine is demonstrated while in Fig. 7, the reaction with diaminostilbene is shown. Unfortunately, these materials do not yield large DFWM signals even though films of excellent optical quality have been obtained.

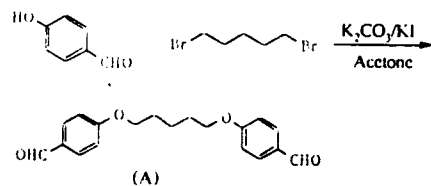


Fig. 4. Synthesis of dialdehyde monomer with flexible chain.

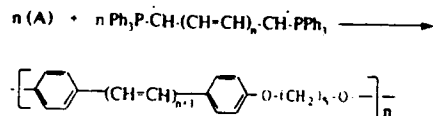


Fig. 5. Preparation of phenylpolyene/flexible chain copolymers.

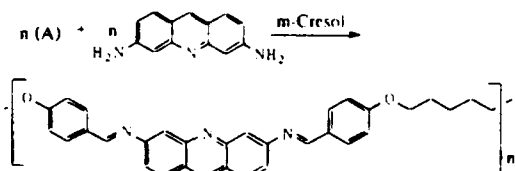


Fig. 6. Synthesis of copolymer containing acridine unit.

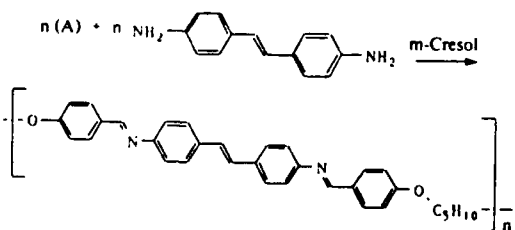
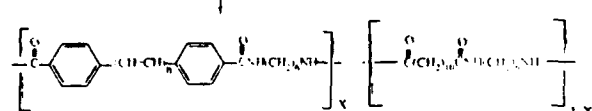
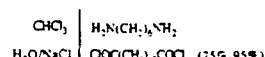
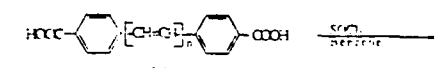


Fig. 7. Synthesis of copolymer containing stilbene unit.

A polymerization based upon condensation reactions involving acetylchloride and amine groups has also been employed to synthesize copolymers containing alternating electroactive and alkoxy segments as shown in Fig. 8. The meracyanine electroactive segment has been incorporated into copolymers as shown in Fig. 9. These films yield large DFWM signals characterized by a  $\chi^{(3)}/\alpha$  value of  $9 \times 10^{-13}$  esu cm.

An analogous reaction incorporating squaric acid units is also shown in Fig. 9.



X = 5, 10, 15, 20, 25 (molar fraction)

Fig. 8. Interfacial polymerization of NLO active monomer.

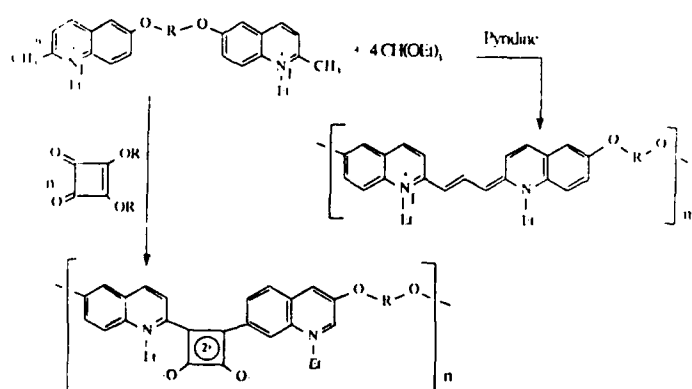


Fig. 9. Syntheses of cyanine-analog copolymers

Various schemes for preparing metal tetraazaannulene copolymers are shown in Figs. 10 and 11. The large optical nonlinearity observed for the annulene metal moiety together with the relative synthetic ease of preparing these materials make these systems attractive for further consideration including the preparation of ordered polymer films.

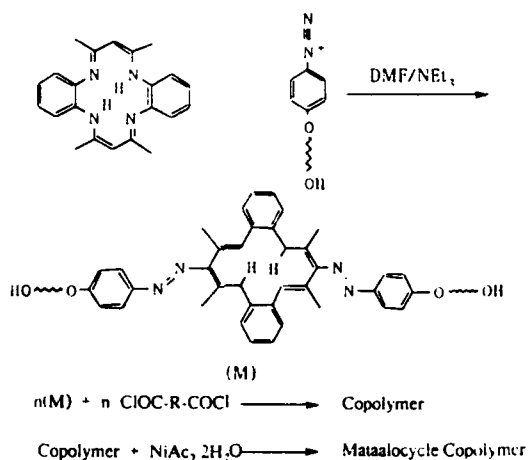


Fig. 10. Synthesis of copolymer containing tetraazoanulene through tetraazo intermediate.

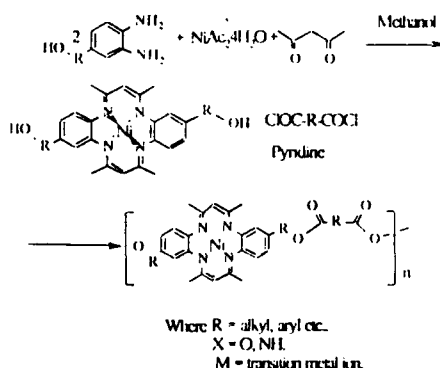


Fig. 11. Polycondensation of tetraazoanulene monomer with diacetyl chloride.

In addition to the investigation of block copolymers, we have pursued the synthesis and characterization of flexible chain backbone polymers containing pendant electroactive units. Such a preparation scheme is illustrated in Fig. 12. The polymer shown in this figure is synthesized by a free radical polymerization of the corresponding  $\alpha$ -vinyl monomer<sup>7</sup>. The final polymer has a molecular weight in the range 4000-10,000 (determined by GPC using polystyrene as a

reference). This material exhibits a large optical nonlinearity, i.e., a  $\chi^{(3)}/\alpha$  value of  $8.5 \times 10^{-13}$  esu cm. Other (e.g., nitrobenzo-2-oxa-1,3-diazole, etc) electroactive units have been incorporated as pendants to a variety of polymers including polystyrene.

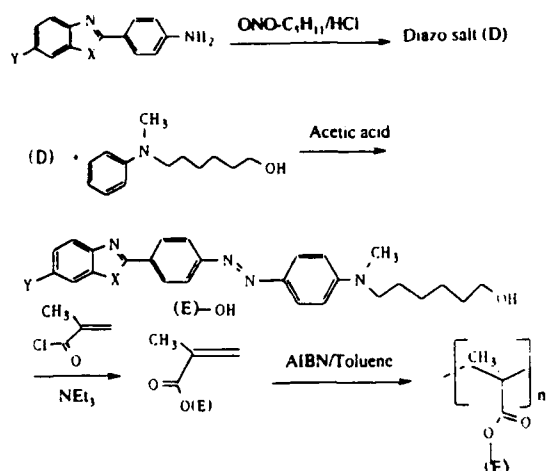


Fig. 12. Synthesis of polymer containing pendant NLO active units.

Investigation of the frequency dependence of  $\chi^{(3)}/\alpha$  establishes an important resonant contribution to observed optical nonlinearity and investigation of the dependence of this ratio upon electroactive unit concentration in composite materials suggests the possible contribution of intermolecular mechanisms. This latter observation needs to be investigated more carefully before unequivocal conclusions can be drawn but clearly preliminary observations argue for the importance of such studies. The procedures considered in this work have all proven successful in terms of producing optical quality thin films with well-defined optical properties (e.g., sharp bandedges, etc.); the advantage of a particular approach in general was determined by solubility considerations. A variety of structures exhibit significant optical nonlinearity and necessary associated properties (e.g., high laser damage threshold, etc.); continued exploration of these structures including quantitative definition of the contributions from various mechanism is appropriate.

### Acknowledgements

This work was supported by the Air Force Office of Scientific Research under contracts F49620-87-C-0100 and F49620-88-C-0071 and by the National Science Foundation under grant DMR-88-15508. We are also indebted to Professor R. W. Hellwarth, Dr. X. F. Cao and J. P. Jiang for DFWM measurements.

### References

1. P. N. Prasad, E. Perrin, and M. Samoc, *J. Chem. Phys.*, 91, 2360 (1989).
2. P. N. Prasad and D. R. Ulrich (eds), *Nonlinear Optical and Electroactive Polymers*, Plenum Press, New York, 1987.
3. J. Messier, et. al. (eds), *Nonlinear Optical Effects in Organic Polymers*, Kluver Academic Publishers, 1989.
4. L. P. Yu and L. R. Dalton, *J. Amer. Chem. Soc.*, 111, 8699 (1989).
5. X. F. Cao, J. P. Jiang, D. P. Bloch, R. W. Hellwarth, L. P. Yu, and L. R. Dalton, *J. Appl. Phys.*, 65, 5012 (1989).
6. L. R. Dalton, R. Vac, and L. P. Yu, in *Handbook of Electroresponsive Polymers*, Marcel Dekkar, New York, 1990.
7. M. Chen, L. P. Yu, and L. R. Dalton, unpublished work.

92-18281



AD-P007 489



345

### MICROPHASE SEPARATION IN TRIBLOCK COPOLYMER MELTS

ANNE M. MAYES AND MONICA OLVERA DE LA CRUZ

Northwestern University, Department of Materials Science and Engineering, Evanston, IL 60208

#### ABSTRACT

Phase diagrams of the microphase morphologies for triblock copolymer melts are calculated for the weak segregation limit. The diagrams are found to be highly asymmetric with block copolymer composition.

#### INTRODUCTION

Block copolymer melts exhibit intriguing microcomposite morphologies with unusual mechanical and rheological properties. Block copolymers are pseudo two-component materials formed by chemically joining chains of incompatible species (A and B), Figure 1. The net repulsion present between segments of A and B drives a local segregation to A-rich and B-rich domains. A macrolattice or microphase evolves with periodicity on the length scale of the radius of gyration of the copolymer chains (typically 10 nanometers). The equilibrium morphology is a strong function of the block copolymer composition; alternating lamellar structures, hexagonally packed cylinders, body-centered cubic spheres and bicontinuous double-diamond nets are observed to be stable.

AB DIBLOCK COPOLYMER



ABA TRIBLOCK COPOLYMER



(AB)<sub>n</sub> STAR COPOLYMER



Fig 1. Several block copolymer architectures.

The disorder-order transition phenomenon in block copolymer melts, called the microphase separation transition, has brought their commercial use as thermoplastic elastomers [1]. At high temperatures the homogeneous melt can be processed like ordinary thermoplastics, while in the temperature range of use, the macrolattice formation provides a kind of thermodynamic cross-linking that dramatically influences the flow characteristics of the material. As one might expect, the properties of the ordered phase depend considerably upon the macrolattice obtained; the lamellar and cylindrical morphologies, for instance, display a high degree of mechanical anisotropy. One commercial example of block copolymers as a multifunctional material is in cable and wire coatings, an application that exploits their rheological, mechanical, and insulating properties. Future applications for block copolymers might take advantage of their microcomposite structure. In electron-beam litho-

graphy, for example, a copolymer with blocks of negative and positive resist could be cast as an alternating lamellar film over the substrate surface. After electron beam exposure one could theoretically obtain linewidths one or two orders of magnitude lower than the present state-of-the-art [2].

Designing materials for such applications requires an understanding of microstructure-property relationships and the equilibrium phase behavior of block copolymer systems. Considerable theoretical and experimental work has been published on the equilibrium phase diagram of the three prominent microphase morphologies, namely bcc spheres, hexagonally packed cylinders (hpc), and alternating lamellar (lam) structures, in diblock copolymer melts [3-5]. The relationship between morphology and mechanical properties in diblock systems has also been examined in detail [6]. In contrast, relatively few studies have focused on other molecular architectures, such as triblock, graft, and star copolymers. This paper discusses the theoretical phase diagrams obtained for triblock copolymers of varying degrees of asymmetry, and points out some particular triblock architectures that may feature microcomposite morphologies with improved mechanical properties.

We study the system near the disorder-order transition, or the weak segregation limit, where the copolymer chains remain nearly Gaussian in configuration such that the domain periodicity scales as the radius of gyration in the homogeneous phase. A Landau mean-field analysis for diblock copolymers in weak segregation predicts a continuous (second order) transition at equal volume fractions of A and B, and a first order transition to bcc spheres at all other compositions [3]. Transitions to other morphologies are predicted (bcc to hpc to lam) with increasing  $x_N$ , where N is the polymerization index and the Flory parameter  $x \sim 1/T$  describes the net interaction between A and B segments. The phase diagram for diblocks (Figure 2) is symmetric about  $f=.5$ , where f is the volume fraction of A segments per copolymer chain. When concentration fluctuations are self-consistently incorporated in the diblock analysis, a first-order transition ensues at  $f=.5$ , and direct transitions from the disordered phase to the cylindrical and lamellar morphologies are found over certain composition ranges for finite molecular weights [4].

The work described here is an extension of the mean-field analysis for diblocks to A-B-A triblock systems of varying degrees of asymmetry [7]. The phase diagram of the microphase morphologies is discovered to change significantly as the triblock architecture is altered. The influence of concentration fluctuations on the phase behavior of triblock melts is also demonstrated.

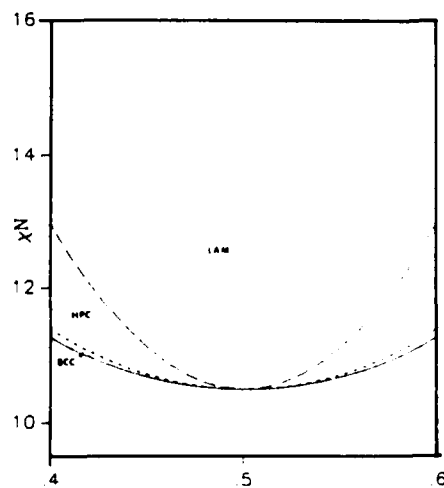


Fig 2. Mean-field diblock phase diagram. [3]

## THEORY

Mean-field approach

We consider a monodisperse incompressible melt of A-B-A triblock copolymer chains. In a Landau analysis of the microphase separation transition the free energy is expanded in a power series of the Fourier components of the order parameter around  $F_0$ , the free energy of the homogeneous disordered state,

$$\begin{aligned} F/kT = F_0/kT + (1/2!) \sum \rho_{Ak} \rho_{A-k} / S(k) + (1/3!V) \sum \Gamma_3(k, k', k'') \\ \times \rho_{Ak} \rho_{Ak'} \rho_{Ak''} \delta(k+k'+k'') + (1/4!V) \sum \Gamma_4(k, k', k'', k''') \\ \times \rho_{Ak} \rho_{Ak'} \rho_{Ak''} \rho_{Ak'''} \delta(k+k'+k''+k''') \end{aligned} \quad (1)$$

The order parameter  $\Delta\rho_A(r)$  is the local deviation in concentration of monomer A from its mean value  $f$ , where  $f=f_1+f_2$ , the sum of the two A-block fractions. A symmetry parameter can subsequently be introduced,  $\tau = f_1/f$ , where  $\tau = 0, 1$  corresponds to a diblock copolymer and  $\tau = .5$  is a symmetric triblock (note that  $\tau = 1-\tau$ ).

The scattering function  $S(k)$  is the Fourier transform of the two-monomer correlation function. In disordered block copolymer melts,  $S(k)$  is peaked around wave vectors of magnitude  $k^*$ , where  $k^* \sim N^{-1/2}$ . The scattering function has the general form

$$S^{-1}(k) = Q(x)/N - 2x \quad (2)$$

where  $x = k^2 N a^2 / 6$  (the parameter  $a$  is the characteristic segment length). The peak intensity grows with increasing  $xN$  and diverges at the spinodal,  $(xN)_s = Q(x^*)/2$ , where the homogeneous melt becomes unstable to fluctuations of wave vector  $k^*$ . At a fixed composition and molecular weight, the spinodal is raised as  $\tau$  increases from 0 to .5; i.e., the symmetric triblock architecture has the most stable disordered state.

To determine the microphase separation transition (MST) and the equilibrium morphologies, the higher order terms in the free energy expansion are required. The  $\Gamma_3(\{k\})$  and  $\Gamma_4(\{k\})$  are functions of the two, three and four-monomer correlation functions, which are specific to the molecular architecture. For any  $\tau$ ,  $\Gamma_3(\{k\})$  is always negative in the limit  $f \rightarrow 0$  and positive as  $f \rightarrow 1$ , and therefore must be zero at some composition  $f=f_c$ , indicating a (mean-field) continuous transition. For triblock polymers  $f_c$  always occurs at compositions  $f > .5$ , and generally does not coincide with the minimum of the spinodal. We have also found continuous transition points in (A-B)<sub>n</sub> star copolymer melts for any arm number  $n$ , and suggest this to be a general feature of the mean-field phase diagrams for all block copolymer architectures [7].

If the MST lies close to the spinodal (a nearly continuous transition), the important wave vector contributions to the free energy functional lie on a sphere of radius  $k^*$ , and the infinite wave vector summations in eq.(1) are replaced by n-vector sums that characterize each morphology;  $n=1, 3$ , and  $6$  for the lam, hpc, and bcc microphases, respectively. The order parameter thus becomes a superposition of compositional fluctuations [3]:

$$\Delta\rho_A(r) = n^{-1/2} \rho_n \sum_{m=1}^n \exp[i(K_m r + \phi_m)] + \text{c.c.} \quad (3)$$

where  $|K_m| = k^*$ . Minimizing the free energy with respect to the phases  $\{\phi_m\}$  always yields a negative third order contribution to the free energy (zero at  $f_c$ ). The set of vectors  $\{K_m\}$  is used to calculate the terms  $(\Gamma_3)_n$  and  $(\Gamma_4)_n$  for each microphase morphology, subject to the translational invariance constraints.

With the above wave vector approximation the Landau free energy for a given morphology reduces to the form

$$(F - F_0)N/kT = 2N(x_s - x)\rho_n^2 + \alpha_n\rho_n^3 + \beta_n\rho_n^4 \quad (4)$$

where  $\alpha_n = N(\Gamma_3)_n/(3!n^{3/2})$  and  $\beta_n = N(\Gamma_4)_n/(4!n^2)$ . For a given  $f$  and  $\tau$ , the free energy is minimized in  $\rho_n$  to determine the value of  $xN$  at which  $F(\bar{\rho}_n) = F_0$  for each morphology. Comparing these values we find the MST for all triblock architectures and compositions  $f \neq f_c$  is a first order transition to bcc spheres. Transitions between morphologies are obtained by equating their respective Landau free energies (4) with  $\rho_n = \bar{\rho}_n$ .

Figures 3 and 4 are mean-field phase diagrams for A-B-A triblock copolymer melts with  $\tau$  values of .25 and .5, respectively. Notable differences are observed in the windows of stability for each morphology with different  $\tau$  values. For example, a second order transition to a lamellar morphology is predicted at  $f=.5$  in diblocks (Figure 2), while the same composition shows large zones of bcc and hpc stability for  $\tau = .25$ . The phase diagrams for triblock systems are also found to be highly asymmetric, in contrast to diblocks. At  $xN = 19$ , for instance, Figure 4 predicts that a symmetric triblock melt ( $\tau = .5$ ) will be homogeneous at  $f = .4$ , whereas at  $f = .6$  one finds close-packed cylinders of B in a matrix of A.

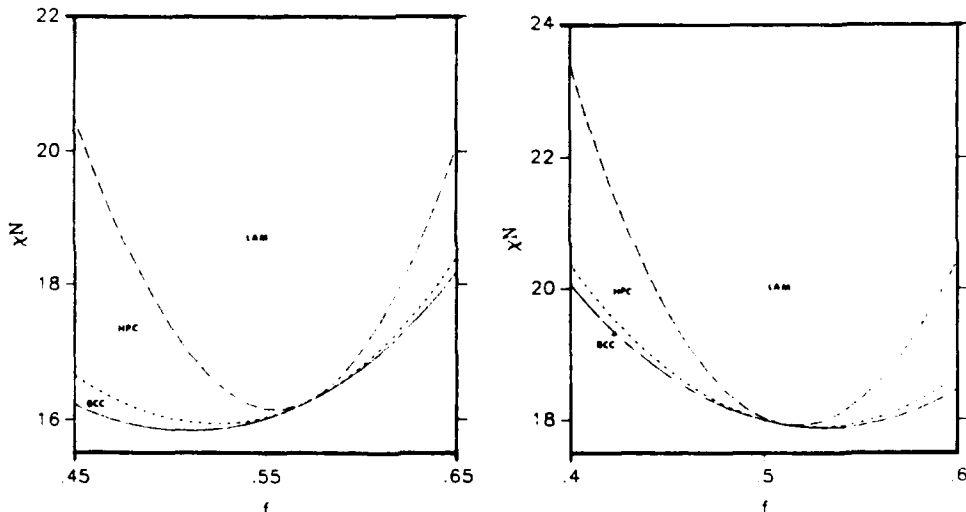


Fig 3. Mean-field triblock phase diagram,  $\tau = .25$ .

Fig 4. Mean-field triblock phase diagram,  $\tau = .5$ .

### Hartree approximation

In disordered block copolymer melts near  $f_c$ , important free energy contributions arise from concentration fluctuations within a shell of wavevectors  $|k| \sim k^*$ . The effects of fluctuations on the MST can be self-consistently taken into account using the Hartree approximation scheme outlined by Fredrickson and Helfand for the case of diblock copolymers [4]. One arrives at an expression for the thermodynamic potential,

$$\begin{aligned}\Phi = & n(r^2 - r_o^2)/2\sum\lambda(h_m) + \alpha_o n\lambda(0)[r^{1/2} - r_o^{1/2}]/\sum\lambda(h_m) + \\ & + 2na^3/3 + n\beta' a_n^4/2\end{aligned}\quad (5)$$

where  $\alpha_o = k^{*2}N^{1/2}/4\pi$ ,  $\alpha'$  and  $\beta'$  are related to  $\alpha_n$  and  $\beta_n$  in eq.(4), and  $r$  and  $r_o$ , the renormalized inverse susceptibility in the ordered and disordered phases, are defined as

$$r = t - \alpha_o\lambda(0)/4 \int_4^0 r(h)^{-1/2} dh + \sum\lambda(h_m)a_n^2 \quad (6)$$

$$\text{with } r(h) = t - \alpha_o\lambda(0)/4 \int_4^0 r(h)^{-1/2} dh + m\lambda(h)a_n^2$$

$$r_o = t + \alpha_o\lambda(0) r_o^{-1/2} \quad (7)$$

where  $t \sim (xN)_s - \gamma N$ . The mean amplitude  $a_n$  for a given morphology is obtained from

$$\beta' a_n^2 + \alpha' a_n + r = 0 \quad (8)$$

For a given  $r$ ,  $f$  and  $N$  one calculates the potential at  $xN$  for each morphology by solving for  $r_o$ ,  $r$  and  $a_n$ . The integral expressions in  $r$  and  $r(h)$  arise as a consequence of retaining the wave vector dependence of the  $\Gamma_4(\{k\})$  in eq.(1). The integral must be calculated numerically since  $\lambda(h)$ , the renormalized quartic term, is a complicated function of  $h$ . As the dependence of  $r$  on  $h$  is small, to simplify the numerical solution of  $r$  and  $a_n$ , we used the approximation  $r(h) = r$ . The MST is defined at  $\Phi = 0$  (the morphology with the lowest calculated value of  $(xN)_s$  is the equilibrium morphology); transitions between morphologies are determined by equating their respective potentials.

Hartree phase diagrams for A-B-A triblock melts with  $r = .25$  and  $.5$  and  $N=10^6$  are given in Figures 5 and 6. As in diblocks, the Hartree approximation for triblocks predicts a first order transition at  $f=f_c$  with corrections to  $(xN)_s$  scaling as  $N^{-1/3}$ . Composition ranges with direct transitions to the hpc and lam structures also appear. The asymmetry of the triblock phase diagrams is preserved. For  $r = .25$ , large windows of bcc and hpc stability are still present for  $f \leq .5$ . This suggests a microphase morphology with large spheres of A in a B matrix. Experimentally it was found that enlarging the spherical polyisoprene domains in poly(styrene-isoprene) diblocks improves the toughness and ductility of the material [6]. Careful experiments on asymmetric

A-B-A triblocks, particularly for  $\tau = .1-.25$  and  $f < .5$ , where a bcc macrolattice with large A domains is predicted, may unveil structures with enhanced mechanical properties.

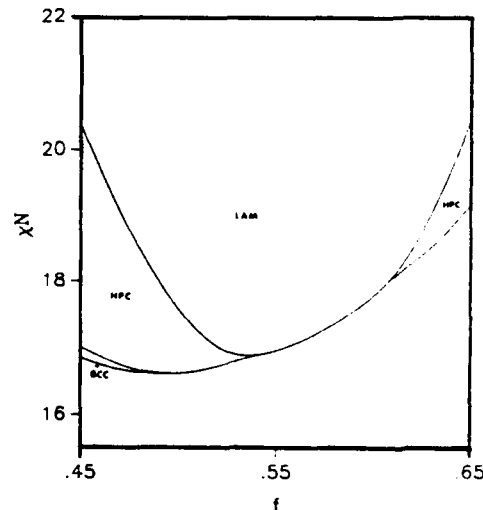


Fig. 5. Hartree triblock phase diagram,  $\tau = .25$ .

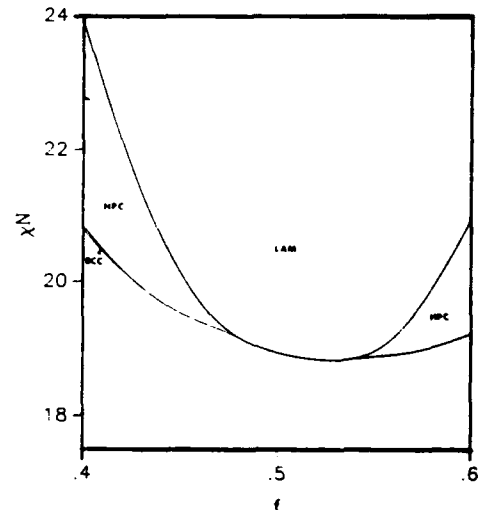


Fig. 6. Hartree triblock phase diagram,  $\tau = .5$ .

#### REFERENCES

1. Thermoplastic elastomers: a comprehensive review, edited by N. R. Legge, G. Holden, and H. E. Schroeder (Hanser, New York, 1987).
2. VLSI technology, edited by S. M. Sze (McGraw-Hill, New York, 1983).
3. L. Leibler, *Macromolecules* 13, 1602 (1980).
4. G. H. Fredrickson and E. Helfand, *J. Chem. Phys.* 87, 697 (1987).
5. E. L. Thomas, D. M. Anderson, C. S. Henkee, and D. Hoffman, *Nature* 334, 598 (1988).
6. H. Kawai, T. Hashimoto, K. Miyoshi, H. Uno, and M. Fujimura, *J. Macro. Sci. Phys.* B17, 427 (1980).
7. A. M. Mayes and M. Olvera de la Cruz, *J. Chem. Phys.*, in press.

92-18282



AD-P007 490



351

SYNTHESIS OF SEGMENTED ANISOTROPIC-ISOTROPIC  
POLY(ARYL ESTER)POLY(ARYLENE ETHER) COPOLYMERS

J. E. McGrath,\* K. L. COOPER, W. WAEHAMAD, H. HUANG, and G. L. WILKES  
Departments of Chemistry, Chemical Engineering and the NSF Science and  
Technology Center: High Performance Polymeric Adhesives and Composites  
Virginia Polytechnic Institute and State University, Blacksburg, Virginia  
24061

\*To whom correspondence should be addressed

ABSTRACT

Carboxyl functional poly(arylene ether) oligomers of controlled number average molecular weight were synthesized via nucleophilic aromatic substitution step polymerization using p-hydroxy benzoic acid as the molecular weight and end group controlling reagents. The subsequent functionalized polyarylene ethers were copolymerized with acetoxy benzoic acid or acetoxyphenoxy benzoic acid via melt acidolysis procedures. Successful copolymers were generated using chlorobenzene as a solvent for the first stage of the reaction followed by melt reaction at temperatures as high as 325°C. Resulting copolymer composition and segment size were investigated. It was possible to prepare improved solvent resistant copolymers through incorporation of the liquid crystal polyester (LCP) segment. Extraction tests using boiling chloroform showed that a high percentage of segmented copolymer were generated. Swelling characteristics were also noted and were observed to decrease as a function of the LCP concentration utilized. Multiple transitions were observed in differential scanning calorimetry consistent with Tg's, Tm's and possibly with liquid crystal transitions. Optical microscopy showed an ordered microstructure developed which is consistent with the presence of liquid crystalline phases. The materials were successfully compression molded to afford tough coherent films at all compositions, implying the likelihood of improved compressive strength relative to the LCP homo- or copolymers.

INTRODUCTION

Lyotropic and thermotropic high strength liquid crystalline polymer systems have become an important area of research and development in polymeric materials. In general, these materials have afforded excellent high temperature stability and high strength in the oriented direction, but not in the transverse direction. Thus, "balancing" the solid state structure in the longitudinal and transverse directions to improve mechanical properties such as compressive strength is an important research frontier.

The basic premise which has guided this research has been to synthesize isotropic-anisotropic segmented copolymers where the isotropic phase is based upon a thermoxidatively stable ductile poly(arylene ether), while the anisotropic segment is based upon a rigid LCP polyester moiety [1-4]. Poly(oxyphenoxybenzoate)-Poly(oxybenzoate) copolymers were chosen as the polyester moiety due to the observation that homo- or statistical copolymers incorporating these structures show both crystallinity and liquid crystallinity [5-8]. The poly(arylene ether)s were synthesized such that they had functional carboxyl group termination [9]. The ester forming monomers were subsequently reacted with the functional endgroups of the poly(arylene ether) via a melt acidolysis procedure to form the segmented copolymers. Characterization of these polymers has included differential scanning calorimetry, thermal mechanical analysis, thermal gravimetric

analysis, FT-IR, hot stage optical microscopy and wide-angle x-ray scattering. Solution behavior (eg. intrinsic viscosity) could only be studied on compositions which were low (eg.  $\leq$  10 weight percent) LCP.

#### EXPERIMENTAL

Materials: 4,4'-dichlorodiphenyl sulfone (DCDPS), 4,4'-difluorobenzophenone (DFBP), hydroquinone, biphenol, and bisphenol A were obtained from commercial sources and purified according to earlier published procedures [10]. N-methyl-pyrrolidone (NMP), dimethyl sulfoxide (DMSO) and chlorobenzene were dried over calcium hydride and vacuum distilled before use. Acetic anhydride was dried over magnesium and distilled before use. p-Hydroxybenzoic acid and p-acetoxybenzoic acid were generously donated by the Amoco Chemical Corporation and were used without further purification.

##### Preparation of Carboxyl Terminated Poly(arylene ether)s:

The carboxyl terminated aromatic poly(arylene ether) oligomers of controlled molecular weight were prepared using a one pot aromatic nucleophilic substitution procedure. To a nitrogen purged 3-neck round bottom flask, fitted with an overhead stirrer, condenser, Dean Stark trap, gas inlet and thermometer, the activated halide (DCDPS, DFBP), bisphenols (biphenol, hydroquinone, or bisphenol A), endcapping reagent (p-hydroxybenzoic acid) and base (potassium carbonate) were added. DMSO or a combination of DMSO and DMAC (2/1) was added to afford a 15% (w/v) solids content. Toluene, used as an azeotropic agent, was then added to the flask at half the volume of DMSO or DMSO/DMAC. The mixture was carefully stirred, and heated to the reflux temperature (135°C-140°C) of DMSO/toluene or DMSO/DMAC/toluene. After 4 to 8 hours the temperature was raised to 160°C to 165°C, for an additional 14 hours, by removing toluene and the water formed during the reaction. The contents of the flask were cooled to 100°C and filtered through a coarse glass frit to remove insoluble salts and excess potassium carbonate. The potassium carboxylate end groups of the oligomer were then acidified by neutralizing with aqueous HCl to a slightly acidic pH. The carboxyl terminated poly(arylene ether) oligomer was precipitated into a five fold excess of methanol in a stirred Waring blender, collected by suction filtration, washed with water and methanol and dried in vacuum oven for 24 hours at 130°C. The oligomer was then redissolved in chloroform and reprecipitated into methanol, filtered and dried in a vacuum oven for an additional 24 hours at 130°C.

##### Preparation of Phenyl Terminated Poly(arylene ether) oligomers:

Non-reactive phenyl terminated poly(arylene ether) oligomers were prepared in a manner similar to the carboxyl terminated oligomers described above except a monofunctional activated halide (4-Fluorobenzophenone or 4-chlorodiphenyl sulfone) was used as the endcapping reagent.

##### Preparation of Poly(arylene ether) - Poly(oxyphenoxybenzoate) - Poly(oxybenzoate) Segmented Copolymers:

The aromatic poly(arylene ether)-poly(oxyphenoxybenzoate)-poly(oxybenzoate) segmented copolymers were prepared using a one pot melt acidolysis procedure. The preformed carboxyl terminated polysulfone was

charged into a 1000 ml wide mouth cylindrical resin kettle. A stoichiometric amount of 2,6 naphthalene diacetate was added to the vessel to offset the number of moles of polysulfone. The p-acetoxybenzoic acid and 4,4'-acetoxyphenoxybenzoic acid (in a 50/50 molar ratio) monomers were then added at various weight percentages. Chlorobenzene, 50% (w/v), was then added to the vessel to enhance mixing of the poly(arylene ether) oligomer and monomers. The top portion of the reactor was fitted with a high torque mechanical stirrer and anchor agitator, teflon seal, N<sub>2</sub> inlet and attached to the bottom of the reactor. The agitated mixture was carefully purged with nitrogen and heated to the reflux temperature (132°C) of chlorobenzene. After 4 to 6 hours at 200-220°C, the temperature was raised to between 300°C and 325°C and the chlorobenzene was completely distilled off, leaving an apparently homogeneous melt. Acetic acid rapidly began to evolve from the mixture and the viscosity was observed to increase. After several hours, the rate of acetic acid evolution diminished, and a vacuum was carefully applied to the system over a period of about a 1/2 hour until pressures approaching 50 mill. Torr were obtained. The molten polymer then rapidly increased in viscosity to the point where it was barely stirrable by the high torque anchor stirrer. Generally, the reaction was stopped after about 2 hours under vacuum and slowly cooled to room temperature under a nitrogen bleed. The polymer was removed from the resin kettle, ground and vacuum dried at 140°C for 24 hours.

The control non-reactive phenyl terminated poly(arylene ether) oligomers were also "reacted" with the ester forming monomers in a similar manner.

#### Preparation of Chain Extended Poly(arylene ether)s:

The chain extended poly(arylene ether) polymers were prepared in a similar manner except that only stoichiometric amounts of the carboxyl terminated poly(arylene ether) oligomer and a diacetate (bisphenol A diacetate) monomer were used.

#### CHARACTERIZATION

The number average molecular weights ( $\langle M_n \rangle$ ) of the starting carboxyl terminated poly(arylene ether) oligomers were determined using a potentiometric titration of the endgroups by a method developed in our laboratory [11]. FT-IR spectra of the poly(arylene ether) oligomers and copolymers were determined using a Nicolet MX-1 spectrophotometer. Differential scanning calorimetry (DSC) was used to elucidate the thermal properties of the polysulfone or polyether ketone oligomers and copolymers. These scans were run at 10°C/min. using a DuPont Model 2100. Wide-angle x-ray scattering (WAXS) was performed on the poly(arylene ether) oligomers and copolymers using a table top Philips generator equipped with a Worchus camera. Optical micrographs of the polysulfone or polyether ketone oligomers and copolymers were taken using a polarizing microscope equipped with a Mettler hot stage. Thermal gravimetric analysis was performed on a DuPont Model 2100. Isothermal scans were run at 350°C and 400°C for 1 to 2 hours under an oxidative atmosphere (20 cc/min.).

#### RESULTS AND DISCUSSION

Characteristics of representative poly(arylene ether) oligomers prepared are shown in Table I.

TABLE I. CHARACTERIZATION OF CARBOXYL FUNCTIONALLY TERMINATED POLY(ARYLENE ETHER) OLIGOMERS

HQ/BP CARBOXYL TERM	THEORETICAL	SMALL GM/MOL		DSC <sup>(2)</sup>	
		ILLUMINATED	[n] <sup>(1)</sup>	Tg (°C)	
HQ/BP 50/50	2000	2400	0.15	146	
HQ/BP 50/50	5000	5800	0.23	176	
HQ/BP 50/50	9000	9900	0.31	189	
HQ/BP 50/50	14000	14100	0.36	195	
HQ/BP 50/50	15000	15800	0.41	203	
HQ/BP 50/50	16000	17500	0.47	210	

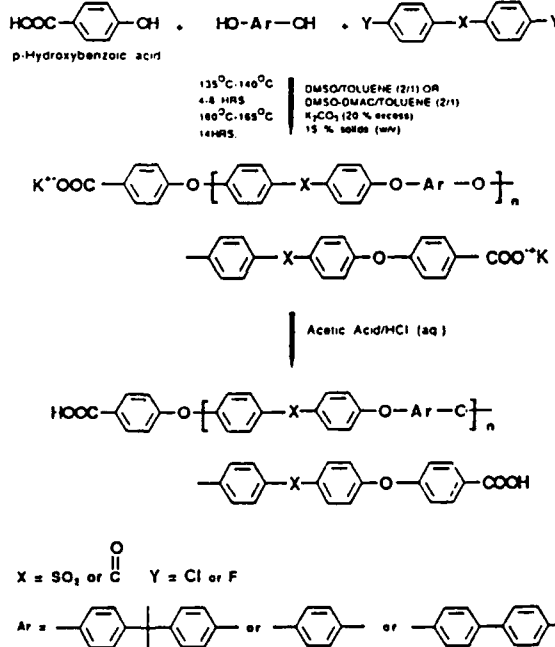
PEK CARBOXYL TERM	
BISPHENOLA	3000
BISPHENOLA	5000
BISPHENOLA	8000
BISPHENOLA	10000

(1) 1-METHYL-2-PYRROLIDONE, 25°C

(2) 10°C/MIN, N<sub>2</sub>, 2nd heating scan

HQ/BP = Hydroquinone/Biphenol 50/50 molar ratio

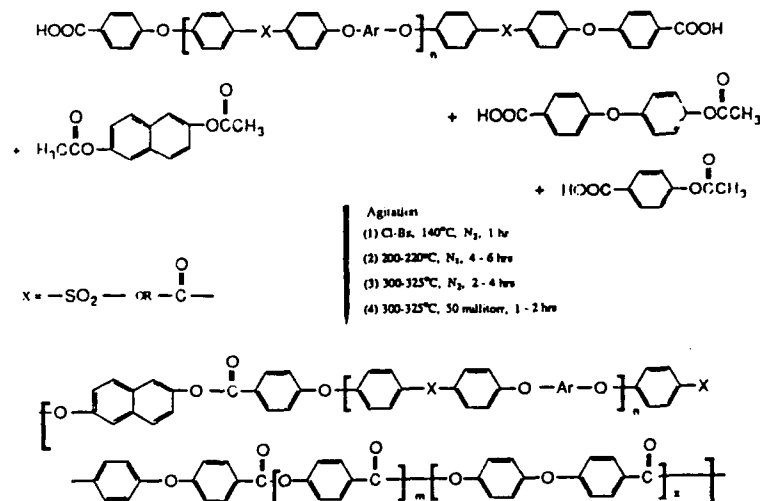
The one-pot synthetic route to the poly(arylene ether)s is shown in Scheme 1.



Scheme 1. Synthesis of Poly(arylene Ether) Carboxyl Functionally Terminated Oligomers

In general, intrinsic viscosities measured in N-methylpyrrolidone and glass transition temperatures measured by DSC, are in the expected range based on considerable research in these laboratories utilizing analogous systems [9,10,12].

Preliminary studies of the poly(arylene ether)-poly(arylate) segmented copolymers have been reported earlier [1]. Those copolymers were synthesized without the use of a solvent. The work reported here deals with segmented copolymers based on poly(oxyphenoxybenzoate)-poly(oxybenzoate) and poly(arylene ether) using a solvent such as chlorobenzene which enhances the mixing of the poly(arylene ether) oligomer and ester forming monomers. The one-pot synthetic route to the poly(arylene ether)-poly(oxyphenoxybenzoate)-poly(oxybenzoate) segmented copolymers is shown in Scheme 2.



SCHEME 2. SYNTHESIS OF POLY(ARYLENE ETHER)-POLY(OXYBENZOATE)-POLY(OXYPHENOXYBENZOATE) SEGMENTED COPOLYMERS VIA MELT ACIDOLYSIS

It was found through FT-IR studies, that if a high degree of agitation and mixing was not employed during the initial stages of the melt acidolysis reaction, p-acetoxybenzoic acid would react with itself forming a homopolymer of poly(oxybenzoate) and the poly(arylene ether) oligomer would be chain extended by a few repeat units of oxybenzoate to produce a chloroform soluble fraction [1]. However, when a solvent such as chlorobenzene which dissolves both the polysulfone oligomer and ester forming monomers, was utilized true segmented copolymers of poly(arylene ether)-poly(oxyphenoxybenzoate)-poly(oxybenzoate) were formed. This was proven by extracting representative samples in a soxhlet with chloroform for 72 hours and drying to a constant weight. In most cases, very little

of the original poly(arylene ether) oligomer was observed to be extracted by refluxing chloroform as shown in Table II. Moreover, the extract itself is often a copolymer, rich enough in isotropic content to permit solubility in hot chloroform.

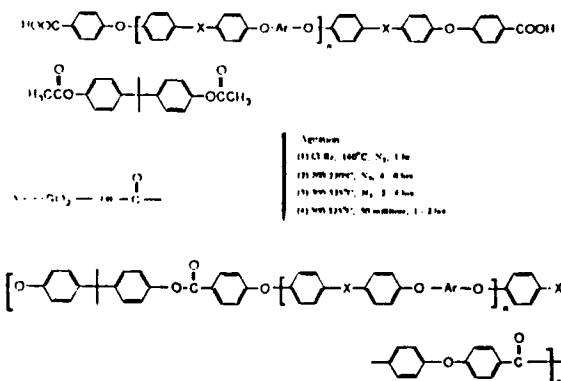
TABLE II. EXTRACTIONS OF A SERIES OF POLY(ARYLENE ETHER SULFONE)-POLY(OXYBENZOATE)-POLY(OXYPHENOXYBENZOATE) SEGMENTED COPOLYMERS

PSF CARBOXYL TERM	$\bar{M}_n$	WT% PSF	% EXTRACTED <sup>(1)</sup>
Hq/Bp	50/50	17500	90
Hq/Bp	50/50	17500	75
Hq/Bp	50/50	17500	50
Hq/Bp	50/50	17500	25
Hq/Bp	50/50	17500	10
Hq/Bp	50/50	15100	25
Hq/Bp	50/50	9900	50
Hq/Bp	50/50	5800	50

(1) Soxhlet Extraction with  $\text{CHCl}_3$  for 72 hr; Constant weight after 1 day

This contrasts with our earlier results [1] and also those reported recently by Auman and Percec et al. on similar materials [13]. The extraction data demonstrates the importance of good mixing (e.g. mutual solvent and/or good agitation in the early stages of the reaction).

Another important criteria for complete reaction between the polysulfone or polyether ketone oligomers and ester forming monomers is to have difunctionally terminated poly(arylene ether) oligomers. This was proven by reacting the carboxyl terminated polysulfone or polyether ketone oligomers with a diacetate monomer under melt acidolysis reaction conditions to form chain extended poly(arylene ether) polymers [Scheme 3].



SCHEME 3. SYNTHESIS OF POLY(ARYLENE ETHER) CHAIN CHAIN EXTENDED POLYMERS VIA MELT ACIDOLYSIS

The large increase in molecular weight, as determined by intrinsic viscosity values, indicates that the polysulfone or polyether ketone

oligomers are highly difunctional (Table III). This demonstrates that the poly(arylene ether) oligomers must be functionally terminated to form true segmented copolymers.

TABLE III. CHARACTERIZATION OF CARBOXYL FUNCTIONALLY TERMINATED POLY(ARYLENE ETHER) CHAIN EXTENDED POLYMERS VIA MELT ACIDOLYSIS

<u>PSF CARBOXYL TERM</u>	<u>THEORETICAL</u>	<u>&lt;Mn&gt; gm/mol</u>	<u>DSC(2)</u>		
			<u>TITRATED</u>	<u>[n]<sup>(1)</sup></u>	<u>Tg(°C)</u>
Hq/Bp 50/50	5000	5800	0.23	176	
BISPHENOL A EXTENDED*	----	----	0.87	205	
<u>PEK CARBOXYL TERM</u>					
BISPHENOL A	5000	5700	0.23	140	
BISPHENOL A EXTENDED*	----	----	0.74	153	

(1) 1-METHYL-2-PYRROLIDONE, 25°C

(2) 10°C/MIN, N<sub>2</sub>, 2nd heating scan

Hq/Bp = Hydroquinone/Biphenol 50/50 molar ratio

\* Bisphenol A diacetate chain extended polymers

The necessity for difunctionality of the poly(arylene ether) was also proven by control experiments with non-reactive phenyl terminated polysulfone or polyether ketone oligomers with ester forming monomers in a melt acidolysis reaction. Extraction of representative samples in a soxhlet with chloroform for 72 hours and drying to a constant weight shows the loss of almost all the polysulfone oligomer originally charged (Table IV).

TABLE IV. EXTRACTIONS OF FUNCTIONALIZED AND NON-REACTIVE POLY(ARYLENE ETHER)-POLY(OXYBENZOATE)-POLY(OXYPHENOXYBENZOATE) SEGMENTED COPOLYMERS

<u>POLY(ETHER SULFONE)</u>	<u>&lt;Mn&gt;</u>	<u>WT% PSF</u>	<u>% EXTRACTED<sup>(1)</sup></u>
Hq/Bp 50/50*	10200	10	8
Hq/Bp 50/50**	10200	10	1
<u>POLY(ETHER KETONE)</u>			
Hq/Bp 50/50*	12200	10	8
Hq/Bp 50/50**	12000	10	1

\* UNFUNCTIONALLY TERMINATED - PHENYL END GROUPS

\*\* FUNCTIONALLY TERMINATED - CARBOXYL END GROUPS

(1) Soxhlet Extraction with CHCl<sub>3</sub> for 72 hrs; Constant weight after 1 day

DSC scans of the copolymers indicated one or two glass transition temperatures, depending on the weight percent of poly(arylene ether) to polyarylate and one endotherm (Table V, Figure 1).

TABLE V. TRANSITION TEMPERATURES OF A SERIES OF  
POLY(ARYLENE ETHER)-POLY(OXYBENZOATE)-  
POLY(OXYPHENOXYBENZOATE) SEGMENTED COPOLYMERS

<u>PSF CARBOXYL TERM</u>	<u>Mn</u>	<u>WT% PAE**/LCP</u>	DSC(°C)(1)		
			$T_{g1}$	$T_{g2}$	$T_m$
Hq/Bp 50/50	17500	90/10	—	203	—
Hq/Bp 50/50	17500	75/25	122	205	312
Hq/Bp 50/50	17500	50/50	123	201	318
Hq/Bp 50/50	17500	25/75	122	202	315
Hq/Bp 50/50	17500	10/90	123	—	313
<u>PEK CARBOXYL TERM</u>					
BISPHENOL A	12200	70/30	—	153	305
BISPHENOL A	12200	60/40	—	152	304
BISPHENOL A	12200	50/50	120	153	306
BISPHENOL A	12200	40/60	120	152	308
BISPHENOL A	12200	30/70	120	153	305
BISPHENOL A	12200	20/80	124	155	308
BISPHENOL A	12200	10/90	119	—	311
LCP(50/50)*	....	....	120	—	309

\* POLY(OXYBENZOATE)-POLY(OXYPHENOXYBENZOATE) 50-50 MOLE%

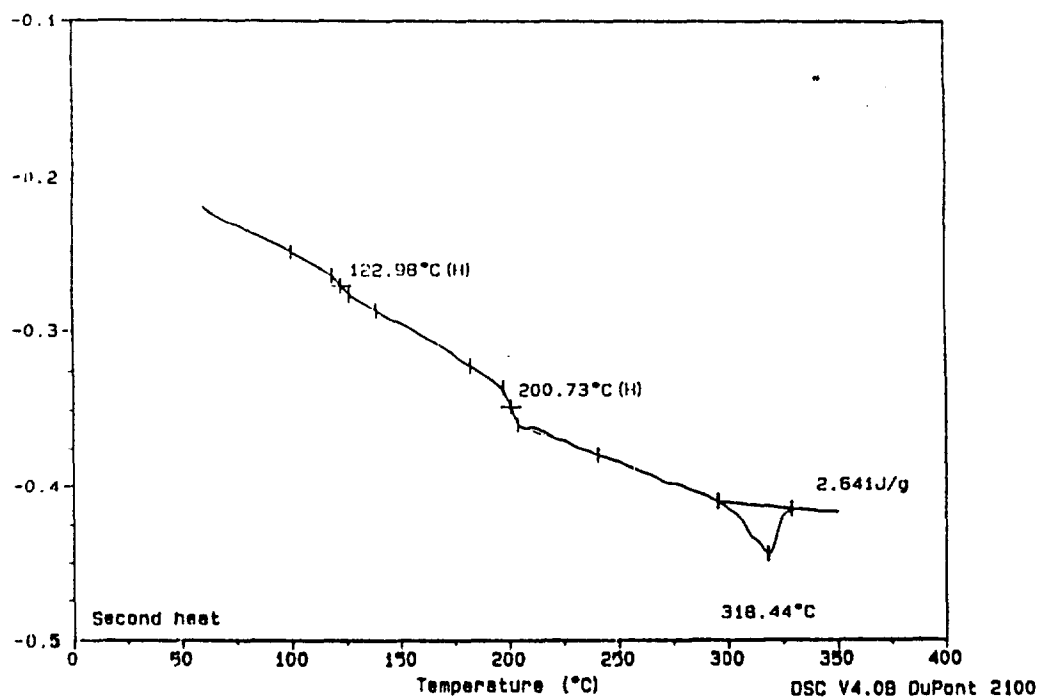
\*\* PAE - POLY(ARYLENE ETHER)

(1) 2nd or 3rd heating scan, 10°C/min, N<sub>2</sub>

Figure 1.

Sample: 17.5K PSF-LCP (50/50) 50/50wt% **DSC**  
 Size: 13.3900 mg  
 Method: 50-350 @ 10C/min, 2 heats  
 Comment: 50-350 @ 10C/min, 2 heats; slow cool @ 2.5C/minute after each H

File: A:COOPERK.53  
 Operator: Paul S. Vail  
 Run Date: 4-Aug-89 15:32



The polyarylate glass transition temperature appears at or near 120°C, whereas, the glass transition temperature for the poly(arylene ether) appears at 150°C for the polyether ketones or 200°C for the polyether sulfones. Wide-angle xray scattering (WAXS) patterns also show that the copolymers are semicrystalline. A sample when viewed between cross polarizers at a temperature below that of the melting endotherm shows a texture similar to that of semicrystalline polymers [5-8]. However, when viewed between cross polarizers above the temperature of the melting endotherm it shows a texture similar to that expected for liquid crystal polymers [5-8]. Thus, it would appear there is probably a liquid crystalline phase, which exists above the melting endotherm.

Although exact molecular weight determinations for the copolymers are not readily accessible, due to their insolubility in any solvent but strong acids, reasonably high molecular weights are indicated by the ability to compression mold the copolymers into coherent films with improved solvent resistance (Table VI). Note that the swelling ratio correlates well with the weight or volume fraction of L.C.P.

TABLE VI. SWELLING EXPERIMENTS PERFORMED ON A SERIES OF POLY(ARYLENE ETHER SULFONE)-POLY(OXYBENZOATE)-POLY(OXYPHENOXYBENZOATE) SEGMENTED COPOLYMERS

CARBOXYL TERM PSF	$\langle M_n \rangle$ PSF	WT% PSF/LCP*	% SWELLING <sup>(1)</sup>
Hq/Bp 50/50	17500	90/10	750
Hq/Bp 50/50	17500	75/25	600
Hq/Bp 50/50	17500	50/50	200
Hq/Bp 50/50	17500	25/75	40
Hq/Bp 50/50	17500	10/90	2
Hq/Bp 50/50	15100	25/75	40
Hq/Bp 50/50	9900	50/50	200
Hq/Bp 50/50	5800	50/50	250
LCP 50/50*	----	----	2

\* POLY(OXYBENZOATE)-POLY(OXYPHENOXYBENZOATE) 50-50 MOLE%

(1) % SWELLING = (SWELLING WT. - ORIGINAL WT. / ORIGINAL WT.) X 100  
SWELLING AFTER 5 DAYS IN  $\text{CHCl}_3$

#### CONCLUSIONS AND FUTURE WORK

These results indicate that poly(arylene ether)-poly(oxyphenoxybenzoate)-poly(oxybenzoate) segmented copolymers can be successfully synthesized as described, using the one pot synthetic procedure which employs chlorobenzene solvent in the initial stages of the melt acidolysis reaction.

It has been possible to prepare well-defined carboxyl functionally terminated poly(arylene ether)s of controlled molecular weights. These endgroups enable the isotropic polysulfone or polyether ketone segment to be incorporated nearly quantitatively into an aromatic, potentially liquid crystalline polyester segmented copolymer via melt acidolysis. The resulting copolymers have improved solvent resistance, which is a function of composition and appear semicrystalline or liquid crystalline above 10 weight percent of the poly(oxyphenoxybenzoate)-poly(oxybenzoate) L.C.P. polyester segment. Future studies will focus on the synthesis of poly(arylene ether)-polarylate segmented copolymers of controlled molecular weight that contain aryl ether arylates to lower the melting transitions for improved melt processability. In addition, the further utilization of optical microscopy, WAXS, and more detailed thermal analysis will be pursued to better determine the nature of the presumed liquid crystal structure. Mechanical properties (e.g. compressive and tensile behavior) will also be assessed.

#### REFERENCES

1. J. M. Lambert, B. E. McGrath, G. L. Wilkes and J. E. McGrath, PMSE Preprints, Vol. 54, p. 1 (1986); J. M. Lambert, Ph.D. Thesis VPI & SU (1986).

2. K. L. Cooper, D. H. Chen, H. Huang, G. L. Wilkes, J. E. McGrath, PMSE Preprints, Vol. 60, p. 322 (1989).
3. K. L. Cooper, W. Waehamad, H. Huang, D. H. Chen, G. L. Wilkes, J. E. McGrath, Polymer Preprints, Vol. 30(2), p. 464 (1989).
4. W. Waehamad, K. L. Cooper, J. E. McGrath, Polymer Preprints, Vol. 30(2) p. 441 (1989).
5. P. W. Morgan, Macromolecules, 10(6), p. 1381, (1977).
6. J. H. Wendorff, H. Finkelmann and H. Ringsdorf, J. Polm. Sci.: Polym. Symp. 63, 245, (1978).
7. R. W. Lenz and J. K. Jin, "Liquid Crystals and Ordered Fluids" #4, p. 347, 1984).
8. W. J. Jackson, Jr., British Polymer Journal, Vol. 12, p. 154 (1980).
9. D. K. Mohanty, J. L. Hedrick, K. Gobetz, B. C. Johnson, I. Yilgor, E. Yilgor, R. Yang and J. E. McGrath, Polymer Preprints, Vol. 23,(1), p. 284, (1982).
10. J. M. Lambert, E. Yilgor, I. Yilgor, G. L. Wilkes and J. E. McGrath, Polymer Preprints, Vol. 26(2), p. 275, (1985).
11. A. J. Wnuk, T. F. Davidson and J. E. McGrath, J. Appl. Poly. Sci.: Appl. Polym. Symp. 34, p. 89, (1978).
12. J. M. Lambert, D. C. Webster, and J. E. McGrath, Polymer Preprints, Vol. 25, (2), p. 14, 1984; ibid, p. 93-112, in Advances in Polymer Synthesis, B. M. Culbertson and J. E. McGrath, Edit., Plenum (1985).
13. B. C. Auman and V. Percec, Polymer (London), 29(5), 938 (1988).

92-18283

AD-P007 491



63

INORGANIC AND ORGANOMETALLIC PRINCIPLES  
IN THE DESIGN OF MULTIFUNCTIONAL MATERIALS

D. MICHAEL P. MINGOS

Inorganic Chemistry Laboratory, University of Oxford, South Parks Road, Oxford OX1 3QR, U.K.

ABSTRACT

The prospects of using the properties of inorganic solids with infinite structures in combination with the spectral, magnetic and chemical characteristics of co-ordination and organometallic compounds are reviewed with particular reference to their potential applications in the electronics, sensors and optoelectronic fields.

Solid state inorganic chemistry provides a great variety of thermally stable and optically transparent host materials which have sufficiently large cavities for the incorporation of small molecules. These include zeolites with either spherical or cylindrical three dimensional cavities, layered compounds with infinite two-dimensional spaces and a variable third dimension, and pillared materials with intersecting one-dimensional channels. These structures may be chosen on the basis of a particular function and a second introduced via the incorporation of molecules in the cavities. Alternatively, they may be viewed as neutral structural materials and the multifunctionality can be introduced via the incorporation of molecules with different spectral or chemical properties.

As guest materials co-ordination and organometallic compounds have the following properties which are important in the context of multifunctionality: the ability to co-ordinate small molecules such as  $O_2$ ,  $SO_2$ ,  $H_2$  reversibly, distinct reversible electrochemical properties, electronic transitions which show an enormous variation in extinction coefficients and oscillator strengths, polarised spectral transition and electrical conductivity properties.

INTRODUCTION

In their own right inorganic elements and compounds have a range of physical, optical, electronic and magnetic properties which form the backbone of the modern materials industry. The range of elements and their associated oxides, fluorides, sulphides, carbides and nitrides provide a tremendous range of possibilities and perhaps the following can be identified as characteristic inorganic properties which have formed the basis of technological devices [1].

Thermal and chemical stability which originate from the strengths of the chemical bonds in both ionic and covalent inorganic solids with infinite structures. Refractory materials are generally brittle, have little tensile strength but exhibit plastic deformations at high temperatures. Their microstructures have an important influence on their strengths. Examples of such materials which are used on a large scale

include silica, chrome-magnesia basic, fired fireclay and high alumina.  $\text{SiC}$  and  $\text{Si}_3\text{N}_4$  have more specialised applications.

Mechanical properties - the range of available metals, alloys, ceramics and polymers in inorganic chemistry permits a high degree of control over such properties as ductility, malleability, brittleness, hardness, resistance to thermal shock and plasticity.

Conductivity properties associated with metals and inorganic compounds remain an important area of development although many of the important scientific principles are well understood. The area of high temperature superconductors represents an important new area where conflicting theoretical interpretations still abound.

Optical properties. The optical transparency of oxides and fluorides is important to many industrial optical applications. Furthermore the addition of activator and sensitizer ions to oxide and sulphide hosts lead to a range of photo-, electro- and cathode-luminescent materials which have been exploited technologically. Of primary importance are the Stokes phosphors based on  $\text{Ca}_5(\text{PO}_4)_3\text{F}$  hosts doped with  $\text{Sb}^{3+}$  and  $\text{Mn}^{2+}$ , and  $\text{YVO}_4$  doped with  $\text{Eu}^{3+}$ . Anti-Stokes phosphors based on  $\text{YF}_3$ ,  $\text{NaLa}(\text{WO}_4)_2$  and  $\text{NaYF}_4$  hosts have been widely developed by the defence industries. Inorganic chemistry also provides important examples of photoconductors, e.g.  $\text{Se}$  used in photocopying processes, and photochromic glasses based on the doping into glasses of small crystals of  $\text{AgCl}$  which are photoreduced to clusters when exposed to bright lights.

Magnetic properties. The detailed understanding of the physics of ferromagnetism, antiferromagnetism and ferrimagnetism has led to the possibility of "crystal engineering" of magnetic materials with the designed characteristics. An impressive range of applications has resulted including:  $\text{MnZn}$  ferrites and  $\text{YIG}$  garnets for transformer cores, because they are magnetically soft and have a large power handling capacity; magnetic bubble and information storage devices which are based either on garnets epitaxially laid down on non-magnetic substrates, or magnetic ferrites.

Dielectric properties arising from ferroelectric, antiferroelectric, ferrielectric, piezoelectric and pyroelectric properties have yielded a number of applications. Ferroelectric materials based on lead zirconate titanate have been used as capacitor materials and  $\text{BaTiO}_3$  and  $\text{PbTiO}_3$  as PTC thermistors. Piezoelectric materials are widely used as transducers.

Catalytic properties. Transition metals are particularly effective in catalysing the reactions of unsaturated molecules either in their own right, dispersed on inert supports or as oxides and sulphides. In addition a range of microporous materials, e.g. zeolites, provide a basis for the size selection of molecules in the catalytic process.

During the last twenty years the attractive possibility of designing materials with specific properties from molecular building blocks has emerged. Attempts have been made to emulate the inorganic properties outlined above using molecular precursors derived from both organic and inorganic chemistry. Particularly noteworthy advances have been made in the following areas.

Conducting materials, based on organic, inorganic, and organometallic subunits are now well established. There are even examples of molecular superconductors although they only exhibit this property at very low temperatures.

Optical materials. The possibility of molecular fine tuning in the development of dyes, luminescent and fluorescent materials is long established. Non-linear optical materials based on molecular organic compounds with donor and acceptor functions represent a noteworthy success in recent years.

Piezoelectric materials. A wide range of piezoelectric polymers notably, polydivinylfluoride, have been developed and have found a wide range of civil and military uses as transducers.

Magnetic materials based on organometallic and co-ordination compounds have recently been developed, but their current effectiveness is limited by their inability to function at ambient temperatures.

In addition there have been attempts to incorporate inorganic characteristics into areas traditionally associated with organic chemistry. Particularly noteworthy has been the development of thermally stable polymers with robust inorganic backbones. Other areas, however, remain the province of molecular inorganic and organic chemists, for example liquid-crystals, chirality and molecules designed for specific molecular recognition.

The possibilities for multifunctionality arising from combinations of these properties are immense but the scientific search for new bifunctional materials must be tempered by the need to combine properties which when taken together represent a positive technological gain. Thus it could be proposed that the combinations listed below:

Metallic - liquid crystals  
Chiral - metal conductors  
Ferroelectric - liquid crystal  
Luminescent - ferroelectric

represent intriguing possibilities, but they are not of equal promise and technological importance. Other speakers in this symposium have concentrated on multifunctionality arising from organic monomers, polymers and liquid crystals. This paper is more speculative in nature and will attempt to evaluate the possibilities for multifunctionality in inorganic chemistry.

## DISCUSSION

Multifunctionality in preformed inorganic materials can be most effectively introduced either by surface modification or by the incorporation of functional molecules into microporous or layered compounds. The alternative procedure, based on organic precedents, of designing multifunctional molecular precursors which are subsequently polymerised is attractive but has few precedents in inorganic chemistry because inorganic polymer chemistry is less well developed.

Surface modification

The possibility of introducing multifunctionality in inorganic chemistry through surface modification has many well established precedents. The chemical finishing of metals for preventing corrosion represents a particularly traditional example of this technology, and depends primarily on the formation of surface layers of insoluble oxides. This type of technology could be adapted by using oxide precursors with functional groups which have a second desirable optical or electronic function. Metal alkoxides provide particularly attractive precursors for this type of surface modification since the second function can be readily incorporated into the sidechains. For the noble metals sulphur compounds are known to adhere well to these metal surfaces and could be used to introduce a second functionality.

The bifunctionality associated with metallic conduction and surface groups able to interact selectively with electrochemically active molecules opens up the possibility of sensors with a high degree of molecular selectivity [3]. The developments in supra-molecular chemistry [4] have demonstrated that molecular recognition based on the matching of molecular size and the specificity of the weak intermolecular forces which can exist between molecules make this a realistic possibility. Recently graphite electrodes have been functionalised in a similar manner by the introduction of surface carboxylate groups by oxidation of specific surfaces [3].

Heterogeneous catalysts depend on many surface modification effects. The dispersion of catalysts on an inert support provided an early and widespread example of the use of this technology. More recently catalytically active transition metal complexes have been anchored on silicate and polystyrene supports. This methodology provides an opportunity for designing more selective catalysts and ultimately can lead to catalysts which can produce optically active organic products rather than enantiomeric mixtures [5].

The addition of promoters and inhibitors to catalytic processes remains something of a black art, but nonetheless represents an important area of surface modification by the creation of alternative active sites. Recently chiral organic molecules have been pre-adsorbed on catalytic metal surfaces to create prochiral catalytically active sites. Furthermore, membrane catalysts which are permeable to hydrogen but not organic compounds provide interesting possibilities for chemical selectivities [5]. The development of metal vapour deposition techniques will certainly play an important role in

the future development of surface modified materials [6]. In addition the introduction of ion implantation techniques with cascade ion mixing and continuous or pulsed laser heating introduces possibilities for new types of surface phases. The vapour deposition of optoelectronic structures made from layer structures whose chemical compositions are modulated from layer to layer represents a particularly exciting future development [6].

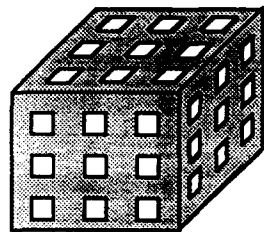
The coming together of the ideas developed above for multifunctional surface modified materials could lead to the design of a new generation of photocatalysts. The electronic band gaps associated with the functional group anchored to the surface of the catalyst could be fine-tuned in such a way to maximise the catalytic effects, particularly if used in conjunction with an electrochemical cell [5]. The development of surface modified  $TiO_2$  electrodes in the study of the photolytic decomposition of water provides an excellent case study of what can be achieved in this area.

#### Pervasive Modification

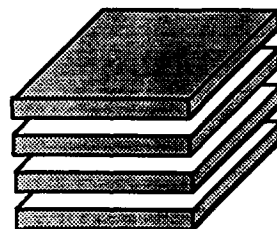
Inorganic chemistry not only provides examples of polymeric materials which are analogous to organic polymers, e.g. the thermally stable silicone polymers and the conducting  $(NS)_x$  polymer, but also regular matrix host structures which are sufficiently open to permit the incorporation of guest molecules. 1-Dimensional chain structures provide vacant lattice channels, e.g.  $K_2[Pt(CN)_4]$ ; 2-dimensional layered structures provide planar lattice sites in the van der Waals' gap which separates the layers, e.g. graphite, metal dichalcogenides; and 3-dimensional framework structures, e.g. zeolites [7] which have well defined cavities. These structures are illustrated schematically in Figure 1. These microporous structures have been studied in some detail and form the cornerstone of intercalation chemistry. The materials which result from intercalation reactions are formed by topotactic solid state processes whereby the defined matrix elements of the solid remain essentially unaltered with respect to structure and composition when the guest molecules are incorporated. All intercalation reactions occur either by the introduction of mobile guest molecules into empty host lattice sites or from exchange reactions involving a guest molecule already in place in the lattice [8].

To date intercalation materials have been studied with the following applications in mind: reversible battery electrodes, electrochemical displays, hydrogen storage devices, shape selective heterogeneous catalysts, ionic and electronic conductors. Such research has been directed primarily towards the development of materials with a single function and there are few examples of attempts to design multifunctional materials. In many examples the intercalation hosts are chosen for their rigidity and thermal stability rather than for their specific functionality. There are two possible strategies for generating poly-function materials based on intercalating hosts:

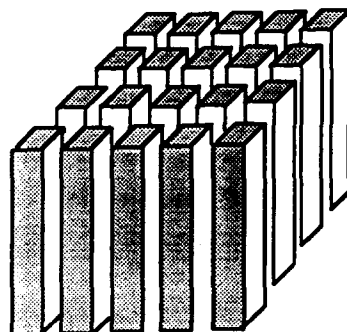
Firstly, the guest molecule would provide a second functionality to the host which itself has a desirable

**Basic host types with different structural dimensionality****3- D**

Three dimensional framework  
containing "channels"

**2- D**

Layered structures,  
provide planar lattice sites in  
Van der Waals gap

**1- D**

Chain structures,  
provides vacant lattice channels

**Figure 1**  
Schematic representations of inorganic host lattices

stereochemical, electronic, magnetic or chemical property.

Secondly, the introduction of two types of guest molecule, perhaps selectively chosen by the presence of two cavity types with different volumes, could provide a basis for bifunctionality.

Although the discussion above has been couched in terms of the introduction of guest molecules into the matrix, their chemical unsaturation could provide a basis for subsequent polymerisation processes. The formation of *in situ* conducting polymers within the channels of these microporous materials opens up the possibility of making complex molecular conducting networks within an insulating framework [9]. Bogomolov's incorporation of selenium chains with controlled lengths in mordenite provides a fine starting point for the development of three dimensional molecular circuits of this type [10]. Small semi-conducting particles based for example on CdS have been introduced by Herron *et al* in X, Y and A zeolites [11].

The stereochemical aspects of the microporous structure can provide an important method of controlling the functionality of the material. For example, the occurrence of non-centrosymmetric microporous zeolite structures has provided the possibility of creating a non-aligned packing regime for organic molecules incorporated into the cavities. For example, Stucky's elegant illustration that para-aminonitrobenzene, which usually crystallises in a non-centrosymmetric space group and therefore does not exhibit second harmonic non-linear optical effects, can be induced to show such effects when acting as a guest in the cavities of a non-centrosymmetric zeolite [12].

The piezoelectric effect associated with microporous structures of this type could perhaps be used as a basis for specific molecular sensors because the magnitude of the piezoelectric effect could be modulated by the presence of size-selected molecules within the cavities.

The major advances in inorganic bifunctionality will arise when the network of the host microporous material has an important electronic or magnetic function in its own right. In particular intercalation hosts with well developed conducting, magnetic or catalytic properties could be made bifunctional by introducing guest molecules with a second function. Therefore the synthesis and characterisation of new classes of microporous materials with a range of cavity sizes and well defined and useful magnetic or optical properties associated with the framework structure represents an important synthetic goal if inorganic multifunctionality is to be transformed from an attractive concept into a technological reality.

#### Acknowledgements

The AFOSR is thanked for financial support and Dr. Don Ulrich in particular for proposing that I consider the possibilities for research in this area. Until that time I had had enough problems introducing a single function into my molecules.

## REFERENCES

1. A. R. West, Solid State Chemistry and its Application, J. Wiley & Sons, 1984.
2. G. M. Ferguson and G. M. Whitesides, Chemtracts, 1, 171 (1986).
3. F. A. Armstrong, H. A. O. Hill and N. J. Walton, Accounts Chem. Res., 21, 407 (1989).
4. J. F. Stoddart, Pure Appl. Chem., 60, 407 (1988).
5. J. M. Thomas, Angew. Chem. Int. Ed. 28, 1079 (1989).
6. J. O. Williams, Angew. Chem. Int. Ed., 28, 1110 (1989).
7. Inclusion Compounds, Vol. 1, edited by J. L. Atwood, J. Davies and D. MacNicol, Academic Press, 1984.
8. Intercalation Chemistry, edited by M. S. Whittingham and A. J. Jacobson, Academic Press, 1982.
9. F. Garnier, Angew. Chem. Int. Ed., 28, 513 (1989).
10. V. N. Bogomolov, S. V. Kholodkevich, S. G. Romanov and L. S. Agroskin, Solid State Commun., 47, 181 (1983).
11. N. Herron, Y. Wang, M. M. Eddy, G. D. Stucky, D. E. Cox, K. Moller and T. Bein, J. Amer. Chem. Soc., 111, 530, (1989).
12. S. D. Cox, T. E. Gier, G. D. Stucky and J. Bierlien, J. Amer. Chem. Soc., 110, 2986 (1988).

92-18284



AD-P007 492



371

## MODELLING MICROSTRUCTURE IN MATERIALS THAT CONTAIN ANISOTROPIC PARTICLES

CHRISTOPHER VINEY\* AND LARRY A. CHICK\*\*

\*Department of Materials Science and Engineering FB-10, and the Advanced Materials Technology Program, University of Washington, Seattle, WA 98195

\*\*Battelle Pacific Northwest Laboratories, P.O. Box 999, Richland, WA 99352

### ABSTRACT

The spontaneous alignment of molecules in liquid crystalline solutions is characteristic of other materials that contain rodlike particles. We are developing a model to predict the evolution of microstructure in these systems. Its starting point is Flory's thermodynamic analysis of liquid crystalline phase separation. Our preferred method dispenses with the traditional lattice model in favor of a Monte Carlo simulation to calculate entropy. Some advantages and consequences of our approach are explored in this paper.

### INTRODUCTION

In all areas of materials science, it is recognized that the properties of a material depend on its micro- and nano-structure in addition to its chemical constitution. Thus the role of controlled grain size, and of eliminating voids or pores, in tailoring mechanical behavior has been characterized extensively for metals and ceramics. Many novel advanced materials, designed to optimize a spectrum of useful properties, contain rodlike particles. These multifunctional materials include polymers for non-linear optical applications, electrically conducting polymers, molecular composites, liquid crystalline materials, and whisker reinforced metals and ceramics. In each case, one or more of the following questions about microstructure pertains to property optimization:

- What is the maximum volume fraction of the rodlike particles that can be accommodated?
- Do the rods spontaneously form clusters / domains, and does this depend on the concentration and axial ratio of the rods?
- What size of clusters are formed?
- What is the distribution of rod orientations within clusters / domains?

For example, minimizing losses due to light scattering at domain boundaries in polymeric non-linear optical materials requires that the domain size be either much greater than or much less than the wavelength of light. As another example, consider whisker-reinforced ceramics, where the strength and stiffness both increase with volume fraction, though toughness may be compromised if the reinforcing rods orient over large distances to provide an easy crack path parallel to the preferred direction of alignment [1].

The present paper shows how some of the questions listed above can be answered in certain simple cases. We will limit the discussion to *athermal* systems, in which the only interactions are steric. In other words, we will be concerned with entropic terms and not enthalpic terms in the thermodynamic analyses that follow. Also, we will consider only *monodisperse* rods.

### FLORY'S LATTICE MODEL

This model [2,3] was devised to predict the formation of nematic liquid crystalline phases by athermal solutions of rodlike molecules. Above a critical concentration that depends on the axial ratio of the molecules, these solutions separate into random (disordered, isotropic) and aligned (ordered, anisotropic) phases. The lattice model considers the placement of rods in a space that is divided into a very large number of cubic cells. Rods have a width equal to the cell dimension, so their specified axial ratio ( $x$ ) then defines the total number of cells occupied by each rod. This number remains unchanged regardless of the orientation of the rod.

The number of ways of placing a given concentration of rods into the lattice is calculated in terms of the product of translational and orientational components, to obtain a value for total

configurational entropy. In this analysis, the orientational contribution to configurational entropy is expressed implicitly in terms of the *average* orientation of rods, without reference to the actual *distribution* of orientations. The total configurational entropy provides a direct measure of free energy (there are no enthalpic terms) for the phase in question, be it random or aligned. The chemical potentials of rods and solvent in the random phase are equated to the corresponding quantities in the aligned phase, and the resulting expressions are solved iteratively to calculate the volume fractions that define a tie line on the phase diagram (Figure 1).

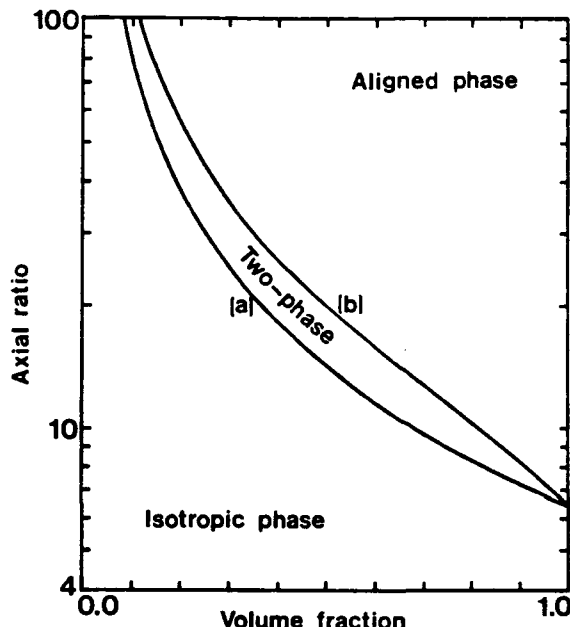


Figure 1

Phase diagram predicted by Flory's lattice model for athermal rods. For a given axial ratio, the diagram predicts the critical volume fractions required for both (a) initial appearance of an aligned phase, and (b) final disappearance of the isotropic phase, as a function of rod axial ratio.

The great strength of Flory's model is that it predicts a phase diagram that is at least qualitatively in agreement with experiment [4]. However, a number of questionable approximations are inherent to this model:

- (a) One principal axis of the lattice is chosen as a reference direction or *director*. Rods inclined at an angle to the director are divided into  $y$  segments, each of which lies parallel to the director and contains  $x/y$  cells. The average value of  $y$  (represented here by  $\langle y \rangle$ ) for the random phase has to equal  $x$ , to ensure internal *mathematical* consistency in the model. In turn, this generates the *physically* impossible requirement that the random phase contain rods for which  $y$  is greater than  $x$ . In other words, these rods consist of more segments than cells. Flory and his collaborators themselves recognize this difficulty [2,3].
- (b) Flory and Ronca [3] use the following formula for  $y$  :

$$y = \frac{4}{\pi} x \sin \psi \quad (1)$$

where  $\psi$  is the angle between rods and the director. If  $\psi = 0$ , this formula yields  $y=0$ . However, the rod in this case consists of a single segment lying parallel to the director, and so, by definition,  $y$  should be equal to 1.

- (c) The algebra contains approximations that presuppose the relative magnitudes of variables. Several of these approximations introduce increasingly significant errors as the rod axial ratio decreases.

- (d) Because rods are a single cell wide, the model does not preclude rods from crossing as shown in Figure 2. In other words, if vacancies on either side of an existing rod share a common edge or vertex, they can be part of the trajectory of a new rod.
- (e) The lattice model allocates rods a finite probability of touching, while in reality the probability should be vanishingly small [1].
- (f) A statistical analysis is used to calculate the translational contribution to total configurational entropy. At high volume fractions of rods, this formula increasingly overestimates the probability that the available / remaining vacancies are arranged to form a connected space capable of accommodating an additional rod. Flory recognized this problem; he later attempted to quantify the unoccupiable volume by using density or thermal expansivity data for neat liquid crystalline fluids [5].

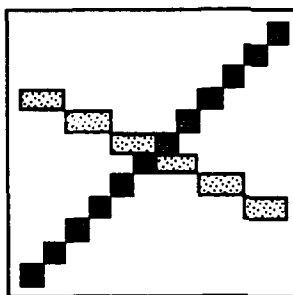


Figure 2

An example of how rods in the lattice model can cross without any of their occupied cells overlapping. Both rods occupy 12 cells, and thus, in terms of the lattice model, both have an axial ratio of 12.

#### COMPUTATIONAL IMPROVEMENTS TO THE LATTICE MODEL

We have found that calculating the equilibrium volume fractions of random and aligned phase can be simplified considerably by *locating the common tangent* to the corresponding free energy curves.

Also, we explicitly specify the *full orientation distribution function* in both phases. From the assumed distribution, we can directly calculate the orientational contribution to total entropy, so our calculation of orientational entropy is *entirely independent of the lattice model*. The orientation distribution function also yields the value of  $\langle y \rangle$  that is used in calculating the translational contribution. We are now in a position to explore how the free energy of the aligned phase is affected by changes in the distribution of rod orientations. This approach removes the problems associated with approximation (a) in the preceding section. As a further improvement, we replace equation (1) with

$$y = 1 + \frac{4}{\pi}(x - 1)\sin\psi \quad (2)$$

to deal with approximation (b) above. No algebraic approximations other than Stirling's formula were used in solving equations to determine the phase diagram, so that (c) in the list above is no longer a concern.

The effect of these improvements is shown in Figure 3, for rods in the aligned phase distributed uniformly over a restricted range of  $\psi$ . (This distribution gives more rods per unit *solid angle* at lower values of  $\psi$ .) We note that the two-phase region converges to a critical axial ratio of 9.6 at the right hand side of the diagram. This differs significantly from the value of 6.417 quoted in ref.3. This result leads us to the following realizations:

- The approximations inherent to the unimproved lattice model do not merit presenting its predictions to 4-figure accuracy.
- Because approximations (d)-(f) are not addressed by the computationally improved model, the predicted critical axial ratio of 9.6 is not necessarily any closer to the true value than the

prediction of Flory and Ronca. However, we are at least able to observe the qualitative effect of those approximations that we *have* eliminated thus far. (Experimental evidence suggests that the critical axial ratio must be at least 6 [4], but the upper limit is less certain.)

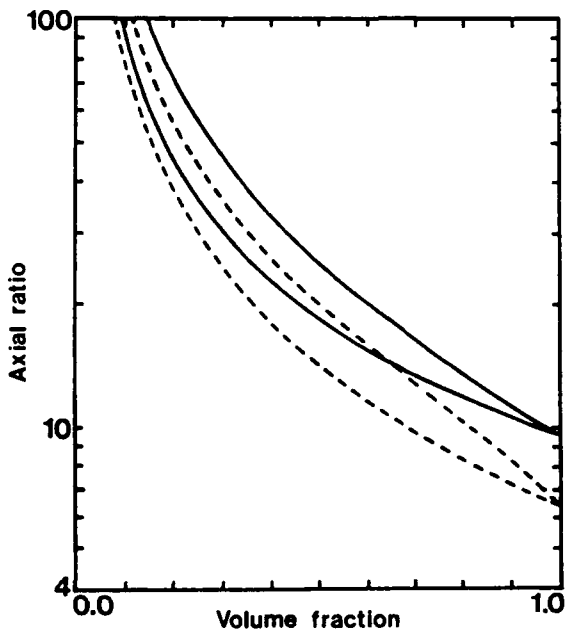


Figure 3

Phase diagram predicted by the computationally improved lattice model (solid lines). The phase diagram shown in Fig. 1 is superimposed for comparison (broken lines).

#### A HIGH RESOLUTION LATTICE MODEL

The approximations (d)-(f) above are all implicit in the equation used to calculate the translational contribution to total configurational entropy (equation 1 in ref. 3). If we increase the resolution of the lattice model by re-scaling the cell size relative to the width of a rod, so that the rod is a very large number of cells in diameter, it is then no longer possible for rods to cross as in Figure 2. No path involving vacant cells that share at least a common vertex can be found crossing an existing rod. Thus approximation (d) in the list above is no longer an issue. Also, as the resolution increases, the effect of approximation (e) is reduced continuously to a point where it becomes insignificant.

Increasing the resolution in this way greatly adds to the complexity of deriving a formula for translational entropy. At the same time, it still does not take account of unoccupiable volume in the lattice. We therefore look for an approach that is independent of lattice model statistics.

#### MONTE CARLO MODELLING

Because of the difficulty in deriving an *a priori* formula for the number of ways of placing the next rod in a partially filled space, we attempt instead to *measure* this quantity. To date, we have carried out this work in two dimensions [1,6]: it is simpler to plot the arrangement of rods in a monolayer than in the bulk of a three-dimensional system, and it facilitates deriving comparative predictions from the high resolution lattice model.

For either phase, the angular orientation of the  $j^{\text{th}}$  rod is chosen randomly from a pre-set distribution (random in the case of the isotropic phase). Next, candidate positional co-ordinates are chosen randomly, and checked to see if they would result in the  $j^{\text{th}}$  rod interpenetrating any of the  $(j-1)$  existing rods. If interpenetration is detected, a new candidate position is chosen for the  $j^{\text{th}}$

rod, while its original orientation is maintained. This search is repeated until a vacancy is found. The necessary number of tries  $T_j$  is then recorded, and the rod is placed in the vacancy. The process subsequently continues with an orientation being chosen for the  $(j+1)^{\text{th}}$  rod.

In our previous description of this approach [7], we have claimed without proof that the number of ways ( $v_j$ ) available for placing the  $j^{\text{th}}$  rod is related to the average value of  $T_j$  by:

$$v_j = \frac{K}{\langle T_j \rangle} \quad (3)$$

where  $K$  is a characteristic constant of the system. This intuitive hypothesis can in fact be proved, on the basis that the probability ( $p$ ) of successfully placing the  $j^{\text{th}}$  rod is the same on each attempt, and is independent of the outcome of previous attempts. The relationship between the number of successes in placing the rod and the number of tries therefore follows a binomial distribution. The expectation value for the number of tries required until the first success is therefore:

$$\langle T_j \rangle = \frac{1}{p} \quad (4)$$

But  $p$  is also equal to the probability of placing the rod on the *first* attempt, and therefore:

$$p = \frac{v_j}{\text{number of ways to place rods in the empty system}} \quad (5)$$

Combining equations (4) and (5) leads directly to equation (3). Values of  $v_j$  are used in our versions of the lattice model described above, modified for two dimensions.

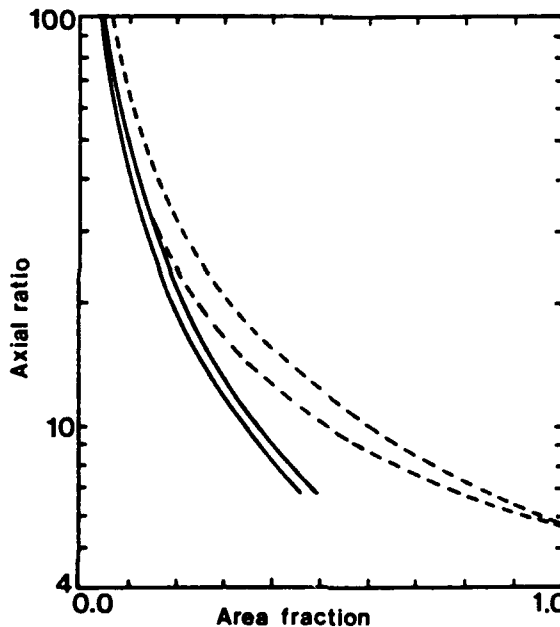


Figure 4

Phase diagram predicted by Monte Carlo modelling of rods packed in two dimensions (solid lines). A phase diagram predicted by the computationally improved lattice model, adapted to two dimensions, is also shown (broken lines).

Figure 4 shows the phase diagram predicted by our Monte Carlo analysis of rods packing in a two dimensional space, for rod orientations in the aligned phase distributed normally over  $\psi$ . For the purpose of comparison, the figure includes the predictions of the computationally improved lattice model, adapted to two dimensions. In the latter case, rods in the aligned phase

were distributed uniformly over a restricted range of  $\psi$ ; normal distributions did not yield phase separation.

We note that the Monte Carlo-generated phase diagram does not converge to predict an aligned  $\leftrightarrow$  random transition in fully dense material. This is because the number of tries needed to place an additional rod increases ever more steeply at higher concentrations, reflecting the fact that less and less of the remaining empty space is occupiable by rods. In other words, much of the vacant space between existing rods is "wasted", because these rods are too crowded to allow an additional rod to be placed amongst them. To illustrate this point, Figure 5 shows how the probability of placing an additional rod is predicted to decrease with increasing concentration in a simple 2-dimensional system consisting of perfectly aligned rods. Each improvement in the model produces a more conservative estimate of the probability, with the difference between predictions becoming increasingly significant at higher volume fractions. We anticipate that the Monte Carlo-generated prediction should be close to the behavior of real systems. However, we are still in the process of investigating the possible effect that rod motion may have on the fraction of occupiable space.

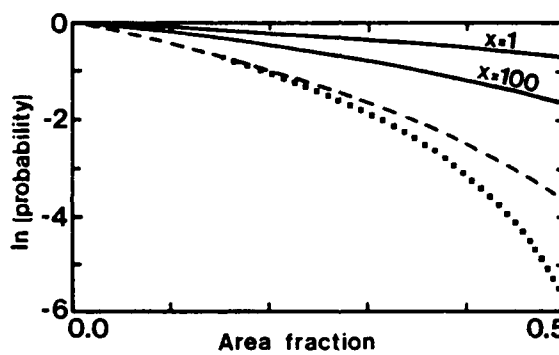


Figure 5

Probability of placing an additional rod in a 2-dimensional assembly of perfectly aligned rods, shown as a function of occupied area fraction (up to 50%).

Three models are represented: Flory's lattice model (equation [1] in ref. 3; solid lines); high resolution lattice model (broken line); Monte Carlo-generated data (dotted line). The probability is independent of rod axial ratio in the last two cases.

Developing the Monte Carlo approach has led us to the following observations:

- As demonstrated in Figure 4, we obtain a phase diagram that is qualitatively still in agreement with Flory's.
- The free energy of the aligned phase appears to be lowest if the constituent rods have orientations that follow a *normal distribution* relative to the director. The width of the normal distribution of orientations decreases as the rod concentration increases.
- The maximum packing fraction for rods in a real composite depends on the extent to which processing provides the rods with mobility to become aligned into clusters.
- Because the Monte Carlo algorithm involves adding rods, one at a time, to a defined region of space, the *evolution of the resulting microstructure can be monitored* by simply plotting the positions occupied by rods at any concentration of interest (Figure 6). Thus we have begun to *quantify the scale* of microstructures; in other words, we can obtain a measure of the typical domain size as a function of concentration and axial ratio [1]. The issue of microstructural scale is not addressed by Flory's approach.

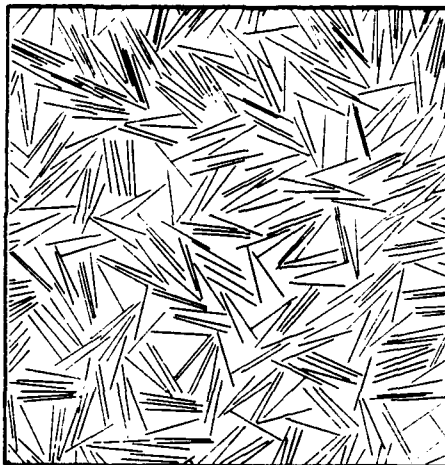


**Figure 6**

Monte Carlo-generated microstructure for rods in two dimensions. Axial ratio 25; area fraction 0.26.

### CONCLUSIONS AND FUTURE GOALS

In progressing to the Monte Carlo analysis described above, we claim a number of improvements relative to the Flory lattice model:

- Rod orientations and positions are continuously variable.
- All recourse to mathematical approximations (other than Stirling's formula) has been eliminated.
- We now have a route to predicting microstructural scale in systems that contain rodlike particles.
- Studies of Monte Carlo-generated microstructures may enable us to quantify theoretically the amount of intrinsically unoccupiable space in these systems.

We are working to further develop our analyses. This includes extending the Monte Carlo calculations to three dimensions. Subsequent enhancement of the algorithm will allow us to work with systems of rods that experience "soft" (i.e., mutually attractive or repulsive) interactions, for example ceramic whiskers that have a surface charge distribution. Also, by suitably defining the anisotropy of the interactions, we anticipate being able to account for the effect of net forces (e.g. shear, gravity) that act on real microstructures during processing.

The cluster sizes that can be measured from our Monte Carlo-generated microstructures may coarsen if rod motion is allowed. We anticipate using a simulated annealing technique to generate coarsened microstructures. Initially, these studies would be attempted for athermal systems only. In order to determine whether or not a particular annealed condition represents a state of lower free energy, we would calculate the total configurational entropy of the microstructure, expressed in terms of the measured average disorientation of the rods. By comparing

- the typical CPU time (or number of iterations) required for a given degree of microstructural coarsening, and
- the diffusion rate of rodlike species in a given real system under defined conditions, we will seek to model the rate at which coarsening occurs.

### ACKNOWLEDGEMENTS

We gratefully acknowledge stimulating discussions with I.A. Aksay. This work was sponsored by the Air Force Office of Scientific Research (AFOSR) and the Defense Advanced Research Projects Agency (DARPA), and was monitored by AFOSR under Grant no. AFOSR-87-0114. Work performed by Larry Chick was sponsored by the Advanced Education and

Training Program from Battelle Pacific Northwest Laboratories and the Department of Energy. We also acknowledge the IBM Corporation for its support as part of a block grant on the microdesigning of ceramics and polymer / ceramic composites.

#### REFERENCES

1. L.A. Chick, C. Viney and I.A. Aksay in Processing Science of Advanced Ceramics, edited by I.A. Aksay, G.L. McVay, and D.R. Ulrich (Mater. Res. Soc. Proc. 155, Pittsburgh, PA 1989) pp.331-342.
2. P.J. Flory, Proc. Roy. Soc. London A 234, 73 (1956).
3. P.J. Flory and G. Ronca, Mol. Cryst. Liq. Cryst. 54, 289 (1979).
4. P.J. Flory and G. Ronca, Mol. Cryst. Liq. Cryst. 54, 311 (1979).
5. P.J. Flory and P.A. Irvine, Chem. Soc. Faraday Trans. I 80, 1807 (1984).
6. L.A. Chick, C. Viney and I.A. Aksay in The Materials Science and Engineering of Rigid Rod Polymers, edited by W.W. Adams, R.K. Eby, and D.E. McLemore (Mater. Res. Soc. Proc. 134, Pittsburgh, PA 1989) pp.27-32.
7. L.A. Chick, C. Viney and I.A. Aksay in Fourth International Conference on Ultrastructure Processing of Ceramics, Glasses and Composites, edited by D.R. Uhlmann, M.C. Weinberg, and S.H. Risbud (Wiley Interscience, New York) in press.

## Author Index

Aksay, I.A., 3  
 Aroca, Ricardo, 61  
 Attard, George S., 239  
  
 Blumstein, A., 265  
 Borchers, Bettina, 249  
 Braun, F., 297  
 Brennan, A., 179  
  
 Carr, Paul L., 289  
 Carr, S.H., 331  
 Chen, S.H., 271  
 Chick, Larry A., 371  
 Cooper, K.L., 351  
 Covino, J., 187  
 Creed, David, 35  
  
 Dalton, L.R., 337  
 Davies, Geoff R., 289  
 Davies, Nicholas A., 135  
 DeGroot, D., 331  
 Dykema, J., 187  
  
 East, A.J., 113  
 Exarhos, Gregory J., 95  
  
 Faubert, F., 265  
 Findlay, Rob, 305  
 Fosmoe, A., 23  
 Francis, C.V., 107  
 Fuso, Francesco, 51  
  
 Garito, Anthony F., 89, 129  
 Gehring, Stefan, 249  
 Gerbi, D.J., 107  
 Gido, Samuel P., 315  
 Ginsburg, E.J., 101  
 Goldberg, H.A., 113  
 Gorman, C.B., 101  
 Griffin, Anselm C., 35  
 Griffith, Michael S., 135  
 Grubbs, R.H., 101  
  
 Haase, Wolfgang, 249, 257  
 Haghighat, R. Ross, 193  
 Hall, Jr., H.K., 51  
 Harestad, R.E., 107  
 Heß, M., 297  
 Hench, L.L., 23  
 Hosoda, Masahiro, 89  
 Hoyle, Charles E., 35  
 Huang, H., 351  
  
 Ikawa, H., 161  
 Ishii, T., 129  
  
 Jacobs, S.D., 271  
 Johnson, R.E., 113  
  
 Kalnin, I.L., 113  
 Karasz, Frank E., 227  
 Karim, D., 113  
 Keosian, R.A., 113  
 Kido, H., 219  
 Klemm, K., 187  
 Komarneni, S., 219  
 Kosfeld, Robert, 297  
 Kovar, Robert F., 193  
 Kumar, R.S., 265  
  
 Lemmon, Tim, 305  
 Leslie, Thomas M., 51  
 Leung, P.C., 107  
 Lipscomb, G.F., 41  
 Liu, J., 3  
 Lusignea, Richard W., 193  
 Lytel, R., 41  
  
 MacArthur, Donald M., 61  
 Mackenzie, John D., 149, 173  
 Maeda, M., 265  
 Malla, P.B., 219  
 Man, H.T., 113  
 Marder, S.R., 101  
 Marks, T.J., 331  
 Mayes, Anne M., 345  
 McGrath, J.E., 179, 351  
 McKinstry, S.E., 161  
 Mingos, D. Michael P., 363  
 Mitchell, Michael A., 51  
  
 Nazemi, Ali, 227  
 Nazri, Gholamabbas, 61  
 Newnham, R.E., 161  
 Ni, Zhende, 51  
 Nonami, Toru, 71  
  
 Ogata, Naoya, 277  
 Oguchi, Kiyoshi, 277  
 Olvera de la Cruz, Monica, 345  
  
 Padias, Anne B., 51  
 Pantano, Carlo, 193  
 Perry, J.W., 101  
 Pfeiffer, Matthias, 257  
 Phillips, Nicholas J., 207  
 Prasad, Paras N., 79  
  
 Rancourt, J., 179  
 Rector, L.P., 331

Roy, Rustum, 15  
Salib, S., 325  
Samuels, William D., 95  
Sanui, Kohei, 277  
Sarikaya, M., 3  
Sasabe, Hiroyuki, 89, 129  
Schaefer, W.P., 101  
Shih, W.Y., 3  
Sixou, P., 265  
Spinu, M., 179  
Stevens, J., 107  
Thomas, Edwin L., 193, 315  
Tripathy, S.K., 265  
Tsai, M.L., 271  
Venkataram, Krishnan, 35  
Viney, Christopher, 371  
Vipulanandan, C., 325  
Wada, Tatsuo, 89, 129  
Waehamad, W., 351  
Ward, Ian M., 289  
White, K.M., 107  
Wilkes, G.L., 179, 351  
Williams, Graham, 227  
Willner, L., 297  
Windle, Alan, 305  
Worboys, Michael R., 135  
Yamada, Akira, 89, 129  
Yokoh, Yasuhiko, 277  
Yu, L.P., 337  
Zheng, Haixing, 173

## Subject Index

- ceramics
  - colloids, 3
  - composites, 3
  - ferroelectric, 151, 161, 166
  - high temperature superconductivity, 173, 175, 325
  - magnetic, 162
  - magneto-optic, 165
  - multifunctional, 149, 151
  - photochromic, 155
  - photorefraction, 151
  - whiskers, 71
- composite structures
  - ceramic/polymer, 179, 193, 325
  - Kevlar/polypyrrole, 331
  - polymer composites, 107
  - devices, 31, 43, 83, 135
  - diamond, 16
  - diopside, 75-76
- ferrimagnetic materials, 19, 20, 151
- inorganic materials, 363
- hydroxyapatite, 71
- liquid crystals
  - metal centers, 249
  - monomers, 242
  - spontaneous alignments, 371
- metallocenes, 89
- nanocomposites, 15-16, 18, 20-21, 161, 166, 168
- non-linear optics
  - electro-optic, 41, 119, 126
  - second order, 53, 99, 101, 129, 154
  - third order, 89, 93, 103, 107
- polymers
  - acrylonitrile copolymers, 59
  - alignment, 44, 117, 227, 236, 285
  - dielectric properties, 121, 231, 236, 257, 289
- liquid crystal polymers, 35, 227, 239, 257, 265, 271, 297, 305, 351
- main chain polymers, 52, 54, 81, 194, 351
- microstructure, 75, 315, 331
- multifunctional, 113, 135, 289, 315
- non-linear optical, 41-44, 51, 56, 79, 89, 101, 277, 289, 337
- organometallic, 101, 363
- phosphazene-based, 95
- piezoelectric, 51, 56, 123, 135, 293, 365
- polymer/salt complexes, 61
- polypeptides, 129
- pyroelectric, 117, 135, 289
- side chain polymers, 55, 149, 227, 241, 257, 265, 305
- silicone containing, 297
- triblock copolymers, 345
- protective coatings, 187
- rod like structures
  - modelling, 371
  - polymers, 194
- silica
  - optics, 23
- sol-gel structures
  - hybrid structures, 179, 193
  - impregnation, 31-33, 156
  - microstructure, 18
  - morphology, 18, 199
  - optical
    - imaging systems, 207
    - properties, 27-28, 84, 207
  - pore size, 24-26, 213, 219
  - process, 25, 176, 179
  - transpiration, 29, 30
- thin films
  - Langmuir-Blodgett, 85, 277
  - polymers, 337
  - solvent casting, 291
  - spin coating, 117

---

---

**MATERIALS RESEARCH SOCIETY SYMPOSIUM PROCEEDINGS**

---

ISSN 0272 - 9172

Volume 1—**Laser and Electron-Beam Solid Interactions and Materials Processing**,  
J. F. Gibbons, L. D. Hess, T. W. Sigmon, 1981, ISBN 0-444-00595-1

Volume 2—**Defects in Semiconductors**, J. Narayan, T. Y. Tan, 1981,  
ISBN 0-444-00596-X

Volume 3—**Nuclear and Electron Resonance Spectroscopies Applied to Materials  
Science**, E. N. Kaufmann, G. K. Shenoy, 1981, ISBN 0-444-00597-8

Volume 4—**Laser and Electron-Beam Interactions with Solids**, B. R. Appleton,  
G. K. Celler, 1982, ISBN 0-444-00693-1

Volume 5—**Grain Boundaries in Semiconductors**, H. J. Leamy, G. E. Pike,  
C. H. Seager, 1982, ISBN 0-444-00697-4

Volume 6—**Scientific Basis for Nuclear Waste Management IV**, S. V. Topp, 1982,  
ISBN 0-444-00699-0

Volume 7—**Metastable Materials Formation by Ion Implantation**, S. T. Picraux,  
W. J. Choyke, 1982, ISBN 0-444-00692-3

Volume 8—**Rapidly Solidified Amorphous and Crystalline Alloys**, B. H. Kear,  
B. C. Giessen, M. Cohen, 1982, ISBN 0-444-00698-2

Volume 9—**Materials Processing in the Reduced Gravity Environment of Space**,  
G. E. Rindone, 1982, ISBN 0-444-00691-5

Volume 10—**Thin Films and Interfaces**, P. S. Ho, K.-N. Tu, 1982, ISBN 0-444-00774-1

Volume 11—**Scientific Basis for Nuclear Waste Management V**, W. Lutze, 1982,  
ISBN 0-444-00725-3

Volume 12—**In Situ Composites IV**, F. D. Lemkey, H. E. Cline, M. McLean, 1982,  
ISBN 0-444-00726-1

Volume 13—**Laser-Solid Interactions and Transient Thermal Processing of Materials**,  
J. Narayan, W. L. Brown, R. A. Lemons, 1983, ISBN 0-444-00788-1

Volume 14—**Defects in Semiconductors II**, S. Mahajan, J. W. Corbett, 1983,  
ISBN 0-444-00812-8

Volume 15—**Scientific Basis for Nuclear Waste Management VI**, D. G. Brookins, 1983,  
ISBN 0-444-00780-6

Volume 16—**Nuclear Radiation Detector Materials**, E. E. Haller, H. W. Kraner,  
W. A. Higinbotham, 1983, ISBN 0-444-00787-3

Volume 17—**Laser Diagnostics and Photochemical Processing for Semiconductor  
Devices**, R. M. Osgood, S. R. J. Brueck, H. R. Schlossberg, 1983,  
ISBN 0-444-00782-2

Volume 18—**Interfaces and Contacts**, R. Ludeke, K. Rose, 1983, ISBN 0-444-00820-9

Volume 19—**Alloy Phase Diagrams**, L. H. Bennett, T. B. Massalski, B. C. Giessen,  
1983, ISBN 0-444-00809-8

Volume 20—**Intercalated Graphite**, M. S. Dresselhaus, G. Dresselhaus, J. E. Fischer,  
M. J. Moran, 1983, ISBN 0-444-00781-4

Volume 21—**Phase Transformations in Solids**, T. Tsakalakos, 1984, ISBN 0-444-00901-9

Volume 22—**High Pressure in Science and Technology**, C. Homan, R. K. MacCrone,  
E. Whalley, 1984, ISBN 0-444-00932-9 (3 part set)

Volume 23—**Energy Beam-Solid Interactions and Transient Thermal Processing**,  
J. C. C. Fan, N. M. Johnson, 1984, ISBN 0-444-00903-5

Volume 24—**Defect Properties and Processing of High-Technology Nonmetallic  
Materials**, J. H. Crawford, Jr., Y. Chen, W. A. Sibley, 1984,  
ISBN 0-444-00904-3

Volume 25—**Thin Films and Interfaces II**, J. E. E. Baglin, D. R. Campbell, W. K. Chu,  
1984, ISBN 0-444-00905-1

---

---

**MATERIALS RESEARCH SOCIETY SYMPOSIUM PROCEEDINGS**

---

Volume 26—Scientific Basis for Nuclear Waste Management VII, G. L. McVay, 1984, ISBN 0-444-00906-X

Volume 27—Ion Implantation and Ion Beam Processing of Materials, G. K. Hubler, O. W. Holland, C. R. Clayton, C. W. White, 1984, ISBN 0-444-00869-1

Volume 28—Rapidly Solidified Metastable Materials, B. H. Kear, B. C. Giessen, 1984, ISBN 0-444-00935-3

Volume 29—Laser-Controlled Chemical Processing of Surfaces, A. W. Johnson, D. J. Ehrlich, H. R. Schlossberg, 1984, ISBN 0-444-00894-2

Volume 30—Plasma Processing and Synthesis of Materials, J. Szekely, D. Apelian, 1984, ISBN 0-444-00895-0

Volume 31—Electron Microscopy of Materials, W. Krakow, D. A. Smith, L. W. Hobbs, 1984, ISBN 0-444-00898-7

Volume 32—Better Ceramics Through Chemistry, C. J. Brinker, D. E. Clark, D. R. Ulrich, 1984, ISBN 0-444-00898-5

Volume 33—Comparison of Thin Film Transistor and SOI Technologies, H. W. Lam, M. J. Thompson, 1984, ISBN 0-444-00899-3

Volume 34—Physical Metallurgy of Cast Iron, H. Fredriksson, M. Hillerts, 1985, ISBN 0-444-00938-8

Volume 35—Energy Beam-Solid Interactions and Transient Thermal Processing/1984, D. K. Biegelsen, G. A. Rozgonyi, C. V. Shank, 1985, ISBN 0-931837-00-6

Volume 36—Impurity Diffusion and Gettering in Silicon, R. B. Fair, C. W. Pearce, J. Washburn, 1985, ISBN 0-931837-01-4

Volume 37—Layered Structures, Epitaxy, and Interfaces, J. M. Gibson, L. R. Dawson, 1985, ISBN 0-931837-02-2

Volume 38—Plasma Synthesis and Etching of Electronic Materials, R. P. H. Chang, B. Abeles, 1985, ISBN 0-931837-03-0

Volume 39—High-Temperature Ordered Intermetallic Alloys, C. C. Koch, C. T. Liu, N. S. Stoloff, 1985, ISBN 0-931837-04-9

Volume 40—Electronic Packaging Materials Science, E. A. Giess, K.-N. Tu, D. R. Uhlmann, 1985, ISBN 0-931837-05-7

Volume 41—Advanced Photon and Particle Techniques for the Characterization of Defects in Solids, J. B. Roberto, R. W. Carpenter, M. C. Wittels, 1985, ISBN 0-931837-06-5

Volume 42—Very High Strength Cement-Based Materials, J. F. Young, 1985, ISBN 0-931837-07-3

Volume 43—Fly Ash and Coal Conversion By-Products: Characterization, Utilization, and Disposal I, G. J. McCarthy, R. J. Lauf, 1985, ISBN 0-931837-08-1

Volume 44—Scientific Basis for Nuclear Waste Management VIII, C. M. Jantzen, J. A. Stone, R. C. Ewing, 1985, ISBN 0-931837-09-X

Volume 45—Ion Beam Processes in Advanced Electronic Materials and Device Technology, B. R. Appleton, F. H. Eisen, T. W. Sigmon, 1985, ISBN 0-931837-10-3

Volume 46—Microscopic Identification of Electronic Defects in Semiconductors, N. M. Johnson, S. G. Bishop, G. D. Watkins, 1985, ISBN 0-931837-11-1

Volume 47—Thin Films: The Relationship of Structure to Properties, C. R. Aita, K. S. SreeHarsha, 1985, ISBN 0-931837-12-X

Volume 48—Applied Materials Characterization, W. Katz, P. Williams, 1985, ISBN 0-931837-13-8

Volume 49—Materials Issues in Applications of Amorphous Silicon Technology, D. Adler, A. Madan, M. J. Thompson, 1985, ISBN 0-931837-14-6

---

---

**MATERIALS RESEARCH SOCIETY SYMPOSIUM PROCEEDINGS**

---

Volume 50—Scientific Basis for Nuclear Waste Management IX, L. O. Werme, 1986, ISBN 0-931837-15-4

Volume 51—Beam-Solid Interactions and Phase Transformations, H. Kurz, G. L. Olson, J. M. Poate, 1986, ISBN 0-931837-16-2

Volume 52—Rapid Thermal Processing, T. O. Sedgwick, T. E. Seidel, B.-Y. Tsaur, 1986, ISBN 0-931837-17-0

Volume 53—Semiconductor-on-Insulator and Thin Film Transistor Technology, A. Chiang, M. W. Geis, L. Pfeiffer, 1986, ISBN 0-931837-18-9

Volume 54—Thin Films—Interfaces and Phenomena, R. J. Nemanich, P. S. Ho, S. S. Lau, 1986, ISBN 0-931837-19-7

Volume 55—Biomedical Materials, J. M. Williams, M. F. Nichols, W. Zingg, 1986, ISBN 0-931837-20-0

Volume 56—Layered Structures and Epitaxy, J. M. Gibson, G. C. Osbourn, R. M. Tromp, 1986, ISBN 0-931837-21-9

Volume 57—Phase Transitions in Condensed Systems—Experiments and Theory, G. S. Cargill III, F. Spaepen, K.-N. Tu, 1987, ISBN 0-931837-22-7

Volume 58—Rapidly Solidified Alloys and Their Mechanical and Magnetic Properties, B. C. Giessen, D. E. Polk, A. I. Taub, 1986, ISBN 0-931837-23-5

Volume 59—Oxygen, Carbon, Hydrogen, and Nitrogen in Crystalline Silicon, J. C. Mikkelsen, Jr., S. J. Pearton, J. W. Corbett, S. J. Pennycook, 1986, ISBN 0-931837-24-3

Volume 60—Defect Properties and Processing of High-Technology Nonmetallic Materials, Y. Chen, W. D. Kingery, R. J. Stokes, 1986, ISBN 0-931837-25-1

Volume 61—Defects in Glasses, F. L. Galeener, D. L. Griscom, M. J. Weber, 1986, ISBN 0-931837-26-X

Volume 62—Materials Problem Solving with the Transmission Electron Microscope, L. W. Hobbs, K. H. Westmacott, D. B. Williams, 1986, ISBN 0-931837-27-8

Volume 63—Computer-Based Microscopic Description of the Structure and Properties of Materials, J. Broughton, W. Krakow, S. T. Pantelides, 1986, ISBN 0-931837-28-6

Volume 64—Cement-Based Composites: Strain Rate Effects on Fracture, S. Mindess, S. P. Shah, 1986, ISBN 0-931837-29-4

Volume 65—Fly Ash and Coal Conversion By-Products: Characterization, Utilization and Disposal II, G. J. McCarthy, F. P. Glasser, D. M. Roy, 1986, ISBN 0-931837-30-8

Volume 66—Frontiers in Materials Education, L. W. Hobbs, G. L. Liedl, 1986, ISBN 0-931837-31-6

Volume 67—Heteroepitaxy on Silicon, J. C. C. Fan, J. M. Poate, 1986, ISBN 0-931837-33-2

Volume 68—Plasma Processing, J. W. Coburn, R. A. Gottscho, D. W. Hess, 1986, ISBN 0-931837-34-0

Volume 69—Materials Characterization, N. W. Cheung, M.-A. Nicolet, 1986, ISBN 0-931837-35-9

Volume 70—Materials Issues in Amorphous-Semiconductor Technology, D. Adler, Y. Hamakawa, A. Madan, 1986, ISBN 0-931837-36-7

Volume 71—Materials Issues in Silicon Integrated Circuit Processing, M. Wittmer, J. Stimmell, M. Strathman, 1986, ISBN 0-931837-37-5

Volume 72—Electronic Packaging Materials Science II, K. A. Jackson, R. C. Pohanka, D. R. Uhlmann, D. R. Ulrich, 1986, ISBN 0-931837-38-3

Volume 73—Better Ceramics Through Chemistry II, C. J. Brinker, D. E. Clark, D. R. Ulrich, 1986, ISBN 0-931837-39-1

Volume 74—Beam-Solid Interactions and Transient Processes, M. O. Thompson, S. T. Picraux, J. S. Williams, 1987, ISBN 0-931837-40-5

---

---

**MATERIALS RESEARCH SOCIETY SYMPOSIUM PROCEEDINGS**

---

Volume 75—Photon, Beam and Plasma Stimulated Chemical Processes at Surfaces, V. M. Donnelly, I. P. Herman, M. Hirose, 1987, ISBN 0-931837-41-3

Volume 76—Science and Technology of Microfabrication, R. E. Howard, E. L. Hu, S. Namba, S. Pang, 1987, ISBN 0-931837-42-1

Volume 77—Interfaces, Superlattices, and Thin Films, J. D. Dow, I. K. Schuller, 1987, ISBN 0-931837-56-1

Volume 78—Advances in Structural Ceramics, P. F. Becher, M. V. Swain, S. Sōmiya, 1987, ISBN 0-931837-43-X

Volume 79—Scattering, Deformation and Fracture in Polymers, G. D. Wignall, B. Crist, T. P. Russell, E. L. Thomas, 1987, ISBN 0-931837-44-8

Volume 80—Science and Technology of Rapidly Quenched Alloys, M. Tenhover, W. L. Johnson, L. E. Tanner, 1987, ISBN 0-931837-45-6

Volume 81—High-Temperature Ordered Intermetallic Alloys, II, N. S. Stoloff, C. C. Koch, C. T. Liu, O. Izumi, 1987, ISBN 0-931837-46-4

Volume 82—Characterization of Defects in Materials, R. W. Siegel, J. R. Weertman, R. Sinclair, 1987, ISBN 0-931837-47-2

Volume 83—Physical and Chemical Properties of Thin Metal Overlays and Alloy Surfaces, D. M. Zehner, D. W. Goodman, 1987, ISBN 0-931837-48-0

Volume 84—Scientific Basis for Nuclear Waste Management X, J. K. Bates, W. B. Seefeldt, 1987, ISBN 0-931837-49-9

Volume 85—Microstructural Development During the Hydration of Cement, L. Struble, P. Brown, 1987, ISBN 0-931837-50-2

Volume 86—Fly Ash and Coal Conversion By-Products Characterization, Utilization and Disposal III, G. J. McCarthy, F. P. Glasser, D. M. Roy, S. Diamond, 1987, ISBN 0-931837-51-0

Volume 87—Materials Processing in the Reduced Gravity Environment of Space, R. H. Doremus, P. C. Nordine, 1987, ISBN 0-931837-52-9

Volume 88—Optical Fiber Materials and Properties, S. R. Nagel, J. W. Fleming, G. Sigel, D. A. Thompson, 1987, ISBN 0-931837-53-7

Volume 89—Diluted Magnetic (Semimagnetic) Semiconductors, R. L. Aggarwal, J. K. Furdyna, S. von Molnar, 1987, ISBN 0-931837-54-5

Volume 90—Materials for Infrared Detectors and Sources, R. F. C. Farrow, J. F. Schetzina, J. T. Cheung, 1987, ISBN 0-931837-55-3

Volume 91—Heteroepitaxy on Silicon II, J. C. C. Fan, J. M. Phillips, B.-Y. Tsaur, 1987, ISBN 0-931837-58-8

Volume 92—Rapid Thermal Processing of Electronic Materials, S. R. Wilson, R. A. Powell, D. E. Davies, 1987, ISBN 0-931837-59-6

Volume 93—Materials Modification and Growth Using Ion Beams, U. Gibson, A. E. White, P. P. Pronko, 1987, ISBN 0-931837-60-X

Volume 94—Initial Stages of Epitaxial Growth, R. Hull, J. M. Gibson, David A. Smith, 1987, ISBN 0-931837-61-8

Volume 95—Amorphous Silicon Semiconductors—Pure and Hydrogenated, A. Madan, M. Thompson, D. Adler, Y. Hamakawa, 1987, ISBN 0-931837-62-6

Volume 96—Permanent Magnet Materials, S. G. Sankar, J. F. Herbst, N. C. Koon, 1987, ISBN 0-931837-63-4

Volume 97—Novel Refractory Semiconductors, D. Emin, T. Aselage, C. Wood, 1987, ISBN 0-931837-64-2

Volume 98—Plasma Processing and Synthesis of Materials, D. Apelian, J. Szekely, 1987, ISBN 0-931837-65-0

---

---

**MATERIALS RESEARCH SOCIETY SYMPOSIUM PROCEEDINGS**

---

Volume 99—High-Temperature Superconductors, M. B. Brodsky, R. C. Dynes, K. Kitazawa, H. L. Tuller, 1988, ISBN 0-931837-67-7

Volume 100—Fundamentals of Beam-Solid Interactions and Transient Thermal Processing, M. J. Aziz, L. E. Rehn, B. Stritzker, 1988, ISBN 0-931837-68-5

Volume 101—Laser and Particle-Beam Chemical Processing for Microelectronics, D.J. Ehrlich, G.S. Higashi, M.M. Oprysko, 1988, ISBN 0-931837-69-3

Volume 102—Epitaxy of Semiconductor Layered Structures, R. T. Tung, L. R. Dawson, R. L. Gunshor, 1988, ISBN 0-931837-70-7

Volume 103—Multilayers: Synthesis, Properties, and Nonelectronic Applications, T. W. Barbee Jr., F. Spaepen, L. Greer, 1988, ISBN 0-931837-71-5

Volume 104—Defects in Electronic Materials, M. Stavola, S. J. Pearton, G. Davies, 1988, ISBN 0-931837-72-3

Volume 105— $\text{SiO}_2$  and Its Interfaces, G. Lucovsky, S. T. Pantelides, 1988, ISBN 0-931837-73-1

Volume 106—Polysilicon Films and Interfaces, C.Y. Wong, C.V. Thompson, K-N. Tu, 1988, ISBN 0-931837-74-X

Volume 107—Silicon-on-Insulator and Buried Metals in Semiconductors, J. C. Sturm, C. K. Chen, L. Pfeiffer, P. L. F. Hemment, 1988, ISBN 0-931837-75-8

Volume 108—Electronic Packaging Materials Science II, R. C. Sundahl, R. Jaccodine, K. A. Jackson, 1988, ISBN 0-931837-76-6

Volume 109—Nonlinear Optical Properties of Polymers, A. J. Heeger, J. Orenstein, D. R. Ulrich, 1988, ISBN 0-931837-77-4

Volume 110—Biomedical Materials and Devices, J. S. Hanker, B. L. Giammara, 1988, ISBN 0-931837-78-2

Volume 111—Microstructure and Properties of Catalysts, M. M. J. Treacy, J. M. Thomas, J. M. White, 1988, ISBN 0-931837-79-0

Volume 112—Scientific Basis for Nuclear Waste Management XI, M. J. Apted, R. E. Westerman, 1988, ISBN 0-931837-80-4

Volume 113—Fly Ash and Coal Conversion By-Products: Characterization, Utilization, and Disposal IV, G. J. McCarthy, D. M. Roy, F. P. Glasser, R. T. Hemmings, 1988, ISBN 0-931837-81-2

Volume 114—Bonding in Cementitious Composites, S. Mindess, S. P. Shah, 1988, ISBN 0-931837-82-0

Volume 115—Specimen Preparation for Transmission Electron Microscopy of Materials, J. C. Bravman, R. Anderson, M. L. McDonald, 1988, ISBN 0-931837-83-9

Volume 116—Heteroepitaxy on Silicon: Fundamentals, Structures, and Devices, H.K. Choi, H. Ishiwara, R. Hull, R.J. Nemanich, 1988, ISBN: 0-931837-86-3

Volume 117—Process Diagnostics: Materials, Combustion, Fusion, K. Hays, A.C. Eckbreth, G.A. Campbell, 1988, ISBN: 0-931837-87-1

Volume 118—Amorphous Silicon Technology, A. Madan, M.J. Thompson, P.C. Taylor, P.G. LeComber, Y. Hamakawa, 1988, ISBN: 0-931837-88-X

Volume 119—Adhesion in Solids, D.M. Mattox, C. Batich, J.E.E. Baglin, R.J. Gottschall, 1988, ISBN: 0-931837-89-8

Volume 120—High-Temperature/High-Performance Composites, F.D. Lemkey, A.G. Evans, S.G. Fishman, J.R. Strife, 1988, ISBN: 0-931837-90-1

Volume 121—Better Ceramics Through Chemistry III, C.J. Brinker, D.E. Clark, D.R. Ulrich, 1988, ISBN: 0-931837-91-X

---

---

**MATERIALS RESEARCH SOCIETY SYMPOSIUM PROCEEDINGS**

---

Volume 122—**Interfacial Structure, Properties, and Design**, M.H. Yoo, W.A.T. Clark, C.L. Briant, 1988, ISBN: 0-931837-92-8

Volume 123—**Materials Issues in Art and Archaeology**, E.V. Sayre, P. Vandiver, J. Druzik, C. Stevenson, 1988, ISBN: 0-931837-93-6

Volume 124—**Microwave-Processing of Materials**, M.H. Brooks, I.J. Chabinsky, W.H. Sutton, 1988, ISBN: 0-931837-94-4

Volume 125—**Materials Stability and Environmental Degradation**, A. Barkatt, L.R. Smith, E. Verink, 1988, ISBN: 0-931837-95-2

Volume 126—**Advanced Surface Processes for Optoelectronics**, S. Bernasek, T. Venkatesan, H. Temkin, 1988, ISBN: 0-931837-96-0

Volume 127—**Scientific Basis for Nuclear Waste Management XII**, W. Lutze, R.C. Ewing, 1989, ISBN: 0-931837-97-9

Volume 128—**Processing and Characterization of Materials Using Ion Beams**, L.E. Rehn, J. Greene, F.A. Smidt, 1989, ISBN: 1-55899-001-1

Volume 129—**Laser and Particle-Beam Modification of Chemical Processes on Surfaces**, A.W. Johnson, G.L. Loper, T.W. Sigmon, 1989, ISBN: 1-55899-002-X

Volume 130—**Thin Films: Stresses and Mechanical Properties**, J.C. Bravman, W.D. Nix, D.M. Barnett, D.A. Smith, 1989, ISBN: 1-55899-003-8

Volume 131—**Chemical Perspectives of Microelectronic Materials**, M.E. Gross, J. Jasinski, J.T. Yates, Jr., 1989, ISBN: 1-55899-004-6

Volume 132—**Multicomponent Ultrafine Microstructures**, L.E. McCandlish, B.H. Kear, D.E. Polk, and R.W. Siegel, 1989, ISBN: 1-55899-005-4

Volume 133—**High Temperature Ordered Intermetallic Alloys III**, C.T. Liu, A.I. Taub, N.S. Stoloff, C.C. Koch, 1989, ISBN: 1-55899-006-2

Volume 134—**The Materials Science and Engineering of Rigid-Rod Polymers**, W.W. Adams, R.K. Eby, D.E. McLemore, 1989, ISBN: 1-55899-007-0

Volume 135—**Solid State Ionics**, G. Nazri, R.A. Huggins, D.F. Shriver, 1989, ISBN: 1-55899-008-9

Volume 136—**Fly Ash and Coal Conversion By-Products: Characterization, Utilization and Disposal V**, R.T. Hemmings, E.E. Berry, G.J. McCarthy, F.P. Glasser, 1989, ISBN: 1-55899-009-7

Volume 137—**Pore Structure and Permeability of Cementitious Materials**, L.R. Roberts, J.P. Skalny, 1989, ISBN: 1-55899-010-0

Volume 138—**Characterization of the Structure and Chemistry of Defects in Materials**, B.C. Larson, M. Ruhle, D.V. Seidman, 1989, ISBN: 1-55899-011-9

Volume 139—**High Resolution Microscopy of Materials**, W. Krakow, F.A. Ponce, D.J. Smith, 1989, ISBN: 1-55899-012-7

Volume 140—**New Materials Approaches to Tribology: Theory and Applications**, L.E. Pope, L. Fehrenbacher, W.O. Winer, 1989, ISBN: 1-55899-013-5

Volume 141—**Atomic Scale Calculations in Materials Science**, J. Tersoff, D. Vanderbilt, V. Vitek, 1989, ISBN: 1-55899-014-3

Volume 142—**Nondestructive Monitoring of Materials Properties**, J. Holbrook, J. Bussiere, 1989, ISBN: 1-55899-015-1

Volume 143—**Synchrotron Radiation in Materials Research**, R. Clarke, J. Gland, J.H. Weaver, 1989, ISBN: 1-55899-016-X

Volume 144—**Advances in Materials, Processing and Devices in III-V Compound Semiconductors**, D.K. Sadana, L. Eastman, R. Dupuis, 1989, ISBN: 1-55899-017-8

---

---

MATERIALS RESEARCH SOCIETY CONFERENCE PROCEEDINGS

---

**Tungsten and Other Refractory Metals for VLSI Applications**, Robert S. Blewer, 1986;  
ISSN 0886-7860; ISBN 0-931837-32-4

**Tungsten and Other Refractory Metals for VLSI Applications II**, Eliot K. Broadbent,  
1987; ISSN 0886-7860; ISBN 0-931837-66-9

**Ternary and Multinary Compounds**, Satyen K. Deb, Alex Zunger, 1987; ISBN 0-931837-57-X

**Tungsten and Other Refractory Metals for VLSI Applications III**, Victor A. Wells, 1988;  
ISSN 0886-7860; ISBN 0-931837-84-7

**Atomic and Molecular Processing of Electronic and Ceramic Materials: Preparation,  
Characterization and Properties**, Ilhan A. Aksay, Gary L. McVay, Thomas G. Stoebe,  
J.F. Wager, 1988; ISBN 0-931837-85-5

**Materials Futures: Strategies and Opportunities**, R. Byron Pipes, U.S. Organizing  
Committee, Rune Lagneborg, Swedish Organizing Committee, 1988; ISBN 1-55899-000-3

**Tungsten and Other Refractory Metals for VLSI Applications IV**, Robert S. Blewer,  
Carol M. McConica, 1989; ISSN 0886-7860; ISBN 0-931837-98-7

**Tungsten and Other Advanced Metals for VLSI/ULSI Applications V**, S. Simon Wong,  
Seiijiro Furukawa, 1990; ISSN 1048-0854; ISBN 1-55899-086-2

**High Energy and Heavy Ion Beams in Materials Analysis**, Joseph R. Tesmer, Carl J.  
Maggiore, Michael Nastasi, J. Charles Barbour, James W. Mayer, 1990;  
ISBN 1-55899-091-7

**Physical Metallurgy of Cast Iron IV**, Goro Ohira, Takaji Kusakawa, Eisuke Niyama,  
1990; ISBN 1-55899-090-9